Proceedings of the National Workshop on the
Global Weather Experiment (1st)
Current Achievements and Future Directions
Volume 2. Part 2

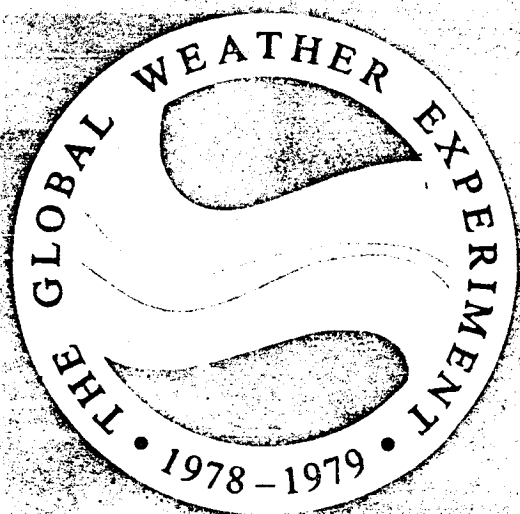National Research Council, Washington, DC

Prepared for

National Science Foundation, Washington, DC

Oct 85

50272-101

REPORT DOCUMENTATION PAGE	1. REPORT NO.	2.	3. Recipient's Accession No. DDO 6 139177 /45

4. Title and Subtitle	5. Report Date
Proceedings of the First National Workshop on the Global Weather Experiment: Current Achievements and Future Directions Volume Two, Part 2 of 2	October 1985
	6.

7. Author(s)	8. Performing Organization Rept. No.

9. Performing Organization Name and Address	10. Project/Task/Work Unit No.
National Research Council Commission on Physical Sciences, Mathematics, and Resources 2101 Constitution Avenue, N.W. Washington, D.C. 20418	11. Contract(C) or Grant(G) No. (C) (G) NSF ATM-8025329

12. Sponsoring Organization Name and Address	13. Type of Report & Period Covered
National Science Foundation National Oceanic and Atmospheric Administration National Aeronautics and Space Administration	Final
	14.

15. Supplementary Notes

Proceedings of a workshop held at Woods Hole, Massachusetts, July 9-20, 1984

16. Abstract (Limit: 200 words)

An assessment of the status of research using Global Weather Experiment (GWE) data and of the progress in meeting the objectives of the GWE, i.e., better knowledge and understanding of the atmosphere in order to provide more useful weather prediction services.

Volume Two of the report consists of a compilation of the papers presented during the workshop. These cover studies that addressed GWE research objectives and utilized GWE information. The titles in Part 2 of this volume include General Circulation Planetary Waves, Interhemispheric, Cross-Equatorial Exchange, Global Aspects of Monsoons, Midlatitude-Tropical Interactions During Monsoons, Stratosphere, Southern Hemisphere, Parameterization, Design of Observations, Oceanography, Future Possibilities, Research Gaps, with an Appendix.

17. Document Analysis   a. Descriptors

meteorology, atmospheric sciences, weather prediction, global circulation, numeric modeling and prediction, objective analysis and assimilation, satellite observing systems, tropical meteorology, oceanography, monsoons, heat sources and sinks, cumulus parameterization

b. Identifiers/Open-Ended Terms

Global Atmospheric Research Program (GARP), Global Weather Experiment (GWE), First GARP Global Experiment (FGGE), Monsoon Experiment (MONEX), Observing Systems Simulation Experiments (OSSE)

c. COSATI Field/Group

18. Availability Statement	19. Security Class (This Report) unclassified	21. No. of Pages
Distribution is unlimited.	20. Security Class (This Page) unclassified	22. Price

(See ANSI-Z39.18)   See Instructions on Reverse   OPTIONAL FORM 272 (4-77) (Formerly NTIS-35)

THE GLOBAL WEATHER EXPERIMENT · 1978–1979 ·

Proceedings of the
First National Workshop on the
Global Weather Experiment

Current Achievements and Future Directions

Volume Two, Part Two

Proceedings of the First National Workshop on the Global Weather Experiment:

Current Achievements and Future Directions

Volume Two, Part II

Woods Hole, Massachusetts
July 9–20, 1984

2<

CONTENTS

4<

5

6

9. GENERAL CIRCULATION PLANETARY WAVES

Organizers	Jay Fein John H.E. Clark
Session Chairmen	Jay Fein John H.E. Clark
Speakers	Ferdinand Baer Richard D. Rosen Richard L. Pfeffer Wayman E. Baker
Rapporteur	John H.E. Clark Tsing-Chang Chen

FGGE AND ATMOSPHERIC PREDICTABILITY

Ferdinand Baer
University of Maryland

ABSTRACT

FGGE data and its analyses have made significant impact on the
prediction community and its understanding of the atmosphere. The
detail available from the FGGE data makes understanding of specific
issues more precise and opens up new questions not previously recog-
nized. The spectrum of issues to which FGGE data may be addressed
includes time scales (stationary and transient), space scales (global
versus local), regionality (tropics, oceans, and so on), specific
weather phenomena (blocking, monsoons, and so on), and energetics, to
name but a few.

In addition to identifying and highlighting atmospheric processes,
FGGE data can and have been applied to improved atmospheric predictabil-
ity. This has been achieved through model initialization, improved
parameterization of model forcing, and more thorough validation of
model forecasts. Of particular interest is the increased understanding
of the atmosphere and subsequently its predictability, which may be
obtained through an assessment of the statistical characteristics of
the FGGE data.

INTRODUCTION

Predictability has taken on a highly sophisticated significance in
meteorological circles over the last few years and has challenged the
minds of our most competent scholars. Despite this apparent ascendancy
of a topical issue, predictability has been in the forefront of
meteorological thought and study during the entire development of our
discipline since the Second World War. The prediction problem,
basically nonlinear and essentially intractable deductively without
substantial computing power (see, for example, Richardson, 1922), was
championed by von Neumann as an ideal candidate for application of his
newly developed digital computer in the late 1940s. Subsequent to
assembling a small group of scientists at the Institute for Advanced
Study in Princeton, a f ecast model was developed and prediction skill
was demonstrated (Charney et al., 1950).

8<

There early experiments were modest, utilizing the barotropic vorticity equation over a limited domain and showed limited success with forecasts not much longer than one day over a region smaller than the North American continent. Not only was the venture a pioneering one requiring simplicity, but computer resources were restrictive and completely extended by the simple models. History now shows that model sophistication developed in consort with the availability of more powerful computers.

As computer capacity grew, assumptions imposed in the simpler models were cast aside. Hemispheric and global models replaced the regional models, eliminating serious lateral boundary problems. (Ironically, more recent efforts with limited-area models to predict the mesoscale have resurrected these early boundary problems). Single-level models were extended to multiple levels, first with quasi-geostrophy imposed, and ultimately using the primitive equations. The transition to model complexity brought with it the issue of proper initial conditions, since more complex models require additional and appropriate initial conditions. It quickly became apparent that observations were not sufficiently complete to adequately specify the initial state for prediction models. A careful study evolved to determine how observations and their analyses could be properly balanced so that prediction skill with models could be enhanced. (See, for example, Bolin, 1956).

Much of the development of predictive skill with numerical models was for short-term forecasts (one to two days) and seemed dependent more on internal and nonlinear dynamics of the fluid as manifest by the model than on the forces imposed on the fluid by physical or mechanical processes. However, the study of physical processes and how they force fluid flow in the models was accelerated, perhaps in association with models designated to simulate the general circulation. Since some of the forcing processes are not on the resolvable scales of models, parameterization techniques were developed that could apply subgrid-scale forcing appropriately to the models' resolvable scales. Topography was also introduced to establish boundary forcing. Details of sea and land processes and their impact on prediction were left to the future.

Throughout this evolutionary period in model development and accompanying predictive skill, it was apparent that our observations of the atmosphere were inadequate. Not only did we not have suitable initial conditions to satisfy the requirements of the evolving models, but we did not have the quality nor quantity of data to understand physical processes that would ultimately lead to improved predictability. This awareness led to the development of the Global Atmospheric Research Program (GARP), which ultimately culminated in the First GARP Global Experiment (FGGE), and gave our community the wherewithal to study more carefully many outstanding problems, intractable without the FGGE data. As plans for the FGGE evolved, new questions about modeling and prediction arose and additional applications of the planned data were conceived.

In the late 1960s, Lorenz (1969) provided a definitive limit to predictability based on theoretical considerations that allowed us to focus our efforts and to identify those issues that have more or less

impact on predictive skill within his established bounds. Since then a large number of factors have been studied to aid in improving prediction, and the solutions to many of these problems have been substantially enhanced by the FGGE data. Models now depend as much on forcing and its parameterization as they do on initial conditions, numerics, and boundary conditions. Models are differentiated by the time scales and space scales that they must predict, and scientists are flirting with procedures for predicting climate far beyond the prediction limitiations set out by Lorenz. There has been strong interaction between the analyses of the FGGE data, their applications to prediction models, their description of physical processes of the atmosphere, and subsequent interpretations.

CURRENT STATUS OF PREDICTABILITY

Having had several decades to develop modeling skills, to exploit the explosion of available computing resources, and more recently to assess a higher quality global data set, what critical problems in predictability have been isolated? There is clearly no unique answer to this question since many problems have surfaced. The process by which this evolution has proceeded is however illuminating. Models are developed, compared to observations, and limitations observed. Adjustments are made to the models, and new comparisons are made. Data deficiencies are discovered that make high quality comparisons questionable, and new and improved data are required. Thus we come to the FGGE era, which provides the most recent and highest quality global data set available. As modeling deficiencies were identified, more and more detailed questions relating to predictability arose. In particular, whereas early modelers were content to evaluate their predictive skill by simple scalar numbers such as the mean height of the 500 mb surface, current modelers ask for more sophisticated measures by which to assess their predictive capabilities. Baumhefner (1984) has recently addressed this problem, suggesting a variety of possible tests and describing predictability as a function of space scales. Anthes (1984) has discussed the question in application to mesoscale predictability. Recognizing that each new development in predictive skill generates new problems, let us assess our current situation.

Methodology

Numerous laboratories in many countries have experimented with representational procedures to optimize the efficiency and quality of predictions at minimum computational cost. These techniques convert differential equations to manageable computational format and include finite differences, finite elements, and spectral expansions. Although not universally adopted, the spectral method is in current fashion for the horizontal representation in most global prediction models. This choice may be based on the ease with which both truncation and interpretation of data may be accomplished.

For model representation with atmospheric height, the preferred variable is currently a σ-coordinate, incorporating the advantages of pressure (the hydrostatic approximation) and utilizing the coordinate to represent the earth's topographic boundary as a surface. However, it has long been known that isentropic surfaces are material surfaces for adiabatic motions and may be quite suitable for the careful analyses of atmospheric behavior. Indeed, recent isentropic analyses of FGGE data by Duncan (1983) and Johnson (1983) support this contention and provide insight into the structure of the longwaves, the forcing of those waves, and the atmospheric mass circulation. Although prediction with entropy as the vertical coordinate is not necessarily recommended, diagnosis of model output as well as observations on such surfaces is insightful.

Perhaps the most exciting and interesting development in the area of modeling methodology has been the application of normal mode theory to prediction models. This process identifies the structures of the linearized prediction equations that are characteristic of the system, i.e., which diagonalize the equations. These structures or vectors also have characteristic frequencies, both Rossby or gravity, that define their temporal motions. As models have become more complex, the corresponding normal mode structures have also become more complex. Yet they can provide deep insight into the behavior and predictability of the atmospheric system they represent. Model forcing can stimulate one or more of these modes and lead to a better understanding of how atmospheric processes evolve. Indeed, nonlinear models can be represented by an expansion in their linear modes and integrated in that format. Experiments utilizing this procedure have been performed with the shallow water equations by Kasahara (1977).

Initial Conditions

The dependence of predictability on observational data is most pronounced in the need for suitable initial conditions. As models evolved in complexity and detail, initial condition requirements grew apace. Since observations are not taken uniformly throughout the atmosphere and models require uniformity of initial conditions, substantial effort has gone into developing suitable interpolation procedures. Two analysis procedures have been prominently used. A local weighting procedure that determines values at a point by weighting observations in the vicinity according to their distance from the point in question was used for many years by NMC and was developed by Cressman (1959). In recent years this method has been supplanted by including data statistics into the weighting functions; it is known as the optimum interpolation analysis. To include a knowledge of known physical relationships between some variables, coupling is included when possible in a multivariate procedure (see Phillips, 1982). This process has been shown to provide superior predictions and is in use at most prediction centers. The alternate procedure, whereby observed data are projected onto global functions that are themselves used as initial conditions or evaluated at the needed points of a model, also incorporates physical

relations between the variables and was used for many years at NMC by projection onto Hough-Rossby modes and denoted as the "Flattery Analysis."

Although the optimum interpolation analysis schemes are considerably more effective in providing adequate initial conditions to models, limitations in density of observations (both time and space) lead to imbalances in initial field variables that can cause severe instabilities in model integrations, thereby destroying predictability. This deficiency has been countered by developing initialization procedures that are based on model characteristics. The most popular of these is normal mode initialization, whereby the initial data are adjusted to the normal modes of the model, reducing or removing the tendencies of the higher frequency gravity modes that are normally not seen in the observations. The effect of this activity has been pronounced improvement in predictability over the first day of global prediction, and the topic has been carefully discussed by Leith (1980) and Daley (1980).

Since some observations are superior in quality and density to others and some observed variables have more impact on prediction systems than others, variational techniques have been devised to incorporate this information into the initializing schemes. Recent studies (Williamson and Daley, 1983) recognize that data analysis and initialization are not independent procedures, but both are related to the adequate preparation of observations for use as initial conditions in prediction systems. Consequently, efforts are now under way to integrate these procedures, analyzing observations to fit most suitably a given model and including the model's idiosyncrasies through initialization into the final objective analysis.

Since data are retrieved and available during the course of a model integration period, incorporation of this data in an asynchronous fashion with time during the model run may have a positive effect on prediction. Success with such data assimilation has been reported by Lorenc (1982) and Stern (1982) as well as by other prediction centers. Yet the FGGE data have pointed out clearly the shortcomings of our routine data observations and their negative impact on predictability. Julian (1982) has shown that tropical analyses, particularly the divergent flow, are poorly represented in initial conditions and inhibit prediction success. Moreover, the shortage of data over large oceanic areas is clearly a limiting factor in advancing our ability to forecast shorter scale events.

Observed Factors Impacting on Prediction

Using the methods and techniques developed over years of research, numerous circulation features have been extracted from atmospheric observations. Analyses of the FGGE data set have been particularly fruitful in isolating processes that, if properly modeled, could yield superior predictive skill. A particularly relevant feature has gradually come to light by separating the wavy flow of the atmosphere into transient and stationary components. Not only have some significant modes with important frequencies come to light, but the impact of

forcing on some of these modes has been investigated. It appears that the transient eddies may determine the character of the stationary flow, and these effects are both of a barotropic and baroclinic nature.

The observations of wave interactions on various time scales was first studied by a simple harmonic decomposition in longitude at various latitudes, and on different pressure surfaces. However, it was noted that the "normal modes" of some atmospheric models, if used for projection of atmospheric observations, might provide even more insight into the interactive forcing process. Analyses of this type have highlighted some forcing processes in the atmosphere. It now appears that Pacific North American (PNA) patterns are set up by certain anomalous forcings of particular modes of the flow field and that sea-surface temperature anomalies can lead to pronounced flow pattern effects. These observations coupled with the transient-stationary wave interactions give a valuable insight into the processes that models must emulate if they are to succeed in extending predictability skill. Observational evidence provided by Holopainen (1983) and Madden and Tribbia (1983) coupled with simple model experiments of Machenhauer (1983) and Simmons et al. (1983) have led the way in this area. Models must be shown to reproduce the observed interactions noted here if they are to succeed predictively.

Other factors applicable to prediction include the persistence of anomalies as described by Dole and Gordon (1984) and the impact of heating on the position of primary troughs in the longwave patterns seen by Paegle (1983). Many of these features can be cataloged and used for testing purposes to assess the quality of prediction models.

Atmospheric Features Tested by Prediction Models

Insight into atmospheric flow gained from observations has led modelers to test their predictions against those observations. The normal mode approach has been particularly useful not only in improving initial conditions, but in diagnosing both observations and model output. Dominant modes can be identified in observed fields and their behavior followed in time, and the corresponding model mode behavior can be compared. Focusing on significant modes, model performance can be evaluated and suitable adjustments tested. This procedure seems to be gradually gaining favor.

Statistics of atmospheric turbulence has long attracted modelers for its potential in parameterization of subgrid-scale interactions. Theory identifies energy and vorticity statistics that are difficult to isolate in observations because of the severity of the approximations required. Model statistics vary from expectations of theory when the models involve more physics and dynamics than theory. Using vertical mean energy statistics derived from FGGE analyses, Boer (1984) observed a $-5/3$ slope in the spectrum of the large waves and a -3 slope in the shorter waves. Other observed statistics were less in agreement with theory. He then derived statistics from the Canadian Meteorological Center's forecast model. Although comparison of these prediction statistics with FGGE observations was not overwhelming, the process

indicates a methodological approach that should lead to improved predictability.

Topography.has long been known to have a pronounced impact on the atmosphere and has been included in most prediction models. Details of space scaling and truncation associated with topography have recently been studied more carefully. As a result, Tibaldi (1984) has shown that appropriate smoothing of topography as input into a model, known as "envelope orography," has a positive effect on model climate drift, thus reducing systematic prediction error. Additional benefit is seen in the ultralong, low-frequency planetary waves that have shown resistance to adequate prediction in the past.

Additional modeling studies involving forcing have been provoked by the availability of the high quality FGGE data set. An incomplete list of forcing factors under investigation include clouds, radiation, vertical diffusion, land-sea surface effects, evapotranspiration, and albedo, to name just a few. Shukla (1984) has pointed out, based on experience with a general circulation prediction model, that growth of dominant instabilities in the atmosphere delimit its predictability. These instabilities depend on season, the circulation regime, and the presence of quasi-stationary asymmetric forcing among other factors. Modeling of these features and comparison with observations should guide us to improved prediction techniques.

Finally, the availability of the FGGE analyses of global data has stimulated a study of large-scale model intercomparisons. As reported by Temperton et al. (1983), no less than eight different models representing forecast centers were compared based on the FGGE analyses as initial conditions. Although this study did not directly support model improvements, it highlighted prediction deficiencies that were seen systematically in all models. Information of this type is invaluable if predictive skill is to be enhanced.

ADDITIONAL APPLICATIONS OF FGGE. DATA

Having seen the wide variety of problems related to predictability to which FGGE data have been directed, one may well ask if other meaningful applications exist. Here the development of the normal mode procedure is briefly reviewed for a clue. Model normal modes have proved exceptionally useful in the initialization problem, allowing modal separation with frequency and suggesting procedures for amplitude control on high frequency gravity modes. The manifold representation presented by Leith (1980) has proved particularly enlightening. Previous discussion indicates that representation in normal modes also gives insight into model forcing, highlighting particularly relevant modes. Models have been presented in normal mode form, where the integration actually is accomplished in modal space. Atmospheric data may be projected onto model modes to give insight into how that data are distributed among the modes as well as to establish how that distribution changes with time.

In these discussions the normal mode problem from the atmospheric perspective has not been considered. Given the nature of the

14<

atmosphere as a continuum, it is reasonable to presume that it has no characteristic modes. However, when viewed as a fluid of discrete points, which corresponds to how its properties are measured, such modes may be definable. Indeed, some few modes seem to be identifiable. Madden (1983) has detected a 16-day wave, and Lindzen et al. (1984) have noted a 5-day wave. Perhaps the data available to date can yield no more. If one sets up a finite net of points over the atmospheric domain, characteristic structures may be established from data (FGGE data in particular) that best fit that data in a statistical sense. Although such a procedure precludes a discussion of frequency, some effort in that direction may be possible. Additionally, some of these statistical modes may have strong persistence.

Characteristic atmospheric structures can be generated from a time series of data by developing a covariance matrix of the data. The eigenvectors of that matrix represent the characteristic vectors and the eigenvalues determine their relative importance in the time record. Data can be considered globally, hemispherically, or regionally. The total field can be analyzed or the time mean can be removed yielding information about the transient component. Details on structures in the vertical coordinate, in the planetary waves, or on latitudinal variability can be determined. Dependence on seasonality can also be assessed.

Some calculations generating structures of the FGGE IIIb SOP1 (Baer, 1982) have been reported on. In those calculations, the hemispheric wind field was projected onto solid harmonics, and stream field coefficients were developed on 12 pressure levels to 50 mb for 120 time records. Characteristic vertical structures were generated from the covariance matrices of each planetary wave. Those structures were compared to corresponding normal mode structures of atmospheric models (see, for example, Kasahara and Shigehisa, 1983) and showed similarities. The data set was then reprojected onto these vertical modes, yielding horizontal coefficients in each vertical mode. For each vertical mode and planetary wave, characteristic latitudinal structures were generated. Since the normal modes in latitude for most models are Hough functions that do not include shearing current, favorable comparison of the statistical modes of the FGGE analysis with Hough modes has not yet been found. However, when the observed data are projected onto the statistical latitudinal modes, a time trend for each mode may be sought. Such trends should give insight into the frequencies of observed atmospheric structures, however this analysis is not yet complete.

Can one gain predictive skill from structure analysis of the type indicated here? Perhaps models could produce improved predictions if integrations were performed in vertical modes rather than on pressure surfaces, particularly if those modes reflected the statistical properties of the atmosphere. Perhaps models could produce improved prediction if integrations were performed in characteristic latitudinal structures rather than at latitudinal gridpoints or Legendre polynomials. Perhaps models could be more effectively truncated if unimportant modes with nonrelevant frequencies could be readily identified. It seems evident that projection of model output on structures that are

particularly significant in observations of the atmosphere should provide more insight into the energy exchange processes that take place in models. Such information should also indicate the modeling changes needed to provide enhanced prediction skill.

CONCLUSIONS

It should be evident from the previous discussion that accessibility of data and predictability of atmospheric events are inseparably intertwined and feed on one another. As one obtains more data, understanding of atmospheric processes grows, and modeling abilities advance. Scientists seek the greatest possible resolution in both time and space from the measurements taken of the atmosphere. These measurements should be of high quality (small errors) and should include as many of the physical and dynamical variables as feasible, within our capabilities. Clearly, the FGGE was a recent high point in such an endeavor and has provided the best global data set yet attainable. Correspondingly, scientists need sophisticated models that can reproduce the processes that occur in the atmosphere in order to achieve the best predictions within theoretically identified limits.

Clearly, observational data are required for model initial conditions; without high quality data, predictions with models are not feasible. Additionally, data of comparable quality are needed to test model predictions, i.e., to determine how well a chosen model can emulate the real atmosphere. Finally, quality data are required to diagnose the processes that the atmosphere undergoes so that this information can be incorporated into models, thereby enhancing the models' prediction skill.

Observed data can be used to achieve improved predictability in several ways. Each observation can be used directly or it can be used statistically by averaging over time and/or space. Data statistics have already shown utility in optimum interpolation analyses as well as for initialization. Statistics aid in diagnosing model inaccuracies and also yield characteristic features of observed fields that may assist in modeling development.

Efforts to make the most of information available from the FGGE data as applicable to the prediction problem are intense. New observations generate excitement about the future potential for detailed prediction. Continuing research should highlight yet undiscovered limitations that will ultimately lead to a need for new and more refined observations, and perhaps for additional and as yet unconsidered variables.

ACKNOWLEDGMENT

REFERENCES

Anthes, R. A. (1984). Predictability of mesoscale meteorological phenomena. Predictability of Fluid Motions, AIP Conf. Proc. #106, Amer. Inst. of Phys., New York, 247-270.

Baer, F. (1982). Characteristic structures of atmospheric flow and temperature as seen from FGGE analyses. Proc. 14th Stanstead Seminar. Meteo. 127, 44-51.

Baumhefner, D. P. (1984). The relationship between present large-scale forecast skill and new estimates of predictability error growth. Predictability of Fluid Motions, AIP Conf. Proc. #106, Amer. Inst. of Phys., New York, 169-180.

Boer, G. J. (1984). Observational aspects of large-scale atmospheric turbulence and predictability. Predictability of Fluid Motions, AIP Conf. Proc. #106, Amer. Inst. of Phys., New York, 55-66.

Bolin, B. (1956). An improved barotropic model and some aspects of using the balance equation for three-dimensional flow. Tellus 8, 61-75.

Charney, J. G., R. Fjortoft, and J. von Neumann (1950). Numerical integration of the barotropic vorticity equation. Tellus 2, 237-254.

Cressman, G. (1959). An operational objective analysis system. Mon. Wea. Rev. 87, 367-374.

Daley, R. (1980). On the optimum specification of the initial state for determinant forecasting. Mon. Wea. Rev. 108, 1719-1735.

Dole, R. M., and N. D. Gordon (1984). Asymmetries in persistence between positive and negative anomalies in persistent anomaly regions. Predictability of Fluid Motions, AIP Conf. Proc. #106, Amer. Inst. of Phys., New York, 181-204.

Duncan, C. N. (1983). Some circulation statistics in isentropic coordinates. IAMAP Symposium on Maintenance of the Quasi-Stationary Components of the Flow in the Atmosphere and in Atmospheric Models, PWPR, WMO, Paris, 29 August to 2 September 1983, 15-18.

Holopainen, E. (1983). Observational studies on the interplay between the long-term stationary flow and two kinds of large-scale transient eddies in the atmosphere. IAMAP Symposium on Maintenance of the Quasi-Stationary Components of the Flow in the Atmosphere and in Atmospheric Models, PWPR, WMO, Paris, 29 August to 2 September 1983, 23-24.

Johnson, D. R. (1983). On the forcing and maintenance of the isentropic zonally averaged circumpolar vortex. IAMAP Symposium on Maintenance of the Quasi-Stationary Components of the Flow in the Atmosphere and in Atmospheric Models, PWPR, WMO, Paris, 29 August to 2 September 1983, 19-22.

Julian, P. R. (1982). Objective analysis of streamfunction and velocity potential for analysis of tropical wind fields. Proc. 14th Stanstead Seminar. Meteo. 127, 100-105.

Kasahara, A. (1977). Numerical integration of the global barotropic primitive equations with Hough harmonic expansions. J. Atmos. Sci. 34, 687-701.

Kasahara, A., and Y. Shigehisa (1983). Orthogonal vertical normal modes of a vertically staggered discretized atmospheric model. Mon. Wea. Rev. 111, 1724-1735.

Leith, C. (1980). Nonlinear normal mode initialization and quasi-geostrophic theory. J. Atmos. Sci. 37, 958-968.

Lindzen, R. S., D. M. Strauss, and B. Katz (1984). An observational study of large-scale atmospheric Rossby waves during FGGE. J. Atmos. Sci. 41 (in press).

Lorenc, A. C. (1982). On direct data assimilation into a forecast model. Proc. 14th Stanstead Seminar. Meteo. 127, 126-131.

Lorenz, E. N. (1969). The predictability of a flow which possesses many scales of motion. Tellus 21, 289-307.

Machenhauer, B. (1983). The quasi-stationary and large-scale transient components of the flow in the atmosphere and in an atmospheric model analyzed in terms of model normal modes. IAMAP Symposium on Maintenance of the Quasi-Stationary Components of the Flow in the Atmosphere and in Atmospheric Models, PWPR, WMO, Paris, 29 August to 2 September 1983, 27-28.

Madden, R. A. (1983). The effect of the interference of traveling and stationary waves on time variations of the large-scale circulation. J. Atmos. Sci. 40, 1110-1125.

Madden, R. A., and J. J. Tribbia (1983). Seasonally forced large-scale waves as depicted by Hough functions. IAMAP Symposium on Maintenance of the Quasi-Stationary Components of the Flow in the Atmosphere and in Atmospheric Models, PWPR, WMO, Paris, 29 August to 2 September 1983, 29-30.

Paegle, J. (1983). Longitudinally asymmetric heating and ultralong waves. IAMAP Symposium on Maintenance of the Quasi-Stationary Components of the Flow in the Atmosphere and in Atmospheric Models, PWPR, WMO, Paris, 29 August to 2 September 1983, 39-42.

Phillips, N. A. (1982). On the completeness of multivariate optimum interpolation for large-scale meteorological analysis. Mon. Wea. Rev. 110, 1329-1334.

Richardson, L. F. (1922). Weather Prediction by Numerical Process. Cambridge University Press, London, 236 pp. (Dover edition, 1965).

Shukla, J. (1984). Predictability of a large atmospheric model. Predictability of Fluid Motions. AIP Conf. Proc. #106, Amer. Inst. of Phys., New York, 449-456.

Simmons, A. J., J. M. Wallace, G. W. Branstator (1983). Barotropic wave propagation and instability, and atmospheric teleconnection patterns. J. Atmos. Sci. 40, 1363-1392.

Stern, W. (1982). Four-dimensional assimilation at GFDL using FGGE data. Proc. 14th Stanstead Seminar. Meteo. 127, 150-159.

Temperton, C., T. N. Krishnamurti, R. Pasch, and T. Kitade (1983). WGNE Forecast Comparison Experiments. Report No. 6, World Climate Research Program, WMO, Geneva, November 1983, 104 pp.

Tibaldi, S. (1984). On the relationships between systematic error of the ECMWF forecast model and orographic forcing. Predictability of Fluid Motions, AIP Conf. Proc. #106, Amer. Inst. of Phys. New York, 397-418.

Williamson, D. L., and R. Daley (1983). A unified analysis-initialization technique. Mon. Wea. Rev. 111, 1517-1536.

IMPACT OF FGGE ON DIAGNOSES OF THE GENERAL CIRCULATION

Richard D. Rosen
Atmospheric and Environmental Research, Inc.

ABSTRACT

Because of the tremendous efforts devoted during the FGGE to the collection and analysis of observations taken over the globe from an unprecedented variety of platforms, expectations were high that new features of the general circulation would be revealed. Comparisons of monthly mean circulation fields derived from Level IIIb analyses with those derived from analyses based on just the conventional rawinsonde data do, indeed, point out a number of features missed by the station network during FGGE, and possibly in earlier years as well. For example, the station-based analysis of the 200 mb field of transient eddy momentum flux in January does not include a significant region of northward flux over the northeast Pacific that is contained in Level IIIb analyses. In addition, experiments in which the impact of the FGGE satellite data was tested by withholding them from IIIb analyses indicate that these data did have some effect on circulation statistics, especially over the southern hemisphere, although the effect generally was not large.

Several studies however have pointed out that a number of significant differences exist in circulation fields derived from the various Level IIIb analyses. For example, differences in the strength of the January Hadley cell between the GFDL and ECMWF analyses are as large as 35 percent, and there are some locations over the northern hemisphere where the 200 mb zonal wind in January differs by 10 m/s between these two analyses. Calculations of the global energy cycle based on the GFDL and ECMWF analyses are significantly different as well. In addition, the uncertain quality of some of the FGGE IIIb moisture and vertical motion fields raises doubts about whether new insights into the role of these fields in the general circulation will be gained from the FGGE data. Overall, therefore, a sense of disappointment emerges that the FGGE analyses have thus far failed to live up to the expectation that they would yield more definitive general circulation statistics. The shortcomings in the Level IIIb analyses need to be rectified before full confidence can be placed in results pertaining to the general circulation that are based on such modern data assimilation approaches.

INTRODUCTION

From the standpoint of general circulation research, the FGGE came at a propitious moment. By the early 1970s, the understanding of the general circulation seemed to be in fairly good order. Indeed, Lorenz (1970) estimated at that time that the theory of the average general circulation was 80 percent complete, at least for an ideal dry atmosphere. Lorenz also noted however that the theory of fluctuations of the general circulation was still in its infancy and that "we do not even know whether the year-to-year variations are mainly systematic or mainly random."

Later during the 1970s, the subject of the general circulation's interannual variability became of more practical concern as a series of unusually severe winters struck many portions of the world. It became clear that if one were to seek the cause for such fluctuations in the general circulation, then more precise measurements of the state of the general circulation would be needed. Although the rawinsonde station network had been sufficient to delineate the average general circulation and its annual cycle (Oort and Rasmusson, 1971), the gaps in this network would have to be filled if we were to unambiguously detect real interannual variations in the general circulation.

Thus the stage was set for FGGE to make an impact on diagnoses of the general circulation. Although FGGE was to represent just a one year effort, the data taken that year were to be the most extensive ever. Expectations were high therefore that the general circulation during that year would be determined to unprecedented accuracy and that new features of the general circulation might be revealed. Moreover, it was hoped that the FGGE data would allow important new progress to be made in two areas of general circulation research that had been stymied for lack of accurate data: the role of vertical fluxes of heat and momentum in the general circulation, and the behavior of water vapor and the hydrological cycle in the general circulation.

If FGGE were to provide more precise circulation statistics, then these would have to be based on more data than those from the existing rawinsonde network. Although efforts were made to upgrade this station network for FGGE, Figure 1 illustrates that significant gaps in the distribution of upper-air stations remained. Of course, the design for FGGE recognized early on that such gaps would exist, and other systems, particularly satellites, were looked upon to fill the voids. The data assimilation task however would then have to take into account the very different natures in time and space of the different observing systems, a complex and relatively novel undertaking. At the time of the experiment, it was certainly unclear what the effect of the assimilation procedures on diagnoses of the general circulation would be.

In the next section, a number of studies that have utilized the various Level IIIb data sets to diagnose the general circulation during FGGE are reviewed. Only IIIb results are dealt with here because these are presumed to be based on the most complete set of observations possible. However many studies of the general circulation have used the operational IIIa data sets from 1979 that did benefit from the enhanced FGGE observations. The studies by Koehler and Min (1984) and

200 mb
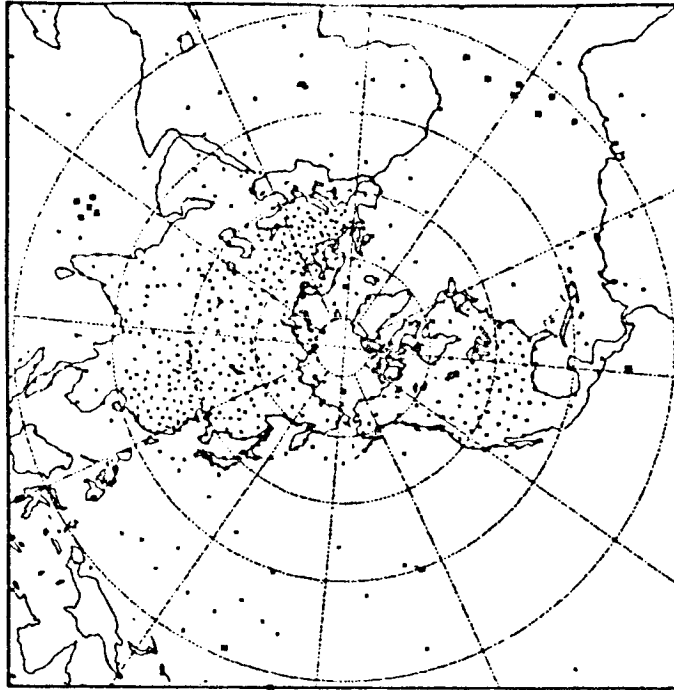
850 mb

FIGURE 1 Maps of rawinsonde stations that could be used to analyze monthly mean winds at 850 and 200 mb during June 1979. Asterisks denote monthly mean location of the tropical wind observing ships (TWOS) that were relatively stationary during the month.

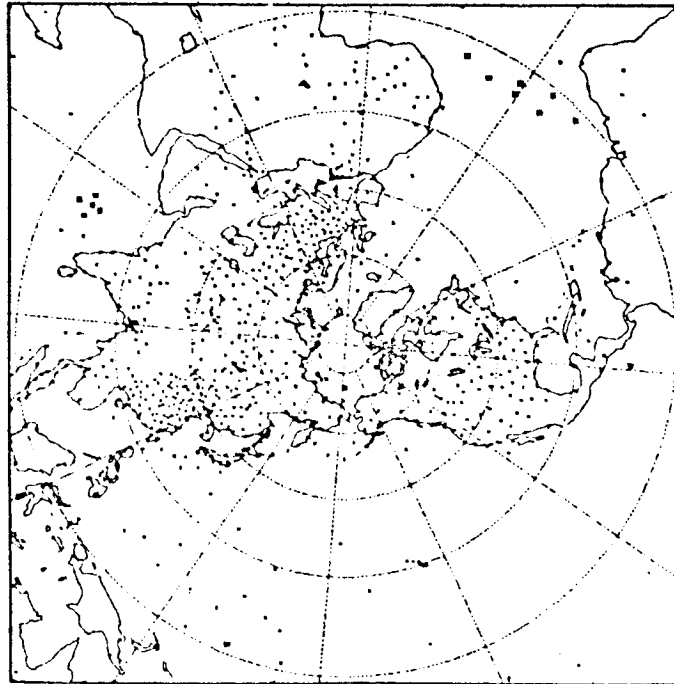van Loon (1980) are relevant examples. Space limitations however preclude a discussion of these or, for that matter, of every one of the general circulation studies that have used the IIIb data. Also, results for the southern hemisphere or for diabatic heating in the general circulation are explicitly dealt with elsewhere in this report. Instead, the focus here is on the subset of studies that reveals information about the impact of FGGE itself on diagnoses of the general circulation, particularly with regard to traditional circulation statistics for the northern hemisphere. Finally, the paper concludes with some perspectives on both the past and possible future impacts of FGGE on general circulation research.

DIAGNOSTIC STUDIES OF THE FGGE GENERAL CIRCULATION

ECMWF Analyses

The first set of FGGE Level IIIb analyses to be completed was that generated by the European Centre for Medium Range Weather Forecasts (ECMWF). Not surprisingly, in light of the above discussion, the earliest diagnostic studies of the general circulation based on these analyses were aimed at discovering not only whether new features of the circulation had been captured, but also what effect the assimilation procedures might have had on circulation statistics. For example, Kanamitsu (1981) concluded that the FGGE observations did have an impact on monthly mean flow fields over ocean regions based on comparisons with older station-based climatologies. It was unclear how much of the difference was real, or how much should be attributed to normal interannual variability or to biases in the ECMWF analyses. With respect to the latter, Kanamitsu noted that the ECMWF initialization procedure yielded unrealistically weak divergences in the tropics, including a weakened Hadley cell. Moreover, although the uninitialized $\underline{u}$ and $\underline{v}$ fields could be used to depict realistic large-scale velocity potential fields, the vertical motions derived from these caused undesirably large residuals in energy budget calculations. Kanamitsu concluded that "the quantitative evaluation of the vertical motion field...still seems to have some difficulties."

Among the more recent evaluations of the ECMWF FGGE analyses is the work by Lorenc and Swinbank (1984), who attempt to assess the accuracy of circulation statistics derived from these analyses in light of what is known about the data assimilation procedures. They conclude that the ECMWF analyses provide useful new information, for example, with regard to height fields over the southern hemisphere. On the other hand, they note that the ECMWF analyses tend to overestimate transient eddy momentum fluxes in data-sparse regions such as over the southern hemisphere. In addition, they point out that a variety of factors, including the smoothing effect of the vertical interpolations in the ECMWF system, make the ECMWF analyses unsuitable for moisture convergence calculations. Indeed, the basic humidity fields themselves are suspect because, as the authors note, humidity observations were erroneously weighted in the assimilation procedures for some portion of

FGGE. Chen and Vorwald (1984) have also pointed out that the ECMWF moisture fluxes are questionable in the tropics.

GFDL Analyses

The other complete set of FGGE Level IIIb analyses now available is that produced by the Geophysical Fluid Dynamics Laboratory (GFDL) of the National Oceanic and Atmospheric Administration. An early comparison between the ECMWF and GFDL analyses was performed by Kung and Tanaka (1983), who computed elements of the global energy budget with both data sets. The authors discovered "a twofold difference in the intensity of the energy cycle" between the two analyses, which "implies some fundamental differences in these data sets and thus in their description of the general circulation." They attributed this difference to the different data assimilation procedures used at the two centers. The GFDL analysis appeared to yield the more realistic energy cycle and was utilized by Kung and Tanaka (1984) to perform more detailed studies of the spectral character of energy transformation during FGGE.

Recently, Rosen et al. (1984) undertook some comparisons of circulation statistics based on the IIIb analyses with those derived from data taken at the FGGE upper air stations such as depicted in Figure 1. Two different versions of station analysis were performed, marked by different types of initial guesses (one utilizes a zonal mean initial guess field; the other allows for zonal asymmetries). In Figure 2, cross-sections of [ū] taken from this study are presented. The agreement between the GFDL and station analyses is generally good, but this belies more significant regional differences such as those evident in Figure 3. For example, the station-based analyses tend to underestimate the extent of the strong winds in the exit region of the east Asian jet, a result obtained in previous studies as well. Also, both station analyses place a local minimum in the zonal wind field east of the Arabian peninsula, whereas the GFDL analysis of ū contains a local minimum over the subtropical Atlantic that is not present in the station analyses. Because all these differences occur in station-sparse regions, Rosen et al. assumed that the GFDL analyses are superior in these areas.

A more surprising result emerges however when the GFDL analyses of ū at 200 mb are compared with those from the ECMWF, as in Figure 4. Differences as large as 10 m/s occur, including in the exit region of the east Asian jet. The other area of large differences is over central Asia where plenty of conventional data were available to both analyses, as shown in Figure 5. Rosen et al. concluded that "the magnitude of these differences in the IIIb analyses of ū provides a disturbing measure of the limitations in our ability to properly depict even this fundamental field." Astling (1984) also presents evidence of important differences between the GFDL and ECMWF 200 mb wind fields. For example, over South America during January 6 to 25, he finds mean wind speeds in the GFDL analysis that were more than double the ECMWF values at many grid points.
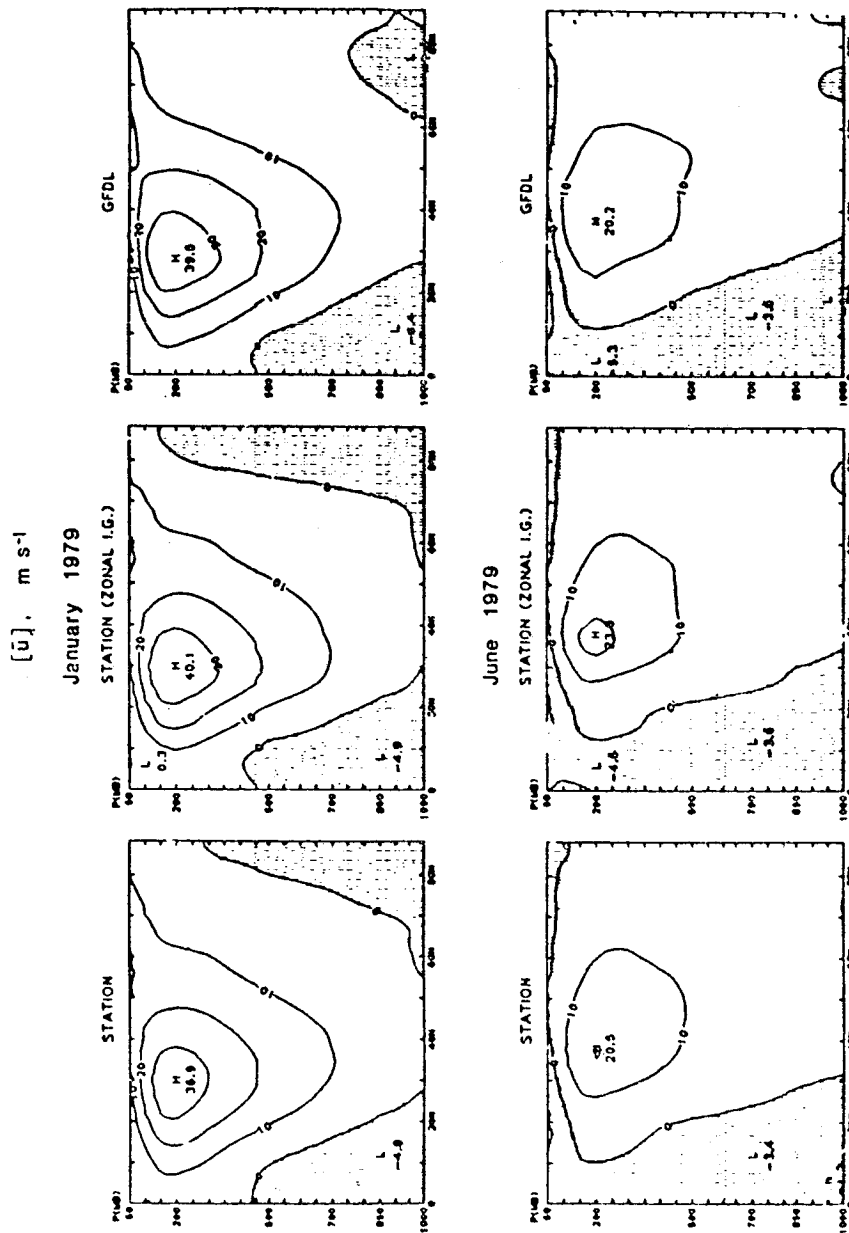
FIGURE 2 Cross-sections of the zonally averaged mean zonal wind for January and June 1979 based on two versions of station analysis and the GFDL level IIIb analysis. Negative values are shaded and indicate easterlies. Locations of extrema in these fields are indicated by the symbols H or L.

$\bar{u}$, m s^{-1} 200 mb   January 1979

STATION   STATION (ZONAL I.G.)
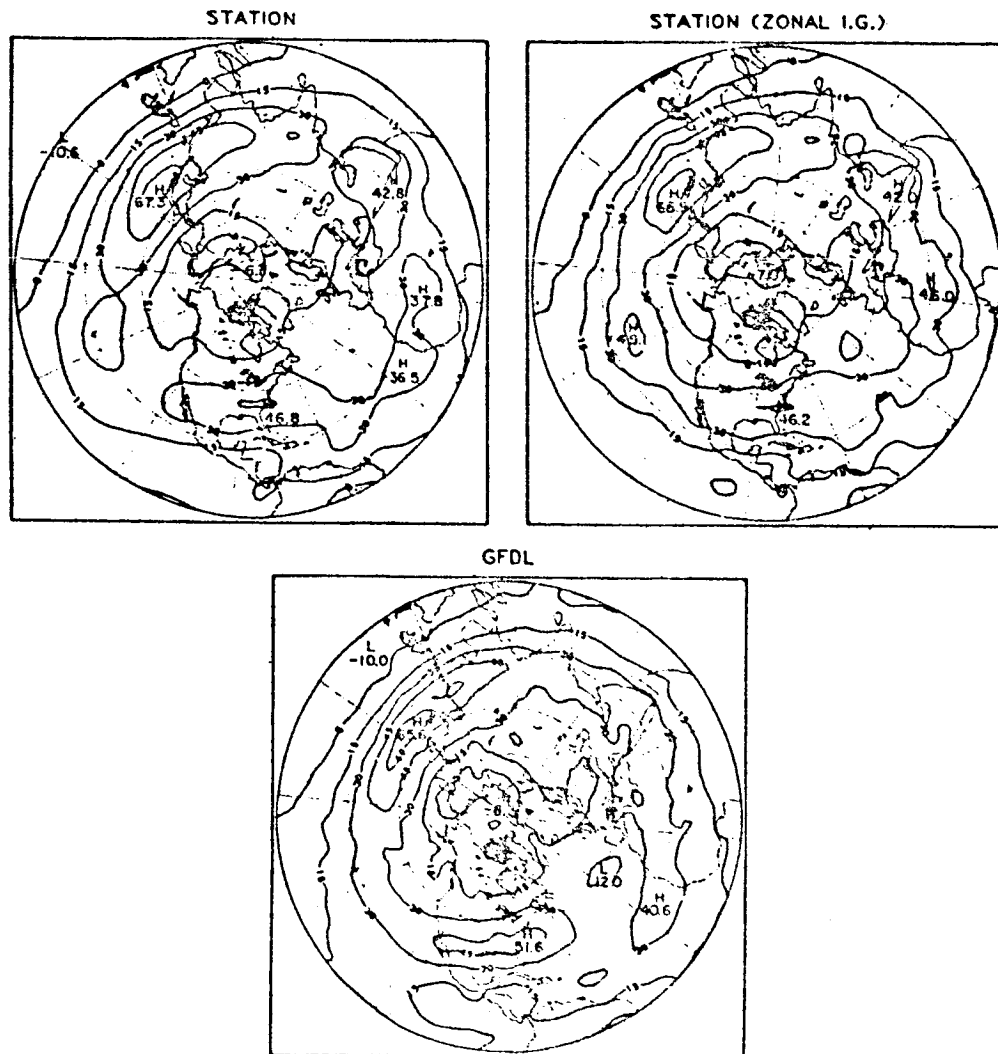
GFDL

FIGURE 3 Hemispheric maps of the mean zonal velocity at 200 mb for
January 1979. Results are derived from two versions of station
analysis and the GFDL level IIIb analysis. Isolines are drawn at
intervals of 15 m/s. Negative values are shaded and indicate
easterlies.

$\bar{u}$, m s^{-1} 200 mb   January 1979
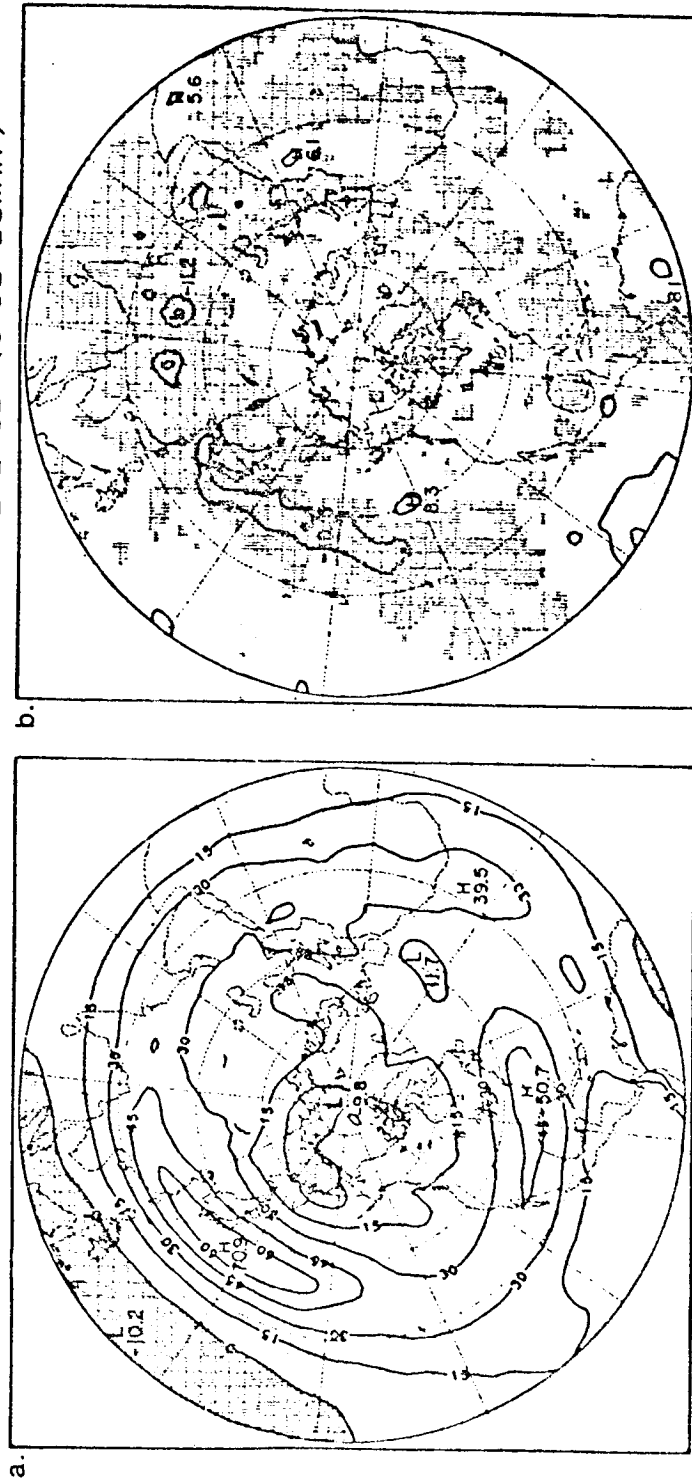
FIGURE 4 (a) Hemispheric map of the mean zonal velocity at 200 mb for January 1979 based on the ECMWF level IIIb analysis. Isolines are drawn at intervals of 15 m/s. Negative values are shaded and indicate easterlies. (b) Hemispheric map of the GFDL field in Figure 3 minus the ECMWF field in Figure 4a. Isolines are drawn at intervals of 5 m/s (the zero line is omitted). Negative values are shaded and indicate regions of stronger westerlies or weaker easterlies in the ECMWF data.
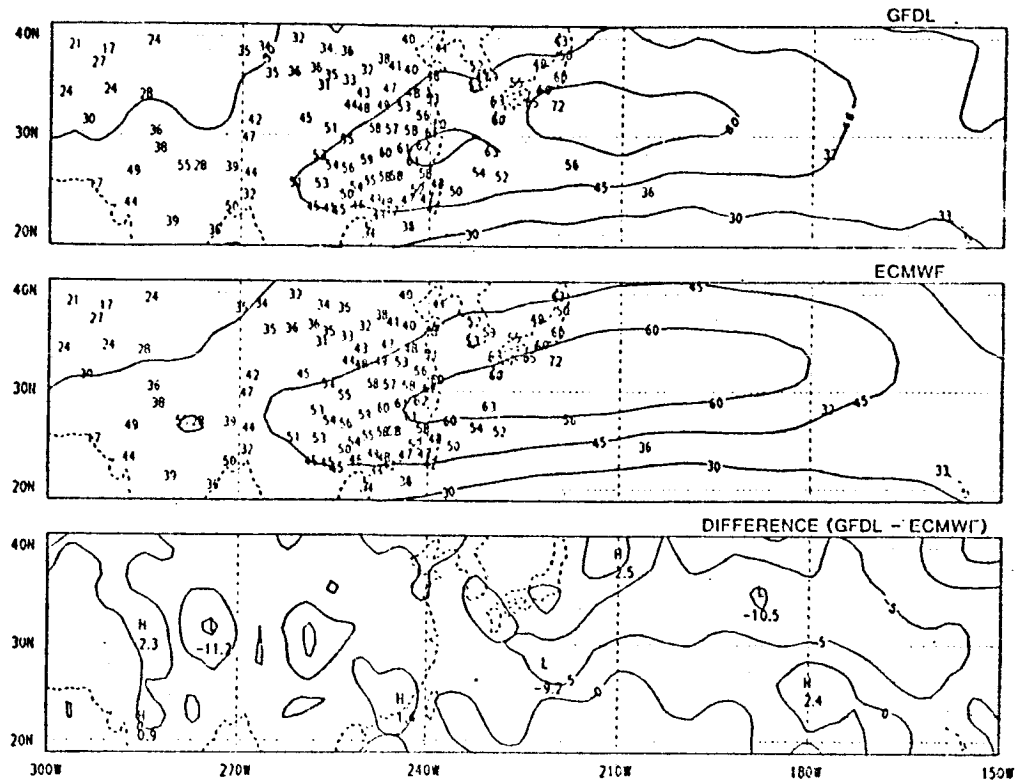
FIGURE 5 Map of the zonal velocity at 200 mb for January 1979 in the
region from 20°N to 40°N and 150°W to 300°W calculated from the
GFDL (top) and ECMWF (middle) Level IIIb analyses. Isolines are drawn
at intervals of 15 m/s; also displayed are the monthly mean values of ū
at the rawinsonde stations that passed the cutoff criterion for the
month. In the bottom panel is the difference, GFDL minus ECMWF, with
isolines drawn at intervals of 5 m/s and negative values shaded.

As for the meridional component of the mean wind field, Figure 6
presents zonal cross-sections of the mass streamfunction for two months
of the FGGE. In agreement with the studies cited earlier, the northern
hemisphere Hadley cell is noticeably weak in the ECMWF analysis both
months. Indeed, the maximum in January is some 35 percent smaller than
in the GFDL analysis. The GFDL streamfunction for January appears to
be realistic and resembles the station analyses but for two particulars.
First, the vertical gradient of ψ in the lower levels of the tropics
is much stronger in the GFDL analysis, leading to a maximum value of
ψ that is 20 percent larger than the average of the two station
maxima. Second, this central value of ψ is located 200 mb closer to
the surface in the GFDL analysis than in the station analyses. These
differences are related to a more intense region of tropical low level
zonal mean northerlies, which are confined more strictly to the lower
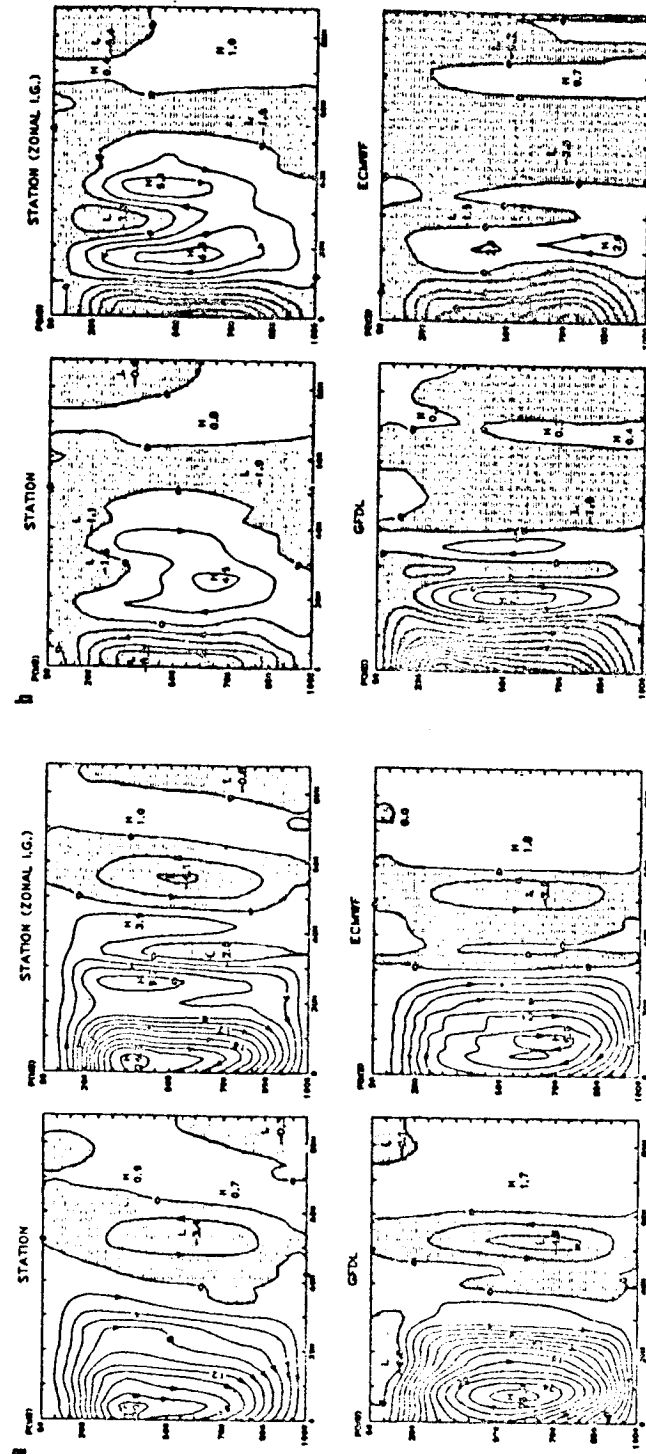
FIGURE 6 (a) Cross-sections of the mass streamfunction for the mean meridional circulation obtained after removal of spurious net mass flows for January 1979. Results are presented for two versions of station analysis and for the GFDL and ECMWF level IIIb analyses. Positive values indicate clockwise circulation. (b) As in a, but for June 1979

half of the atmosphere in the GFDL analysis. This may be an instance in which the FGGE data have provided us with a more precise measurement of the Hadley cell, historically a difficult feature of the general circulation to quantify. Note, by the way, that in June the GFDL analysis yields a southern hemisphere Hadley cell that is considerably stronger than in the other analyses.

Questions have been raised by Julian (1984), however, about the quality of the GFDL analyses in the tropics. He suggests that the analyses often "ignore the observed data" and "on scales less than the planetary are much too creative." On this second point, there seems to be little doubt that the GFDL analyses contain a great deal of detailed structure. This is evident, for example, in the maps of the transient eddy momentum flux, $u'v'$, in Figure 7. Also evident from this figure is that the station network appears to have missed some important features in the field, most notably over the Pacific between Hawaii and the west coast of the United States, but elsewhere over the Atlantic as well. Presumably, the intensity of such features as the east Pacific center has also been missed by earlier general circulation studies that were based on the conventional rawinsonde network. On the other hand, it is interesting to note that the east Pacific center can be generated by a general circulation model into which no data have been assimilated (Figure 8), thereby raising the question of how model dependent this feature may be in the Level IIIb analyses.

The zonal mean field of transient eddy momentum flux, $[\overline{u'v'}]$, in Figure 9 does indicate that differences as large as 30 percent exist between the station and GFDL analyses in the region of the maximum in this field. Interestingly, the results from the ECMWF analysis given by Kanamitsu (1981) for January agree more closely with the station-based results than with the GFDL results. The ECMWF picture also agrees with the station analysis in the tropical upper atmosphere in January, with both yielding much smaller values of $[\overline{u'v'}]$ than the GFDL analysis.

Although it would appear from the comparisons of $[\overline{u'v'}]$ that there is considerable uncertainty in the assessment of second-order circulation statistics with the FGGE data, this is not universally true. Thus, the cross-sections of $[\overline{v'T'}]$ in Figure 10 show generally close agreement between the station and GFDL analyses. The maps of $\overline{v'T'}$ in Figure 11 also show good overall agreement, particularly in June. The more detailed structure in the GFDL analysis is plainly evident however, a result which is highlighted in Figure 12. In addition, there is at least one area of substantive disagreement in January, namely, in the north Pacific near the dateline, where the station analysis appears to have missed a local positive maximum in the field.

The eddy flux fields can be used to help quantify the atmosphere's energy cycle during FGGE, and a number of studies on this subject have already been undertaken. In addition to the works by Kung and Tanaka (1983, 1984), Chen and Buja (1983) have used the ECMWF IIIb analyses to study the difference between the two hemispheres in the annual variation and in the vacillation of atmospheric energetics. As for the energy cycle in the northern hemisphere from the GFDL analysis, Figure 13 indicates that it is not very different from what could be deduced from

STATION   GFDL

DIFFERENCE (STATION-GFDL)

FIGURE 7   (a) Hemispheric maps of the transient eddy flux of momentum
at 200 mb for January 1979 based on the station and the GFDL level IIIb
analyses.   Isolines are drawn at intervals of 50 m^{2}s^{-2}.   Negative
values are shaded and indicate southward fluxes.   (b) Difference,
station analysis minus GFDL analysis, of the two fields in 7a.   Isolines
are drawn at intervals of 50 m^{2}s^{-2}.   Negative values are shaded and
indicate stronger northward or weaker southward fluxes in the GFDL
analysis.
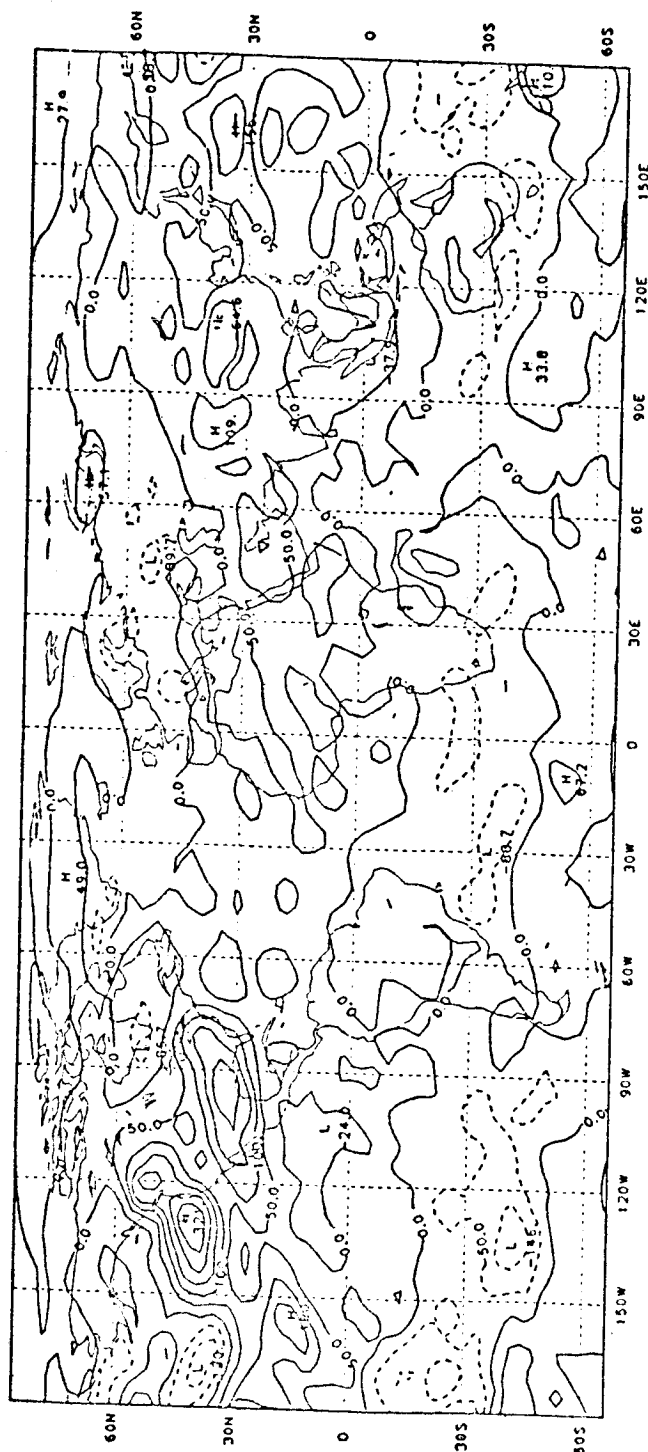
FIGURE 8 Map of the transient eddy flux of momentum at 200 mb generated by the GLAS general circulation model for January. The model run was initialized with the ECMWF analysis for December 15, 1978, but no further data were assimilated. Isolines are drawn at intervals of 50 m^2s^{-2}. Negative values are dashed and indicate southward fluxes.

January 1979
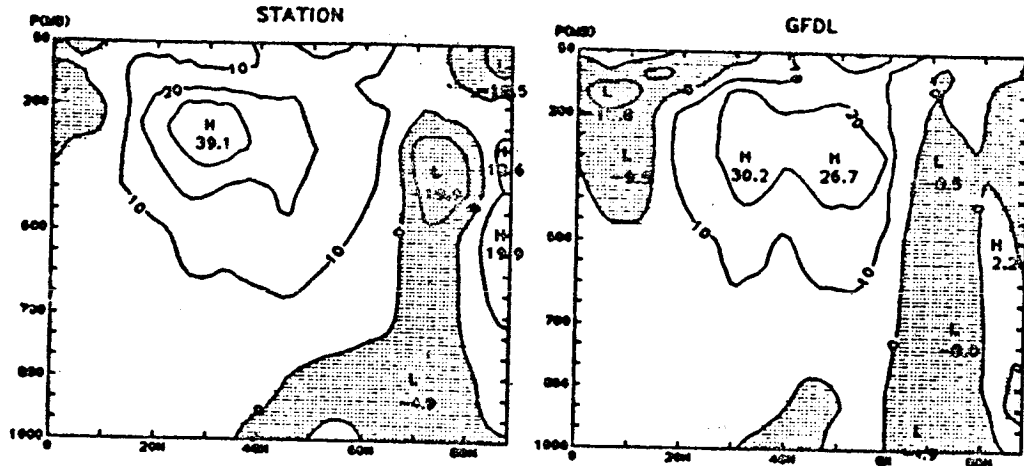
June 1979
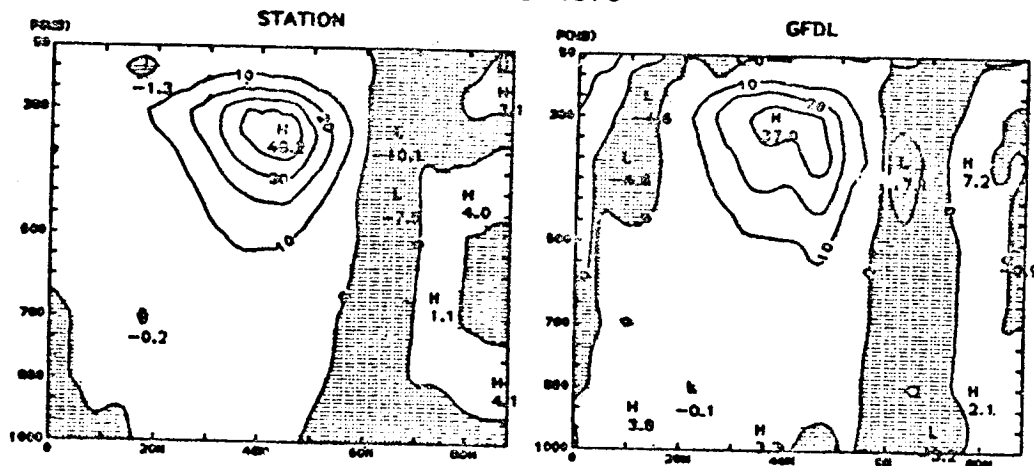
FIGURE 9   Cross-sections of the transient eddy flux of momentum for January and June 1979 based on the station and the GFDL level IIIb analyses.   Negative values are shaded and indicate southward fluxes.

the station data alone.   There are two differences worth noting however.   The first of these is in $C(P_M, K_M)$ in both months shown, not a surprising result in light of this term's dependence on $[\bar{v}]$.   The second difference is in $C(K_{TE}, K_M)$ in January, when the GFDL analysis actually yields a negative value for this barotropic conversion term.   This behavior results in large measure from the strong downgradient flux of $[\overline{u'v'}]$ in the GFDL tropical upper atmosphere, which, as noted above, is not so prominent in either the station or ECMWF analyses that month.

January 1979
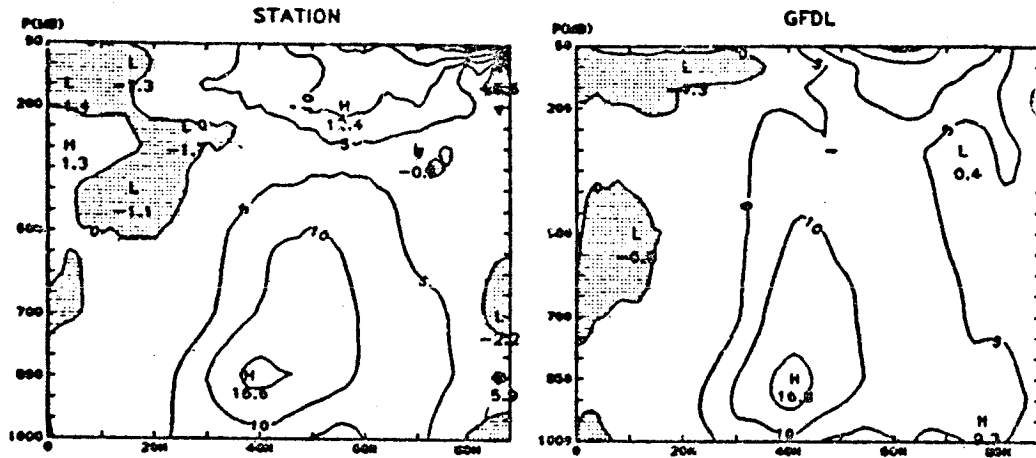
June 1979
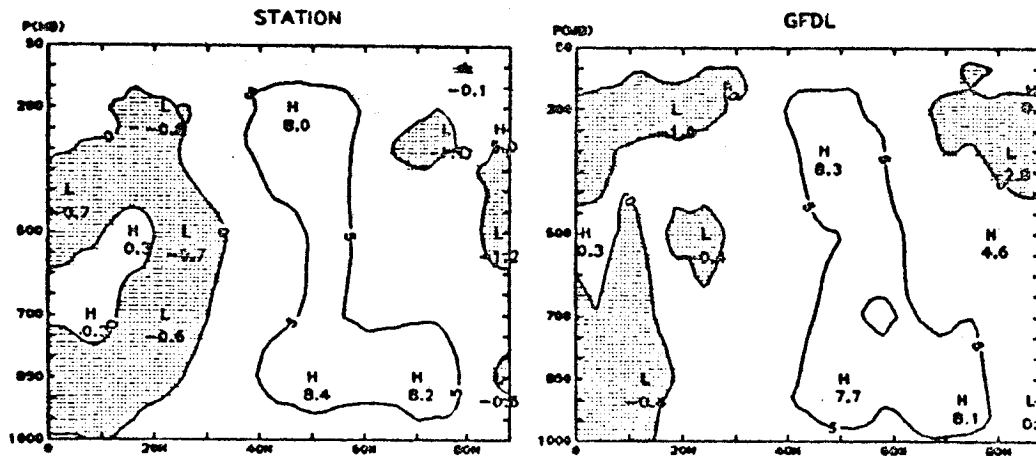
FIGURE 10   Cross-sections of the transient eddy flux of heat for
January and June 1979 based on the station and the GFDL level IIIb
analyses.   Negative values are shaded and indicate southward fluxes.

Finally, with regard to the GFDL analyses, Figure 14 presents the
field of monthly mean specific humidity at 850 mb for June.   It is
worth noting that the moisture data available to the GFDL analysis were
drawn almost entirely from the very same station data used to construct
the station analysis (the aircraft dropwinsonde data being the only
important difference).   It is somewhat surprising therefore to see such
large differences between the two analyses, which must reflect in part
the influence of the GFDL model used in their data assimilation.   The

413

$$\overline{v'T'}, \qquad m\ s^{-1}\ {}^\circ C \qquad 850\ mb$$

January 1979

STATION   GFDL
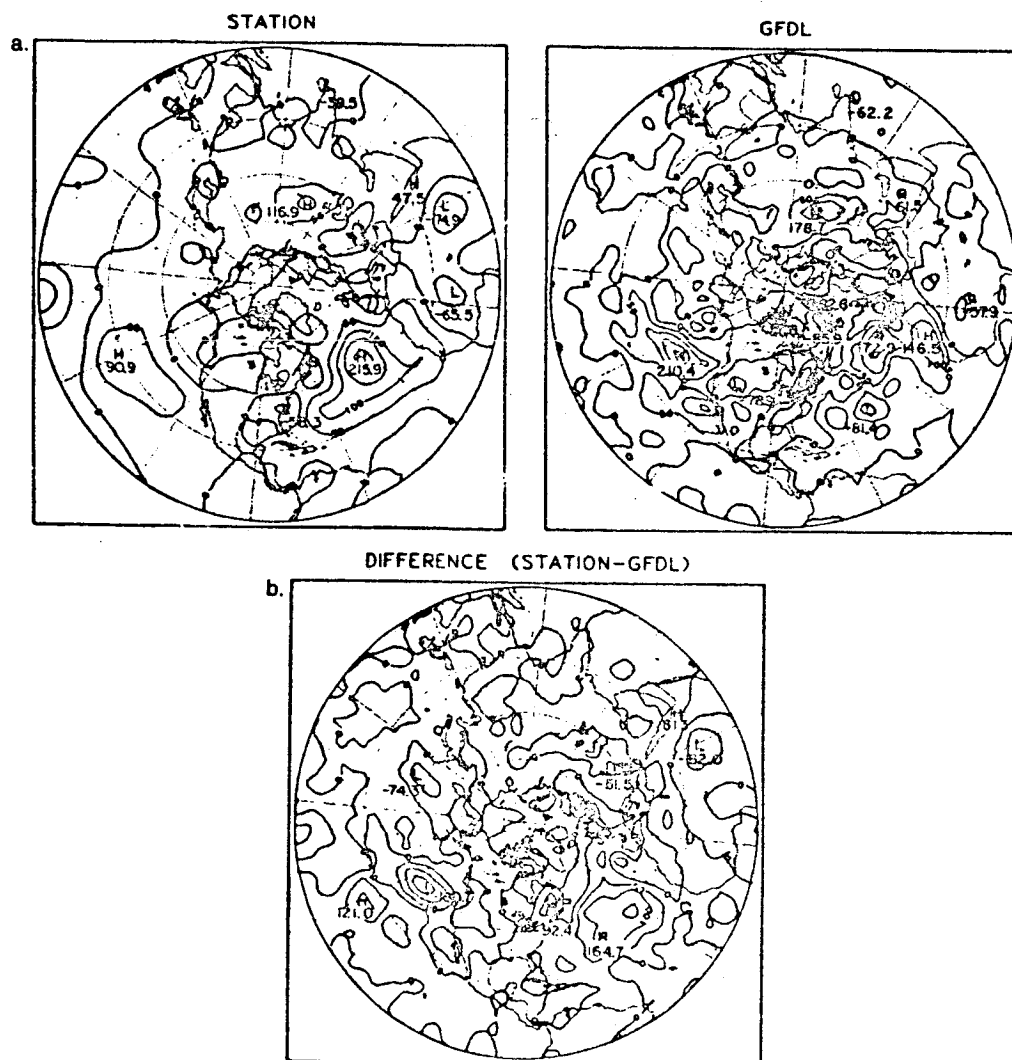

June 1979
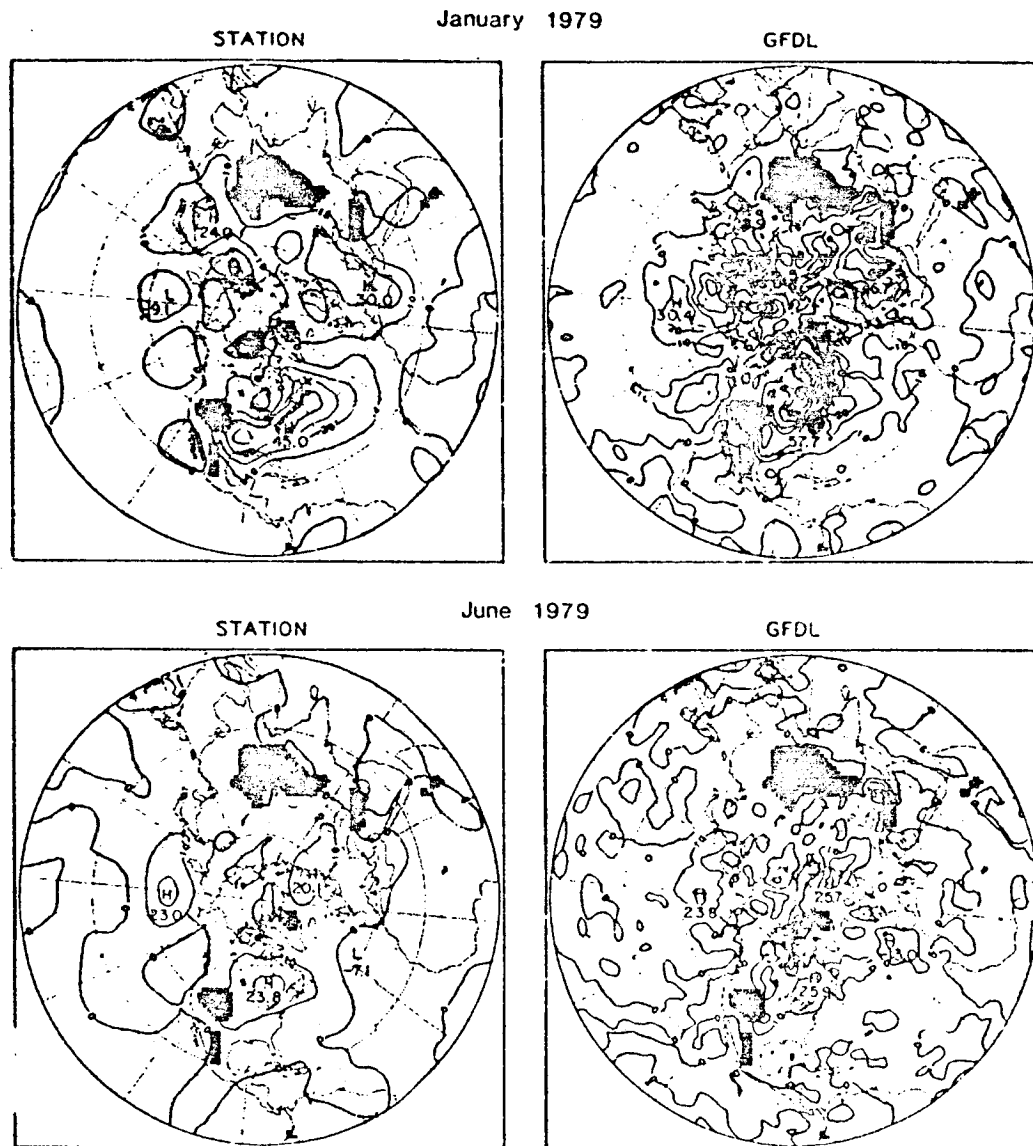
STATION   GFDL

FIGURE 11 Hemispheric maps of the transient eddy flux of heat at 850
mb for January and June 1979 based on the station and the GFDL level
IIIb analyses. Isolines are drawn at intervals of 10 m/s ${}^\circ C$.
Negative values are shaded and indicate southward fluxes. Regions
where the topography is at pressures less than 850 mb are indicated by
the heavy shading.

34

414
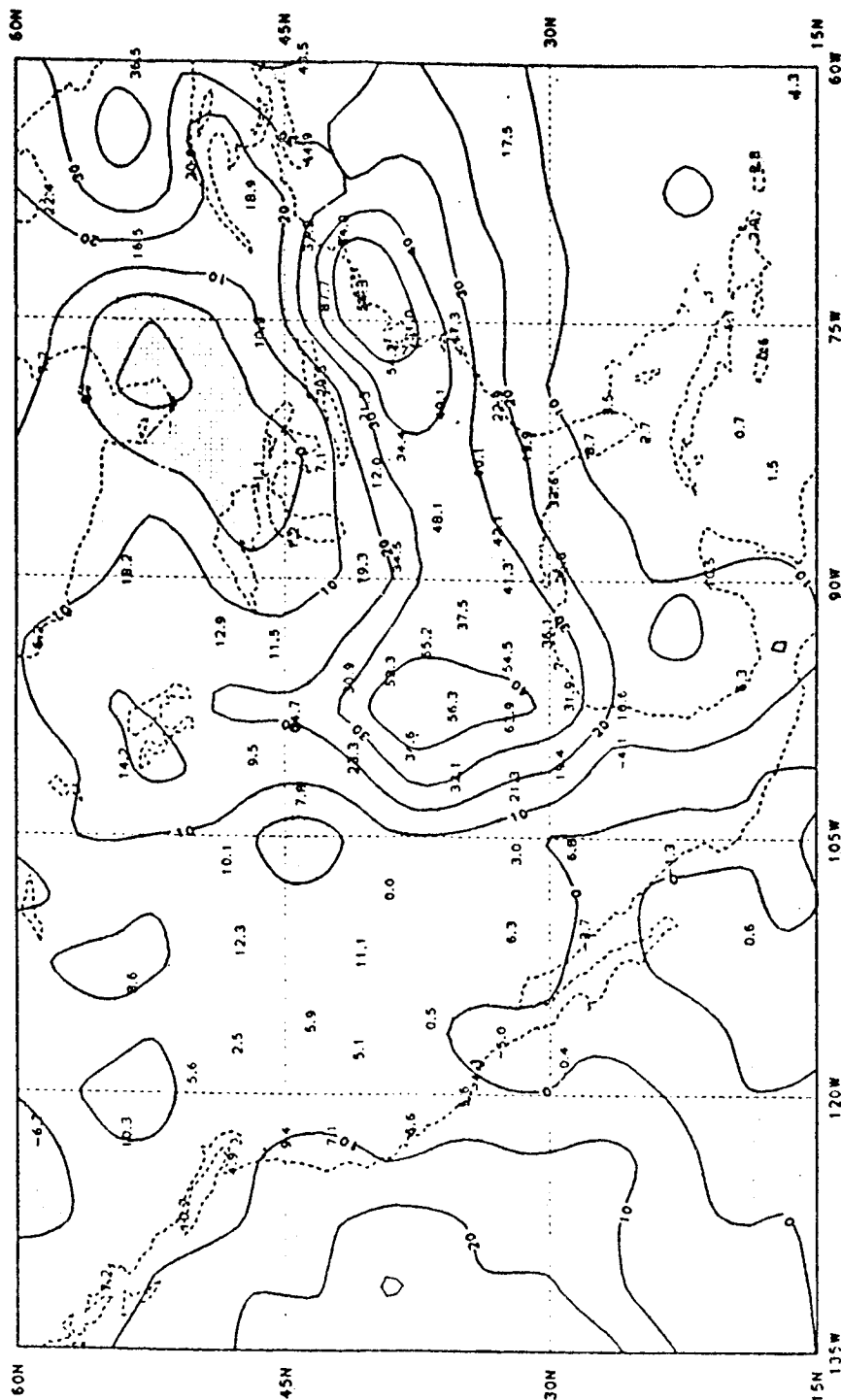
FIGURE 12 Map of the transient eddy heat flux at 850 mb for January 1979 over North America calculated from the GFDL Level IIIb analysis. Isolines are drawn at intervals of 10 m/s °C; negative values are shaded. Also displayed are the monthly mean values of $\overline{v'T'}$ at the rawinsonde stations that passed the cutoff criterion for the month.
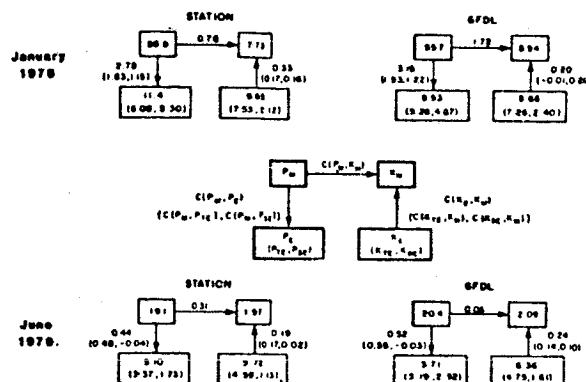
FIGURE 13 Partial energy cycle diagrams based on the station and the GFDL level IIIb analyses for January and June 1979. Values are for the northern hemisphere mass between 1000 and 100 mb. The schematic in the center indicates the layout of the diagrams. Units for energies are 10^5 J m^{-2}, and for conversions W m^{-2}.

GFDL analysis is noticeably noisy, and differences of a factor of 2 between it and the station analysis exist over some portions of the hemisphere, for example, in the subtropical Atlantic.

The field of $\overline{q'v'}$ in Figure 15 demonstrates quite clearly how noisy some of the GFDL analyses can be. It also serves to illustrate a point concerning the quality control of the FGGE water vapor data. Note the extraordinarily large value for the flux over the Arabian peninsula in the GFDL analysis. This unlikely feature can be traced to the erratic soundings during June from Riyadh, which was eliminated from the station analysis. Screening humidity data (or the resultant analyses) for errors is not a well-developed procedure in the current state-of-the-art, and clearly there is a significant disagreement in this instance.

GLAS Analyses

For the Special Observing Periods (SOPs) of FGGE, NASA's Goddard Laboratory for Atmospheric Sciences (GLAS) has also produced Level IIIb analyses, as described by Baker (1983). Baker noted that the GLAS analyses yield realistic mean meridional circulations, and indeed the Hadley cell in the GLAS analysis resembles that in the GFDL analysis shown earlier. Paegle and Paegle (1984) have compared the GLAS 200 mb winds with those from GFDL and ECMWF for 10- and 12-day averaging periods during SOP-1. They concluded that the GLAS analyses resemble those of GFDL with regard to the divergent component of the wind but more closely resemble those of ECMWF with regard to rotational wind amplitudes.

The GLAS analyses have already found considerable use in studies of planetary scale waves (for example, Paegle and Baker, 1982), a subject covered elsewhere in this report. The GLAS analyses have also been

STATION

GFDL

a.

DIFFERENCE (STATION-GFDL)

b.
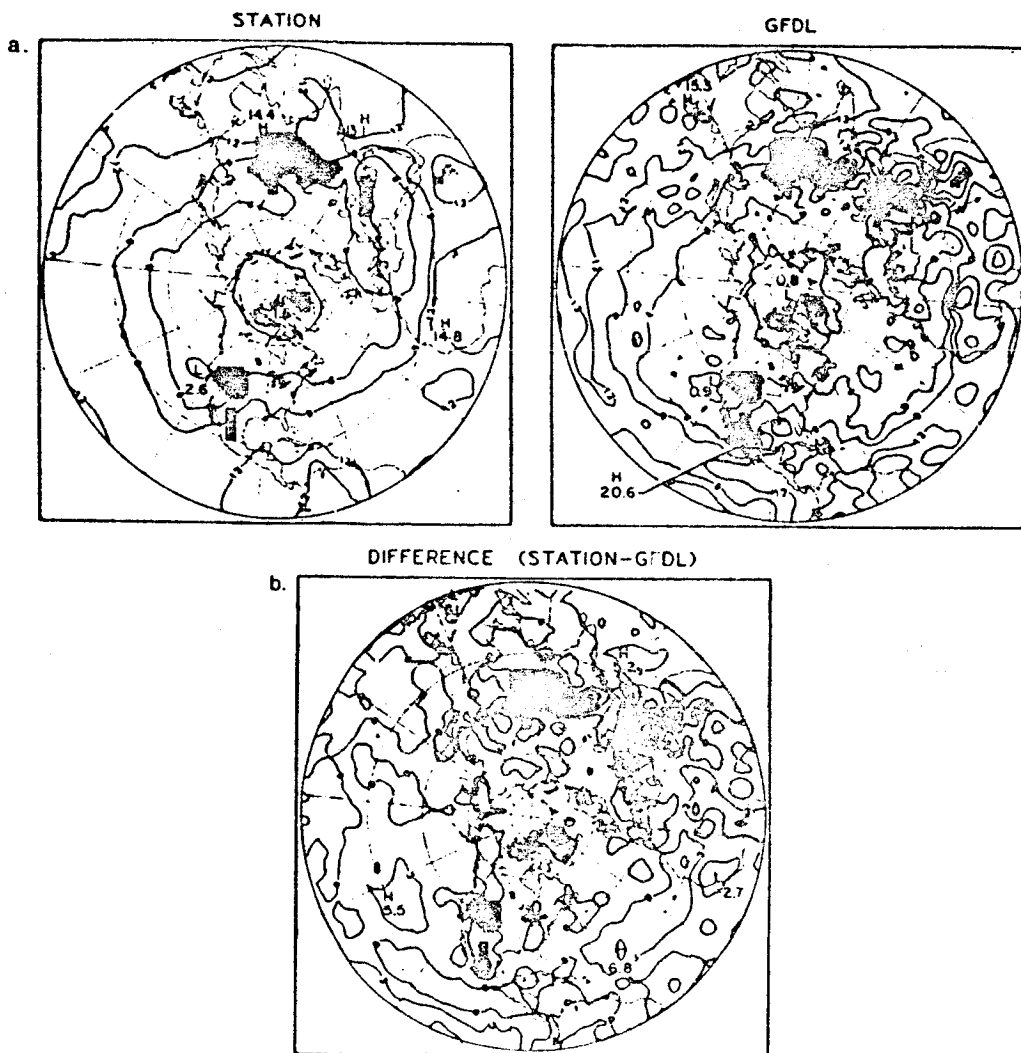
FIGURE 14   (a) Hemispheric maps of the specific humidity at 850 mb for
June 1979 based on the station and the GFDL level IIIb analyses.
Isolines are drawn at intervals of 3 g kg^{-1}. Regions where the
topography is at pressures less than 850 mb are indicated by the heavy
shading. (b) Difference, station analysis minus GFDL analysis, of the
two fields in a. Isolines are drawn at intervals of 3 g kg^{-1}.
Negative values are shaded and indicate higher values of specific
humidity in the GFDL analysis.
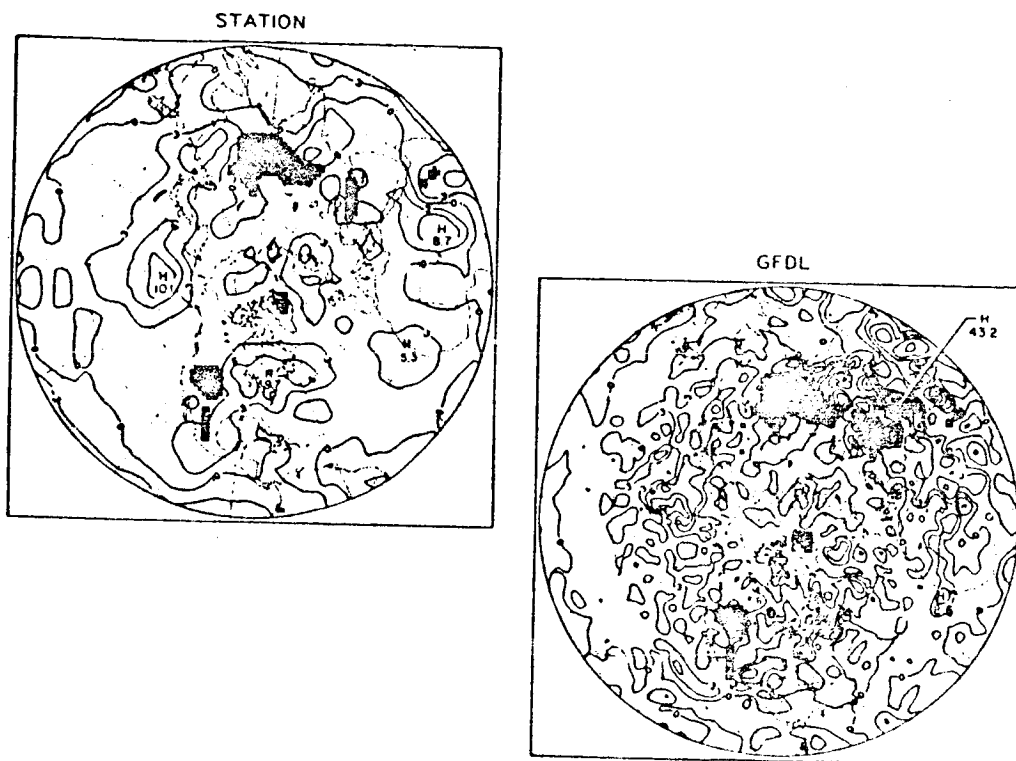
STATION

GFDL

FIGURE 15 Hemispheric maps of the transient eddy flux of moisture at 850 mb for June 1979 based on the station and the GFDL level IIIb analyses. Isolines are drawn at intervals of 3 g kg^{-1} m/s. Negative values are shaded and indicate southward fluxes. Regions where the topography is at pressures less than 850 mb are indicated by the heavy shading.

used to investigate the impact of the FGGE satellite data on general circulation statistics by Salstein et al. (1984). In this work, output from two experiments (described by Halem et al., 1982) was used to form statistics for the 30-day period from January 6 to February 4. In one experiment, all the FGGE data were assimilated; in the other, satellite-related data were withheld (NOSAT). Figures 16 and 17 contain the fields of $\bar{u}$, and $\bar{T}$ derived from the two experiments. Although some locally large differences between the FGGE and NOSAT experiments do exist (particularly over the southern hemisphere), the overall impression is that the two analyses are fairly similar.

DISCUSSION AND FINAL REMARKS

The extensive data collection effort that marked FGGE raised the hope that substantially better data sets would be available with which to
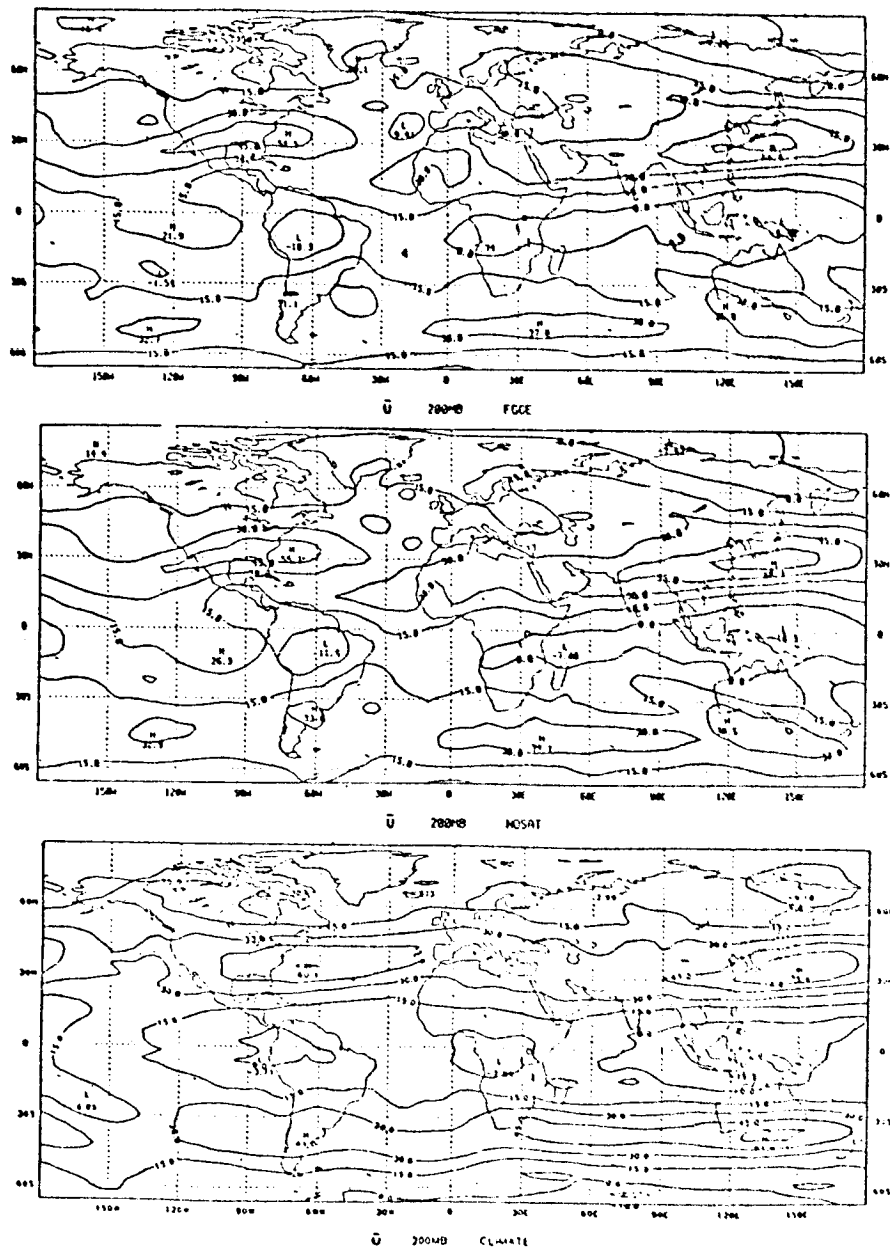
FIGURE 16 Maps of the mean zonal velocity at 200 mb for the period
January 6 to February 4, 1979 based on GLAS analyses utilizing all FGGE
data (FGGE) and all but satellite related FGGE data (NOSAT). Also
shown is the field generated by the GLAS general circulation model
without the benefit of data. Isolines are drawn at intervals of 15 m/s.
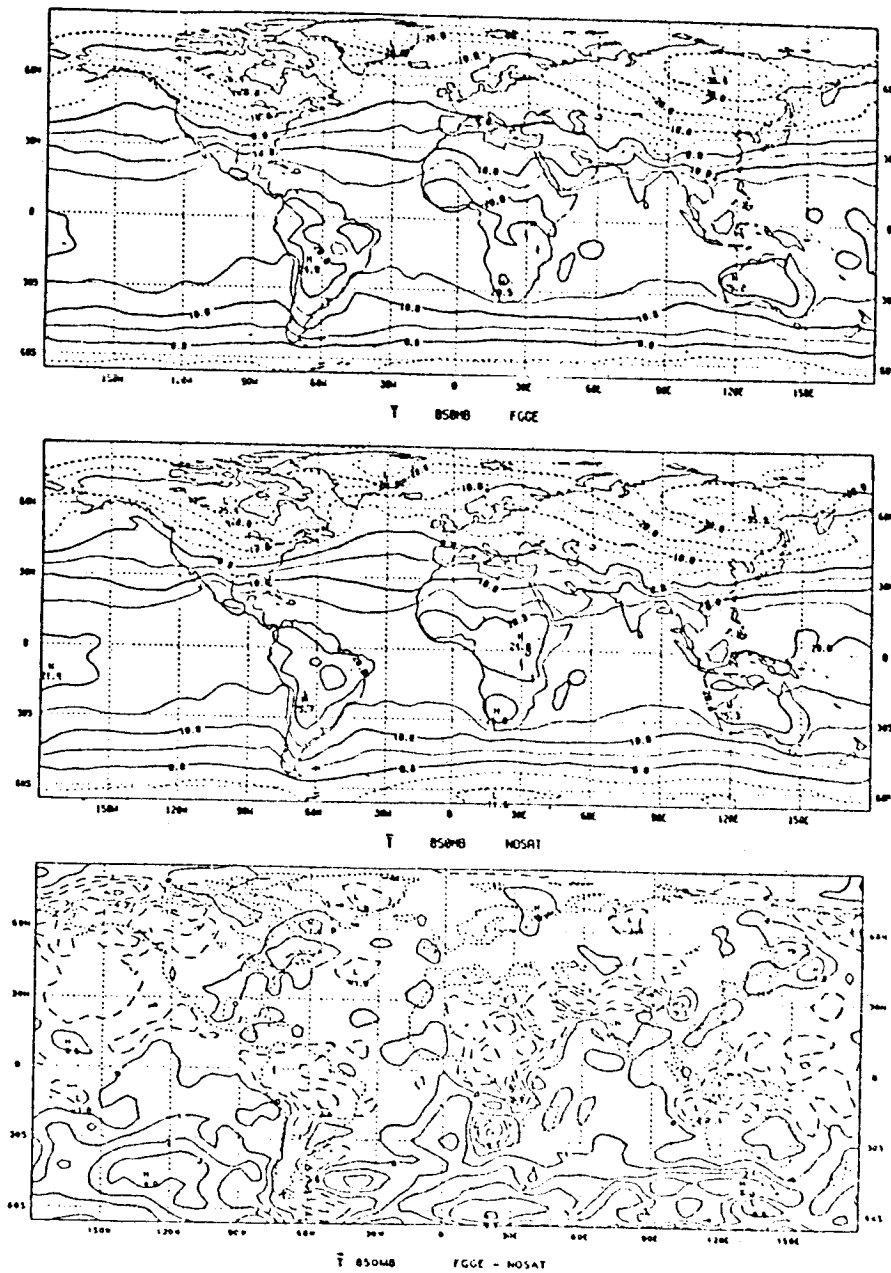
FIGURE 17 As in Figure 16, but for the mean temperature at 850 mb.
Isolines are drawn at intervals of 5°C and negative values are
shaded. In the bottom panel, the difference field, FGGE minus NOSAT;
isolines are drawn at 1°C and negative values are shaded.

study the general circulation. As has been seen however, the impact of the new FGGE observing systems, at least over the northern hemisphere, has not been especially dramatic. To be sure, traditional analyses based on the upper air station network alone display some important shortcomings. For example, they seem to miss some extrema in the circulation fields over station-sparse regions. Presumably, such features have also been missed in climatologies based on the station network in the past. Overall, though, the circulation statistics derived from the station analyses during FGGE appear rather good.

On the other hand, circulation statistics from the Level IIIb analyses raise a number of questions. It is not this author's intention to appear unduly critical of the IIIb data sets. Most of the deficiencies perceived can be traced to known shortcomings in the schemes used to produce them. Nevertheless, when viewed as an ensemble, the differences among the analyses are often large enough to suggest that considerable uncertainty remains in the ability to quantify the general circulation. Certainly, the level of uncertainty seems too high in the current IIIb analyses to encourage renewed efforts at evaluating the roles of vertical fluxes and of water vapor in the general circulation.

This situation may well improve. Much has been learned about data assimilation techniques since (and because of) the production of the original IIIb analyses. Plans do exist to create a second generation of Level IIIb analyses utilizing improved assimilation models and IIb data. These efforts should be supported, along with efforts to reassess the use of these data for studying outstanding problems in general circulation research. One note of caution must be sounded, however. The work cited here suggests that, regardless of which IIIb assimilation model is used, the FGGE observations may not have been sufficient in themselves to define the real circulation more accurately. If this is so, the next generation of IIIb analyses may still be less adequate than hoped for.

ACKNOWLEDGMENT

REFERENCES

Astling, E. G. (1984). A comparison of 200 mb wind fields from ECMWF and GFDL level IIIb analysis data. Global Weather Experiment Newsletter 3, 15-19.

Baker, W. E. (1983). Objective analysis and assimilation of observational data from FGGE. Mon. Wea. Rev. 111, 328-342.

Chen, T.-C., and L. E. Buja (1983). A comparison study for the time variation of the atmospheric energetics between two hemispheres during the FGGE year: Annual variation and vacillation. First International Conference on Southern Hemisphere Meteorology, Amer. Meteorol. Soc., 21-24.

Chen, T.-C., and J. G. Vorwald (1984). A comparison of moisture transport analysis using ECMWF and GFDL FGGE IIIb data. *Global Weather Experiment Newsletter 4*, 8-10.

Halem, M., E. Kalnay, W. E. Baker, and R. Atlas (1982). An assessment of the FGGE satellite observing system during SOP-1. *Bull. Amer. Meteorol. Soc. 63*, 407-426.

Julian, P. R. (1984). Some comparisons of ECMWF IIIb and GFDL IIIb analyses in the tropics. *Global Weather Experiment Newsletter 3*, 20-22.

Kanamitsu, M. (1981). Some climatological and energy budget calculations using the FGGE IIIb analyses during January 1979. *Dynamic Meteorology: Data Assimilation Methods* (L. Bengtsson et al., editors), Springer-Verlag, 263-318.

Koehler, T. L., and K. D. Min (1984). Available potential energy and extratropical cyclone activity during the FGGE year. *Tellus 36A*, 64-75.

Kung, E. C., and H. Tanaka (1983). Energetics analysis of the global circulation during the Special Observing Periods of FGGE. *J. Atmos. Sci. 40*, 2575-2592.

Kung, E. C., and H. Tanaka (1984). Spectral characteristics and meridional variations of energy transformations during the First and Second Special Observing Periods of FGGE. Unpublished manuscript.

Lorenc, A. C., and R. Swinbank (1984). On the accuracy of general circulation statistics calculated from FGGE data--a comparison of results from two sets of analyses. *Quart. J. Roy. Meteorol. Soc.*, in press.

Lorenz, E. N. (1970). Forecast for another century of weather progress. *A Century of Weather Progress*, Amer. Meteorol. Soc., 18-24.

Oort, A. H., and E. M. Rasmusson (1971). *Atmospheric Circulation Statistics*. NOAA Prof. Paper No. 5, 323 pp. (NTIS COM-72-50295).

Paegle, J., and W. E. Baker (1982). Planetary-scale characteristics of the atmospheric circulation during January and February 1979. *J. Atmos. Sci. 39*, 2521-2538.

Paegle, J. N., and J. Paegle (1984). Selected comparisons of FGGE level IIIb 200 mb winds. *Global Weather Experiment Newsletter 3*, 6-14.

Rosen, R. D., D. A. Salstein, J. P. Peixoto, A. H. Oort, and N.-C. Lau (1984). Circulation statistics derived from level IIIb and station-based analyses during FGGE. Unpublished manuscript.

Salstein, D. A., and R. D. Rosen (1984). Impact of satellite data on large-scale circulation statistics as determined from GLAS analyses during FGGE SOP-1. Unpublished manuscript.

van Loon, H. (1980). Transfer of sensible heat by transient eddies in the atmosphere on the southern hemisphere: An appraisal of the data before and during FGGE. *Mon. Wea. Rev. 108*, 1774-1781.

REVIEW OF RESEARCH ON WAVE MEAN FLOW
INTERACTIONS USING FGGE DATA

Richard L. Pfeffer
Florida State University

ABSTRACT

Comparison is made between the conventional Eulerian diagnostics of
wave mean flow interactions in the atmosphere and the diagnostics
introduced by Andrews and McIntyre (1976). In the latter, the
meridional circulation is represented by a "residual" circulation, and
the eddy torque in the zonal momentum equation by the Eliassen-Palm
(1960) flux divergence (or equivalently, by the poleward eddy flux of
geostrophic potential vorticity). It is found that, while the new
diagnostics are useful in studying stratospheric warmings and transports
of conservative quantities, the conventional diagnostics are more
useful in studying global energetics and wave mean flow interactions in
the troposphere and lower stratosphere. Case studies diagnosed with
FGGE IIIb data are presented to illustrate this point.
    Kung and Tanaka's (1983) comparisons of the atmospheric energy cycle
for SOP-1 and SOP-2, estimated with the use of the ECMWF and GFDL FGGE
IIIb data bases, are used to assess the uncertainty in calculations of
energetics based on the use of FGGE IIIb data. These results demon-
strate the high degree of model dependence in the FGGE IIIb data sets.

BACKGROUND

The maintenance of the zonally averaged westerly wind current and the
interaction between this current and synoptic-scale atmospheric waves
have been the subject of much attention in the meteorological litera-
ture. Starr and his colleagues (Starr, 1968; Starr et al., 1970)
demonstrated that the rate of production of zonal kinetic energy
through the action of Reynolds' stresses associated with large-scale
atmospheric eddies is of the correct order of magnitude to maintain
this energy against friction. Later, Andrews and McIntyre (1976), Boyd
(1976), and others stressed the need to take into account the secondary
meridional circulations produced by the eddies in order to assess
properly the net effect of the eddies on the mean zonal flow.
    Pfeffer (1981) presented calculations of the acceleration of the
zonally averaged current ($\bar{u}$) by synoptic-scale waves in the atmosphere
using the conventional Eulerian formalism. In this formalism, the eddy

422

43<

flux convergence of momentum appears in the $\partial\bar{u}/\partial t$ equation as a mechanical torque that, according to the data, acts to accelerate the upper tropospheric westerlies in midlatitudes and to decelerate them in the tropics and in the Arctic. The eddy induced 3-cell mean meridional circulation redistributes zonal momentum in the vertical direction. In the northern hemisphere winter, slightly more than half the zonal momentum increase in midlatitudes, which is brought about by the eddy flux convergence of momentum in the upper troposphere, is communicated to the lower troposphere mainly through the action of the Coriolis force on the eddy induced Ferrel cell. The net effect of the eddies, including the eddy induced meridional circulation, is to accelerate the air from west to east in midlatitudes and to decelerate it in the tropics and in the Arctic. This acceleration is in the same direction as the upper tropospheric eddy torque but is redistributed more evenly in the vertical. Pfeffer's calculations showed also that the rate of production of zonal kinetic energy by the eddies, including the contribution of the eddy induced meridional circulation, is of the order of 70 percent (or greater) the rate of production calculated by Starr et al. (1970) excluding this contribution. In winter, the eddy induced meridional circulation actually appears to augment the rate of production of zonal kinetic energy.

Andrews and McIntyre (1976) introduced an alternative formalism in which the mean meridional circulation is represented by a "residual circulation," which is closely related to the zonally averaged Lagrangian mean circulation, and the eddy torque in the zonal momentum equation is represented by the Eliassen-Palm flux divergence, or equivalently, by the poleward eddy flux of quasi-geostrophic potential vorticity. Their transformed system of equations has been found to be useful in studying stratospheric dynamics for several reasons.

1. The changes that take place in the strength and direction of the polar night jet at times of stratospheric warmings are generally in the same direction as the "eddy torque" in this formalism, but not necessarily in the conventional formalism.

2. More often than not, the terms in the transformed equations are all of the same order of magnitude during stratospheric warmings, whereas in the conventional Eulerian formalism the local acceleration of the zonally averaged zonal wind is often given by a small difference between large eddy and meridional circulation terms.

3. It is easier to explain how certain features of the ozone and water vapor distribution in the stratosphere arise in terms of the Lagrangian or residual mean meridional circulation than it is in terms of the conventional Eulerian mean meridional circulation.

In the troposphere and lower stratosphere, which comprise 90 percent of the mass of the atmosphere, the present author finds, however, that in the transformed equations the eddy induced zonal wind acceleration $(\partial\bar{u}/\partial t)$ is a very small difference between the divergence of the Eliassen-Palm flux and the Coriolis force acting on the residual mean meridional circulation. Moreover, since $\partial\bar{u}/\partial t$ is usually of the same sign as the "eddy torque" in the conventional formalism but of

opposite sign in the new formalism, the former gives a clearer description of the effect of the eddies on the mean zonal current.

In the present paper, case studies diagnosed with the use of FGGE IIIb data will be presented to illustrate the value of the new formalism in studying stratospheric warmings (as reported by Palmer, 1981a,b) and the value of the conventional formalism in studying the dynamics of wave mean flow interactions in the troposphere and lower stratosphere (as investigated by the speaker). In order to assess the uncertainty of the results, the conventional energy cycle for SOP-1 and SOP-2 calculated from the ECMWF and GFDL FGGE IIIb data bases as reported by Kung and Tanaka (1983) will be compared.

THE STRATOSPHERIC WARMING OF FEBRUARY 1979

Figure 1, after Palmer (1981a), shows the evolution of the zonal westerlies north of 20°N latitude during the period February 17 to 27, 1979. Here, the breakdown of the stratospheric polar night jet and the reversal to equally strong easterlies by the end of this period are seen. Palmer (1981b) diagnosed the evolution of $\bar{u}$ averaged from 60° to 80°N at 1 mb using the conventional and transformed zonal momentum equations. His results are shown in Figure 2. Here, $\bar{v}$ is the zonally averaged northward component of velocity; v^* is the residual mean meridional circulation; $\nabla \cdot F$ is the divergence of the Eliassen-Palm flux; $\overline{u'v'}$ is the poleward eddy flux of momentum; ρ is density; $z = H \ln(p/1000)$, where p is pressure, and H, scale height; ϕ is latitude; and r_o is the radius of the earth. Palmer's results show that, in the conventional formalism, $\partial u/\partial t$ is a small difference between two large and oppositely directed terms, namely, the "eddy torque"

$$(- \frac{1}{r_o \cos^2 \phi} \frac{\partial \overline{u'v'} \cos^2 \phi}{\partial \phi})$$

and the Coriolis force ($f\bar{v}$), and that $\partial \bar{u}/\partial t$ does not appear to correlate well with either quantity. In the transformed equations, $\partial u/\partial t$ appears to correlate much better, although not perfectly, with the "eddy torque"

$$(\frac{1}{\rho_o r_o \cos\phi} \ell z/H \nabla \cdot F)$$

which is generally larger by a factor of 2 than the Coriolis force ($f\bar{v}^*$) acting on the residual mean meridional circulation. The Coriolis terms were calculated as residuals in the momentum equation. Assuming that diabatic effects are negligible, $\bar{v}$ and $\bar{v}^*$ can be interpreted as the meridional circulations induced by the eddies, plus the sum of the errors in estimating the magnitudes of $\partial \bar{u}/\partial t$ and the eddy torques.
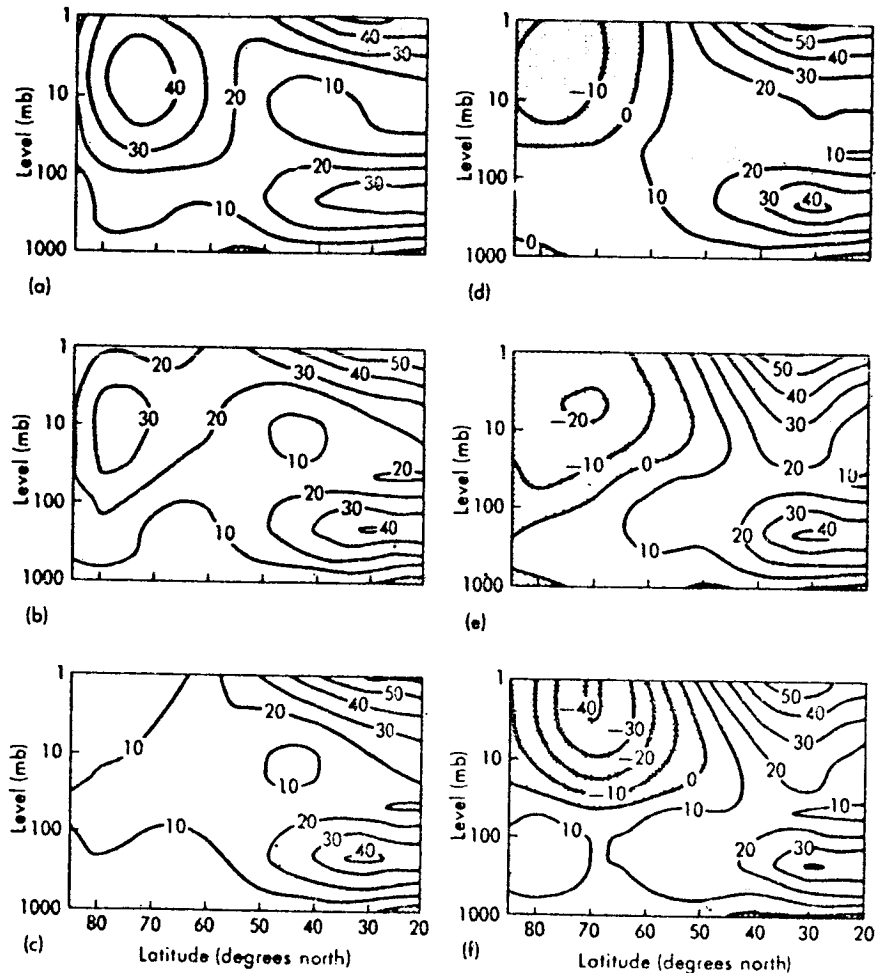
FIGURE 1 Meridional cross-section of zonal mean wind velocity (m/s). Regions of easterly winds are stippled: (a) February 17, (b) February 19, (c) February 20, (d) February 21, (e) February 23, and (f) February 27. The values of the pressure coordinates used are related to the scale-height coordinates 100 mb, 14.7 km; 40 mb, 20.5 km; 10 mb, 29.4 km; 4 mb, 35.2 km; and 1 mb, 44.1 km (after Palmer, 1981a).

In terms of the transformed equations, stratospheric warming and the deceleration and reversal of the polar night jet can be considered to take place when and where there is a strong convergence of the Eliassen-Palm flux. Figure 3 clearly shows this convergence. This concept is consistent with our previous understanding that stratospheric warmings are produced by adiabatic wave propagation from the troposphere, since the Eliassen-Palm flux may be interpreted as the flux of wave activity
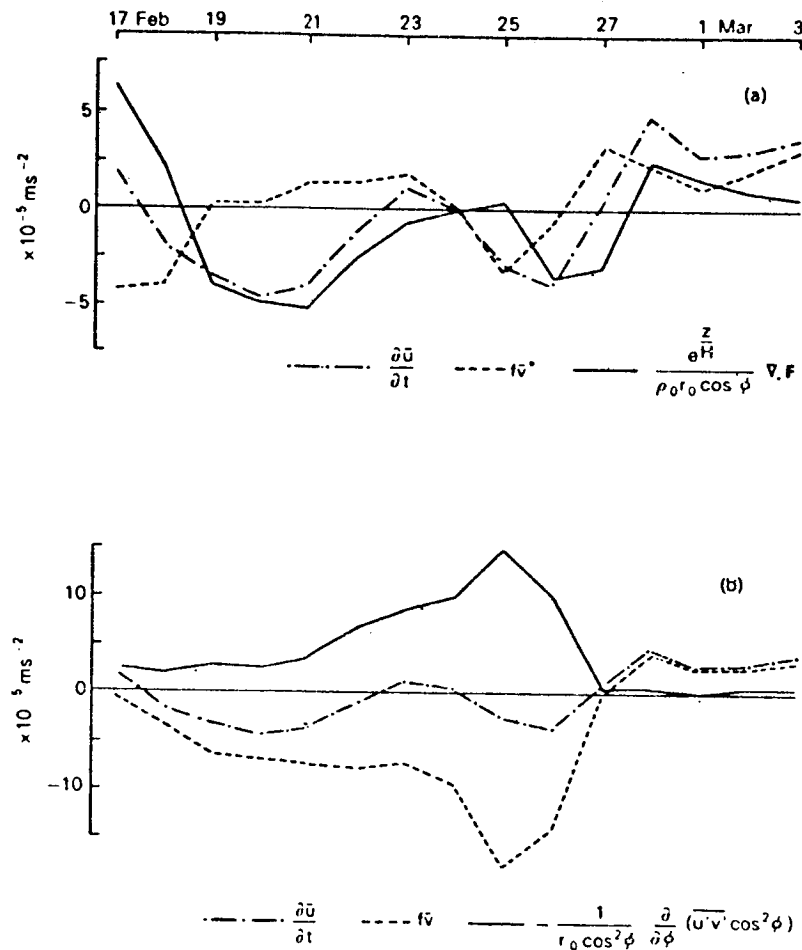
FIGURE 2 Momentum budget averaged with cosine of latitude weighting between 60°N and 80°N for the period February 17 to March 3, 1979, at 1 mb. (a) Transformed formalism, (b) standard formalism (after Palmer, 1981b).

from one latitude and height to another when the eddy dynamics are similar to Rossby waves (Edmond et al., 1980).

TROPOSPHERIC DYNAMICS

Figure 4, after Pfeffer (1981), shows the zonal momentum tendency in the northern hemisphere winter and summer brought about by the eddies, together with the contributions to this tendency from the "eddy torque" and Coriolis force ($\bar{v}$, $\bar{\omega}$ terms) in the conventional Eulerian formalism.
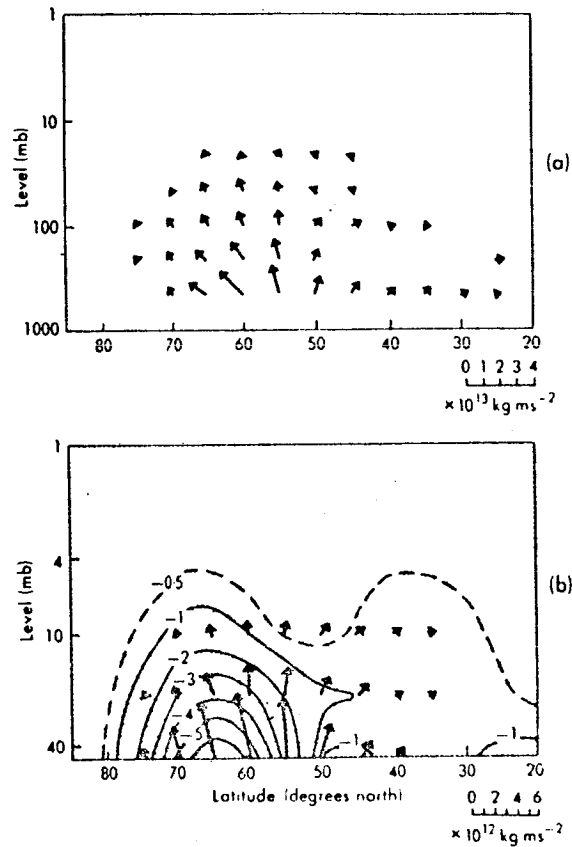
FIGURE 3 Total Eliassen–Palm flux and divergence for February 21, 1979. (a) Troposphere and stratosphere, (b) stratosphere only. Contours of divergence are labeled in units of 10^8 kg s^{-2}. Magnitudes of arrows are given by the scales (after Palmer, 1981b).

According to this formalism, the eddy flux of momentum exerts a torque on the zonal current, mainly in the upper troposphere, accelerating the air from west to east in midlatitude and from east to west at lower and higher latitudes. The eddy induced meridional circulation redistributes some of this momentum in the vertical through the action of the Coriolis force, with the result that the net westerly acceleration in each latitude band is more evenly distributed with altitude. The zonal momentum tendency ($\partial \bar{u}/\partial t$) in the upper troposphere correlates well with the eddy torque

$$\left(- \frac{1}{r_o \cos^2 \phi} \; \frac{\partial \; \overline{u'v'} \cos^2 \phi}{\partial \phi} \right) - \frac{\partial \; \overline{u'\omega'}}{\partial p}$$
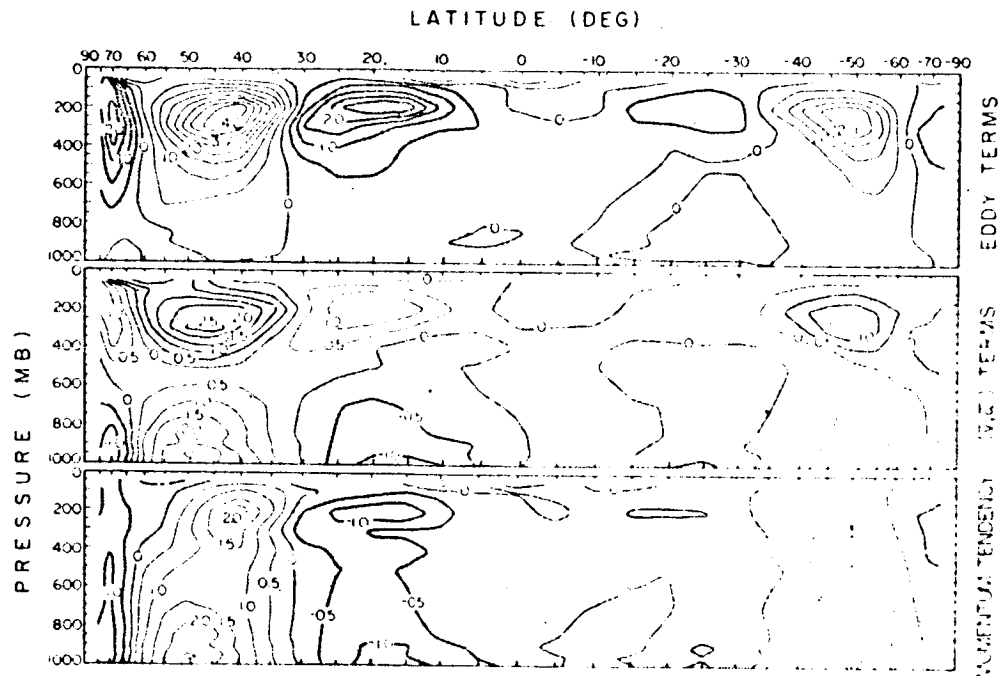
LATITUDE (DEG)

FIGURE 4 Winter (positive latitudes) and summer (negative latitudes) momentum budget due to eddy forcing (after Pfeffer, 1981, Figure 8) using the conventional Eulerian formalism. Units are 10^{-5} m s^{-2}. The peak value of the momentum tendency in winter represents an acceleration of 2 m/s day^{-1}. (Data source: Oort and Rasmusson, 1971.)

which is from 1.5 to 2 times larger than the Coriolis force. Clearly, $\partial \bar{u}/\partial t$ is not determined as a small difference between large quantities.

Figure 5 shows the momentum balance in the transformed formalism calculated recently by the author from the same data. In this formalism, the zonal momentum tendency appears as a small difference between very large and oppositely directed forces, in this case the poleward eddy flux of potential vorticity, which is proportional to the Eliassen-Palm flux divergence, and the Coriolis force acting on the residual mean meridional circulation. The pattern of $\partial u/\partial t$ is uncorrelated with either force and, in the midlatitude troposphere, is for the most part of opposite sign to the "eddy torque." Clearly the new formalism is not as useful in the diagnostics of wave mean flow interactions in the troposphere as is the conventional formalism.

In order to understand the reason for the foregoing result, we must examine the nature of the residual circulation. The equation governing this circulation is
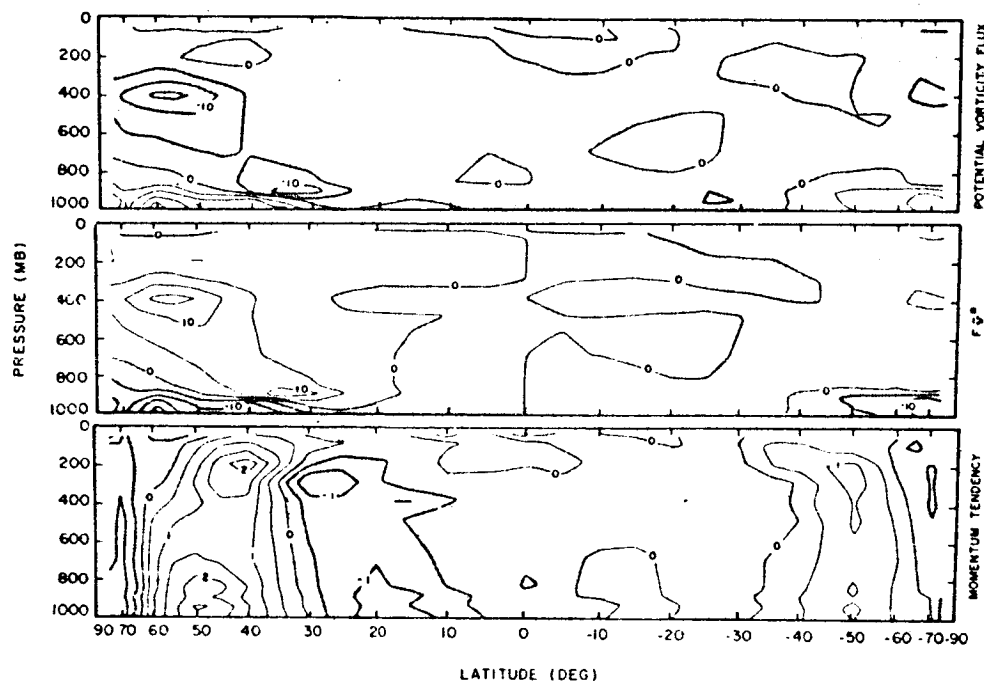
FIGURE 5 Winter (positive latitudes) and summer (negative latitudes) momentum budget due to eddy forcing using the transformed formalism of Andrews and McIntyre (1976). Units are 10^{-5} m s^{-2}. The peak value of the momentum tendency in winter represents an acceleration of 2 m/s day^{-1}. (Data source: Oort and Rasmusson, 1971.)

$$ A \frac{\partial^2 \psi^*}{\partial \eta^2} + \frac{\partial}{\partial p} \left(C \frac{\partial \psi^*}{\partial p} \right) = - D \frac{\partial \overline{v'q'}}{\partial p} \tag{1} $$

with the boundary conditions

$$ \psi^* = \begin{cases} \overline{v'\theta'}\cos\psi / - \dfrac{\partial \overline{\theta}}{\partial p} & \text{at the lower and upper boundaries} \\ 0 & \text{at the poles} \end{cases} $$

Here, θ is the potential temperature; q, the geostrophic potential vorticity; v, the northward component of velocity; $\eta \equiv \sin\phi$, A, C, and D are functions of latitude and pressure; and

$$ \overline{v}^* = \frac{1}{\cos\phi} \frac{\partial \psi^*}{\partial p} ; \quad \overline{\omega} = - \frac{1}{r\cos\phi} \frac{\partial \psi^*}{\partial \phi} , $$
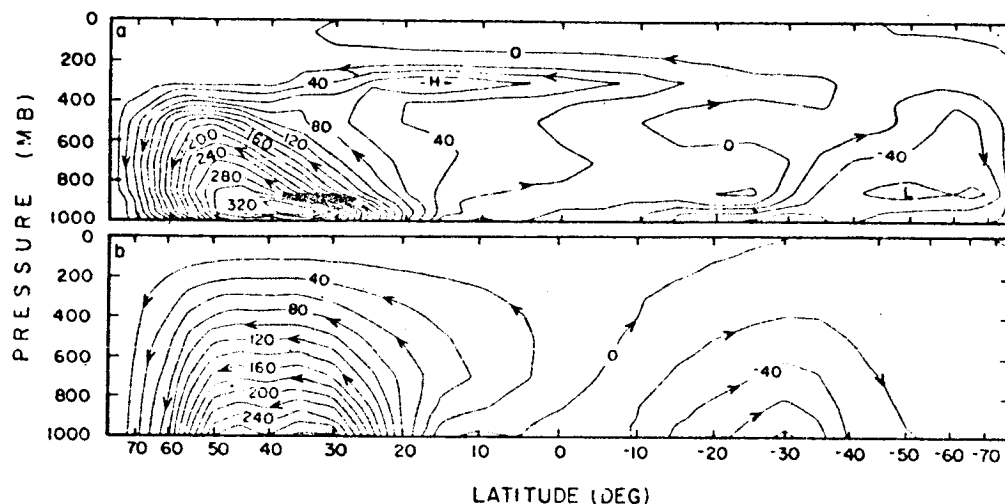
FIGURE 6 (a) Streamfunction (ψ*) for the eddy induced residual mean meridionala circulation. Winter is at positive latitudes; summer is at negative latitudes. Units are m mb s^{-1} (a m mb s^{-1} is equivalent to 0.41 x 10^{12} g s^{-1} mass flow). Data source: Oort and Rasmusson (1971). (b) Component of ψ* induced by the poleward eddy flux of heat at the lower boundary.

where ω is the vertical component of velocity in pressure coordinates. A similar equation (Eliassen, 1952; Kuo, 1956) with ψ = 0 on all boundaries governs the mean meridional circulation in the conventional Eulerian formalism.

At the top of the atmospheric, ψ* may be considered to vanish because of the very large magnitude of $\partial\bar{\theta}/\partial p$. But, at the lower boundary, there are strong poleward fluxes of heat and moderate values of $\partial\bar{\theta}/\partial p$, with the result that the lower boundary condition exerts a strong influence on the solution of ψ* throughout the troposphere and lower stratosphere. This influence may be assessed by solving equation (1) with $\overline{v'q'}$ = 0 everywhere. This solution and the solution with the forcing function and boundary conditions fully specified from the data are shown in Figures 6b and 6a, respectively. It is seen that the lower boundary condition contributes substantially to the eddy induced residual circulation (ψ*) serving to enhance the positive contribution of f$\bar{v}$* to the zonal acceleration throughout the troposphere and lower stratosphere. In midlatitudes, where locally $\overline{v'q'}$ (and therefore ∇· F) is negative, the ψ* circulation induced by the poleward eddy heat flux at the lower boundary causes the positive contribution of f$\bar{v}$* to exceed the negative contribution of $\overline{v'q'}$, with the result that the air is accelerated locally from west to east. It is therefore incorrect to conclude, as some investigators have done, that because $\overline{v'q'}$ (or ∇· F) is the only wave induced forcing of the mean state in the transformed system of equations, the distribution of
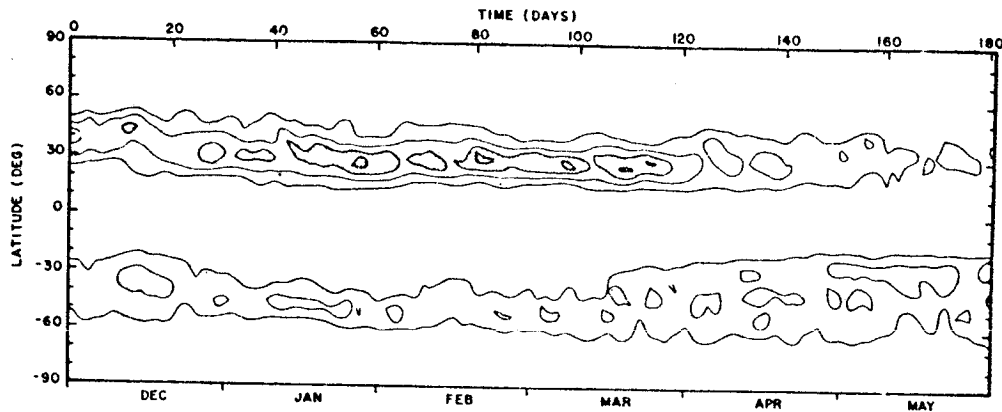
FIGURE 7   Distribution of zonal kinetic energy (K_Z) per unit mass at 200 mb from December 1, 1978 through May 31, 1979. Contour intervals are 250 m^2 s^{-2}. Shaded area represents values greater than 750 m^2 s^{-2}.

$\partial \bar{u}/\partial t$ in space and time should correlate better with the divergence of the Eliassen-Palm flux than it does with the eddy momentum flux convergence. The fact that it does so in stratospheric warmings must be due in part to the distance from the lower boundary and in part to the relative magnitudes of the poleward fluxes of heat and momentum and the coefficients A and C.

THE ONSET OF THE WINTER JET IN DECEMBER 1978

Having established the greater usefulness of the conventional Eulerian formalism in diagnostic studies of wave-mean flow interactions in the troposphere and lower stratosphere, a case study during FGGE is now discussed. Figure 7 shows the distribution of zonal kinetic energy (K_Z) per unit mass at 200 mb during the first five months of FGGE. In the northern hemisphere, the maximum of K_Z shifts equatorward from midlatitudes to the subtropics during the period December 15 to 20 and remains there for the rest of the winter season. The evolution of the zonal momentum distribution in the meridional plane during this five-day period is shown in Figure 8. Here, $\bar{u}$ is weighted by $\cos\phi$ in order to take into account the convergence of the meridians since the abscissa is linear in ϕ. It is seen that the maximum of $\bar{u} \cos\phi$ at 200 mb moves progressively equatorward and strengthens from December 15 to 20. The average rate of change of $\bar{u} \cos$ during this period is shown in Figure 9.

Figure 10 presents the conventional Eulerian diagnostics of the zonal momentum tendency due to the eddies. The figure shows a pattern of eddy flux convergence and divergence of momentum that is reflected in the zonal momentum tendency, after taking into account the Coriolis
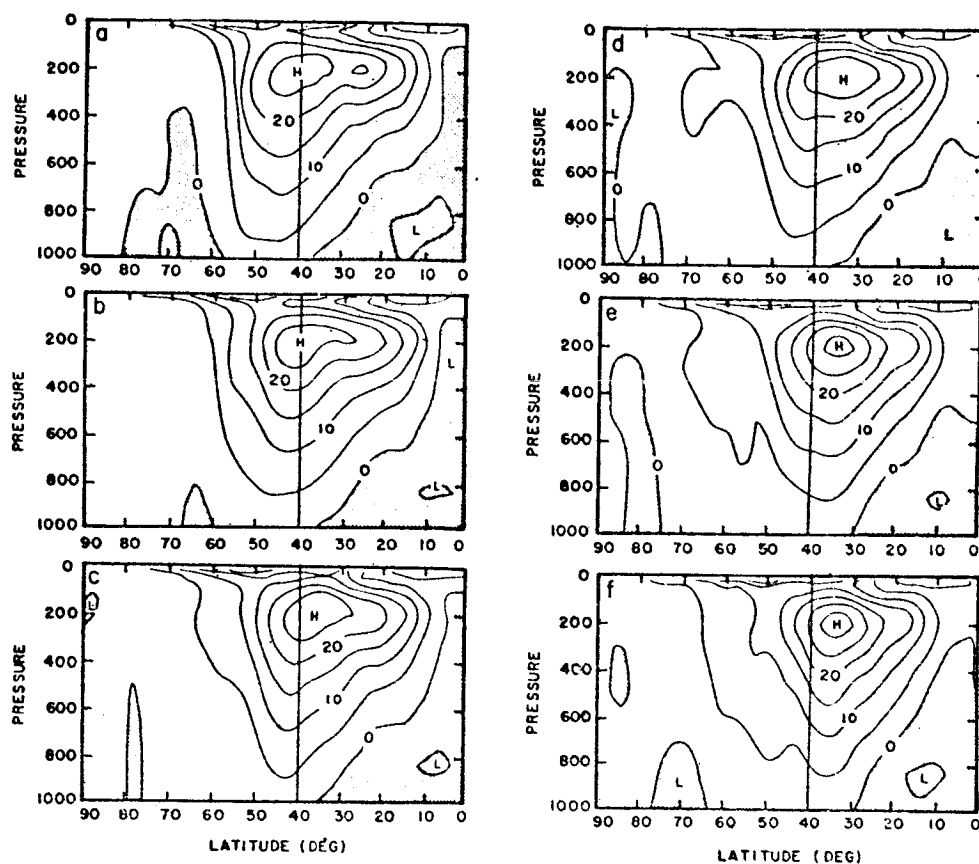
FIGURE 8. Sequence of distributions of u cos in the meridional plane from December 15 through December 20, 1979 (Figure 8a to Figure 8f). The vertical line at 40°N is for reference. Units are m/s. (Data source: ECMWF FGGE IIIb.)

force ($\bar{v}$, $\bar{\omega}$ terms) acting on the mean meridional circulation. This pattern appears to account for most but not all of the actual change of zonal momentum that takes place during this period. Some of the change during the five-day period could have been brought about by diabatic effects. In this connection, it is interesting to look at the evolution of the eddy induced mean meridional circulation (ψ) during the period under consideration. Figure 11 reveals that a weak and diffuse circulation at the beginning of the period became organized into a pattern with a strong eddy induced Hadley cell by the end of the period. Such a cell could be expected to draw moisture toward the equator and develop or intensify the ITCZ which, in turn, would feed back to intensify the Hadley cell. Similarly, the rising motion at 60°N could be expected to increase the release of latent heat of condensation
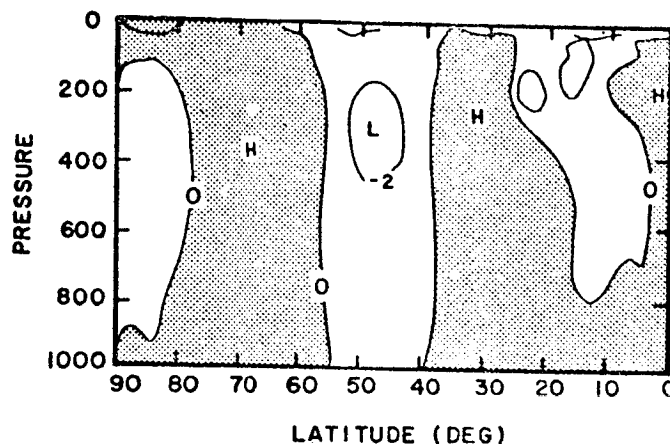
FIGURE 9. The average rate of change of u cos from December 15 to December 20, 1978. Units are 10^{-5} m s^{-2}. (Data source: ECMWF FGGE IIIb.)

at that latitude and intensify the Ferrel cell. Through the action of the Coriolis force, the meridional circulations enhanced by such latent heat release would alter the zonal current, possibly accounting for the differences between the actual rate of change (Figure 9) and the eddy generated momentum tendency (Figure 10).

ENERGETICS: ECMWF VERSUS GFDL DATA SETS

Kung and Tanaka (1983) have calculated the global energy balance during the FGGE SOP-1 and SOP-2 using both the ECMWF and GFDL data sets. Their comparisons are shown in Figure 12. In both periods, the intensity of the conversions from potential to kinetic energy and, in particular, from zonal potential (P_M) to zonal kinetic (K_M) are much greater when calculated from the GFDL data set. Kung and Tanaka (1983) attributed this to the initialization procedure. They pointed out that the adiabatic nonlinear normal mode initialization used in the ECMWF model suppresses the divergent component of the wind. Moreover, the assimilation of the ECMWF data set assumes a geostrophic-type relationship between the pressure height and the wind at middle and high latitudes, whereas the assimilation of the GFDL data set does not.

The implication by Kung and Tanaka (1983) is that the GFDL data set is better than the one prepared by ECMWF. The present author reserves judgment on this point, particularly since the ECMWF model is known to give better five-day forecasts than other models. Because of the strong dependence of the data on the model used in the analysis, the estimates of the energy cycle based on FGGE IIIb data sets differ from each other by as much as they differ from estimates for different years based on different data sets (see Kung and Tanaka, 1983, Table 2).
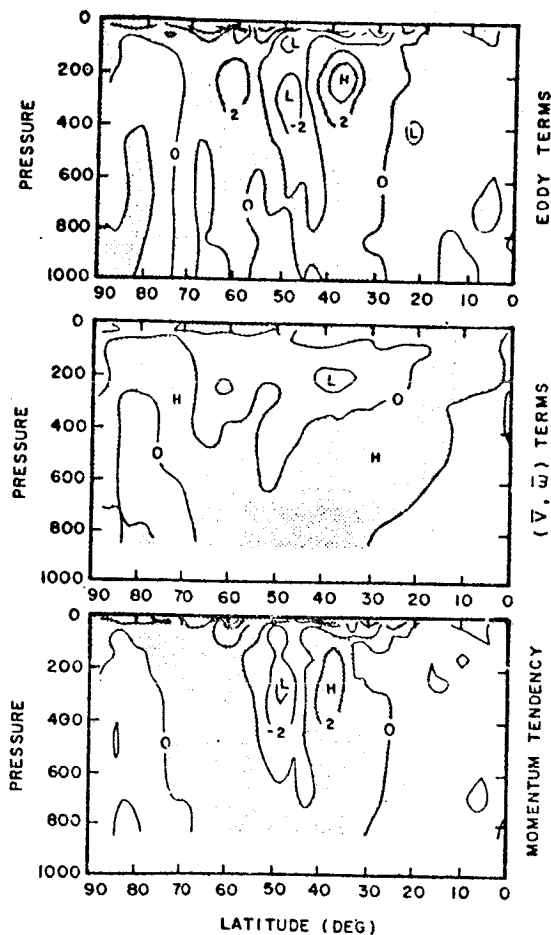
FIGURE 10 Conventional Eulerian diagnostics of the momentum budget
(i.e., u cos / t) due to eddy forcing from December 15 to December 20,
1978. Units are 10^{-5} m s^{-2}. The peak negative value of the
momentum tendency represents a deceleration of about 4 m/s day^{-1}.
(Data source: ECMWF FGGE IIIb.)

There is clearly a need to prepare other data sets for the FGGE year
for comparison using different GCMs and to investigate carefully the
reasons for the differences.

CONCLUSIONS

Conventional diagnostics are most appropriate in studies of global
energetics and wave mean flow interactions in the troposphere and lower
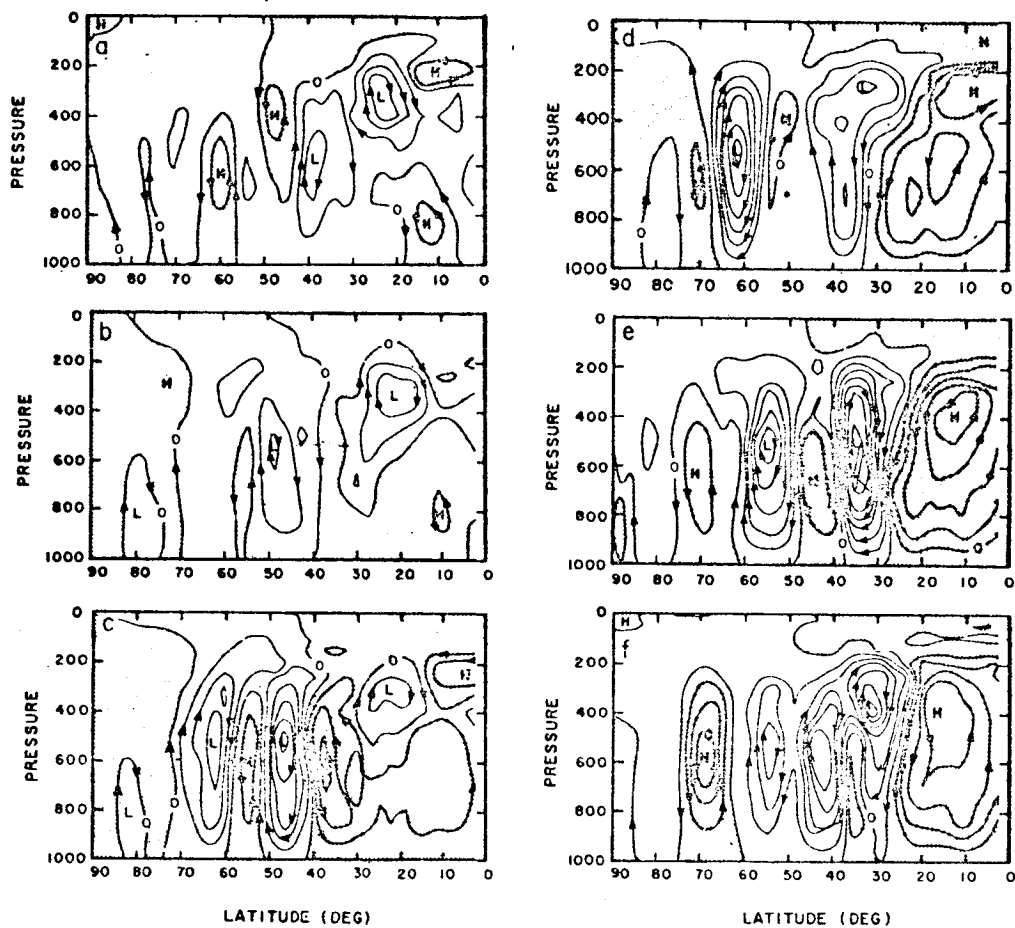
FIGURE 11 Sequence of distributions of the streamfunction ( ) for the eddy induced mean meridional circulation from December 15 through December 20, 1978 (Figure 11a to 11f). Units are m mb s^{-1} (1 m mb s^{-1} is equivalent to 0.41×10^{12} g s^{-1} mass flow). Data source: ECMWF FGGE IIIb.

stratosphere, while the transformed equations are more useful in studies of stratospheric warmings. FGGE IIIb data is highly model dependent, with the result that estimates of the energy cycle during the FGGE year differ from each other by as much as each differs from estimates for different years based on different data sets. It is suggested that new data sets using different GCMs be prepared for FGGE for comparison with the existing ones and that investigations be undertaken to determine the reasons for the differences.

(a) SOP-1
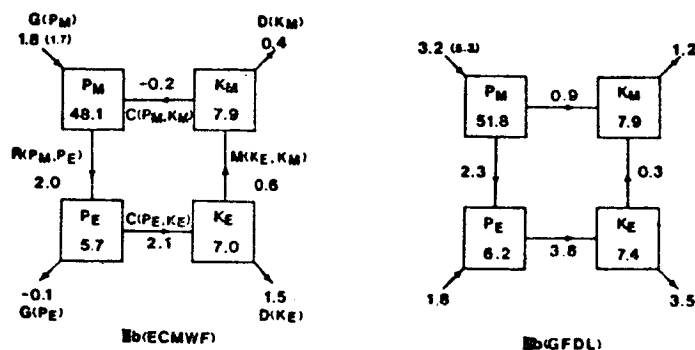
(b) SOP-2
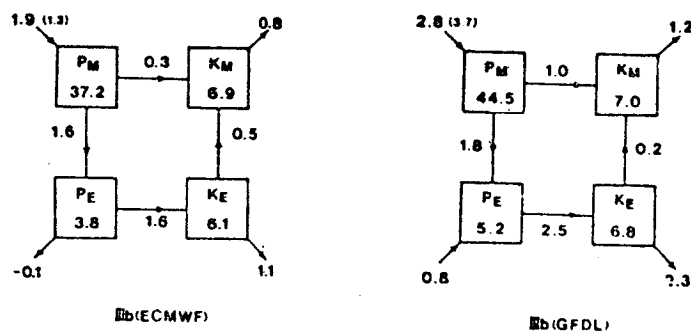
FIGURE 12   Global energy blanace during the FGGE SOP-1 and SOP-2 using both the ECMWF and GFDL data sets (after Kung and Tanaka, 1983).

REFERENCES

Andrews, D. G., and M. E. McIntyre (1976). Planetary waves in a horizontal and vertical shear: The generalized Eliassen-Palm relation and the mean zonal acceleration. J. Atmos. Sci. 33, 2031-2048.

Boyd, J. (1976). The noninteraction of waves with the zonally averaged flow on a spherical earth and the interrelationships of eddy fluxes of energy, heat, and momentum. J. Atmos. Sci. 33, 2285-2291.

Edmon, H. J., B. J. Hoskins, and M. E. McIntyre (1980). Eliassen-Palm cross-sections for the troposphere. J. Atmos. Sci. 37, 2600-2616.

Eliassen, A. (1952). Slow thermally or frictionally controlled meridional circulation in a circular vortex. Astrophys. Norv. 5, 19-60.

Eliassen, A., and E. Palm (1960). On the transfer of energy in
stationary mountain waves. Geofys. Publ. 22, 1-23.

Kuo, H. L. (1956). Forced and free meridional circulations in the
atmosphere. J. Meteorol. 13, 561-568.

Kung, E. C., and H. Tanaka (1983). Energetics analysis of the global
circulation during the special observing periods of FGGE. J. Atmos.
Sci. 40, 2575-2592.

Oort, A., and A. B. Rasmusson (1971). Atmospheric Circulation
Statistics. NOAA Prof. Paper 5, U.S. Department of Commerce,
Washington, D.C., 323 pp.

Palmer, T. N. (1981a). Diagnostic study of wavenumber-2 stratospheric
sudden warming in a transformed Eulerian mean formalism. J. Atmos.
Sci. 38, 844-855.

Palmer, T. N. (1981b). Aspects of stratospheric sudden warmings
studied from a transformed Eulerian mean viewpoint. J. Geophys.
Res. 86, 9679-9687.

Pfeffer, R. L. (1981). Wave mean flow interactions in the atmosphere.
J. Atmos. Sci. 38, 1340-1359.

Starr, V. P. (1968). Physics of Negative Viscosity Phenomena.
McGraw-Hill, 254 pp.

Starr, V. P., J. P. Peixoto, and J. E. Sims (1970). A method for the
study of the zonal kinetic energy balance in the atmosphere. Pure
Appl. Geophys. 80, 346-357.

THE ROLE OF FGGE DATA IN THE UNDERSTANDING AND PREDICTION OF ATMOSPHERIC PLANETARY WAVES

Wayman E. Baker
NASA/Goddard Space Flight Center

INTRODUCTION

The augmented observational data base provided by FGGE offers a unique opportunity to improve our understanding and prediction of atmospheric planetary waves. Substantial progress has been made, but a number of problems remain.

This paper attempts to review the research on planetary waves conducted thus far with FGGE data. Areas of progress are summarized in section 2, and some remaining problems are discussed in section 3.

FGGE RESEARCH ON PLANETARY WAVES

An attempt is made to summarize the FGGE planetary wave research by topical area with the main findings briefly discussed.

Planetary Wave Predictability

One of the remarkable findings resulting from research with FGGE data has been the successful prediction of atmospheric blocking patterns beyond one week (e.g., Bengtsson, 1981; Halem et al., 1982). For example, Bengtsson et al. (1981) obtained an accurate eight-day prediction of a blocking pattern over the North Atlantic shown in Figure 1, with a high-resolution spectral model from initial conditions that included satellite cloud-track wind data. In subsequent integrations in which the resolution was degraded, less sophisticated physical parameterizations were utilized, and satellite data were deleted, a noticeable degradation in predictive skill was obtained.

Similarly, Halem et al. (1982) obtained a skillful eight-day forecast of a Pacific blocking pattern (see Figure 2) using a high-resolution gridpoint model from an initial state that utilized all the FGGE data. Again, less skill was obtained without satellite data using a coarse resolution model.

However, as noted by Bengtsson (1981), there is considerable variation in predictability from day to day. Baumhefner and Bettge (1981) examined the planetary wave forecast error obtained from the NMC
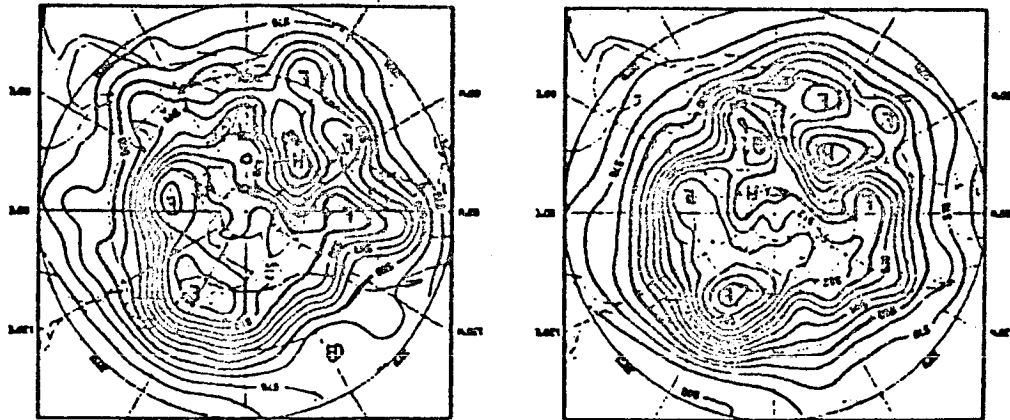
FIGURE 1 500 mb geopotential for an 8-day forecast (shown on the left)
for January 24, 1979 with the ECMWF high resolution spectral model.
Shown on the right is the ECMWF analysis for January 24 (from
Bengtsson, 1981).

forecasts during FGGE SOP-1 and concluded that the best forecast skill
is associated with quasi-stationary planetary wave behavior, and the
poorest skill occurs during periods of planetary wave transition. The
lagged average forecast (LAF) method developed by Hoffman and Kalnay
(1983) seems promising in that regard. By providing an a priori
estimate of forecast skill, the time at which individual forecasts lose
their skill can be predicted.

   In an analysis of planetary wave systematic forecast error, Bettge
(1981) found a strong persistence in the error from one month to the
next and for the same month in different years, as may be seen in
Figure 3. A large negative error was noted over northern Eurasia,
indicative of a continental ridge weaker than observed. Positive
errors were noted in the vicinities of the northern Pacific and
Atlantic Oceans, indicative of troughs weaker than observed.

Tropical Influences on Planetary Waves

Several studies have examined the role of the tropics in affecting the
extratropical circulation using pre-FGGE data sets. For example, a
study by Paegle (1978) indicated that tropical disturbances may
influence the subtropical jet streams, while analyses of a Data Systems
Test (DST) assimilation experiment (Paegle et al., 1979) suggested that
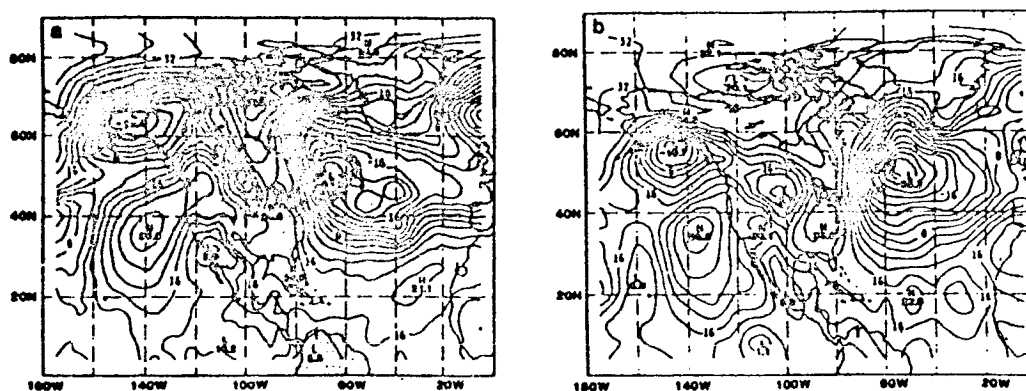
FIGURE 2   Sea level pressure for 0000 GMT February 6, 1979.   (a) 8-day forecast with the 2.5° x 3° GLAS fourth order model, (b) GLAS FGGE IIIb analysis.   Pressure minus 1000 is in mb (from Halem et al., 1982).

low-latitude convective activity may propagate energy outside the tropics on short time scales. More recently, Somerville (1980) suggested that tropical data may affect the forecast of ultralong waves.

Because of the abundance of the FGGE tropical wind data, primarily cloud-track winds, Baker and Paegle (1983) conducted a sensitivity study to examine the Somerville (1980) hypothesis. Two separate assimilation experiments were performed. One experiment utilized tropical wind data and the other did not. Six forecasts were generated from the initial conditions provided by each experiment. The tropical wind data were found to have a positive effect (reduced the error) on the 72-hour planetary wave prediction in four cases and to have a negative effect (increased the error) in two cases. The study also revealed significant differences in the rotational wind component at all latitudes after 72 hours, while the differences present in the initial divergent wind field remained largely restricted to the tropics as may be seen by comparing Figures 4 and 5. This suggests that the differences in the planetary wave predictions in the extratropics resulted from initial differences in the rotational wind field in agreement with the findings of Daley et al. (1981) for a barotropic model.

Planetary Wave Teleconnections

The abundant FGGE data have provided an opportunity to gain further insight into possible atmospheric teleconnections. Such a study was
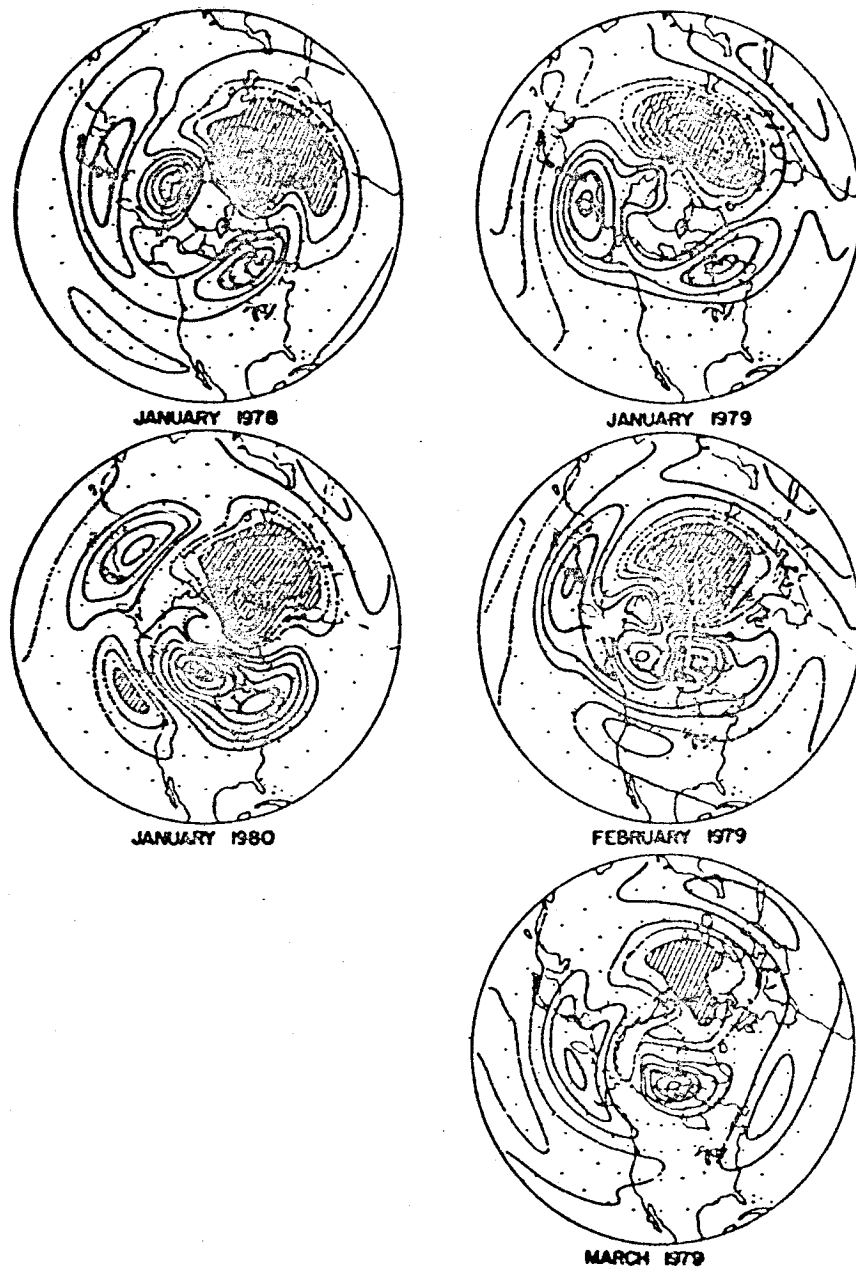
FIGURE 3 Systematic planetary wave errors over the northern hemisphere for 72-hour NMC forecasts by month in 1979, and year from January 1978 to January 1980 (from Bettge, 1981). Contour interval is 10 m. Errors greater than ± 30 m are shaded.
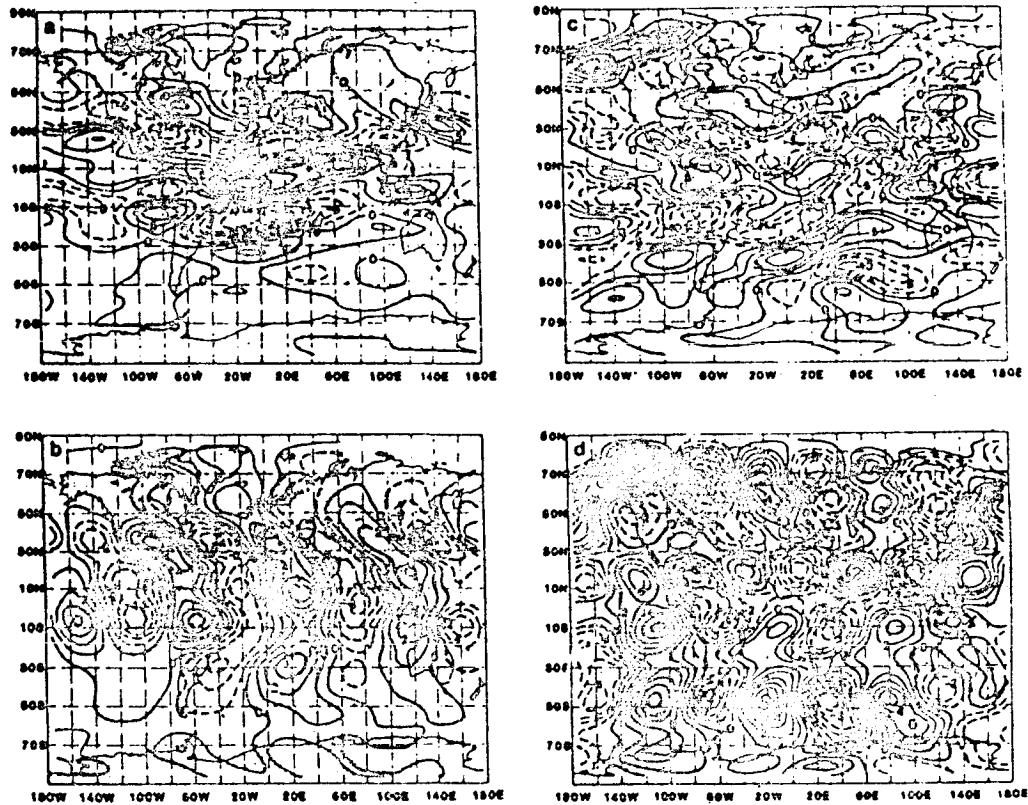
FIGURE 4   Rotational wind differences (tropical winds minus no tropical winds) at 200 mb in terms of a spherical harmonics sum with a longitudinal truncation beyond m = 4 for the 0000 GMT January 15, 1979 case (from Baker and Paegle, 1983).   (a) Initial differences in the zonal component, (b) Initial differences in the meridional component, (c) 72-hour differences in the zonal component, and (d) 72-hour differences in the meridional component.

conducted by Lau et al. (1983) with the FGGE/MONEX data to examine planetary scale teleconnections between the tropics and midlatitudes. They composited 11 episodes of cold surges over the South China Sea during December 1978 to February 1979 and noted the following: A convective heat source, which was found over the equatorial central Pacific, was enhanced 3 to 5 days after surge onset. As Lau et al. (1983) point out, the 200 mb zonal wind and streamfunction maps shown in Figures 6 and 7, respectively, indicate that the enhancement of the convective heat source coincides with the occurrence of a subtropical jet stream and a pronounced upper level trough/ridge system extending from the equatorial central Pacific to the west cost of North America.
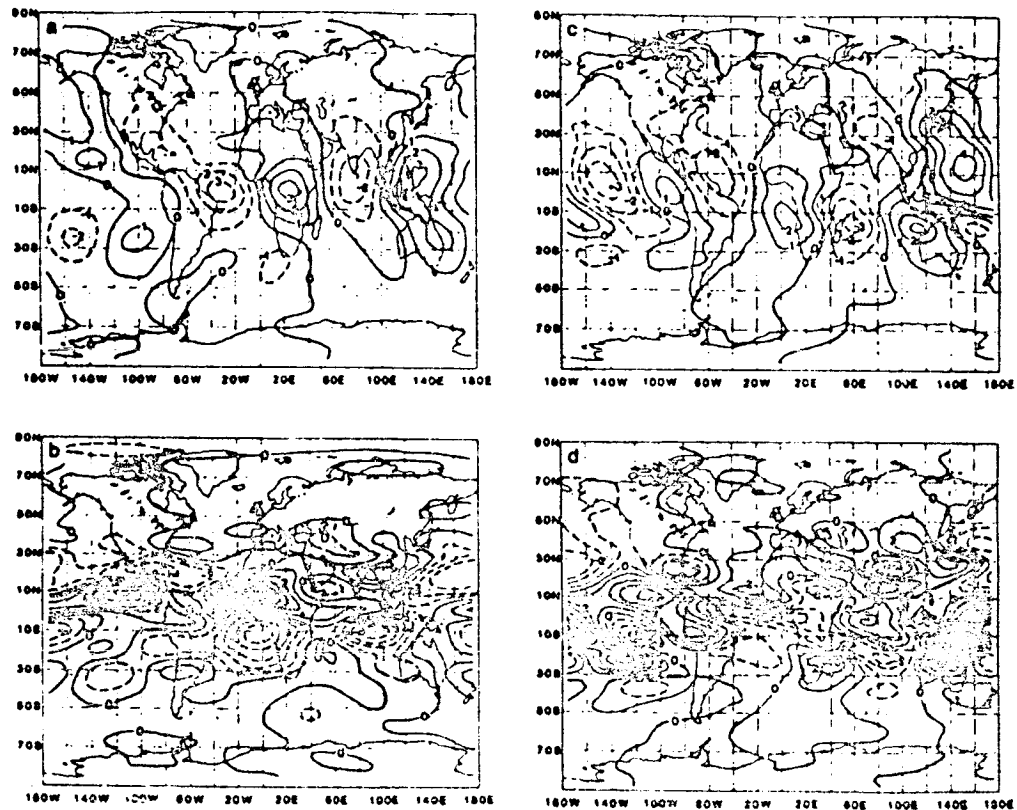
FIGURE 5   As in Figure 4, except for the divergent wind.

As noted in a study by Paegle and Baker (1982), January 1979 had many characteristics in common with the abnormal winter of 1977, particularly the deep North Pacific cyclone and the strong anticyclone over the Rocky Mountains. This pattern was reversed in February 1979. The subtropical jet over the central Pacific was found to be 15 m/s stronger during January than during February, as may be seen in Figure 8.   The January cross-equatorial divergent flow was considerably stronger as well, but weaker than in February in the tropical Atlantic. These characteristics may indicate possible teleconnections.

Southern Hemisphere Planetary Waves

Our understanding of the southern hemisphere planetary waves has been significantly advanced with the FGGE data.   For example, Paegle et al. (1983) found a distinct southward divergent flow from the convective regions of the tropics into regions of kinetic energy generation over Australia, South America, and Africa.   They, therefore, suggested the
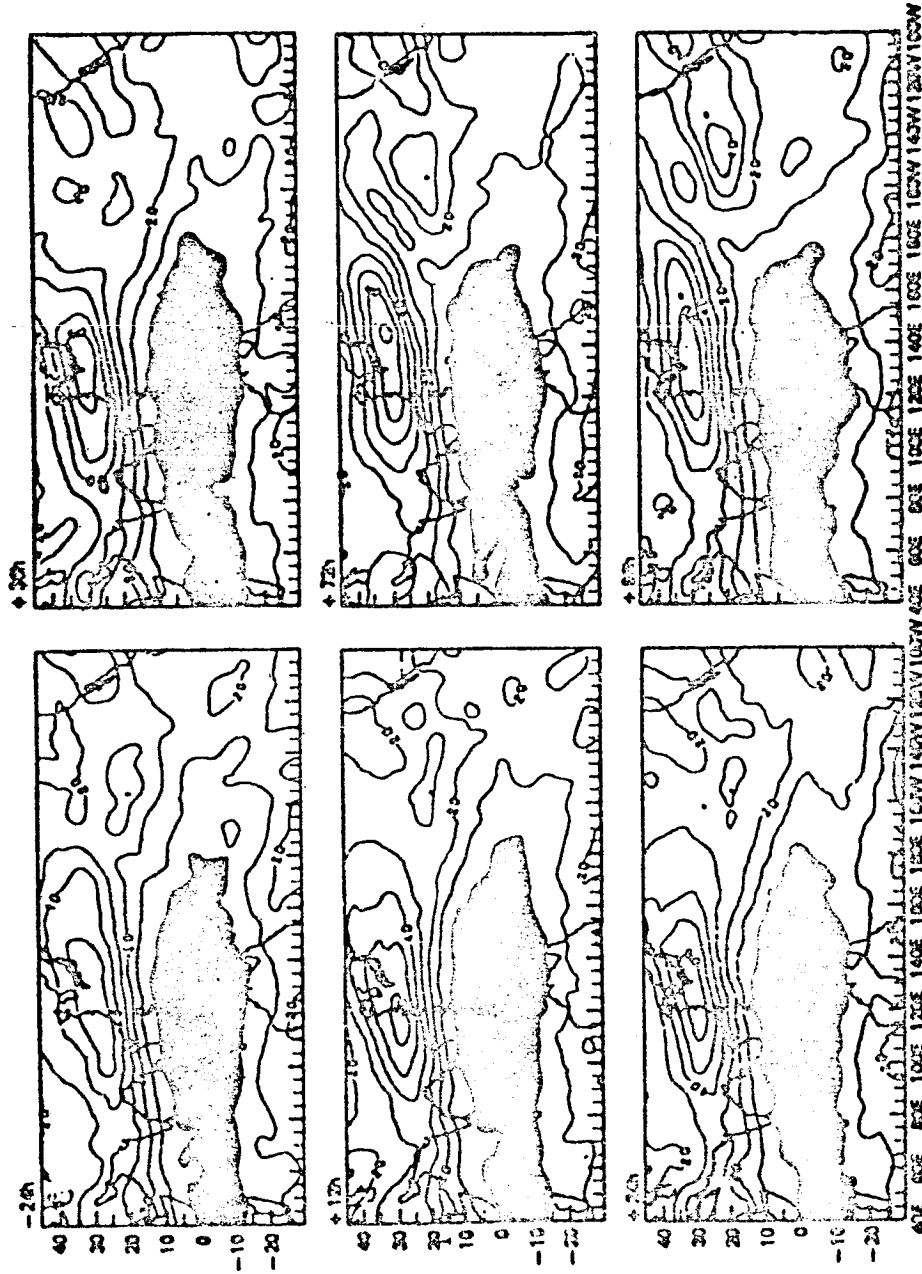
FIGURE 6 Composite maps of 200 mb zonal wind speed over the greater Winter MONEX area at selected time intervals (from Lau et al., 1983). Regions of easterly wind are shaded. Contour interval is 10 m/s.
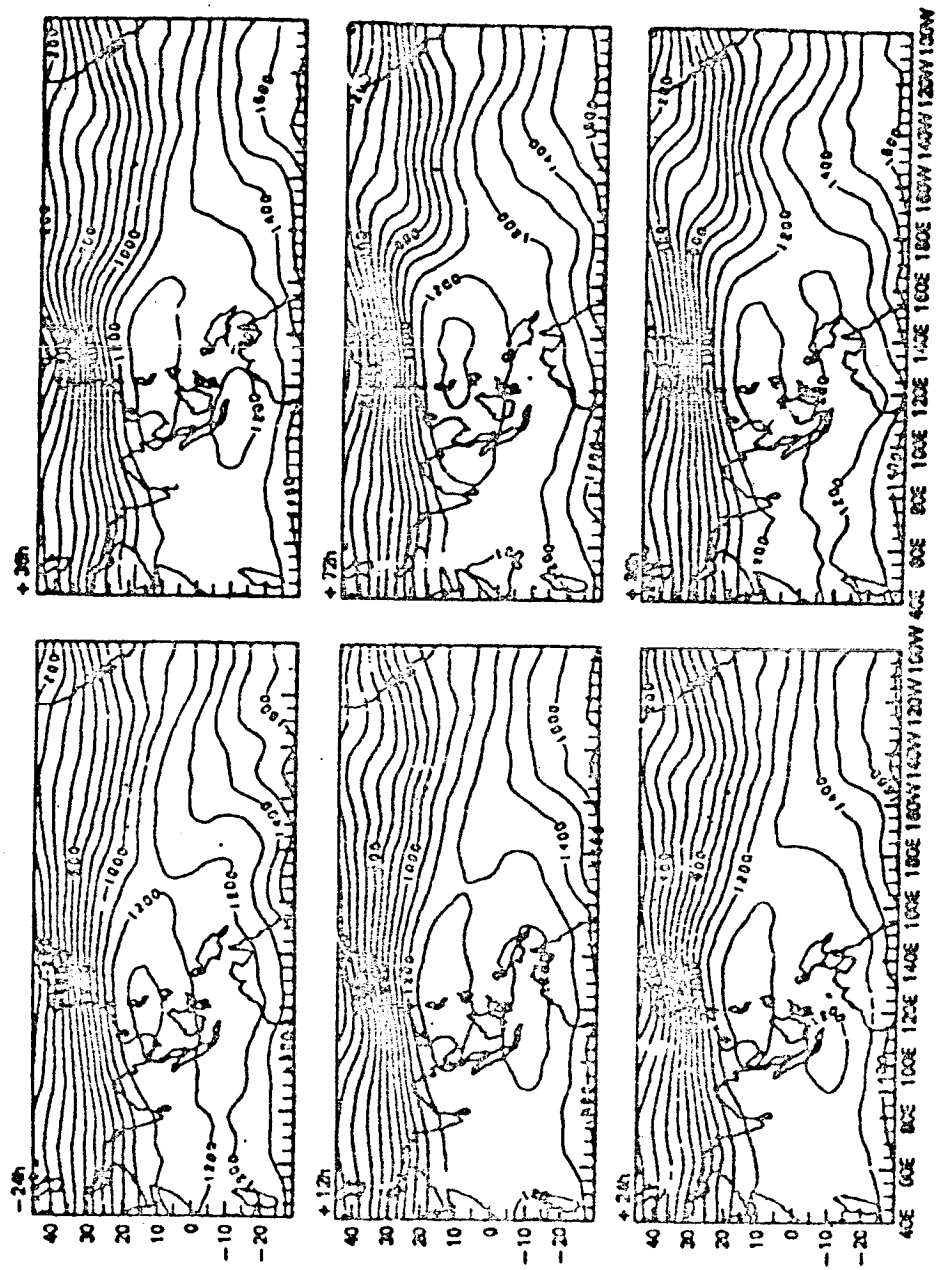
FIGURE 7 As in Figure 6, except for the 200 mb streamfunction. Contour interval is 100 $\times 10^5 m^2 s^{-1}$.
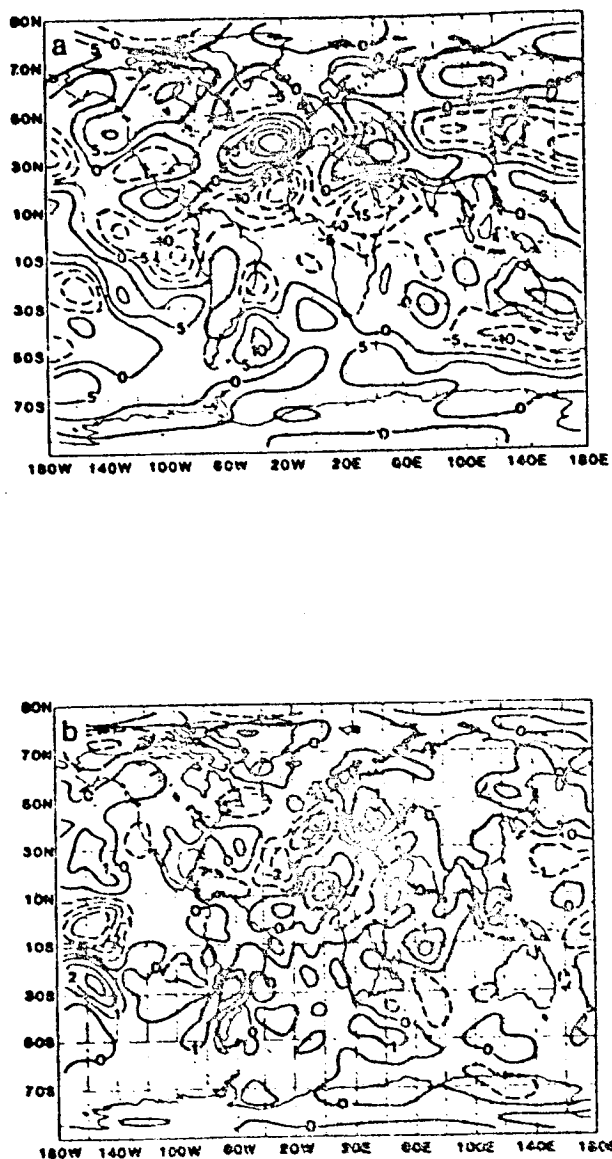
FIGURE 8 Time change (February minus January) of components of the 200
mb wind field from Paegle and Baker (1982). (a) Rotational zonal
component, (b) Divergent meridional component.

possibility that the subtropical jet structure in the southern
hemisphere may be strongly determined by longitudinal gradients of
tropical heating and may explain the standing wave pattern of the
southern hemisphere winter.

Mechoso and Hartmann (1982) performed an observational study of southern hemisphere traveling planetary waves for the period May to September 1979. They found that westward-moving waves have a structure characteristic of barotropic external modes and are coherent across a broad range of latitudes from the surface to 2 mb. On the other hand, eastward-moving waves were found to have more phase variation, especially in the troposphere, and are more baroclinic.

Rossby Waves as Depicted by FGGE Observations

Lindzen et al. (1984) have performed an observational study of Rossby waves during the FGGE year with ECMWF analyses. They found that, for the largest scales, global Rossby waves exist in agreement with theory, and pointed out that since both symmetric and antisymmetric modes appear equally vigorously, a global domain is needed to correctly analyze and/or forecast these waves.

SOME REMAINING PROBLEMS

It is not surprising that in the course of pursuing the FGGE objectives a number of questions have been raised related to planetary waves for which further research with the FGGE data may provide answers. An attempt is made to summarize the unresolved questions by topical area.

Planetary Wave Predictability

Why is there considerable variation in planetary wave predictability from day to day? Bengtsson (1981) found that integrations using different models, data, resolutions, and parameterizations all resulted in poor forecasts on some days, while on other days all the forecasts were generally good.

Why does the best forecast skill seem to occur during periods of quasi-stationary planetary wave behavior and the poorest skill during periods of planetary wave transition, as noted by Baumhefner and Bettge (1981)?

What are the sources of the model planetary wave systematic error? Bettge (1981) has suggested that data inadequacies could result in the improper partitioning of the initial stationary and transient components of the flow, producing large errors early in the forecasts. He also suggested that the regional coherence of the errors later in the forecast may indicate incorrect external forcing such as land/sea contrasts or topography.

Tropical Influences on Planetary Waves

What are the limits of linear theory in explaining the observed tropical/extratropical interactions through regions of easterly flow found by Paegle et al. (1983)?

Planetary Wave Teleconnections

The abundant FGGE data provide an opportunity to gain further insight into atmospheric teleconnections. Wallace and Gutzler (1981) have noted some key unresolved questions: Are teleconnection patterns apparent in the stratosphere and, if so, are they related to stratospheric warmings? How should teleconnection patterns be viewed in relation to synoptic patterns associated with blocking? Are they mutually exclusive or should one set be a subset of the other?

As noted by Paegle and Baker (1982), January 1979 was characterized by a deep North Pacific cyclone with a strong anticyclone over the Rocky Mountains. The pattern was reversed in February 1979. What role, if any, did sea-surface temperatures play in the marked January to February 1979 transition?

REFERENCES

Baker, W. E., and J. Paegle (1983). The influence of the tropics on the prediction of ultralong waves. Part I: Tropical wind field. Mon. Wea. Rev. 111, 1341-1355.

Baumhefner, D. P., and T. W. Bettge (1981). Characteristics of atmospheric planetary circulations and associated model forecast skill during FGGE case studies selected by WGNE. International Conference on Early Results of FGGE and Large-Scale Aspects of Its Monsoon Experiments, Condensed Papers and Meeting Report, Tallahassee, Florida, U.S.A., 12-17 January 1981. Global Atmospheric Research Programme, World Meteorological Organization, Geneva, 1981-4.

Bengtsson, L. (1981). Numerical prediction of atmospheric blocking--A case study. Tellus 33, 19-42.

Bettge, T. W. (1981). An examination of the characteristics of planetary scale systematic forecast errors. Preprints Fifth Conference on Numerical Weather Prediction, Monterey, Calif., American Meteorological Society, 109-114.

Daley, R., J. Tribbia, and D. L. Williamson (1981). The excitation of large-scale free Rossby waves in numerical weather prediction. Mon. Wea. Rev. 109, 1836-1861.

Halem, M., E. Kalnay, W. E. Baker, and R. Atlas (1982). An assessment of the FGGE satellite observing system during SOP-1. Bull. Amer. Meteorol. Soc. 63, 407-426.

Hoffman, R. N., and E. Kalnay (1983). Lagged average forecasting, an alternative to Monte Carlo forecasting. Tellus 35a, 110-118.

Lau, K.-M., C.-P. Chang, P. H. Chan (1983). Short-term planetary scale interactions over the tropics and midlatitudes. Part II: Winter-MONEX period. Mon. Wea. Rev. 111, 1372-1388.

Lindzen, R. S., D. M. Straus, B. Katz (1984). An observational study of large-scale atmospheric Rossby waves during FGGE. J. Atmos. Sci. 41 (in press).

Mechoso, C. R., and D. L. Hartmann (1982). An observational study of traveling planetary waves in the southern hemisphere. *J. Atmos. Sci.* 39, 1921–1935.

Paegle, J. (1978). The transient mass-flow adjustment of heated atmospheric circulations. *J. Atmos. Sci.* 35, 1678–1688.

Paegle, J., and W. E. Baker (1982). Planetary scale characteristics of the atmospheric circulation during January and February 1979. *J. Atmos. Sci.* 39, 2521–2538.

Paegle, J., J. N. Paegle, F. P. Lewis, and A. J. McGlasson (1979). Description and interpretation of planetary flow structure of the winter 1976 DST data. *Mon. Wea. Rev.* 107, 1506–1514.

Paegle, J. N., F. P. Lewis, and J. Paegle (1983). Observed and modeled longwave patterns of the southern hemisphere. *First International Conference on Southern Hemisphere Meteorology*, Sao Jose dos Campos, Brazil, American Meteorological Society, August 1983, 37–40.

Somerville, R. C. J. (1980). Tropical influences on the predictability of ultralong waves. *J. Atmos. Sci.* 37, 1141–1156.

Wallace, J. M., and D. S. Gutzler (1981). Teleconnections in the geopotential height field during the northern hemisphere winter. *Mon. Wea. Rev.* 109, 1150–1162.

10. INTERHEMISPHERIC

Organizer	Julia N. Paegel
Session Chairman	Wayman E. Baker
Speakers	Jan Paegle
	Richard C.J. Somerville
Rapporteur	Richard C.J. Somerville

INTERHEMISPHERIC INTERACTIONS

Jan Paegle
University of Utah   *Dept of Meteorology*

ABSTRACT

Diagnoses of global data sets are presented that indicate strong coupling between the regions of enhanced tropical convection of the summer hemisphere and subtropical jet stream maxima of the winter hemisphere. One curious aspect of this coupling is that it tends to occur through zones of easterly winds at upper tropospheric levels. This characterizes the El Niño event of 1983, an upper connection of the Asian monsoon to the Australian jet in FGGE and DST data and shorter term transitions during the First Special Observing Period of FGGE. The reasons for the apparent propagation through easterly wind zones remain to be clarified.

MODELS

One of the major goals of the First GARP Global Experiment has been to improve weather prediction by expanding into the tropics and southern hemisphere the domain of useful data coverage for model initialization and verification. In recent years, it has become apparent that correct global initialization is essential not only for the accurate prediction of tropical weather but also for accurate midlatitude predictions of a few days or longer (Somerville, 1980; Daley et al., 1981; Baker and Paegle, 1983; Paegle and Baker, 1983).

The short time scale of such deep latitudinal interaction is rather surprising in view of the extensive theoretical evidence that efficient Rossby wave propagation between the deep tropics and higher latitudes is impeded by the typical zonal wind structure. The zonally averaged wind usually possesses a deep and extensive layer of easterly flow in the tropics throughout the middle and lower troposphere, while the midlatitudes display strong westerlies. Meridional Rossby wave propagation through such a shearing flow would be strongly inhibited for all modes that do not have a westerly propagation rate in excess of the strongest easterly wind (Charney, 1969; Mak, 1969; Bennett and Young, 1971; Geisler and Dickinson, 1974).

In its simplest form, for purely rotational flow on the beta plane, the nondivergent vorticity equation linearized about a zonally uniform flow produces a latitude structure equation of the form:

$$\frac{d^2\psi}{dy^2} + \left[\frac{\partial}{\partial y}\left(f - \frac{\partial u}{\partial y}\right)\right]/(U - c) - k^2 \;\psi = 0 \qquad (1)$$

Here x, y represent eastward, northward distances, respectively, ψ is the y-dependent amplitude of Fourier wavenumber k in x, U is the x-independent eastward basic flow, and c is the phase speed of wavenumber k.

The divergent quasi-geostrophic version discussed by Charney (1969) has a similar latitude structure equation, with a slight modification due to divergence. As pointed out by Charney, propagating wavelike solutions in y can exist only if the bracketed coefficient of ψ is positive, implying (for the typical case that absolute vorticity increases poleward) the necessity to have U > c, i.e., westerly phase propagation with respect to the basic flow. Otherwise, the response to localized forcings will be trapped on the forcing side of any latitude where U = c (the "critical latitude"). Much research has been focused on the singular point represented by this critical latitude. A summary of recent work is given in Held (1983).

To the level of Charney's (1969) quasi-geostrophic treatment, the presence of divergent effects does not modify the substance of the critical latitude trapping conclusions, but only shifts the spectral range of propagating modes. The situation for the highly nonbalanced divergent component suggested in the FGGE data is not covered by this case but may be described in linearized treatments of the primitive equations. In view of this, it is somewhat surprising that the bulk of such analyses support the conclusions of the simpler balanced case to a remarkable extent.

Apart from some tropical easterly waves (Zangvil and Yanai, 1980), the theory suggests that slight short-term coupling may be expected between midlatitudes and the tropics. Indeed, Daley et al (1981) suggest that the meridional propagation of forecast error out of the tropics may not be very important to the degradation of the midlatitude forecast. That study concludes that the projection of the initially erroneous tropical fields on global normal modes produces erroneous midlatitude dispersion for <u>longitudinal</u> propagation, and this accounts for the major part of the midlatitude error structure. Thus the aforementioned theories are not obviously violated in predictability studies suggesting strong tropical data impact on short-term prediction for midlatitudes by global models.

Nevertheless, there is extensive observational evidence of a meridional connection between the most active quasi-stationary tropical convection areas and the subtropical jet streams of the opposite hemisphere. This has been suggested in studies of the time differences of monthly averages by Bjerknes (1966, 1969) and Ramage (1968). Such teleconnections may also be inferred in seasonal averages described by Krishnamurti (1973) and Murakami (1978). Several FGGE studies also imply similar interactions between the tropics and midlatitudes (Paegle
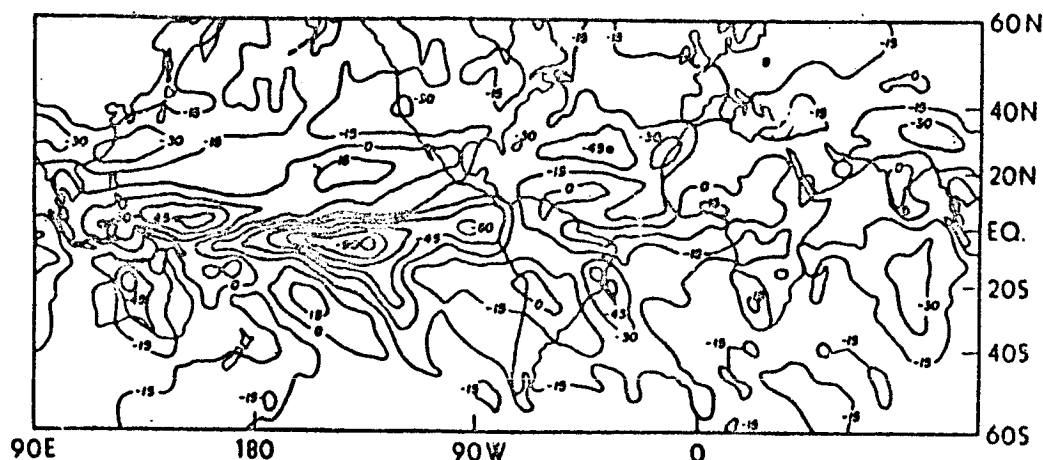
FIGURE 1 Anomalous outgoing infrared radiation for March 1983 in units
of W m^{-2}, with an analysis interval of 15 W m^{-2}. This diagram is
taken from the Spcial Climate Diagnostics Bulletin Update on the
1982-1983 Equatorial Pacific Warm Episode produced by the Diagnostics
Brnach of the Climate Analysis Center/NMC/NWS/NOAA.

and Baker, 1982a,b). The study by Paegle and Baker (1982b) concludes
that the weekly and monthly averages of highly truncated circulation
components behave qualitatively in agreement with the weekly and
monthly evolution of the upper tropospheric zonal wind field and the
theory of critical latitude trapping. However, that study could not
confirm the applicability of the theory to less truncated fields that
carry most of the kinetic energy.

We now review the recent observations that suggest pronounced
connections of quasi-stationary tropical convection of one hemisphere
with the subtropical jet streams of the opposite hemisphere. Three of
the more striking cases involve the strong El Niño event of the
northern winter and spring seasons of 1983, explanations of the
stationary wave pattern of the southern hemisphere that invoke the
strong heat source of the Asian monsoon, and apparently corresponding
adjustments of tropical heating and global waves observed during FGGE.

THE EL NIÑO EVENT OF 1983

The El Niño data to be summarized are taken from the Special Climate
Diagnostics Bulletins of the Climate Analysis Center of the National
Meteorological Center. Figure 1 presents the anomalous outgoing
infrared radiation for the month of March, 1983. The large negative
values centered at about 135°W represent greatly enhanced deep cloud
systems for this month that were presumably associated with the
anomalously strong east Pacific El Niño current of this period.
Figure 2 presents the anomaly streamfunction at 200 mb for this month.
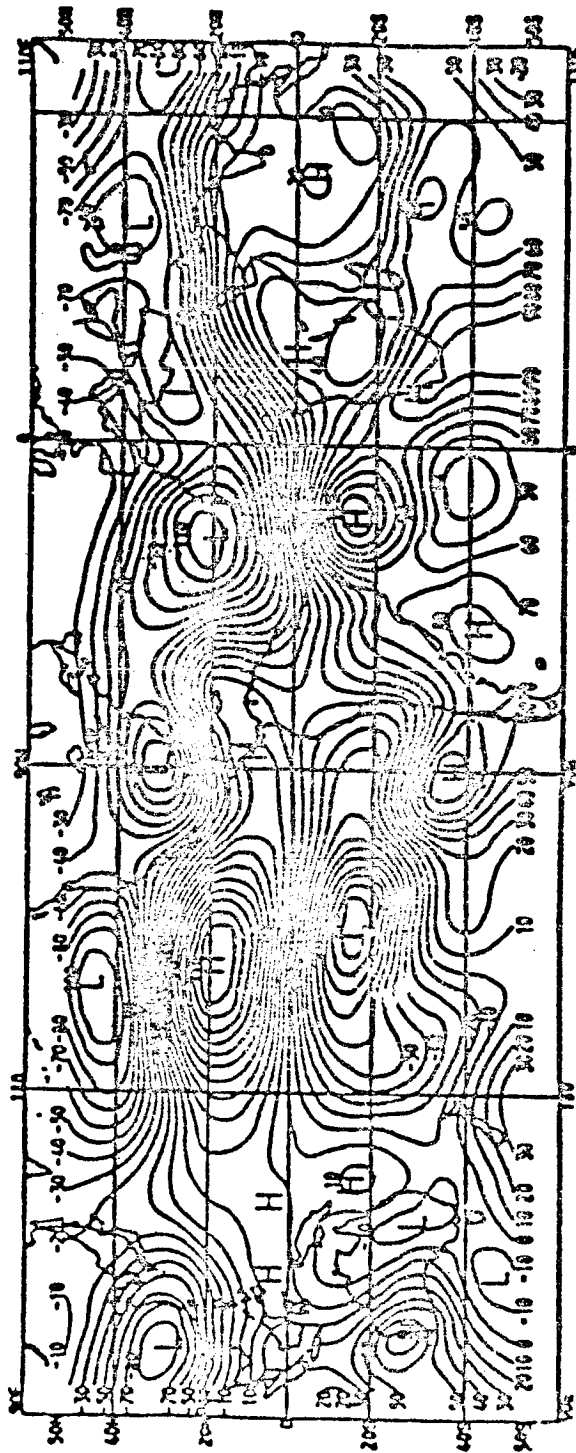
FIGURE 2 Anomaly streamfunction field at 200 mb for March 1983 in units of m^2 s^{-1}, with an analysis interval of 10^6 $m^2 s^{-1}$. This diagram is taken from the same source as Figure 4.

The two anticyclonic gyres located just north and south of the outgoing radiation anomaly center in the Pacific Ocean produce local intensifications of the westerly flow amounting to about 25 m/s at 30°N and somewhat lesser intensifications in the southern hemisphere.

The total flow picture for March 1983 (Figure 3) shows that this enhancement of the northeast Pacific subtropical jet stream produces a pronounced elongation of the speed maximum ordinarily found off the Asian coast. This picture is certainly consistent with Bjerknes' (1966) original concept of local Hadley cell enhancement by local tropical heating. However, it does not easily fit into the theory of meridional Rossby wave propagation because most of the heating anomaly implied by the infrared anomaly of Figure 1 occurs in the southern hemisphere in regions of upper level easterly winds (Figure 3), while the maximum response in the zonal wind is in the upper levels of the northern hemisphere (Figure 2). It also does not fit Gill's (1980) recent analysis for equatorially forced waves, because the deviation pattern of the streamfunction appears to center on the heating anomaly as implied by the satellite infrared anomaly instead of being centered to the west.

An alternative explanation of this phenomenon may be that during periods of locally enhanced tropical heating, the entire tropical belt commonly warms, and the principal response is in the zonally averaged structure (Horel and Wallace, 1981). Although this may partly reconcile these observations with theory, the idea does not easily apply to the next two examples of tropical-subtropical connections.

STATIONARY KINETIC ENERGY DISTRIBUTION
OF THE SOUTHERN HEMISPHERE

The surface of the earth underlying the atmosphere of the southern hemisphere in midlatitudes is much more nearly uniform than is the northern hemisphere surface at similar latitudes. Consequently, to the extent that the horizontal gradient of surface conditions reflects the distribution of quasi-stationary wave kinetic energy, much stronger gradients of kinetic energy may be expected in the northern hemisphere than in the southern hemisphere during equivalent seasons. The observations to be presented, however, do not support this inference.

Figure 4 presents the stationary wave kinetic energy at the 200 mb level (the level that contributes most strongly to the global kinetic energy field) during the summer and winter seasons of the 1976 DST data (a pre-FGGE data systems test conducted by NASA). As expected, these results show more stationary wave kinetic energy in the northern winter than in the southern winter. However, the longitudinal gradients of this field differ much less than would be expected from simple models reacting to local forcing.

Figure 5 shows that the ECMWF analyses of the FGGE data for February and August of 1979 are similar to the DST results. In this year, the stationary wave kinetic energy of the southern winter month of August was greater than the stationary wave kinetic energy of the northern winter month of February. Scientists conclude that a rather prominent
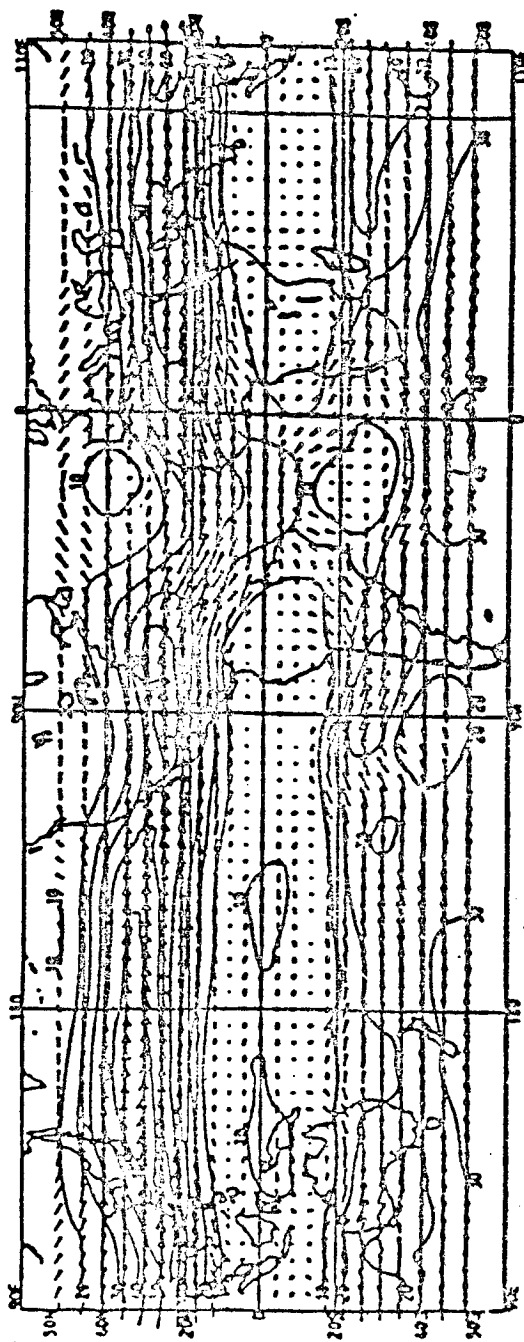
FIGURE 3 The horizontal wind vectors and isotach analysis at 200 mb for March 1983 in units of m/s with an analysis interval of 10 m/s. This diagram is from the same sources as Figure 4.

DST Winter (1976)

DST Summer (1976)
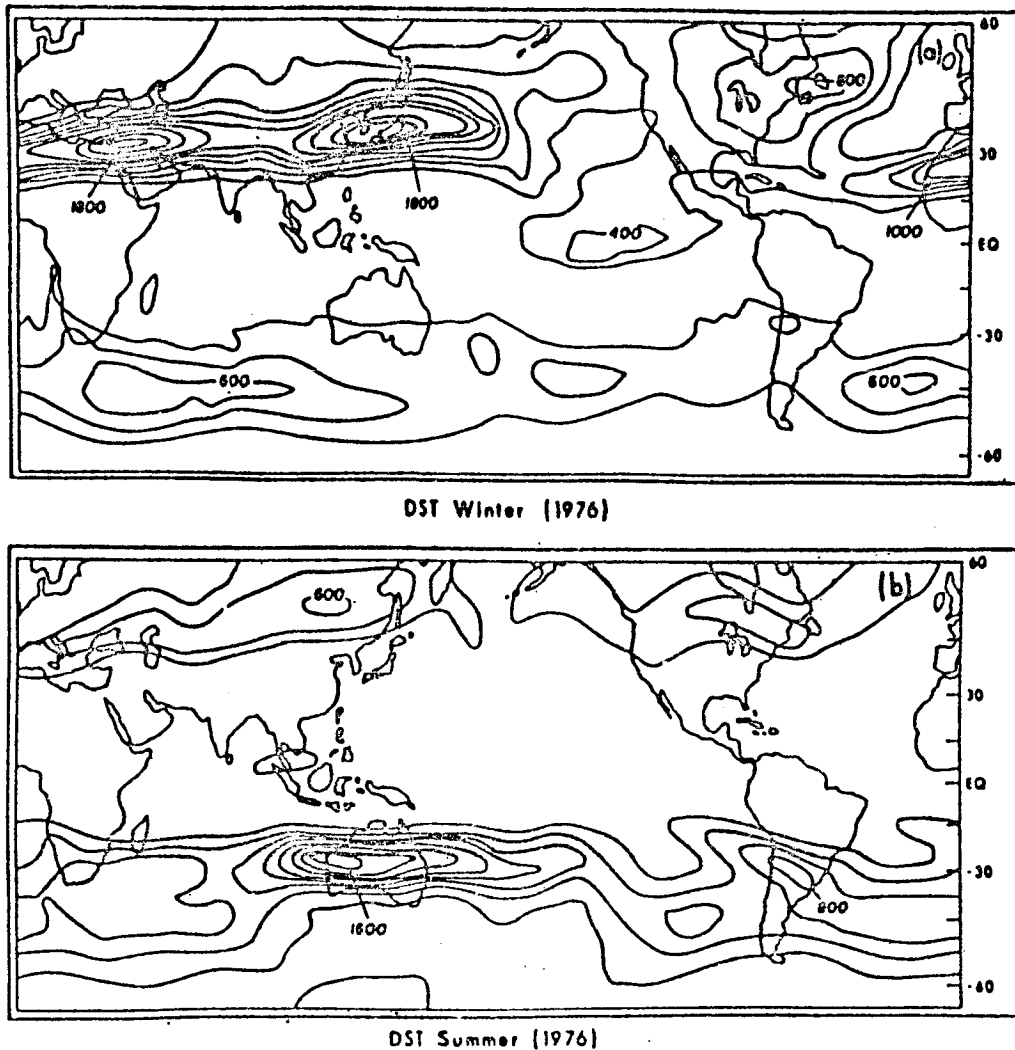
FIGURE 4   (a) Kinetic energy at 200 mb for the northern winter season of the 1976 DST data (January 29 to March 3, 1976).   The units are m/s^2 and the analysis interval is 200 m^2 s.   (b) As in (a), for the northern summer season of the 1976 DST data (August 21 to September 4, 1976).

southern hemisphere longwave pattern is apparent in different years and is present in different analyses.   Furthermore, the kinetic energy of this pattern is dominated by the structure of the subtropical jet stream.

These observations present a dilemma for many theories of the generation of stationary waves.   Topography is generally thought to

February 1979
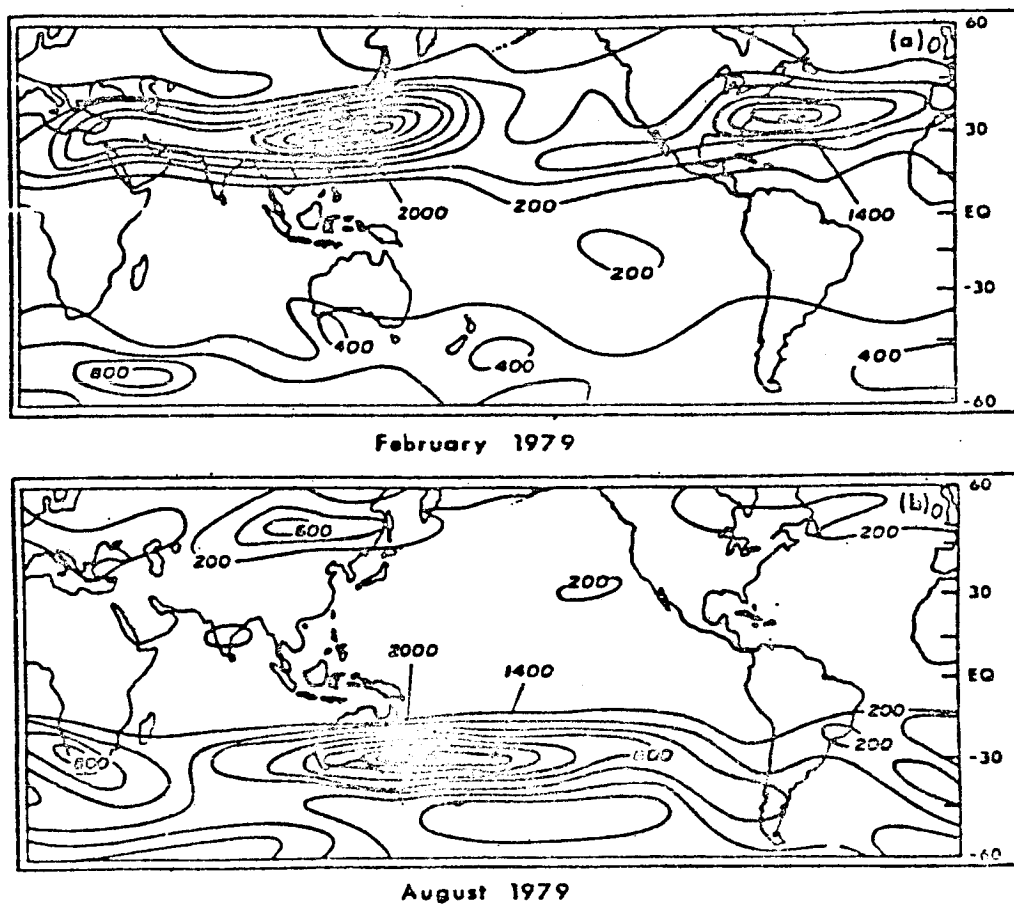
August 1979

FIGURE 5 (a) Kinetic energy at 200 mb for the month of February 1979. The units are m/s^2, and the analysis interval is 200 m/s^2. The calculation is based on the gridded archives of ECMWF. (b) As in (a), for the month of August 1979.

produce much of the stationary wave pattern of the northern hemisphere winter season (e.g., Charney and Eliassen, 1949; Grose and Hoskins, 1979; Held, 1983). While many aspects of topographically shaped flows in these models are reasonable, simple versions of the models do not produce significant stationary wave kinetic energy in the southern hemisphere when forced with relaxation to zonally symmetric flow in the presence of mountains (see Figure 4 of Paegle et al., 1983).

An alternative driving mechanism may involve baroclinic instability that may be preferentially triggered in certain locations by topography, but integrations of the simplest two-layer global model that may capture such an effect (Lewis, 1979) do not support this possibility.

DST Summer (1976)
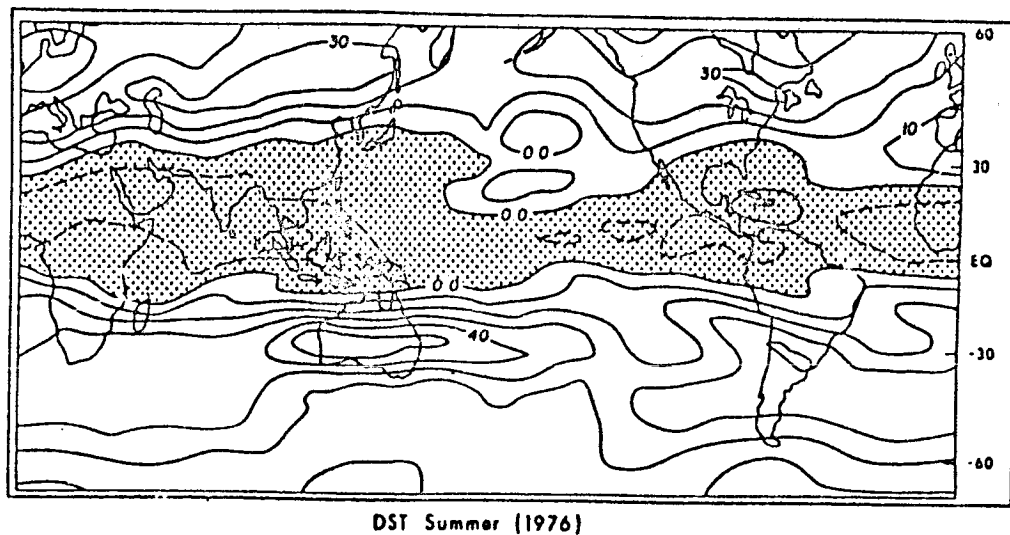
FIGURE 6   Zonal wind component at 200 mb for the northern summer season of the 1976 DST datat (August 21 to September 4, 1976).   The units are m/s, and the analysis interval is 10 m/s.   The region of easterly winds is shaded.k

Another potential explanation of the southern hemisphere stationary wave pattern is that it may be produced by longitudinal gradients of tropical heating.   There is an apparent correspondence between the kinetic energy maxima located around Australia and secondary maxima sometimes seen around South America and South Africa, with the enhanced tropical convection in similar longitudes.   The strongest of these heatings occurs in association with the Asian monsoon, which is in the same longitude sector as the strongest southern hemisphere jet streams.

The study by Physik (1981) suggests that the ageostrophic meridional wind is the major driving mechanism of the subtropical jet around Australia during FGGE.   Such circulation features may relate to the southward branch of the upper tropospheric divergent wind emanating from the Asian monsoon (Krishnamurti, 1971).   However, a straightforward connection of these heating fields to the subtropical jets of the southern hemisphere is incompatible with critical latitude trapping because the heating maxima are embedded within extensive tropical easterlies (see the 200 mb zonal flow in Figure 6).

FGGE OBSERVATIONS OF SOP-1

The intervals from January 10 to 23 (period 1) and January 26 to February 7 (period 2) were used for the present study of tropical heating redistributions and subtropical jet rearrangements during FGGE.   Figure 7 shows the averaged outgoing infrared radiation obtained
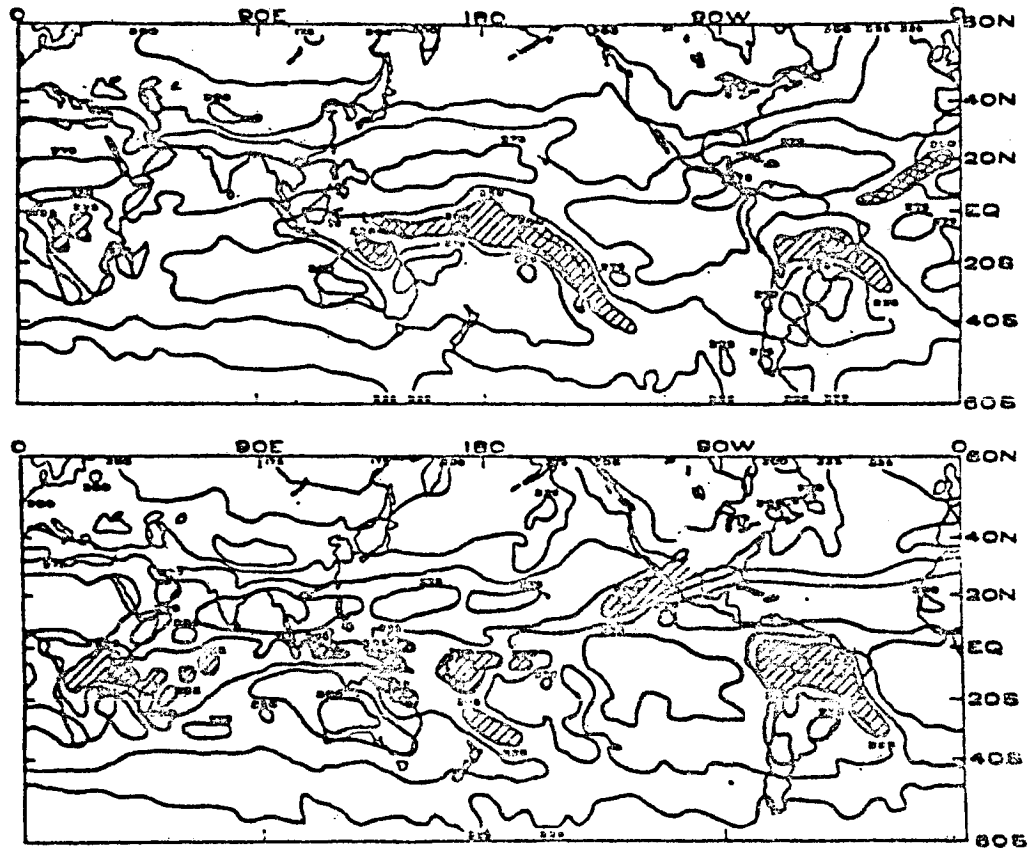
FIGURE 7 Averaged outgoing infrared radiation in W m^{-2} for January 10 to January 23, 1979 (top) and January 26 to February 7, 1979 (bottom). The analysis interval is 25 W m^{-2}. Local tropical minima are shaded. Hatched and cross-hatched regions indicate areas with high cloudiness.

from the TIROS-N radiation data for the two periods. Areas with relatively low values between 45°S and 30°N have been shaded to denote areas with high (presumably convective) clouds. The three typically cloudy areas of the southern hemisphere summer (i.e., Krishnamurti et al., 1973) clearly appear in this figure.

One difference between the periods occurs over the Pacific Ocean where the well-developed northwest to southeast convective band centered about 140°W during period 1 has shifted closer to the dateline and decreased in magnitude during period 2. The tropical convection appears over the Indian Ocean during period 2.

Gridded analyses of FGGE data were obtained from the European Centre for Medium Range Weather Forecasts for the FGGE enhanced data sets. The objective analysis of these data has been documented by Lorenc
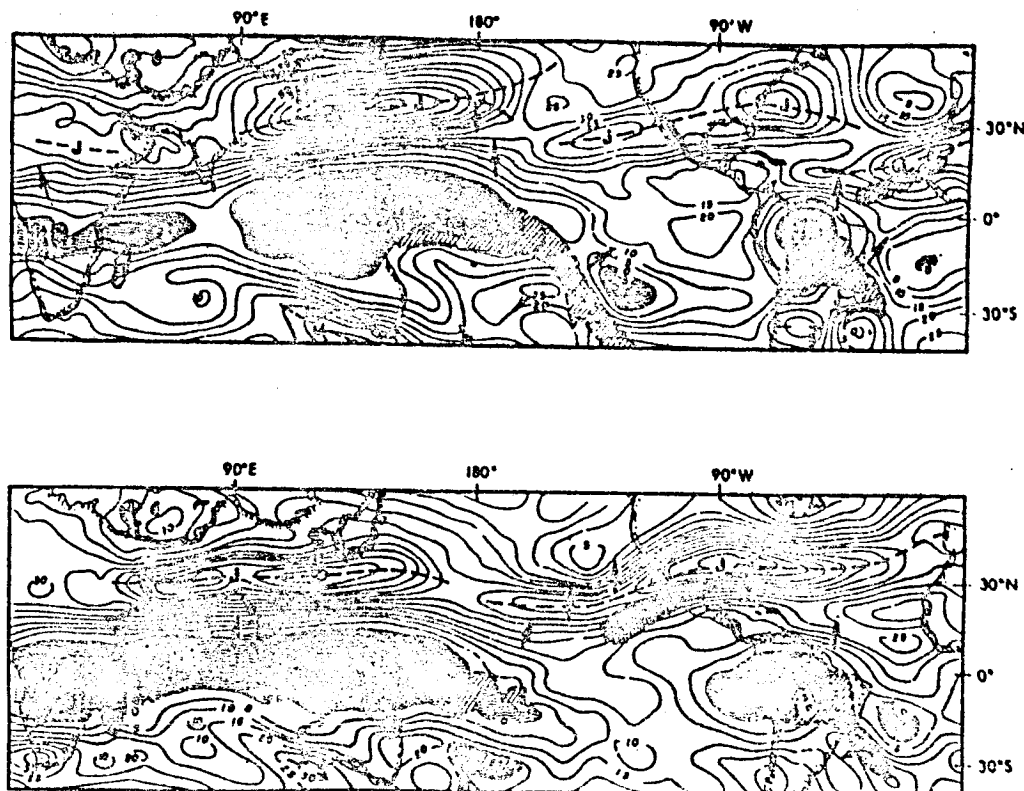
FIGURE 8   Average zonal wind component at 200 mb for January 10 to
January 23, 1979 (top) and January 26 to February 7, 1979 (bottom).
The units are in m/s, and the analysis interval is 5 m/s.   Arrows
indicate the direction of divergent winds at 200 mb, and easterlies are
denoted by horizontal wiggly lines.   The hatched areas indicate the
cloudy regions also depicted in Figure 7.   Thick dashed lines show jet
stream cores.   This wind analysis is based on data gridded by ECMWF.

(1981).   The strongest winter jet streams, as analyzed from this data
set in Figure 8, appear over or off the east coasts of the main
continents.   There is a tendency for the tropical easterly zones to
move westward with the subtropical jet maxima of the northern
hemisphere from the first to the second period.   If there is a
tropical, extratropical connection in the present data, it occurs
through local easterly flow.   The divergent component of the wind
associated with the entrance and exit regions of the jets are sketched
in Figures 9 and 10.   Similar circulations have been previously
discussed by many authors (e.g., Blackmon et al., 1977; Lau, 1978;
Mori, 1959; Murakami and Unninayar, 1977; and Newton, 1959).
   Cressman (1981) suggests that the West Pacific jet stream results
from the solenoidal circulation associated with the strong baroclinic
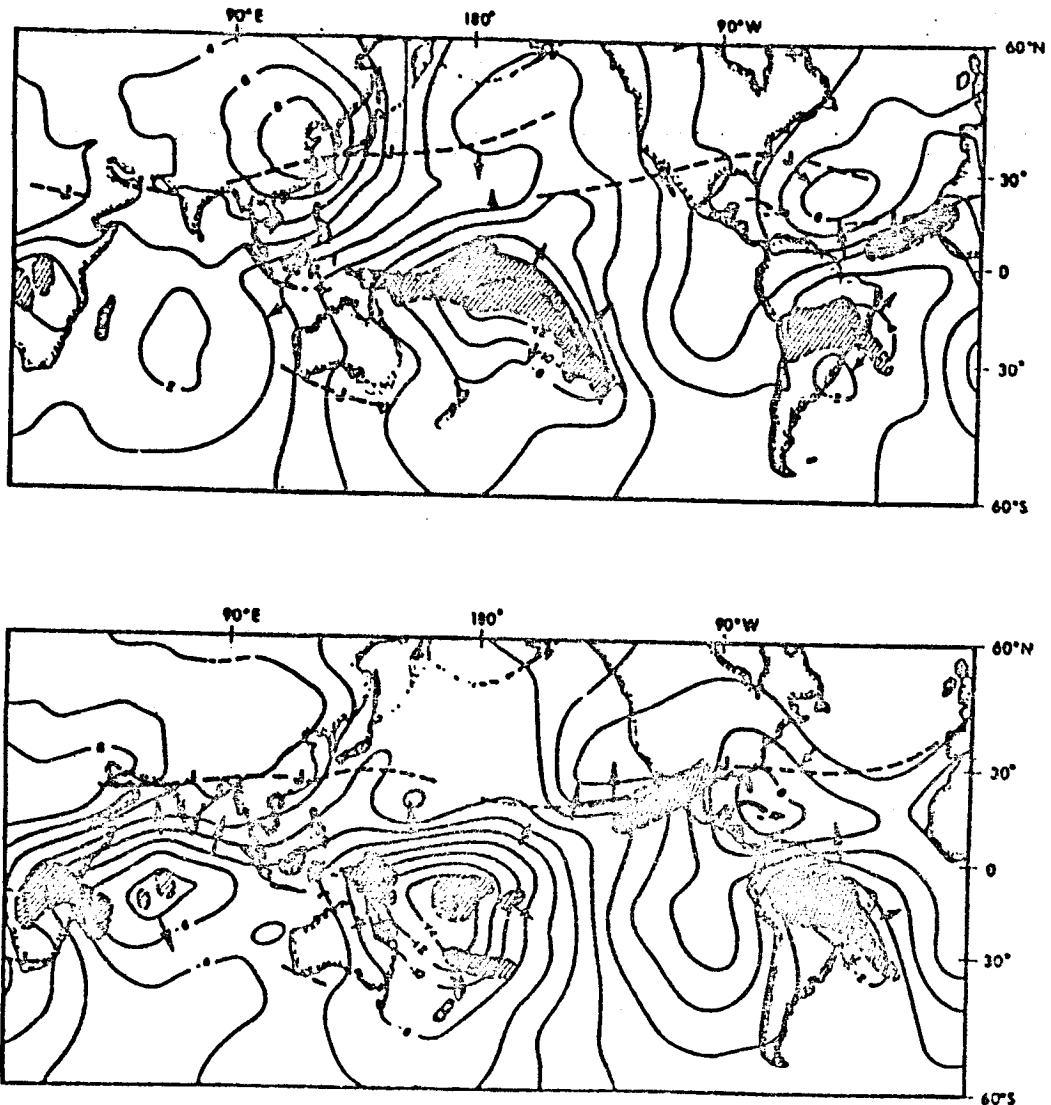
FIGURE 9 As in Figure 8, for the 200 mb velocity potential analyzed every 2×10^6 m^2 s^{-1}.

activity near Japan. He also suggests that the exit region of this jet is a direct consequence of the inertial cycle started by the ageostrophic wind component in the entrance region. Many of the features for this case apply to the west Pacific jet for period 1. The position and extent of the winter jet streams for this period resemble climatological averages (Newell et al., 1972) more clearly than do those of period 2. The main differences between the periods appear in a broad zone centered at about 90°E and in a more narrow region west of Africa.
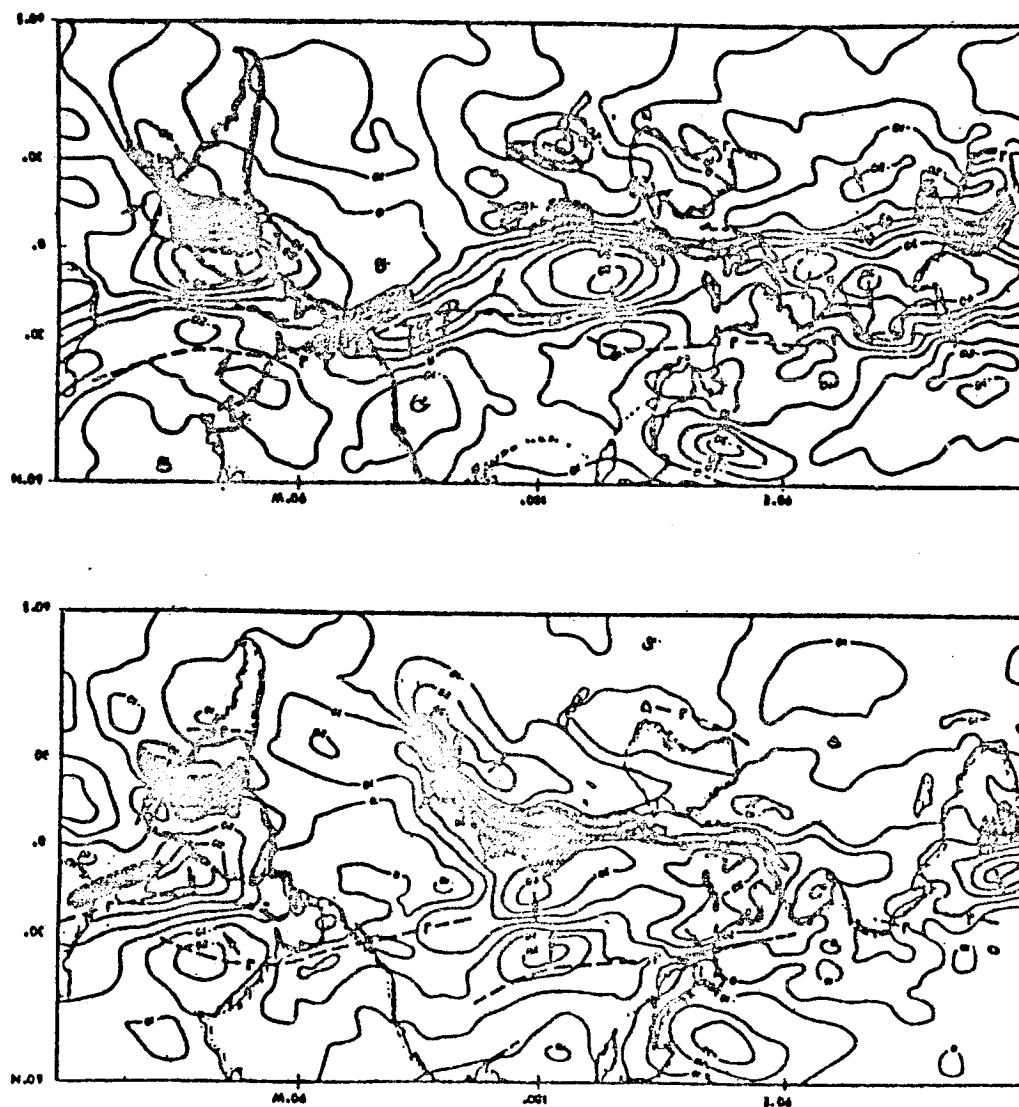
FIGURE 10 As in Figure 8, for the 200 mb divergent meridional wind. component analyzed at an interval of 1 m/s. The unit is 10^{-1} m/s.

The zonal wind maxima above the northwest Pacific and south of Australia shift westward from period 1 to period 2 in an amount approximately equal to the westward shift of maximum infrared brightness and heating over the South Pacific. Zonal wind maxima also appear over India and South Africa for period 2.

The northward/southward divergent wind components over the entrance/ exit regions of the jets are clearly seen in Figures 9 and 10. The.

major differences between the velocity potentials for periods 1 and 2 seem to be correlated with the local changes of the kinetic energy distribution and brightness features. These include the displacement of the center of velocity potential from about 160°W (period 1) to about 170°E (period 2) and the development of a mass source over the equatorial Indian Ocean (period 2).

It appears that many of the differences in the distribtuion of the zonal wind for these two periods can be related to large-scale changes in tropical convection. These convective motions may be triggered by higher latitude effects or by local forcings and instabilities. Whichever may be the initiation mechanism for convection, the present analyses suggest a connection between deep tropical convection and associated changes in the position of the subtropical jet maxima.

CONCLUSIONS

There is a strong apparent interhemispheric interaction of the tropical heating regions of one hemisphere with subtropical jet enhancements of the other hemisphere. The connections for the zonally averaged Hadley cell are explicable by linear Hadley cell dynamics (Dickinson, 1971). However, the apparent connection of the wave components has at present no clear explanation in terms of Rossby waves. To the contrary, the tendency for local interactions to occur through easterly wind zones is at variance with current theory.

Scientists are unaware of convincing theories that may reconcile these issues, although some attempts are made in a review paper by Paegle et al. (1984). Those analyses suggest a prominent role for the strong divergent wind modes of the tropics and emphasize the restrictions of quasi-rotational idealizations for this problem. Careful examination of the tropical divergent motions, of the heating field that drive these motions, and of the normal mode decomposition of these patterns would be useful to clarify the apparent discrepancies between theory and observation. Until a better data set emerges, such studies are best done on the FGGE archives.

ACKNOWLEDGEMENTS

REFERENCES

Baker, W. E., and J. Paegle (1983). The influence of the tropics on the prediction of ultralong waves. Part I: Tropical wind field. Mon. Wea. Rev. 111, 1341-1355.

Bennett, J. R., and J. A. Young (1971). The influence of latitudinal wind shear upon large-scale wave propagation into the tropics. Mon. Wea. Rev. 99, 202-214.

Bjerknes, J. (1966). A possible response of the atmospheric Hadley circulation to equatorial anomalies of ocean temperature. Tellus 18, 820-829.

Bjerknes, J. (1969). Atmospheric teleconnections from the equatorial Pacific. Mon. Wea. Rev. 97, 163-172.

Blackmon, M., J. M. Wallace, N.-C. Lau, and S. L. Mullen (1977). An observational study of the northern hemisphere wintertime circulation. J. Atmos. Sci. 34, 1040-1053.

Charney, J. G. (1969). A further note on large-scale motions in the tropics. J. Atmos. Sci. 26, 182-185.

Charney, J. G., and A. Eliassen, 1949. A numerical method for predicting the perturbations of the middle latitude westerlies. Tellus 1, 38-54.

Cressman, G. P. (1981). Circulations of the west Pacific jet stream. Mon. Wea. Rev. 109, 2450-2463.

Daley, R., J. Tribbia, and D. L. Williamson (1981). The excitation of large-scale free Rossby waves in numerical weather prediction. Mon. Wea. Rev. 109, 1836-1861.

Dickinson, R. E. (1971). Analytic model for zonal winds in the tropics. II. Variation of the tropospheric mean structure with season and differences between hemispheres. Mon. Wea. Rev. 99, 511-523.

Geisler, J. E., and R. E. Dickinson (1974). Numerical study of an interacting Rossby wave and barotropic zonal flow near a critical level. J. Atmos. Sci. 31, 946-955.

Gill, A. E. (1980). Some simple solutions for heat-induced tropical circulations. Quart. J. Roy. Meteorol. Soc. 106, 447-462.

Grose, W. L., and B. J. Hoskins (1979). On the influence of orography on large-scale atmospheric flow. J. Atmos. Sci 36, 223-234.

Held, I. M. (1983). Stationary and quasi-stationary eddies in the extratropical troposphere: Theory. Large-Scale Dynamical Principles in the Atmosphere. B. Hoskins and R. Pearce, eds., Academic Press.

Horel, J. D., and J. M. Wallace (1981). Planetary scale atmospheric phenomena associated with the southern oscillation. Mon. Wea. Rev. 109, 813-829.

Krishnamurti, T. N. (1971). Observational study of the tropical upper tropospheric motion field during the northern hemisphere summer. J. Appl. Meteorol. 10, 1066-1096.

Krishnamurti, T. N., M. Kanamitsu, W. J. Koss, J. D. Lee (1973). Tropical east-west circulations during the northern winter. J. Atmos. Sci. 30, 780-787.

Lau, N. C. (1978). On the three-dimensional structure of the observed transient eddy statistics of the northern hemisphere wintertime circulation. J. Atmos. Sci. 35, 1900-1923.

Lewis, F. P. (1979). Latent heat induced divergence and the ultralong waves of the subtropics and midlatitudes. Doctoral dissertation, University of Utah, Salt Lake City, Utah. 239 pp.

Lorenc, A. (1981). A global three-dimensional multi-variate statistical interpolation scheme. Mon. Wea. Rev. 109, 701-721.

Mak, M.-K. (1969). Laterally driven stochastic motions in the tropics. J. Atmos. Sci. 26, 41-64.

Mohri, K. (1959). Jet streams and upper fronts in the general circulation and their characteristics over the Far East (Part II). Geophys. Mag. 29, 333-412.

Murakami, T., and M. Unninayar (1977). Atmospheric circulation during December 1970 through February 1971. Mon. Wea. Rev. 105, 1024-1038.

Murakami, T. (1978). Winter circulations and wave number domain energetics at 200 mb. J. Meteorol. Soc. Japan 56, 215-231.

Newell, R. E., J. W. Kidson, D. G. Vincent, and G. J. Boer (1972). The general circulation of the tropical atmosphere and interactions with extratropical latitudes. Vols. 1 and 2. The MIT Press.

Newton, C. W. (1959). Axial velocity streaks in the jet streams: Ageostrophic "inertial" oscillations. J. Meteorol. 16, 638-645.

Paegle, J., and W. E. Baker (1982a). Planetary scale characteristics of the atmospheric circulation during January and February 1979. J. Atmos. Sci 39, 2521-2538.

Paegle, J., and W. E. Baker (1982b). Global scale weekly and monthly energetics during January and February 1979. J. Atmos. Sci. 39, 2750-2759.

Paegle, J., and W. E. Baker (1983). The influence of the tropics on the prediction of ultralong waves. Part II: Latent heating. Mon. Wea. Rev. 111, 1350-1371.

Paegle, J., J. N. Paegle, and Y. Hong (1983). The role of barotropic oscillations within atmospheres of highly variable refractive index. J. Atmos. Sci. 40, 2251-2265.

Physik, W. L. (1981). Winter depression tracks and climatological jet streams in the southern hemisphere during the FGGE year. Quart. J. Royal Meteorol. Soc. 107, 883-897.

Ramage, C. S. (1968). Role of tropical "maritime continent" in the atmospheric circulation. Mon. Wea. Rev. 96, 365-370.

Somerville, R. C. J. (1980). Tropical influence on the predictability of ultralong waves. J. Atmos. Sci. 37, 1141-1156.

Zangvil, A., and M. Yanai (1980). Upper tropospheric waves in the tropics. Part I: Dynamical analysis in the wavenumber frequency domain. J. Atmos. Sci. 37, 283-298.

PLANETARY WAVE PREDICTION:
BENEFITS OF TROPICAL DATA AND GLOBAL MODELS

Richard C.J. Somerville
Scripps Institution of Oceanography

ABSTRACT

Skillful numerical predictions of midlatitude atmospheric planetary waves generally require both tropical data for the initial conditions and a global domain for the forecast model. The lack of either adequate tropical observations or a global domain typically leads to a significant degradation of forecast skill in middle latitudes within the first one to three days of the forecast period. These effects were first discovered by numerical experimentation. They were subsequently explained theoretically, and their importance for practical forecasting has been confirmed in a series of prediction experiments using FGGE data.

INTRODUCTION

Tropical initial data and a global forecast domain have strong effects on the midlatitude planetary wave components of numerical weather predictions. Operational forecasts today, such as those at the European Centre for Medium-Range Weather Forecasts (ECMWF), are routinely carried out using global models initialized with global observational data. The skill of such forecasts is due, of course, to progress in many areas, including physical parameterizations, numerical methods and fine spatial resolution, objective analysis and initialization, and improved initial data.

A significant part of the improved skill of modern large-scale forecasts, relative to those of the pre-FGGE era, may be attributed, however, simply to the use of a global forecast domain and tropical initial data. The crucial importance of these factors to forecast skill, within the first few days of the forecast period, has become recognized and understood only within about the last five years. The purpose of this brief note is to list some papers, appearing from 1980 to 1983, which have helped to illuminate this subject. This list of papers is strictly limited to the tropical data and domain effect, and no attempt is made to survey the many other factors that affect planetary wave predictability.

88<

DATA AND DOMAIN EFFECTS

The strong influence of tropical initial data and a global forecast domain was first shown clearly in an ensemble of primitive-equation, real-data numerical predictions using both global and hemispheric models (Somerville, 1980). This paper, which also contains a summary of earlier work, was itself an outgrowth of the model intercomparison study of Baumhefner and Downey (1978) and used the same ensemble of six pre-FGGE test cases. These cases were originally chosen by Druyan et al. (1975) for one of the earliest examinations of the extended-range forecasts of a more-or-less modern global general circulation model (Somerville et al., 1974). The intercomparison of Baumhefner and Downey (1978) found that this model had superior planetary wave skill, relative to that of the other models tested. Somerville (1980) showed that this superior skill was essentially due simply to the use of a global forecast domain and tropical initial data. A major result of Somerville (1980) also suggested that the resulting errors might be associated with the spurious excitation of large-amplitude external modes, consistent with earlier diagnostic studies of planetary wave predictions (Lambert and Merilees, 1978).

THEORETICAL UNDERSTANDING

The most comprehensive and thorough theoretical treatment of this problem is that of Daley et al. (1981). Using one of the cases of Somerville (1980), Daley et al. extensively analyzed the modal structure of both observational data and numerical integrations. They treated three distinct phenomena, denoted as the tropical data effect, the hemispheric/global domain effect, and the tropical wall effect. Daley et al. (1981) showed that all three may largely be understood in terms of the spurious excitation of transient external large-scale Rossby modes. Such modes can be sufficiently energetic and fast-moving to produce significant forecast errors in as little as one day.

In an independent and complementary study, Roads and Somerville (1982) used an extremely simple theoretical framework: a quasi-linear, quasi-geostrophic barotropic model, including orography, zonal forcing and frictional dissipation. Roads and Somerville were able to show that a hemispheric version of this model could excite anomalous Rossby waves and produce erroneous short-range planetary wave forecasts in middle latitudes.

PREDICTION EXPERIMENTS

Several aspects of tropical data and domain effects on midlatitude large-scale forecasts were clarified by an exchange of correspondence between Gadd (1981) and Somerville (1981). These papers cite the results of several numerical prediction experiments. Perhaps the most striking experimental result was that of Bengtsson et al. (1980) who used a version of the ECMWF operational model to determine the effect

of a global domain on "useful predictability." In an ensemble of eight cases, they found that for the planetary waves the useful predictability increased on average by 16 hours when a global rather than a hemispheric domain was used. Of the eight cases, three showed no improvement, three showed a clear improvement, and two showed a substantial improvement of more than 36 hours. The strong case-dependence appears to be consistent with the theoretical results of Roads and Somerville (1982).

Subsequently, Baker and Paegle (1983) studied the influence of FGGE tropical wind data on the numerical prediction of planetary waves in an ensemble of six cases, with the Goddard fourth-order model. They too found a noticeable effect, "consistent with the results of Somerville (1980)." Baker and Paegle also confirm that the forecast error "appears in a predominantly barotropic mode as was found in studies by Daley et al. (1981) and Roads and Somerville (1982)."

Finally, Temperton (1983) reports results of FGGE experiments in which a global version of the Canadian operational spectral model produced clearly more skillful forecasts of planetary waves than a hemispheric version.

ACKNOWLEDGMENT

REFERENCES

Baker, W.E., and J. Paegle (1983). The influence of the tropics on the prediction of ultralong waves. Part I: Tropical wind field. Mon. Wea. Rev. 111, 1341-1355.

Baumhefner, D.P., and P. Downey (1978). Forecast intercomparisons from three numerical weather prediction models. Mon. Wea. Rev. 106, 1245-1279.

Bengtsson, L., U. Cubasch, and M. Jarraud (1980). Interhemispheric influences on the predictability of the ultralong waves. GARP Working Group on Numerical Experimentation, Research Activities in Atmospheric and Oceanic Modelling, Rept. No. 21, 55-56, World Meteorological Organization, Geneva.

Daley, R., J. Tribbia, and D.L. Williamson (1981). The excitation of large-scale free Rossby waves in numerical weather prediction. Mon. Wea. Rev. 109, 1836-1861.

Druyan, L.M., R.C.J. Somerville, and W.J. Quirk (1975). Extended-range forecasts with the GISS model of the global atmosphere. Mon. Wea. Rev. 103, 779-795.

Gadd, A.J. (1981). Comments on tropical influences on the predictability of ultralong waves. J. Atmos. Sci. 38, 2542-2543.

Lambert, S.J., and P.E. Merilees (1978). A study of planetary wave
   errors in a spectral numerical weather prediction model.
   Atmos.-Ocean 16, 197-211.
Roads, J.O., and R.C.J. Somerville (1982). Predictability of
   ultralong waves in global and hemispheric quasi-geostrophic
   barotropic models. J. Atmos. Sci. 39, 745-755.
Somerville, R.C.J. (1980). Tropical influences on the predictability
   of ultralong waves. J. Atmos. Sci. 37, 1141-1156.
Somerville, R.C.J. (1981). Reply. J. Atmos. Sci. 38, 2544-2546.
Somerville, R.C.J., P.H. Stone, M. Halem, J.E. Hansen, J.S. Hogan,
   L.M. Druyan, G. Russell, A.A. Lacis, W.J. Quirk, and J. Tenenbaum
   (1974). The GISS model of the global atmosphere. J. Atmos. Sci.
   31, 84-117.
Temperton, C. (1983). Survey of forecasts starting from a particular
   SOP-I initial state. WGNE Forecast Comparison Experiments. World
   Climate Research Programme, Numerical Experimentation Programme,
   Rept. No. 6, 9-71, World Meteorological Organization, Geneva.

11.   CROSS-EQUATORIAL EXCHANGE

Organizer	Julia N. Paegel
Session Chairman	William M. Gray
Speaker	John A. Young
Rapporteur	Richard S. Greenfield

ANALYSIS OF CROSS-HEMISPHERIC INFLUENCES ON THE MONSOON TROUGH
AND TROPICAL CYCLONE GENESIS DURING FGGE
AND DIURNAL SUBSIDENCE DIFFERENCES

William M. Gray and Cheng-Shang Lee
Colorado State University

ABSTRACT

For a number of years our project has been studying the cross-equatorial
(winter to summer hemisphere) processes that can lead to the day-to-day
alterations in the strength of the monsoon trough. These processes are
also related to the genesis and intensification of tropical storms.
The cross-hemispheric processes that occurred during the FGGE year are
currently being studied with the use of the ECMWF analysis. This paper
briefly describes how the winter hemisphere can affect (1) low-level
cold surge penetration across the equator following cold front passage,
and (2) how upper tropospheric anticyclones of the winter hemisphere
can produce an intensification of a tropical cyclone of the opposite
hemisphere.

This paper also presents ECMWF analysis of the 00Z versus 12Z
diurnal difference in the clear region (10° diameter) subsidence
occurring in the subtropical Pacific Ocean during FGGE. These
calculations agree with previous rawinsonde composite results and
appear to offer further substantiation to the previously hypothesized
response process of the troposphere to its large 2-to-1 night versus
daytime differences in net radiational cooling.

We also attempt to show the general reliability of the FGGE ECMWF
analysis with regad to the specification of the large-scale structure
of tropical cyclones. We are optimistic as to the general validity of
the ECMWF wind analysis, particularly those analyses of the large-scale
that primarily involve the rotational component of the wind field.

INTRODUCTION

Our tropical research project has been performing analysis on the
physical processes associated with tropical cyclone genesis, structure,
and intensity change for a number of years.

The more tropical cyclones are studied, the more we are coming to
realize to what extent these storm systems, and indeed the monsoon
trough itself, is the product of their larger scale surrounding
circulations. One cannot properly understand the formation and the
intensity change of tropical cyclones without often consulting the

475

meteorological conditions of the opposite hemisphere. To a large extent, this is also true of the monsoon trough.

We have started analysis of all 80 tropical cyclones that occurred during the FGGE year through the use of ECMWF 1.875° grid level IIIb data. Although this ECMWF analysis cannot well describe the inner structure of the tropical cyclone, it does show a very good resolution of the cyclones surrounding flow features at radii greater than 3° to 4° from the storm center. It is this information we have been concentrating on. This analysis of individual case ECMWF FGGE data agrees, in general, with what we would have expected from the information that had been gained from our project's previous rawinsonde composite analysis of these storm systems.

We are finding that there are distinctive large-scale circulation features that act to bring about the genesis of tropical cyclones. Cyclone genesis appears to be largely a product of lower tropospheric processes. By contrast, cyclone intensification or the later increase in a cyclone's central inner core wind strength appears to be related in a substantial way to the strength of cyclone's upper tropospheric outflow channels. Upper tropospheric anticyclonic processes of the winter hemisphere often appear to play a primary role in the change of maximum wind strength of a cyclone of the summer hemisphere.

Our beginning look at the question of the diurnal variability occurring during the FGGE year with the ECMWF analysis indicates that if one analyzes the divergence over a broad area in the oceanic subtropical clear zones, the large diurnal cycle of vertical motion and divergence is obtained. In agreement with our previous rawinsonde composite analysis of 00Z and 12Z rawinsonde data, we find that the 00Z and 12Z ECMWF FGGE year analysis of subsidence over oceanic 5° radius (10° diameter) clear regions also show a distinctive 2-to-1 morning versus evening (morning maximum) subsidence difference. This agrees very well with the composite results we obtained in earlier years and with our general ideas on night versus daytime tropospheric radiation being the primary driving mechanism for this diurnal subsidence cycle.

LOW LEVEL CROSS HEMISPHERIC INFLUENCES ON THE VARIATION OF THE MONSOON TROUGH--WINTER HEMISPHERE COLD SURGE INFLUENCE

Western Pacific

The rises in sea level pressure (SLP) that occur behind vigorous wintertime cold front passage can often be tracked to the equator and beyond into the opposite hemisphere. This can lead to pressure rises near the equator and the establishment of west-east pressure gradients at low latitudes of both hemispheres. This pressure typically occurs in a surge-type fashion. The equatorward movement of 15 to 20 m//s of this pressure surge is faster than that of the individual air parcels. Surges often cause an increase in the cross-equatorial wind and a strengthening of the monsoon westerly flow of the summer hemisphere.
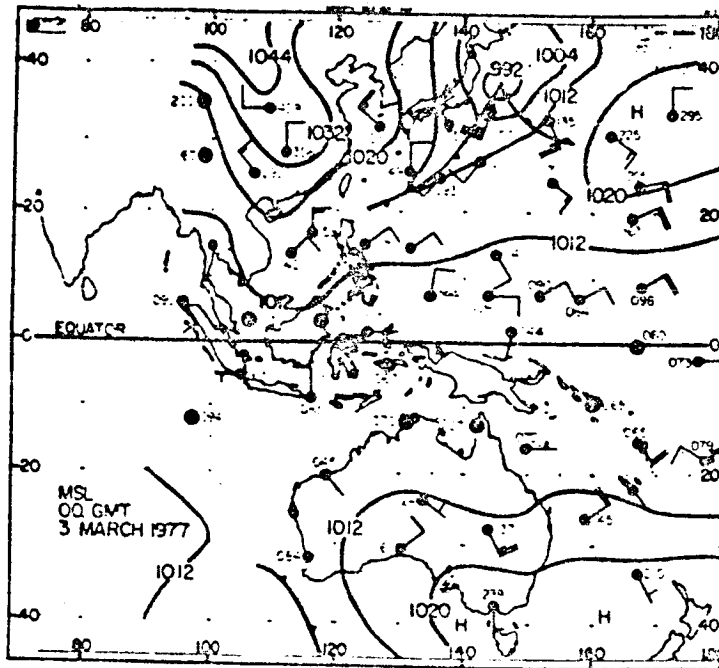
FIGURE 1   Mean sea level pressure and gradient level wind analysis for
3 March 1977.   Pressure in millibars, wind speed in conventional format
(full barb = 5 m s^{-1}).   (From Love, 1982).

Enhanced westerly wind effects are typically observed through a
tropospheric deep layer from the surface up to at least 400 to 500 mb.
Figures 1 and 2 are a typical example of how a wintertime baroclinic
cyclone system coming out of east Asia can lead to the enhancement of
gradient level winds in Indonesia and North Australia two days later.
     This sequence of events is especially active if the near equatorial
SLP 5° to 10° longitude to the east of the cold surge is lower than
normal.   The monsoon trough region can thus have different receptabil-
ities to these winter surges.   If pressures along the equator are
already low in the equatorial region to the east of the position where
the surge will penetrate, then the enhancement of westerly winds is
much less noticeable.   For instance, if the Solomon and Marshall Island
pressures (see Figure 3) are lower than normal, then surge induced
pressure rises in the Borneo area will be more effective at westerly
wind enhancement.   Disregarding abnormal equatorial SLP, day-to-day
changes in SLP are generally correlated with SLP changes in the winter
hemisphere subtropics.   The relationship varies however from year to
year in both the strength of the correlation and in the location of the
equatorial response.
     Inspection of the synoptic charts reveals that during the 1978 to
1979 season the northern hemisphere cold surges were much further east
than usual.   This is quantified in Figure 5, which shows a histogram of

478
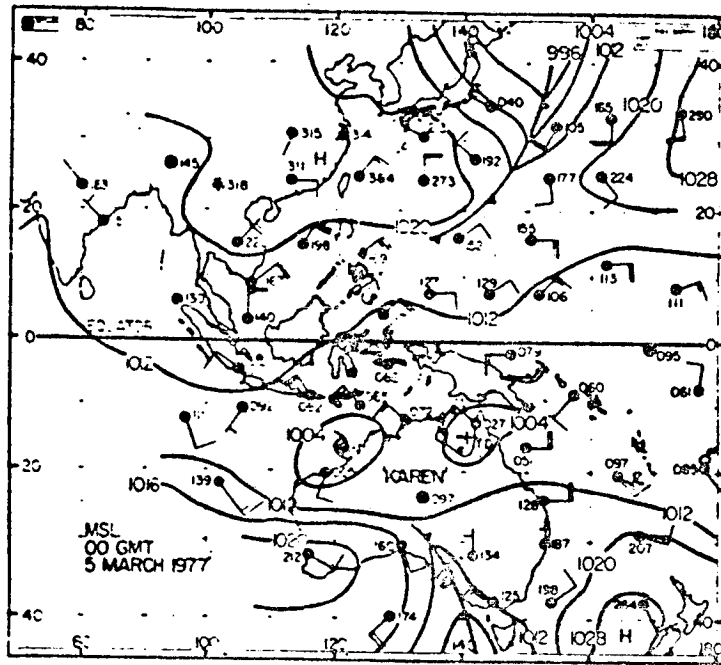
FIGURE 2   Mean sea level pressure and gradient level wind analysis for
5 March 1977.   Units as for Figure 1.   (From Love, 1982).

the locations of the western edge of cold surges in the MONEX season
compared with the average locations occurring during six other seasons
(including MONEX).

East-west equatorial pressure gradients respond quickly to changes
in pressure in the winter hemisphere subtropics.   Love (1982) has made
calculations of the relationships of cold surges to surface pressure
difference for 100 days during the FGGE period of December 1 to March 5
and the period of June 1 to September 7.   Figure 4 shows the 600 mb
westerly wind component at Port Moresby and the Borneo-Solomon Island
pressure gradients for the southern hemisphere summer during the 1978
to 1979 FGGE period.   Note how closely related Port Moresby 600 mb
westerly wind speed is to Borneo minus Solomon Island pressure gradient.

Indian Ocean

Observational evidence also indicates that the increase of summertime
westerly winds over the Indian continent (and sometimes also the
formation of monsoon depressions in the north Indian Ocean) is often
associated with the passage of strong southern hemisphere cold front
penetration across the Cape of Africa and into the Mozambique Channel
as indicated by Figure 6.   Sikka and Gray (1981) have made preliminary
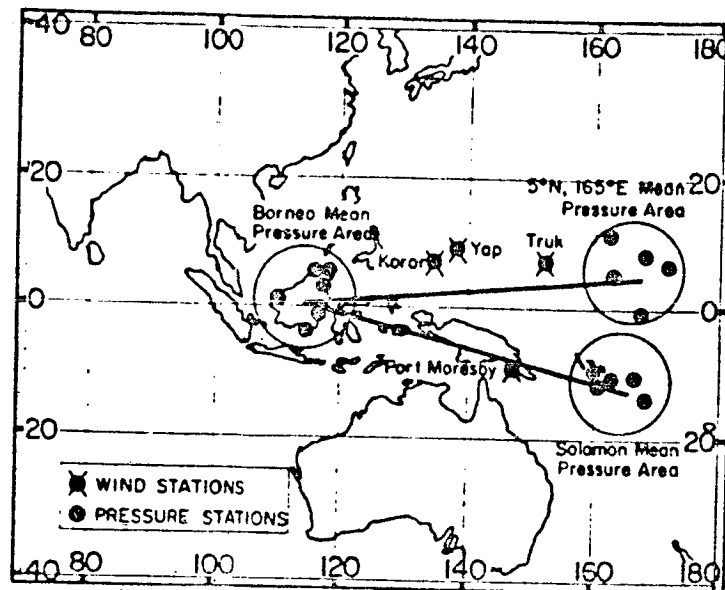
FIGURE 3 Locations of areas for which large-scale pressure gradients
were calculated and intervening stations whose wind fields were
correlated with the pressure difference time series.

analysis of eight years of daily weather chart data, using South
African 1960s and IGY period of 1957 to 1958 plus the 1979 MONEX period.

The phase lag between the southern hemisphere wintertime events and
the northern hemisphere summer events often appears to be related to
the occurrence of vigorous cold air advection and pressure rises that
pass through the Mozambique Channel and along the east African coast to
the equator or beyond. These northward moving pressure pulses move
faster than the individual northward moving air particles and appear to
be similar to the type of cold air surges that occur along the Asian
coast in winter.

Such east African cold air induced pressure rises often cause an
enhancement of cross-equatorial flow and a resulting increased west to
east pressure gradient over the Indian region. This enhancement of the
Indian monsoon low level westerly winds may not take place, however, if
conditions within the Indian subcontinent or to the east are not
receptive to the receipt of these southern hemisphere cold surge
influences.

It appears that these southern hemisphere surge influences over
India are strongest when SLP over southeast Asia is lower than normal.
About one third of these east African cold surges are effective at
bringing about a noticeable increase in subcontinent low level
westerlies.
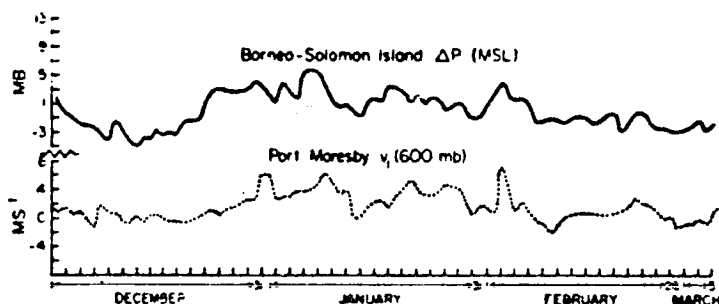
FIGURE 4   The 600 mb westerly wind component at Port Moresby and the
Borneo-Solomon Islands pressure difference for the winter MONEX
period.   (From Love, 1982).

LOW-LEVEL CROSS-HEMISPHERIC INFLUENCES
ON TROPICAL CYCLONE GENESIS

This section discusses how winter hemisphere baroclinic events can
influence the genesis of tropical cyclones in the summer hemisphere
monsoon trough.

There is considerable evidence that tropical cyclone genesis occurs
only when the surrounding large-scale tangential flow to 4° to 8°
radius about a tropical disturbance becomes greater than 2 to 3 m/s.
This is primarily accomplished by surrounding environmental processes
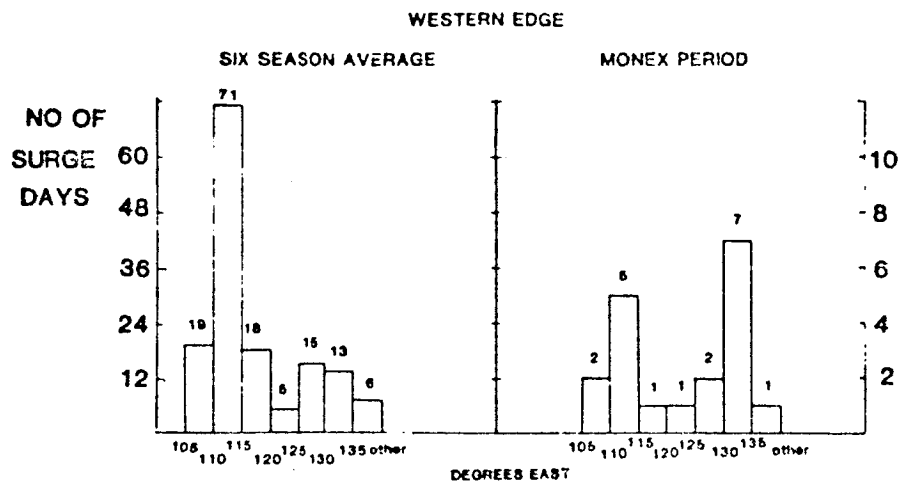
FIGURE 5   Histograms giving the longitude of the western edge of
Northern Hemisphere winter cold surges.   The long-term (six season)
distribution is contrasted with that for the 1978-79 winter MONEX
period.   (From Love, 1982).
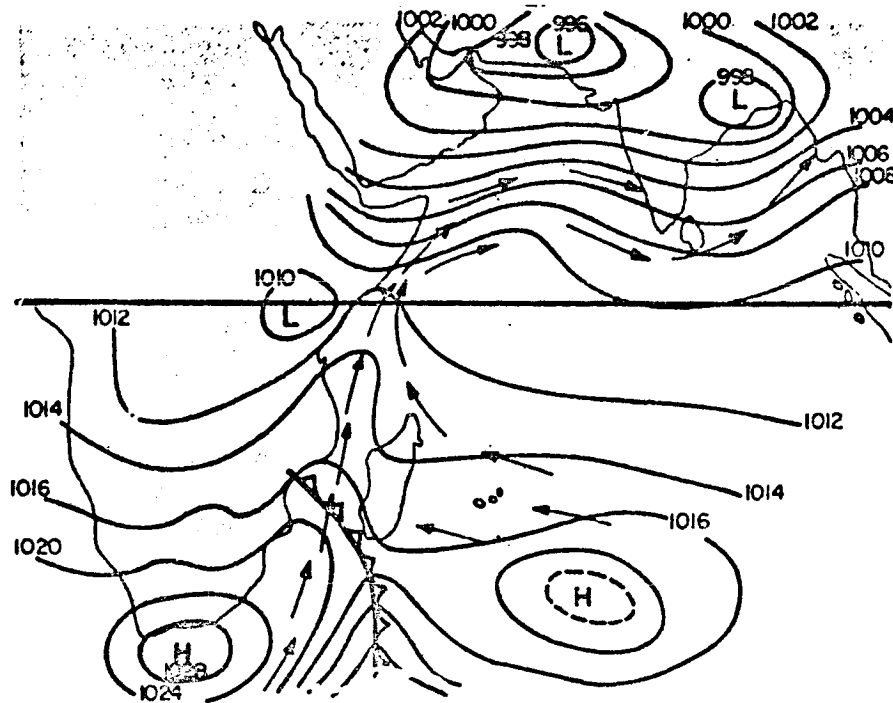
FIGURE 6 Idealized view of how a wintertime surge off of South African east coast can enhance the North Indian low-level westerly current.

that act to convey angular momentum about the center of tropical disturbance. Angular momentum transport calculations reveal that the surrounding large-scale changes in such a manner that it increases the import of angular momentum to the genesis point.

Our rawinsonde and individual case analysis finds strong evidence that tropical cyclone development is often influenced by events in the winter hemisphere. The transition from a quiet (noncyclogenesis) state to the precyclone condition is often marked by an intensification of the winter hemisphere Hadley cell. Corresponding to this, there is an increase in the strength of the monsoon westerlies equatorward of the precyclone disturbance and in the strength of the upper level equatorial easterlies. Both the increased cross-equatorial inflow to the monsoon trough and the increased monsoon westerlies occur through a deep layer from the surface up to about the 400 mb level. The composite analyses also reveal that the transition to the pregenesis state takes place over a very large scale.

It appears the forcing from northern to southern hemisphere during the southern hemisphere summer is quite similar to that operating in the other direction six months later. The case studies indicate it is favorable to have a minimum of lower tropospheric baroclinic action poleward of the developing disturbance, with an upper level (200 mb) tropical upper tropospheric trough (TUTT) type disturbance impinging on
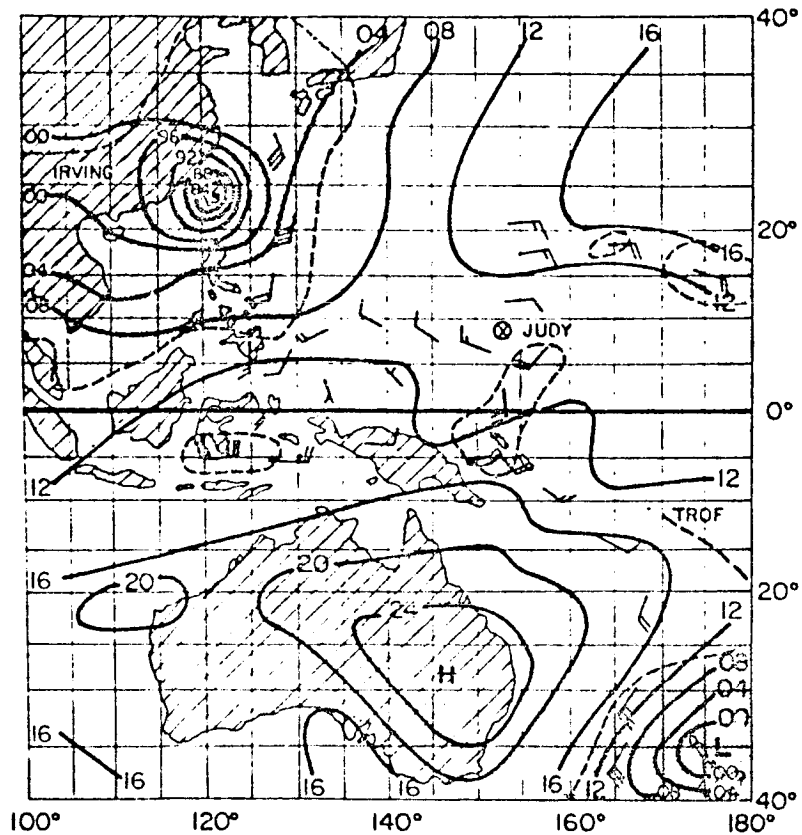
FIGURE 7 Low-level synoptic/wind map for 00Z 15 August 1979. The position of TD 13 (Judy) is given by the symbol ⊗. Thick lines mark the surface pressure and frontal patterns. Representative 850 mb winds are shown. The thin dashed lines delineate areas with wind speeds of 10 m s^{-1} (20 kt) or greater. (Adapted from ECMWF and NCC analyses). (From Askue, 1984b).

it. Baroclinic action pushing relatively close to the equator in the winter hemisphere appears to be a consistent feature. Figure 7 shows the southern hemisphere forcing for the early stage building of a tropical disturbance, which eventually became Typhoon Judy on August 19, 1979. Note the strong low-level southern hemisphere winds feeding into the southern portion of this precyclone on August 15. This southern hemisphere forcing occurred behind a cold surge moving eastward from Australia with a high pressure cell over eastern Australia. From consideration of our case studies of tropical cyclone genesis and from rawinsonde composite analysis of genesis, our idealized scenario for an equatorial trough tropical cyclone genesis case can be prepared. The following important synoptic events appear to occur:

1. There is intense midlatitude cyclogenesis at about the genesis longitude in the winter hemisphere three days before genesis.

2. The strong anticyclogenesis in the wake of the developing winter hemisphere trough moves equatorward to reinforce the subtropical ridge near latitude 25°.

3. A cold surge in the winter hemisphere propagates equatorward, raising pressures from the subtropics to the equator in an area west of the genesis point.

4. With the establishment of east-west equatorial pressure gradients, down-gradient westerly winds occur equatorward of the equatorial trough.

5. Around the time of enhanced equatorial westerlies an anticyclone has moved slowly eastwards, polewards of the pregenesis cluster, intensifying the summer hemisphere trade easterlies.

6. Enhanced low level convergence into the intertropical convergence zone increases convection, with stronger outflow occurring aloft in the layer 250 mb to 100 mb.

7. The large-scale vertical wind shears induced by the strengthened Hadley cell lead to warming of the core of the equatorial trough. Such flows also allow the necessary transports of angular momentum to support an intensifying vortex.

An idealized picture of northern hemisphere influences on southern hemisphere cyclone genesis is shown in Figure 8. That of southern hemisphere influences on northern hemisphere cyclone genesis is shown in Figure 9.

For a more detailed description of this research, the reader may consult the CSU project report of Love (1982).

CROSS-HEMISPHERIC INFLUENCES AT UPPER TROPOSPHERIC LEVELS

The FGGE year ECMWF analysis is also demonstrating that, in addition to the frequently observed low-level cross-hemispheric influences just discussed, there is also a large number of important and distinctly upper level cross-hemispheric processes. This is particularly true of the winter hemisphere's role in the intensification of summer hemisphere tropical cyclones.

Tropical cyclone intensification is defined as the spin up of the cyclone's central region of maximum winds. Recent research at CSU (Holland and Merrill, 1984), too involved to discuss here, is indicating that the tropical cyclone inner region intensification (inside 1° to 2° radius) is likely the result of processes that act to enhance the cyclone's surrounding upper level outflow channels. Such an outflow channel enhancement causes a compensating inner region lower-level inflow and a consequent inner-core wind spin-up. This type of upper level cross hemispheric influences on tropical cyclone intensity change are distinctive from the much larger scale cross-hemispheric processes occurring at lower levels that bring about the enhancement of the monsoon trough or that lead to cyclone genesis (increase of tangential wind over a broad 10° wide belt).
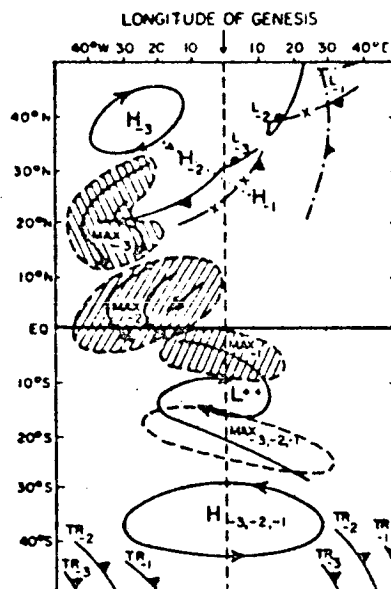
FIGURE 8   Idealized gradient level streamline chart for three days preceding tropical cyclone genesis in the Southern Hemisphere. Subscripts -3, -2, -1 refer to the position of the synoptic feature that number of days before genesis. The momentum burst (isotach maximum) has been shaded. (From Love, 1982).

Impact of the Southern Hemisphere on Northern Hemisphere Tropical Cyclone Intensification

A strong equatorial anticyclone over the southern hemisphere's tropical region is extremely favorable for enhancing the equatorward outflow of a tropical cyclone in the northern hemisphere and vice versa. In particular, when an equatorial anticyclone of increasing intensity to the southeast of a northern hemisphere tropical cyclone moves westward, this acts to strengthen the equatorward outflow channel of the tropical cyclone, often leading to its rapid intensification.

Example. On August 16, the tropical depression, which became Typhoon Judy, was located over the northwest Pacific. It had light southeast winds above it and a weak upper tropospheric outflow (Figure 10a). During August 17-19, an equatorial anticyclone in the southern hemisphere to the southeast of this storm moved westward and increased in intensity (Figures 10b and 10c). This process dramatically changed the strength of the storm's upper level outflow from southeast to northeast on August 17. A very strong equatorward outflow channel was thus established during this period. Following the enhancement of the equatorward outflow, the tropical cyclone dramatically intensified from August 17 to 20. A tropical storm was formed on August 17, and by
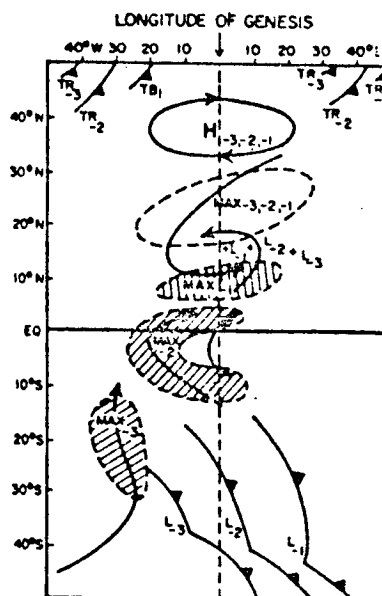
FIGURE 9   Idealized gradient level streamline chart for three days preceding tropical cyclone genesis in the Northern Hemisphere. Subscripts -3, -2, -1 ref r to the position of the synoptic feature that number of days before genesis. The momentum burst (isotach maximum) has been shaded.   (From Love, 1982).

August 20 Typhoon Judy reached its sustained wind speed of 135 kts. A large number of other examples of similar cyclone intensification have been found during the FGGE year. This also includes northern hemisphere 200 mb anticyclone enhancement of southern hemisphere tropical cyclones.

USE OF ECMWF FGGE IIIb DATA FOR THE STUDY OF THE SURROUNDING FLOW CONDITIONS RESPONSIBLE FOR TROPICAL CYCLONE GENESIS

The FGGE Level IIIb data used are zonal and meridional components of horizontal wind. These data are extracted directly from the analyzed pressure levels and have not been subject to any vertical interpolation. The analysis procedure used a primitive equation forecast for the first guess, but after the initial analysis step, no model initialization has taken place. The data are available at 1.875° latitude/longitude grids and at 15 vertical pressure levels. The pressure levels used in this study are 100, 150, 200, 250, 300, 400, 500, 700, 850, and 1000 mb, but the following discussion is based on the low level winds only.
     For our tropical cyclone studies, the FGGE data that were initially on spherical grids have been linearly interpolated onto cylindrical

FIGURE 10 200 mb streamline patterns at 00Z. A Northern Hemisphere tropical cyclone (Judy) with an equatorward outflow channel intensified when an anticyclone over the opposite hemisphere moved close to it. From 17 to 19 August Judy's maximum sustained wind increased from 50 to 125 kts. (a) 16 August 1979 (V_{max} = 50 km), (b) 17 August 1979 (V_{max} = 80 kts) and (c) 19 August 1979 (V_{max} = 135 kts). (From Chen and Gray, 1984).

grids. There are 13 radial and 16 azimuthal grid segments. The grid spacing is 1^O latitude radius (starting from 2^O out from the cyclone center) and 22.5^O azimuth. The cylindrical grid point data of zonal and meridional wind components (u, v) are then converted to radial and tangential wind components (v_r, v_t) with respect to the cyclone center. The results presented in this paper use only the tangential winds, which are considered more reliable than the radial wind.

RESULTS FROM FGGE DATA FOR TYPHOON JUDY:

$V_{MAX}=20$KTS

$V_{MAX}=135$KTS
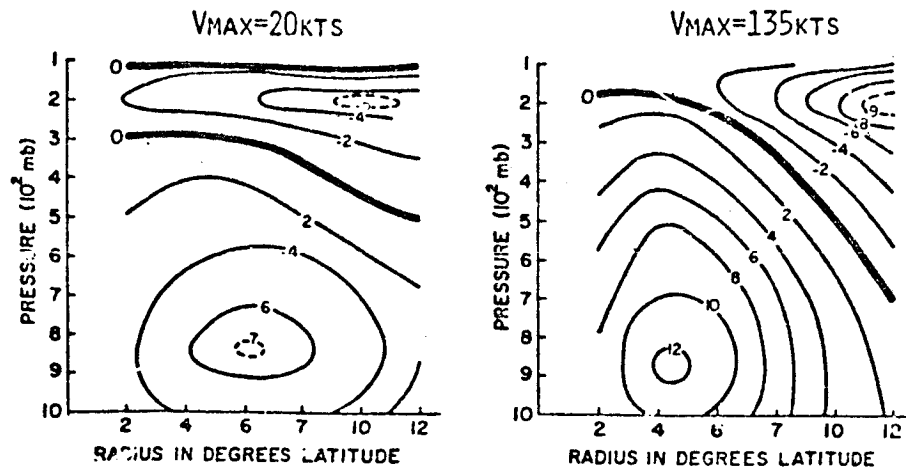
COMPOSITE RESULTS (McBRIDE AND ZEHR, 1981):
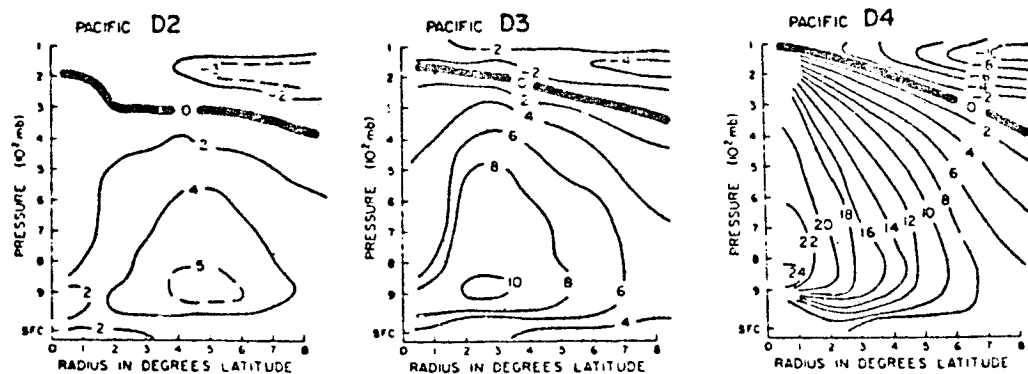
FIGURE 11 Comparison of FGGE year tangential wind for Typhoon Judy in its early and late stage with results of rawinsonde composite analysis.

A question that must be answered is: How well can the FGGE data represent the surrounding circulation of the tropical cyclone? To answer this, the azimuthal average of the tangential wind obtained from the FGGE data was compared to the composite results of McBride and Zehr (1981). Although the variations among individual cases are large, the composite wind field is still a good aid for comparison purpose. Figure 11 shows the results of a typical case (Typhoon Judy) compared to the composites. The figure reveals that beyond 4° to 5° latitude radius from the cyclone center the composites and FGGE analyses are very similar. At the early stage of development, the FGGE

data seem to be able to resolve the circulation as close as 2° latitude from the cyclone center. These comparisons indicate that it appears reasonable to use the FGGE IIIb data to quantitatively study large-scale influences on tropical cyclone development if some caution is taken.

We have extensively studied the low level surrounding circulation patterns and the maximum sustained wind near the center, V_{max}, for all 39 tropical cyclone systems in the northwest Pacific, northwest Atlantic, and north Indian Oceans during the 1979 FGGE year (see Table 1). Results indicate that there is generally not a simultaneous and direct change in V_{max} near the center and 850 mb tangential wind at 6° radius. Results also show that for two thirds of the cases, the buildup of the surrounding circulation occurred prior to major intensification near the center. The time period during which the system's surrounding circulation undergoes significant buildup (without major increase in V_{max}) is defined as the tropical cyclone genesis stage. The next developmental stage, in which the inner core maximum sustained winds increase, is defined as intensification. The intensification stage often is accompanied by a decrease in the surrounding circulation tangential winds. This indicates that intensification is more of a concentration process of angular momentum.

The buildup of the surrounding circulation requires an inward horizontal angular momentum transport. Results have indicated that the surrounding large-scale low level flow, such as the cross-equatorial surge discussed in section 3, forces the circulation to spin up at larger radii in the genesis stages. This buildup then moves slowly inward as the large-scale forcing is maintained resulting in the genesis of a tropical cyclone.

<div align="center">

DIURNAL VARIATION OF CLEAR REGION SUBSIDENCE
CALCULATED FROM ECMWF ANALYSIS

</div>

For a number of years our CSU project has been investigating the large diurnal variation of tropospheric vertical motion which the first author has long hypothesized is primarily a result of the known 2-to-1 differences in night versus daytime net tropospheric radiational cooling. Our previous rawinsonde composite analysis of 00Z versus 12Z clear region subsidence (as detected from satellite images) in the western Pacific (see Figure 12), western Atlantic, and GATE regions have consistently shown or implied a distinct morning maximum and an evening minimum in clear region subsidence (see McBride and Gray, 1980a,b). These nearly 2-to-1 differences in observed clear region subsidence closely correspond in magnitude to the differences of daytime versus night net radiational cooling with a time lag of about 4 to 6 hours for the adjustment of the wind to the radiational forcing.

A question arises as to whether the ECMWF IIIb analysis fields as they were developed for FGGE year analysis were capable of detecting such 00Z versus 12Z clear region diurnal subsidence variations from calculations of the horizontal divergence of the wind fields. Some meteorologists have voiced the opinion that the ECMWF initialization

TABLE 1 Summary of 1979 Tropical Cyclones in NW Pacific, NW Atlantic and N Indian Ocean

System Name	Period (No. of days)	Maximum surface wind (kts) and minimum sea level pressure (mb)	V_{max} (kts) at initial time	No. of days to reach maximum intensity
NW Pacific				
TY Bess	March 18-25 (8)	90(958)	15	5.0
TY Cecil	April 08-20 (13)	80(965)	15	7.5
TS Dot	May 06-15 (10)	40(984)	15	8.0
TD 05	May17-24 (8)	30(998)	20	7.0
TY Ellis	June 23-July 05 (13)	85(955)	10	10.0
TS Faye	June 29-July 07 (9)	40(998)	15	5.0
TD 08	July 23-26 (3.5)	20(1004)	15	0.5
TS Gordon	July25-29 (5)	60(980)	15	2.5
STY Hope	July 24-Aug. 03 (11)	130(898)	20	7.0
TD 11	Aug. 02-06 (5)	25(997)	15	5.0
TY Irving	Aug. 07-17 (11)	90(954)	20	7.5
STY Judy	Aug. 15-26 (12)	115(887)	15	5.5
TD 14	Aug. 16-20 (5)	20(1006)	10	2.5
TS Ken	Aug. 30-Sept. 04 (6)	60(985)	15	5.0
TY Lola	Aug. 31-Sept. 08 (9)	90(950)	10	6.5
TY Mac	Sept. 11-24 (14)	70(984)	10	6.0
TS Nancy	Sept. 17-22 (6)	45(993)	20	2.25
TY Owen	Sept. 19-30 (12)	110(918)	10	7.0
TS Pamela	Sept. 23-26 (4)	45(1002)	15	2.5
TS Roger	Sept. 30-Oct. 07 (8)	45(985)	10	5.0
TY Sarah	Oct. 01-15 (15)	110(929)	15	9.0
STY Tip	Oct. 03-19 (17)	160(870)	10	9.0
STY Vera	Oct. 28-Nov. 07 (11)	140(915)	10	7.0
TS Wayne	Nov. 07-13 (7)	50(990)	15	3.0
NW Atlantic				
TS Ana	June 19-23 (5)	50	25	3.0
HC Bob	July 09-16 (8)	65	20	1.5
TS Claudette	July 15-29 (15)	35(45)*	20	2.0*
HC David	Aug. 25-Sept. 08 (15)	150	25	5.5
TS Elena	Aug. 30-Sept. 02 (3.5)	35	25	1.0
HC Frederic	Aug. 29-Sept. 14 (17)	65(115)*	25	3.0*
HC Gloria	Sept. 04-15 (12)	85	25	8.5
HC Henri	Sept. 15-24 (10)	75	25	2.5
N. Indian Ocean				
TC 17	May 05-12 (8)	85(967)	20	6.0
TC 18	June 17-20 (4)	50(985)	25	3.0
TC 22	Sept. 20-23 (4)	25(1000)	20	1.5
TC 23	Sept. 18-24 (7)	55(980)	15	5.0
TC 24	Oct. 29-Nov. 01 (4)	35(995)	20	2.5
TC 25	Nov. 14-17 (4)	40 (994)	20	2.5
TC 26	Nov. 20-25 (6)	30(995)	15	3.5

*There were 2 peaks for V_{max}. The values within the parenthesis are the second peak. This study only considers the first peak.

procedures tend to eliminate the larger portion of the divergence fields and would, consequently, suppress much of the real diurnal divergence signal. Although there have been problems with ECMWF diurnal analysis using 06Z and 18Z data, we have been led to believe through discussion with Paul Julian of the National Center for Atmospheric Research that the ECMWF IIIb divergence field may be reasonably satisfactory if one uses only 00Z and 12Z data and if one
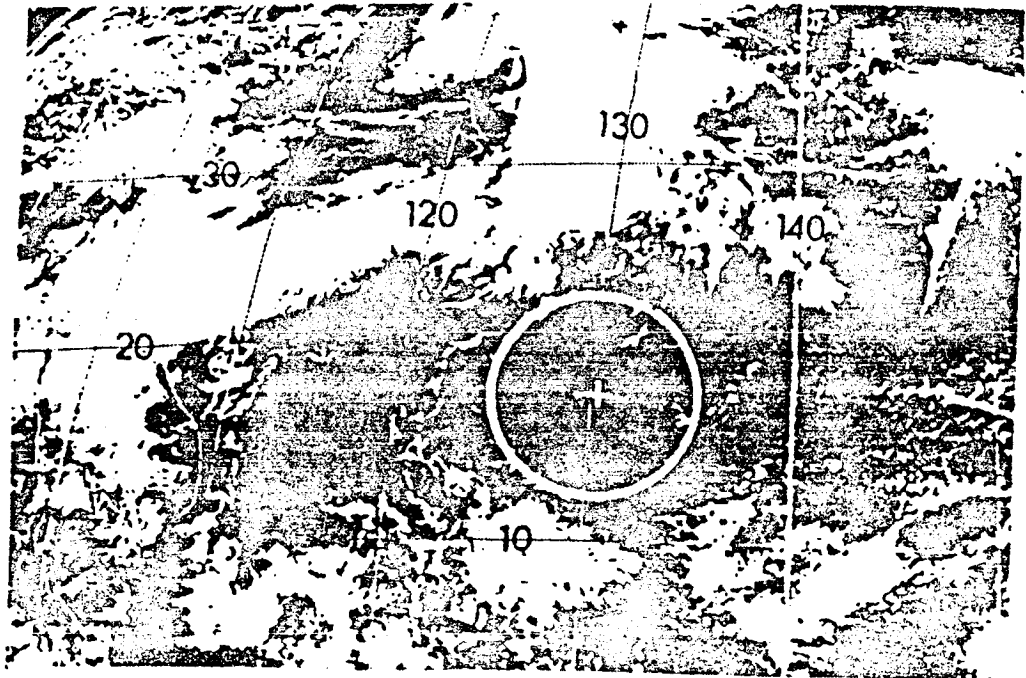
FIGURE 12 Portrayal of the typical western Pacific subtropical clear
regions used in the calculation of 00Z vs. 12Z subsidence.

only attempts to estimate the divergence on large horizontal scales of
10° latitude or more.

To verify how well the ECMWF IIIb uninitialized analyzed wind fields
might represent the expected differences in 00Z versus 12Z subsidence
occurring in subtropical clear regions we have made direct calculations
of such subsidence at these time periods in western Pacific subtropical
clear regions during May and June 1979. The Japanese SMS satellite was
used to locate the clear regions that were cloud free or nearly cloud
free over a 10° latitude-longitude belt (Figure 12). ECMWF 1.875°
initial unsmoothed wind data were obtained from NCAR and converted to a
cylindrical grid that we use for our tropical cyclone studies. Mean
divergence values were made relative to the center of each clear region
at 5° radius (or 10° diameter) at all tropospheric levels up to 100
mb. A mass balance correction was applied to each level to assure that
the 1000 mb to 100 mb net divergence was zero. Vertical motion was
then kinematically calculated from the individual level corrected
divergences.

Thirty-one cases of 00Z versus 12Z subsidence were calculated in May
and 33 cases in June. Figure 13 shows a composite analysis of 00Z
versus 12Z subsidence for the May and for the June cases separately.
Note how distinctly greater the 00z subsidence (09 to 10 LT) is
compared with the 12Z subsidence (21 to 22 LT). These calculations

491
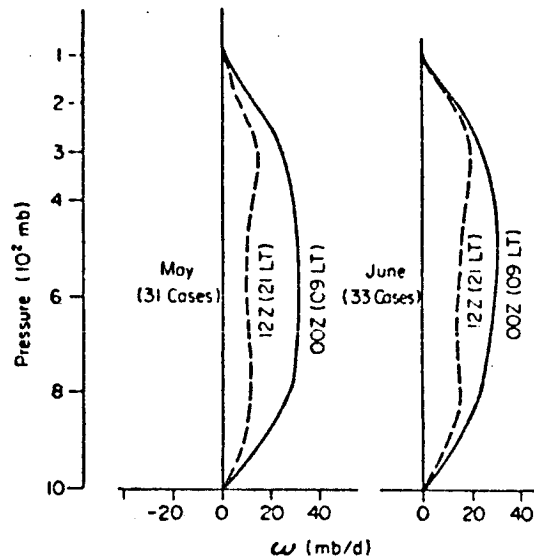
FIGURE 13   Comparison of 00Z vs 12Z 10° wide subsidence in western Pacific subtropical clear regions.

agree very well with the independently calculated composite diurnal vertical motion variation that we have previously made directly from our rawinsonde data sets (Figure 14) where none of the usual modeling smoothing or filtering analysis procedures have been employed.

Discussion.   Note that these 00Z versus 12Z subsidence differences are close to the expected differences in clear region subsidence due to 2-to-1 night versus day differences in net radiational cooling (with a 4 to 6 hour lag) and to the previous rawinsonde composite results.   It would appear that the ECMWF FGGE unsmoothed IIIb level wind analysis gives reasonably accurate divergence and vertical motion values if such divergence and vertical motion analysis is applied on a large enough scale.

If these western Pacific diurnal subsidence calculations are correct, then a compensating diurnal variation in upward vertical motion must be occurring somewhere else.   It is of interest to note that heavy rain events (>1 cm/hr) in the western Pacific have a very distinctive morning maximum and a quite pronounced evening minimum.

For many years the first author has believed in the fundamental importance of the inclusion of tropospheric radiational cooling in the hemispheric and global PE models.   It would appear that for the proper initialization of the global models, with as representative a divergence field as possible, that consideration will have to be given to the large 2-to-1 night versus day radiation differences and the consequent differences in wind divergence that these radiational differences generate.   To make use of diurnal radiation information for global model initialization, one would have to take into account the time of day as well as cloudiness.   We are somewhat surprised at the

492

WEST PACIFIC CLEAR AREAS
VERTICAL VELOCITY
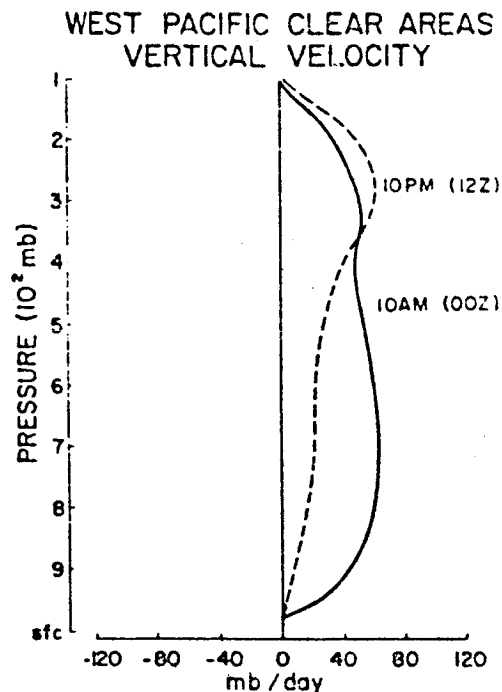
FIGURE 14 Mean vertical velocity within the r = 0-3° area for
western Pacific clear areas.

slowness of the global community to incorporate radiation and its
obvious large day versus night differences into their models.

Does the inclusion of radiation in the global models require so much
computation time and need to be so vigorously applied? Could not
radiation be included in the global model in a rather simple empirical
manner in terms of time of day and upper tropospheric vertical motion
(cloudiness)? Might it not be better to have some representation of
the diurnal radiation cycles in the numerical models (no matter how
imperfect) than none at all? One of the big lessons to be learned from
the various oceanic tropical experiments over the last 15 years has
been the large magnitude of the diurnal cyclone of vertical motion over
the ocean regions where lapse rate conditions do not undergo their
usual diurnal variation as they do over land. Many tropical land areas
also have a morning maximum of deep convection.

SUMMARY AND DISCUSSION

We are finding the FGGE ECMWF IIIb analysis a unique and special data
set compared with anything that has been available in the past. This
data set is particularly valuable if it is used in conjunction with SMS
satellite images. But much hard work and frustration are involved in

rendering the raw IIIb rectangular grid point information available on magnetic tape for useful individual weather system calculations in other coordinate arrangements.

Nevertheless, this quite special data set employing identical analysis procedures at all time periods allows us at CSU the ability to begin quantitative case analysis of the individual tropical cyclone and of other weather phenomena, where in the past, poor data coverage and non-uniform analysis procedures have required us to rely more on a composite as compared to an individual case approach. This new FGGE ECMWF analysis is now allowing us the ability to handle the individual case.

ACKNOWLEDGEMENTS

REFERENCES

Askue, C. A. (1984a). A study of the genesis and intensification of two 1979 northwest Pacific supertyphoons. Paper presented at the 15th Tech. Conf. on Hurricanes and Tropical Meteorology, January 9-13, 1984, Miami, Fl., 6 pp.

Askue, C. A. (1984b). Varying structure and intensity change characteristics of four western North Pacific tropical cyclones. Department of Atmospheric Science Master's Thesis, Colorado State University, Fort Collins, Colo.

Chen, L, and W. M. Gray (1984a). Global view of the upper level outflow patterns associated with tropical cyclone intensity changes during FGGE. Paper presented at the 15th Tech. Conf. on Hurricanes and Tropical Meteorology, January 9-13, 1984, Miami, Fl., 8 pp.

Chen, L., and W. M. Gray (1984b). Global view of the upper level outflow changes during FGGE. Department of Atmospheric Science, Colorado State University, Fort Collins, Colo.

Holland, G. J., and R. T. Merrill (1984). Tropical cyclone intensification mechanisms. Paper submitted to the Quart. J. Roy. Meteorol. Soc.

Lee, C. S. (1984). Large-scale influences on individual cases of tropical cyclone genesis during the FGGE year. Paper presented at the 15th Tech. Conf. on Hurricanes and Tropical Meteorology, January 9-13, 1984, Miami, Fl., 8 pp.

Love, B. (1982). The role of the general circulation in western Pacific tropical cyclone genesis. Department of Atmospheric Sciences Paper No. 340, Colorado State University, Fort Collins, Colo., 230 pp.

McBride, J. L., and W. M. Gray (1980a). Mass divergence and vertical velocity in tropical weather systems, Part I: Diurnal variation. Quart. J. Roy. Meteorol. Soc. 106, 501-516.

McBride, J. L., and W. M. Gray (1980b). Mass divergence and vertical velocity in tropical weather systems, Part II: Large-scale controls on convection. Quart. J. Roy. Meteorol. Soc. 106, 517-538.

McBride, J. L., and R. Zehr (1981). Observational analysis of tropical cyclone formation, Part II: Comparison of nondeveloping versus developing systems. J. Atmos. Sci. 6, 1132-1151.

Sikka, D. R., and W. M. Gray (1981). On the possible linkage between tropical depression formation in the north Indian Ocean and cold front penetration across the South Pacific. (Research performed at Colorado State University; paper still in preparation.)

CROSS-EQUATORIAL AND BOUNDARY LAYER EXCHANGE: A FGGE REVIEW

John A. Young
University of Wisconsin, Madison

ABSTRACT

The Global Weather Experiment (FGGE) provided unique data on the interesting phenomenon of cross-equatorial flow. Such motion is a key element of the seasonal cycle of the tropics, especially in monsoonal regions. This paper reviews the IIb observations, IIIb assimilations, and implied dynamics of the flows. Additional emphasis is given to the low-level branches concentrated in the planetary boundary layer, including air-sea interaction and vertical turbulence processes. The results of a recent MONEX Boundary Layer Workshop are summarized at the end.

LARGE-SCALE FLOW DYNAMICS

Geostationary satellite data were essential to FGGE because (a) wind observations are critical in the tropics and (b) the entire tropical belt was covered. More than a million wind vectors described the 900 mb flow on the oceans very well, and the 200 mb flow adequately. The Indian Ocean data were especially unique in that they provided the first complete view of the Indian monsoon system (e.g., Young et al., 1980; Virji, 1981). Figure 1 shows the mean July flows (m/s) from those data. Both levels tend to contain some of the strongest cross-equatorial motion. These satellite data were supplemented on occasion by FGGE and MONEX (May-July) dropsonde winds and the BALSAMINE low-level free balloon flights (Cadet et al., 1981).

Low-Level Flow

A valuable IIb surface data set has been constructed for the FGGE tropical belt at the University of Wisconsin-Madison (e.g., preliminary note, Wylie et al., 1983). It is based on a merger of ship winds and satellite winds modified empirically. Figure 2 shows means for January and July: northward cross-equatorial winds of 3 m/s or more are typical in both seasons over the eastern Pacific and eastern Atlantic. In contrast, the Asian monsoon creates significant cross equatorial flow toward the summer hemisphere over the Indian Ocean and western
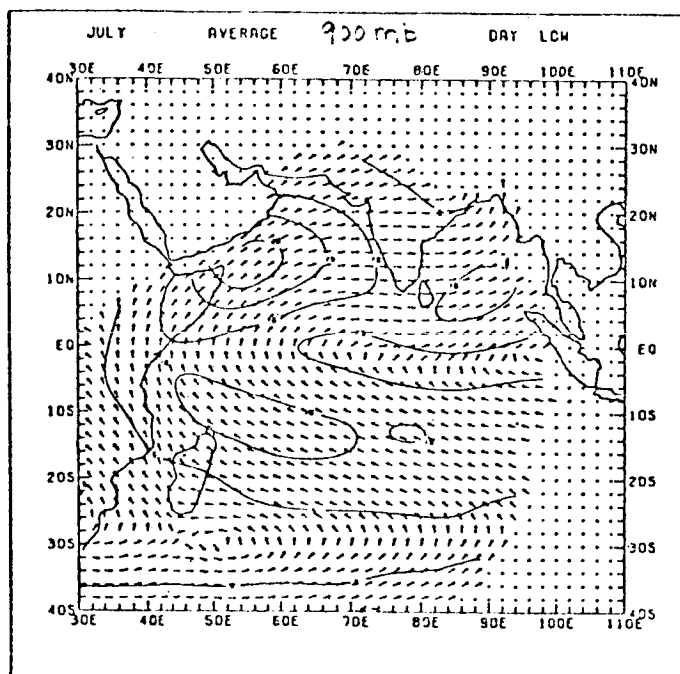
FIGURE 1 Mean 900 mb July 1979 flow (m/s) from GOES winds (Young et al., 1980).

Pacific. The strongest case is found in the entrance to the Somali Jet/Southwest Monsoon complex, which maximizes near 900 mb (Figure 1). ψ and χ fields computed by Krishnamurti and Ramanathan (1982) show that this cross-equatorial wind contains a divergent component that is nearly as strong as the rotational one (Figure 3).

Information on the interannual variability of surface cross-equatorial flow has been emerging: (1) over the Indian Ocean, Cadet and collaborators (1981, 1983) have studied the year 1975; (2) over the Pacific, O'Brien and Goldenberg (1983) have produced an atlas of monthly means during 1961-1970. Analyses of 850 mb monthly mean equatorial flows for 1965-1974 are given in Krishnamurti et al. (1983). These studies are useful in characterizing interannual variability, but the FGGE year needs to be included in future work.

Equatorial flow variability on the synoptic time scales during FGGE has focused on the 40-day time scale (e.g., Murakami et al., 1983; Krishnamurti and Gadgil, 1984). The results indicate planetary scale anomalies with meridional propagation in the Asian summer monsoon region. The latter shows maximum cross-equatorial variability in the upper troposphere, with a secondary maximum at 850 mb over the Indian Ocean (Krishnamurti and Gadgil, Figures 4e, 6c) that ties in with active/break phases of the monsoon. The author is currently comparing global longitude-time sections of this flow for the years 1974-1982 from NMC data.

JAN. SFC.
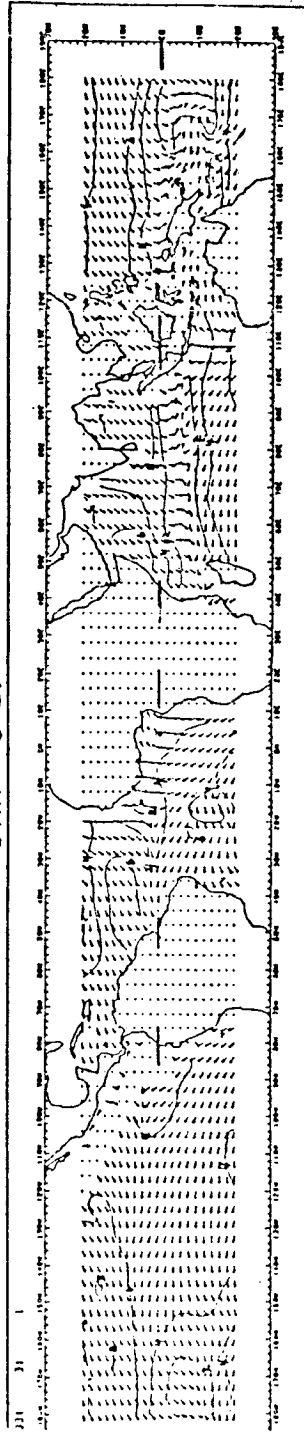
JULY SFC.
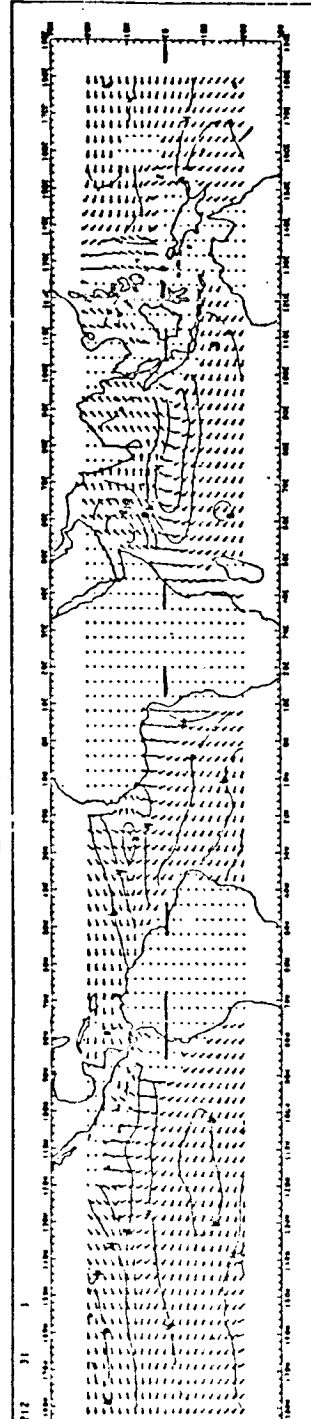
FIGURE 2 Mean surface flows (m/s) in 1979 from ship and GOES winds (recent work of Wylie, Hinton, and Howland, 1984).

850 mb
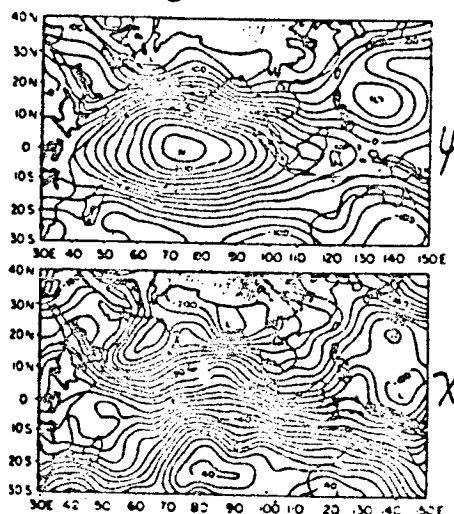
FIGURE 3   Stream function and velocity potential at 850 mb during MONEX, June 1979 (Krishnamurti and Ramanathan, 1982).

Shorter-period equatorial disturbances v(x,t) have been calculated from satellite winds using the data of Young et al. (1980), and Stout and Young (1983) showed that rms wind deviations were a minimum (3 m/s) in the region of strong cross-equatorial flow of 11 m/s. A complete analysis of possible cross-equatorial surges in MONEX has not been made. Gray and Lee (1984) interpret cold surges from the extratropics as being important for subsequent establishment of zonal pressure gradients, cross-equatorial flow, westerlies, and tropical cyclogenesis in the summer hemisphere. Rao and Haney (1982) studied parts of two surges up the African coast, but it is clear that FGGE data represent the best opportunity, as yet unrealized, to describe and understand the possible connections completely.

Uppe.-Level Flow

Less attention has been given to analyzing IIb data for the upper troposphere because it is sparser. However useful results have been obtained from IIIb data produced by ECMWF, GFDL, and GLAS. Silva-Dias and Paegle (1984) have confirmed that the divergent meridional wind is smaller in the ECMWF data, a probable result of the initialization procedure used in the 1980 assimilations. New assimilations for the SOPs are expected to be conducted in 1984. Silva-Dias and Paegle (1984) also show that the slow tropical circulations are mainly internal vertical modes, so that their upper and lower tropospheric divergent motions are closely coupled. In addition, the cross-equatorial component v tends to be more divergent than rotational

v-- Divergent Component --Jan.'79
200 Mb

50 N

30 N

10 N

10 S

30 S
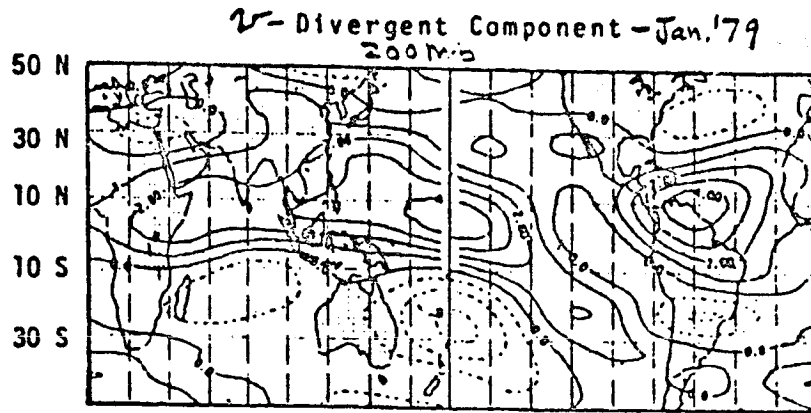
FIGURE 4   Divergent meridional wind component (m/s) at 200 mb for January 1979 (Silva-Dias and Paegle, 1984).

(Figure 4).   Thus we conclude that persistent cross-equatorial flows are strongly divergent and vertically internal. They possess important intraseasonal variability that could arise from diabatic anomalies or propagation from the extratropics (e.g., Webster, 1983) during persistent westerly regimes at the equator. Paegle et al. (1984) contrast the global fields of v_x for two periods in January-February 1979 (Paegle et al., Figure 13). This v_x variability probably reflects non-Kelvin gravitational modes. For example, Figure 5 (excerpted from Silva-Dias and Paegle, 1984, Figure 8b, 8d) shows that the mean internal mode cross-equatorial flow is described by (1) gravity-inertia waves (diagram b) that concentrate near the Asian monsoon and shift longitudinally with season, and (2) mixed Rossby-gravity waves (diagram d) that shift from the western to eastern hemisphere from January to July 1979.

Dynamics

To the extent that model parameterizations and assimilation procedures are correct, FGGE IIIb data allow the computation of fields that are hard to obtain by direct observation. However IIb data may also yield important results by residual calculations and may be particularly valuable when there are some modeling difficulties.

   A number of results have been obtained for the strongest cross-equatorial flow, that of the Indian summer monsoon. Stout and Young (1983) diagnosed the satellite wind field to solve the divergence and vorticity equations for pressure and friction force, respectively. The resulting cloud-level isobars (Figure 6) show a distinctive "reversed S" signature connecting the hemispheres and supporting strong cross-equatorial flow. This corresponds (Young, 1983) to an eastward acceleration $v\ \partial u/\partial y$ (associated with cross-equatorial motion v) produced by a zonal gradient $- 1/\rho\ \partial p/\partial x$. The diagnosed pattern

500

5a

5b
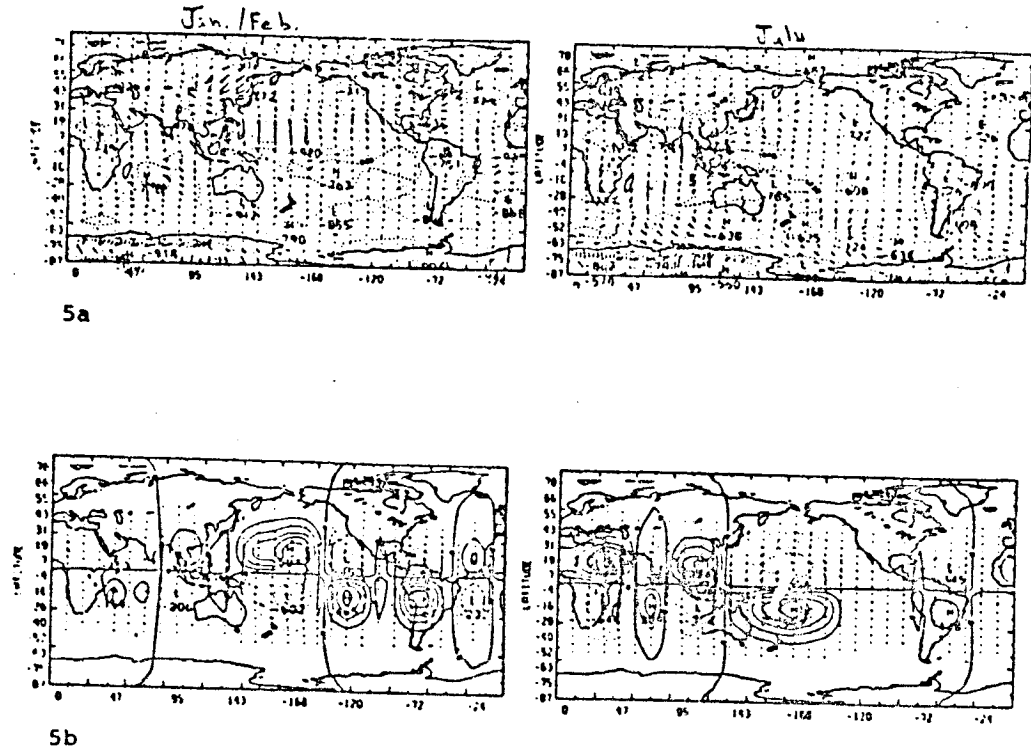
FIGURE 5 Mean internal observed modes showing cross-equatorial flow
during 1979 (January/February, left; July, right). Gravitational (top)
and mixed Rossby-gravity (bottom) (Silva-Dias and Paegle, 1984).

of Figure 6 has found by the author to agree well with the mean 850
geopotential pattern from ECMWF IIIb data. The 900 mb friction force
derived by Stout and Young (1983) is consistent with the wind data and
the constraint of zero curl for pressure gradient force field. Figure
7 shows that it tends to oppose the wind (which of course is not a
physical requirement) and has a magnitude less than 2×10^{-4} ms^{-2},
smaller than is found near the surface. This result confirms that the
friction layer in this flow is somewhat thinner than the planetary
boundary layer defined by temperature, moisture, and clouds.

Reverdin and Sommeria (1983) also estimated friction as a residual
by using observed wind (from free balloons near 900 mb) together with
ECMWF IIIb model pressure field; such a technique may introduce errors
when the model winds and observed wind do not agree. However, the
overall 900 mb friction magnitudes they found were in broad agreement
with those of Stout and Young (1983).

Force evolutions along cross-equatorial trajectories are shown in
Figures 8a and 8b. Figure 8a is a mean picture gotten from an Eulerian

501
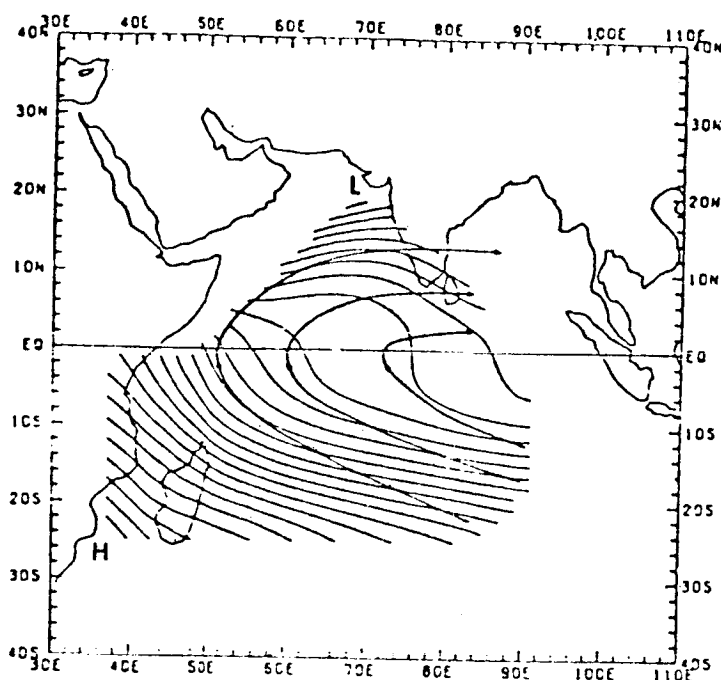
July 900 mb geopotential height from ϕ field estimated for the monsoon period including friction term in the boundary conditions; contour intervals relative to arbitrary value are 5 m. Selected mean streamlines have arrows.

FIGURE 6   July 1979 geopotential estimated from divergence equation using GOES winds (Stout and Young, 1983).

analysis by Stout and Young (1983), while Figure 8b is an instantaneous Lagrangian one by Reverdin and Sommeria (1983) following a balloon. The figures portray an increasing imbalance and reduced forces as the equator is approached, an eastward pressure gradient force near the equator and its rapid rotation to the left of the flow in the downwind hemisphere, where a strong balanced flow is approached.   In both figures at 900 mb, friction never dominates, tends to oppose the wind, and has a component to the left of the wind over the Arabian Sea.   Many of the above properties were duplicated in the PBL wind simulation for a single MONEX day by Krishnamurti et al. (1983).

The force results in Figures 8a and 8b suggest a major nonlinear "adjustment" region downwind of the equator: Stout and Young (1983) characterized it as essentially an inertial transition from cyclostrophic to geostrophic conditions and found that the Rossby number exceeded 0.4 up to 9°N.   In addition, Young (1981) showed that much of this transition belt contained a region of negative absolute vorticity with implied growth rates for divergent motions as large as 10^{-5} s^{-1}.   In such a region the rotational wind cannot be obtained from the mass field using the balance equation, but the reverse can be accomplished (e.g., Stout and Young, 1983 for MONEX; Paegle et al.,

502

Non-divergent friction force **F**, at 900 mb esumated from the vorticity equation (4.6) for the monsoon period. Contour interval for magnitude (solid lines) is 1×10^{-3} m s^{-2}, arrows indicate direction.
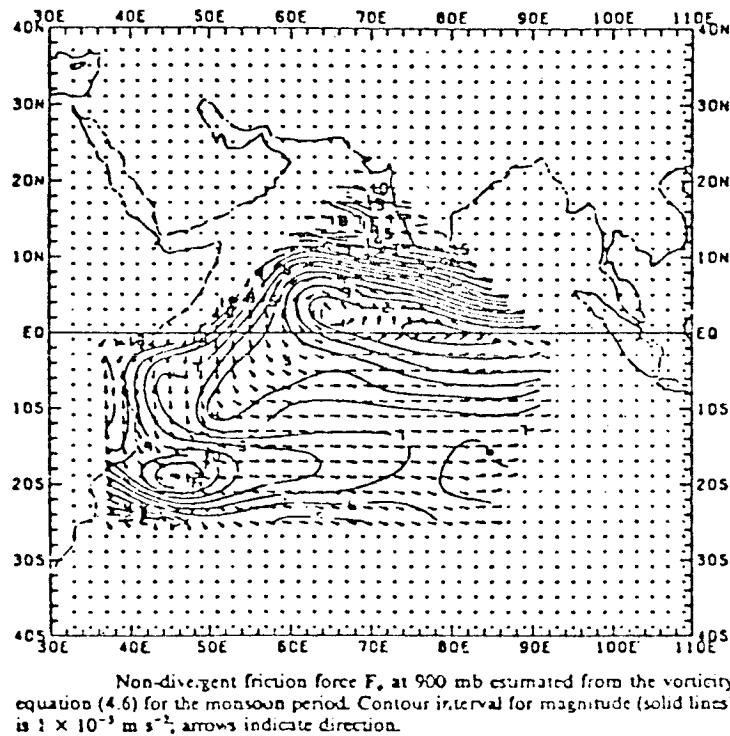
FIGURE 7 July 1979 friction force estimated from vorticity equation using GOES winds (Stout and Young, 1983).

1983 for GATE). The divergent wind is probably not obtainable by a diagnostic approach in these strong inertial regions (e.g., VanTuyl and Young, 1983); Paegle et al. (1983) had to assume Lagrangian steady state for their GATE study, which is unlikely to be correct with strong cross-equatorial flow. The implications of this region of anticyclonic absolute vorticity for the inertial stability of the mean ageostrophic flow are not yet resolved, but work by Stevens (1983) and others may contribute to the answers.

BOUNDARY LAYER DYNAMICS

Some of the most important cross-equatorial flow is concentrated at low levels in the planetary boundary layer (PBL) where turbulence processes influence its distribution and strength. This flow transfers atmospheric properties (such as water vapor) from one hemisphere to another and modulates the surface fluxes into the PBL as well.

503
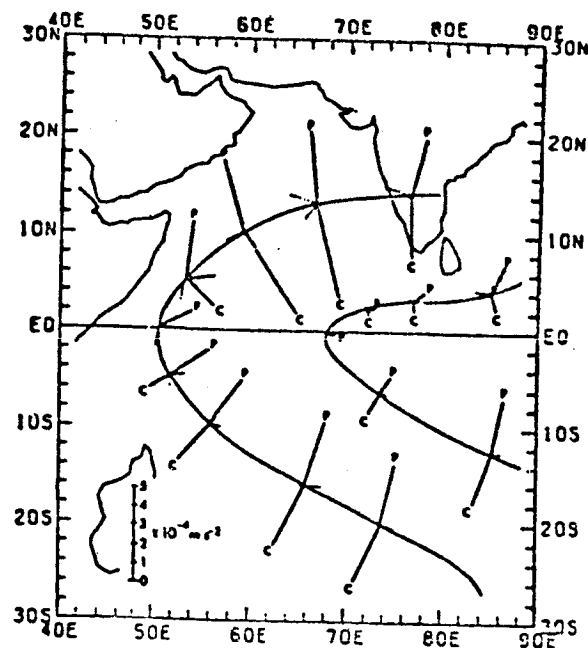
(a)   Balance of mean vector forces along selected trajectories in the monsoon period. Vectors are drawn without arrowheads and are understood to point away from their origin on the trajectory. The vectors labeled P and C are pressure gradient force and Coriolis force, respectively; the unlabeled solid vector is relative acceleration; the dotted vector is nondivergent friction force.

(b)
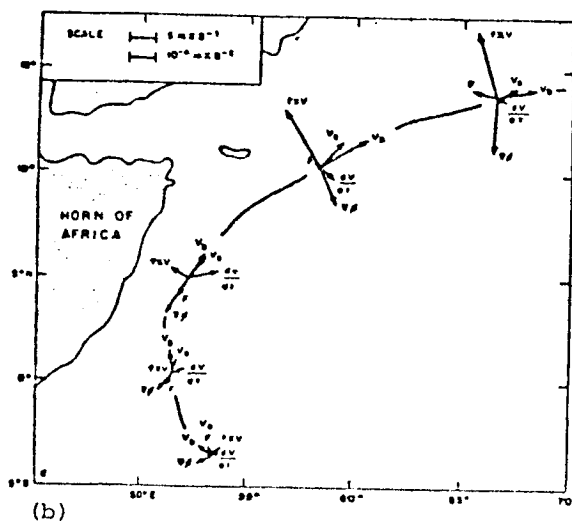
FIGURE 8   Force evolutions along summer monsoon trajectories in 1979. Top, from GOES analysis (Stout and Young, 1983); bottom, from BALSAMINE and ECMWF IIIb analyses (Reverdin and Sommeria, 1983).

504
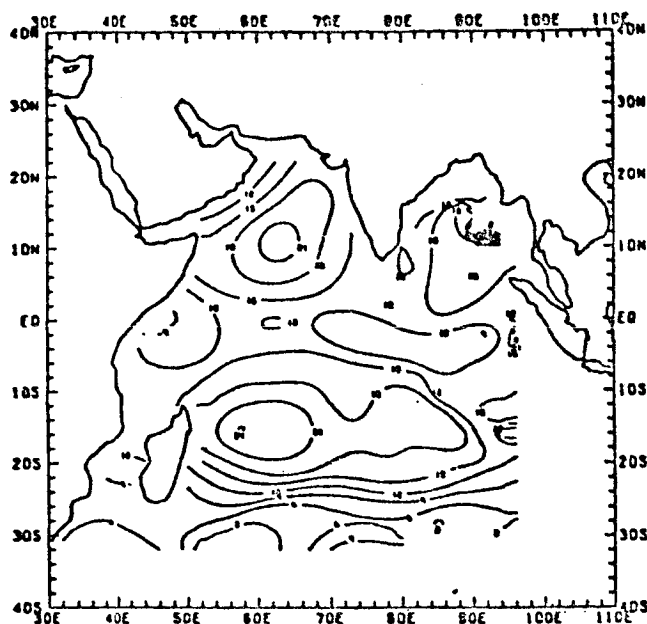
FIGURE 9 Mean flux of moist static energy from the sea into the air
for July 1979. Units 10 W/m^2 (Wylie and Hinton, manuscript in
preparation).

Air-Sea Interaction

FGGE data will provide the best chance to estimate surface fluxes and
their synoptic variability over the entire equatorial belt. Some
unpublished preliminary estimates have been made at ECMWF and GLAS from
IIIb data, but significant questions remain regarding ocean tempera-
ture, relative humidity, and the quality of current IIIb data in the
PBL. In the meantime, estimates from IIb data (primarily ship and some
satellite data) have recently been intercompared at the MONEX Layer
Workshop held in May 1984 at the University of Wisconsin. This work is
based on analyses by Cadet (Florida State University) and Wylie, Hinton,
and Howland (University of Wisconsin) and will allow large-scale
estimates with a time resolution better than 10 days. Figure 9 shows
an example of the moist energy flux for July 1979 over the Indian Ocean.
    The analysis of surface momentum fluxes has progressed further.
Satellite and ship winds have been merged by Wylie and Hinton to
produce 10-day Indian Ocean stress fields through the 1979 summer
monsoon (1982) and monthly fields throughout the year 1979 (1983).
Figure 10 shows an example for the retreat of the monsoonal meridional
stress at the equator.
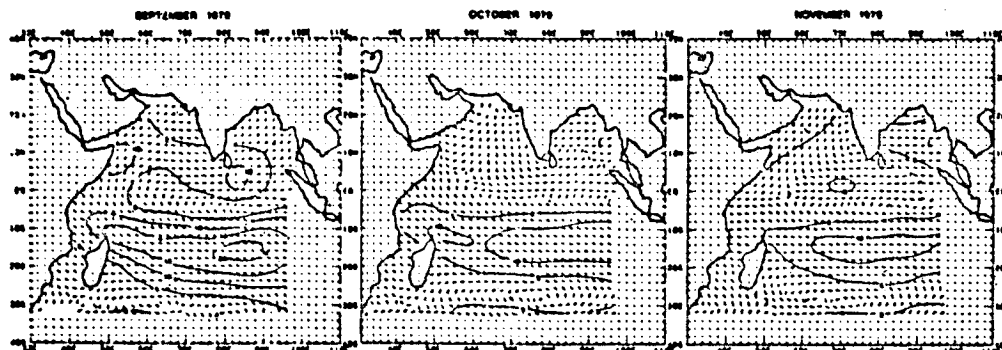
FIGURE 10 Surface stress during retreat of monsoonal cross-equatorial flow in 1979. Units 0.1 dynes cm^{-2} (Wylie and Hinton, 1982b).

Cross-Equatorial Water Vapor Transport

A long-standing question of monsoon studies has been the source of water vapor reaching land areas. The answer for 1979 will ultimately require refined treatment of water vapor in IIIb data. In the meantime, Cadet (1983) has merged satellite and IIIb water vapor estimates to produce fields of precipitable water over the Indian Ocean during summer 1979. Such data should provide a basis for combining with wind data and calculating cross-equatorial water vapor transport in the future.

Vertical Structure

Five sources of data on the vertical variations of FGGE cross-equatorial PBL flow systems exist.

1. Satellite and ship winds. The excellent satellite coverage, intermittent ship coverage, and time averaging provide a basis for resolving many large-scale differences between 900 mb and the surface. Relations over all the tropical oceans for the entire FGGE year could be obtained. Results to date have focused on the Indian Ocean. Wylie and Hinton (1982a, 1984) have calculated the large-scale shear statistics for all seasons of FGGE and interpreted the results in terms of boundary layer theory, including latitude, baroclinity, and stability effects. They find that surface equatorial speed is less (~25 percent) than at 900 mb during northern summer but is comparable to it during northern winter.

2. Operational aircraft data. Dropwindsonde data were collected during winter and summer SOPs in areas with significant cross-equatorial flow: Indian Ocean, eastern and central Pacific, Atlantic (U.S. FGGE Project Office, 1981). No special effort has yet been made to analyze these IIb data alone, partly because the required averaging eliminated wind data points below 950 mb.

506
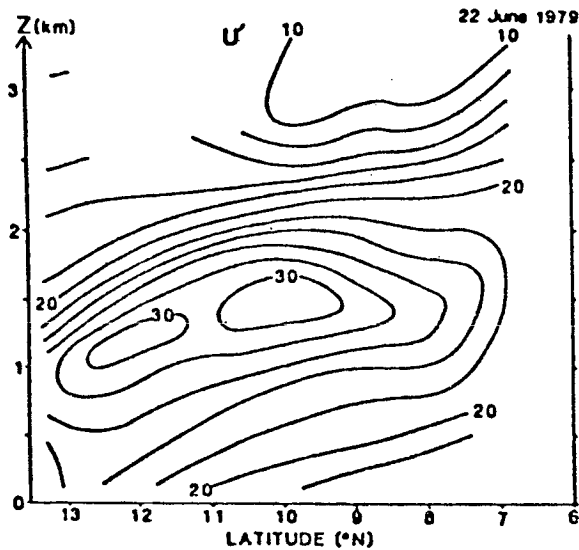
FIGURE 11 Somali jet wind structure from June 22, 1979 aircraft penetration (m/s) (Nordgarden and Young, 1984).

3. Research aircraft data. Special MONEX flights were made: Winter MONEX, South China Sea; Summer MONEX, Arabian Sea and Bay of Bengal. Two U.S. aircraft made a limited number of flights in the boundary layer as close to the equator as 5°N. Five NCAR Electra flights produced 0.1 second gust-probe turbulence data (June 20, 24 and July 14; December 4, 12). Meyer and Rao (1984) analyzed the June 20 and June 24 thermodynamic turbulence data. Grossman and Sethu Raman are currently analyzing turbulence data for June 24 and the June 20, July 14 flights, respectively (private communication).

Two special P-3 flights produced 1 second data in the boundary layer on "sawtooth" profiling missions (June 22, 24) across the Somali Jet. For example, Figures 11 to 13 (Nordgarden and Young, 1984) give revealing vertical cross sections for this most intense (30 m/s) downwind brand of cross-equatorial flow. Other analyses (for June 24) had been made by Rao et al. (1980) and LaSeur (1981). Figure 11 shows the jet is concentrated on a sloping axis in the PBL, with very strong shears at the PBL top and variable shear in the bottom. A separate analysis showed the upper shear to be associated with strong baro-clinity, where wind direction changes were concentrated. This was also the boundary between two branches of a direct secondary circulation (Figure 12) possessing vertical motions up to several cm/sw, especially above the PBL. Figure 13 shows that the absolute angular momentum equalled that of the earth at the equator (M = 0 in Figure 7) up to 13°N, with an isolated maximum at 7°N and apparent inertially unstable region extending southward along the flow to the equator. The density of plotted circles is proportional to the potential vorticity of the flow, which is concentrated in the upper PBL and its "lid".
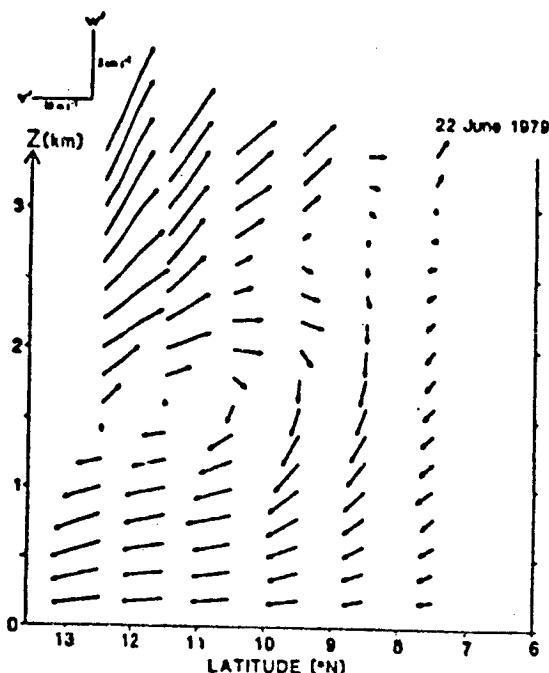
FIGURE 12 Somali jet transverse circulation from June 22, 1979 aircraft penetration (m/s) (Nordgarden and Young, 1984).

The equatorial area upwind of the Somali Jet core was not sampled in MONEX, although good data (e.g., Hart et al., 1978) is available from 1977. The decelerating flow downwind of the core was measured on the PBL mission of June 24 (see Grossman and Durran, 1984).

4. BALSAMINE balloon observations. These provided winds in the upper half PBL at various latitudes spanning both hemispheres. Reverdin and Sommeria (1983) presented statistical results on speed and direction which confirm that (a) speed shear is greater in the southwest monsoon area than in the southern trades, (b) directional veering shifts to backing at about 4^ON (not at the equator) and (c) directional veering/backing is nearly zero above 2 km.

5. Numerical boundary layer models. Currently most of the FGGE PBL data from numerical models are those available in IIIb data sets. The GFDL data set apparently has the best resolution, as all 19 predictive levels (including 3 within the boundary layer above the surface) are archived. The ECMWF set does not archive the 2 internal boundary layer levels that are contained in the prediction model. The NASA GLAS data consists of a single mixed layer to produce the surface wind. Both the GFDL and ECMWF have PBL physics described by K theory with no internal clouds. This may be a shortcoming, for the recent work of Yuen (1984a, b) suggests that clouds may contribute to the friction field and hence alter the flow between 850-950 mb. Yuen's results apply to cold surge situations, and the model has been tested against AMTEX data. Winter MONEX simulations at the equator remain to be done.

508
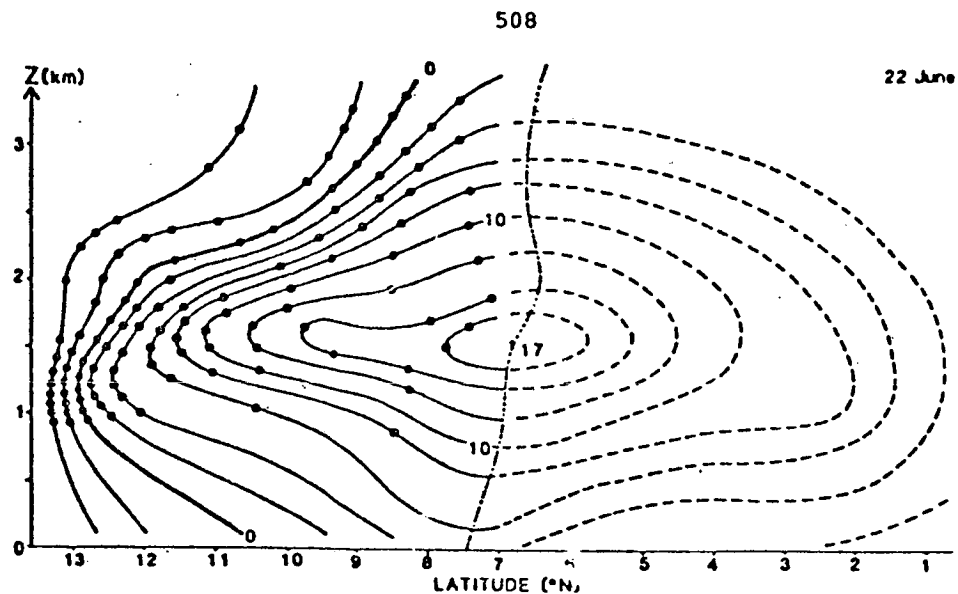
FIGURE 13 Somali jet angular momentum deviation (expressed in m/s) from Figure 11. Circles show intersections with surfaces of virtual potential temperature; their local density is proportional to potential vorticity.

The only pure research simulations of FGGE/MONEX cross equatorial flow to date appeared in KW for a single realization of June 27, 1979. The model used neutral K theory and assumed steady state conditions. The simulated structures seemed in broad agreement with some observations, although the simulated shear, directional change, and surface wind suggest that further refinements and assimilations are desirable.

Friction Variations

PBL flow near the equator shows variations in forces (particularly friction) with height and latitude. Many of the variations reflect large-scale dynamics in addition to local surface forcings. For example, even classical Ekman theory predicts that the vertical structure depends on latitude.

The most comprehensive attempt to characterize the (y, z) force regimes was the diagnosis of the simulation by KW. They confirmed that the inertial regimes near the equator would have latitudinal limits that depended on altitude. Figure 14 shows force vectors at 200 m (2 = inertial acceleration, 3 = Coriolis, 4 = pressure gradient, 5 = friction). These results, and especially comparable ones at $z = 1$ km (not shown), are very similar to the horizontal fields diagnosed for MONEX by Stout and Young (1983) and Reverdin and Sommeria (1983).

509
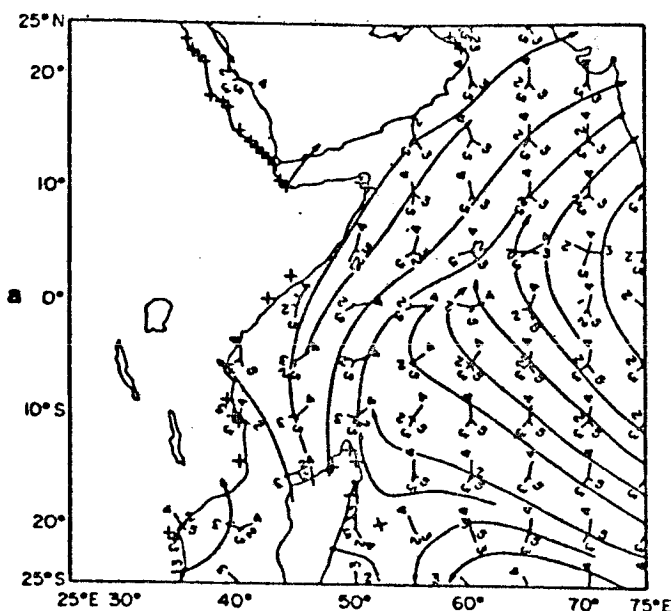
FIGURE 14 Forces simulated at 200 m altitude for June 27, 1979 (2 = inertial acceleration, 3 = Coriolis, 4 = pressure gradient, 5 = friction) (Krishnamurti et al., 1983).

Results for the observed vertical variation of friction must be considered to be preliminary. Stout and Young estimated that friction near cloud base was on the order of 20 percent of the surface value, while RS' statistical analysis suggests a larger fraction ~50 percent. The smaller value was consistent with the simulation of KW. The associated decay times from SY and RS at 1 km were of the order of 0.7×10^{-5} s^{-1}. A continuous profile of friction (component normal to the wind) is suggested by the Somali Jet wind profiles (observed, estimated geostrophic, and gradient) of Nordgarden and Young (1984) (see Figure 15). The difference (u'-ugr') decreases at a variable rate, with 1 km values equalling about 50 percent times the surface values.

Model results to date cannot be expected to clarify the factors influencing the vertical variation of friction: the GCM data lack good vertical resolution and PBL clouds, while KW lacks clouds and stability dependence. The model of Yuen (1984a) includes clouds, but it has not yet been applied to summer MONEX. Preliminary experiments (Young and Yuen, 1982) suggest that vigorous clouds may create a complicated friction profile, especially in monsoonal baroclinic situations.

MONEX Boundary Layer Workshop

This interim workshop, sponsored by the National Academy of Sciences, was held at the Department of Meteorology, University of Wisconsin,

510

(a)

(b)
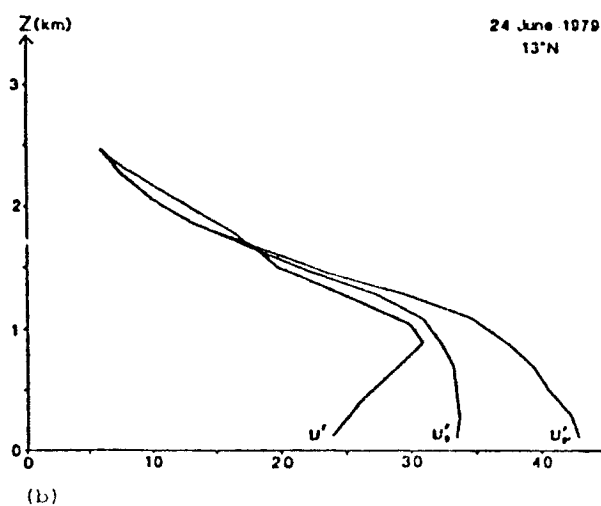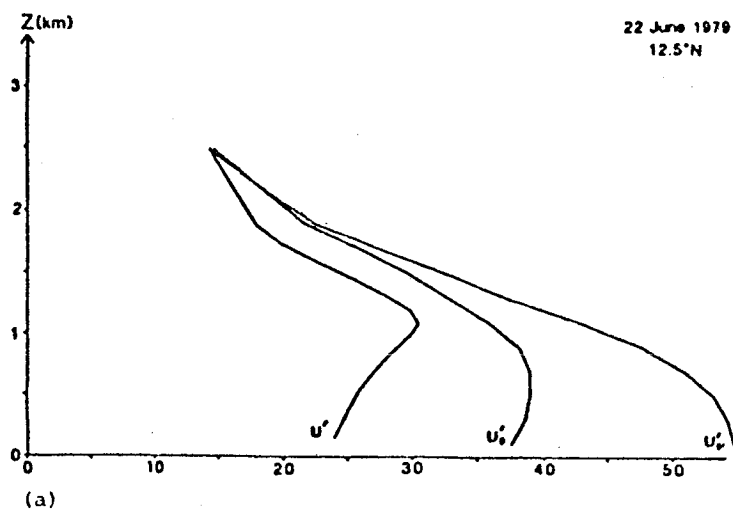
FIGURE 15 Vertical profiles of observed and estimated geostrophic and gradient winds (m/s) in Somali jet from aircraft data of June 1979. Deviations imply transverse friction force component. (Nordgarden and Young, 1984.)

Madison, on May 21-24, 1984. The chairman was John Young; group leaders were Daniel Cadet (large-scale) and S. SethuRaman (turbulence); V. Wong led a subgroup on numerical modeling. A report including consensus statements and recommendations is available from Young.

SUMMARY OF SCIENTIFIC ISSUES

The monsoon boundary layer is unique because of its large horizontal scale, strong jet-like winds, and imbedded clouds. The first two properties provided foci for the large-scale group, while the latter two were topics of analysis and discussion by the turbulence group. Good progress has been made in both areas, with prospects for most MONEX projects to be completed within about two years. However, the MONEX results should provide a basis for studying the large-scale tropical boundary layer flows of FGGE in future years. At the same time, an increased role for numerical modeling is seen, both as a natural, culmination of MONEX boundary layer studies and as a needed application to FGGE data.

The large-scale group emphasized surface interactions over the Indian Ocean during summer MONEX. Four research groups used various combinations of ship data, satellite cloud wind vectors, satellite water vapor, and IIIb assimilated model data to produce gridded surface fields for detailed comparisons. Bulk formulae were applied to yield maps of stress, sensible heat, and latent heat fluxes during various stages of the 1979 summer monsoon, including active and break phases. These views of monsoonal surface interactions during a single season are the most complete ones ever obtained, and the results are encouraging. Careful intercomparisons are planned as a next step in order to produce an optimum data set for future studies. The techniques might improve our ability to estimate surface fluxes over the entire tropical belt during all seasons of the FGGE year. Satellite derived estimates of net solar radiation appear to be consistent with other results and will be included in future intercomparisons. A serious gap in the current heat budget data is net long wave radiation, and efforts will be made to estimate it from sea surface temperature and cloud data. In addition, increased attention may be given to the effect of dust over the ocean. One satellite study showed a strong event after the monsoon onset, with high optical depths and horizontal transport. The variability of horizontal water vapor transport was documented using satellite and IIIb data during the active/break cycle, suggesting that the relative importance of cross-equatorial flux is less dominant in break conditions. Further work is envisi ed on modeling and analysing the top of the moist boundary layer, its vertical structure, and synoptic variability of the Somali Jet system and related surface interactions. Finally, work on regional winter MONEX circulations, especially in cold surge situations, is under way using a combination of IIb and IIIb data with a simple boundary layer model.

The turbulence group emphasized vertical profile and turbulence measurements from summer research aircraft flights. Both analyses reflect physical processes in the boundary layer, and the profiles will

be of general importance in large-scale syntheses of ship, cloud wind, and satellite sounding data. Three key regions were sampled in 1979 (Somali Jet core and exit region, and the Bay of Bengal). Together with two upwind areas sampled in 1977 (equatorial African coast, southern trade wind core), excellent snapshots along mean monsoonal trajectories now exist. In most cases the turbulence variances seem to be correct in magnitude and vertical variation. The calculated fluxes raise questions. Some seem to be too small (especially in the middle and upper PBL) or are of unexpected sign. The implied flux convergences give large values over layers thin compared to the PBL depth. There is a possibility that the fluxes are largely correct; PIBAL data on the Bay of Bengal coast and some aircraft probes indicated unexpected wind maxima in the lower PBL. Our ultimate goal is to clarify these uncertainties. Refined calculations will attempt to identify possible sampling or cloud contamination problems. In this effort, attention will be given to isolating cloud scale events in the time series and cloud regimes on satellite imagery. This may allow determination of the special role played by cumulus clouds. In the meantime, it is expected that radiation profiles for these and other flights will be available for integration with the turbulence results. The final studies of vertical profile data should be aimed at mapping gross boundary layer regimes for reference in large-scale analyses and numerical models. Bulk stability parameters may be mapped from IIb or IIIb data, for both ocean and land surfaces. Special attention would be given to relating these variables to convective cloud type in order to clarify the mechanism for onset of convective rains. Finally, it seems that preliminary analyses of two winter MONEX gust-probe flights during cold surge conditions should be conducted.

The boundary layer modeling group discussed a variety of PBL models, some tested on GARP data. A K-theory model had success in simulating several fundamental properties of summer monsoon flow, while another model demonstrated the importance of parameterized cumulus clouds. A combined approach is likely to yield the best simulations and should be developed and tested against aircraft data. All models confirmed the importance of horizontal advection in the strong monsoonal flow, and suggest that the models should increasingly be driven by MONEX and FGGE data, thus yielding new sets of assimilated surface data. Such fields could then be compared with existing large-scale analyses and to indicate the breakdown of stabilities and the development of deep convective rain.

ACKNOWLEDGMENTS

REFERENCES

Cadet, D., 1983: Tellus 329-345.

Cadet, D., Ovarlez, H., and G. Sommeria, 1981: BAMS, 381-388.

Gray, W. and C.S. Lee, 1984: U.S. FGGE Workshop preprint.

Grossman, R. and D. Durran, 1984: to appear in MWR.

Hart, J., Rao, Van de Boogaard, Young, and Findlater, 1978: MWR 1714-1724.

Krishnamurti, T.N. and S. Gadgil, 1984: Structure of 30-50 Day Mode over the Globe During FGGE, F.S.U. Report 84-1.

Murakami, T., H. Pan, R. Pasch, and D. Subrahmanyam, 1983: Interannual Variability of the Tropical Motion Field, F.S.U. Report 83-3.

Krishnamurti, T.N. and Y. Ramanathan, 1982: JAS, 1290-1306.

Krishnamurti, T.N., V., Wong, Pan, Molinari, and Ardanuy, 1983: JAS 894-908.

La Seur, N., 1981: WMO Tallahassee Conf. Report.

Meyer, D., and G.V. Rao, 1984: submitted to JAS.

Murakami, T., T. Nakazawa, and J.H. He, 1983: U. Hawaii Tech. Report UHMET 83-02.

Nordgarden, R. and J. Young, 1984: manuscript in preparation.

O'Brien, J. and S. Goldenberg, 1982: Pacific Wind Stress Atlas 1961-1970, Florida St. Univ.

Paegle, J., J.N. Paegle, and G. Dodd, 1983: MWR 1709-1723.

Paegle, J., J.N. Paegle, and F. Lewis, 1984: submitted to PAGEOPH.

Rao, G.V., N. LaSeur, and D.N. Sikdar, 1980: FGGE Operations Report 9 (Part A) WMO, 234-237.

Rao, G.V. and J. Haney, 1982: QJRMS 957-974.

Reverdin, G. and G. Sommeria, 1983: JAS 1435-1452.

Silva-Dias, P. and J.N. Paegle, 1984: U.S. FGGE Workshop preprint.

Stevens, D. 1983: JAS 882-893.

Stout, J.E., and J.A. Young, 1983: MWR 774-798.

U.S. FGGE Project Office, 1981: FGGE Final Operations Report.

VanTuyl, A., and J. Young, 1982: MWR 2038-2054.

Virji, H., 1981: WMO Tallahassee Conf. Report.

Webster, P., 1983: Southern Hem. Conf. Proc. (Brazil).

Wylie, D., and B. Hinton, 1982a: JPO 186-199.

Wylie, D., and B. Hinton, 1982b: BLM 197-208.

Wylie, D., and B. Hinton, 1984: BLM (in press).

Wylie, D., B. Hinton, and M. Howland, 1983: T.O.A.N.L., May (18) 2-4.

Yang, D.S., and T.N. Krishnamurti, 1981: JAS 2676-2695.

Young, J., 1981: WMO Tallahassee Conf. Report.

Young, J., 1982: WMO Bali Conf. Report.

Young, J., 1983: Southern Hem. Conf. Proc. (Brazil).

Young, J., H. Virji, D. Wylie, C. Lo, 1980: MONEX GOES Wind Atlas, U. of Wisconsin NSF Report.

Young, J.A., and C.W. Yuen, 1982: San Diego AMS Conf. presentation.

Yuen, C.W., 1984a: submitted to JAS.

Yuen, C.W., 1984b: submitted to JAS.

12. GLOBAL ASPECTS OF MONSOONS

Organizer   T. N. Krishnamurti

Session Chairman   C. P. Chang

Speaker   Takio Murakami

Rapporteurs   William M. Gray
                             John A. Young

132<

GLOBAL ASPECTS OF MONSOONS

Takio Murakami
University of Hawaii

This paper surveys recent developments in three areas of monsoon research: (1) global aspects of the monsoon onset, (2) the orographic influence of the Tibetan Plateau on the summer monsoon circulations, and (3) tropical 40 to 50 day oscillations. Reference was made only to those studies that are primarily based on FGGE Level IIIb data. To save space, only a brief summary is given in the sections that follow.

GLOBAL ASPECTS OF THE MONSOON ONSET

The importance of differential heating in the evolution of monsoons has been well recognized. However the lack of data prior to FGGE prohibited the evaluation of large-scale heat sources and moisture sinks. Masuda (1984) and Kasahara and Mizzi (1984) evaluated the vertically inte- grated, large-scale apparent heat sources Q_1 during the 1978-197? FGGE year. In winter (Figure 1, top), Q_1 exceeds 100 W m^{-2} over the southern hemisphere monsoon region (Indonesia, New Guinea, northern Australia, and the western South Pacific). Q_1 is also substantial over equatorial Africa and South America. In the middle latitudes of the northern hemisphere, large heating occurs along the cyclone tracks to the east coasts of Asia and North America. In summer (Figure 1, bottom), the Asiatic summer monsoon is characterized by large Q_1 over central India, the southeastern Tibetan Plateau and the South China Sea.

It appears that FGGE Level IIIb data is subject to large errors in the immediate vicinity of high mountains, such as the Tibetan Plateau, the American Rockies, and the Andes. This is particularly true when horizontal divergence (vertical velocity) is computed. A distinct band of large negative Q_1 along the southern periphery of the Tibetan Plateau in summer is questionable, since this region experiences large amounts of rainfall. A marked band of positive Q_1 over the north- eastern Tibetan Plateau in winter is similarly questionable.

Symmetric and Asymmetric Heating Fields

Following Webster (1984), we separate Q_1 into two important com- ponents. The first component is symmetric about the equator and shows
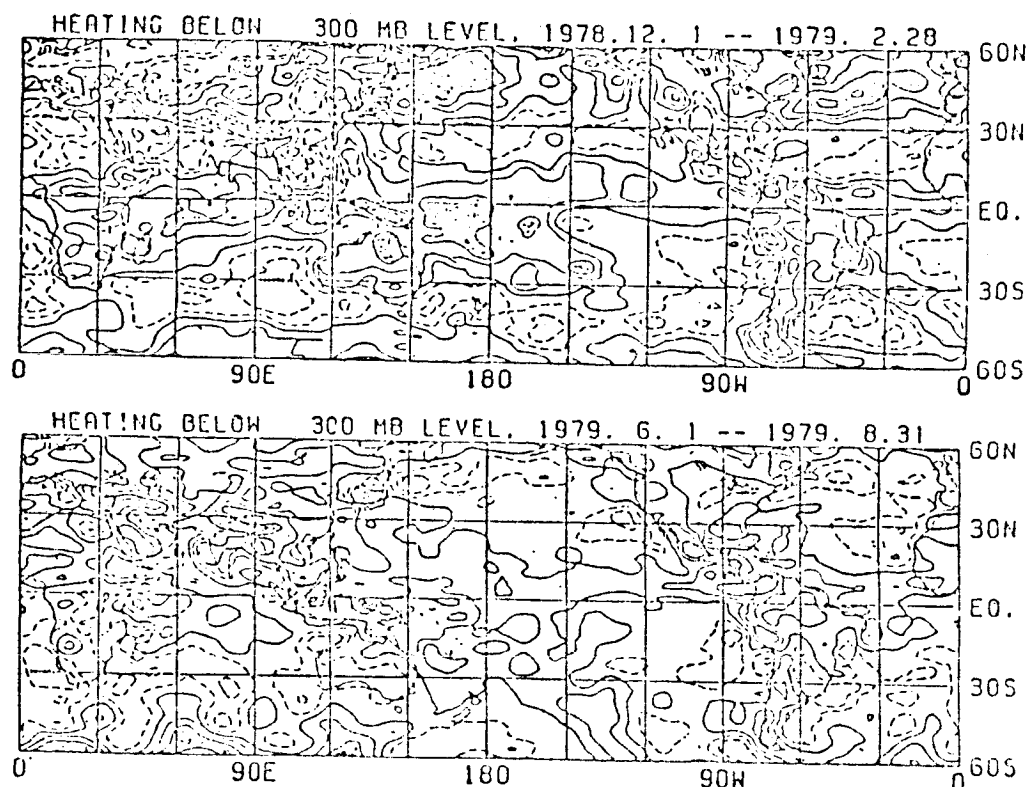
FIGURE 1 Vertically integrated, large-scale apparent heat sources Q_1 evaluated from FGGE Level IIIb data for winter (top) and summer (bottom). Thick hatching indicates regions of Q_1 greater than 100 W m^{-2}.

relatively small seasonality. The second component is asymmetric about the equator with convective zones showing a distinct seasonal pattern between the southern and northern hemisphere summer. Q_1 can be partitioned into two components as follows:

$$Q_1^+ = 1/2 \ (Q_N + Q_S),$$

$$Q_1^- = 1/2 \ (Q_N - Q_S),$$

where Q_1^+ and Q_1^- represent the symmetric and asymmetric components, respectively; Q_N (Q_S) denotes Q_1 in the northern (southern) hemisphere. Q_1^+ is positive and substantial, irrespective of season, over equatorial Africa ($20°$ to $40°E$), the maritime continent ($100°$ to $160°E$), and equatorial South America ($110°$ to $70°W$). These are three of the most convectively active regions near the equator. Response to Q_1^+ is generally confined to the equatorial latitudes and is often called the "Walker circulation" (Gill, 1981; Lim and Chang, 1983; Lau and Lim,

1984). Lau and Lim (1984) investigated the effect of nonlinearity in modifying the forced teleconnection by Q_1^+ near the dateline at the equator. The response is of Kelvin (Rossby) type east (west) of the Q_1^+ center. O particular interest is the equatorward penetration of midlatitude upper tropospheric westerlies over the eastern North and South Pacific. This is associated with the development of upper tropospheric troughs to the northeast and southest of the Q_1 center due to the nonlinearity. As will be shown in Section 3, when the summer monsoon is active over South Asia, Q_1 is also above normal over the equatorial central Pacific, and the Walker circulation along the equator is stronger than usual. At this time, the eastern North and South Pacific are characterized by strong westerlies at 200 mb, favoring interhemispheric interaction due to transient disturbances.

Q_1^- is negative and substantial over the maritime continent (Sumatra, Borneo, New Guinea) during the southern hemisphere summer monsoon. The response is of Rossby type with cross-equatorial low-level northerlies and upper-level southerlies (Hadley circulation). During the northern hemisphere summer monsoon, Q_1^- becomes positive over the equatorial Indian Ocean where cross-equatorial low-level southerlies are capped by cross-equatorial upper-level northerlies.

Transition from the Southern to Northern Hemisphere Summer Monsoon

The longtitudinal dependency of Q_1^+ along the equator is nearly identical to that of the symmetric component of outgoing longwave radiation (hereafter signified as OLR^+). Over the three equatorial convective regions near $30^\circ E$, $140^\circ E$, and $80^\circ W$; OLR^+ seldom exceeded 240 W m^{-2} throughout the five-month period from February 15 to June 20, 1979 (Murakami and Nakazawa, 1984b). Namely, OLR^+ over these three regions exhibits little (if any) indication of seasonality. Associated with this OLR^+ field is a near permanent Walker circulation along the equator. This was confirmed from an inspection of longitude-time sections of U^+ at 850 and 200 mb. (As will be shown in Section 3, the Walker circulation is subject to substantial intraseasonal (not interseasonal) variations with a period range of 40 to 50 days.)

The asymmetric component OLR^-, measured at 10° of latitude away from the equator, changes from positive to negative during the transition from the southern to northern hemisphere summer monsoon. Near equatorial North Africa and the maritime continent, OLR^- becomes zero around April 15, while over Central America, near zero OLR^- occurs at the end of March. In association with the occurrence of near zero OLR^-, 850 mb U^- at 10° of latitude away from the equator changes from negative (easterly) to positive (westerly) near the three equatorial convective regions. This corresponds to the withdrawal of the southern hemisphere monsoonal westerlies and the first establishment of the northern hemisphere monsoonal westerlies at 850 mb.

The timing of near zero OLR^- and/or U^- differs considerably from one region to another. It ranges from about March 20 to April 20. Murakami and Nakazawa (1984b) then computed the differences in OLR, and u and v winds between the two contrasting periods, i.e., February 15 to

520
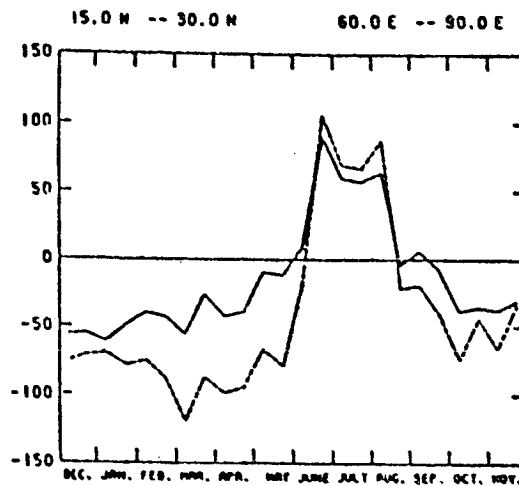
FIGURE 2 Annual march of half-monthly Q_1 (full line) and Q_2 (dashed line) over the Indian region (15° to 30°N, 60° to 90°E).

March 20 and April 20 to June 20, over the entire tropics. These difference fields depict the existence of three distinct regions of monsoon-type circulations: over equatorial North Africa, the Indochina-Malaysian Peninsula region, and Central America. In short, Murakami and Nakazawa's study indicates the importance of the global-scale thermal effects during the transition from the southern to northern hemisphere summer monsoon. The monsoon onset over Indochina and the Malaysian Peninsula occurs as a paart of the global-scale phenomenon. Over central India, the monsoon begins about the beginning of June, i.e., about two months later than the transition from the southern to northern hemisphere summer monsoon. This transition takes place in an abrupt manner on the seasonal time scale. What mechanisms are responsible for such a rapid transition? Further study is needed to answer this question.

Monsoon Onset over Central India

There appears to be marked regional differences in the manner and timing of the onset of summer monsoon over South and East Asia. In this section, the term onset refers to the monsoon onset over central India.

The monsoon onset is rarely sudden and dramatic on the day-to-day time scale. However, it is certainly a dramatic event on the seasonal time scale. This can be seen in Figure 2 for the Indian summer monsoon onset (Masuda, 1984), which exhibits a sharp increase in Q_1 and Q_2 in the middle of June. Prior to this period, both Q_1 and Q_2 are negative (cooling), congruent with persistent dry weather during the pre-monsoon. After the onset, Q_1 and Q_2 are positive and nearly equal ($\sim$70 W m^{-2}), indicating heavy rainfall.

521
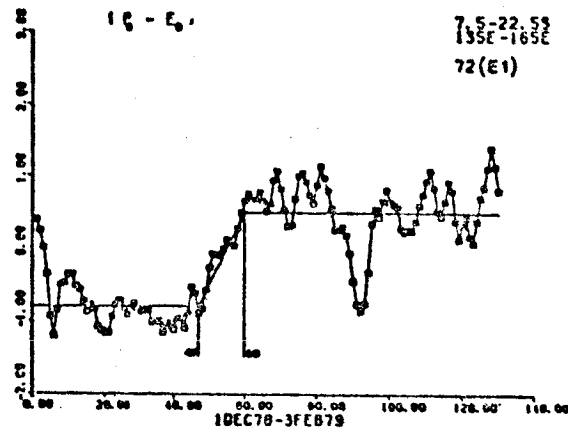
FIGURE 3   Time series of twice-daily moisture budget (P_0 to E_0) over the Australian region (7.5° to 22.5°S, 135° to 165°E) from December 1, 1978 to February 3, 1979.

To test the sensitivity of the monsoon onset to initially imposed fields of differential heating, Krishnamurti and Ramanathan (1982) conducted a series of numerical prediction experiments. In all these experiments, essentially the same initial state was used, i.e., the flows during a one-week period (June 5 to 11, 1979). The irrotational part of this initial state was replaced by these from three periods representing late spring, pre-onset, and post-onset phases. The moisture fields for these three periods also replaced the weekly average of the above initial state. Thus the three initial states differ in their description of inital moisture and mass convergence. This provides a different field of differential heating at the initial time. Figure 4a-c show the 800 mb flow fields at 96 hours for the late spring, pre-onset, and post-onset experiments. The structure of the cross-equatorial flows is a measure of the evolution of the monsoons. The first two experiments do not show any evolution of the typical monsoonal Somali jet. The third experiment exhibits a rapid evolution of the monsoons. Figure 4d shows the establishment of the well-marked cross-equatorial flow at 72 hours after the initial state. From these experiments, it follows that the onset evolution is quite sensitive to the initial fields of divergent circulations and the differential heating.

Pasch (1984) attempted to identify the key physical processes that operate during the buildup of the planetary-scale monsoon system during the 1979 early summer. Figure 5 clearly demonstrates the drastic amplification of both APE (eddy available potential energy) and KE (eddy kinetic energy) on the planetary-scale (wavenumbers 1 to 3) during the onset period (June 16 to 20). This confirms the presence of planetary-scale manifestation of the regional onset phenomenon. To further investigate the planetary-scale wave behavior, Pasch performed a global weather prediction using the FSUGSM model from an initial
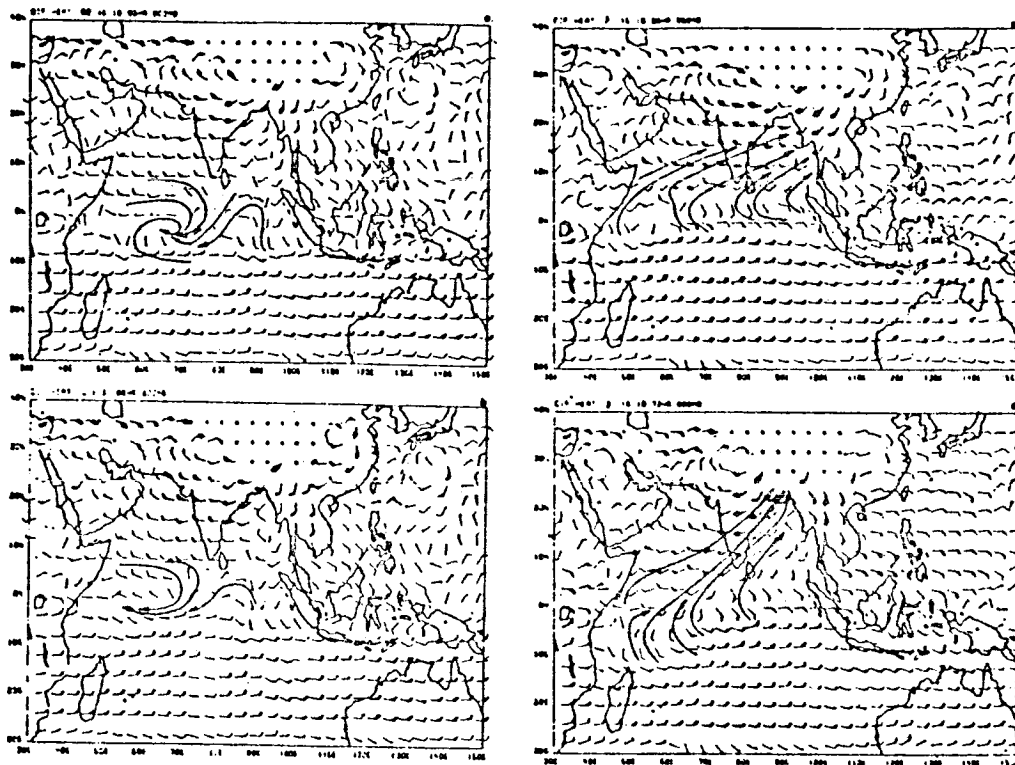
FIGURE 4 Predicted 850 mb wind field for the four experiments: (a)
late spring at 96 h, (b) pre-onset at 96 h, (c) post onset at 96 h, and
(d) post-onset at 72 h.

state of June 16, 1979, 1200 GMT for a 96-hour forecast period. A
complete planetary-scale energy budget from the model results is shown
in Figure 6. The most important energy exchanges are the generation of
APE by cumulus convection and the conversion from APE to KE. It is
clear that the most significant energy exchanges occur directly on the
planetary scales themselves. Interactions between other scales or with
the zonal mean motions are of secondary importance. Furthermore, Pasch
found that the most important geographical regions for the convective
generation are the Tibetan Plateau and Indochina. This, in turn,
indicates the importance of the orographic influence of the Tibetan
Plateau on the determination of planetary-scale heating and vertical
motion during the monsoon onset.
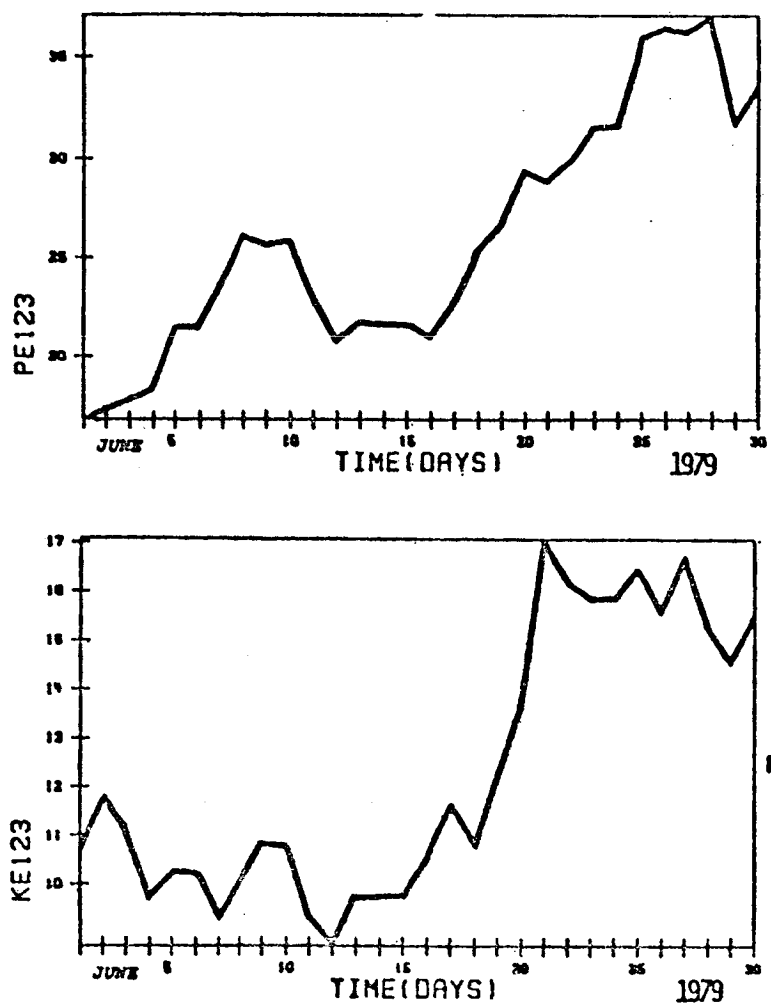
FIGURE 5 Time series from June 1 to 30, 1979 of planetary scale (sum of wavenumbers 1 to 3) energetics: (a) APE, and (b) KE.

It may be of interest to perform similar numerical experiments, as employed by Krishnamurti and Ramanathan (1982) and by Pasch (1984), during the withdrawal of the Asiatic summer monsoon. It would also be instructive to carry out numerical experiments to investigate the key physical processes that are responsible for the onset and withdrawal of the southern hemisphere summer monsoon. The Indonesia-Australia region, where the southern hemisphere summer monsoon is most active, is basically free from high mountains. Yet this monsoon onset is as clearly defined as in the Asiatic monsoon. In Figure 3 for Q_2 over the Australian summer monsoon region (Lubis and Murakami, 1984), a step-like time variation occurs during the eight-day span from t = 47
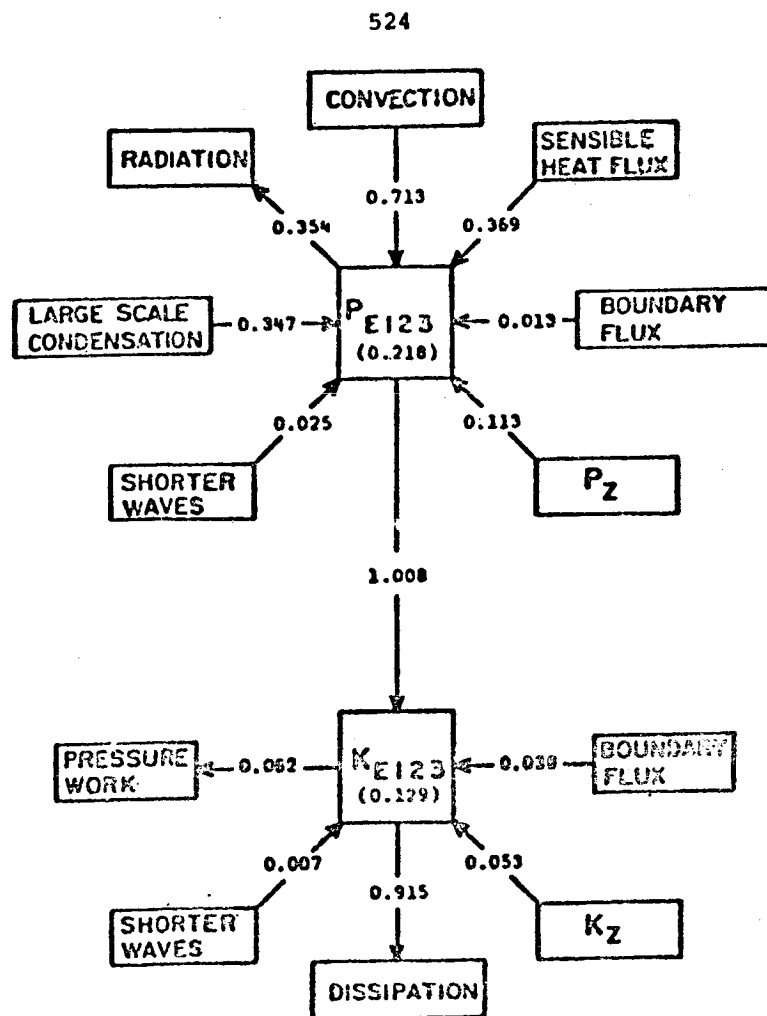
FIGURE 6 Mean energy budget of the sum of wavenumbers 1 to 3 for hours
0 to 96 of the prediction experiment, integrated from 2.5°S to
42.5°N and from 200 to 1000 mb.

(00 GMT, December 24) to 60 (12 GMT, December 30). Prior to t = 47,
$(P_0 - E_0)$ is negative, indicating that evaporation exceeds
precipitation. After t = 60, P_0 is much greater than E_0. What
mechanisms are responsible for the sharp and dramatic onset of the
southern hemisphere summer monsoon? One effective way to answer this
question is to perform a series of numerical prediction experiments and
to examine the sensitivity of the monsoon onset to various
meteorological parameters.

OROGRAPHIC INFLUENCE OF THE TIBETAN PLATEAU
ON THE NORTHERN HEMISPHERE SUMMER MONSOON

Since the Tibetan Plateau is a huge massif of extremely high elevation,
it receives a large amount of solar radiation which effectively heats
the mountain surface, causing a strong heat contrast with the sur-
rounding free atmosphere. This heat contrast at the mid-tropospheric
level (4 to 5 km) can be as important as the Eurasian continent-Indian
Ocean heat contrast at the earth's surface. Many investigators
emphasized the importance of thermal effects of the Tibetan Plateau on
the rapid northwaqrd jump of the westerly jet across these high
mountains and the establishment of the upper tropospheric Tibetan high
in early June. This view was questioned by Murakami and Ding. (1982),
who analyzed the temperature changes at 700 and 300 mb over Eurasia
between the pre- and post-onset periods, and found a well-organized
east-west oriented band of positive temperature changes at about 30°
to 540°N across Eurasian with three distinct centers: near Japan,
the western end of Tibet, and the Saudi Arabian desert. Namely,
Murakami and Ding's study indicates the importance of the thermal
effect of the Eurasian continent as a whole. However, the Tibetan
Plateau is instrumental in causing a local enhancement of the
temperature increase and associated jete stream jump during the onset
period.
   Despite the efforts of many synoptic meteorologists, there continues
to be no unified and detailed description of the exact role of Tibetan
Plateau in maintaining the summer monsoon circulation. To overcome
this difficulty, several authors have used other approaches, including
numerical model experiments.

Simplified Model Experiments

Murakami et al. (1970) used an eight-layer, two-dimensional numerical
model of the summer monsoon at 80°E. It exhibited the strong impact
of Tibet on the monsoon circulation. Another informative experiment,
without any mountains, was conducted by Webster and Cho (1980). This
experiment used a two-level primitive equation model in which a con-
tinental cap north of 18°dN is surrounded by interactive and mobile
oceans. When hydrologic processes are included, the upper-level zonal
winds undergo substantial interseasonal changes from westerly (30 m/s
at 30°N) during winter to easterly (-20 m/s at 10°N) in summer even
without the effects of the Tibetan Plateau. Thus the continent-ocean
heat contrast appears to be a crucial element in determining the
seasonal variation of the upper-level circulation. In the real
atmosphere however, the northern hemisphere westerly jet is much
stronger than 30 m/s. As shown by Murakami (1981a), the Tibetan
Plateau plays an important role in the intensification of the world's
strongest westerly jet over East Asia during the northern hemisphere
winter. In Webster and Cho's model, the annual changes over the
southern hemisphere are much reduced as compared to the corresponding
changes in the northern hemisphere. In fact, their model failed to

produce upper tropospheric easterly winds during the southern hemisphere summer. Perhaps, this indicates the importance of the orographic influence of the Australian continent in the development of the southern hemisphere summer monsoon.

Based on a primitive equation model with five atmospheric layers and one oceanic layer over the 0° to $180^\circ E$, $25^\circ S$ to $55^\circ N$ region, Kuo and Qian (1982) investigated the relative importance of orography, radiative heating, cumulus condensation, and initial conditions for the development of the monsoon circulation from June to July. The low-level monsoonal flows are largely determined by the diabatic heating distribution and influenced somewhat by orography, but are almost independent of the initial state. The essential features of the monsoonal flows cannot be reproduced without radiative heating and cumulus condensation. However, the precipitation distribution is found to be critically influenced by both radiative heating and orography. Without orography, maximum precipitation occurs only in the coastal regions. One important aspect of Kuo and Qian's experiments is that the time requirement for the atmosphere to establish the planetary-scale monsoon circulation under the combined radiative/convective heating effects is only about 5 days when the diurnal variation was included. Perhaps, this is due to the increase in dry and moist convective activities produced by strong insolation during the day over and around the Tibetan Plateau regions.

Global GCM Numerical Experiments

A series of numerical experiments using a global GCM can be performed both with and without the mountains, and comparisons of the results can provide useful information about orographic influences. Such experiments have been conducted by several authors, e.g., Hahn and Manabe (1975) for summer, and Manabe and Terpstra (1974) for winter. Recently, Lau (1984) performed 15-year integrations of GFDL GCMs with mountains (M-model) and without mountains (NM-model).

Figure 8 depicts the vectorial difference patterns of streamfunction and velocity potential between M- and NM-models for winter (left) and summer (right). The following points are noteworthy:

1. The streamfunction response to orography in the winter season is dominated by two well-defined wavetrains (Figure 8a). One such group of perturbations L_1, H_1, and L_2 is forced by the Tibetan Plateau, whereas the other group of waves H_2, L_3, and H_3 is essentially a response to the Rockies.
2. Figure 8b for winter exhibits the enhanced thermally direct circulation over East Asia, with rising motion over the warm western Pacific, and sinking motion over the cold northern China and Siberia area. Associated with this direct cell is the presence of 200 mb divergent southerlies near Japan, which account for the enhanced westerly jet in that region (Figure 8a).
3. The summertime streamline pattern (Figure 8c) is dominated by anticyclonic centers over the Eurasian and North American continents, and cyclonic centers over the Pacific and Atlantic Oceans. The
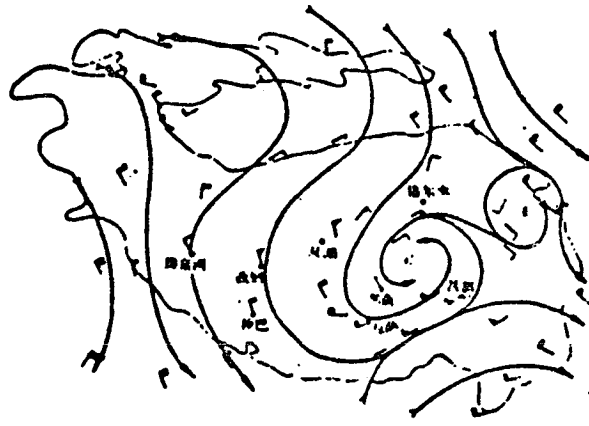
图5h 1979 年 6 月 8 日 20 时 100 毫巴流场
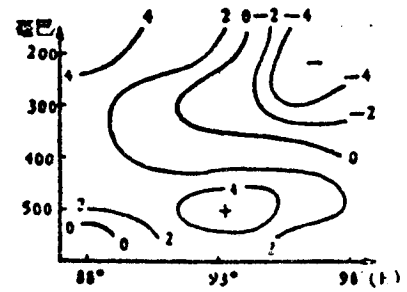
图5b 1979 年 6 月 8 日 20 时 35°N
涡度(10⁻⁵ 秒⁻¹)垂直分布
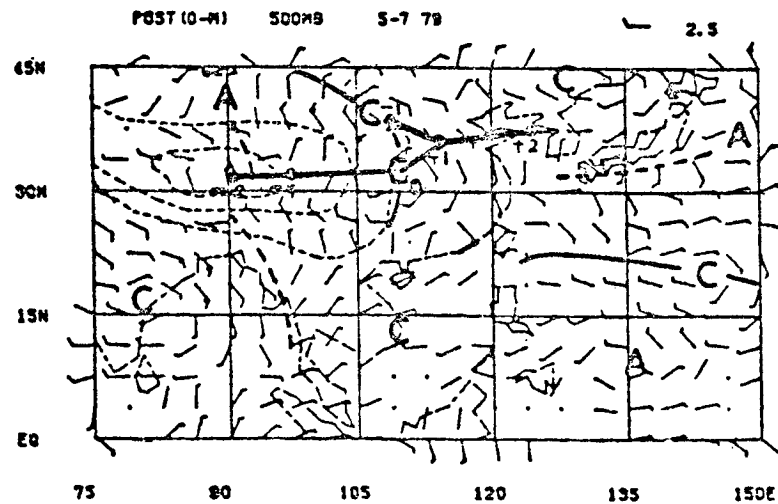
FIGURE 7 (a) 500 mb winds on June 8, 1979; (b) Vorticity $(10^{-5}s^{-1})$ on June 8, 1979; and (c) 500 mb winds at 0 day. Heavy full lines indicate the trajectories of cyclonic vortices from day -2 to +2.

528

M-NM

DJF JJA

(a) ψ° (c) ψ°

C.l. 2×10⁶ m²s⁻¹   C.l. 2×10⁶ m²s⁻¹

(b) X (d) X

C.l. 5×10⁵ m²s⁻¹   C.l. 1×10⁶ m²s⁻¹
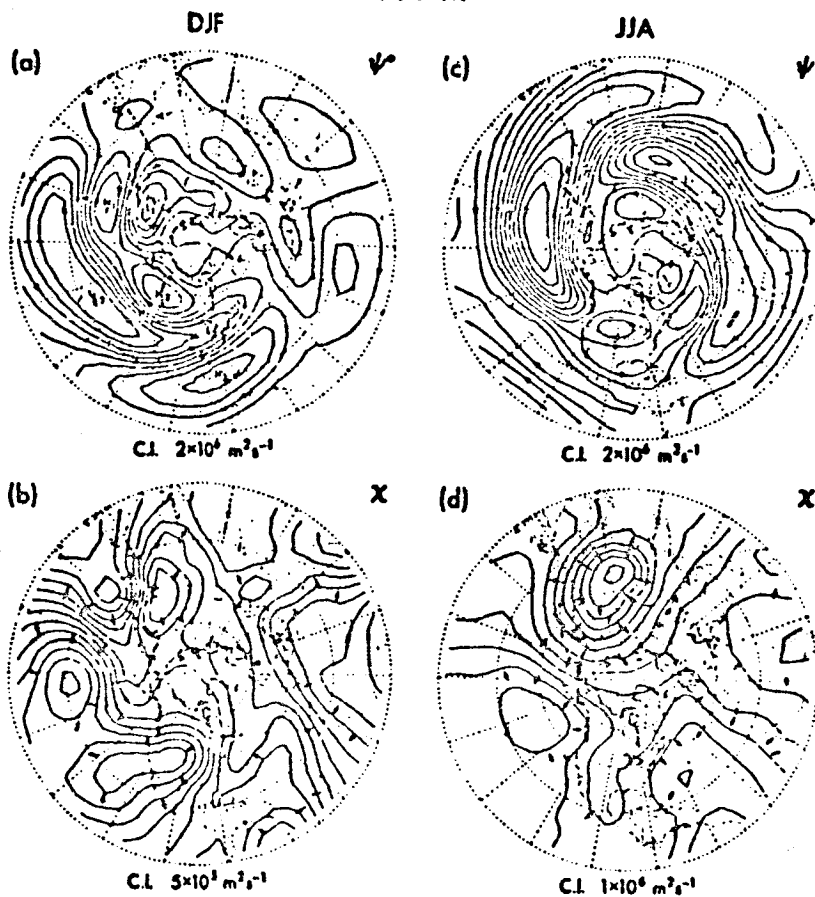
FIGURE 8 Top: Difference patterns for 200 mb streamfunction between
experiment M and NM for winter (a) and summer (c). Bottom: Difference
patterns for 200 mb velocity potential for winter (b) and summer (d).

features in Figure 8d are characterized by rising motions over Asia and
North America, and sinking motions over the midlatitude Pacific and
Atlantic.

In Figure 9, which shows the distribution of diabatic heating for M
and NM during winter (a and b) and summer (c and d), noteworthy are the
following:

1. In winter, the patterns for both M and NM experiments are
dominated by elongated maxima over the two ocean basins, which are
associated with latent heat release along the wintertime storm tracks,
and by cooling over the continental land masses.

111

VERTICALLY AVERAGED DIABATIC HEATING

DJF

JJA

CONTOUR INTERVAL

0.5 K/day

CONTOUR INTERVAL

1 K/day
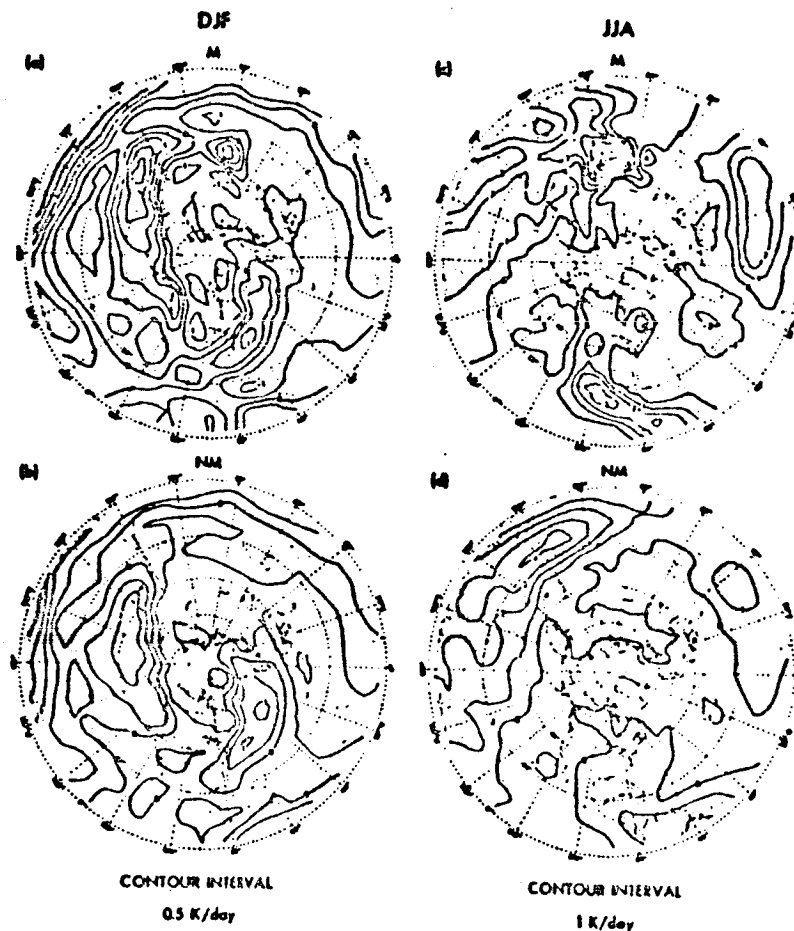
FIGURE 9 Vertically averaged diabatic heating for experiment M in winter (a) and summer (c), and for experiment NM in winter (b) and summer (d).

2. The impact of orography on the diabatic heating pattern is much more notable in summer than in winter. The M pattern exhibits a distinct land-sea contrast, with heating over the eastern Tibetan Plateau, the eastern Rockies, Central America, and the African continent equatorward of $10°N$. Cooling prevails over the eastern Pacific and Atlantic.

Kuo and Qian (1981) investigated the influence of the Tibetan Plateau on the diurnal changes of the meteorological fields during summer. Their five-layer primitive equation model created pronounced diurnal variations. The predominance of diurnal variations was also

noted by Nitta (1983) and Murakami (1983). The Tibetan Highlands produce a variety of atmospheric circulation systems with different time and space scales. It may be interesting to examine the nature of synoptic-scale disturbances over and around the Tibetan Plateau using data of extremely fine time and vertical resolution obtained from numerical prediction models.

SYNOPTIC-SCALE DISTURBANCES OVER AND AROUND THE TIBETAN PLATEAU

Tibetan Vortices

Observational information is scanty pertaining to the nature of transient and synoptic-scale disturbances developing over the Tibetan Plateau. To remedy this deficiency, Chinese scientists conducted the Qinghai-Xizang Plateau Meteorology Experiment (QXPMEX) during the 1979 summer (May to August). In addition to the FGGE Level IIb data, QXPMEX provides many more surface station data, four upper air station data, and six radiation station data over the central and eastern Tibetan Plateau. Based on QXPMEX data, Tao et al. (1984) observed the frequent development of Tibetan vortices during the 1979 summer (refer to Figure 7a). These vortices develop within the mixed boundary layer (~1 km) above the Tibetan Plateau (Figure 7b). Although they are very shallow in the vertical depth, associated rainfall is substantial, occasionally exceeding 100 mm/day. They slowly propagate eastward and dissipate near the eastern edge of the Tibetan Plateau. However, some of the Tibetan vortices propagate eastward across central China to as far east as Japan. Utilizing a limited area version of the ECMWF forecasting model, Dell'osso and Chen (1984) emphasized the importance of moisture supply from the Indian monsoon region for the development of Tibetan vortices.

Based on FGGE Level IIIb data, Huang and Murakami (1984) investigated the nature of Tibetan vortices during the 1979 summer. Figure 7c shows the composite 500 mb maps on day 0, when the rainfall reaches a maximum over the Yangtze River region. Also shown are the trajectories of cyclone centers at 500 mb between day -2 and +2. A Tibetan vortex forms on day -2 over the central Tibetan Plateau (33°N, 90°E). This Tibetan vortex leaves the Plateau around day 0. At this time, the cyclonic cell exhibits the midlatitude frontal charcter in the lower troposphere. Between days 0 and +1, the Tibetan vortex merges with the major cyclonic system and develops into a deep (200 to 1000 mb), mature midlatitude system. It is a general belief that disturbances develop over central China when the low-level monsoonal flows from South Asia intensify. No such intensification of monsoon westerlies can be seen in Figure 7c. At day 0, a cyclonic cell developing over India is of tropical character with cold core in the lower troposphere and warm core in the upper troposphere. Although they are of different character, both China and India disturbances tend to develop nearly simultaneously, causing widespread rainfall over South and East Asia. Thus these disturbances are important energy producing systems during the summer monsoon.

531

Edge Cyclones

Murakami and Huang (1984) showed that the northeastern edge of the
Tibetan Plateau is the birthplace of a small-scale low-level cyclone
trapped below 700 mb during the early summer (May to June) of 1979.
This edge cyclone then propagates southward along the eastern periphery,
reaching the upper reaches of the Yangtze River. Here, the low-level
edge cyclone merges with an eastward propagating upper trough. The
merged cyclone moves eastward along the "Meiu" front causing wide-
spread rainfall over central China and Japan. Murakami (1981b) and
Murakami and Nakamura (1983) showed that these edge distrubances and
associated cold surges represent major and unique wintertime synoptic
systems over East Asia. As mentioned earlier, edge disturbances
develop even inearly summer when the upper tropospheric westerlies
still predominate over and around the Tibetan Plateau. These oro-
graphically induced edge disturbances are of Kelvin-type wave char-
acter. Edge cyclones resemble coastal lows of southern Africa. Gill
(1977) interpreted these African coastal lows as Kelvin waves, while
Bannon (1981) postulated that the formation of coastal lows is due to
the scattering of eastward-propagating synoptic-scale disturbances at
the meridional boundary.

TROPICAL FORTY TO FIFTY DAY OSCILLATIONS

Recently, several investigators documented the nature of long-period
oscillations during the 1978-1979 FGGE year. Krishnamurti and
Subrahmanyam (1982) presented a mapping of the 30 to 50 day filtered
wind fields at 850 mb over the Indian summer monsoon region. Murakami
et al. (1984) postulated that the low-frequency modes propagate
northward and become most intensified near 10° to 20°N through
mutual interaction between synoptic-scale disturbances (convection),
the local Hadley circulation and the zonal mean flows over the monsoon
region (30° to 150°E). The existence of 40 to 50 day oscillations
throughout the 1978-1979 FGGE year was confirmed by Lorenc (1984).
Based on an empirical orthogonal function (EOF) analysis of the velocity
potential fields, Lorenc detected eastward propagating divergent
modes with a zonal wavenumber 1 and a period range of 40 to 50 days.
Recently, Krishnamurti et al. (1984) examined the divergent circula-
tions on the time scale of 30 to 50 days during the FGGE year. Their
analysis identified a planetary-scale, eastward propagating (8°
longitude/day), divergent wave throughout the FGGE year. The amplitude
of this divergent wave is largest during the summer season over the
monsoon region and the western Pacific.
   To reduce the chances of combining entirely different seasonal
characteristics, EOF analysis should not be performed over too long
records of data (one year data, for example). Hence Murakami and
Nakazawa (1984a) applied EOF analysis to 40 to 50 day filtered data
during the 1979 summer (May to September). This was followed by an EOF
analysis of 40 to 50 day filtered data during the transition from the
1979 winter to summer, i.e., February 15 to June 20 (Murakami and

532
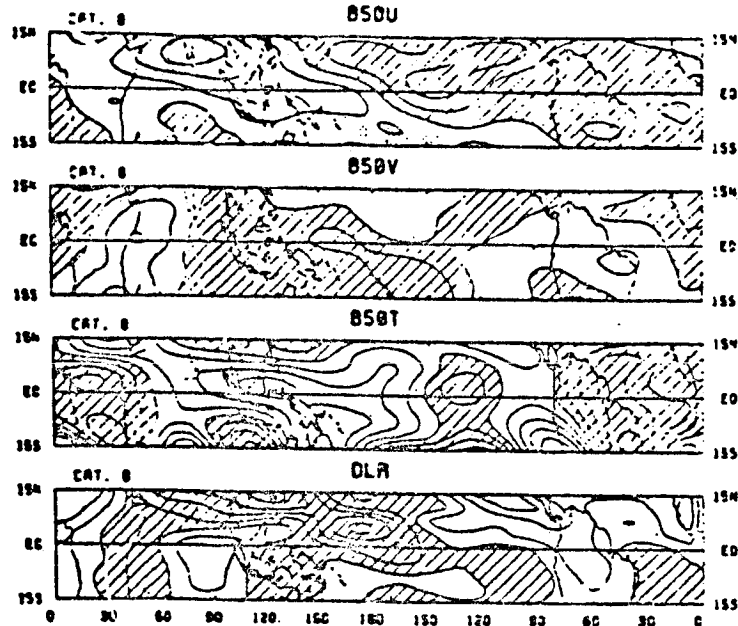
FIGURE 10 Composite charts for u, v, and T at 850 mb and OLR (outgoing longwave radiation) at category 8 (active monsoon phase over South Asia). Shading indicates regions of negative anomaly.

Nakazawa, 1984b). These studies indicate evidence of vertical trapping with the amplitude of the 40 to 50 day perturbations decreasing with increasing height between 200 and 100 mb. Shrestha and Murakami (1984) extended the analysis into the stratosphere, so that the vertical coupling between the troposphere and stratosphere could be investigated. In the following, a brief description will be given for each of three recent studies at the University of Hawaii.

Relationship between Forty to Fifty Day Oscillations
and Active and Break Monsoons during the Northern Hemisphere Summer

Murakami and Nakazawa's (1984a) results can be summarized as follows:

1. When the Asiatic monsoon is active, a distinct WNW-ESE oriented zone of westerly winds (anomaly) at 850 mb extends from South Asia to the central South Pacific, crossing the equator around New Guinea. This contrasts with regions of strong 850 mb easterlies (anomaly) over the equatorial Indian Ocean and the eastern North Pacific east of the dateline (Figure 10, top). At 200 mb, prominent easterlies over the Indian Ocean contrast with strong westerlies (anomaly) over the eastern Pacific east of the dateline between 15°N and 15°S (Figure 11,

533
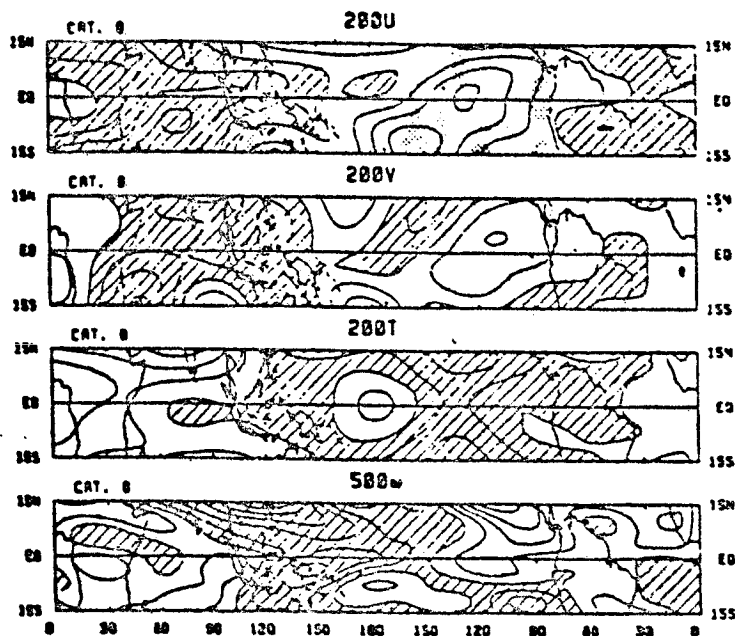
FIGURE 11   As in Figure 10, except for u, v, and T at 200 mb, and ω
at 500 mb.

top).   Perhaps this favors the occurrence of interhemispheric coupling
over the eastern Pacific.

   2.   At the equator, the Walker circulation becomes most pronounced
during the active monsoon phase.   The equatorial eastward propagating
40 to 50 day zonal wind perturbations tilt westward with increasing
height.   Thus their vertical phase propagation is upward with an
approximate speed of 0.7 km/day.

   3.   The active monsoon is associated with anomalous 200 mb
westerlies (easterlies) along the equator east (west) of New Guinea
where the equatorial rainfall is above (below) normal (refer to Figures
10 and 11, bottom).   These features resemble the theoretically
predicted equatorial modes forced by prescribed diabatic heat sources
(Gill, 1980; Lim and Chang, 1983; Lau and Lim 1984)).

   4.   Anomalous features shown in Figures 10 and 11 tend to propagate
eastward while weakening in intensity.   They reintensify again after
passing halfway around the globe.   This corresponds to the break phase
of the monsoon over South Asia.   The anomalous features during the
break monsoons are identical to those shown in Figures 10 and 11,
except for a change of sign.   Low-level winds become easterlies
(anomaly) over South Asia, while they are westerlies (anomaly) over the
eastern North Pacific.   The Walker circulation becomes much less
pronounced than normal.
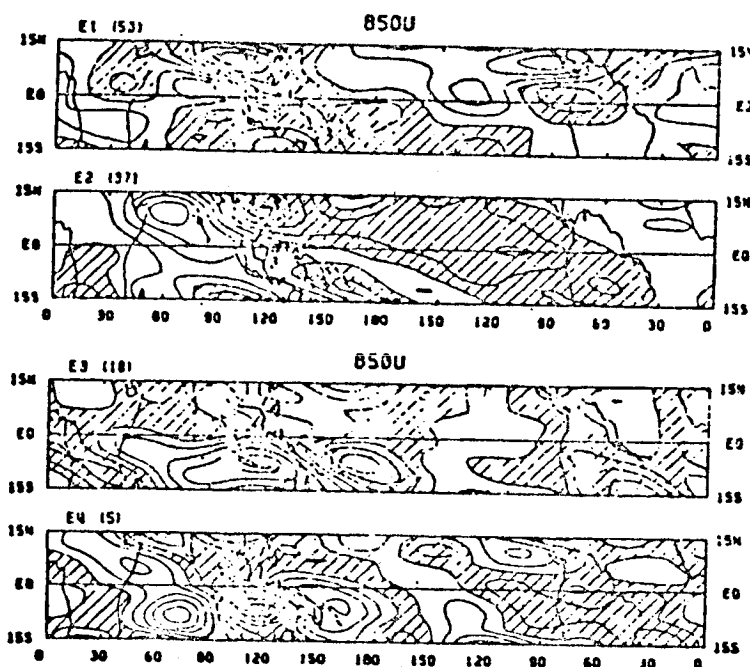
FIGURE 12 First four empirical orthogonal functions for 850 mb u during the transition period (February 15 to June 20, 1979). Shading indicates regions of negative anomaly.

Behavior of Forty to Fifty Day Oscillations during
the Transition from the Southern to Northern Summer Monsoon

Main results obtained by Murakami and Nakazawa (1984b) are summarized as follows:

1. During the transition from the 1979 winter to summer, the first two EOF eigen modes for 40 to 50 day filtered zonal winds resemble the first two eigen modes for summer (compare Figure 12, top with Figure 10, top), while the third and fourth modes exhibit the similarity to those for winter (Figure 12, bottom).

2. The amplitude of the third and fourth modes (Figure 13, bottom) decreases sharply between days 46 (March 22) and 67 (April 22). In comparison, the amplitude of the first and second modes increases monotonically from March to June (Figure 13, top).

3. Figure 14 shows the time-latitude sections of the amplitude of 200 mb U_1 (wavenumber 1, 40 to 50 day 200 mb, zonal winds, top), 850 mb U_1 (wavenumber 1, 40 to 50 day 850 mb zonal winds, middle), and OLR_1 (wavenumber 1, 40 to 50 day filtered, outgoing longwave radiation). Prior to day 44 (March 30), both 850 U_1 and OLR_1 perturbations are of standing-wave character in the southern hemisphere around $15°S$, while the standing character of 200 mb U_1 is evident

535

$$\sqrt{C1^2+C2^2}$$

Feb. | Mar. | Apr. | May | Jun.

$$\sqrt{C3^2+C4^2}$$
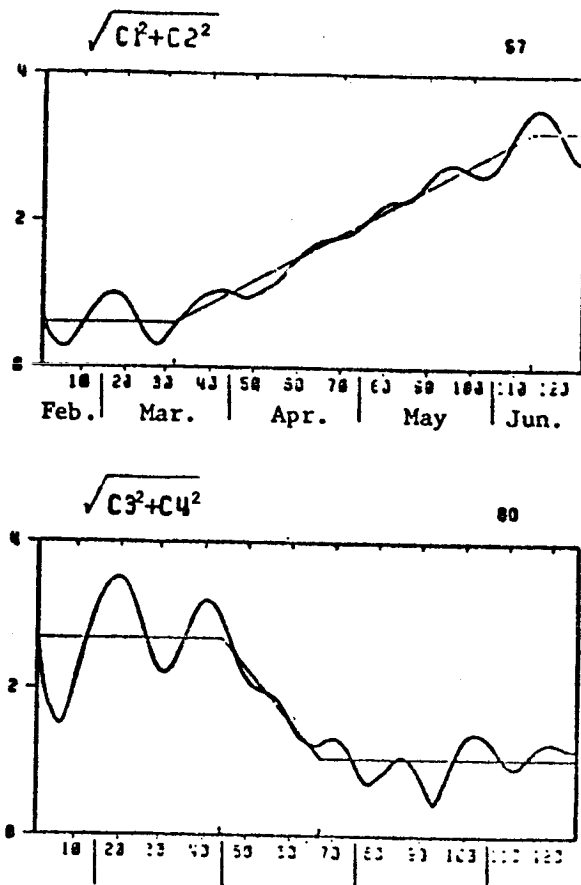
FIGURE 13 Time series of the amplitude of the first and second empirical orthogonal functions (top) and the third and fourth EOF functions (bottom) for 850 mb u from day 1 (February 15) to day 126 (June 20).

in the northern hemisphere around $15°N$. These features are of winter character. After day 67, 200 U_1, 850 U_1, and OLR$_1$ all show the summer character of eastward propagation, which is most prominent between the equator and $20°N$.

Stratospheric Forty to Fifty Day Oscillations
during the 1979 Northern Summer

This section summarizes results obtained by Shrestha and Murakami (1984).

AMPLITUDE   WN 1   200 U

AMPLITUDE   WN 1   850 U

AMPLITUDE   WN 1   OLR

FEB   MAR   APR   MAY   JUN
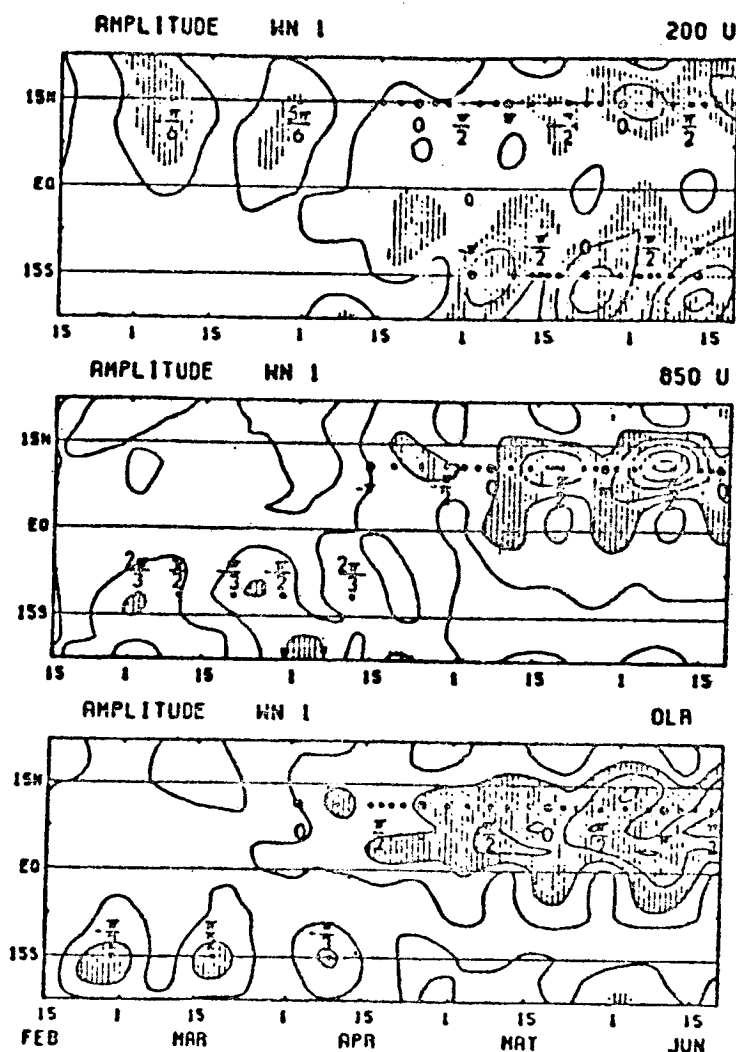
FIGURE 14   Latitude-time section of wavenumber 1 amplitude for 200 mb U (top), 850 mb U (middle), and OLR (bottom).

1. Figure 15 presents spectral analysis results of wavenuber 1 zonal winds (U_1) at 10, 50 and 100 mb, respectively. At 100 mb, eastward propagating modes are prominent between 20°N and 60°S.

2. Near 15°N, 40 to 50 day oscillations attenuate rapidly upward above 100 mb. In this vicinity, the zonal mean winds are easterly in the stratosphere.

3. Although the stratospheric zonal mean winds are easterly at the equator, prominent 40 to 50 day modes are found near 10 mb. These modes in the equatorial upper stratosphere propagate westward.
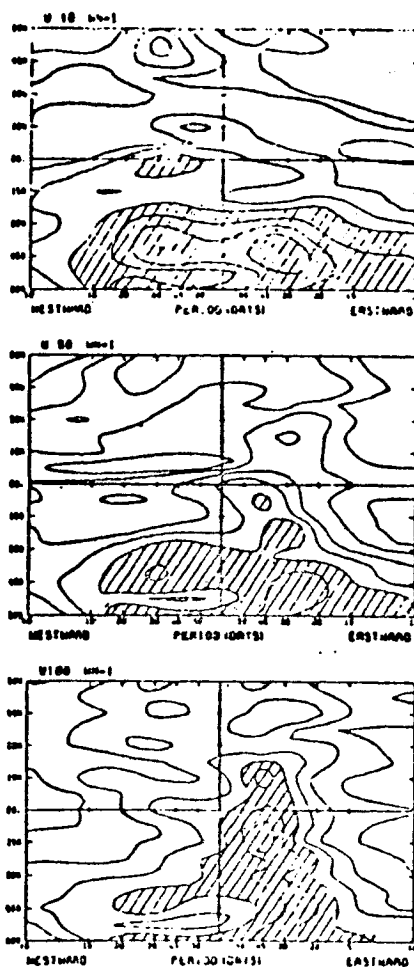
FIGURE 15 Power spectra for u perturbations with wavenumber 1 at 10, 50, and 100 mb, respectively.

4. Around 45°S where the stratospheric wintertime westerlies are strong, the amplitude of 40 to 50 day oscillations (expressed in M^2 s^{-2}) increases sharply from 100 to 10 mb. These low-frequency modes are of standing wave character.

In summary, the main point of Section 3 is that 40 to 50 day oscillations resemble, in many respects, the interannual variations associated with the Southern Oscillation. Further study is needed to investigate the changes in structural features (phase propagation, vertical tilt) of 40 to 50 day oscillations from one year to another. It is also important to investigate the vertical coupling between the troposphere and stratosphere. Also needed is an investigation of lateral coupling between higher and lower latitudes for 40 to 50 day perturbations.

REFERENCES

Bannon, P. R. (1981). Synoptic-scale forcing of coastal lows: Forced double Kelvin waves in the atmosphere. Quart. J. Roy. Meteorol. Soc. 107, 313-327.

Gill, A. E. (1977). Coastally trapped waves in the atmosphere. Quart. J. Roy. Meteorol. Soc. 103, 431-440.

Gill, A. E. (1980). Some simple solutions for heat-induced tropical circulation. Quart J. Roy. Meteorol. Soc. 106, 447-462.

Kasahara, A., and A. P. Mizzi (1984). Preliminary evaluation of diabatic heating distribution from FGGE Level IIIb analysis data. Report No. 84-6. National Center for Atmospheric Research, Boulder, Colo., pp. 32.

Krishnamurti, T. N., and Y. Ramanathan (1982). Sensitivity of the monsoon onset to differential heating. J. Atmos. Sci. 39, 1290-1306.

Krishnamurti, T. N., and D. Subrahmanyam (1982). The 30 to 50 day mode at 850 mb during MONEX. J. Atmos. Sci. 39, 2088-2095.

Krishnamurti, T. N., P. K. Jayakumar, J. Sheng, N. Surgi, and A. Kumar (1984). Divergent circulations on the 30 to 50 day time scale. Dept. of Meteorology, Florida State University, Tallahassee, Fl., 20 pp.

Kuo, H. L., and Y. F. Qian (1981). Influence of the Tibetan Plateau on cumulative and diurnal changes of weather and climate in summer. Mon. Wea. Rev. 109, 2337-2356.

Kuo, H. L., and Y. F. Qian (1982). Numerical simulation of the development of mean monsoon circulation in July. Mon. Wea. Rev. 110, 1879-1897.

Lau, N.-C. (1984). The influences of orography on large-scale atmospheric flow simulated by a general circulation model. Geophysical Fluid Dynamics Laboratory, Princeton Univ., Princeton, N.J., 17 pp.

Lau, K.-M., and H. Lim (1984). ON the dynamics of equatorial forcing of climate teleconnections. J. Atmos. Sci. 41, 161-176.

Lim, H., and C.-P. Chang (1983). Dynamics of teleconnections and Walker circulations forced by equatorial heating. J. Atmos. Sci. 40, 1897-1915.

Lorenc, A. C. (1983). The evolution of planetary-scale 200 mb divergences during the FGGE year. Met O 20 Technical Note II/210, Meteorol. Office, Bracknell, Berkshire, U.K., 13 pp.

Lorenzo, D., and S.-J. Chen (1984). Genesis of vortex and shear line over the Qinghai-Tibetan Plateau--Numerical experiment. Presented at the Symposium on the Tibetan Plateau and Mountain Meteorology, Beijing, March 19-24, 1984.

Lubis, S. M., and T. Murakami (1984). Moisture budget during the 1978-1979 southern hemisphere summer monsoon. Submitted to J. Meteorol. Soc. Japan.

Manabe, S., and T. B. Terpstra (1974). The effects of mountains on the general circulation of the atmosphere as identified by numerical experiments. J. Atmos. Sci. 31, 3-42.

Masuda, K. (1984) Diabatic heating during the FGGE: A preliminary report. Submitted to J. Meteorol. Soc. Japan.

Murakami, M. (1983). Analysis of the deep convective activity over the western Pacific and Southeast Asia. Part I: Diurnal variation. _J. Meteorol. Soc. Japan 61_, 60-76.

Murakami, T. (1981a). Orographic influence of the Tibetan Plateau on the Asiatic winter monsoon circulation. Part I: Large-scale aspects. _J. Meteorol. Soc. Japan 59_, 40-65.

Murakami, T. (1981b). Orographic influence of the Tibetan Plateau on the Asiatic winter monsoon circulation. Part III: Short-period oscillations. _J. Meteorol. Soc. Japan 59_, 173-200.

Murakami, T., R. V. Godbole, and R. R. Kelker (1970). Numerical simulation of the monsoon along $80°E$. _Proc. Conf. Summer Monsoon Southeast Asia_, C. S. Ramage, ed., Norfolk, Navy Weather Research Facility, 39-51. (NTIS AD-876-677).

Murakami, T., and Y.-H. Ding (1982). Wind and temperature changes over Eurasian during the early summer of 1979. _J. Meteorol. Soc. Japan 60_, 183-196.

Murakami, T., and H. Nakamura (1983). Orographic effects on cold surges and lee-cyclogenesis as revealed by a numerical experiment. Part II: Transient aspects. _J. Meteorol. Soc. Japan 61_, 547-567.

Murakami, T., W.-G. Huang (1984). Orographic effects of the Tibetan Plateau on the rainfall variations over central China during the 1979 summer. Submitted to _J. Meteorol. Soc. Japan_.

Murakami, T., and T. Nakagawa (1984a). Tropical 40-50 day oscillations during the 1979 northern hemisphere summer. **Dept. of Meteorology, University of Hawaii, Honolulu, 27 pp.**

Murakami, T., and T. Nakagawa (1984b). Tropical 40-50 day oscillations during the transition from the southern to northern hemisphere summer monsoon. (In preparation).

Murakami, T., T. Nakagawa, and J. He (1984). On the 40-50 day oscillations during the 1979 northern hemisphere summer. Part I: Phase propagation. Submitted to _J. Meteorol. Soc. Japan_.

Nitta, T. (1983). Observational study of heat sources over the eastern Tibetan Plateau during the summer monsoon. _J. Meteorol. Soc. Japan 61_, 606-618.

Pasch, R. J. (1984). On the onset of the planetary-scale monsoon. _15th Conference on Hurricanes and Tropical Meteorology_, Amer. Meteorol. Soc., 367-369.

Shrestha, M. L., and T. Murakami (1984). Stratospheric 40-50 day oscillations during the 1979 northern hemisphere summer. (In preparation).

Tao, S., S. Luo, and H. Zhang (1984). A composite report on the QXPMEX in May-August 1979. Presented at the Symposium on the Tibetan Plateau and Mountain Meteorology, Beijing, March 19-24, 1984.

Webster, P. J. (1984). The relationship of monsoons to extratropical and tropical systems. _Monsoons_, J. S. Fein and P. L. Stephens, ed.

Webster, P. J., and L. C. Chou (1980). Seasonal structure of a simple monsoon system. _J. Atmos. Sci. 37_, 354-367.

13. MIDLATITUDE-TROPICAL INTERACTIONS DURING MONSOONS

Organizer	T. N. Krishnamurti
Session Chairman	John A. Young
Speaker	C.P. Chang
Rapporteurs	Takio Murakami
	T. N. Krishnamurti

156<

MIDLATITUDE TROPICAL INTERACTIONS DURING WINTER

C.-P. Chang
Naval Postgraduate School

ABSTRACT

Pre-FGGE and FGGE/MONEX data are used t.. identify short-term midlatitude tropical and longitudinal interactions during the winter monsoon. These interactions occur as cold surges, which develop over the East Asian continent and penetrate deep into the tropics with fast gravity-wave speed. The observed interactions that occur after a surge include cyclogenesis and enhanced convection in the equatorial region, feedback **from equatorial convection to midlatitude circulation systems, tropical east-west (Walker) circulations, and cross-equatorial influences.** These interactions are also studied theoretically by analytical solutions of linearized shallow water equations. Responses to transient forcing (monsoon surges) are mainly in Rossby and Kelvin modes. When the forcing time scale is short, significant gravity modes are also excited. The responses closely resemble observed winter monsoon flow. Responses to stationary forcing show that deep (barotropic) motions propagate energy away into high latitudes and that shallow (baroclinic) motions are trapped around the equator. While both Rossby and Kelvin modes are important, the former is always more dominant, even in the case of Walker-type circulations. It is shown that the barotropic teleconnection-type response to tropical sources found in previous numerical studies was due to the specified vertical wind shear and surface friction. Furthermore, comparison between the baroclinic stationary responses and the transient response suggests that monsoon surges play an important role in the maintenance of the mean tropical motions.

INTRODUCTION

During the northern winter, a strong baroclinic zone between the cold air mass over Siberia/northern China and the warm tropical air mass over the South China Sea/maritime continent manifests itself in the quasi-steady subtropical jetstreak over the East Asian coast. The passage of a deep upper trough in the midlatitudes often triggers intense baroclinic development causing the pressure gradient across the
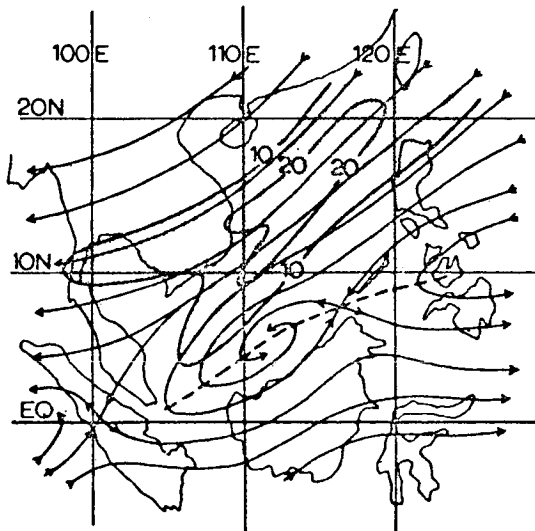
FIGURE 1 A schematic diagram of surface wind field during active
winter monsoon surge. The isotachs are in units of m/s and areas with
larger than 10 m/s wind speed are shaded. T⁻⁻ thick dashed-line
indicates the useful position of the quasi-permanent equatorial shear
line (trough) north of Borneo.

East China coast to tighten. This leads to cold air bursting
equatorward, and a cold surge is initiated.

In the midlatitudes, a surge arrives with a steep rise of surface
pressure, a sharp drop of temperature, and a strengthening of the
monsoon winds. Although the front associated with the surge cannot
normally be followed southward of about $20^\circ N$, the surge propagates
equatorward in a dramatic fashion. As a vigorous surge reaches the
South China coast, the monsoon winds freshen almost simultaneously
several hundred kilometers to the south, far beyond the region where
the winds could have pushed the front (Ramage, 1971; Chang et al.,
1979). A belt of strong northeasterly winds forms within 24 hours off
the South China coast and leads to a strengthening of a quasi-stationary
cyclonic circulation embedded in an eastnortheast-westsouthwest oriented
equatorial trough just north of the Borneo coast (Figure 1). This
region is within the maritime continent, where extensive cumulus
convection is often observed during winter. The convection supplies a
large amount of latent heat to the atmosphere and is believed to be one
of the most important energy sources that drive the winter general
circulation (Ramage, 1971).

In the first half of this paper, several observational studies will
be reviewed that portray the events of monsoonal surges and reveal a
wide range of planetary-scale interactions apparently triggered by an
intense surge. These synoptic time-scale interactions observed during
the winter monsoons pose interesting theoretical questions on the

dynamics involved. In the second half, some recent theories on atmospheric response to forcings and the dynamics of midlatitude tropical, interhemispheric, and equatorial east-west interactions will be described. A critical appraisal of these theories and a discussion of their implications will be given in relation to the observed phenomena of the East Asian winter monsoon.

OBSERVATIONAL STUDIES

Chang et al. (1979) described the interactions between cold surges and tropical convective systems. They noticed that cold surges over the South China Sea come in two phases--a rapid freshening of northeasterly winds followed after a few days by an incursion of cold air. Tropical convective systems, either the quasi-stationary system embedded within the equatorial trough or migratory systems moving in from the east, were observed to intensify on the arrival of the surge winds. This enhancement of convection continued until the arrival of cold air, which stabilizes the tropical atmosphere.

Chang et al. (1983) noticed a gravity-wave characteristic in the equatorward propagation of cold surges. Surface pressure, dew point, and wind data over the South China Sea and vicinity during Winter MONEX showed that although the surface front of a surge pushes southward at about 10 m/s, there is a much faster propagating signal of the cold surge that spread southward at about 40 m/s (Figure 2). This signal is not associated with significant synoptic events but is characterized by a sharp pressure rise and enhanced cross-isobaric winds. This cold surge signal is probably a gravity-wave mode motion and appears to offer a possible mechanism for the often mentioned rapid southward spread of surge winds over the South China Sea.

Chang and Lau (1980, 1982) examined the changes in the planetary-scale circulations following a strong surge and summarized their findings in the schematic diagram reproduced here in Figure 3. They noted that cold surges are often preceded by intense cooling over northern China. Such cooling appears to be due to the advection of polar air behind upper level troughs that move rapidly eastward and deepen over northern Japan. The sinking cold air over the continent accelerates the east Asian local Hadley cell. Almost simultaneously, the east Asian jetstream centered over Japan intensifies due to the Coriolis acceleration by the ageostrophic southerly flow of the enhanced Hadley circulation (Figure 3a, b). There is also a weakening of the west Asian jetstream after a small time lag, possibly due to an induced reverse local Hadley-type circulation as indicated in the figure.

As a surge arrives at the equatorial South China Sea, the existing synoptic-scale convective systems flare up and warm the tropical atmosphere by release of latent heat (Figure 3c). This enhanced tropical heat source not only helps maintain the enhanced Hadley cell but also produces upper level outflow that spreads east and west, driving two Walker circulations (Figure 3d).
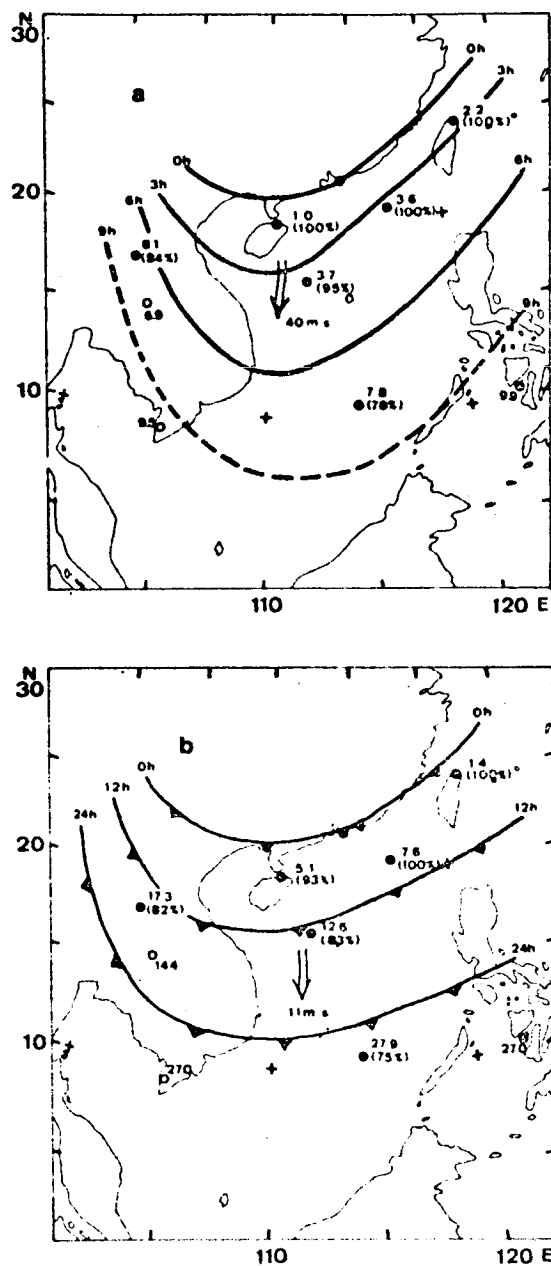
FIGURE 2 Schematic diagram for the progression of (a) the edge of the leading pressure-rise zone, and (b) a cold front, associated with a cold surge event.
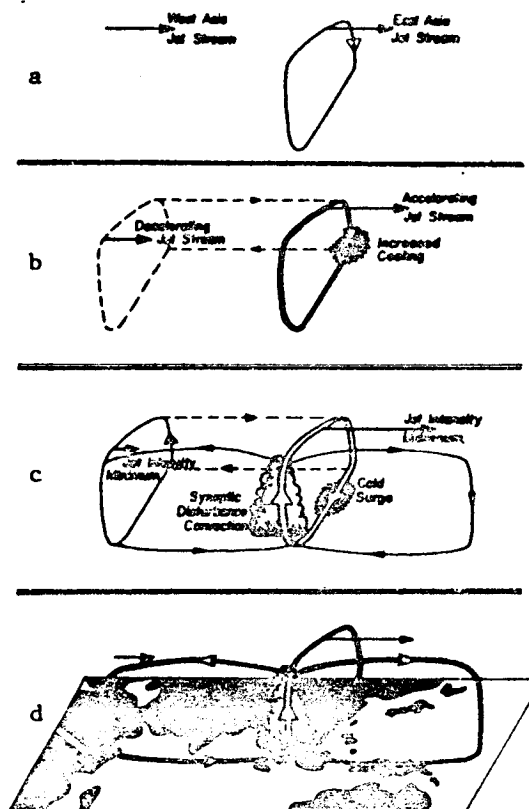
FIGURE 3 Schematic diagram showing the sequence of events before and after the cold surge in the South China Sea. See text for details.

ın this panoramic view, cold surges are seen to be an important link in a complicated chain of midlatitude tropics and equatorial east-west interactions. Through these interactions, the effect of an intense baroclinic development over the east Asian continent is spread deep across a wide equatorial belt ranging from East Africa to mid-Pacific Ocean.

The cold surge related midlatitude tropical interactions contain significant interannual variations. Lau et al. (1983) observed that during Winter MONEX, the area of maximum tropical convective activity occurred in the central Pacific rather than the maritime continent. These central Pacific convective systems responded to cold surges ˉs the maritime continent convective systems but at a 3 to 4 day lag. This shift in the maximum convection center might be related to the 1975-1976 El Niño/Southern Oscillation event, when the Southern Oscillation was still in the Low/Wet phase during the Winter MONEX period. This shift appeared to decrease the feedback effect from tropical convective systems and led to a weakened local Hadley

circulation. Although the maritime continent convective systems still responded to the cold surges, the presence of a stronger convection center in the central Pacific suppressed the Walker circulation connecting the two locations during a strong winter monsoon.

The enhancement of the central Pacific convective systems were also accompanied by the occurrence of a subtropical jetstream over Hawaii and a pronounced upper level trough-ridge system extending from the equatorial central Pacific to the west coast of North America. Thus a chain of midlatitude tropical teleconnections were initiated that resulted in increased downstream midlatitude eddy activities.

Williams (1981) described a case of the cross-equatorial influence of cold surges. About three days after a surge crossed the South China coast, he observed a slow pressure rise over western Indonesia. As if accelerated by the east-west pressure gradient, westerly winds strengthen, and convective systems were observed to develop in the southern equatorial region and drift eastward at a speed of 10 m/s. His observation was supported by Lau (1982), who found similar eastward moving systems in composite satellite imageries.

In an observational study of the Winter MONEX data, Davidson et al (1983) reported that the onset of the Australian monsoon is mostly due to southern hemisphere midlatitude baroclinic development. However, some of the data presented by them actually suggested a possible relation between the onset and the cold surges from the northern hemisphere (Figure 4). In Figure 4a, the strong northerly winds over the South China Sea show that a cold surge was in progress. Four days later, the surge winds penetrated deep into the southern hemisphere and the Australian monsoon sets in (Figure 4b). It may be noted that the extensive cloud system associated with the Australian monsoon onset was embedded within the belt of cross-equatorial flow. This observation and the overall flow pattern give one a strong impression that the Australian monsoon and the east Asian winter monsoon are not independent events. Cross-equatorial influences of monsoon surges have also been reported by Love (1984a,b) who observed tropical cyclogenesis in the southwestern Pacific following surges from the north.

Using the December 1983 to January 1984 data, Chang et al. (1984) studied the midlatitude tropical interactions by analyzing the correlation between tropical divergence and midlatitude zonal wind acceleration at 200 mb. Figure 5 shows that in the northern hemisphere the tropical upper divergence is positively correlated with the zonal acceleration at longitudes of major jet entrance and exit regions. Detailed examinations of individual synoptic events revealed that most episodes of increased tropical divergence are due to tropical convective activities, such as typhoons and cold surge-enhanced tropical convection. These episodes are correlated with the acceleration of the subtropic jet farther north and clearly indicate the immediate influence by tropical outflow to the acceleration of the midlatitude jet through the local meridional circulation. Figure 6 shows that the southern hemisphere correlation is much weaker, a reflection of the much weaker Hadley circulation of the southern hemisphere.
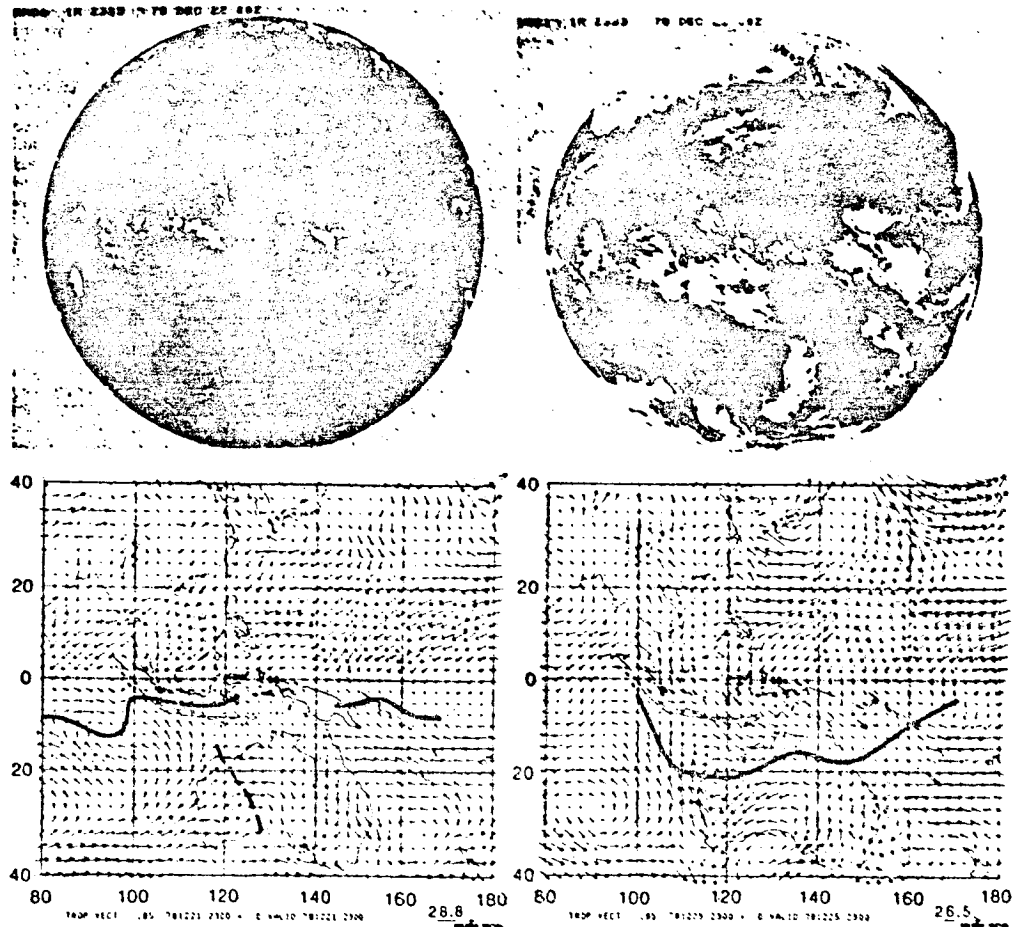
FIGURE 4 The 0000 GMT December 22 and 0000 GMT December 26, 1978,
(a) infrared satellite image, (b) analyzed wind field (m/s) at sigma =
0.95. (Full line denotes monsoon shear line. Dashed line denotes
subtropical trough.)

THEORETICAL STUDIES USING SHALLOW WATER EQUATIONS

Lim and Chang (1981, 1983) investigated the dynamics of the observed
midlatitude tropical, interhemispheric, and equatorial east-west
interactions described in the last section using equatorial β-plane
shallow water equation models. Although the equations seemingly
describe the barotropic motions of a fluid layer, they may also be
regarded as the horizontal structure equations for the various vertical
normal modes with the equivalent depth equal to the scale height (H).
Modes with $c = (gH)^{1/2} = 30$ to 50 m/s have a typical baroclinic
structure with one reversal of the flow fields at midtroposphere.
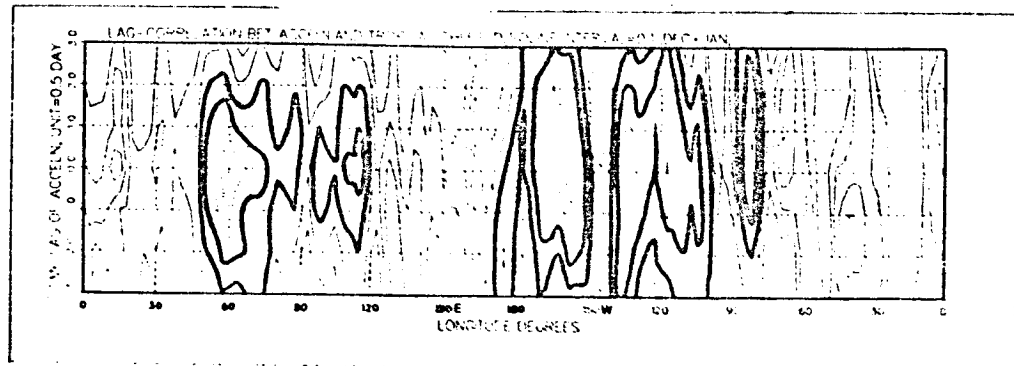
FIGURE 5 Time-lag correlation coefficients (r) between tropical X (averaged over $0°$ to $20°N$) and midlatitude jet acceleration, du/dt (averaged over $25°$ to $40°N$), at the same longitude for December 1983 to January 1984. Lag interval is 12 hours. Positive lag indicates midlatitude leading. Thick lines indicate r = 0.3 and 0.4, or significant levels 95 and 99 percent, respectively.

Atmospheric motions within this category include the Hadley and the **Walker circulations. Modes with c > 120 m/s have a barotropic** structure with the flow fields having the same sign throughout the troposphere. An example of such barotropic motions is the teleconnection patterns observed by Horel and Wallace (1981).

Tropical Response to Transient Midlatitude Pressure Surges

The response in the tropics to midlatitude pressure surges was studied by Lim and Chang (1981) by solving analytically an initial-value problem for the linearized shallow water equations with c = 30 m/s. A mass source with a Gaussian distribution with a half width equal to 1/5 of the earth's radius was specified to simulate the anticyclogenesis over the east Asian continent. The forcing rises rapidly from zero to maximum within 1 day and then decays slowly over 2 to 4 days.

A typical result is shown in Figure 7. The forcing initially generated gravity-wave type motions with strong northerly winds that surge rapidly equatorward. After crossing the equator, the surge winds turn both eastward and westward. The eastward branch consists of Kelvin wave, inertia-gravity wave, and mixed Rossby-gravity disturbances. These disturbances offer a possible interpretation of the eastward moving cloud patterns observed by Williams (1981) and Lau (1982).

The westward branch and the midlatitude response consist of mainly Rossby wave disturbances. These Rossby wave disturbances exhibit a midlatitude anticyclonic circulation that gradually develops a pronounced northeast-southwest tilt. To its south is a belt of strong northeasterly winds resembling the surge wind belt observed over the
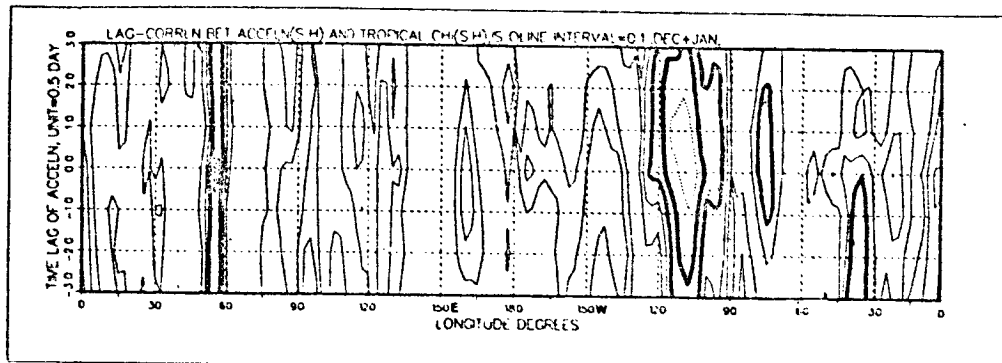
FIGURE 6 Same as Figure 5 except for the southern hemisphere.

South China Sea. Further south is found a stream of southwesterly
cross-equatorial flow and, in between this cross-equatorial flow and
the northeasterly surge wind belt, an equatorial trough (shear line)
extending east-northeastward from the equator to about 15°N. This
flow pattern bears a remarkable resemblance to the typical winter
monsoon flow over the South China Sea shown in Figure 1. The results
**suggest that the quasi-steady equatorial trough north of Borneo Island
is an inherent feature of the Rossby mode response dynamics,** which
could develop without any orographical forcing.

In the equatorial region around the longitude of the midlatitude
high, a general east-west pressure gradient is built up as observed by
Williams (1981) and Love (1984a, b). In the southern tropics, a
cyclonic vortex develops. This cross-equatorial effect may have some
relevance to Love's (1984a, b) observation of southern tropical
cyclogenesis after a winter cold surge.

Large-Scale Response to Steady-State Tropical Heating

Lim and Chang (1983) analyzed the characteristics of atmospheric
response to equatorial heating by solving shallow water equation models
using the method of expansion in terms of equatorial β-plane wave
modes (Matsuno, 1966). The scale height was chosen to give $c = 120$ m/s
for the study of teleconnection-type responses and to give $c = 40$ m/s
for the study of Walker circulation responses.

The solutions for $c = 120$ m/s are shown in Figure 8. The response
in westerly mean wind consists mainly of poleward propagating Rossby
modes resembling the teleconnection patterns. A ray tracing analysis
demonstrated the importance of the rotational and divergence effects on
the propagation of deep internal mode responses. An equatorial wave
mode analysis revealed the existence of equatorial "lee waves" when the
mean wind is weak to moderate westerly.

The solutions for $c = 40$ m/s are shown in Figure 9. The responses
take the form of diverging zonal wind bands resembling Walker
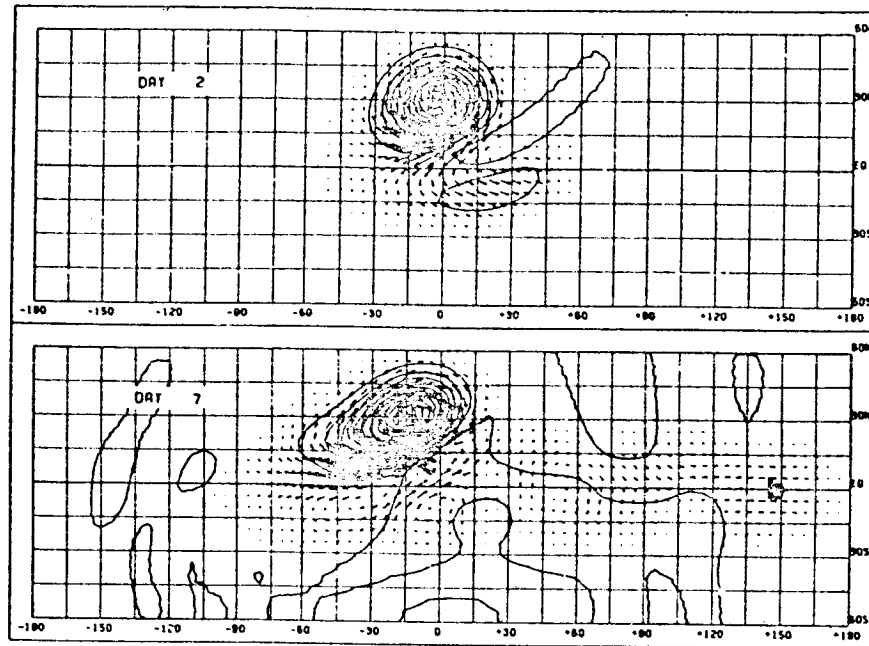
FIGURE 7 The velocity and geopotential fields for days 2 and 7 for a transient forcing.

circulations. In westerly mean winds, the Rossby mode lee waves break up the eastern wind band into segments of lengths comparable to those of observed Walker circulations. In all responses, including both branches of the Walker-like circulation, the Rossby modes were found to dominate over the Kelvin modes as the principal component.

A normal mode consideration showed that the barotropic type of response is difficult to excite by internal heating. Surface heating, which was neglected in most theoretical studies, is important for direct forcing of the barotropic responses. The presence of external mode responses in earlier model studies (e.g., Hoskins and Karoly, 1981; Webster, 1981) were attributed to the intervening effect of vertical wind shear, lower boundary layer, or differential damping at different model levels.

Further analysis using a two-level model demonstrated that surface effects (either direct heating or boundary layer pumping) is necessary to force an external-mode divergent flow. On the other hand, external-mode rotational flow may be forced by surface effects, vertical wind shear, or differential damping. In fact, the ratio of the rotational flow amplitudes of the external and the internal modes is found to be

$$[ik (U_3 - U_1) - (D_3 - D_1) - f\alpha] : [-ik (U_3 + U_1) - (D_3 + D_1) - f\alpha],$$
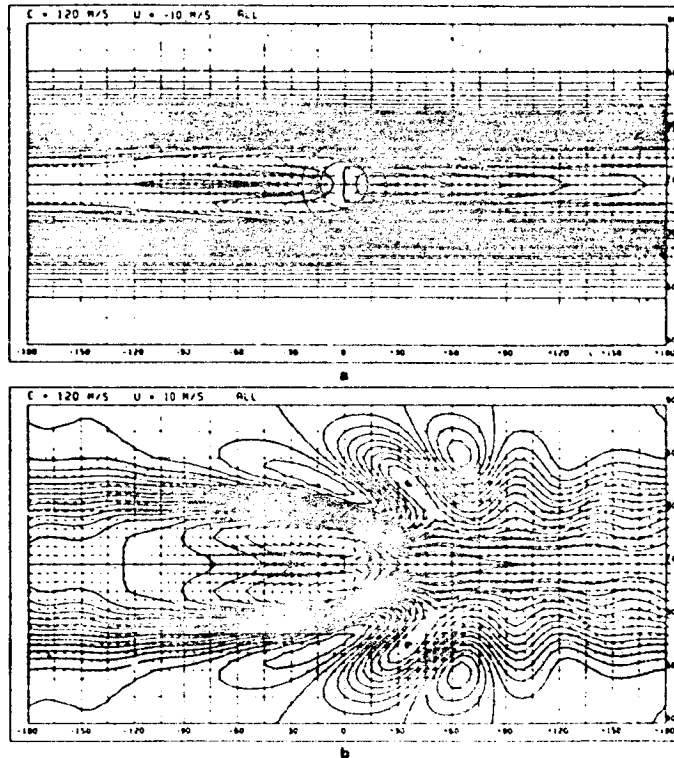
FIGURE 8 Steady-state geopotential and wind responses to an equatorial forcing with c = 120 m/s, for (a) U = 10 m/s, and (b) U = 10 m/s.

where U_1, U_3, D_1, and D_3 are the mean zonal winds and damping coefficients at the upper and the lower levels, and $(f a)^{-1}$ is the spin down time scale of the surface Ekman layer.

The two-level model solutions contain a term that represents the baroclinically unstable disturbances excited by the heating. This term has been suppressed in previous model studies and represents a downstream development of baroclinic waves from the heat source region. Considering a quasi-stationary heat source, such downstream developments will also contribute to the long-term mean flow fields.

When effects such as vertical wind shear are present, the concept of the vertical normal modes is mathematically no more valid but may still be very useful for description and analysis of atmospheric motions. An example of such application is the normal mode initialization used in numerical weather prediction. In this framework, effects such as wind shear will be comparable to those of the nonlinear advection terms in usual, linear analyses--they may in most circumstances be considered modifying effects that facilitate exchange of energy between the linear normal modes. This concept will be especially useful in discussions of the external mode response in strong vertical wind shear regions excited by heating embedded in weak vertical wind shear regions.

554
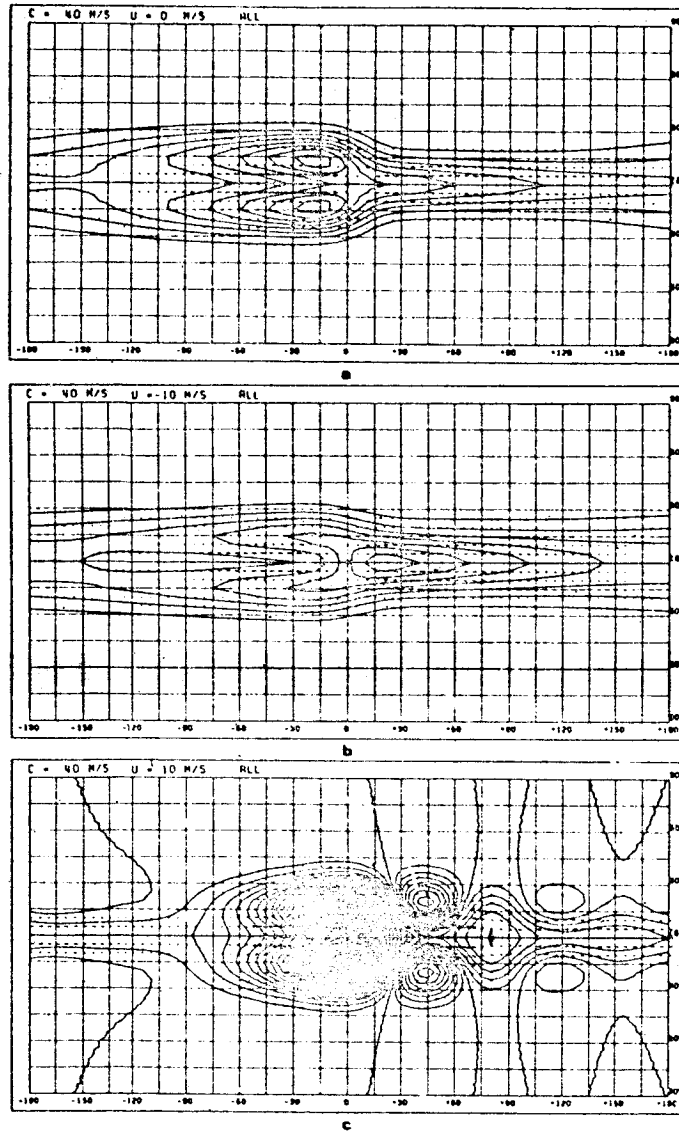
FIGURE 9 Same as Figure 8 except for c = 40 m/s and (a) U = 0, (b) =
-10 m/s, and (c) U = 10 m/s. Note that in (c) the equatorial westerly
wind to the east of the forcing is broken up by Rossby lee waves into a
short intense section followed by a region of weak disturbance and then
a long band of weak westerlies.

168<

Differences between Responses to Transient
and Steady-State Forcings

Lim and Chang (1983) noted that the tropical baroclinic response to stationary forcing in mean westerlies resembles the observed Walker circulations closer than that in mean easterlies does. They further noted that the transient nature of tropical heat sources may have the effect of making the atmospheric response to take on the "westerly mean wind" characteristics. For a single wave component, say $\zeta e^{i(\omega t - kx)}$, the linearized $d\zeta/dt$ term contains the following two terms: $i\omega\zeta - ikU\zeta$, where U is the mean zonal wind. If $U = 0$, for equatorial Rossby waves of Hermite mode n,

$$\omega \simeq - \frac{\beta k c^2}{(2n + 1)\, \beta c + k^2 c^2}$$

The transient nature of the forcing, represented by the i term, may be expected to endow the response with some characteristics similar to those of a steady-state forcing in a "westerly mean wind" with a speed of

$$U^* = \frac{\beta c^2}{(2n + 1)\, \beta c + k^2 c^2}$$

As U* varies with k and n, some qualitative differences in the transient and steady-state westerly mean wind response may be present. For instance, the shorter transient waves will experience smaller effective "mean wind," resulting in shorter wavelength "lee waves" for the transient response as compared to those of the westerly mean wind response. Since all the effective U* are within the range (0, c/(2n + 1)), we expect wave-like characteristics in the response to transient forcing similar to those in the westerly mean wind steady-state response.

To check the validity of such arguments, the responses to steady-state forcings and transient forcings were computed using a 20-level β-plane model. The equations were first separated into 20 vertical modes with the horizontal structure of each of these modes solved as in Lim and Chang (1981) for transient forcings, and as in Lim and Chang (1983) for steady-state forcing. The heat source specified is purely internal with a sin (πσ) vertical profile. In agreement with Lim and Chang (1983), this heat source excites mostly baroclinic responses.

Figures 10 and 11 show the steady-state responses to a forcing centered at 20°N and embedded in a constant mean zonal wind U = -10 m/s and U = 10 m/s, respectively. For U = -10 m/s (and also for U = 0, not shown), the ascending motion is concentrated around the region of heating with descending motions spreading over the remaining area of the globe. for U = 10 m/s, the response shows a complicated structure with the 500 mb omega showing a train of descending and ascending motion centers reflecting the presence of the Rossby lee waves (Lim and Chang, 1983).
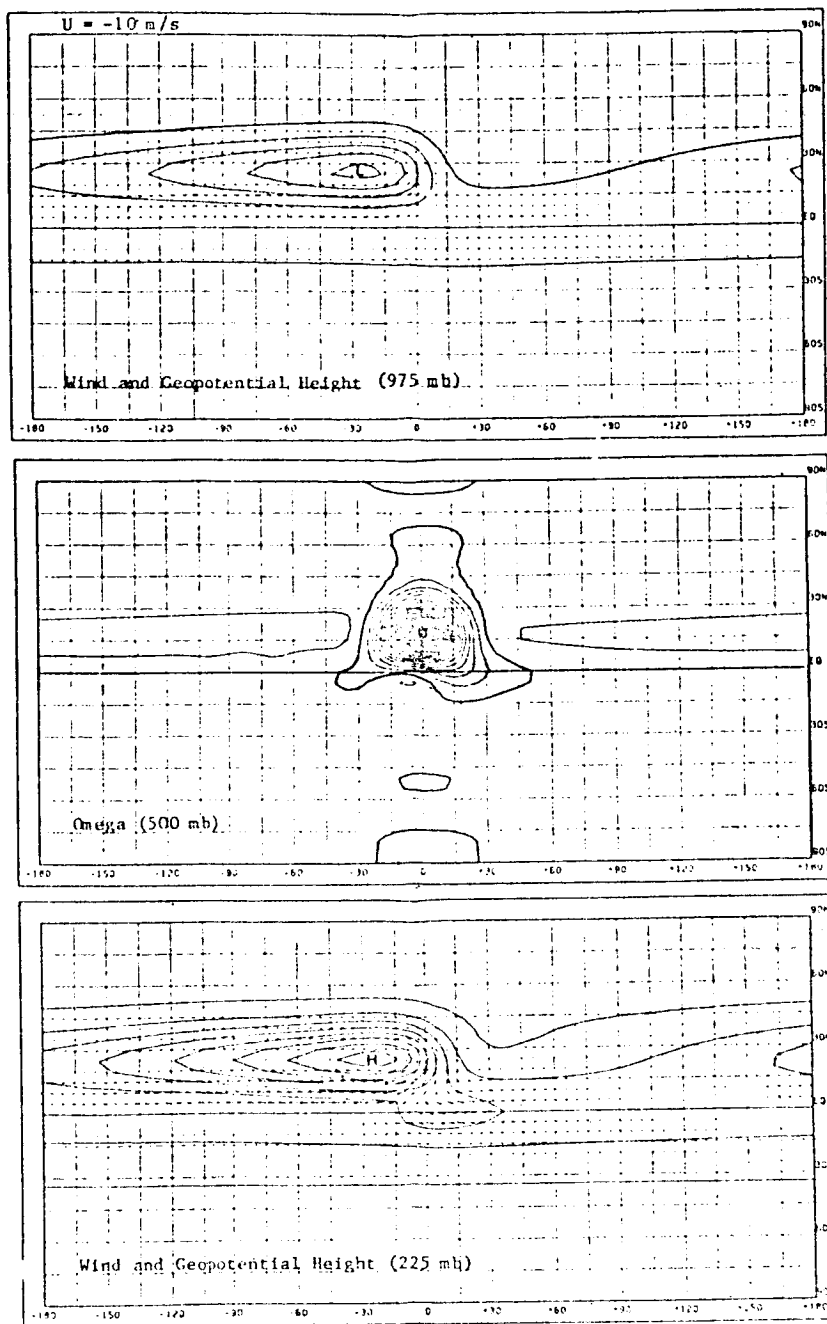
FIGURE 10   Steady-state response to a heat source centered at 20°N with U = -10 m/s.
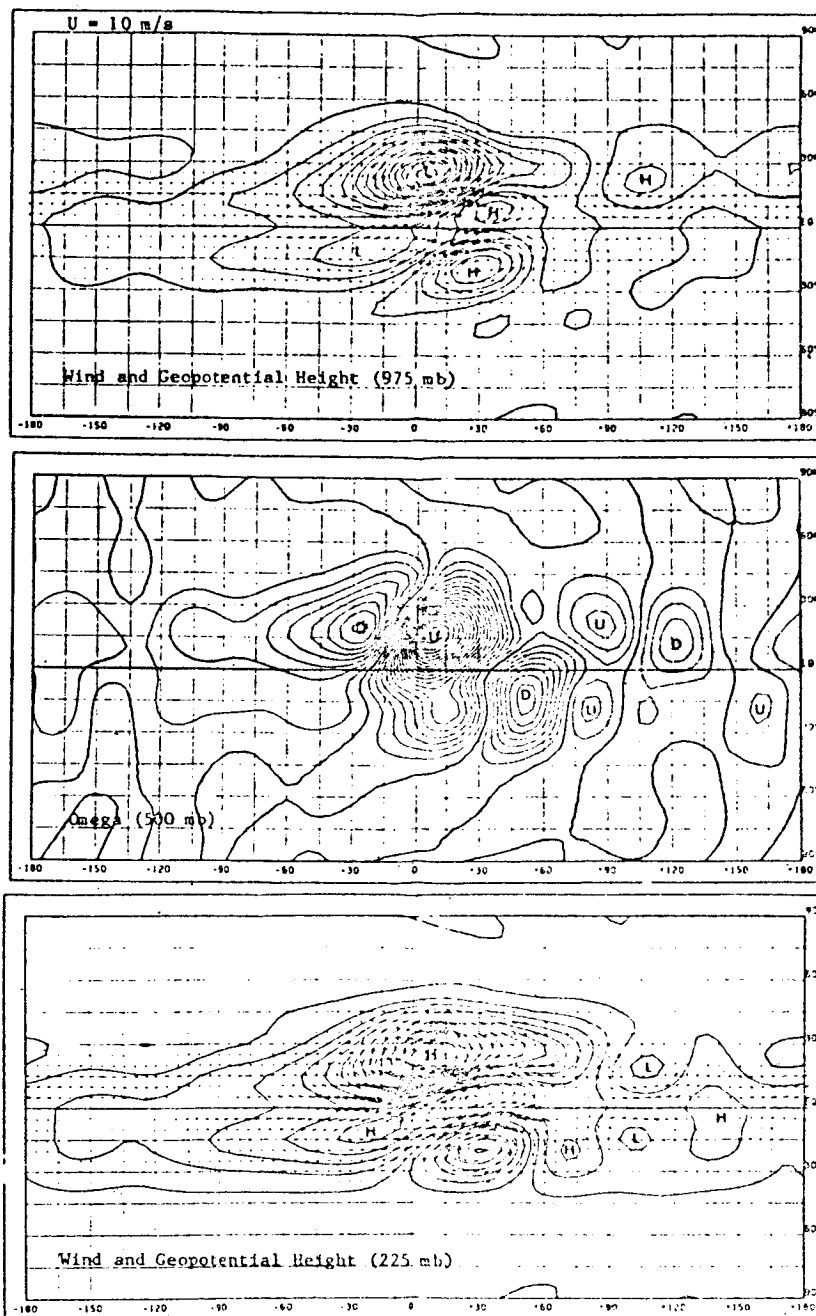
FIGURE 11 Steady-state response to a heat source centered at 20°N with U = 10 m/s.

558
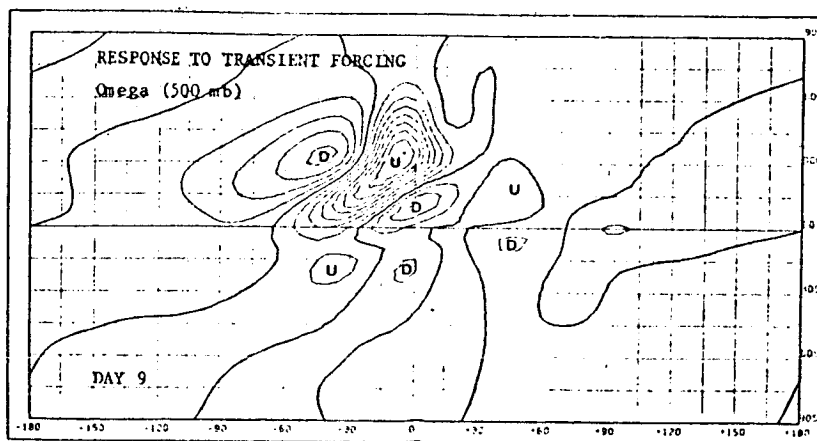
FIGURE 12   Day 9 omega field response to a transient forcing centered
at 27°N with U = 0.

The response to a transient forcing centered at 27°N is similar to
what was described in Lim and Change (1981). Figure 12 shows the 500
mb omega on Day 9 after the forcing was switched on. A comparison with
Figures 11 and 12 shows that the response to a transient forcing indeed
possesses pronounced "westerly mean wind" characteristics.

Since monsoon surges cause the tropical heat source to fluctuate in
time, the motions excited may be expected to have "westerly mean wind"
characteristics even though the organized cumulus convection may be in
an easterly mean wind. This possibility may have far-reaching
implications for the interpretation of tropical climatological mean
flow patterns.

REFERENCES

Chang, C.-P., E. Erickson, and K. M. Lau (1979). Northeasterly cold
    surges and near-equatorial disturbances over the Winter MONEX area
    during December 1974. Part I: Synoptic aspects. Mon. Wea. Rev.
    107, 812-829.
Chang, C.-P., and K. M. Lau (1980). Northeasterly cold surges and
    near-equatorial disturbances over the Winter MONEX area during
    December 1974. Part II: Planetary-scale aspects. Mon. Wea. Rev.
    108, 298-312.
Chang, C.-P., and K. M. Lau (1982). Short term planetary-scale
    interactions over the tropics and midlatitudes during northern
    winter. Part I: Contrast between active and inactive periods.
    Mon. Wea. Rev. 110, 933-946.
Chang, C.-P., K. G. Lum, and H. Lim (1984). Midlatitude tropical
    interactions during the 1983/1984 winter monsoon. (Manuscript in
    preparation).

Chang, C.-P., J. E. Millard, and G. T. J. Chen (1983). Gravitational character of cold surges during Winter MONEX. *Mon. Wea. Rev. 111*, 293-307.

Davidson, N. E., J. L. McBride, and B. J. McAvaney (1983). The onset of the Australian monsoon during Winter MONEX: Synoptic aspects. *Mon. Wea. Rev. 111*, 496-576.

Horel, J. D., and J. M. Wallace (1981). Planetary-scale atmospheric phenomena associated with the Southern Oscillation. *Mon. Wea. Rev. 109*, 813-829.

Hoskins, B. J., and D. J. Karoly (1981). The steady linear response of a spherical atmosphere to thermal and orographic forcing. *J. Atmos. Sci. 38*, 1179-1196.

Lau, K. M. (1982). Equatorial responses to northeasterly cold surges as inferred from cloud satellite imagery. *Mon. Wea. Rev. 110*, 1306-1313.

Lau, K. M., C.-P. Chang, and P. H. Chan (1983). Short-term planetary-scale interactions over the tropics and midlatitudes. Part II; Winter MONEX period. *Mon. Wea. Rev. 111*, 1372-1388.

Lim, H., and C.-P. Chang (1981). A theory for midlatitude forcing of tropical motions during winter monsoons. *J. Atmos. Sci. 38*, 2377-2392.

Lim, H., and C.-P. Chang (1983). Dynamics of the Walker circulation and teleconnection forced by equatorial heating. *J. Atmos. Sci. 40*, 1897-1915.

Love, G. (1984a). Cross-equatorial influence of winter hemisphere cold surges. *Mon. Wea. Rev. 112* (in press).

Love, G. (1984b). Cross-equatorial interactions during tropical cyclogenesis. *Mon. Wea. Rev. 112* (in press).

Matsuno, T. (1966). Quasi-geostrophic motions in the equatorial area. *J. Meteorol. Soc. Japan 44*, 25-43.

Ramage, C. S. (1971). *Monsoon Meteorology*. Academic Press, 296 pp.

Webster, P. J. (1981). Mechanisms determining the atmospheric response to sea-surface temperature anomalies. *J. Atmos. Sci. 38*, 554-571.

Williams, M. (1981). Interhemispheric interaction during Winter MONEX. *Proc. Int. Conf. on Early Results of FGGE and Large-Scale Aspects of Its Monsoon Experiments*, WMO, 10, 12-16.

14. STRATOSPHERE

Organizer	Eugenia Kalnay
Session Chairman	Eugenia Kalnay
Speaker	Carlos R. Mechoso
	Conway B. Leovy
Rapporteur	John H. E. Clark

174<

STRATOSPHERIC WARMINGS DURING THE WINTER OF 1979

Carlos R. Mechoso
University of California, Los Angeles

ABSTRACT

Some of the arguments crucial to our current understanding of
stratospheric warmings are recapitulated briefly. The circulation at
10 mb during the winter of 1979 is described. A review of numerical
forecasts of stratospheric warmings reveals that, in general, these
events are predictable from several days in advance. In some cases,
however, relatively small errors in the predicted tropospheric zonal
mean wind produce large differences in upward wave propagation and,
consequently, in the stratospheric forecast.

INTRODUCTION

A minor and a major stratospheric warmings occurred in the northern
hemisphere during the winter of 1979. In mid-January, the circumpolar
vortex typical of the wintertime circulation was displaced from the
polar position by a growing Aleutian High. The polar temperature
increased at 10 mb reaching a maximum around the end of January. The
above circulation changed dramatically toward the end of February, and
a sudden warming developed. The circulation after the sudden warming
consisted of an anticyclonic vortex over the polar region and two
well-separated cyclonic vortices.

In this paper, some of the theoretical and numerical studies that
have contributed to current understanding of the stratospheric warmings
are briefly reviewed. Successful numerical forecasts of the warmings
during the winter of 1979 are shown, the predictability of those events
is discussed, and the evolution of the sudden warming in one of the
forecasts is described.

REVIEW

Stratospheric warmings have motivated many studies and a substantial
number of review articles. This section touches lightly on the reviews
of Quiroz et al. (1975), Holton (1980), and McIntyre (1982).

175<

Major warmings are defined in Quiroz et al. (1975) as those events in which the poleward movement of planetary-scale thermal systems results in a reversal of the polar circulation at 10 mb. Minor warmings are those in which the polar warming is insufficient to reverse the circulation. Quiroz et al. (1975) indicate that there are strong upward fluxes of geopotential from the troposphere preceding the warming. They review numerical simulations of stratospheric warmings performed by several authors, particularly that by Matsuno (1971). Matsuno's conceptual model of the sudden warming is based on the decelerating effect on the mean flow by large amplitude, transient planetary waves propagating vertically from the troposphere. Such an effect becomes very rapid once a level where the flow reverses (critical level) appears. Matsuno performed calculations with a quasi-geostrophic model of the stratosphere, in which the initial flow and a forcing at the lower boundary consisting of a perturbation that rapidly amplifies and then sustains large amplitude are all prescribed. Those calculations succeeded in simulating several aspects of the sudden warmings.

Schoeberl (1978) identifies two types of planetary wave behavior before the onset of the warming. Type A is characterized by an intensification of wavenumber 2 about two weeks before the onset, followed by an amplification of wavenumber 1, and a subsequent weakening of wavenumber 2. Type B is characterized by a sustained amplification of wavenumber 1. He presents a record of northern hemisphere stratospheric warmings, describes their observed vertical structure, and summarizes diagnostic studies of their energetics. Schoeberl indicates that instability models tend to rule out barotropic or baroclinic instability as the principal mechanism for generation of sudden warmings, a statement that remains the consensus view. He extensively reviews critical level arguments, Matsuno's mechanistic model, and the results of Holton (1976). Holton performed simulations similar to Matsuno's, with a slightly different model. He found that the deceleration of the flow during the most rapid warming period results from slight imbalances between the effects of the mean meridional circulation and horizontal momentum flux convergence. Schoeberl describes the numerical forecast of a sudden warming by Miyakoda et al. (1970). Finally, he reviews studies of mechanisms for large amplification of planetary waves, since such amplification accompanies stratospheric warmings.

Holton (1980) recasts Matsuno's model in terms of potential vorticity flux. The transformed Eulerian mean zonal momentum equation (Andrews and McIntyre, 1976; Boyd, 1976; Edmon et al., 1980; Palmer, 1981) is given by

$$\partial_t \bar{u} - f\bar{v}^* - \bar{F} = \nabla \cdot F / (\rho_o a \cos\phi) \, , \tag{1}$$

$$\bar{v}^* = \bar{v} - \rho_o^{-1} \partial_z (\rho_o \overline{v'\theta'} / \partial_z \bar{\theta}) . \tag{2}$$

Here, u and v are the zonal and meridional components of the horizontal velocity, θ is the potential temperature, F is the sub-grid scale momentum source, ϕ is latitude, $z = -H\ell n \ (p/p_s)$ where H is the scale height and p_s is the surface pressure, $\rho_0(z) = \rho_s \exp(-z/H)$ where $_s$ is the surface air density, f is the Coriolis parameter, and a is the radius of the earth. Overbars represent zonal averages, and primes represent deviations from those averages. The Eliassen-Palm (E-P) flux vector is defined by

$$F = \rho_0 \ a\cos\phi \ (-\overline{u'v'}, \ f \ \overline{v'\theta'}/_{\partial z} \ \overline{\theta}). \tag{3}$$

The E-P flux vector represents the direction of Rossby wave propagation, and its divergence is related to the northward quasi-geostrophic potential vorticity flux. Holton indicates that in the case of a sudden warming, the forcing is primarily due to the nonzero potential vorticity flux ($\nabla.F \neq 0$) caused by wave transience. Hence, momentum and heat fluxes have to be considered combined in $\nabla.F$, rather than separately. Holton refers to the Lagrangian-mean theory of Andrews and McIntyre (1978). The Lagrangian-mean motion is the motion of the center of mass of a line of fluid parcels that would be along a latitude circle if unperturbed by waves. Finally, Holton discusses the Lagrangian-mean model of the sudden warming by Matsuno and Nakamura (1979). In this model, the deceleration of the mean flow is caused by the radiation stress divergence that, in the Lagrangian version of the momentum equation, replaces the eddy flux term in the Eulerian version (1).

McIntyre (1982) discusses the fact that large amplitude planetary waves are not always associated with stratospheric warmings. He indicates that for a major warming, the waves must be unusually well focused into the polar region. This implies a special configuration of the mean zonal flow. The event that occurred during January 1979 might have preconditioned the flow so that waves were focused into the polar cap region during the major warming that occurred in February. A theory for the propagation of unsteady planetary waves is needed to quantify such concepts as focusing. Butchart et al. (1982) argue that it is useful to use E-P flux and quasi-geostrophic refractive index squared Q_k as complementary diagnostics for wave, mean-flow interactions. Q_k for a wave with zonal wavenumber k is defined by

$$Q_k = a \ \partial_\phi \overline{q}/\overline{u} - k^2/\cos^2\phi - a^2 f^2/(4N^2 H^2), \tag{4}$$

where $\overline{q}$ is the zonally averaged potential vorticity, and N is the Brunt-Väisälä frequency. The divergence of the E-P flux represents the effects of the waves on the acceleration of the mean zonal flow, as indicated above. The refractive index squared, on the other hand, represents the effects of mean zonal flow on the propagation of a steady wave. Butchart et al. (1982) performed several numerical experiments with a mechanistic model forced at the lower boundary (8 km) by idealized stationary or progressive height fields . The

566

initial conditions were either zonally averaged climatological fields
or those observed on February 16. Only the experiment from the latter
initial conditions and with progressive forcing shows a reversal of the
mean zonal wind at high latitudes similar to that observed during the
February 1979 sudden warming (see Figure 1a). Butchart et al. showed
that higher (negative) values of the refractive index squared increase
(prevent) wave propagation even in unsteady cases. We shall return to
further work by McIntyre in Section 5.

THE CIRCULATION AT 10 MB DURING THE WINTER OF 1979

In this section, selected features of the circulation at 10 mb for the
period from January 12 to February 27 are presented. The dataset
consists of the FGGE Level IIIb analysis by the European Centre for
Medium Range Weather Forecasts (ECMWF).
   The time evolution of the zonal mean wind and temperature are shown
in Figures 1a and 1b, respectively. The amplitude of wavenumber 1 and
2 at 60°N at 10 and 500 mb are shown in Figures 1c and 1d,
respectively. Accelerations of the flow at very high latitudes and
decelerations at lower latitudes during the early part of the periods
were associated with an increase in polar temperatures, which reached a
maximum around January 25. This minor warming was accompanied by a
large amplification of wavenumber 1 throughout the troposphere and
stratosphere, as shown in Figures 1c and 1d. An acceleration of the
flow at high latitudes followed by a rapid deceleration toward the end
of the period were associated with a sudden warming in the polar
region. This was accompanied by a large amplification of wavenumber 2
throughout the troposphere and stratosphere.
   The zonal mean horizontal eddy momentum flux convergence and the
difference between the zonal mean flow acceleration and that flux
convergence are shown in Figures 2a and 2b, respectively. The most
important contributor to the residual shown in Figure 2b must be the
mean meridional circulation. Figures 1 and 2 show that, during the
sudden warming, wavenumber 2 amplified and the mean meridional
circulation had a decelerating effect on the flow slightly over-
compensating the accelerating effect of the eddies. Therefore the
sudden warming evolved as in the idealized model of Matsuno (1971),
modified by Holton (1976).
   Palmer (1981) found that the direction of the E-P flux in the
stratosphere changed several times during the sudden warming so that
deceleration was more (less) intense when the flux was poleward
(equatorward) and upward. Palmer and Hsu (1983) investigated the
mid-January transition from the typical wintertime circulation with a
circumpolar vortex to a pattern that consisted of a cyclonic vortex
with strong cross-polar flow and a well-defined Aleutian High. Smith
et al. (1984) showed that interactions between wavenumbers 1 and 2 were
important, particularly after both warming events.

(a)

(b)

(c)

(d)
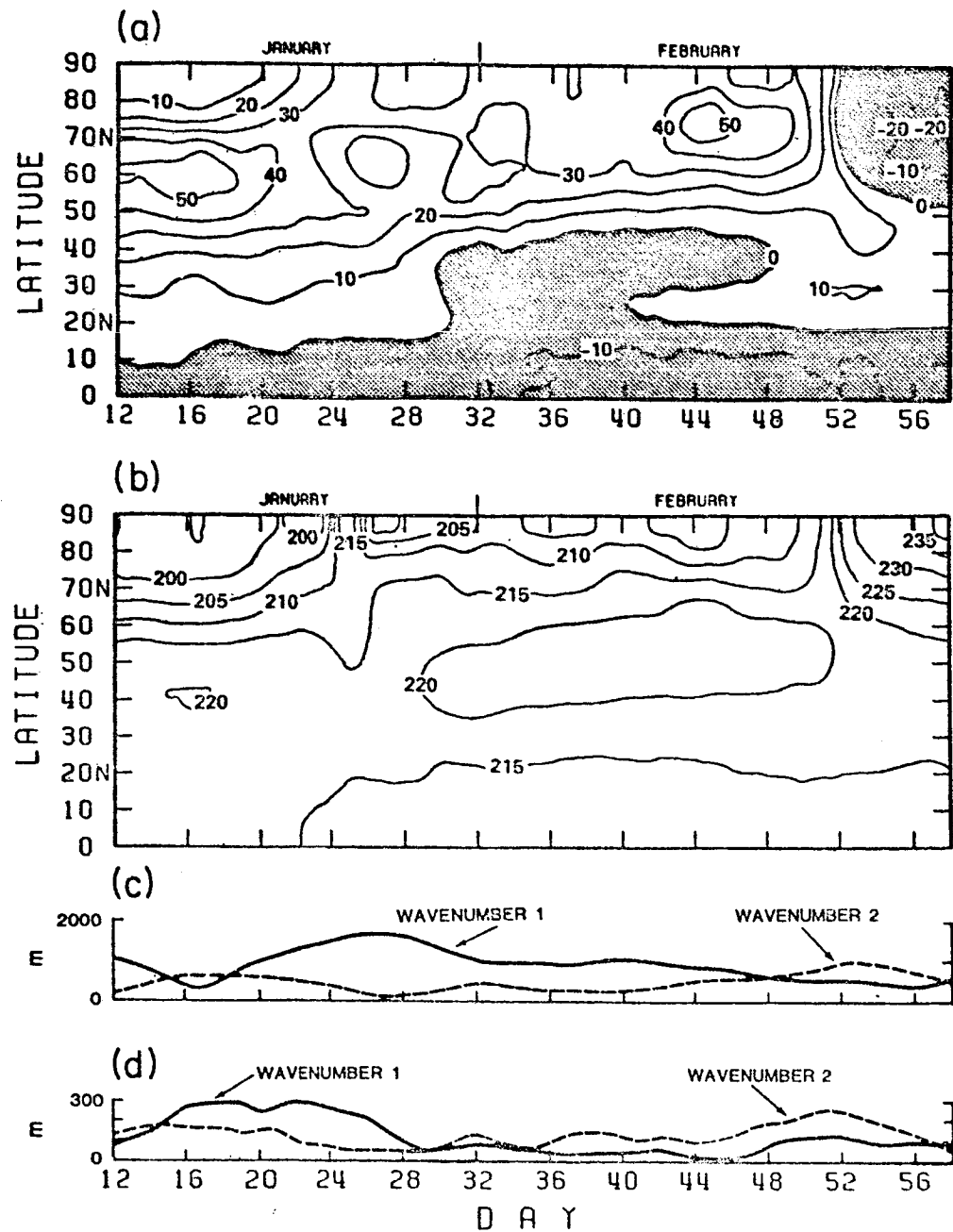
FIGURE 1   Zonal mean (a) wind (m/s), and (b) temperature (K) at 10 mb for the period January 12, 1979 to February 23, 1979. Amplitude of wavenumbers 1 and 2 in geopotential height at (c) 60°N, 10 mb, and (d) 60°N, 500 mb during the same period.
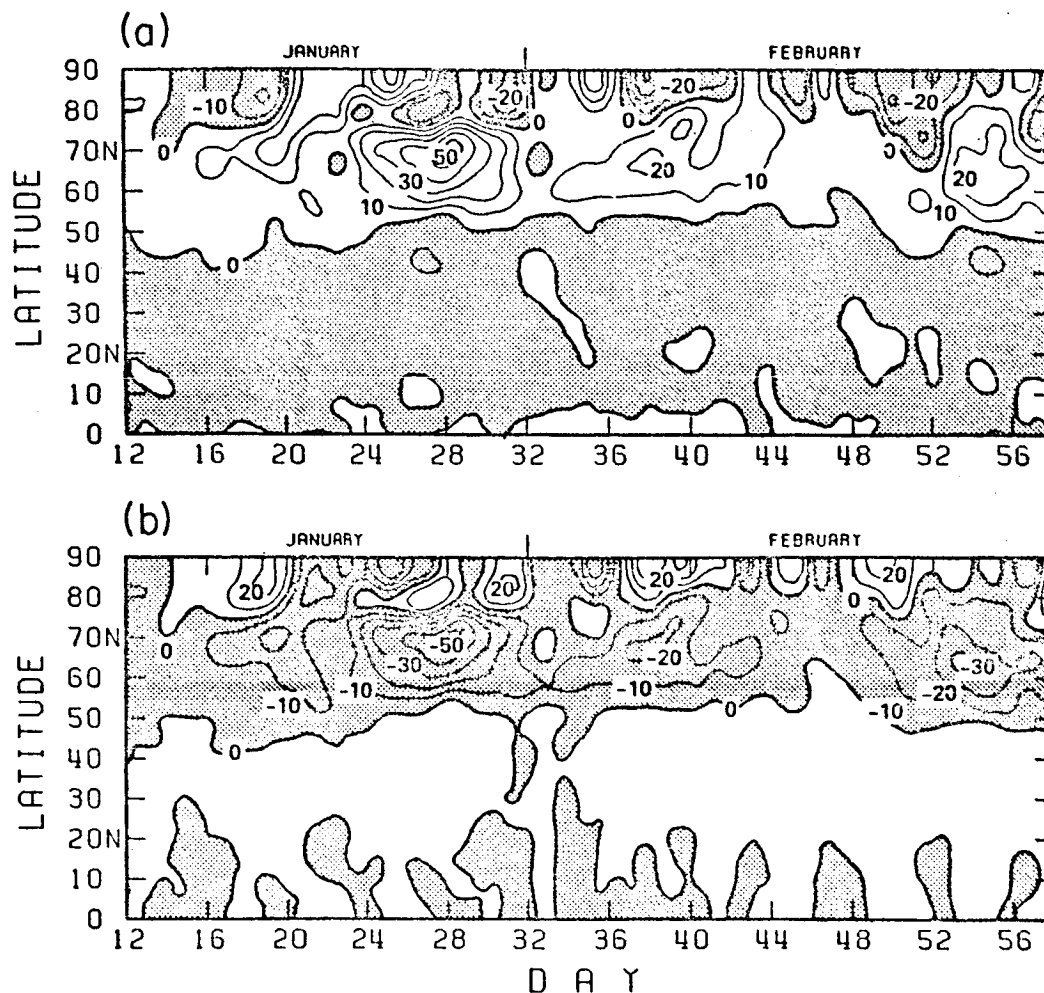
FIGURE 2 As in Figure 1, except for (a) the horizontal eddy momentum flux convergence (m/s day^{-1}), and (b) the difference between the flow acceleration and that flux convergence (m/s day^{-1}).

FORECASTS OF STRATOSPHERIC WARMINGS

There are very few successful forecasts of stratospheric sudden warmings reported in the literature. A forecast of the sudden warming that occurred in March 1965 was attempted by Miyakoda et al. (1970) with a 9-layer, N40 version of the model at the Geophysical Fluid Dynamics Laboratory. They could predict the tendency of the circumpolar vortex toward breakdown but could not capture the complete splitting of the vortex. More recently, forecasts of the stratospheric events during the winter of 1979, including the sudden warming, were performed

by Simmons and Strüfing (1983) with modified versions of the operational model at ECMWF. These versions have the same horizontal resolution (1.875° of latitude and longitude) and differ in the vertical resolution (14, 16, and 18 levels with the top at 50, 25, and 10 mb, respectively). They obtained very realistic forecasts of those events and concluded that substantial changes in the stratospheric circulation up to 10 mb may be predicted at least 10 days in advance.

In Mechoso et al. (1984), the predictability of the stratospheric warming events during the winter of 1979 is investigated by performing a series of 10-day forecasts. The low and high horizontal resolution (4° of latitude by 5° of longitude and 2.4° of latitude by 3° of longitude, respectively) versions of the 15-layer UCLA general circulation model that has the top at 1 mb are used. The initial conditions for the forecasts are obtained from the FGGE analysis by ECMWF below 10 mb, and from the analysis by the U.S. National Meteorological Center of height and temperature fields above that level. In this section, the major results obtained in that study are summarized.

January Forecasts

Results of forecasts from 0000 GMT January 16 and from 0000 GMT January 21 are presented. The geopotential fields at 10 mb for 0000 GMT January 16 and 26 and the 10-day low-resolution forecast from the first of those dates are shown in Figure 3. The observed flow on January 26 shows a pattern consisting of a cyclonic vortex with strong cross-polar flow and a well-defined Aleutian High. The corresponding forecast is very successful both in general patterns and details. The predicted zonal mean temperature at 10 mb (not shown) captures the polar warming that occurred during this forecast period.

The low-resolution and high-resolution forecasts from January 21 also predict the breakdown of the polar vortex and the associated increase in polar temperatures. It is concluded that the January warming event that was associated with a large amplification of wavenumber 1 is highly predictable.

February Forecasts

Results of forecasts from 0000 GMT February 15 and from 0000 GMT February 17 are presented. The geopotential fields at 10 mb for 0000 GMT February 17 and 27 and the 10-day high-resolution forecast from the first of those dates are shown in Figure 4. The observed flow on February 27 shows a well-established anticyclone in the polar region separating two cyclonic vortices. The corresponding high-resolution forecast is very accurate. The predicted zonal mean wind and temperature at 10 mb are shown in Figures 5a and 5b, respectively. They capture the observed wind reversal and polar warming that occurred during the forecast period.
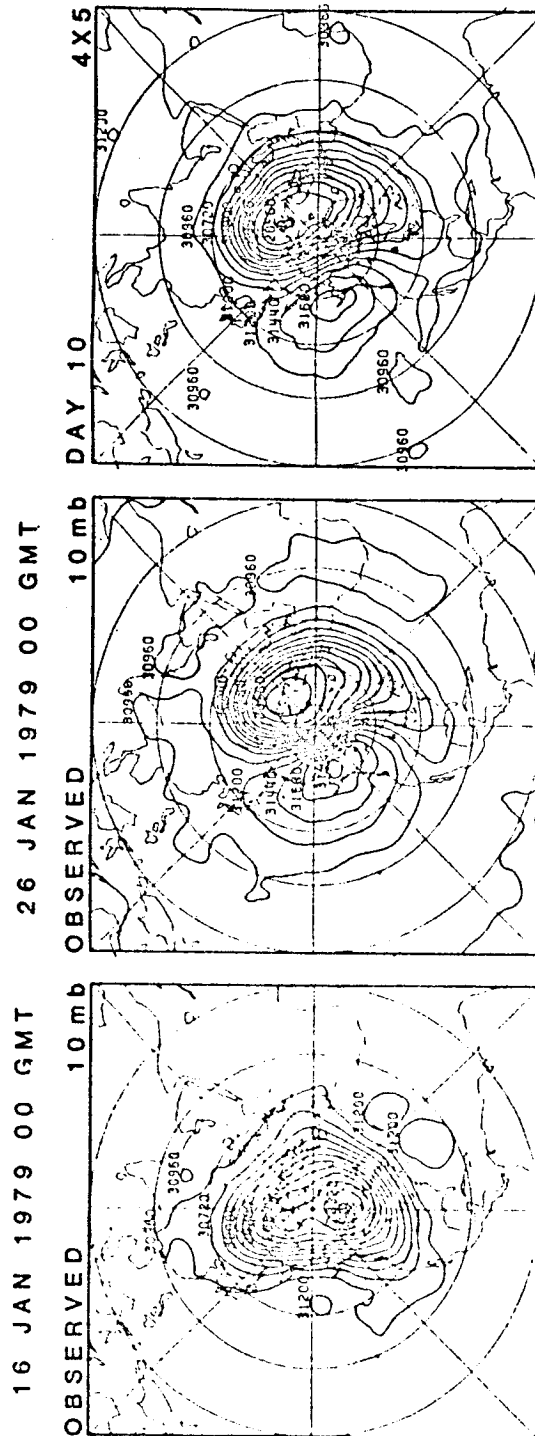
FIGURE 3 Low-resolution forecast from 0000 GMT January 16: initial geopotential field at 10 mb (left), observed field for 0000 GMT January 26 (center), and corresponding predicted field (right).

571

17 FEB 1979 00 GMT   27 FEB 1979 00 GMT

OBSERVED 10 mb   OBSERVED 10 mb   DAY 10   2.4 X 3
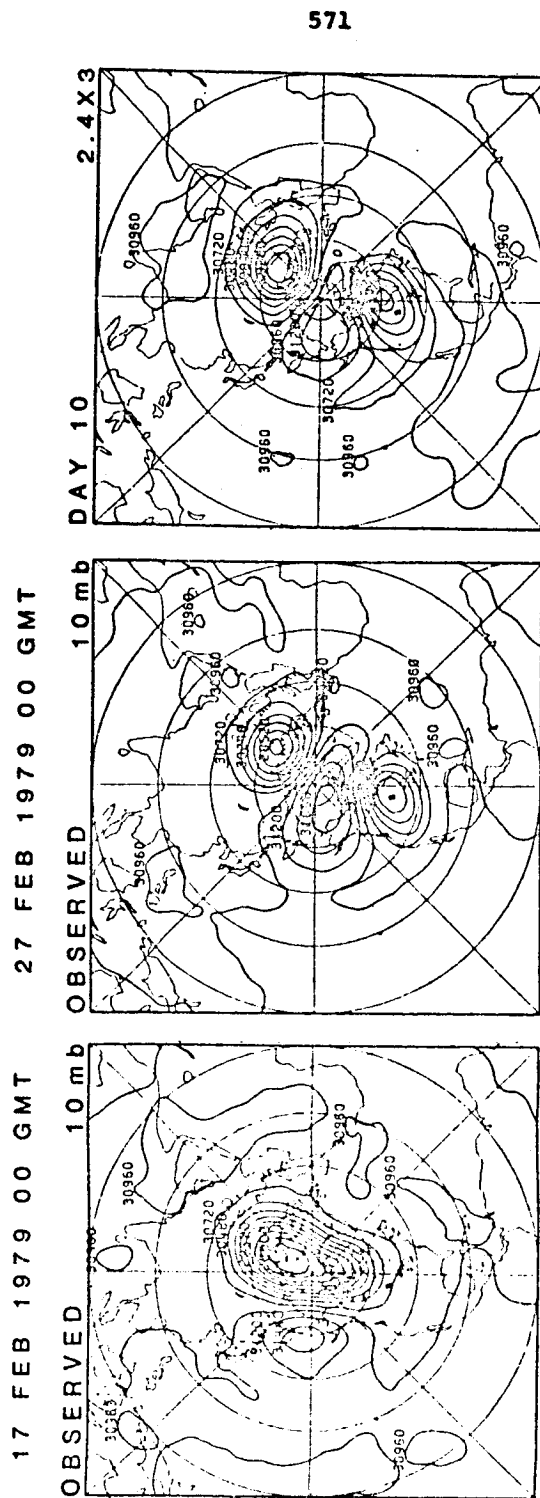
FIGURE 4 As in Figure 3, except for the high-resolution forecast from 0000 GMT February 17.
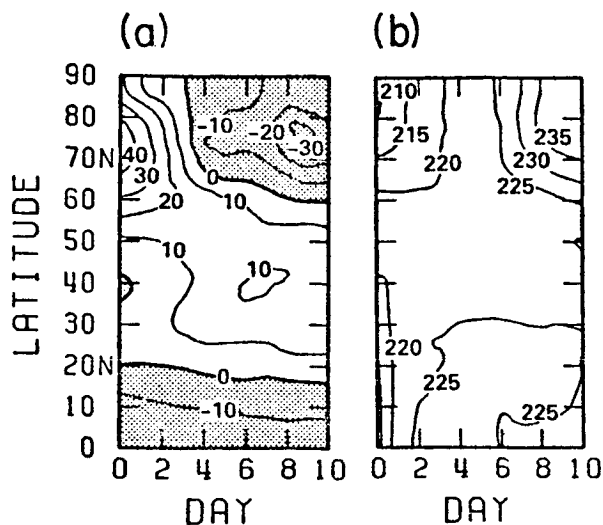
FIGURE 5 Zonal mean (a) wind (m/s) and (b) temperature (K) at 10 mb for the high-resolution forecast from 0000 GMT February 17.

Comparison of Figures 4 and 6 indicates that the 10-day low-resolution forecast from February 17 is not as accurate as the high-resolution forecast. The differences between the two forecasts with different horizontal resolutions become clearly noticeable during the second half of the period. Those differences are associated with a better prediction of the forcing from below with the high-resolution version for the second half of the forecast period. The low-resolution version does not underpredict the forcing near the surface, but the wave propagation into the stratosphere is poor because of errors in the predicted zonal mean wind. This point is illustrated in Figures 7a and 7b, which show the predicted refractive index squared, Q_2, averaged over days 7 and 8 for the low-resolution and high-resolution forecasts, respectively. The low-resolution forecast shows a region of negative values in the upper troposphere around $75^\circ N$, while the high-resolution forecast shows positive values there.

The geopotential fields at 10 mb for 0000 GMT February 15 and 25 and the 10-day high-resolution forecast from the first of those dates are shown in Figure 8. The high-resolution version predicts two distinct low centers, but fails in capturing the anticyclonic circulation in the polar region and the associated zonal mean wind reversal and sudden warming. Since the forecast from February 15 beyond day 2 is the forecast using the prediction for February 17 as the initial condition, the above difference in the two forecasts should be due to errors in the 2-day prediction from February 15. The influence of such errors in the propagation characteristics of the waves is illustrated in Figures 9a and 9b, which are combined plots of E-P flux and Q_2 for 0000 GMT February 17 and predicted from February 15, respectively. The predicted middle tropospheric region of positive Q_2 is significantly

573

27 FEB 1979 00 GMT
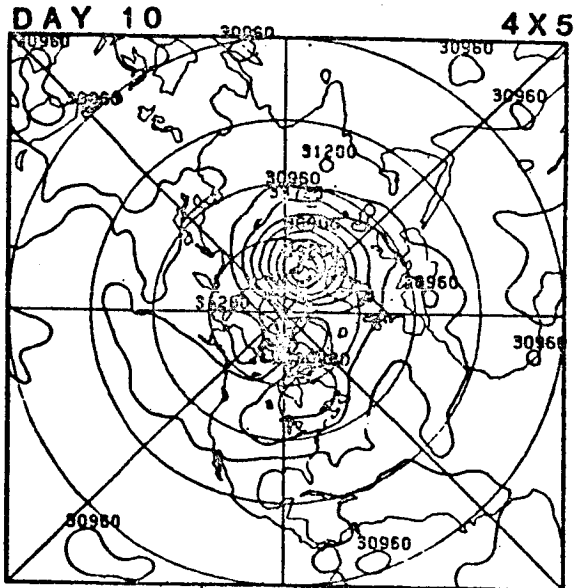
FIGURE 6 Low-resolution forecast from 0000 GMT February 17: Predicted geopotential field at 10 mb for 0000 GMT February 27.

narrower than observed, and consistently the E-P fluxes in that region are significantly weaker than observed. This error in the E-P flux implies differences in wave, mean-flow interactions between the two forecasts at this time. The different degree of success of the two forecasts indicates that those differences have a crucial impact on the subsequent evolution of the flow. Therefore it is concluded that the accuracy of stratospheric forecasts can be very sensitive to the accuracy in predicting the zonal mean tropospheric wind. In this way, the horizontal resolution of the model can significantly influence the quality of stratospheric forecasts.

EVOLUTION OF THE WARMING IN THE HIGH-RESOLUTION FORECAST FROM FEBRUARY 17

The thickness of the layer between 10 and 30 mb (expressed in K) for 0000 GMT February 27 is shown in Figure 10. The maximum temperature of the hemisphere is over the pole at that time, while there are local minima over North America and Europe. The thick dashed lines indicate the predicted trajectories of the temperature maxima, and the solid lines indicate those observed. The open (solid) circles show predicted (observed) locations at 1-day intervals. All trajectories show zonal movement followed by poleward migration. In both the forecast and the
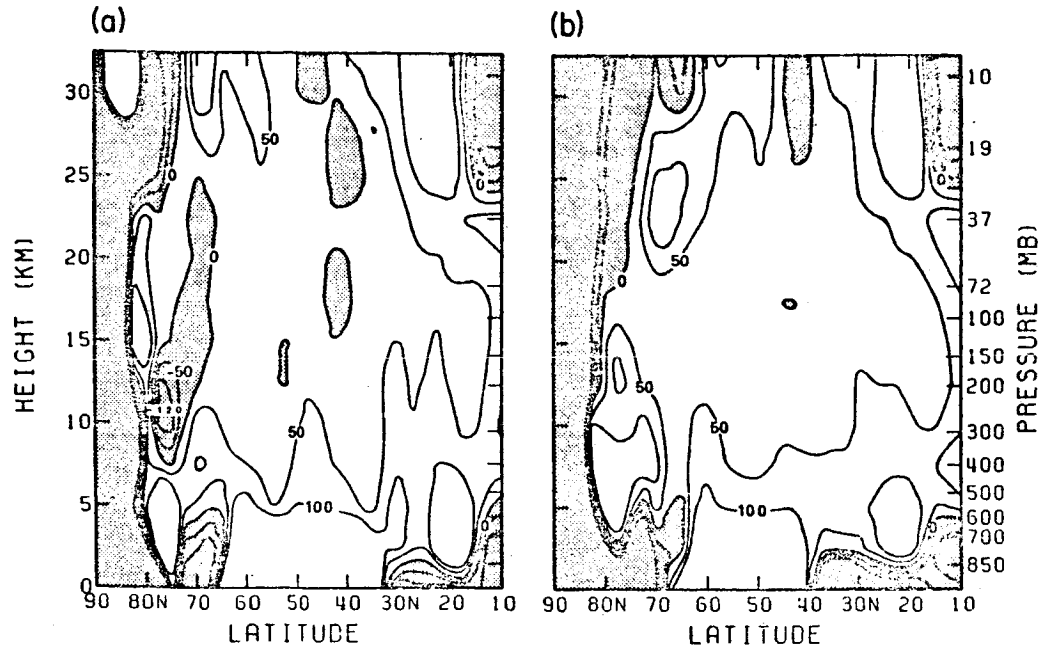
FIGURE 7   Refractive index squared Q_2 averaged over the period 0000
GMT February 23 to 0000 GMT February 25 with (a) the low-resolution
version, and (b) the high-resolution version. Values larger than 100
or smaller than -100 are not contoured.

observation, the stronger (weaker) maximum approaches the polar region
from the Siberian (Atlantic) sector. The maximum temperature in the
forecast does not get as close to the pole as the observed.

The sudden warming is an essentially adiabatic process. The
potential temperature of a fluid parcel θ, and its Ertel's potential
vorticity Q, defined by

$$Q = (2\vec{\Omega} + \nabla \times \vec{v}) \cdot \nabla\theta/\rho, \tag{5}$$

where Ω is the earth's angular velocity, do not change if the parcel moves
adiabatically. Therefore, a sequence of plots of these two quantities at
different stages during the warming might illustrate the behavior of the
fluid parcels (Dunkerton et al., 1981). The left column in Figure 11 is a
series of predicted Q maps on the 850 K isothermal surface in units of 10^{-4}
$K\ m^{-1}s^{-1}$. The projection is polar stereographic, and the southernmost
latitude circle is $20^{\circ}N$. The patterns are similar to the coarse-grain
estimates of Q obtained by McIntyre and Palmer (1983) from observed data.
The forecast for February 20 shows a region of high values with two relative
maxima. On February 22, that region has split into two subregions. On
February 24, one of the subregions is diffusing. On February 26, that
subregion is very elongated to the west, while the other is still sharply

FIGURE 8   As in Figure 4, except for the forecast from February 15.
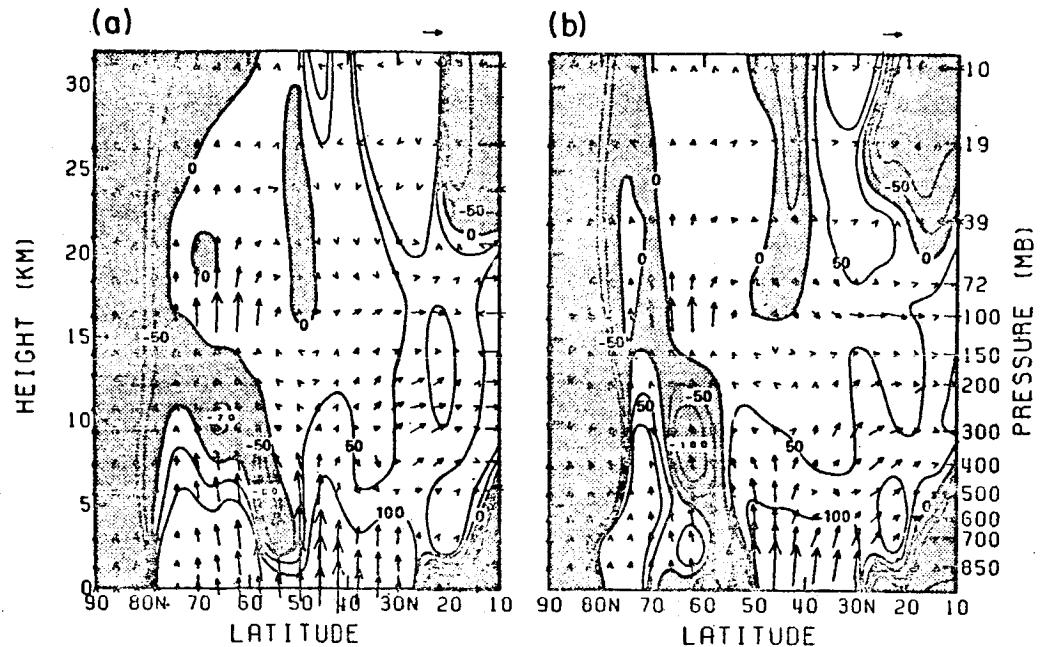
FIGURE 9 E-P fluxes (reference arrow: 10^{-16} kg m/s below 100 mb and 10^{-15} kg m/s above 100 mb) and refractive index squared Q_2 for (a) 0000 GMT February 17, and (b) forecast from February 15 with the high resolution version. Values larger than 100 or smaller than -100 are not contoured.

defined. The low Q region that is on the Aleutian area on February 22 is in a polar position on February 26. The right column in Figure 11 is a three-dimensional plot of the 850 K surface in which pressure (increasing upward from 6.7 mb) is the vertical coordinate. Regions where Q is less than 4 are lightly shaded, while regions where Q is larger than 6 are heavily shaded. The polar warming and the sinking of parcels in the polar region are clearly seen.

McIntyre and Palmer (1983) have indicated that Q maps such as these might make visible the "breaking" of planetary Rossby waves that might be characteristic of the circumstances leading to major stratospheric warmings. Further, they have suggested that the area of the main vortex might be found to decrease systematically during the buildup to a major warming.

SUMMARY

The availability of the FGGE datasets for the stratospheric warmings that occurred during the First Special Observing Period have stimulated research on such phenomena. There are also, for the first time,
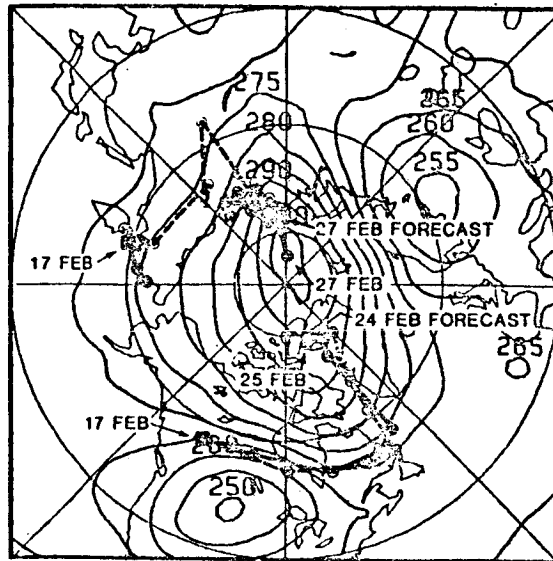
FIGURE 10 Contour plot of the observed 10 to 30 mb thickness (K) for
0000 GMT February 17. Thick solid (dashed) lines indicate observed
(predicted) trajectories of temperature maxima. Solid and open circles
indicate 1-day intervals.

dynamically consistent datasets obtained from successful forecasts of
the warming events with high-resolution numerical models. Diagnostic
techniques suggested by a growing body of theory on the subject have
been used by several authors to describe in detail the evolution of the
warming process, and the effects of the eddies (mean-flow) on the
mean-flow (eddies).

All the evidence seems to confirm that wave, mean-flow interactions
perform the major role in the generation of sudden stratospheric
warmings. The difficulty remains, however, in the prediction of a
warming event. It has been found that forecasts of the warmings can be
very sensitive to details in the initial conditions. The current
theory on wave, mean-flow interactions cannot fully explain such a
sensitivity.

ACKNOWLEDGMENTS
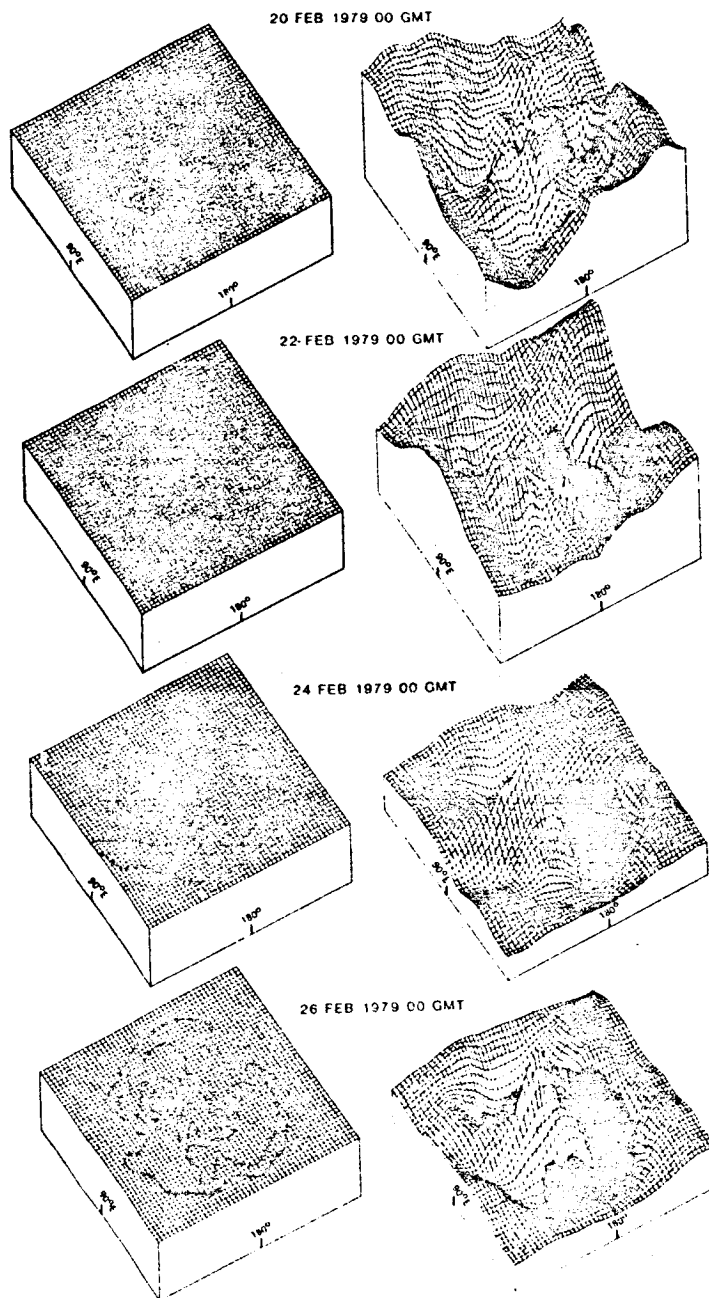
FIGURE 11 Ertel's potential vorticity on the 850 K isothermal surface in units of 10^{-4} K m^{-1} s^{-1}. The vertical coordinate for the three-dimensional plots is pressure, increasing upward from 6.7 mb.

REFERENCES

Andrews, D. G., and M. E. McIntyre (1978). An exact theory of nonlinear waves on a Lagrangian-mean flow. J. Fluid Mech. 89, 609-646.

Andrews, D. G., and M. E. McIntyre (1976). Planetary waves in horizontal and vertical shear: The generalized Eliassen-Palm relation and the mean zonal acceleration. J. Atmos. Sci. 33, 2031-2048.

Boyd, J. P. (1976). The noninteraction of waves with the zonally averaged flow on a spherical earth and the interrelationships of eddy fluxes of energy, heat and momentum. J. Atmos. Sci. 33, 2285-2291.

Butchart, N., S. A. Clough, T. N. Palmer, and P. J. Trevelyan (1982). Simulations of an observed stratospheric warming with quasigeostrophic refractive index as a model diagnostic. Quart. J. Roy. Meteorol. Soc. 108, 475-502.

Dunkerton, T., C.-P. F. Hsu, and M. E. McIntyre (1981). Some Eulerian and Lagrangian diagnostics for a model stratospheric warmings. J. Atmos. Sci. 38, 819-843.

Edmon, H. J., Jr., B. J. Hoskins, and M. E. McIntyre (1980). Eliassen Palm cross sections for the troposphere. J. Atmos. Sci. 37, 2600-2616.

Holton, J. R. (1976). A semi-spectral numerical model for wave-mean flow interactions in the stratosphere: Application to sudden stratospheric warmings. J. Atmos. Sci. 33, 1639-1649.

Holton, J. R. (1980). The dynamics of sudden stratospheric warmings. Ann. Rev. Earth Planet. Sci. 8, 169-190.

Matsuno, T. (1971). A dynamic model of the stratospheric sudden warming. J. Atmos. Sci. 28, 1479-1494.

Matsuno, T., and K. Nakamura (1979). The Eulerian and Lagrangian-mean meridional circulations in the stratosphere at the time of a sudden warming. J. Atmos. Sci 36, 640-654.

McIntyre, M. E. (1982). How well do we understand the dynamics of stratospheric warmings. J. Meteorol. Soc. Japan 60, 37-65.

McIntyre, M. E., and T. N. Palmer (1983). Breaking planetary waves in the stratosphere. Nature 305, 593-600.

Mechoso, C. R., K. Yamazaki, A. Kitoh, and A. Arakawa (1984). Numerical forecasts of stratospheric warming events during the winter of 1979. Submitted to Mon. Weather Rev.

Miyakoda, K., R. F. Strickler, and G. D. Hembree (1970). Numerical simulation of the breakdown of a polar-night vortex in the stratosphere. J. Atmos. Sci. 27, 139-154.

Palmer, T. N. (1981). Diagnostic study of a wavenumber-2 stratospheric sudden warming in a transformed Eulerian-mean formalism. J. Atmos. Sci. 38, 844-855.

Palmer, T. N., and C.-P. F. Hsu (1983). Stratospheric sudden coolings and the role of nonlinear wave interactions in preconditioning the circumpolar flow. J. Atmos. Sci. 40, 909-928.

Quiroz, R. S., A. J. Miller, and R. M. Nagatani (1975). A comparison of observed and simulated properties of sudden stratospheric warmings. J. Atmos. Sci. 32, 1723-1736.

Schoeberl, M. R. (1978). Stratospheric warmings: Observations and theory. Rev. Geophys. Space Phys. 16, 521-538.

Simmons, A. J., and R. Strufing (1983). Numerical forecasts of stratospheric warming events using a model with a hybrid vertical coordinate. Quart. J. Roy. Meteorol. Soc. 109, 81-111.

Smith, A. K., J. C. Gille, and L. V. Lyjak (1984). Wave-wave interactions in the stratosphere: Observations during quiet and active wintertime periods. J. Atmos. Sci. 41, 363-373.

DYNAMICAL PHENOMENA IN THE EQUATORIAL MIDDLE ATMOSPHERE DURING NORTHERN WINTER 1978-1979

Conway B. Leovy and Matthew H. Hitchman
University of Washington

ABSTRACT

Data from the Limb Infrared Monitor of the Stratosphere (LIMS) on the Nimbus-7 spacecraft have been used to delineate the temperature and zonal wind structure of the equatorial stratosphere and lower mesosphere during the period October 25, 1978 to May 28, 1979. Interactions between the descending westerly shear zone of the semiannual oscillation and upward propagating Kelvin waves are described. Inertial instability may be influencing the zonal wind in midwinter.

INTRODUCTION

The middle atmosphere was exceptionally well observed by satellite sensors during the winter of 1978-1979. For this reason and because of the occurrence of an interesting stratospheric warming episode, this particular winter has probably been more extensively studied than any other.

The Limb Infrared Monitor of the Stratosphere (LIMS) was one of the satellite instruments that obtained infrared radiance data during the period October 25, 1978 through May 28, 1979 (Gille and Russell, 1984). Because of the relatively high vertical resolution (2 to 4 km) and coincident retrievals of temperature, ozone, water vapor, nitric acid vapor, and nitrogen dioxide in the altitude range 15 to 60 km, these data have been particularly useful. In this paper, findings based on LIMS measurements in the area of equatorial dynamics will be reviewed.

EQUATORIAL MEAN ZONAL WINDS

An example of zonal mean winds derived from LIMS temperature retrievals is shown in Figure 1. These winds were obtained by using the gradient wind approximation with geopotential tied onto National Meteorological Center (NMC) geopotential height at 100 mb. Temperature and geopotential height were obtained at 4° latitude intervals, and

582
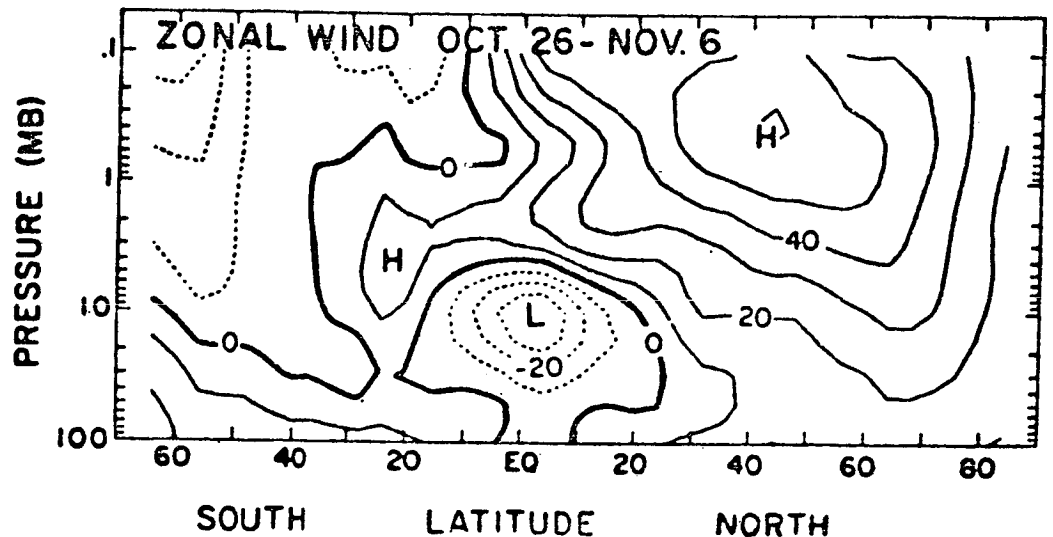
FIGURE 1   Zonally averaged zonal wind derived from LIMS (units = m/s).

winds, derived by finite differencing the geopotential heights, were
smoothed in the latitude range 16°S to 16°N with a 1-2-1 running
mean filter.

Outside the equatorial zone, these winds are in good agreement with
those derived from nadir viewing satellite radiance sensors, but it has
not been possible to derive gradient winds in the equatorial zone from
nadir viewing sensor data. There is also good agreement between LIMS
and rocketsonde zonal wind measurements at all latitudes. In
particular, comparisons with rocketsonde winds at Kwajalein (8.7°N),
Fort Sherman (9.3°N), and Ascension Island (8.0°S) have been used
to validate the equatorial zonal wind structure derived from the LIMS
data. An example of a comparison between time-averaged LIMS zonal wind
and rocketsonde zonal winds at Kwajalein is shown in Figure 2. Note
the good agreement between LIMS and the rocketsondes in depicting the
shear zones between 10 and 60 mb, 3 and 10 mb, and 0.2 and 0.6 mb.

During the period October 26 to November 6, there was an intense
equatorially centered easterly jet near the 10 mb level associated with
the easterly phase of the quasi-biennial oscillation (QBO). Higher up,
near the 0.5 mb level, a tongue of easterlies or weak westerlies
extended across the equator. Easterly flow in this tongue intensified
from late October until early January. The thermal structure
associated with these two wind field features consisted of a series of
warm and cool anomalies: warm in regions of westerly shear and cool in
regions of easterly shear. Accurate depiction of such features from
radiance measurements requires the high vertical resolution of a limb
scanning instrument.

Figure 3 is a time-height cross-section of zonally averaged wind
over the latitude interval 8°S to 8°N. The region near and just
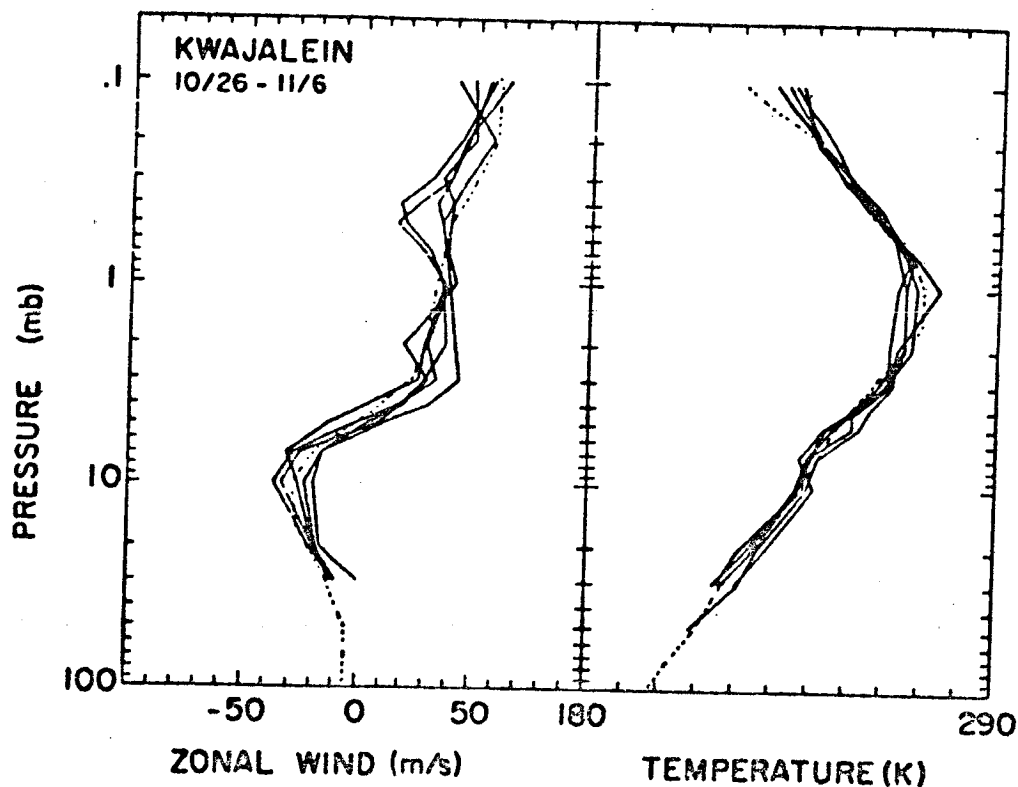
FIGURE 2 LIMS zonal wind and temperature profiles at Kwajalein averaged over the period Octobver 26 to November 6, 1979 (dashed curves) compared with individual rocketsonde ascents (solid curves).

below 10 mb was occupied by slowly descending QBO easterlies throughout the period, but above 10 mb the structure was dominated by the descending semiannual oscillation (SAO). The northward incursion of easterly winds that appeared as a weak feature near 0.5 mb in Figure 1 reached maximum intensity near 0.3 mb in late December. This intensification was followed by a rapid transition to westerlies above the 0.3 level followed by steady descent of the shear zone separating the easterlies from overlying westerlies. The general structure and phasing of these features is consistent with previous depictions of the SAO based on rocketsonde observations (Hirota, 1978, 1979), but the features in Figure 3 are generally stronger, particularly the easterly and westerly wind maxima above 1 mb in December and January.

KELVIN WAVES

The LIMS data also show temperature structure associated with equatorial Kelvin waves. Properties of these waves during January to

584
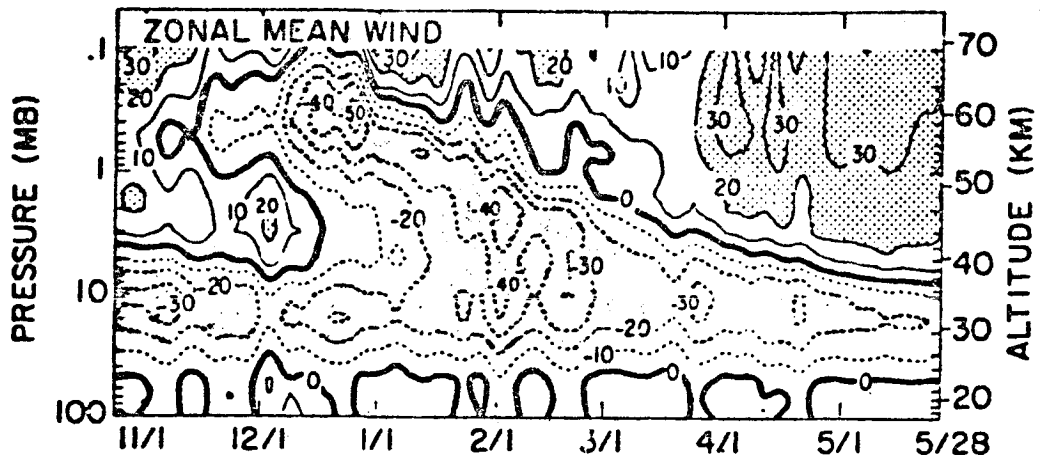
FIGURE 3 Zonally averaged zonal winds averaged over the latitude band
8°S to 8°N versus time and pressure level for the period October
25, 1978 to May 28, 1979.

February 1979 have been documented by Salby et al. (1984). Coy and
Hitchman (1984) have shown that these waves can be interpreted in terms
of the vertical propagation of individual Kelvin wave packets.

Examples of Kelvin wave signatures in equatorial temperature are
shown in Figures 4 to 6. An alternating series of warm and cool
anomalies in the zonal wavenumber 2 component of temperature at 0°
longitude can be seen in the 100 to 4 mb layer between November 7 and
November 21 (Figure 4). Although the individual anomalies propagate
downward with time, the entire pattern gives the distinct impression of
upward propagation with time from a source near 100 mb beginning about
November 8. Similar wavenumber 2 disturbances can be seen above 30 mb
during late January and early February (Figure 5). These midwinter
features, which are responsible for the Kelvin wave structures reported
by Salby et al., also appear as distinct upward propagating wave
packets. All three of the wave packet events shown in Figures 4 and 5
were associated with wavenumber 1 events of comparable amplitude.

Figure 6 shows a wavenumber 1 temperature disturbance during early
May. In contrast to the features shown in Figures 4 and 5, this
disturbance was not associated with a wavenumber 2 disturbance, and it
seems to be connected with rather steady forcing from below over a
month or more rather than with a discrete source event. Consequently,
wave packet behavior is not so obvious for this feature.

Properties of the disturbances shown in Figures 4 to 6 are
summarized in Table 1. Equatorial Kelvin waves should satisfy the
propagation relations valid for long internal gravity waves in a
non-rotating system
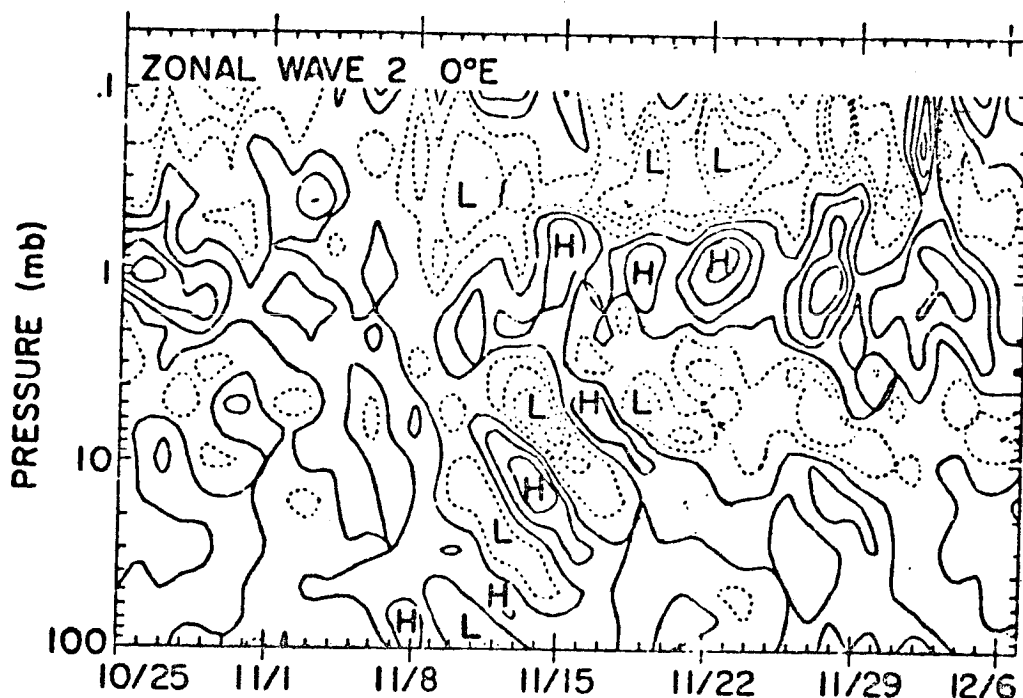
FIGURE 4 Temperature departures from the time mean averaged over the latitude band 8°S to 8°N versus time and pressure level for the period October 25 to December 7, 1978. Contour interval 2°C.

$$| 2\pi (\bar{u} - c)/D | \approx N$$

and $$W_p \approx W_g$$

(see Table 1 for notation). Within the errors of estimation from the data in Figures 4 to 6, these relationships are satisfied. The meridional structure of these features is further strong evidence that they are due to Kelvin waves (Salby et al., 1984).

Individual upward propagating Kelvin wave packets may arise from discrete synoptic events in the tropical troposphere. Even if localized in longitude, such events could be responsible for generating low wavenumber stratospheric Kelvin waves as a result of dispersion and the wave response characteristics of the atmosphere (Salby 1984). M. Williams (personal communication, 1984) has pointed out that the late January and early February wave packets in the middle and upper stratosphere may have been caused by an intense cold outbreak over east Asia between January 10 and January 20. This event severely disturbed the equatorial tropospheric circulation with cold air crossing the equator over Indonesia (Huang and Vincent, 1984; Vincent, 1984).

Coy and Hitchman (1984) have discussed the interactions between these waves and the mean wind shear. The November and April to May
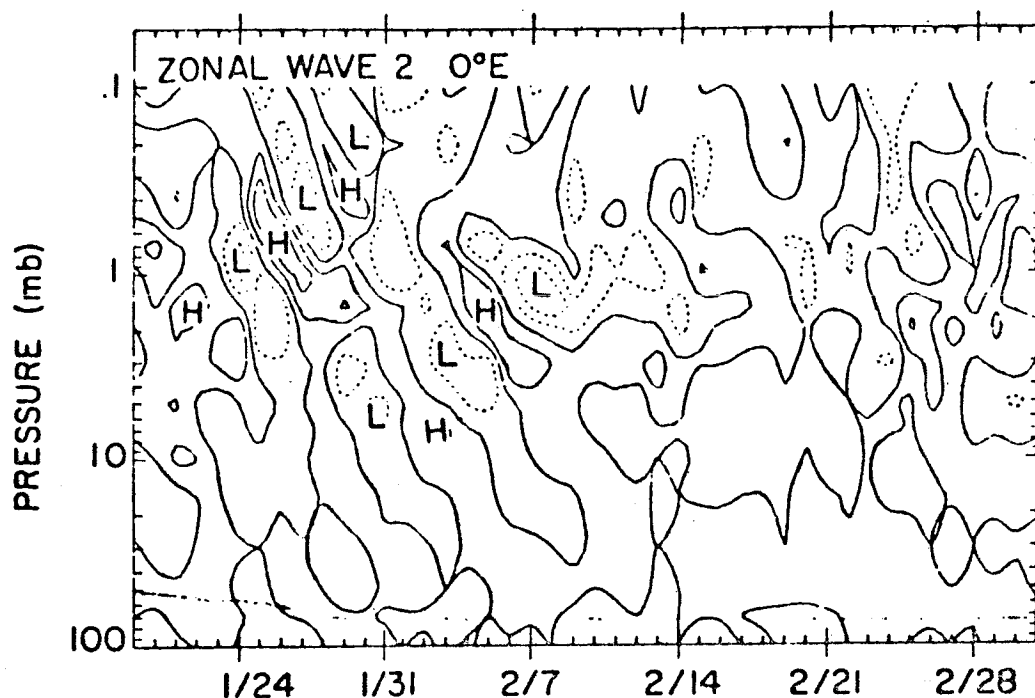
FIGURE 5 Temperature departures from the time mean averaged over the latitude band 8°S to 8°N versus time and pressure level for the period January 19 to March 3, 1979. Contour interval 2°C.

waves interact strongly with westerly shear zones around 5 mb, but during late January and early February, there is no strong westerly shear zone below about 0.5 mb. Consequently, wave packets during this period propagate upward through the mesopause. As Coy and Hitchman (1984) have shown, one effect of wave packet interactions with westerly shear zones is to split the wave packets, with the high frequency low vertical wavenumber components transmitted upward while low frequency components are delayed in the shear layer for a time that may be considerably longer than the time interval over which the disturbance was originally forced. This delay of wave activity in the shear layer tends to smooth wave momentum flux convergence in time so that there can be relatively steady forcing of the zonal winds despite the discrete nature of the Kelvin wave events. Evaluating the zonal wind forcing due to the wave events shown in Figure 5, Coy and Hitchman showed that these events, although important, were probably not sufficient by themselves to account for the rapid downward propagation of the westerly shear zone during January and February. Evidently either the wave amplitudes are underestimated in the LIMS data or other waves that have not been detected are also important. The model results of Hayashi et al. (1984) suggest that intermediate scale internal gravity waves may be as important as long Kelvin waves in forcing the zonal flow.
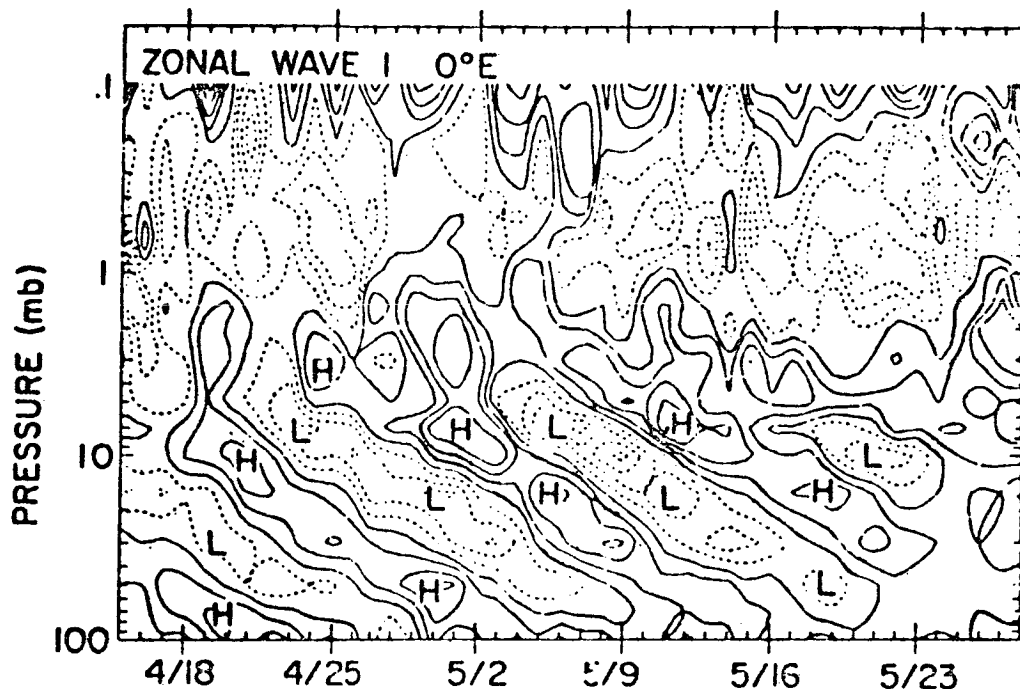
FIGURE 6 Temperature departures from the time mean averaged over the latitude band 8°S to 8°N versus time and pressure level for the period April 15 to May 28, 1979. Contour interval 2°C.

The cause of the rapid easterly acceleration near 0.3 mb during early December (Figure 2) remains unclear. Although westward propagating Rossby gravity waves could drive such an easterly acceleration, as yet no such waves have been isolated in the LIMS data.

POSSIBLE INERTIAL INSTABILITY

Strong cross-equatorial zonal wind shear like that shown in Figure 1 must be associated with an inertially unstable region near the equator. The inertial stability parameter $f(f - u_y)/|f|$ on November 17 is shown in Figure 7. Above 1 mb there is a broad inertially unstable region with positive but weak inertial stability extending northward to about 15°N at the 0.5 mb level. Layers of northward and southward flow, alternating in the vertical, could arise from this instability in the zonal mean and in disturbances of low zonal wavenumber (Dunkerton, 1981, 1982, 198?; Boyd and Christidis, 1982).

The incursion of the tongue of zonal mean easterlies across the equator at 0.5 mb during November and December may have been due to response of the mean meridional flow to this destabilizing influence.

TABLE 1 Properties of Some Kelvin Wave Events

	Fig. 4	Fig. 5	Fig. 5	Fig. 6
Time interval	11/7–11/21 1978	11/21–1/31 1979	1/31–2/10 1979	4/18–5/23 1979
Pressure level range (mb)	100–4	2–0.2	30–0.7	100–4
Vertical wavelength, D (km)	11	17	16	13
horizontal wave-length, L (km)	20,000	20,000	20,000	40,000
Eastward phase speed, c (m/s)	40	60	40	40
mean zonal wind, $\bar{u}$ (m/s)	–10	–20	–30	–10
$2\pi(\bar{u}-c)/D$ (s^{-1})	.028	.029	.028	.023
Buoyancy frequency, N, (s^{-1})	.024	.021	.023	.024
Vertical phase speed, W_p (cm/s)	2.1	5.3	3.2	1.2
Vertical group speed, W_g (cm/s)	2.1	3.5	2.4	–
Estimated date of origin of wave group at 100 mb	11/8	1/12	1/17	–

During November and December, there were also some low wavenumber disturbances in the temperature field that may have arisen from inertial instability. For example, between mid-November and early December, there was a quasi-stationary wavenumber 2 disturbance in equatorial temperatures, with a warm anomaly centered near 0.8 mb, a cold anomaly centered near 0.2 mb and a corresponding vertical half wave length of about 9 km (Figure 4).

One of the problems in the theory of equatorial inertial instability is the unknown mechanism that selects a vertical scale. In its simplest form, the theory of inertial instability predicts disturbances of infinite vertical wavenumber. This defect can be remedied by incorporation of an eddy viscosity in the theory (Dunkerton, 1982, 1983), but without some means of estimating the eddy viscosity, the vertical scale of inertially unstable overturning circulations is still unexplained.

Alternatively, the vertical scale may be determined by a restriction on the Richardson number. The vertical separation between
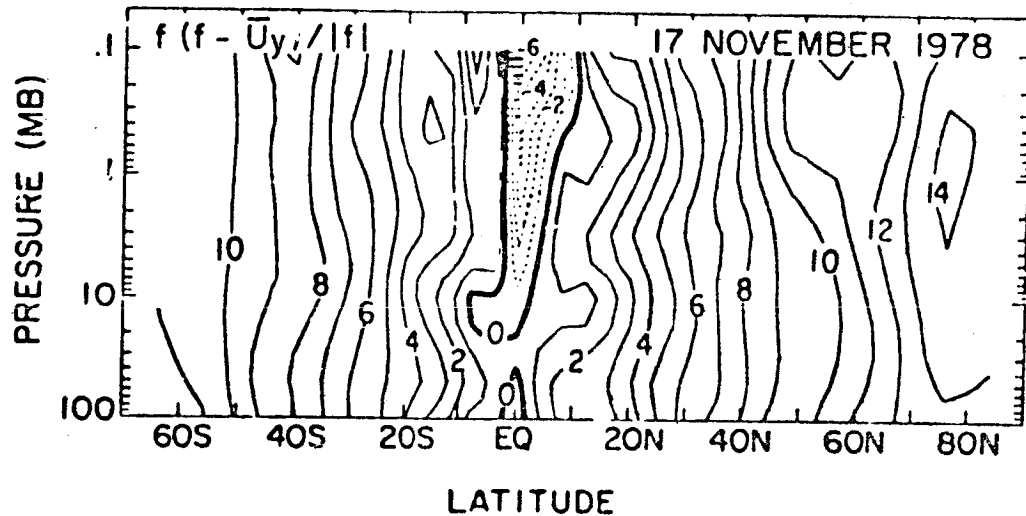
FIGURE 7 Inertial stability parameter expressed in terms of the coriolis parameter f and mean zonal wind shear u_y. The region of **negative values is inertially** unstable (units: $10^{-5}s^{-1}$).

alternating easterly and westerly wind maxima in overlying northward and southward flows must be large enough that the minimum Richardson number exceeds a critical value of 1 or greater, the exact value depending on the amplitude of other types of vertical wind variation superimposed on the inertially unstable flow. Any inertially unstable oscillations that initially fail to satisfy this criterion will deepen rapidly as a result of vertical mixing until the Richardson number criterion is satisfied. Since the zonal wind difference between alternating northward and southward layers would depend on the meridional width of the circulation, the vertical scale would then be determined ultimately by the width of the inertially unstable region. There is some indication in the LIMS data that this Richardson number limitation is important. The minimum value of the Richardson number in the westerly shear region near 0.2 mb in early January is less than 4.

The temperature perturbations associated with these possible inertially unstable layers can be identified in rocketsonde data. In Figure 8, zonally averaged LIMS temperatures, LIMS temperatures at the longitude of Fort Sherman, and a Fort Sherman rocketsonde are compared. The double stratopause structure in both the rocketsonde and the LIMS temperature profile for the same longitude corresponds to the alternating warm and cool layer structure in the wavenumber 2 temperature field shown in Figure 4 and tentatively identified as due to inertial instability. This double stratopause structure is characteristic of wavenumber 1 and 2 temperature anomalies in the LIMS data that are not vertically propagating. It is a clear signature that may make it possible to use the existing lengthy series of rocketsonde measurements to trace interannual variability in inertially unstable oscillations near the equatorial stratopause.
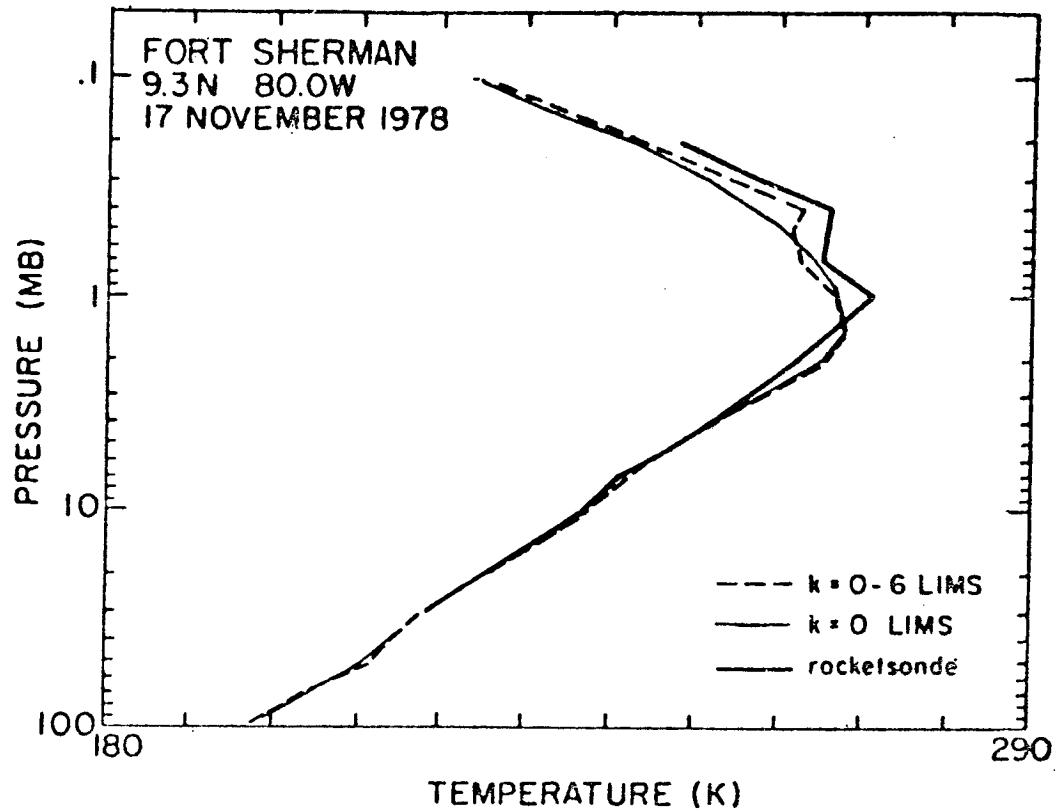
FIGURE 8 Comparison of zonal winds between an individual rocketsonde ascent at Fort Sherman. LIMS evaluated at the latitude and longitude of Fort Sherman (k = 0 - 6), and LIMS zonal mean evaluated at the latitude of Fort Sherman (k = 0).

CONCLUDING REMARKS

The infrared limb scanning data have provided a new viewpoint on several important processes in the middle atmosphere. Studies of equatorial dynamics are particularly promising, and much remains to be learned from further analyses of these data.

ACKNOWLEDGMENTS

REFERENCES

Boyd, J. P., and Z. D. Christidis (1982). Low wavenumber instability on the equatorial beta-plane. Geophys. Res. Lett. 9, 769-772.

Coy, L., and M. Hitchman (1984). Kelvin wave packets and flow acceleration: a comparison of modeling and observations. J. Atmos. Sci. 41 (in press).

Dunkerton, T. J. (1981). On the inertial instability. J. Atmos. Sci. 38, 2354-2364.

Dunkerton, T. J. (1982). The double diffusive modes of symmetric instability on an equatorial beta-plane. J. Atmos. Sci. 39, 1653-1657.

Dunkerton, T. J. (1983). A nonsymmetric equatorial inertial instability. J. Atmos. Sci. 40, 807-813.

Gille, J. C., and J. M. Russell III (1984). The limb infrared monitor of the stratosphere (LIMS): An overview of the experiment and results. J. Geophys. Res. (in press).

Hayashi, Y., D. G. Golder, and J. D. Mahlman (1984). Stratospheric and mesospheric Kelvin waves simulated by the GFDL "SKYHI" general circulation model. J. Atmos. Sci. 41 (in press).

Hirota, I. (1978). Equatorial waves in the upper stratosphere and mesosphere in relation to the semiannual oscillation of the zonal wind. J. Atmos. Sci. 35, 711-714.

Hirota, I. (1979). Kelvin waves in the equatorial middle atmosphere observed by the Nimbus 5-SCR. J. Atmos. Sci. 36, 217-222.

Huang, H.-J., and D. G. Vincent (1983). Major changes in the circulation features over the South Pacific during FGGE, 10-27 January 1979. Mon. Wea. Rev. 111, 1611-1618.

Salby, M. (1984). Transient disturbances in the stratosphere: Implications for theory and observing systems. (submitted for publication).

Salby, M. L., D. L. Hartmann, P. L. Bailey, and J. C. Gille (1984). Evidence for equatorial Kelvin modes in Nimbus-7 LIMS. J. Atmos. Sci. 41, 220-235.

Vincent, D. G. (1982). Circulation features over the South Pacific during 10-18 January 1979. Mon. Wea. Rev. 110, 981-993.

15. SOUTHERN HEMISPHERE

Organizer   Julia N. Paegle

Session Chairman   Peter J. Webster

Speakers   Harry van Loon
                             Kevin E. Trenberth

Rapporteur   Hassan Virji

204<

THE ZONAL HARMONIC AND THE YEARLY AND HALF-YEARLY WAVES ON THE SOUTHERN HEMISPHERE IN FGGE COMPARED WITH THE MEAN

Harry van Loon
National Center for Atmospheric Research
and
Kingtse C. Mo
Goddard Space Flight Center
National Aeronautics and Space Administration

ABSTRACT

The dominant component in the mean annual cycle of sea level pressure in the latitudes north of ~40°S is the yearly wave, whereas to the south of this latitude a half-yearly wave dominates. In FGGE, however, the usually small yearly wave was large in the Antarctic, owing to the extraordinarily low pressure there in the winter of 1979. The half-yearly wave's amplitude was appreciably above normal in the center of each ocean in middle latitudes, and below normal at high latitudes. The yearly wave in the zonal geostrophic wind was larger than normal over the Antarctic Ocean. Similar results are obtained at 500 mb.

The three-month mean stationary waves (zonal harmonic waves) were larger than the mean in FGGE. The intra-annual variation of both amplitude and phase of the monthly mean harmonic waves in FGGE was large, which is not surprising as they contain an appreciable transient component, unlike the long-term monthly mean waves.

INTRODUCTION

Several studies of the First GARP Global Experiment (FGGE) have dealt with the representativeness of the circulation over the southern hemisphere during that year and with the quality of the analyses: Bengtsson et al. (1982), Guymer and LeMarshall (1981), Physick (1981), Streten and Pike (1980), Trenberth (1984), Trenberth and van Loon (1981), Tucker and Physick (1980), Tucker (1981), van Loon (1980), and van Loon and Rogers (1981a). As far as is known, nobody has studied the stationary waves in FGGE, and the waves in time (here only the yearly and half-yearly waves) were but briefly considered in van Loon and Rogers (1981b; 1984a, b).

The analyses in this paper principally cover the area south of 15°S, but the latitudes between the equator and 30°S will receive more attention in a similar paper to be written for the World Meteorological Organization later this year. Data from Level IIIb analyzed in the European Centre for Medium Range Weather Forecasts are

205<

the main source for the analyses, and the period used is December 1978 to November 1979. Some of the analyses below are from our already published studies and are based on operational analyses from the Australian Bureau of Meteorology for the period January to December 1979. These will be pointed out.

In addition to grid points of the elements, observations from stations are used to judge FGGE's place in the spectrum of variability, as it is possible to get much longer periods from stations than from synoptic map analyses. Only some major points will be stressed in the text owing to the limits set for the length of this paper, but enough material has been included in the tables and figures for the reader to extend the comparison of FGGE with the mean.

TIME WAVES IN SEA LEVEL PRESSURE

The Yearly Wave

Figures 1a and 1b show the average distribution of sea level pressure (SLP) in January and July from two different sources: 1955 to 1958 from the historical map series analyzed in the South African Weather Bureau, and 1972 to 1980 from daily operational analyses made in the Australian Bureau of Meteorology. The maps are meant to help the reader relate the phase and amplitude of the yearly and half-yearly waves to the features of the mean pattern. Figure 2 gives the location of the stations used in the illustrations and tables. The word maximum in the description below denotes the largest ordinate of a harmonic, and the word peak refers to the largest value in space. Three-month running means are used in the time series of station data, but the yearly and half-yearly waves are computed from monthly means.

The yearly wave (the first harmonic in a 12-month series) in a 12 to 13 year mean of SLP appears in Figure 3. As far south as 35° to 40°S, but in the Atlantic all the way to the Antarctic, the wave has its maximum in the southern winter, and the peaks are over or near the three lower-latitude continents. There is one noteworthy peak over the oceans in middle and high latitudes: the one in the South Pacific where the maximum is in the southern summer. The yearly wave is the dominant component of the annual cycle north of 40°S (see van Loon and Rogers, 1984b, where the interannual variation of the wave is also treated). In individual years it is often large in different places over the ocean south of 40°S, but its phase there is variable so that it tends to cancel itself in a long-term mean.

The yearly wave in 1979 (Figure 4, January to December 1979) was close to the average shown in Figure 3 in the tropics and subtropics and in middle latitudes of the Pacific Ocean. At high latitudes, the wave was bigger than normal, its maximum was in summer, and it explained much more than usual of the annual variance (cf. van Loon and Rogers, 1984b, Figure 2C). The long-term mean annual curve of stations in different latitudes, the long-term standard deviation (σ), and the FGGE values in Figure 5, all three-month running means, and Table 1, make it possible to judge the seasonal cycle in FGGE against a longer
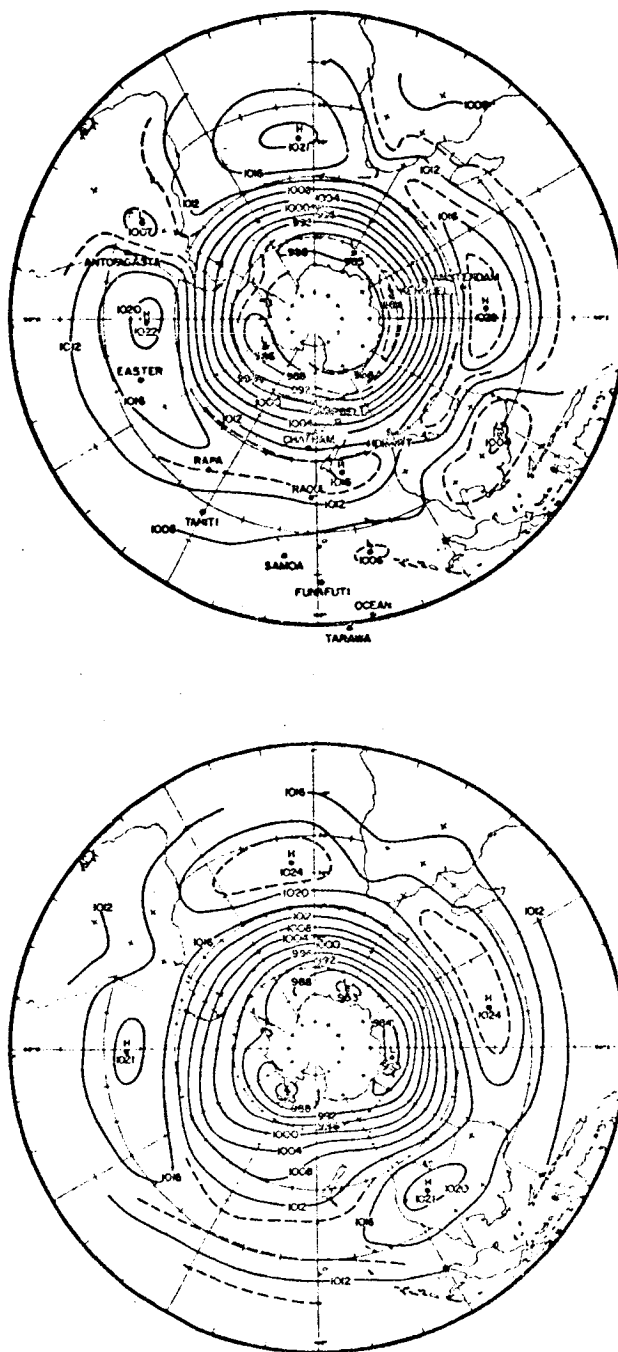
FIGURE 1 Mean sea level pressure in (a) January, (b) July (from van Loon and Rogers, 1984b).
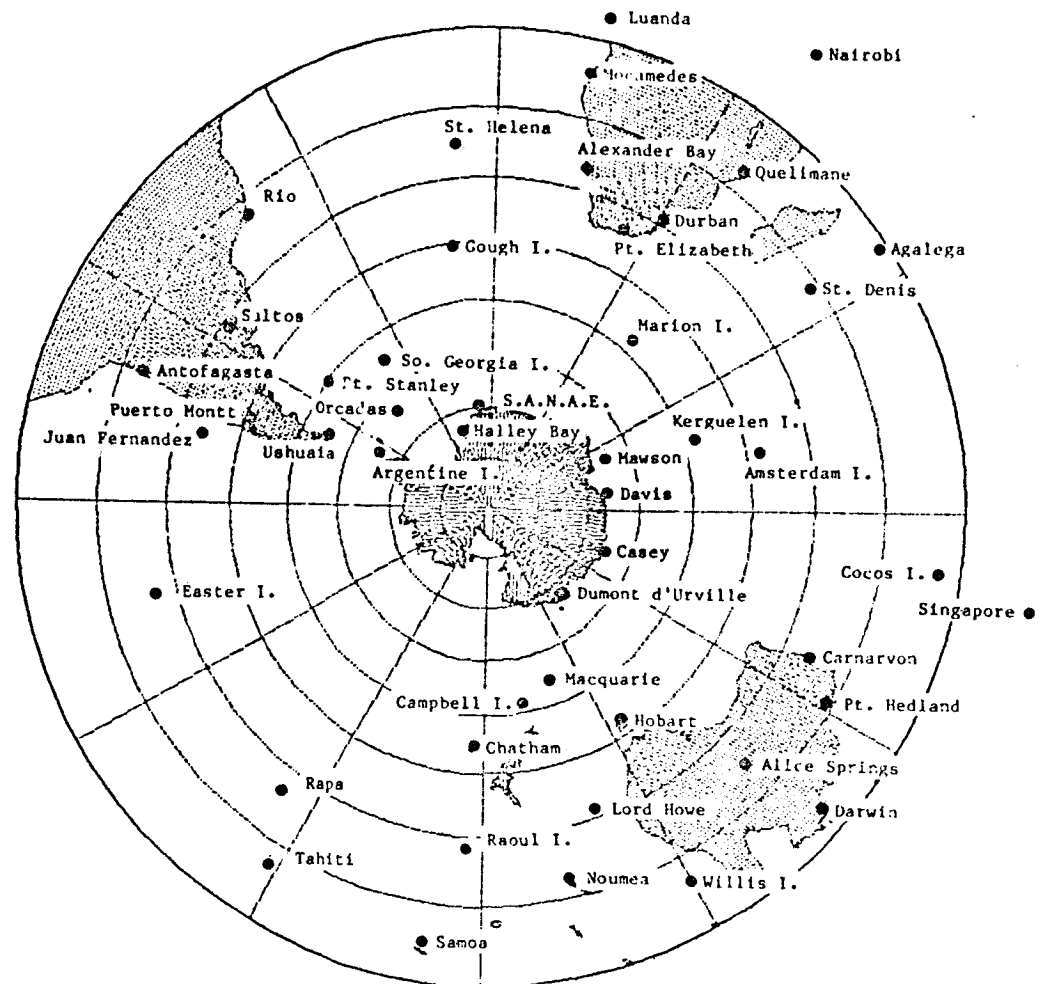
FIGURE 2 Position of stations.

period. The length of period for the stations is in Table 2. It is
evident from a comparison of Figure 5 with Table 1 that the large
yearly wave in FGGE in the Antarctic with maximum in summer is caused
by the extraordinarily low pressure in the winter of 1979: as much as
three standard deviations below the long-term, three-month average at
Halley Bay and Davis. The pressure in middle latitudes was near and
above normal, and as a result, the meridional contrast of pressure in
the sub-Antarctic was above normal during much of FGGE. In summer
(DJF), the zonally averaged pressure difference 50°S to 65°S was
1.40 σ above average and in winter (JJA), 2.50 σ above average (van
Loon and Rogers, 1981a). See also Trenberth (1984) and Trenberth and
Christy in this report.
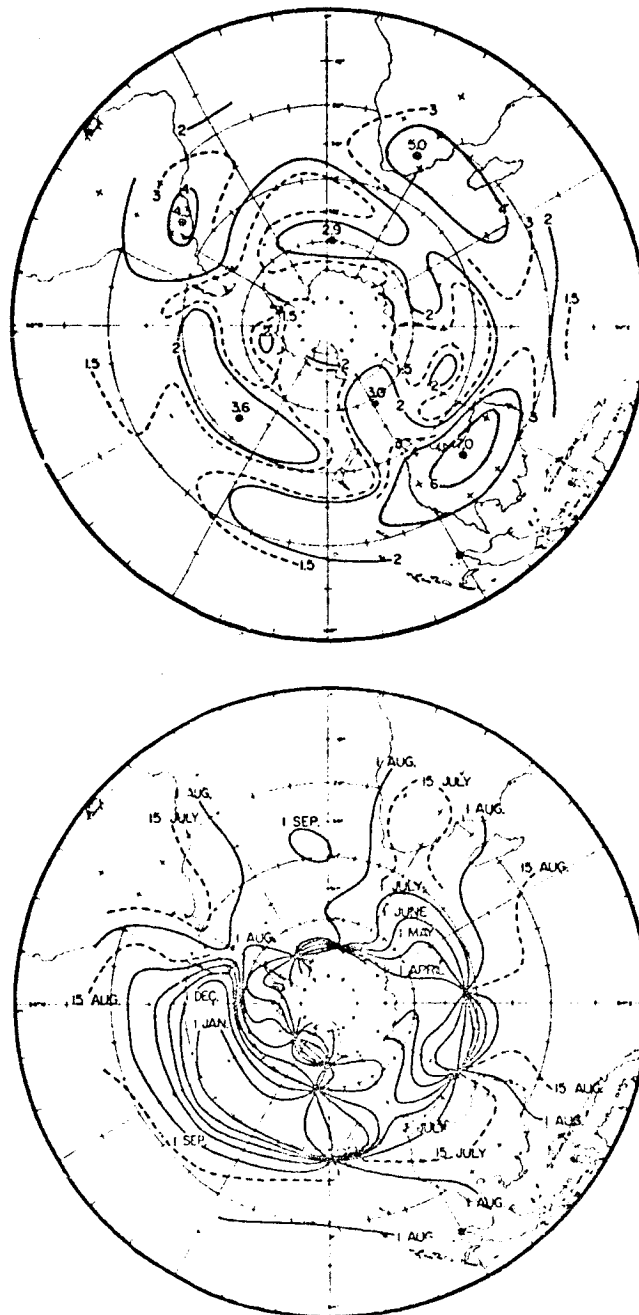
FIGURE 3 First harmonic (yearly wave) in sea level mean pressure (a) amplitude (mb), (b) phase (date of maximum) (from van Loon and Rogers, 1984b).
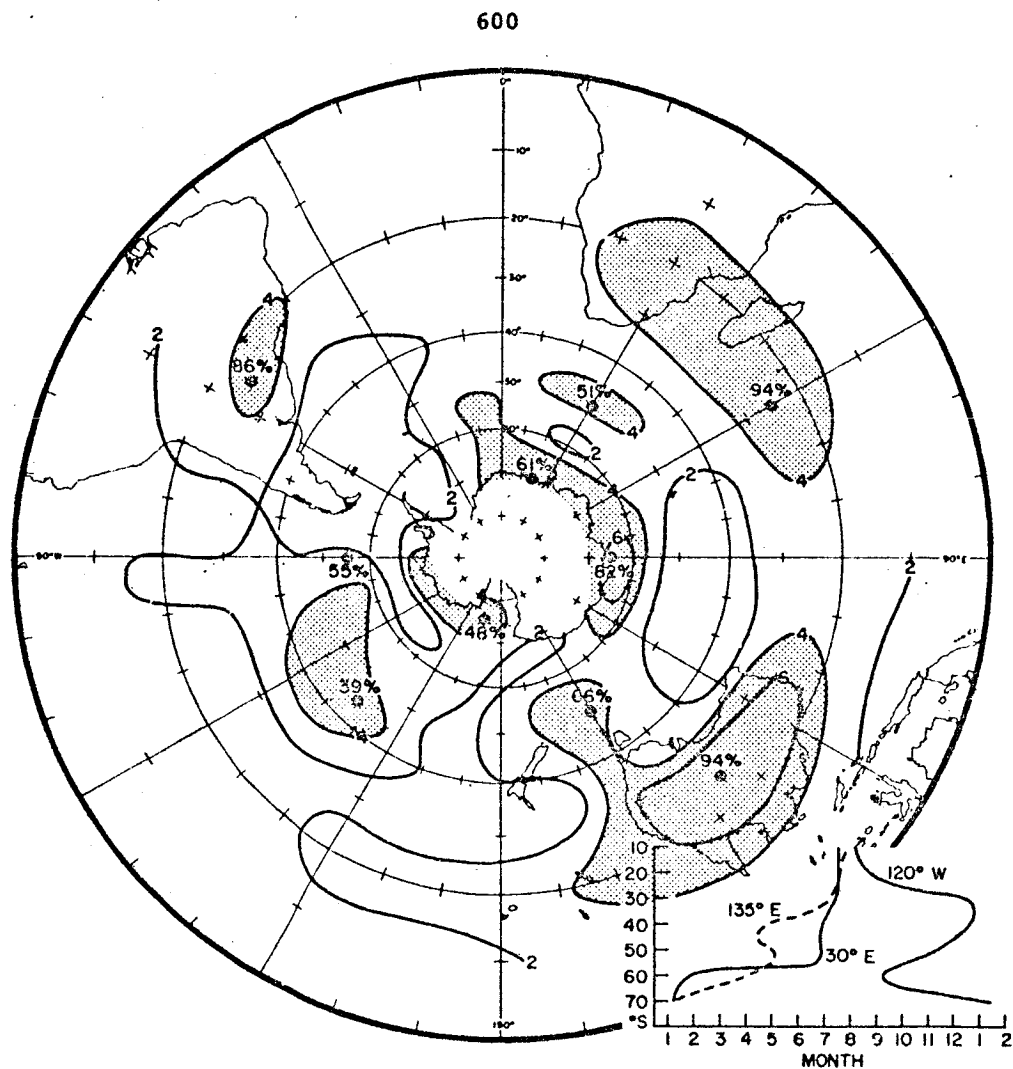
FIGURE 4 Amplitude of the yearly wave in sea level pressure in 1979
(mb).   Inset shows phase (date of maximum) at three meridians.
Percentages are some of the largest percentages of the variance in 1979
explained by the wave (van Loon and Rogers, 1984b).

The Half-Yearly Wave

Figures 6a and 6b show the mean amplitude and phase of the half-yearly
wave in SLP; its interannual variation is discussed in van Loon and
Rogers, 1984a.   The mean wave has a peak in middle latitudes with
maxima near the equinoxes, and another in the Antarctic with solstitial
maxima.   The same pattern is evident in 1979, January to December 1979
in Figure 7, but the amplitude is appreciably above normal in middle
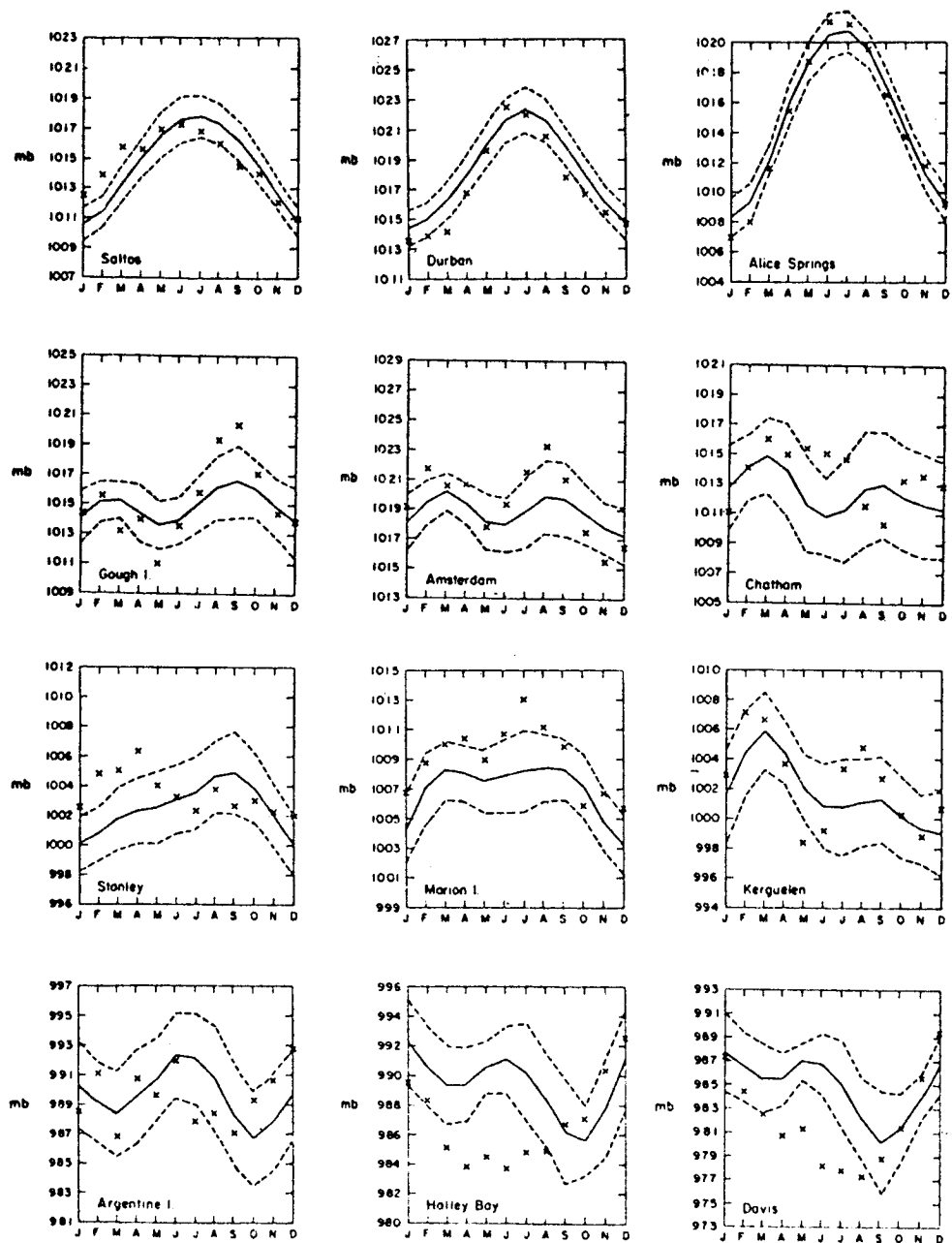
FIGURE 5 Long term mean sea level pressure, three-month running means
(solid line); one standard deviation on either side of the mean (dashed
lines); three-month running means in FGGE (crosses).

TABLE 1 Sea Level Pressure Yearly and Half-Yearly Waves

station	Climatology							FGCE						
	mean	a_1	ϕ_1	%	a_2	ϕ_2	%	mean	a_1	ϕ_1	%	a_2	ϕ_2	%
St. Helena	1017	2.64	Aug 1	97	0.46	Jul 7	3	1018	2.41	Aug 7	86	0.66	Jul 18	7
Agalega	1011	2.45	Aug 5	99	0.02	May 7	<1	1011	2.60	Aug 2	93	0.42	Jun 11	<1
St. Denis	1016	4.98	Aug 4	99	0.23	May 3	<1	1016	5.0	Aug 8	91	0.54	Jun 2	1
New Amsterdam	1019	0.81	Jun 18	15	1.82	Mar 12	77	1019	1.4	Jun 5	8	3.7	Feb 4	59
Kerguelen	1002	2.48	Apr 17	44	2.67	Mar 4	51	1002	1.55	Feb 10	5	4.87	Feb 7	48
Quelimane	1015	5.58	Jul 2	99	0.54	Dec 9	1	1016	5.78	Jul 4	90	1.14	Dec 15	4
Alexander Bay	1016	3.08	Jun15	99	1.32	Mar 6	1	1016	4.06	Jul 2	93	0.67	Dec 12	3
Port Elizabeth	1017	3.46	Jul 6	99	0.10	Jan 12	<1	1018	3.61	Jul 1	69	1.99	Dec 10	21
Durban	1018	4.26	Jul 1	99	0.32	Jan 6	<1	1017	4.62	Jul 4	83	1.60	Dec 21	10
Gough I	1015	0.84	Sep 10	21	1.52	Mar 8	70	1015	2.91	Sep 11	27	3.11	Feb 19	31
Marion I	1007	2.07	Jun 6	43	2.03	Mar 4	41	1009	2.83	Jun 1	26	1.85	Feb 2	11
Antofagasta	1016	1.91	Aug 7	97	0.32	May 1	3	1015	1.82	Aug 6	86	0.03	Jun 15	<1
Easter I	1020	1.66	Sep 9	80	0.5?	Feb 10	8	1018	1.12	Nov 14	9	0.16	Jan 14	<1
Juan Fernandez	1019	1.53	Oct 5	81	0.72	Mar 7	18	1022	0.90	Sep 2	12	0.92	May 6	13
Saltos	1015	3.99	Jul 5	93	0.50	Apr 9	2	1015	2.88	Jun 4	69	0.56	Mar 6	2
Stanley	1002	2.18	Aug 10	67	1.35	Mar 10	26	1004	1.48	Apr 8	21	1.23	Mar 7	15
So. Georgia	997	2.57	Aug 5	68	1.49	Sep 5	23	995	0.54	Jan 17	1	4.39	Feb 9	76
Argentine I	989	1.67	Jun 10	26	2.46	Jan 9	58	989	0.97	Apr 7	2	1.42	De: 4	4
Halley Bay	989	2.0	Mar 10	29	2.97	Jan 18	63	986	2.93	Dec 29	40	1.22	Jan 3	7
Noumea	1013	3.85	Aug 11	97	0.67	Apr 10	3	1013	4.05	Aug 9	92	0.72	Apr 1	3

Samoa	1010	2.12	Jul 12	95	0.47	Mar 13	5	1015	1.83	Jul 5	74	0.61	Mar 1	8
Tahiti	1012	1.78	Aug 11	92	0.44	Mar 7	6	1012	1.96	Jul 8	75	0.42	Feb 14	4
Campbell	1004	1.70	May 2	48	1.54	Feb 9	40	1004	3.44	Jun 7	35	1.79	May 13	1
Chatham	1012	1.04	Feb 14	17	2.14	Mar 4	73	1013	2.07	Apr 3	17	1.20	May 6	8
Raoul	1016	2.05	Aug 1	88	0.73	Apr 8	11	1016	1.24	Aug 12	14	1.80	May 6	30
Darwin	1009	3.38	Jul 10	99	0.25	Apr 11	<1	1010	3.07	Jul 10	92	0.56	Apr 3	3
Willis I	1011	4.01	Aug 10	98	0.57	Apr 13	2	1012	4.94	Jul 14	97	0.55	Apr 1	1
Carnarvon	1014	5.23	Jul 11	97	0.77	Apr 11	2	1014	5.83	Jul 10	97	0.64	May 21	1
Port Hedland	1011	5.57	Jul 2	99	0.36	May 2	<1	1011	5.79	Jul 1	97	0.42	Jun 7	<1
Alice Springs	1014	6.81	Jul 7	99	0.50	May 4	<1	1014	7.75	Jul 7	97	0.78	May 3	1
Hobart	1013	2.94	May 3	97	0.25	Mar 6	<1	1013	3.65	May 3	72	0.94	Jun 15	5
Lord Howe	1015	1.71	Jul 1	72	0.99	Apr 12	25	1017	2.42	Jul 7	44	0.43	Jun 7	2
Macquarie	1000	2.17	May 11	59	1.50	Jan 1	30	1000	3.64	May 13	35	1.35	May 4	5
Cocos I	1011	1.71	Sep 12	95	0.35	Apr 9	4	1012	1.60	Aug 13	56	0.56	Feb 10	7
Davis	988	2.40	Apr 5	47	2.36	Jun 9	46	984	3.67	Jan 1	51	1.69	Jun 9	11
Casey	985	2.90	Mar 3	44	3.11	Jun 7	50	982	4.97	Jan 3	53	2.01	Jun 3	9
Mawson	989	2.92	Apr 7	73	1.66	Jun 7	24	986	3.85	Feb 7	60	1.66	May 4	11

TABLE 2 Sea Level Pressure Stations and the Number of Years

Agalega	1951-1981	SANAE	1957-1981
St. Denis	1951-1981	Halley Bay	1956-1981
New Amsterdam	1952-1981	Davis	1961-1981
Kerguelen	1951-1981	Noumea	1941-1980
Luanda	1901-1981	Samoa	1890-1981
Mocamedes	1944-1981	Tahiti	1935-1982
Quelimane	1926-1981	Rapa	1952-1981
Alexander Bay	1951-1981	Campbell I	1941-1981
Durban	1884-1981	Chatham	1930-1981
Port Elizabeth	1941-1981	Raoul	1940-1980
Gough I	1955-1981	Darwin	1882-1981
Marion I	1948-1981	Willis I	1951-1981
Antofagasta	1951-1981	Carnarvon	1951-1981
Easter I	1942-1981	Port Hedland	1951-1981
Juan Fernandez	1911-1981	Alice Springs	1941-1981
Puerto Montt	1967-1981	Lord Howe	1931-1981
Saltos	1951-1981	Macquarie	1948-1981
Ushuaia	1951-1981	Dumont d'Urville	1956-1980
Stanley	1922-1981	Cocos Island	1952-1981
So. Georgia	1905-1981	St. Helena	1941-1980*
Argentine I	1947-1981	Hobart	1896-1981

*1958-1976 missing

latitudes (e.g., Kerguelen and Gough in Table 1) and below normal at
high latitudes (Davis, Casey, Mawson, Halley Bay in Table 1). The
phase is two to three weeks early in middle latitudes, and normal to
early in high latitudes (see the same stations in Table 1). The peaks
in the Pacific lie farther east than on the mean map of the wave, and
as a result the wave at Chatham Island, Table 1, explains only 8
percent of the annual variance in FGGE against 73 percent in the mean.
   One can compare the annual curves of the zonally averaged SLP in
FGGE (Australian data set) at 45°S and 65°S with those obtained
from the long-term means in Taljaard et al. (1969) and with those based
on the combined South African and Australian daily maps (Figure 8).

605
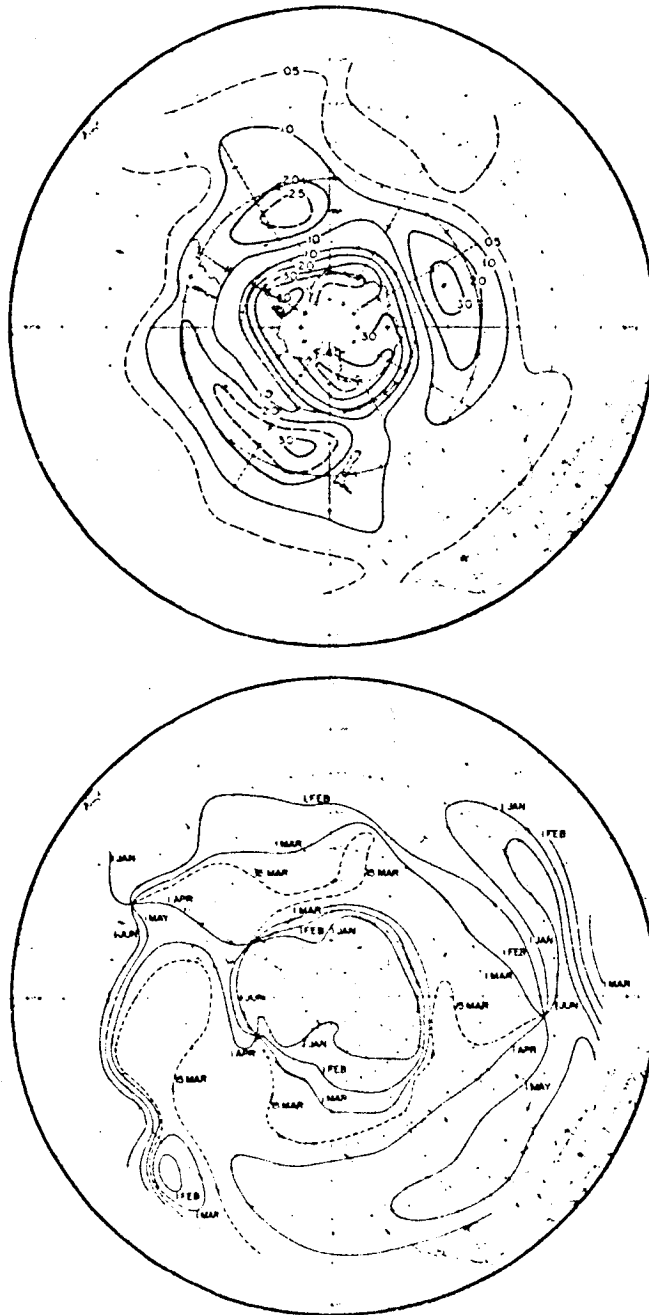
FIGURE 6 Second harmonic (half-yearly wave) in sea level mean pressure
(a) amplitude (mb), (b) phase (date of first maximum) (from van Loon
and Rogers, 1984b).

SOUTHERN HEMISPHERE

a_2 SLP 1979
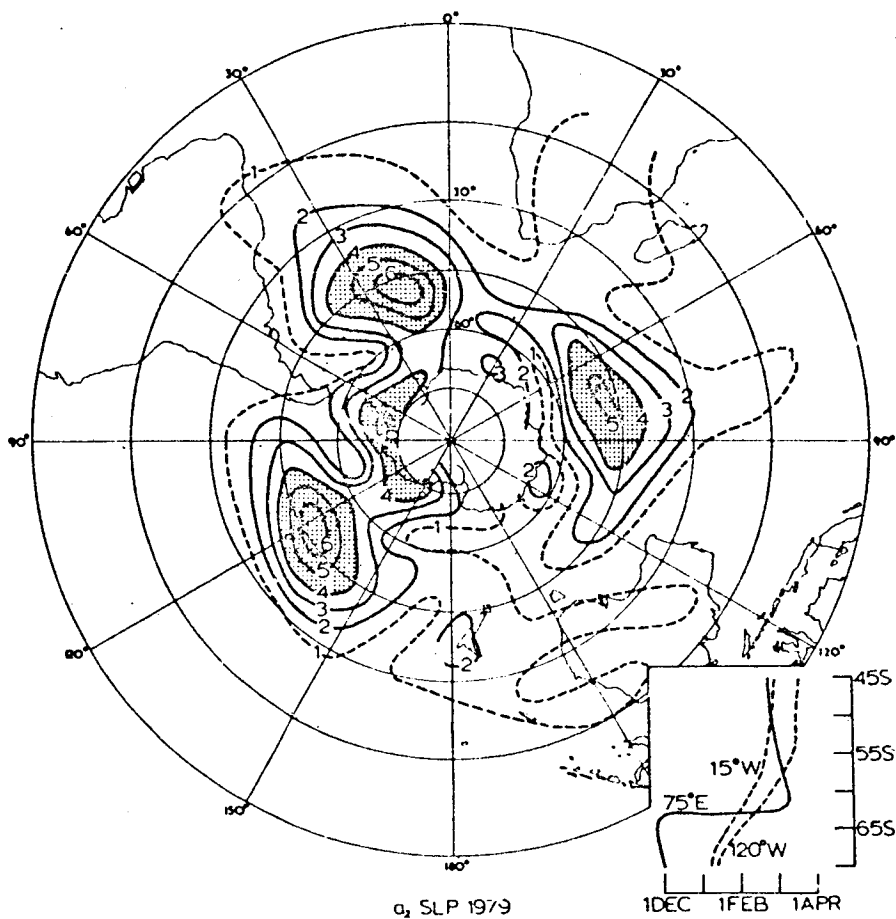
FIGURE 7 Amplitude (mb) of the half-yearly wave in sea level pressure in 1979. Inset shows phase at three longitudes (date of first maximum) (from van Loon and Rogers (1984a).

The curves from the last two sources show clearly the double waves of opposite phase in middle and high latitudes. The zonal mean pressure at 45°S in FGGE follows the shape of these two curves well, being sometimes a little above, sometimes a little below the others. At 65°S, the two long-term means are still close but that of FGGE lies
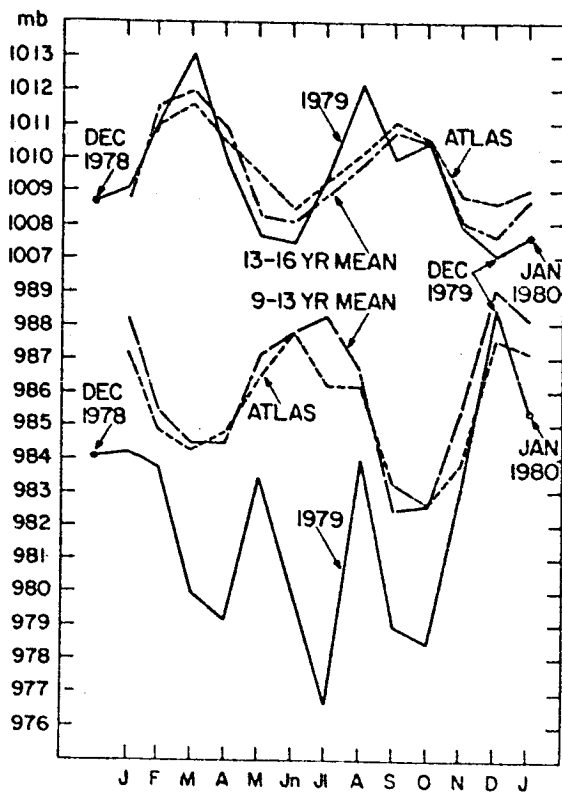
FIGURE 8   Annual curves of the zonally averaged sea level pressure at
(top) 45°S and (bottom) 65°S.   From daily South African and
Australian analyses (9 to 13 and 13 to 16 year means) from Australian
analyses in 1979 (IIIA), and from Taljaard et al.'s (1969) atlas.

below the others until November 1979,* in agreement with Halley Bay and
Davis in Figure 5.

TIME WAVES IN THE SEA LEVEL ZONAL GEOSTROPHIC WIND

The Yearly Wave

The yearly wave in the mean zonal geostrophic wind at sea level
(Figures 9a and 9b) is largest in the tropics and subtropics. Its
phase appears in four concentric belts as follows: maximum westerlies

---

*See Trenberth and Christy (this report) on the question of the
intensity of the circumpolar trough in the Australian operational
analyses.
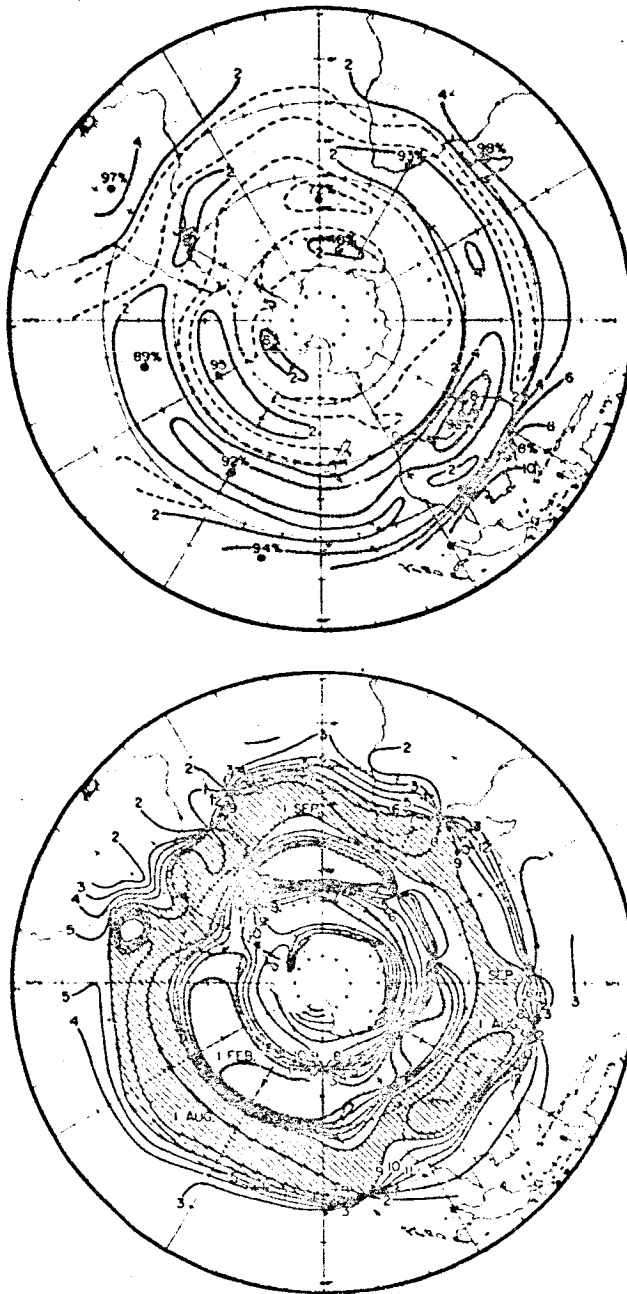
FIGURE 9 Yearly wave in the mean zonal geostrophic wind at sea level.
(a) amplitude (m/s). The percentages are the largest shares of the
mean annual variance accounted for by the yearly wave. (b) phase
(month of maximum, summer maximum is shaded).
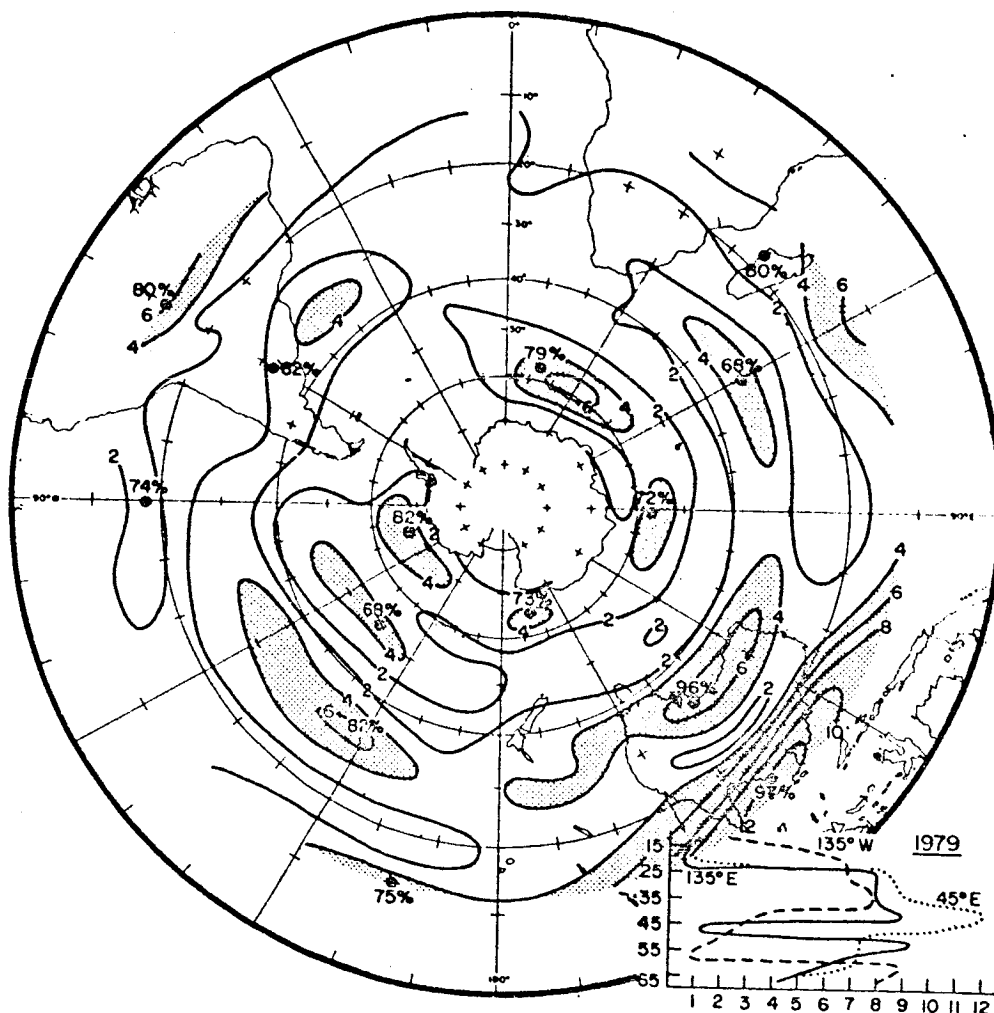
FIGURE 10 Amplitude of the yearly wave in zonal geostrophic wind at
sea level in 1979 (m/s). Inset shows phase (date of maximum) at three
longitudes. Percentages show some of the largest shares of the annual
variance in 1979 explained by the yearly wave (van Loon and Rogers,
1984b).

(minimum easterlies) in summer in the tropics; maximum westerlies
(minimum easterlies) in winter in the subtropics; maximum westerlies in
45°S to 55°S during summer (unlike the northern hemisphere); and
maximum westerlies (minimum easterlies) in winter over most of the area
covered by sea ice in winter. In 1979 (January to December 1979,
Figure 10), the distribution was quite similar, the only notable
difference being the large role that the wave played over the Antarctic
Ocean where the maximum was reached in winter. This is, of course,

ANNUAL WAVE (ᴜg)
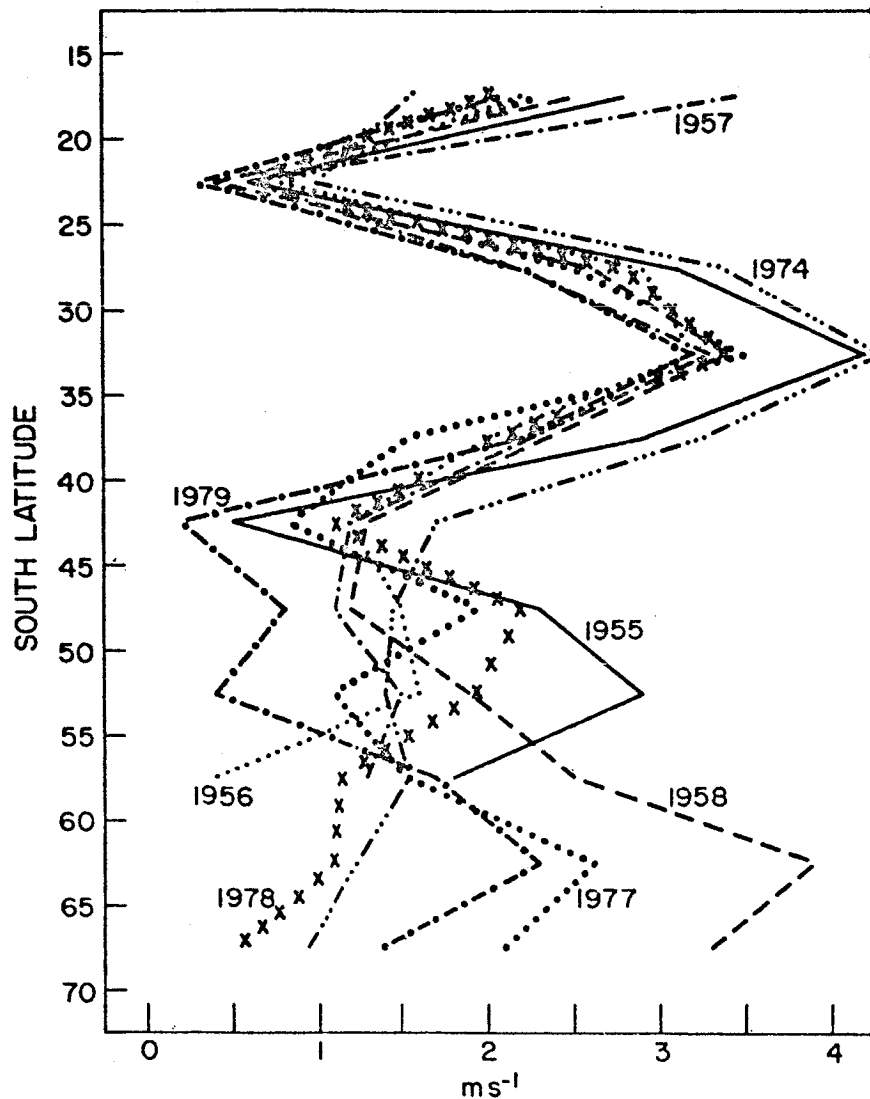
FIGURE 11 Meridional vertical section of the amplitude (m/s) of the
yearly wave in the zonally averaged geostrophic wind at sea level in
eight single years (van Loon and Rogers, 1984b).

associated with the abnormally low pressure in the Antarctic noted
above.

The yearly wave in the zonally averaged geostrophic wind in 1979 can
be compared with that of seven other years in Figure 11: In the peaks

at 15°S to 20°S and 30°S to 35°S, the yearly wave in 1979 was
among the weakest, and a weak wave was characteristic of that year as
far as 55°S. South of this latitude, the 1979 wave is among the
strongest, but even there two years, 1977 and 1958, have a bigger
amplitude.

The Half-Yearly Wave

The annual curve of the mean zonal geostrophic wind is dominated by a
half-yearly wave with equinoctial maxima over the Antarctic Ocean and
solstitial maxima north of 50°S (Figures 12a and 12b). Near 60°S
the mean wave explains over 80 percent of the annual variance along
more than half the circumference, and near 40°S it accounts for more
than 50 percent in many places (van Loon and Rogers, 1984a, Figure
9C). This distribution of phase and amplitude is repeated in 1979
(Figure 13), but the wave explains less of the annual variance than in
the mean. One major difference from the mean is the location of the
peaks in the Pacific Ocean. In 1979, the peaks are in the central part
of the ocean; in the mean, the largest amplitudes are on either side of
the ocean. It is of interest that in the International Geophysical
Year (1957, Figure 14) the half-yearly wave in the Pacific was also
abnormal with an amplitude peak of almost 8 m/s centered on the North
Island of New Zealand.

The anomalous position of the lower latitude peak of the half-yearly
wave in the Pacific in FGGE is reflected in the half-yearly wave in the
difference of SLP between Raoul and Chatham (Figure 15 and Table 3),
where in the mean the wave has an amplitude of 2.2 mb, but one of only
0.6 mb in FGGE.

The diagram in Figure 16 makes it possible to compare the yearly and
half-yearly waves in 1979 with those in other years for the zonally
averaged pressure differences 50°S to 70°S and 35°S to 70°S.
In Figure 16a, the first harmonic accounts for 24 percent of the
variance in 1979, which is in the middle between the years with the
lowest (2) and highest (61) percentages. The phase of the first
harmonic however varies widely from one year to another, and it is
therefore comparatively unimportant in the mean. The second harmonic's
share of the variance in 1979 is 43 percent, whereas the highest and
lowest percentages in other years are 67 and 23.

In the SLP difference between 35°S and 50°S, the second
harmonic's part of the variance in 1979 was also larger than that of
the first harmonic. The first harmonic's role in 1979 was small in
comparison with other years, only 1955 was smaller; the second
harmonic's share of the variance fell midway between the extremes of
the other years.
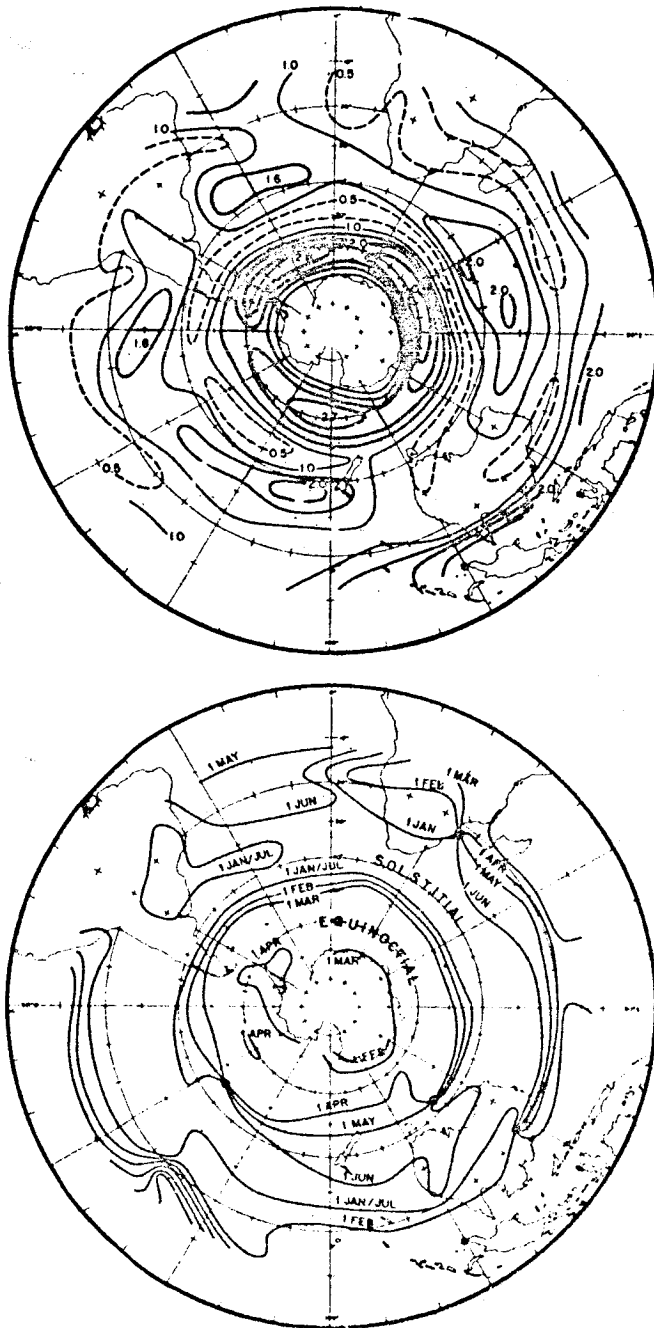
FIGURE 12 The half-yearly wave in the mean zonal geostrophic wind at
sea level (a) amplitude (m/s), (b) phase (date of first maximum).
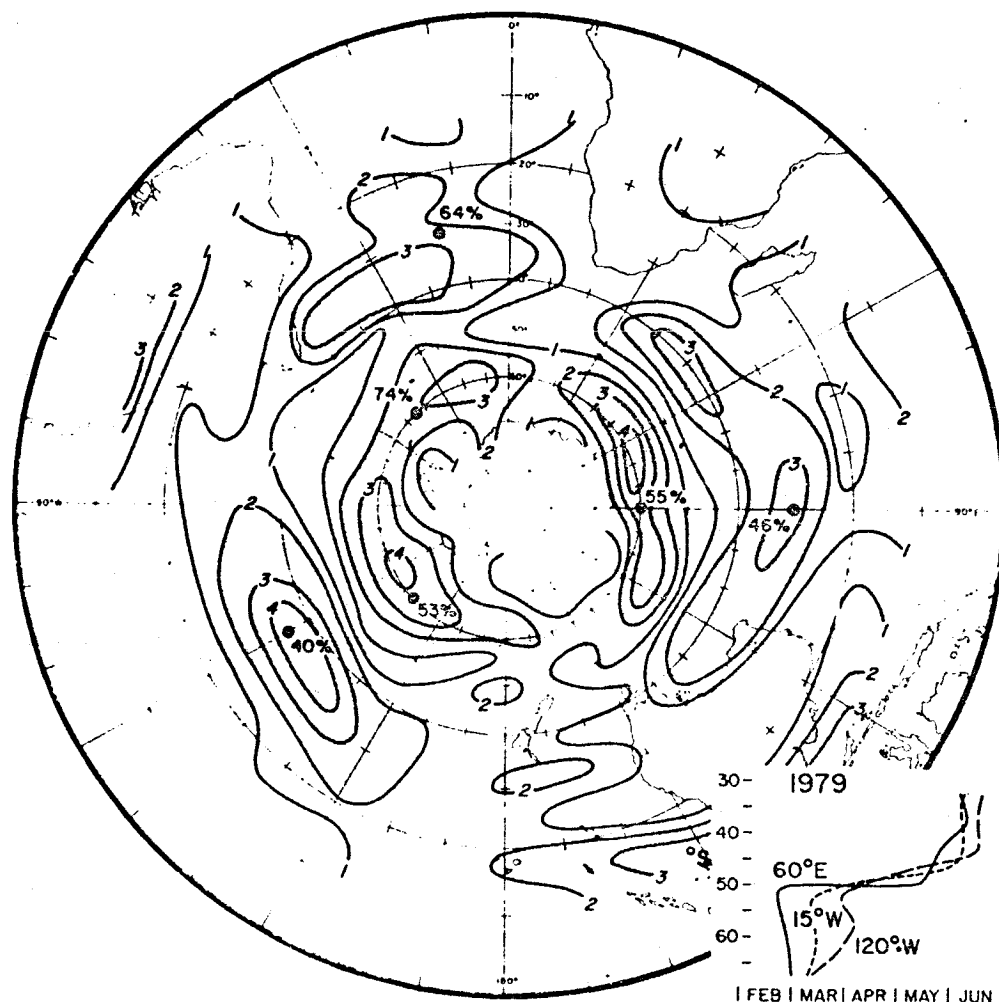
FIGURE 13 The half-yearly wave (amplitude, m/s) in the zonal
geostrophic wind at sea level in 1979. Inset shows phase (date of
first maximum) at three meridians. Percentages are some of the largest
percentages of the annual variance in 1979 explained by the half-yearly
wave (van Loon and Rogers, 1984a).

THE YEARLY AND HALF-YEARLY WAVES AT 500 MB

Geopotential Height

The long-term mean amplitudes of the two waves are shown in Figures 17
and 18; the station data are in Table 5 and the length of observation
in Table 4. South of about 25°S, the maximum of the first wave is in
February, over part of Antarctica it is in January; the second wave has

614
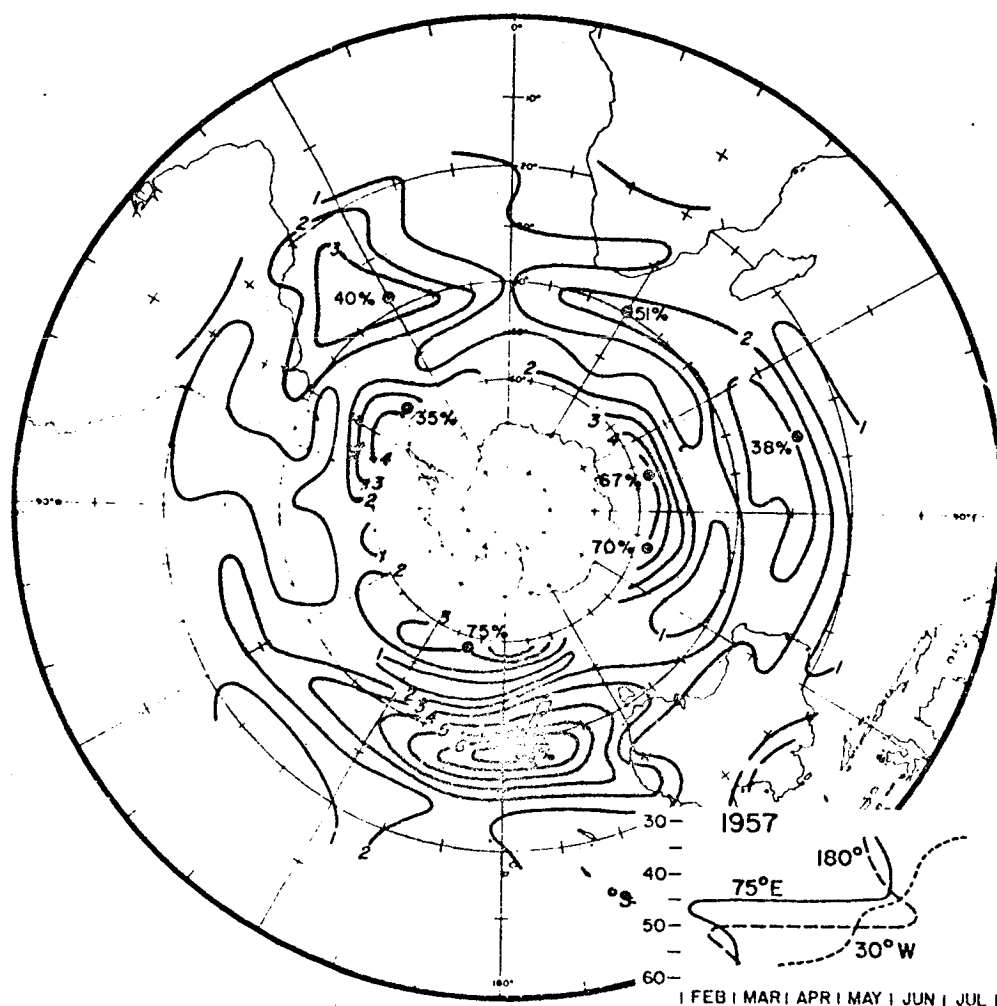
FIGURE 14 The half-yearly wave (amplitude, m/s) in the zonal geostrophic wind at sea level in 1957. Inset shows phase (date of first maximum) at three meridians. Percentages are some of the largest percentages of the annual variance in 1957 explained by the half-yearly wave (van Loon and Rogers, 1984a).

a similar opposition of phase as at sea level (Figure 6b)   The first maximum of the second wave at middle latitudes in FGGE is in February/March, and over Antarctica in December/January (Table 5), that is, somewhat earlier than at sea level. The change of phase between the two regions in FGGE is less than 180°, whereas at sea level the change in most longitudes is close to 180°. In the Antarctic (Table 5), the yearly wave in FGGE was larger than the mean and the half-yearly smaller (cf. Figures 18 and 19), owing to the low
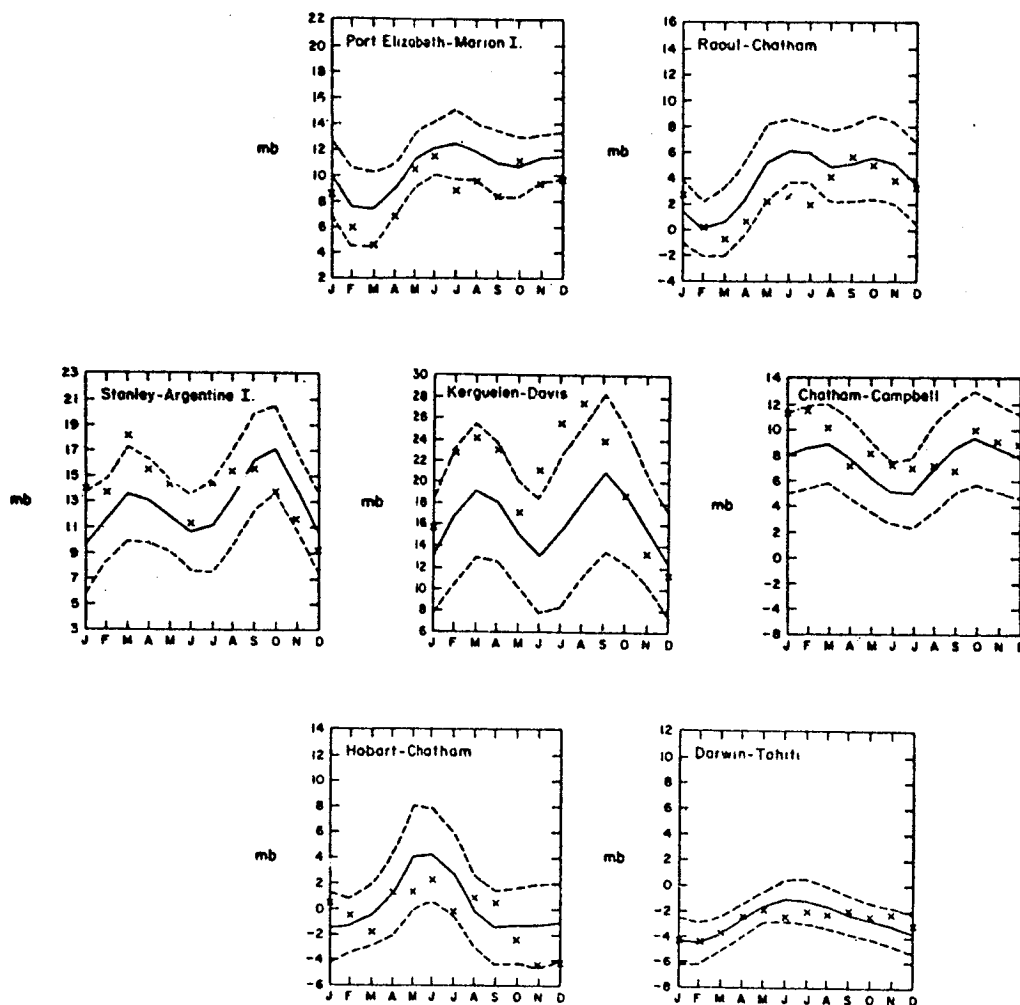
FIGURE 15 Three-month running means of sea level pressure differences: solid lines are long term means, dashed lines are one standard deviation on either side of the mean, crosses are three-month running means of the pressure differences in FGGE.

geopotential heights in winter (Figure 20). At most midlatitude stations, the heights were above normal during much of the colder part of the year, but apart from the central indian and Atlantic Oceans (Kerguelen and Gough in Table 5, Figure 19) the first and second harmonics were not much different from the mean. Unfortunately, the data for November and December 1979 were not available for the stations in the western Pacific (Campbell, Chatham, and Raoul) so a harmonic analysis could not be performed there; but a comparison between the half-yearly wave in 1979 (Figure 19) and the mean (Figure 18) suggests

TABLE 3 Sea Level Pressure Differences Yearly and Half-Yearly Waves

station	Climatology							FGGE						
	mean	a_1	ϕ_1	%	a_2	ϕ_2	%	mean	a_1	ϕ_1	%	a_2	ϕ_2	%
Kerguelen-Amsterdam	17.2	2.37	Sep 2	78	0.96	Jun 10	13	17.2	2.34	Jul 5	26	1.34	Jun 9	9
Raoul-Chatham	3.86	3.03	Aug 2	64	2.16	May 12	33	2.59	2.57	Sep 10	40	0.61	May 6	2
Agalega-St. Denis	-4.88	2.37	Feb 7	99	0.1	Feb 1	<1	-4.83	2.47	Jan 13	81	0.19	Feb 10	1
Cocos I-Amsterdam	-7.68	1.46	Sep 1	37	1.76	Jun 14	54	-7.75	1.88	Oct 2	18	3.17	May 2	50
Samoa-Raoul	-5.72	0.65	May 21	74	0.31	Jan 11	17	-5.6	0.68	Jun 9	4	2.12	Feb 3	41
Port Elizabeth-Marion I	10.13	1.93	Aug 13	39	2.15	Jun 24	48	8.82	1.89	Sep 12	1	3.04	Jun 3	25
Hobart-Macquaire	12.6	0.79	Jun 12	15	1.25	Apr 2	37	13.8	1.07	Feb 5	5	0.65	Jan 13	2
Chatham-Campbell	7.6	1.59	Dec 2	41	1.86	Mar 11	56	8.77	2.42	Jan 1	25	0.70	Jan 10	2
Port Stanley-Argentine I	7.3	0.22	Sep 5	23	3.8	Mar 11	65	5.7	0.2	Jul 13	5	6.7	Feb 10	56

617

Tahiti–Easter I	-7.48	1.47	Jun 9	88	0.23	May 3	2	-5.5	2.38	Jun 10	40	0.37	Mar 5	1
Easter I–Antofagasta	3.75	1.50	Dec 2	69	0.79	Feb 7	20	2.91	2.03	Jan 9	32	0.15	Feb 12	1
Hobart–Chatham	0.29	3.0	May 30	58	2.14	Jun 8	30	-0.23	1.78	Jun 12	11	0.81	Jul 1	3
Darwin–Tahiti	-2.76	1.71	Jul 1	88	0.56	May 14	1	-2.78	1.15	Jul 14	40	0.76	May 10	20
Gough–So. Georgia	17.04	1.82	Jan 3	86	0.09	Apr 9	<1	19.87	3.01	Sep 1	52	1.41	May 1	11
Kerguelen–Davis	16.42	1.15	Jan 12	7	4.27	Mar 4	89	18.16	2.67	Jun 9	9	6.43	Feb 11	52

618
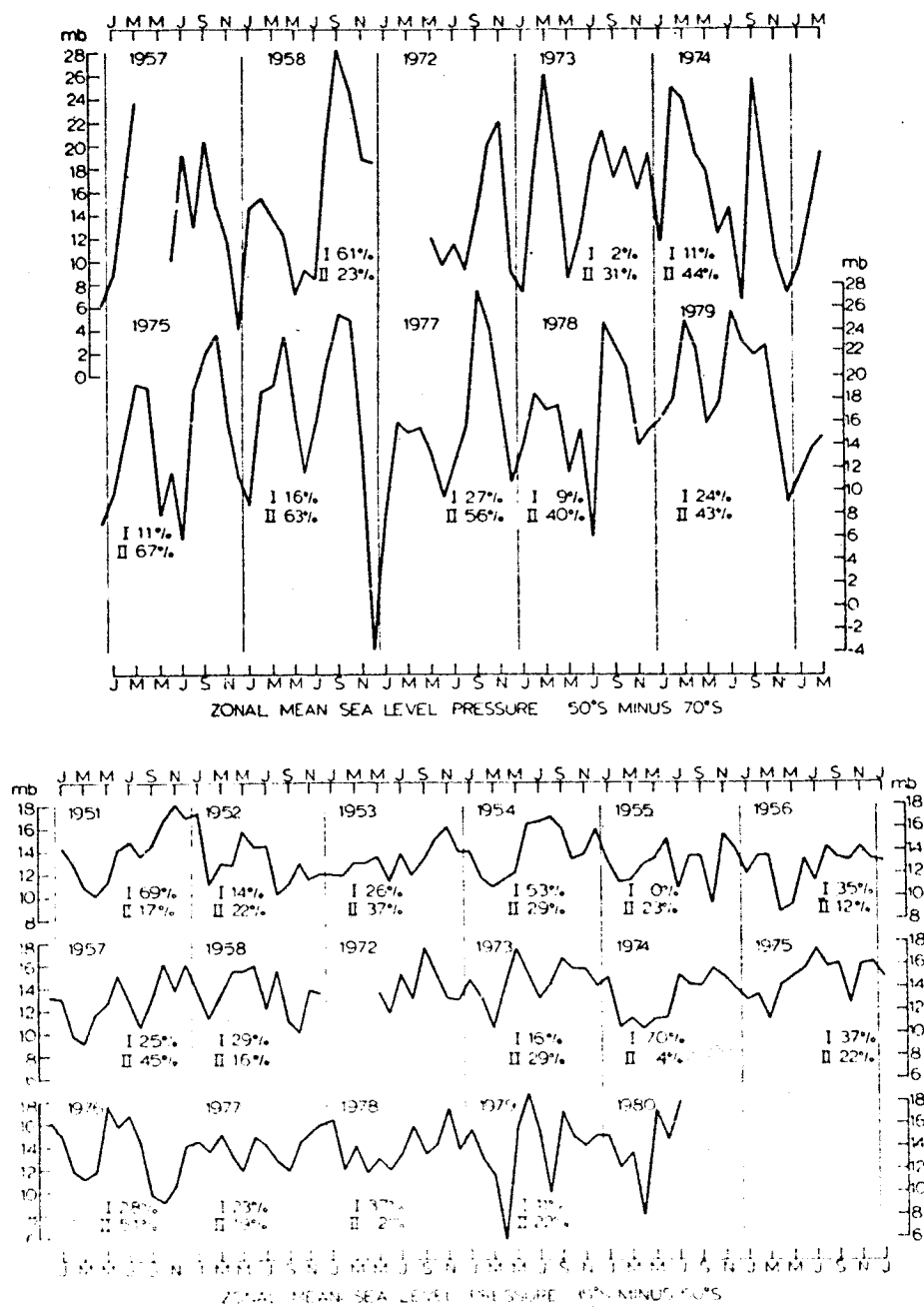
FIGURE 16 Differences in zonally averaged sea level pressure. I. The
percentage of the annual variance explained by the yearly wave in the
pressure difference. II. The percentage explained by the half-yearly
wave. (a) 50°S minus 70°S. (b) 35°S minus 50°S.
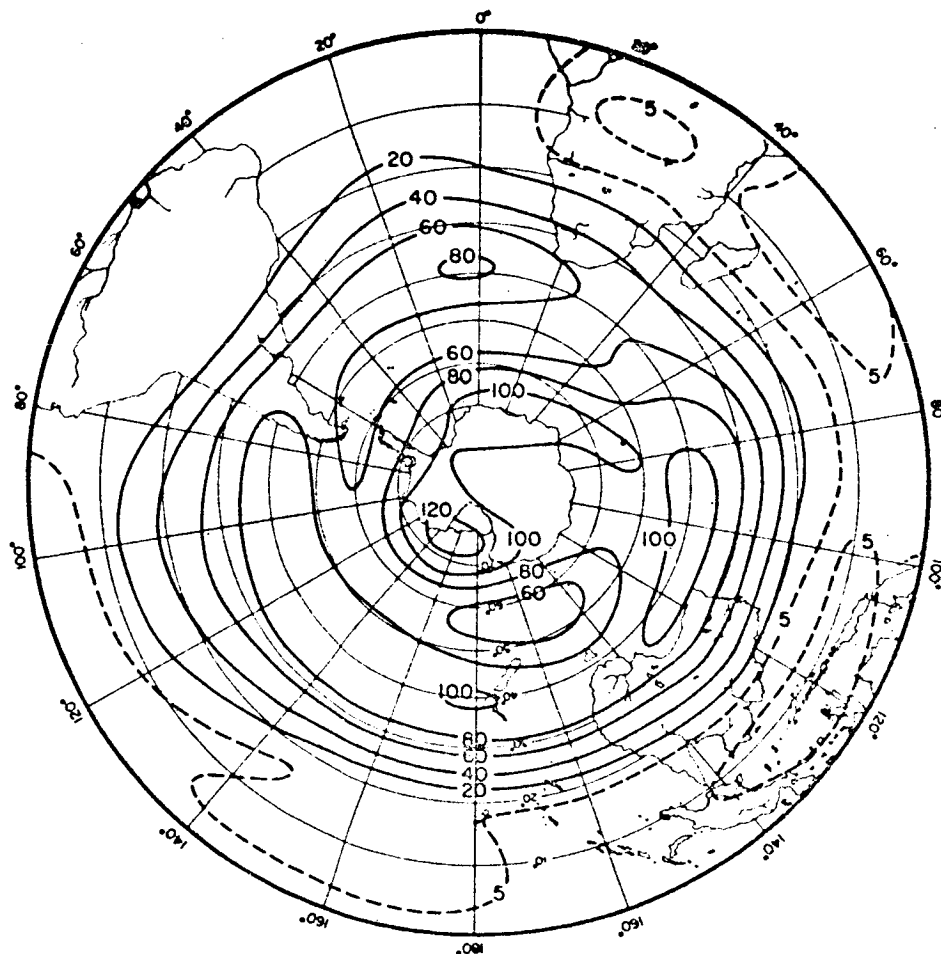
500 MB HEIGHT 1st HARMONIC, AMPLITUDE

FIGURE 17 Amplitude (m) of the yearly wave in the 500 mb mean height (van Loon, 1972).

that the wave was weaker than usual in the western and stronger in the central and eastern parts of the ocean.

Some north-south height differences are shown in Table 6 and Figure 21. Note in the table that the annual mean difference between Kerguelen and Davis was bigger in FGGE than in the mean, but that the amplitudes of the two waves were near normal, although their phase was three to four weeks early.

620
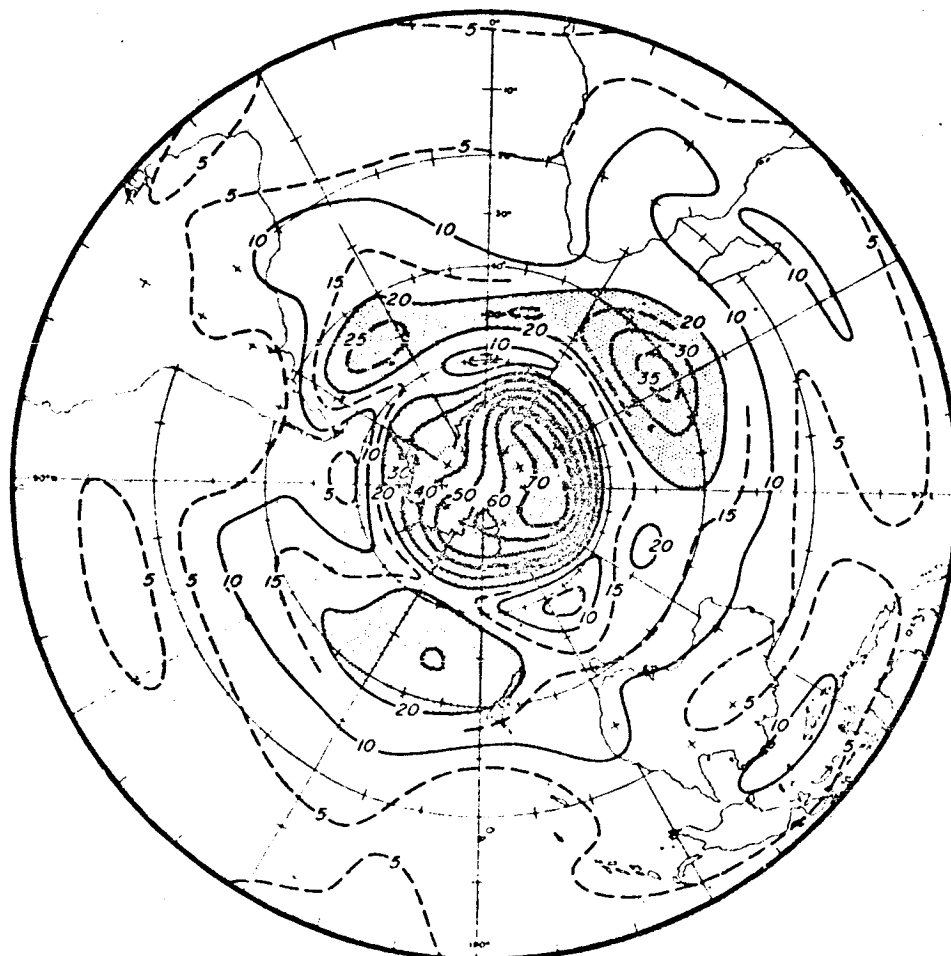
500 mb Ht, 2nd Harmonic, Amplitude

FIGURE 18   Amplitude (m) of the half yearly wave in the 500 mb mean
height (van Loon, 1972).

Temperature

The reader is referred to Figure 22 and Table 7 for the 500 mb
temperature data.   Note the high temperatures at Kerguelen ar.d Marion
in January, February, and March, which are responsible for the large
first harmonic.

The mean yearly and half-yearly waves in the zonally averaged
temperature are given in Figures 23 and 24, and those for FGGE in
Figure 25.   The phases in FGGE that are similar to those in Figures 23
and 24 are not shown.   The amplitude of the first harmonic is
unrealistically high in the FGGE data over the polar region abuve 500

TABLE 4 Upper Air Stations

New Amsterdam I	55-81		Noumea	59-81
Kerguelen	68-81		Samoa	66-81
Luanda	54-81		Tahiti	57-81
Alexander Bay	52-81		Rapa	69-81
Durban	52-81		Campbell	57-81
Port Elizabeth	54-81		Chatham	56-81
Gough I	57-81		Raoul	52-80
Marion	50-81		Darwin	50-81
Rio	67-81		Willis I	60-81
Antofagasta	57-81		Carnarvon	61-81
Quelimane	57-81		Port Hedland	50-81
Puerto Montt	57-81		Alice Springs	50-81
Argentine I	57-81		Hobart	50-81
SANAE	57-81		Mawson	55-81
Halley Bay	57-81		Lord Howe	55-81
Davis	59-81		Macquarie	50-81
Casey	58-81		Cocos I	53-81

mb, according to the archived temperature analyses in ECMWF, but
elsewhere the year is close to the mean, and the same holds true for
the second harmonic.

THE YEARLY AND HALF-YEARLY WAVES
IN THE ZONALLY AVERAGED GEOSTROPHIC WIND

The meridional vertical sections of the annual mean zonal component of
the geostrophic wind in Figure 26 shows that for the year as a whole
there was little difference between FGGE and the mean. The double
maximum is visible in both sections as far down as between 300 and 400
mb, and the peaks are only slightly stronger in FGGE. Note that the
subtropical peak lies closer to the equator in FGGE than in the mean,
25°S against 28°S.

   The mean yearly and half-yearly waves are shown in Figure 27, the
FGGE waves in Figure 28. The phases of the FGGE waves are similar to
those of the mean, and they are therefore not shown. The amplitude of
the yearly wave is a little stronger in FGGE than the mean, but the
distribution is similar. For instance, the two peaks with winter

TABLE 5 500 mb Heights Yearly and Half-Yearly Waves

station	Climatology							FGGE						
	mean	a_1	ϕ_1	%	a_2	ϕ_2	%	mean	a_1	ϕ_1	%	a_2	ϕ_2	%
New Amsterdam	5683	89.3	Feb 10	92	22.5	Feb 13	6	5710	64.7	Feb 9	69	37.2	Feb 4	23
Kerguelen	5381	84.8	Feb 13	89	26.5	Mar 7	9	5408	127.8	Feb 6	56	84.4	Feb 5	24
Durban	5817	37.4	Jan 10	91	10.9	Feb 13	8	5816	40.0	Feb 9	93	0.7	Feb 12	<1
Port Elizabeth	5775	51.5	Feb 9	95	10.3	Feb 4	4	5768	54.6	Feb 1	96	2.7	Jan 3	<1
Gough I	5620	82.9	Feb 9	95	17.6	Feb 15	4	5639	53.4	Jan 9	58	31.0	Feb 14	20
Marion I	5454	54.7	Mar 10	74	26.9	Mar 9	18	5482	69.9	Mar 1	67	22.6	Jan 10	7
Antofagasta	5846	26.4	Feb 9	99	2.4	Apr 13	1	5896	15.7	Feb 6	56	3.0	Jan 14	2
Quintero	5752	62.2	Feb 9	99	2.0	Feb 5	<1	5762	41.5	Feb 14	69	17.9	Jan 27	12
Puerto Montt	5625	83.8	Feb 12	99	8.8	Mar 7	1	5636	95.6	Feb 3	93	13.2	Jan 17	2
Argentine I	5121	59.3	Feb 1	85	23.1	Jan 22	13	5130	70.6	Feb 7	52	9.7	Dec 6	1
Halley Bay	5002	107.4	Jan 20	89	34.9	Jan 15	9	4975	123.8	Jan 2	89	8.9	Jan 21	<1
Davis	5000	87.8	Feb 15	70	52.7	Jan 16	25	4967	129.6	Jan 3	81	36.7	Dec 5	7
Mawson	5003	116.2	Feb 13	86	42.3	Dec 10	12	4974	141.8	Jan 7	88	33.9	Dec 15	5
Casey	5020	95.9	Jan 20	73	56.8	Dec 4	26	4995	124.6	Jan 1	83	40.4	Dec 5	9
Noumea	5827	24.2	Feb 8	97	3.5	Mar 7	2	5822	26.6	Feb 13	61	8.6	Apr 4	6
Samoa	5871	10.4	Jun 11	87	2.9	Apr 9	7	5880	12.6	Jul 15	88	0.9	Dec 13	<1
Darwin	5855	4.8	Jul 4	36	6.3	Apr 13	62	5811	8.9	Jul 9	39	9.6	Apr 3	45

Carnarvon	5797	50.4	Feb 12 97	8.3	Mar 12 3	5797	51.7	Feb 13 67	7.4	Mar 3 2
Port Hedland	5833	21.8	Jan 15 93	3.9	Apr 12 3	5829	25.1	Jan 12 60	8.7	Apr 6 7
Alice Springs	5824	42.4	Jan 21 97	6.4	Apr 13 2	5822	38.7	Jan 5 78	14.2	Mar 12 11
Hobart	5589	88.9	Feb 2 96	14.6	Feb 14 3	5592	91.9	Feb 4 87	16.1	Jan 1 3
Lord Howe	5718	84.1	Feb 14 97	10.5	Mar 2 2	5728	72.3	Feb 8 73	3.3	Jan 8 <1
Macquarie	5352	53.8	Feb 10 83	22.1	Jan 9 14	5351	57.8	May 10 49	14.2	May 5 3
Cocos Island	5846	2.2	Jun 13 18	4.4	Apr 9 74	5845	2.9	Aug 3 8	6.7	May 4 44

SOUTHERN HEMISPHERE

a₂ 500mb 1979
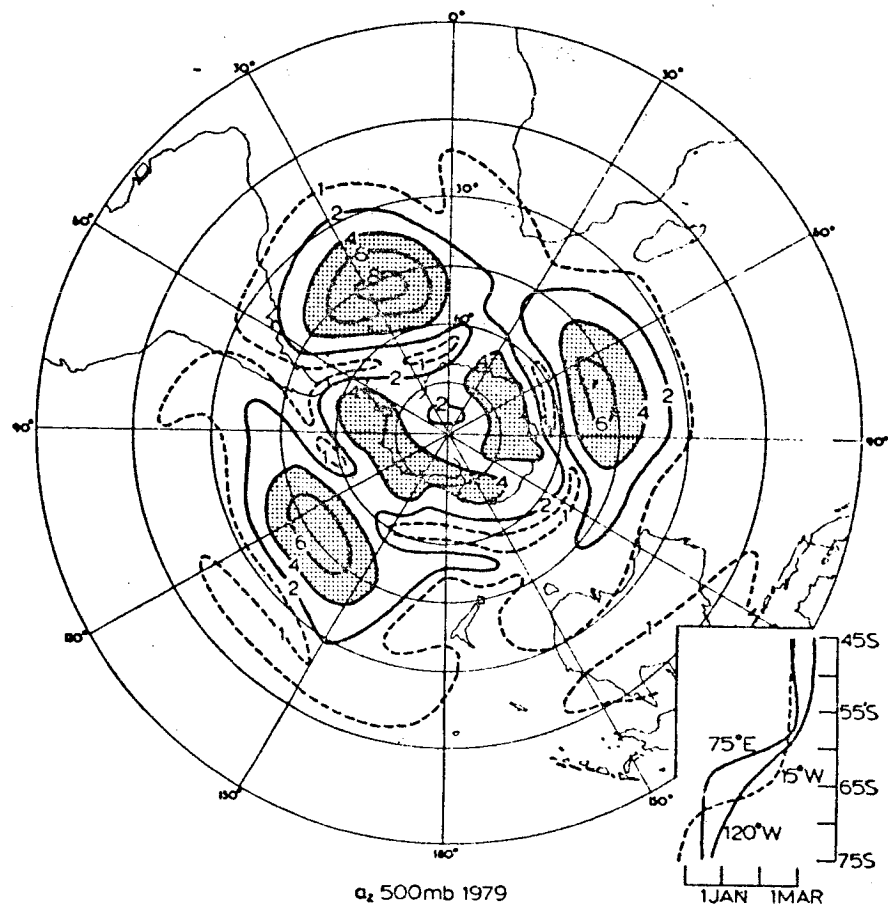
FIGURE 19 Amplitude (dkm) of the half-yearly wave in the 500 mb height
of 1979. Inset shows the phase (date of first maximum) at three
meridians (van Loon and Rogers, 1981b).

maximum in the tropics and the sub-Antarctic are separated by the peak
in middle latitudes with a maximum in summer.

The half-yearly wave in the sub-Antarctic with equinoctial maxima
lies $3°$ to $4°N$ of the mean position in FGGE and is weaker than the
mean. The tropical peak, about $15°S$, with maxima in May and November
does not reach so far down in FGGE as in the mean.
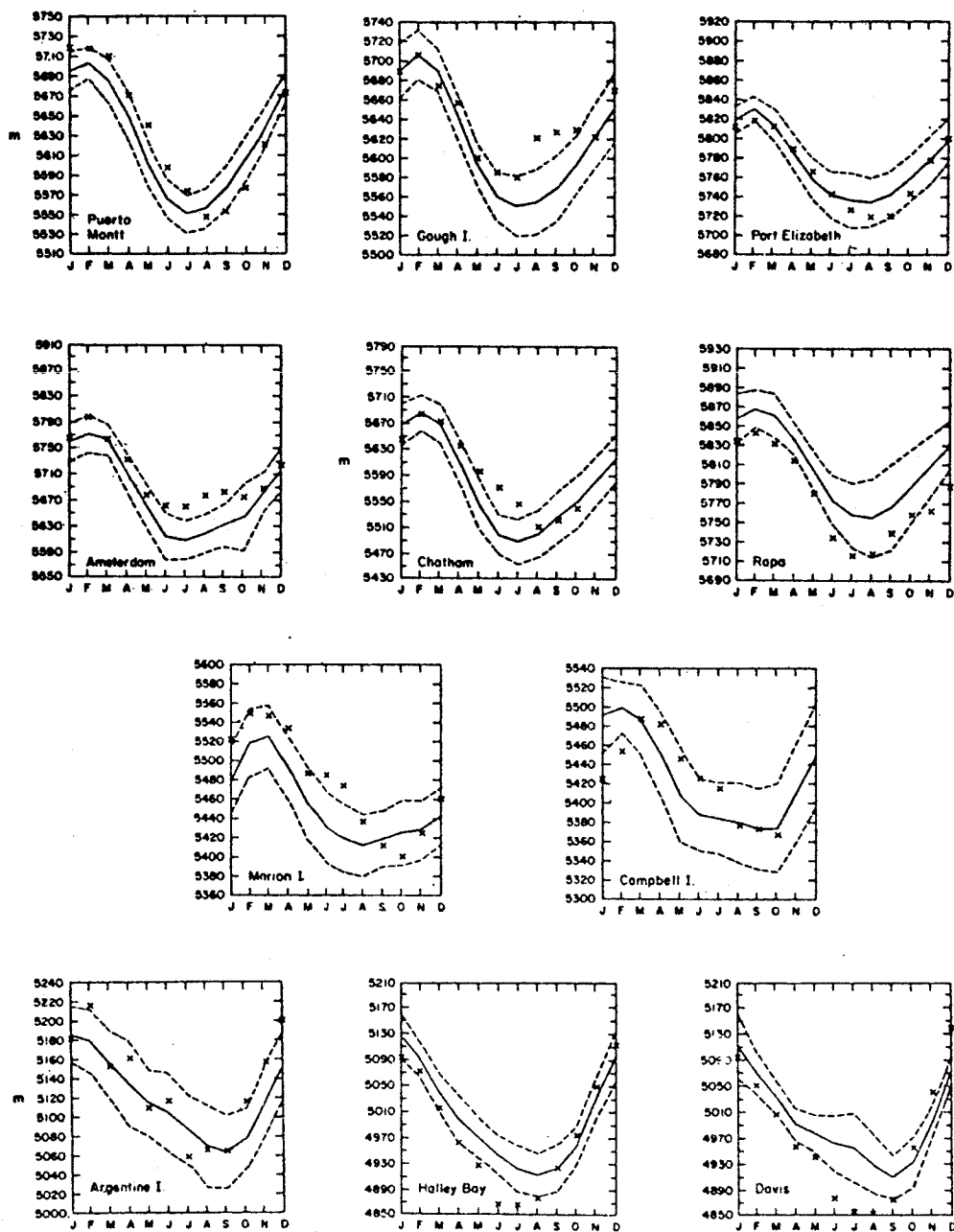
FIGURE 20 Three-month running means of 500 mb heights (m). Solid lines are long term means, crosses are 1979 values, and dashed lines are one three-month standard deviation on either side of the mean.

TABLE 6 500 mb Height Differences (m) Yearly and Half-Yearly Waves

station	Climatology							FGGE						
	mean	a_1	ϕ_1	%	a_2	ϕ_2	%	mean	a_1	ϕ_1	%	a_2	ϕ_2	%
Cocos Island-New Amsterdam	164.7	88.7	Jul 20	92	23.3	May 8	6	135.0	67.5	Aug 7	64	43.9	May 4	27
New Amsterdam-Kerguelen	316.5	33.2	Nov 8	77	16	Jun 2	18	302.1	63.1	Aug 5	34	50.1	May 10	22
Kerguelen-Davis	362.2	44.3	Jun 5	15	100	Mar 6	76	441.0	49.1	May 16	12	106.0	Feb 5	59
Port Elizabeth-Marion	321.1	25.7	Nov 13	54	16.5	Jun 2	23	285.6	36.2	Nov 10	35	20.3	Apr 11	11
Hobart-Macquarie	238.1	38.1	Feb 9	65	21.3	Apr 10	20	241.4	56.3	Jan 4	37	25.5	Feb 14	7

FIGURE 21 Three-month running means of 500 mb height differences (m). Solid lines are long term means, crosses are 1979 values, and dashed lines are one three-month standard deviation on either side of the mean.
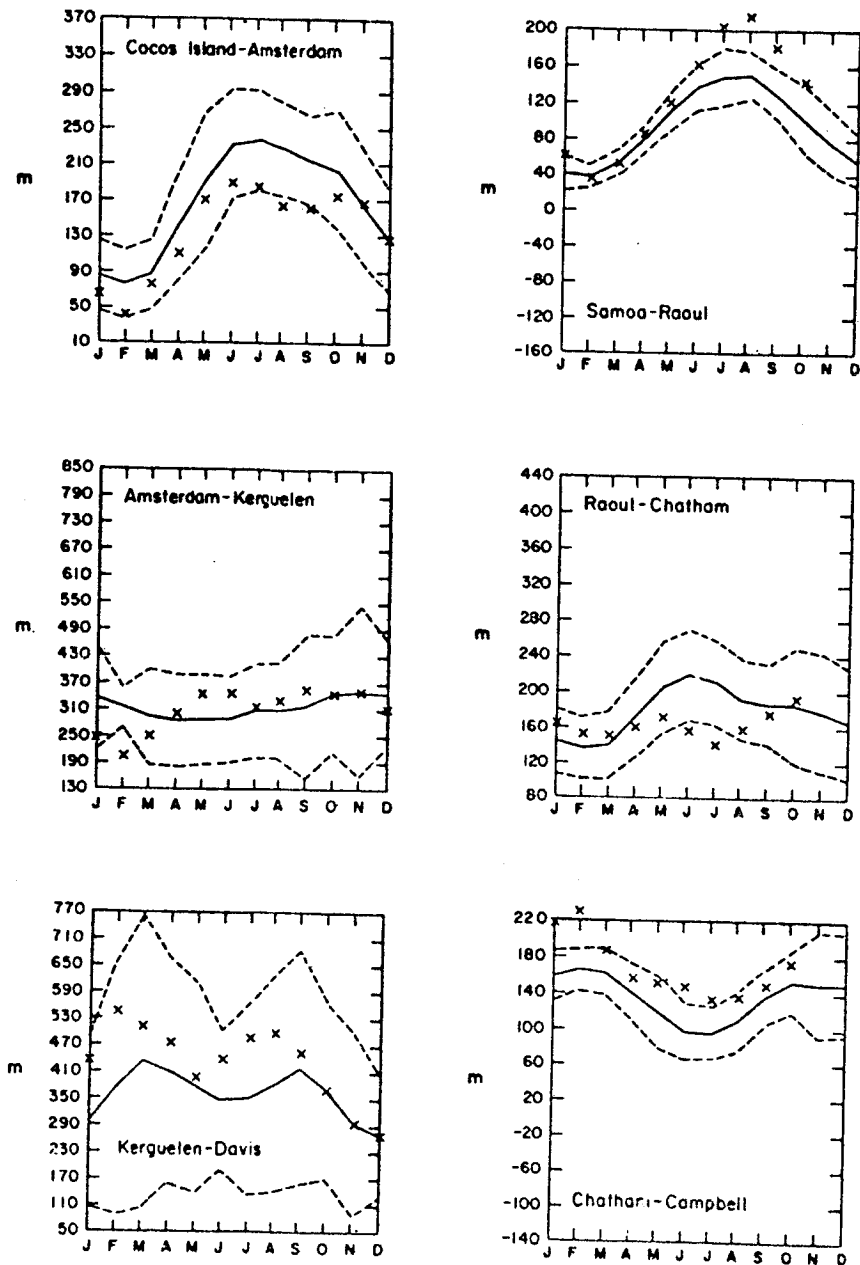
TABLE 7 500 mb Temperature Yearly and Half-Yearly Waves

station	Climatology							FGGE						
	mean	a_1	ϕ_1	%	a_2	ϕ_2	%	mean	a_1	ϕ_1	%	a_2	ϕ_2	%
New Amsterdam	-16.0	4.89	Jan 15	99	0.44	Mar 6	<1	-15.1	4.15	Feb 13	94	0.43	Feb 5	1
Kerguelen	-23.8	4.06	Feb 2	97	0.64	Mar 15	2	-22.8	5.66	Feb 1	75	0.29	Feb 3	20
Durban	-11.1	3.68	Jan 7	97	0.62	Feb 10	3	-11.1	3.39	Jan 6	95	0.24	Mar 7	<1
Port Elizabeth	-12.6	4.07	Jan 10	98	0.53	Feb 8	2	-13.1	4.23	Jan 12	97	0.30	Mar 4	<1
Gough	-17.9	4.61	Feb 9	98	0.55	Feb 1	1	-17.5	3.78	Feb 6	85	0.33	Feb 1	<1
Antofagasta	-8.3	2.91	Jan 13	99	0.21	Feb 6	<1	-8.0	2.37	Jan 12	86	0.12	Mar 9	<1
Quintero	-14.3	4.12	Feb 10	99	0.29	Feb 10	<1	-13.7	3.56	Feb 9	77	1.24	Jan 1	9
Puerto Montt	-19.8	4.61	Feb 9	99	0.35	Feb 7	<1	-18.9	5.09	Feb 3	92	0.89	Jan 7	3
Argentine I	-32.3	3.42	Feb 10	99	0.25	Jan 2	<1	-31.9	4.28	Feb 9	92	0.24	Feb 2	<1
Halley Bay	-36.4	4.19	Jan 6	98	0.46	Jan 9	1	-36.4	4.72	Jan 13	92	0.28	Feb 13	<1
Casey	-34.7	3.92	Jan 13	91	1.22	Dec 13	9	-34.4	4.61	Jan 2	87	1.46	Jun 1	9
Noumea	-7.0	2.08	Feb 2	95	0.47	Feb 6	5	-7.5	1.93	Feb 6	84	0.54	Feb 1	6
Samoa	-5.5	0.51	Feb 1	86	0.19	Dec 13	13	-5.1	0.32	Jan 19	16	0.49	Jun 13	39
Darwin	-5.5	0.55	Mar 4	83	0.20	Mar 3	11	-5.2	0.61	Mar 3	57	0.29	Jun 4	13
Carnarvon	-10.2	2.36	Feb 14	84	1.03	Feb 1	16	-10.5	3.54	Feb 14	82	0.75	Feb 7	4
Port Hedland	-7.5	0.97	Feb 1	61	0.75	Feb 2	36	-7.8	1.16	Feb 11	50	0.66	Feb 4	16
Alice Springs	-9.7	2.45	Feb 6	89	0.82	Feb 6	10	-9.8	2.99	Feb 3	78	1.15	Feb 3	12
Hobart	-20.2	5.35	Feb 14	99	0.46	Mar 10	<1	-20.4	5.59	Jan 13	95	0.82	Jan 13	2

629

Mawson	-35.6	4.32	Jan 10	89	1.41	Jan 9	10	-36.0	5.69	Jan 6	89	1.03	Nov 5	3
Lord Howe	-14.9	5.28	Feb 15	99	0.53	Mar 10	1	-15.2	5.02	Feb 14	91	0.21	Mar 13	<1
Macquarie	-25.6	3.71	Feb 9	99	0.24	Feb 2	<1	-25.2	3.69	Feb 1	88	0.29	May 4	<1
Cocos Island	-5.7	0.12	Mar 10	31	0.95	Apr 6	20	-5.5	0.26	Sep 9	13	0.27	Jun 6	15
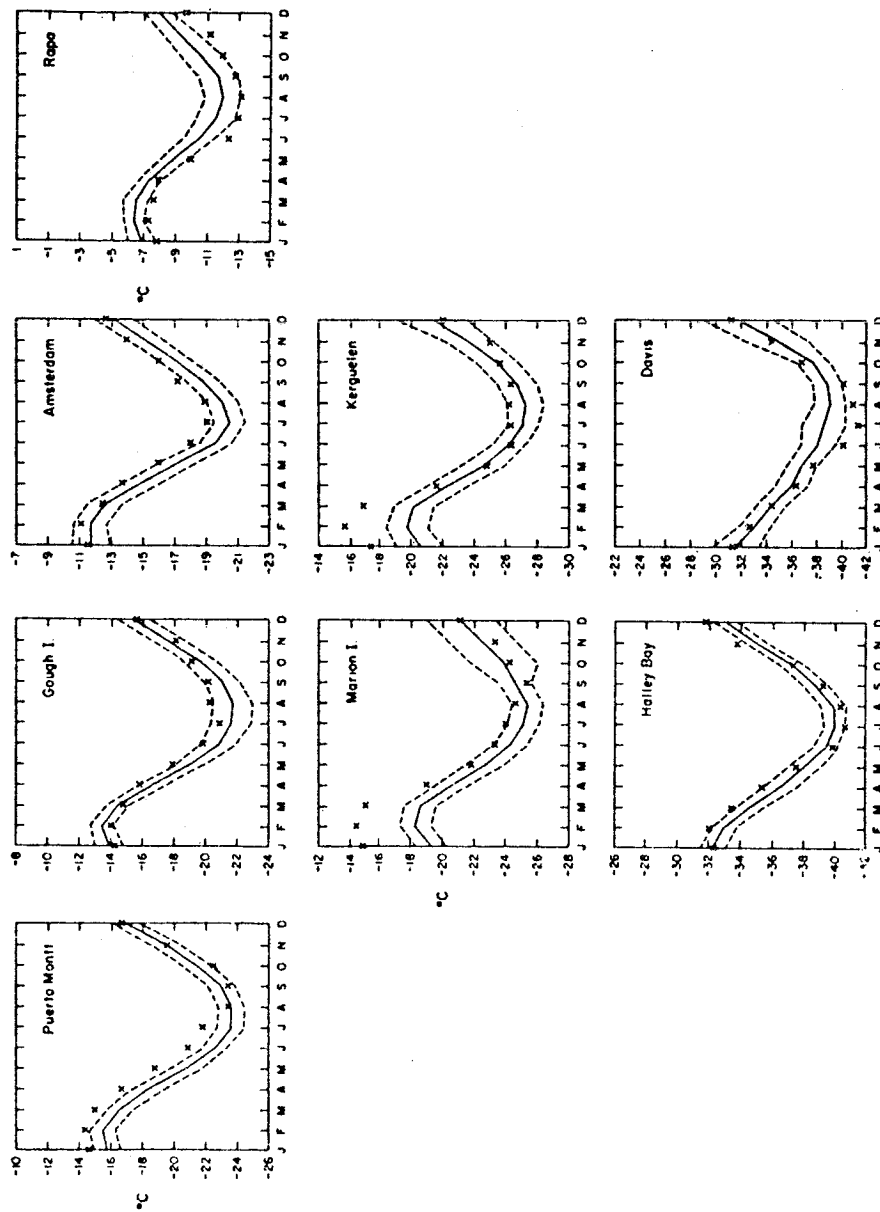
FIGURE 22 Three-month running means of 500 mb temperature (°C). Solid lines are long term means, crosses are 1979 values, and dashed lines are one three-month standard deviation on either side of the mean.

631
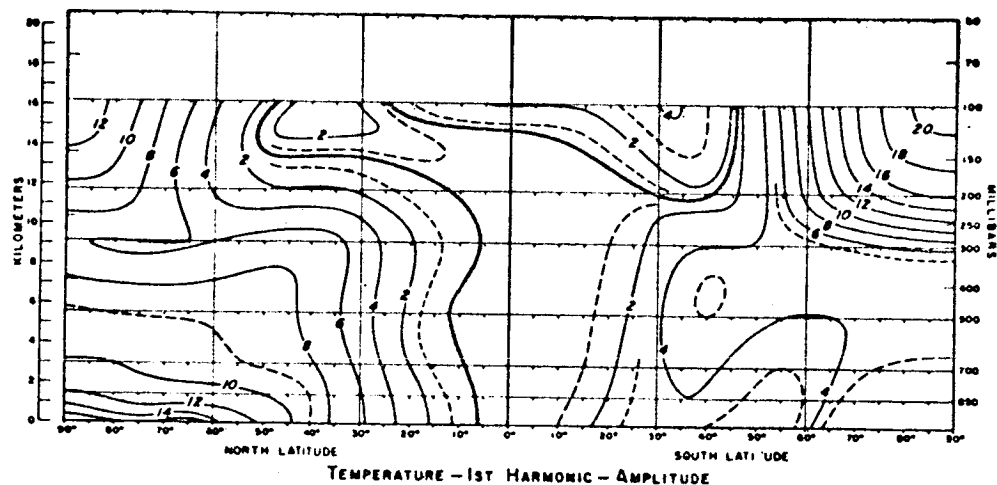
TEMPERATURE – 1ST HARMONIC – AMPLITUDE
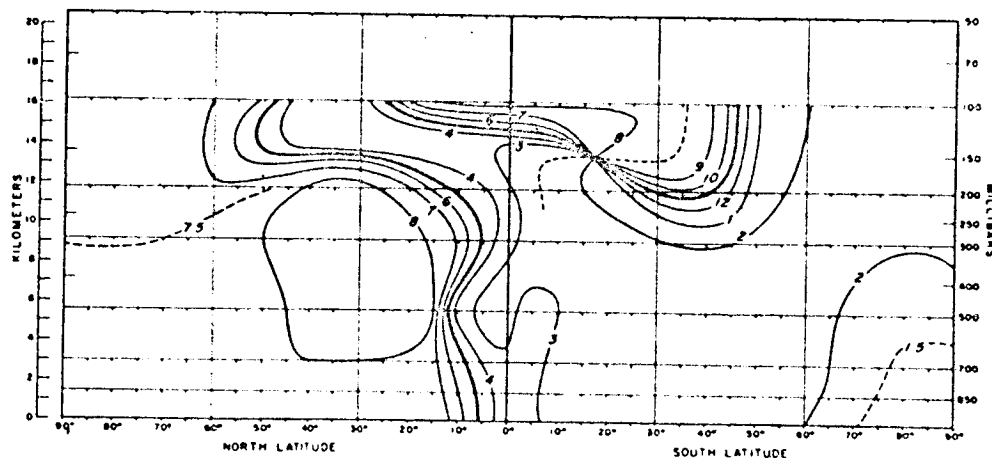
TEMPERATURE – 1ST HARMONIC – PHASE (MONTH)

FIGURE 23   Yearly wave in the zonally averaged temperature,
(a) amplitude (°C), (b) phase (date of maximum) (from van Loon, 1974).

THE QUASI-STATIONARY WAVES

The quasi-stationary waves in the following have been computed for
three-month mean 500 mb height fields (Figure 29) and SLP (Figure 30)
and are shown as running means: January is the mean of December,
January, and February, and so on.   In addition to the mean waves based
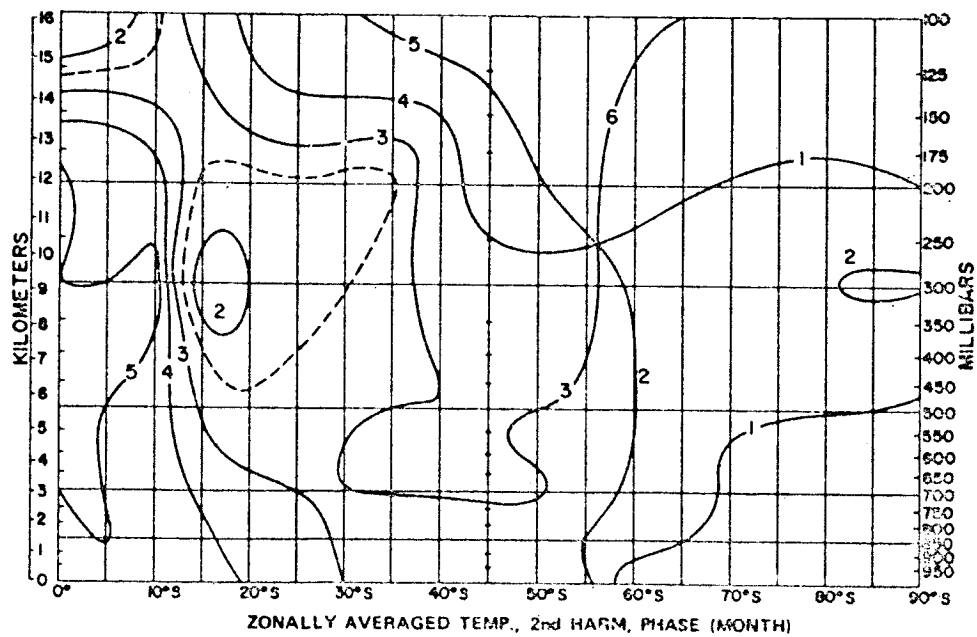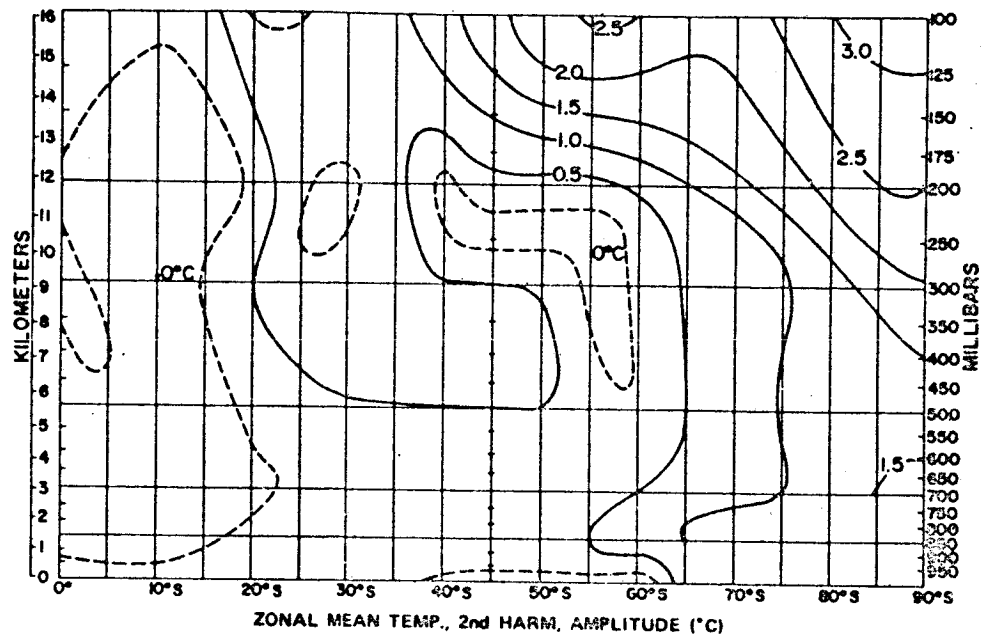
FIGURE 24 Half-yearly wave in the zonally averaged temperature, (a) amplitude ($^{\circ}$C), (b) phase (date of first maximum) (from van Loon, 1972).
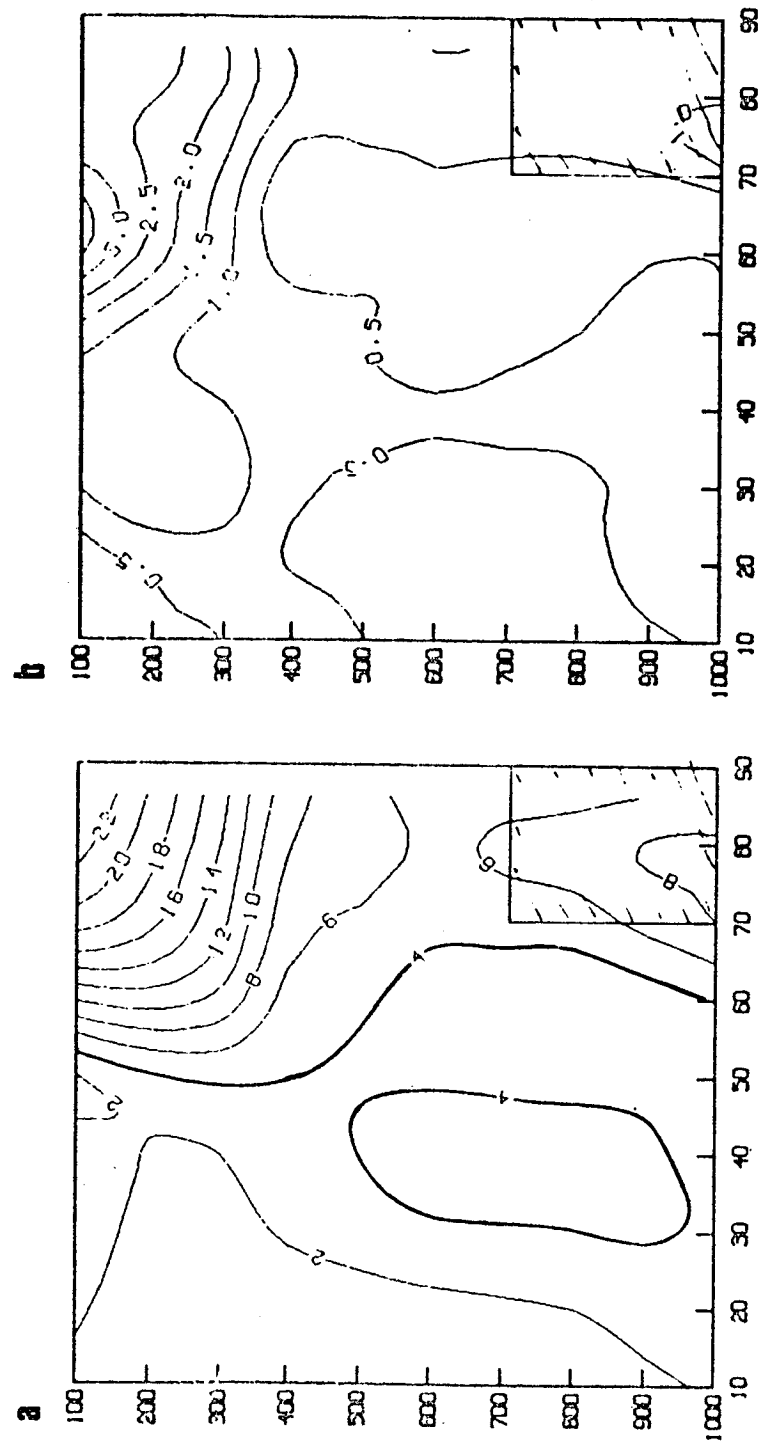
FIGURE 25 Amplitude (°C) in the zonally averaged temperature in FGGE (a) of the yearly wave, (b) of the half-yearly wave.

a
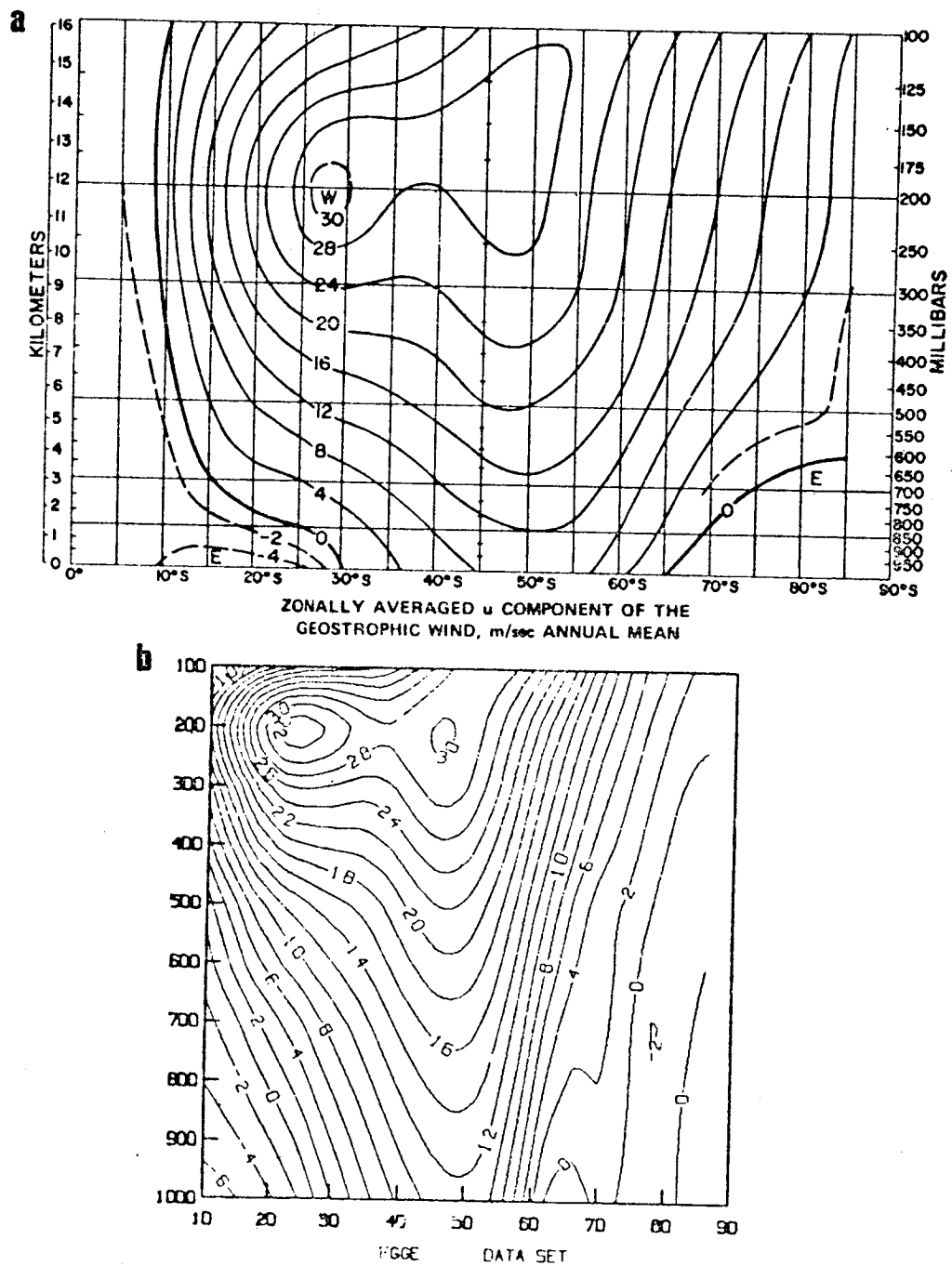
FIGURE 26   Zonally averaged geostrophic wind (m/s).   (a) Long term annual mean (van Loon et al., 1968), (b) FGGE, annual mean.
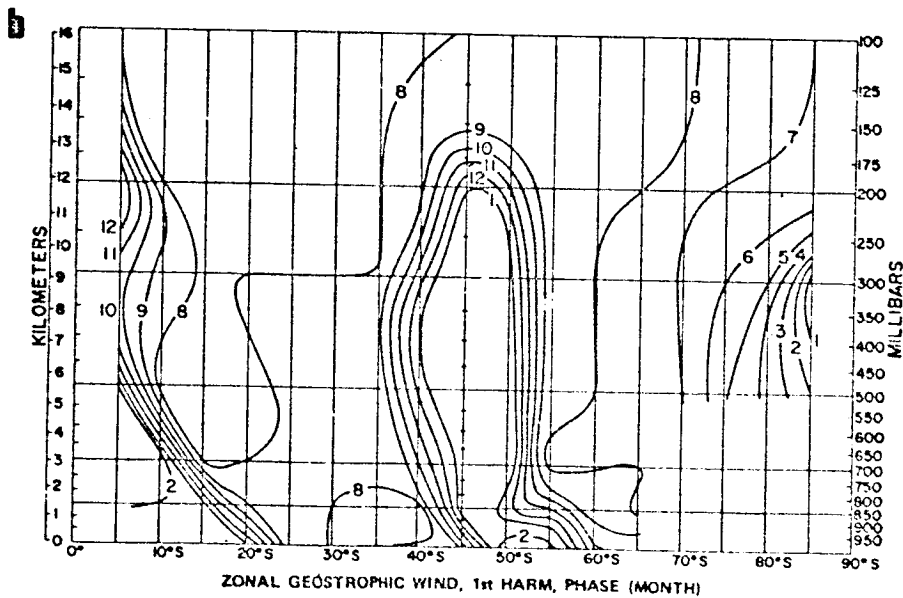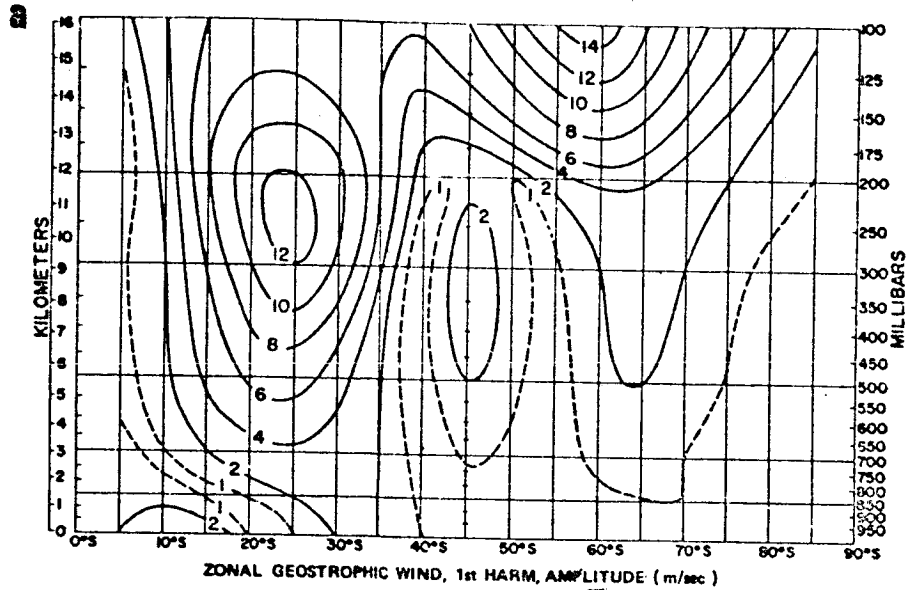
FIGURE 27 (a) Amplitude (m/s) of the mean yearly wave in the zonal mean geostrophic wind. (b) Phase (date of maximum). (c) Amplitude (m/s) of the mean half-yearly wave in the zonal mean geostrophic wind. (d) Phase (date of first maximum). From van Loon, 1972.

ZONAL GEOSTROPHIC WIND, 2nd HARM, AMPLITUDE (m/sec)

ZONAL GEOSTROPHIC WIND, 2nd HARM, PHASE (MONTH)

FIGURE 27 continued

FIGURE 28 Amplitude (m/s) in the zonal mean geostrophic wind in FGGE (a) of the yearly wave, (b) of the half-yearly wave.

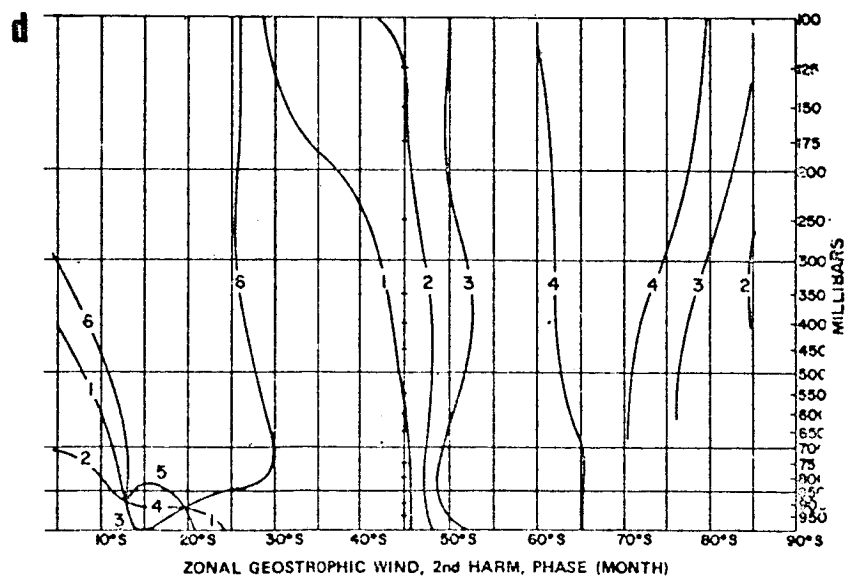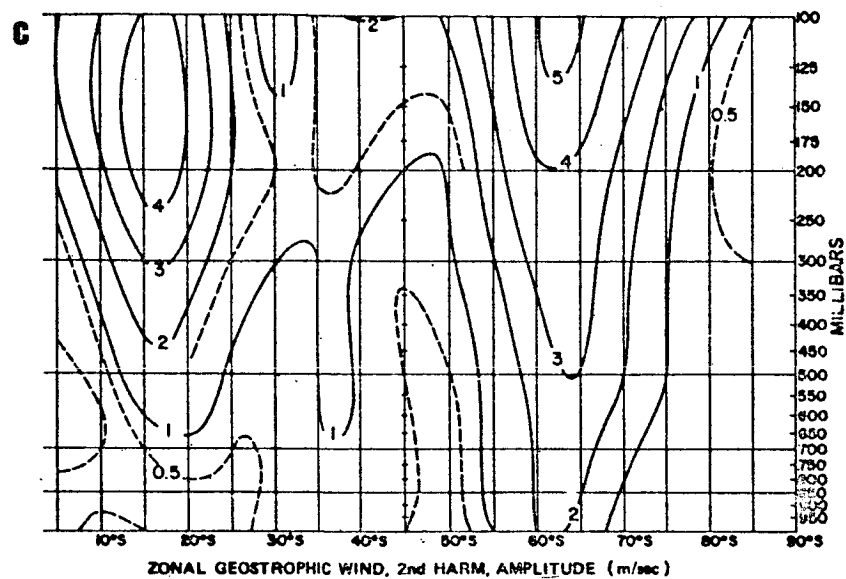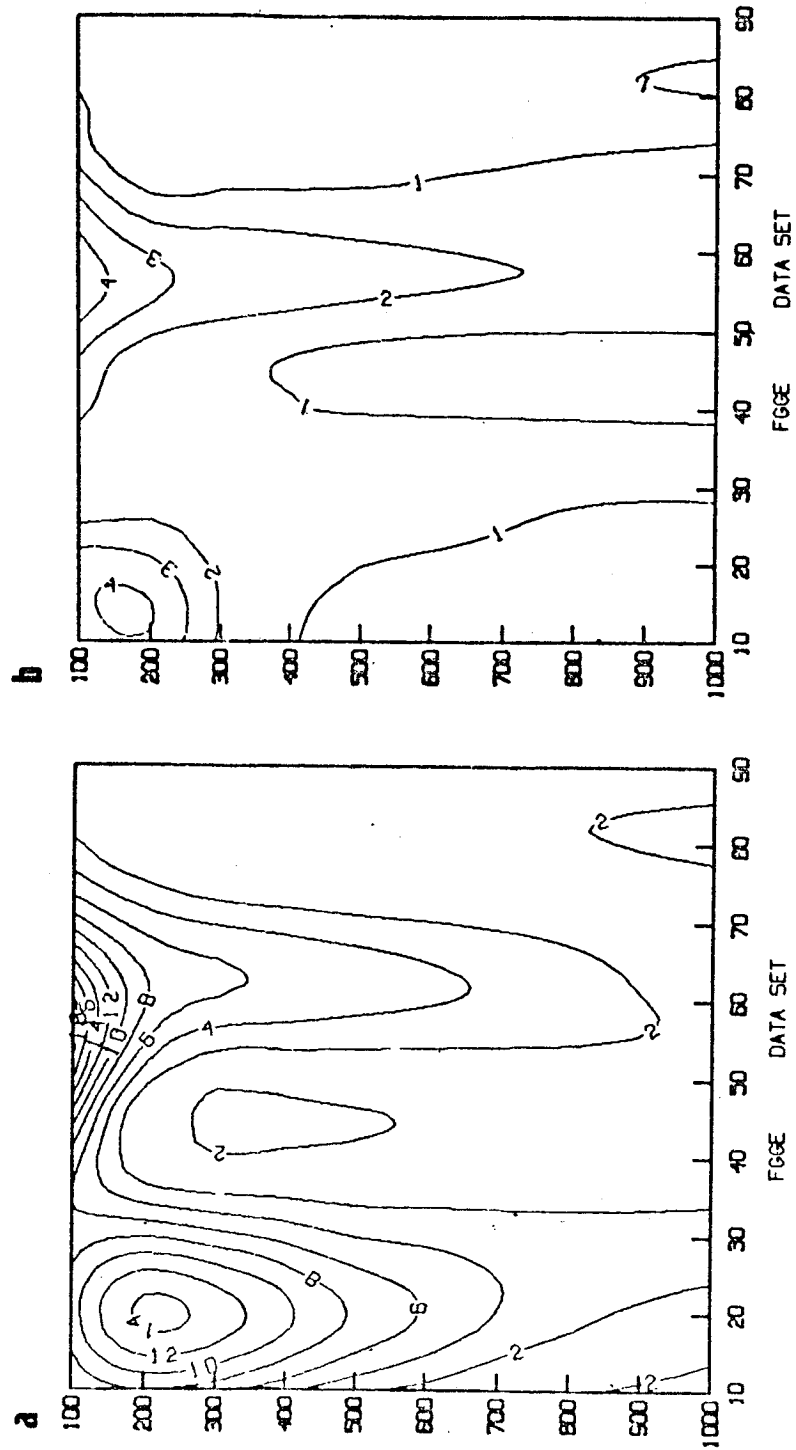on the Australian data (1972-1980), without FGGE) and the waves in FGGE, the waves in SLP for the International Geophysical Year are also shown.

It is immediately apparent that, except for wave 4 at sea level, the stationary waves are larger in FGGE than in the other data sets, but that the distribution of the peaks is fairly similar to that of the mean. The difference between FGGE and the other periods is biggest south of 45°S.

The phases of the peaks of the first three waves at 500 mb in FGGE and in the mean can be compared in Table 8 for single months. The location of the largest amplitude of wave 1 in the 8-year mean ranges over 8° latitude, from 54°S in summer to 62°S in winter. The range in FGGE was larger, 12° latitude, and did not have the gradual north-to-south movement of the mean. The mean wave moves east and west twice in the year, covering 30° longitude (11 percent of the wavelength), whereas in FGGE it changes irregularly from month to month over 78° longitude (22 percent of wavelength). The mean amplitude is smallest in February, 64 m, and biggest in September, 104 m. September in FGGE has the biggest amplitude as well, 143 m, but the smallest, 64 m, is found in three different months.

Wave 2's two average peaks are in the latitudes from 50° to 58°S and 74° to 78°S; the latitude was considerably more variable in FGGE than in the mean: 24° and 16° latitude, respectively (Table 8), and so was the longitude whose normal intra-annual variation is 22 to 24 percent of the wavelength, but in FGGE was 49 to 52 percent.

The mean amplitude range of wave 3 is 29 m, in FGGE it was 75 m (Table 8). The wave's range of latitude in FGGE was normal, 20° latitude; the intra-annual range of its longitude is normally 48 percent of the wavelength; in FGGE, it was somewhat larger: 57 percent, but the wave described its usual westward movement from the end of the southern summer to the beginning of winter, and consequent eastward movement from winter to spring (van Loon and Rogers, 1984a). It must be kept in mind that a monthly mean zonal harmonic wave in a given year is likely to contain an appreciable transient component unlike a three-month mean wave.

CONCLUSION

The dominant component in the mean annual cycle of sea level pressure in the latitudes north of ~40°S is the yearly wave, whereas to the south of this latitude a half-yearly wave dominates. In FGGE however, the usually small yearly wave was large in the Antarctic, owing to the extraordinarily low pressure there in the winter of 1979. The half-yearly wave's amplitude was appreciably above normal in the center of each ocean in middle latitudes and below normal at high latitudes. The yearly wave in the zonal geostrophic wind was larger than normal over the Antarctic Ocean. Similar results are obtained at 500 mb.

The three-month mean stationary waves (zonal harmonic waves) were larger than the mean in FGGE. The intra-annual variation of both

FIGURE 29 Three-month running means of the amplitudes (m) of the first four zonal harmonic waves in FGGE and in the eight-year mean Australian data.
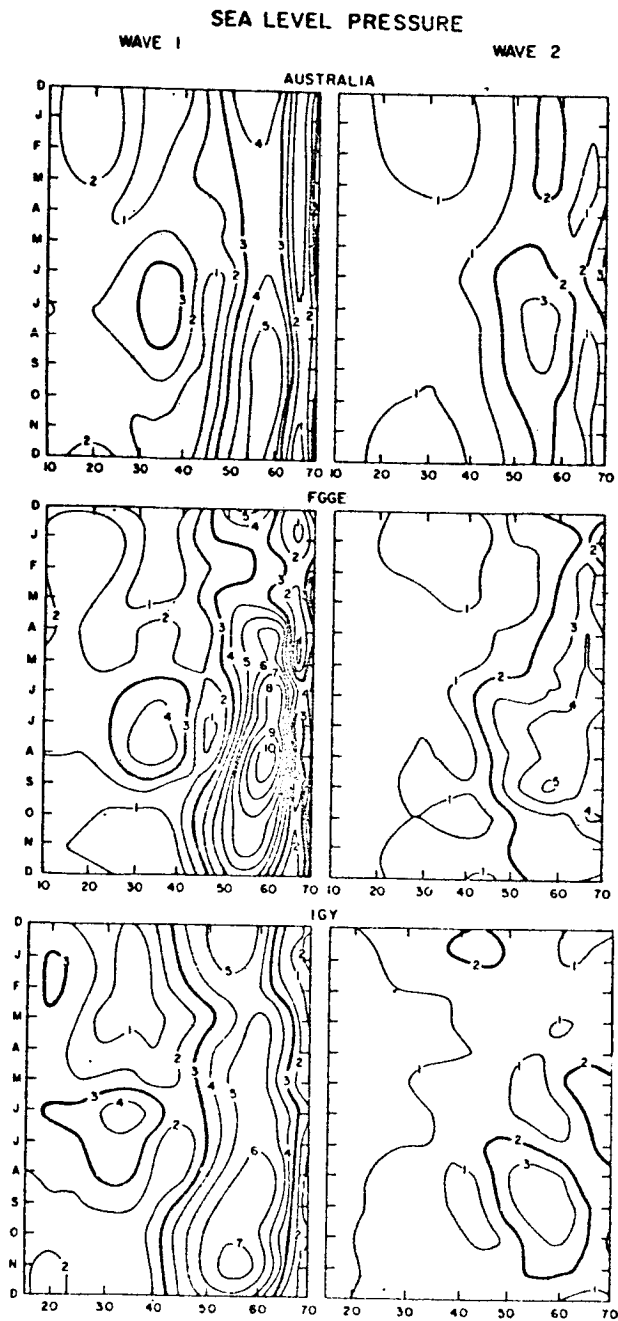
SEA LEVEL PRESSURE

FIGURE 30   Three-month running means of the amplitudes (mb) in the
Australian eight-year means, FGGE, and IGY (a) of waves 1 and 2,
(b) waves 3 and 4.

641

SEA LEVEL PRESSURE

WAVE 3   WAVE 4
AUSTRALIA

FGGE

IGY
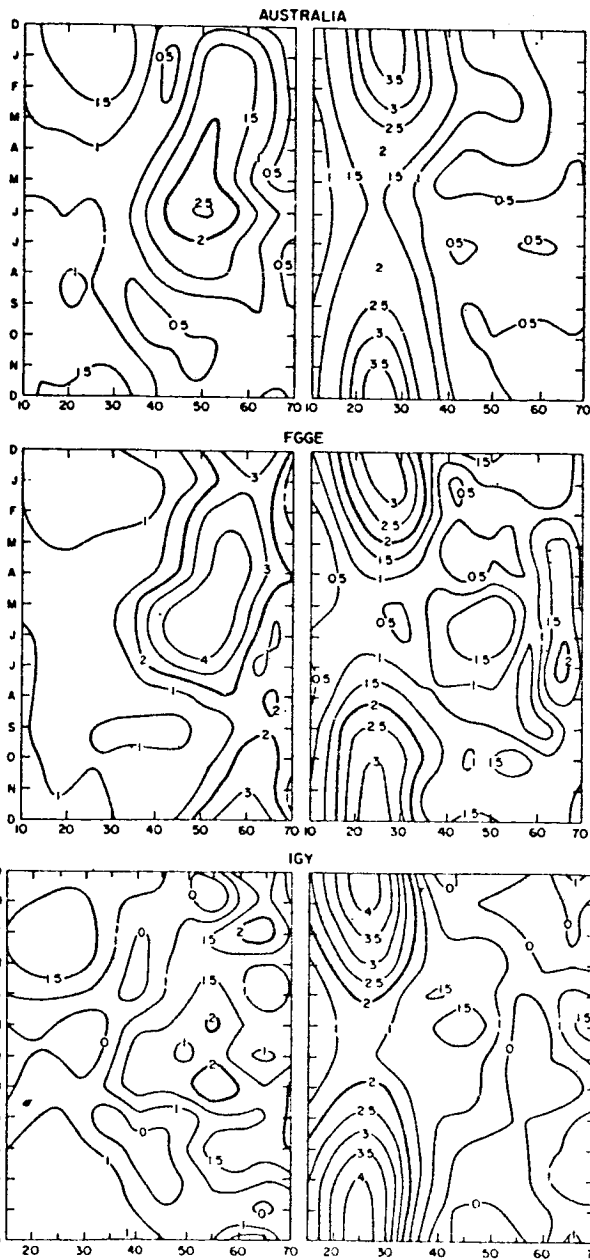
FIGURE 30 continued

251<

TABLE 8 (a) Wave Number 1 500 mb, (b) Wave Number 2 500 mb, (c) Wave Number 3 500 mb

Month	8-year mean (Australia)		FGGE	
	Max Amp. (m)	Location	Max Amp. (m)	Location
1	77	54S, 137W	64	54S, 90W
2	64	54S, 137W	64	50S, 163W
3	78	58S, 124W	73	58S, 112W
4	85	58S, 133W	96	54S, 143W
5	68	62S, 109W	131	62S, 104W
6	74	62S, 118W	64	58S, 123W
7	89	62S, 125W	115	62S, 115W
8	96	62S, 126W	127	62S, 132W
9	104	62S, 109W	143	58S, 112W
10	91	58S, 98W	110	54S, 120W
11	83	58S, 115W	89	54S, 152W
12	98	54S, 132W	124	54S, 168W

Range: latitude 8°
longitude 39°
amplitude 40 m

Range: latitude 12°
longitude 78°
amplitude 79 m

Month	8-year mean (Australia)				FGGE			
	Max$_1$ (m)	Location	Max$_2$ (m)	Location	Max$_1$ (m)	Location	Max$_2$ (m)	Location
1	21	58S, 179E	17	78S, 71E	20	58S, 110E	25	78S, 78E
2	22	58S, 180E	20	78S, 86E		no peak	32	78S, 75E
3	26	58S, 173W	19	78S, 93E		no peak	44	78S, 119E
4	25	50S, 168W	20	78S, 88E		no peak	33	62S, 169E
5	25	50S, 160W	23	78S, 115E	30	50S, 160E	65	70S, 90E
6	26	54S, 174E	32	74S, 100E		no peak	47	70S, 120E
7	32	58S, 160E	40	74S, 101E	40	50S, 175W	39	70S, 108E
8	46	58S, 178W	33	74S, 104E	92	62S, 180W	40	72S, 116E
9	37	54S, 175W	30	78S, 92E	20	54S, 174E	43	74S, 122E
10	24	54S, 178W	30	78S, 99E	70	58S, 161W		no peak
11	28	54S, 165W	21	74S, 92E	21	38S, 175E	40	70S, 100E

Range$_1$ latitude 8°, longitude 40°
Range$_2$ latitude 4°, longitude 44°
amplitude 24 m amplitude 23 m

Range$_1$ latitude 24°, longitude 89°
Range$_2$ latitude 16°, longitude 86°
amplitude 72 m amplitude 40 m

TABLE 8 (continued)

Month	8-year mean (Australia)		FGGE	
	Max Amp. (m)	Location	Max Amp. (m)	Location
1	19	50S, 49E	44	58S, 75E
2	43	50S, 56E	36	58S, 83E
3	35	54S, 58E	78	58S, 57E
4	29	50S, 52E	66	58S, 58E
5	43	50S, 44E	49	50S, 27E
6	38	50S, 30E	100	50S, 34E
7	42	54S, 41E	53	46S, 53E
8	26	46S, 43E	37	66S, 85E
9	22	46S, 48E	42	62S, 88E
10	22	66S, 86E	25	50S, 20E
11	14	66S, 88E	49	62S, 70E
12	20	54S, 61E	34	58S, 66E

Range: latitude 20°
      longitude 58°
      amplitude 29 m

Range: latitude 20°
      longitude 52°
      amplitude 75 m

amplitude and phase of the monthly mean harmonic waves was large in FGGE.

Trenberth and Christy (this report) discuss the FGGE objectives. We agree with their points and wish only to add two recommendations:

1. A comparison should be made of the FGGE analyses of the southern hemisphere from the different centers. At least five such data sets are available.

2. Associated with this comparison, a small team of analysts thoroughly experienced with large-scale synoptic analysis, and preferably also with the southern hemisphere, should redo the maps for two to three weeks in each of the Special Observing Periods of, say, sea level pressure, sea surface temperature, and 500 and 200 mb height, temperature, and humidity. This would serve as a check on the models' handling of the data and on possible biases in the models.

ACKNOWLEDGMENT

REFERENCES

Bengtsson, L., M. Kanamitsu, P. Kallberg, and S. Uppala (1982). Bull. Am. Meteorol. Soc. 63, 277-303.

Guymer, L. B., and J. F. LeMarshall (1981). Bull. Am. Meteorol. Soc. 62, 38-47.

Physick, W. L. (1981). Quart. J. Roy. Meteorol. Soc. 107, 863-898.

Streten, N. A., and D. J. Pike (1980). Austr. Meteorol. Mag. 28, 201-215.

Taljaard, J. J., H. van Loon, H. L. Crutcher, and R. L. Jenne (1969). NAVAIR 50-1C-55.

Trenberth, K. E. (1984). Mon. Wea. Rev. 112, 108-123.

Trenberth, K. E., and H. van Loon (1981). Bull. Am. Meteor. Soc. 62, 1486-1489.

Tucker, G. B. (1981). FGGE Conference Proc., Bergen. ICSU, WMO, 362-376.

Tucker, G. B., and W. L. Physick (1980). Preprints GARP Symposium Melbourne, 80-90.

van Loon, H. (1972). Meteorol. Monogr. A.M.S. 35, 25-112.

van Loon, H. (1974). Bonner Meteorol. Abh. 17, 223-237.

van Loon, H. (1980). Mon. Wea. Rev. 108, 1774-1781.

van Loon, H., R. L. Jenne, J. J. Taljaard, and H. L. Crutcher (1968). Notos 17, 53-62.

van Loon, H., and J. C. Rogers (1981a). Mon. Wea. Rev. 109, 2255-2259.

van Loon, H., and J. C. Rogers (1981b). Acad. of Athens, Publication 5, 45 pp.

van Loon, H., and J. C. Rogers (1984a). Tellus 36A, 76-86.

van Loon, H., and J. C. Rogers (1984b). Tellus 36A, in press.

THE SOUTHERN HEMISPHERE CIRCULATION DURING THE FGGE
AND ITS REPRESENTATIVENESS

Kevin E. Trenberth
National Center for Atmospheric Research
and
John R. Christy
University of Illinois, Urbana

ABSTRACT

An analysis of the global redistribution of mass during the FGGE year indicates that the global circulation was highly anomalous in several respects, especially from April to July 1979. For the 56-year period 1924-1980, sea-level pressures over the northern hemisphere during the FGGE year were second highest in spring and highest in summer. In April and June, the anomalies were 1-in-100-year events. At the same time, sea-level pressure deficits and an exceptionally deep circumpolar trough were recorded over the southern hemisphere. Such compensation between the hemispheres, through the constraint of conservation of mass, provides support for the highly atypical nature of the circulation analyzed to exist over the southern hemisphere throughout the FGGE year.

The southern hemisphere circulation was characterized by an exceptionally deep circumpolar trough, an increase in westerlies from $40°$ to $70°S$, and a decrease in westerlies to the north. In winter, the subtropical jet was weaker and the polar jet stronger than normal, so that a pronounced double jet structure prevailed. In summer, the jet was shifted south by $3°$ latitude. A southward shift in storm tracks accompanied these changes year round in a manner consistent with theory.

Much work remains to be done to meet FGGE objectives over the southern hemisphere. Large discrepancies between analyses at different centers belie the improvements in the observational network and limit the value of diagnostic studies. In addition, tuning models to simulate the atypical circulation during the FGGE year would be ill advised unless the reasons for the anomalies are known and incorporated into the models.

INTRODUCTION

The atmosphere and climate system are global in extent. Although this is obvious, meteorologists have frequently attempted to carry out numerical weather prediction and climate studies with considerably less than global data. In large part, this arose from expediency, although

256<

lack of adequate data over the southern hemisphere has always been a problem.

Only during the Global Weather Experiment, otherwise known as the First GARP Global Experiment (FGGE), has the entire atmosphere been comprehensively observed for a full year (December 1978 to November 1979). Paralleling the observational effort has been the development and adoption of global numerical weather prediction models and global climate models. Validation of these will rely heavily on FGGE data sets. However, Trenberth and van Loon (1981) and Trenberth (1984) have pointed out the rather anomalous nature of the circulation over the southern hemisphere during FGGE. In fact, as shown here, several aspects of the global circulation were highly atypical during FGGE. It is therefore necessary to be cautious in using the FGGE data sets for testing the performance of GCMs, since the tuning that results may not be desirable for simulating the overall climate.

In this paper, the main focus is on documenting aspects of the circulation during FGGE over the southern hemisphere and establishing how representative the circulation was. Differences in the analyzed circulation during FGGE arise from both real changes and the improved data base. It is difficult to separate out these effects, but several features can be confirmed by using constraints on the circulation and long-term station data. In particular, it will be demonstrated that during the months April to July 1979 sea-level pressures over the southern hemisphere were abnormally low while they were extraordinarily high over the northern hemisphere. The long record in the northern hemisphere can be used to establish a perspective and the statistical significance of the result, which can then be carried over to the southern hemisphere analyses through the constraint of conservation of mass.

More detailed results are highlighted by contrasting the analyzed southern hemisphere circulation during both summer and winter of FGGE with that in another year. Thus the summer of 1978-1979 is contrasted with 1976-1977, and winter 1979 is contrasted with 1980. The representativeness of the eddy statistics has been dealt with in more detail by Trenberth (1984), and only a few of those results will be noted here.

DATA

In order to study the representativeness of the circulation during FGGE, a long record is needed. Consequently, the FGGE IIIb analyses have not been used. The main data set consists of 0000 GMT southern hemisphere analyses from the World Meteorological Centre in Melbourne, Australia, which extends from May 1972 to November 1980. Only sea-level pressure and 1000 and 500 mb analyses are considered in detail, since other levels are less reliable. Discussion of the data set and its shortcomings is given by Trenberth (1981a, 1982).

It is not yet possible to obtain a truly global data set for a long period. In order to provide nearly global coverage, sea-level pressure analyses from the U.S. Navy as archived in the historical series at the
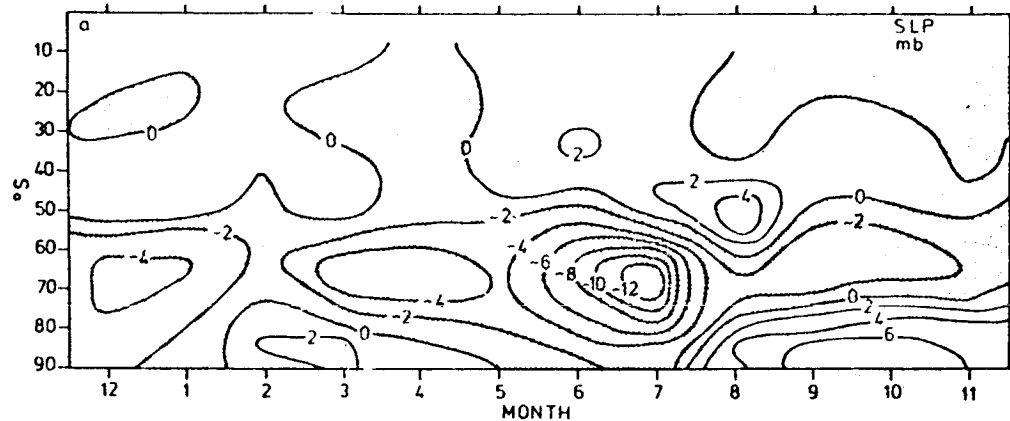
FIGURE 1 Anomalies in the zonal mean sea level pressures from 10° to 90°S for December 1978 to November 1979, the FGGE year. The anomalies are departures from the mean of other months May 1972 to November 1980.

National Center for Atmospheric Research have also been used. These analyses are available from 1899-1980 but are much less reliable prior to 1924 (Trenberth and Paolino, 1980).

In deriving eddy statistics, "seasons" of 128 days have been used (Trenberth, 1982, 1984); summer is defined to be from November 4 to March 11, and winter from May 15 to September 19. There are nine winters and eight summers in the southern hemisphere data set.

GLOBAL SEA-LEVEL PRESSURES DURING FGGE

Figure 1 shows the monthly sea-level pressure anomalies for the FGGE year. Here the anomaly is the departure from the mean of all other values for the same month from May 1972 to November 1980. No smoothing has gone into Figure 1 other than the use of monthly means. It is remarkable how persistent the anomalies were. Negative anomalies occurred in the circumpolar trough near 65°S throughout the year. July 1979 was the most extreme of all months with the largest anomaly of -13 mb at 70°S. A similar pattern is found at 500 mb with negative height anomalies over 55° to 75°S for all months of the FGGE year (Trenberth, 1984).

In viewing the hemisphere south of 10°S as a whole, the exceptionally low circumpolar trough pressures were often compensated to some extent by high pressures near 40°S, implying much stronger than normal surface westerlies. Nevertheless, throughout most of the FGGE year the analysis indicates a net deficit of pressure over the southern hemisphere (10° to 90°S). The exception was in August, while the hemispheric anomalies were small and insignificant in
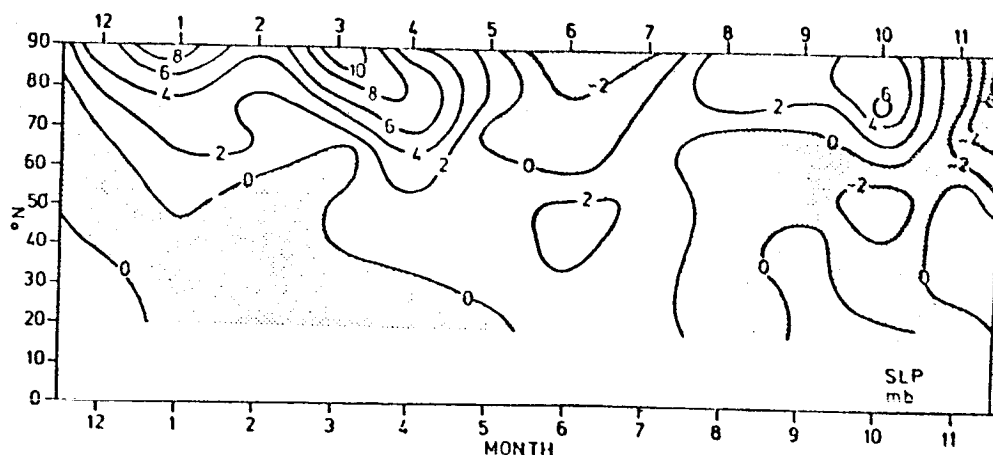
FIGURE 2 Anomalies in the zonal mean sea level pressures from 20° to 90°N for December 1978 to November 1979, the FGGE year. The anomalies are departures from the 1925 to 1980 mean.

September and October. Conservation of mass implies that there should be a surfeit of pressure over the rest of the globe.

Figure 2 shows the sea-level pressure anomalies from 20° to 90°N **for the FGGE year using the 56-year base period from 1925-1980. As** anticipated, positive anomalies are predominant, especially in the northern hemisphere spring and summer months. When the "hemispheric" (17.5° to 90°N) mean northern hemisphere pressures are computed, the anomalies in the 1979 summer are found to be the hignest since 1924 (Figure 3a), and in spring they are the second highest since 1924 (Figure 3b). In Figure 3, the anomalies are computed relative to the 1925-1980 mean. Values prior to 1925 are known to be spuriously high and should be disregarded (Trenberth and Paolino, 1980).

Table 1 shows the "hemispheric" anomaly in mb and the anomaly normalized by the 56-year standard deviation. In April through July 1979, the anomaly exceeds 1 standard deviation and, in April and June 1979, was, respectively, 2.5 and 2.6 standard deviations above normal, i.e., such anomalies would normally be expected about 1 year in 100 (2 tailed).

In order to assess the global redistribution of mass during FGGE, the sea-level pressures should be area weighted. Thus Figure 4 shows the sea-level pressures multiplied by the cosine of the latitude. Also, in this figure, the anomalies were all recomputed in the same way using the same base period of May 1972 to November 1980.

In Figure 4 the large positive anomalies in April over the northern hemisphere took place mostly in middle to high latitudes, while in June pressures were high in the subtropics and apparently throughout the tropics. At 40°N in June, this anomaly is 3.5 standard deviations above normal. In July, Figure 4 implies that high pressures over the tropics and over most of the northern hemisphere may have compensated for the exceedingly low pressures near 65°S.
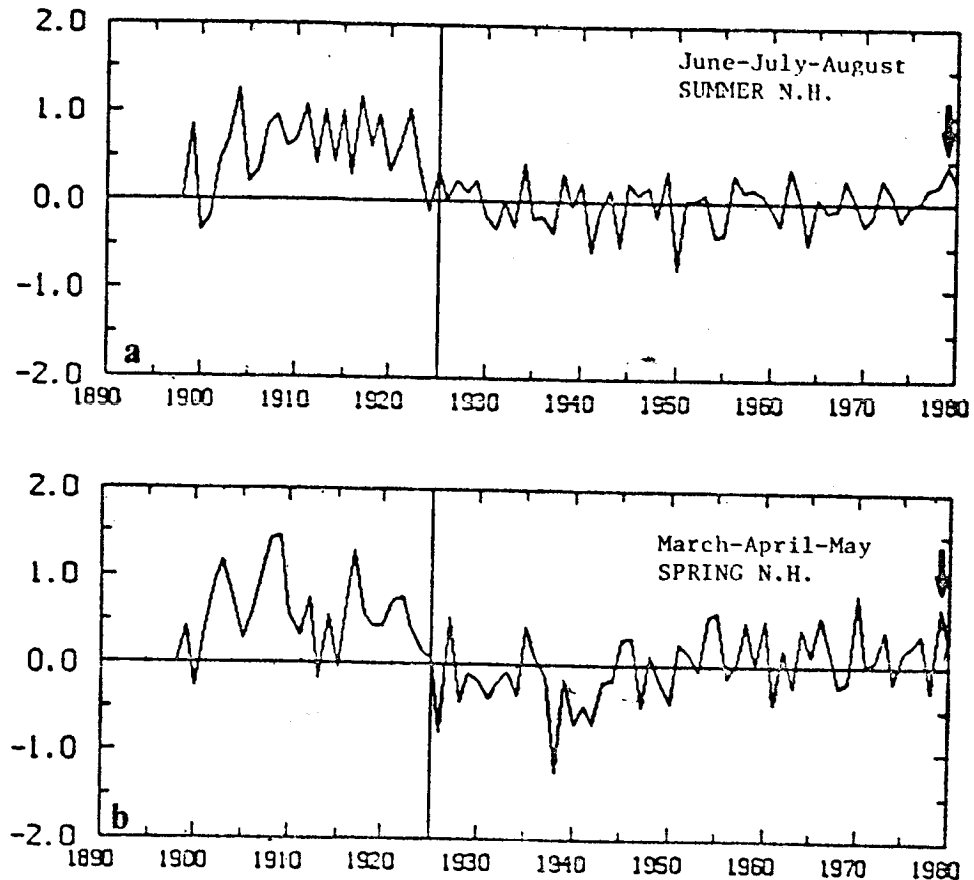
FIGURE 3 Hemispheric (17.5° to 90°N) mean northern hemisphere sea
level pressure anomalies computed relative to the 1925 to 1980 mean.
Values prior to 1925 are erroneously high. (a) Summer (June, July,
August), and (b) spring (March, April, May). The vertical arrow
indicates the 1979 FGGE value.

   Table 2 summarizes this figure by integrating over the available
data and computing a global residual by assuming that the missing
tropical regions are linearly interpolated from the anomalies at 20°N
and 10°S. In most months, there is quite good compensation between
the hemispheres, especially in the months with large anomalies from
April to July 1979. In August 1979, there was also good compensation
but with the signs reversed. The worst agreement is in December 1978
and October 1979. Overall, the global residual tends to be slightly
negative, which may imply that some of the low pressures over the
southern hemisphere were analyzed to be too low during FGGE. For
instance, the National Meteorological Center (NMC) analyses are
systematically higher from 50° to 70°S by 1 to 4 mb (Table 3). On

TABLE 1 Departures from 1925-1979 (55 years) Means of "Hemispheric" (17.5°N to 90°N) Mean Sea Level Pressures for FGGE Year

Month	1978					1979						
	12	1	2	3	4	5	6	7	8	9	10	11
Departure mb	-.40	.39	-.30	.14	1.53	.43	1.00	.69	-.33	.07	-.45	.22
Normalized Departure in S.D.	-.59	.57	-.34	.21	2.47	1.08	2.63	1.64	-.87	.13	-.90	.42

the other hand, the NMC analyses also tend to be higher than the Navy analyses from 20° to 40°N and, in the summer of 1979, averaged 1.0 mb higher at 30° to 35°N (Table 3).

THE SOUTHERN HEMISPHERE GENERAL CIRCULATION DURING FGGE

Figure 5 shows the mean meridional cross section of the zonally averaged wind for January and July 1979 along with the differences from a six-year (1972-1978) mean cross-section from the Australian analyses given by Swanson and Trenberth (1981) and Trenberth (1984). These departures should be interpreted with caution since the Australian cross-section used geostrophic winds. However, they provide an overall guide as to the nature of the circulation anomalies during these two months.

In both months, there was a positive anomaly south of 50°S and a negative anomaly to the north. In January, there was a southward shift in the main jet by about 3° latitude relative to the mean. The strength of the jet however was not changed. In July, the anomaly shows that the subtropical jet was weaker than normal while the polar jet was greatly enhanced. Strong westerlies existed 55° to 60°S from the surface into the stratosphere. Thus there was a pronounced double jet structure in July. Such a strong double jet has been found in other years and was more pronounced in the earlier mean analyses by van Loon (1972). From Figure 1, January can be seen as fairly typical of other summer months, while July was similar but more extreme than other winter months.

The above interpretation can be confirmed by comparing the profile during FGGE with that in other years taking the interannual variability into account. Thus Figures 6 and 7 show the long-term mean over all nine winters or eight summers of the zonal mean westerly wind at 500 mb $\pm$ 1 standard deviation. Here the mean includes the FGGE year. The profile from the FGGE year is plotted as well for comparison. Here, all winds are geostrophic and computed in the same way. In winter (Figure 6), there are slightly weaker winds in the subtropics, but at
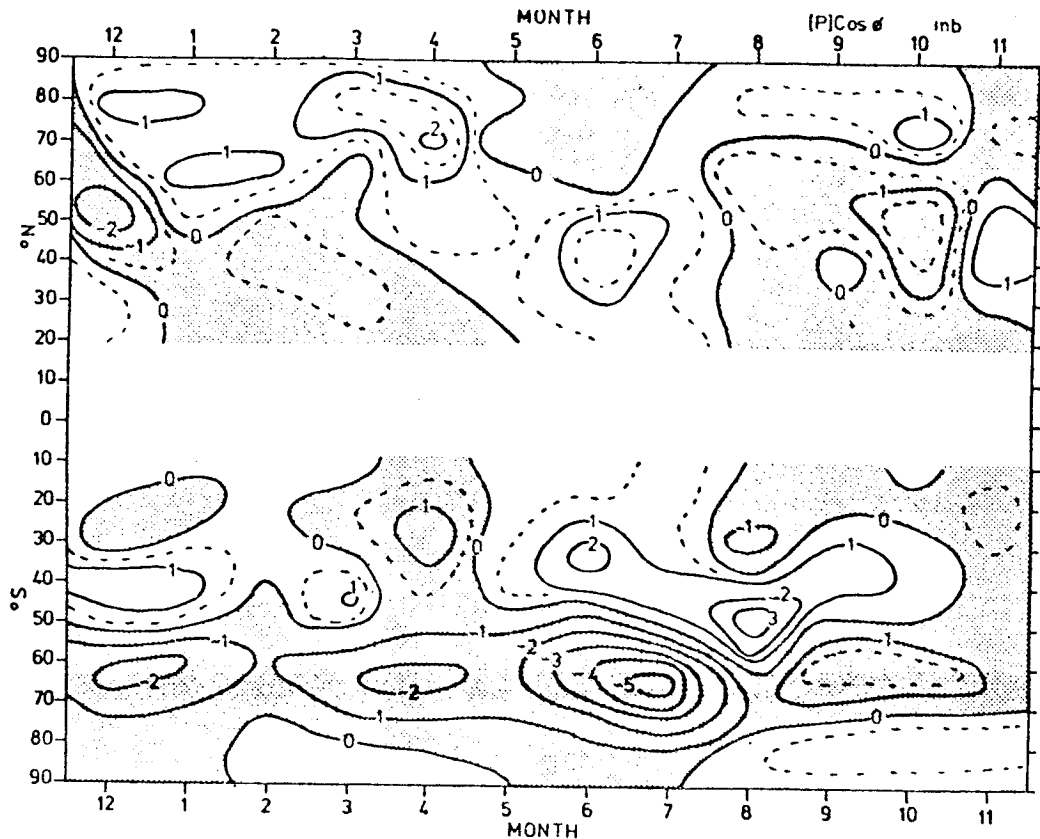
FIGURE 4 Anomalies in the zonal mean sea level pressures weighted by the cosine of the latitude for the FGGE year. All values are departures from the mean of the other months from May 1972 to November 1980.

50° and 60°S the anomalies are statistically significant at the 95 and 99.5 percent confidence level (CL) (see Trenberth, 1984 for details of tests used). In summer (Figure 7), the southward shift in the jet is confirmed with negative anomalies at 40°S exceeding the 95 percent CL and positive anomalies at 50°S exceeding the 90 percent level.

Figures 8 and 9 show the corresponding profiles for the geopotential height variance at 500 mb. The total variance is given along with the contributions from the 2-8 day period and 8-64 day period band. These variances are based on departures from the mean annual cycle consisting of the mean plus four harmonics (Trenberth, 1984).

The 8-64 day period variances were close to normal in both seasons. In summer (Figure 9), the 2-8 day period variances and the total were somewhat greater than normal, but not unusually so. In winter (Figure 8) however, the 2-8 day variances significantly depart from

653

TABLE 2 Departures from Mean for Other Years from May 1972 to November 1980 of Mean Hemispheric Sea Level Pressures for the Year of the GWE in mb. (Hemispheric refers to 17.5° to 90°N and 7.5° to 90°S in the northern and southern hemispheres, respectively. Also shown is the area mean over the globe assuming the missing tropical regions can be interpolated from the anomalies at 20°N and 10°S.

| Month | 1978 | 1979 | | | | | | | | | | |
	12	1	2	3	4	5	6	7	8	9	10	11
NH	-.29	.70	.11	.09	1.25	.29	.85	.75	-.54	-.26	-.80	.52
SH	-.42	-.41	-.18	-.41	-1.53	-.56	-.97	-1.14	.60	-.06	0.00	-.36
"Globe"	-.21	.05	-.06	-.16	-.29	-.12	-.08	-.08	.02	-.18	-.25	-.07

TABLE 3 Differences in Zonal Mean Sea Level Pressures (mb) during the Four FGGE Seasons (a) December 1978 to February 1979, (b) March to May, (c) June to August, and (d) September to November 1979 between (1) NMC-U.S. Navy Analyses over the Northern Hemisphere, and (2) NMC-Australian Analyses over the Southern Hemisphere.

| | | Latitude | | | | | | | |
		20	30	40	50	60	70	80	90
NH	DJF	0.2	0.2	-0.7	0.3	0.2	0.3	-0.2	-2.1
	MAM	0.3	0.4	-0.2	-0.3	-0.4	-0.4	-0.6	0.3
	JJA	0.3	1.0	0.3	-0.3	-0.4	0.0	0.2	0.2
	SON	0.2	0.5	-0.2	-0.3	-0.4	0.0	-0.3	-0.3
SH	DJF	0.6	0.1	0.5	1.4	4.6	2.0	2.8	1.7
	MAM	0.3	0.1	0.4	1.3	2.7	3.1	1.0	-4.3
	JJA	0.2	0.2	1.0	1.1	3.0	3.9	-0.4	-5.4
	SON	0.1	-0.1	0.6	1.8	4.6	3.7	-1.0	-5.6
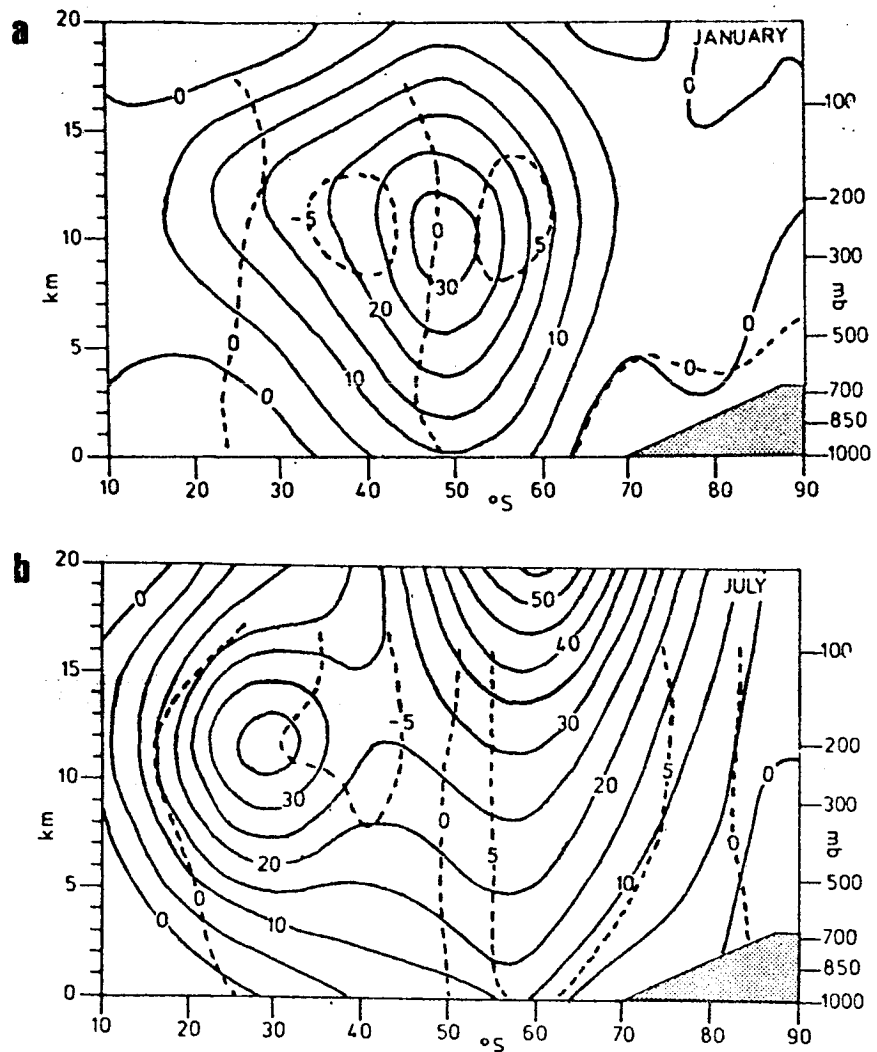
FIGURE 5 Meridional cross-section of zonally averaged wind (m/s) in 1979 for (a) January and (b) July (adapted from Bengtsson et al, 1982). The dashed contours show the differences from the 6-year mean profile given by Trenberth (1984).

normal at most latitudes. From 20° to 40°S it is much less than normal (significant at the 90 to 98 percent CL) while at 60°S it is much greater than normal (95 percent CL). This is mimicked in the total variance. Since the 2-8 day band reflects the high frequency baroclinic eddy activity and the location of storm tracks (Trenberth, 1981, 1982), it reveals a southward shift and strengthening of the storm track activity during FGGE. These results and those for other

FIGURE 6 Meridional profile of the winter zonal mean 500 mb wind
(solid) plus and minus one standard deviation (shaded) and the
corresponding profile during FGGE (dashed) in m/s.

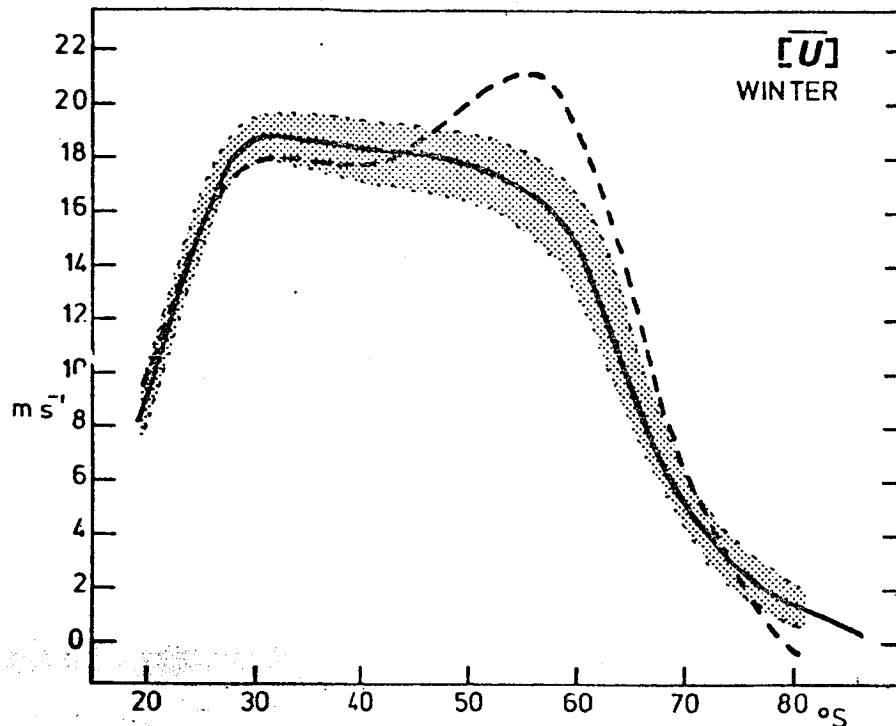variance and covariance statistics are explored in more detail in
Trenberth (1984).

CONTRASTING CIRCULATIONS IN DIFFERENT YEARS

In winter, the year that most closely exhibited contrasting anomalies
was 1980. The mean geopotential height anomalies at 1000 and 500 mb
for winter of 1979 and 1980 are shown in Figure 10. The similarity in
anomaly at the two levels is immediately apparent although more intense
at 500 mb. Note that the anomalies exceeded 50 gpm over wide areas in
both years with a fair degree of zonal symmetry. Also note the mostly
opposite location of the positive and negative anomalies in each year,
implying stronger polar westerlies in 1979 and weaker westerlies in
1980.

Figure 11 shows the zonal mean difference in the strength of the
westerlies at 500 mb between the two years. The pattern, as in
Figure 6, is for much stronger westerlies at 50° to 70°S and weaker
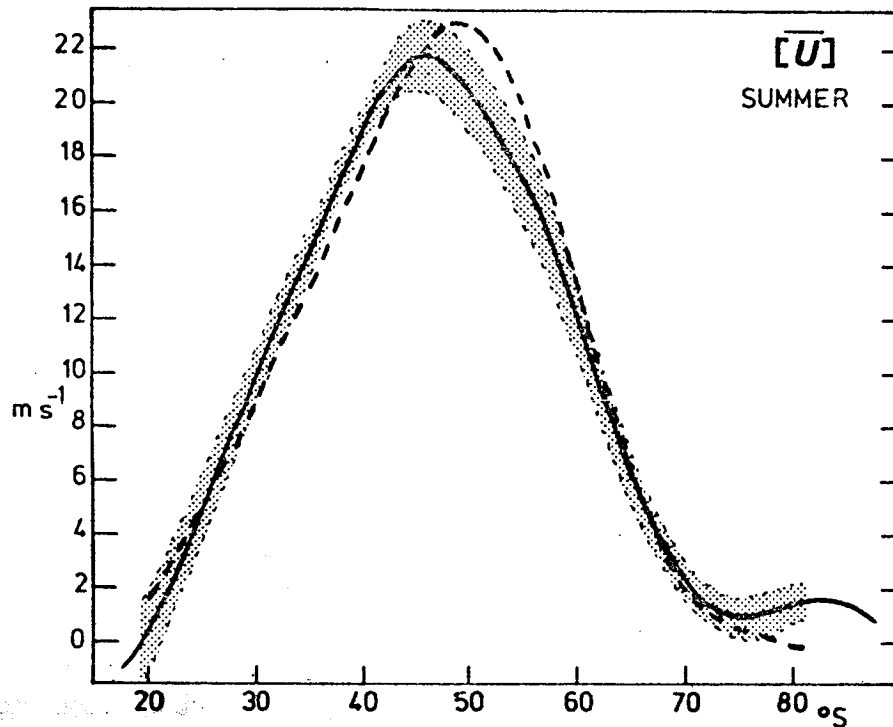westerlies 30° to 40°S during FGGE. Also shown is the 2-8 day band

FIGURE 7 Meridional profile of the summer zonal mean 500 mb wind
(solid curve) plus and minus one standard deviation (shaded), and the
corresponding profile for FGGE (dashed), m/s.

zonal mean difference in the variance of geopotential height and
northward velocity, both key indicators of the location and intensity
of storm tracks. At the bottom of the figure is the contribution to
the change in westerly wind due to convergence of momentum by the
eddies. It reveals that the eddy transports were acting to maintain
the anomalous westerly distribution by feeding momentum into the storm
track. All three are consistent with the view that the stronger and
poleward shifted polar jet stream was accompanied by a southward shift
and stronger baroclinic eddy activity in the main storm track of the
southern hemisphere during FGGE.

   Figure 12 shows the regional distribution of the 2-8 day band of
$\overline{z'^2}$. The main storm tracks, accentuated by the heavy dashed lines,
are all shifted south during FGGE relative to 1980.

   In summer, the contrast is most pronounced between 1976-1977 and the
FGGE summer of 1978-1979. The 1000 and 500 mb height anomalies are
presented in Figure 13. Once again note the strong zonal symmetry to
the anomaly fields and the stronger westerlies in 1978-1979 versus
1976-1977.

FIGURE 8 Meridional profile of the variance of geopotential height for winter, g p dam^2; mean (solid curve), plus and minus one standard deviation (shaded), and the profile for GWE (dashed). Shown are the total variance and the contributions from the 2-8 day and 8-64 day period bands. The scale of the latter is offset.
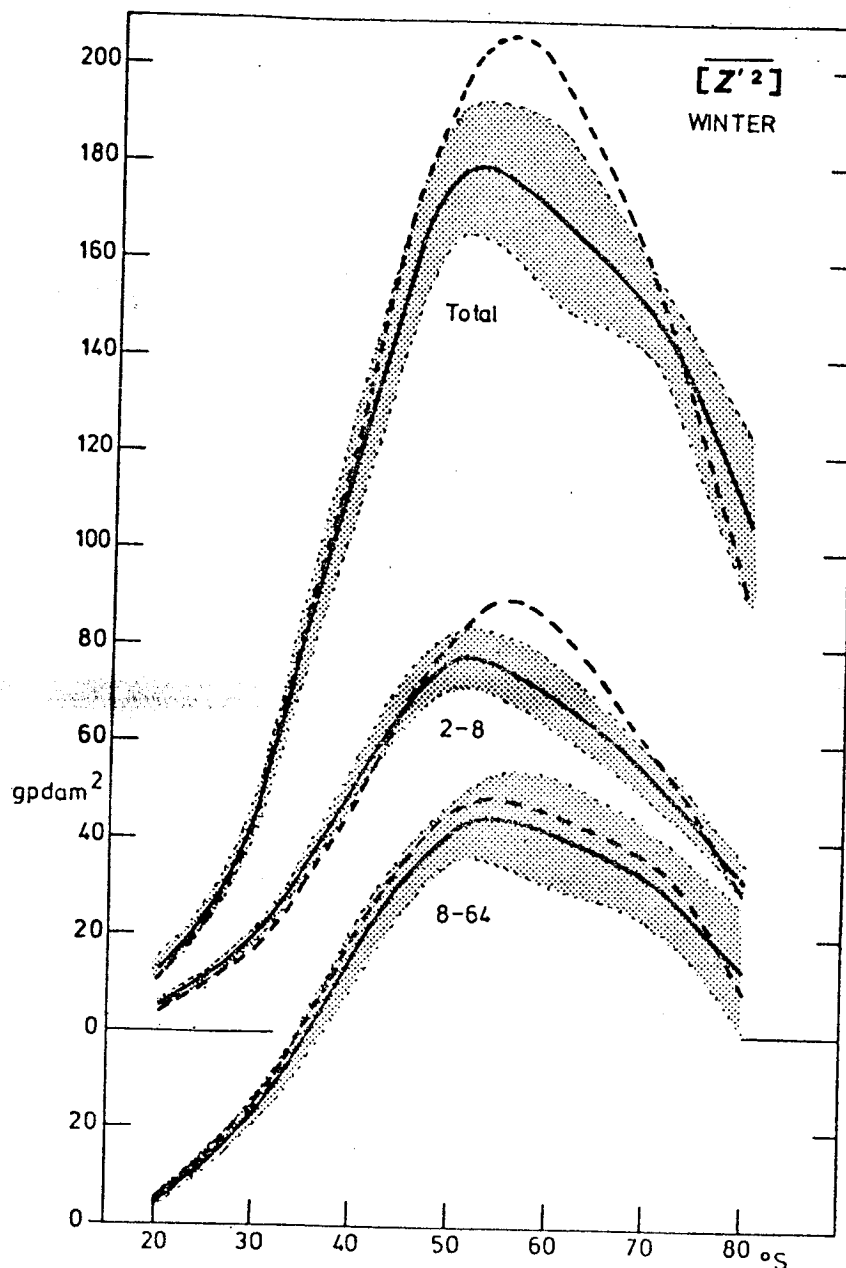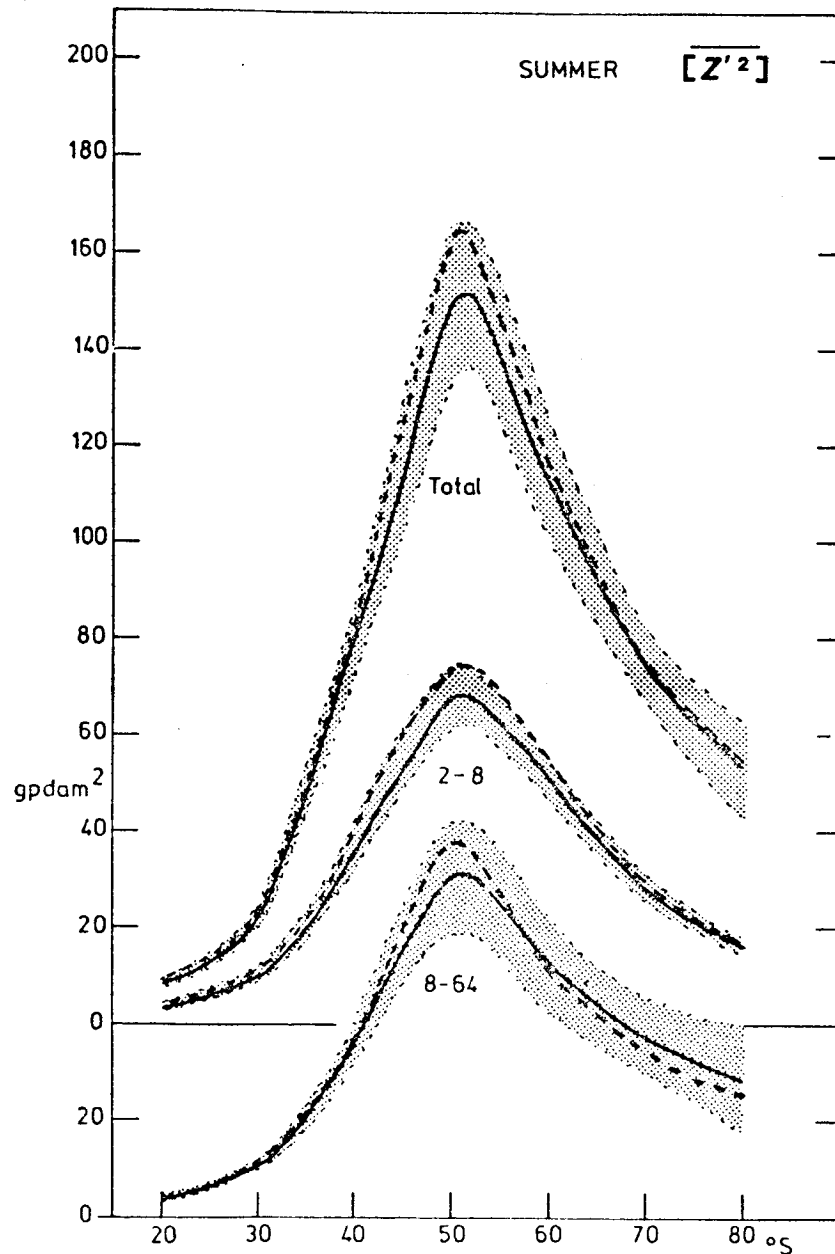
FIGURE 9 Meridional profile of the variance of geopotential height for summer, g p dam^2; mean (solid curve), plus and minus one standard deviation (shaded), and the profile for GWE (dashed). Shown are the total variance and the contributions from the 2-8 day and 8-64 day period bands. The scale of the latter is offset.

FIGURE 10   Anomalies in geopotential height (gpm) at 1000 mb (left) and
500 mb (right) for the winters of 1979 (top) and 1980 (bottom).   The
contour interval is 10 gpm.   Negative contours are dashed.

This is seen more clearly in Figure 14 which presents the same
quantities as for Figure 11.   The pattern is much the same, too.   The
southward shift in the jet of about 5° latitude between the two years
led to a distinct southward shift in the storm track as shown by the
eddy statistics.   The regional differences in $\overline{z'^2}$ for the 2-8 day
band are shown in Figure 15.   The main gain in activity is seen to be
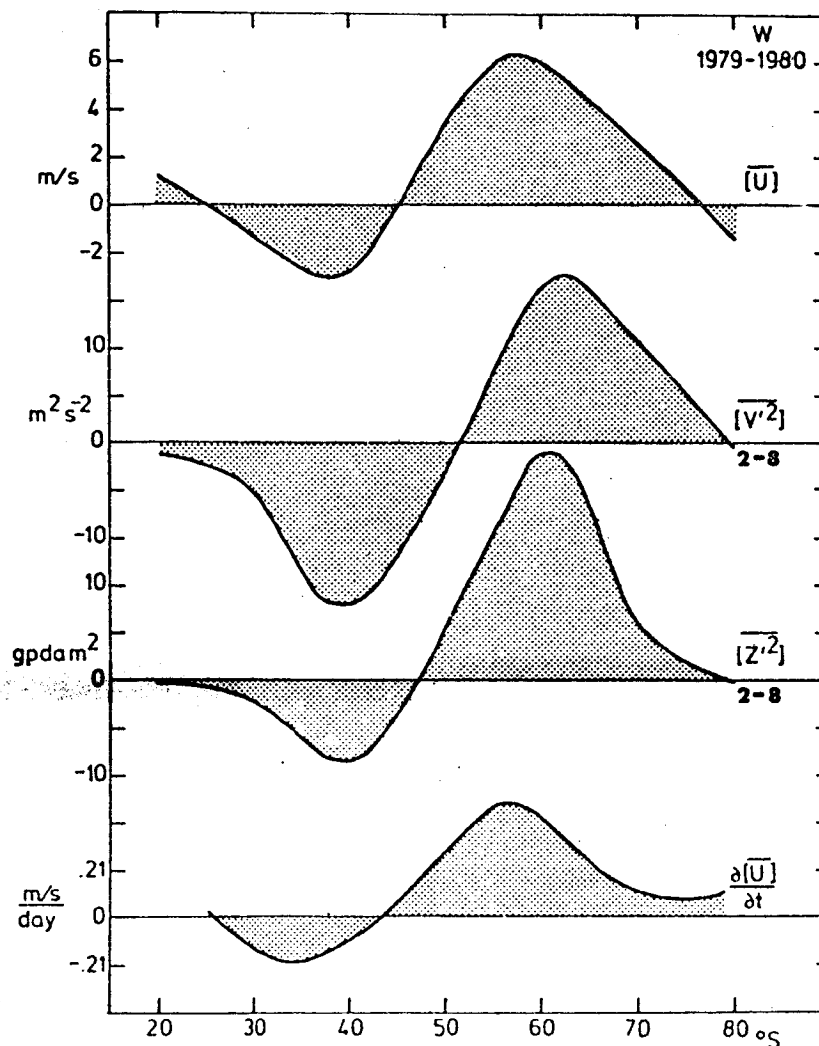
FIGURE 11 Differences in the zonal mean quantities for the winters of 1979 minus 1980. From top to bottom are shown $[\overline{u}]$, $[\overline{v'^2}]$ 2-8 day, $[\overline{z'^2}]$ 2-8 day, and $\partial[\overline{u}]/\partial t$ due to convergence of momentum by the eddies.
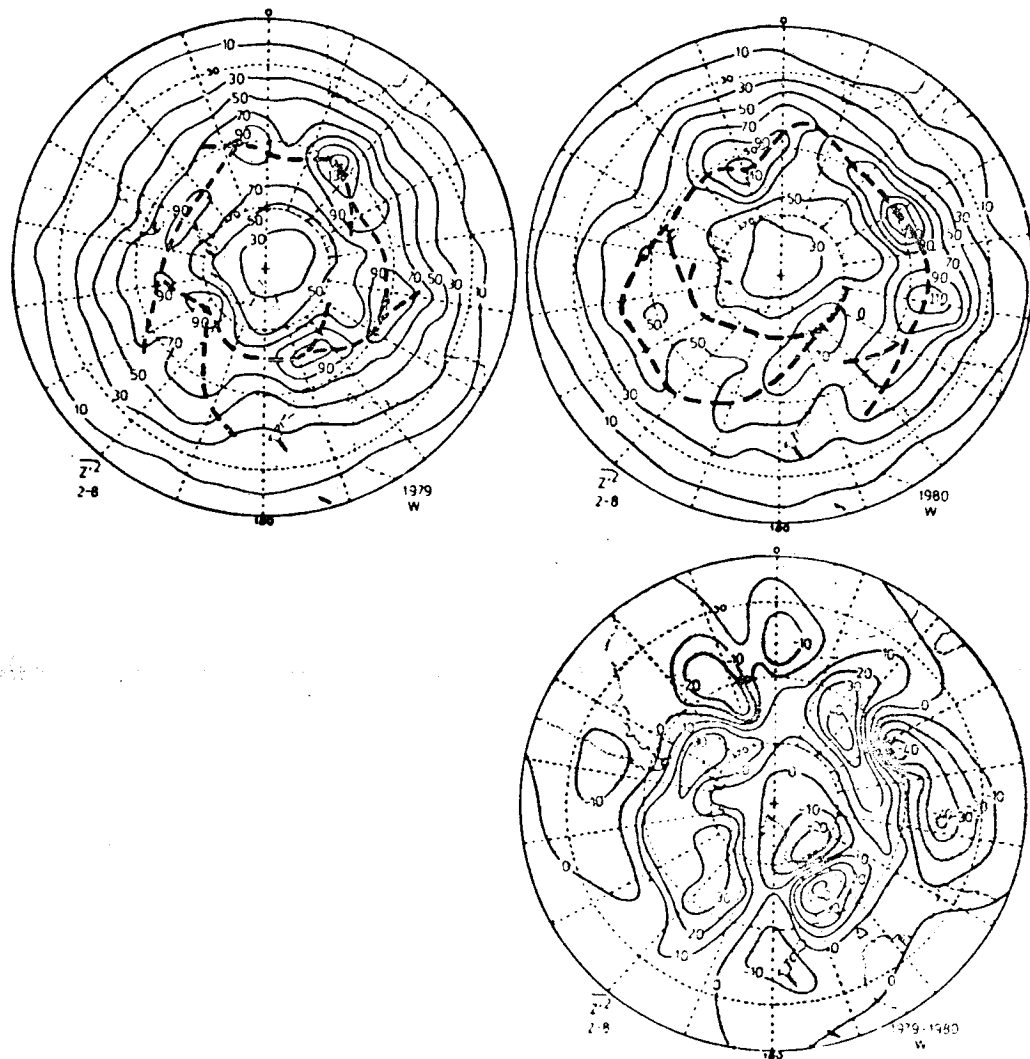
FIGURE 12   The 2-8 day period band contribution to the variance of geopotential height $\overline{z'^2}$ (a) winter 1979, (b) winter 1980, and (c) their difference 1979-1980; in g p dam^2.   The heavy dashed lines denote the locus of the maxima and thus the main storm tracks.
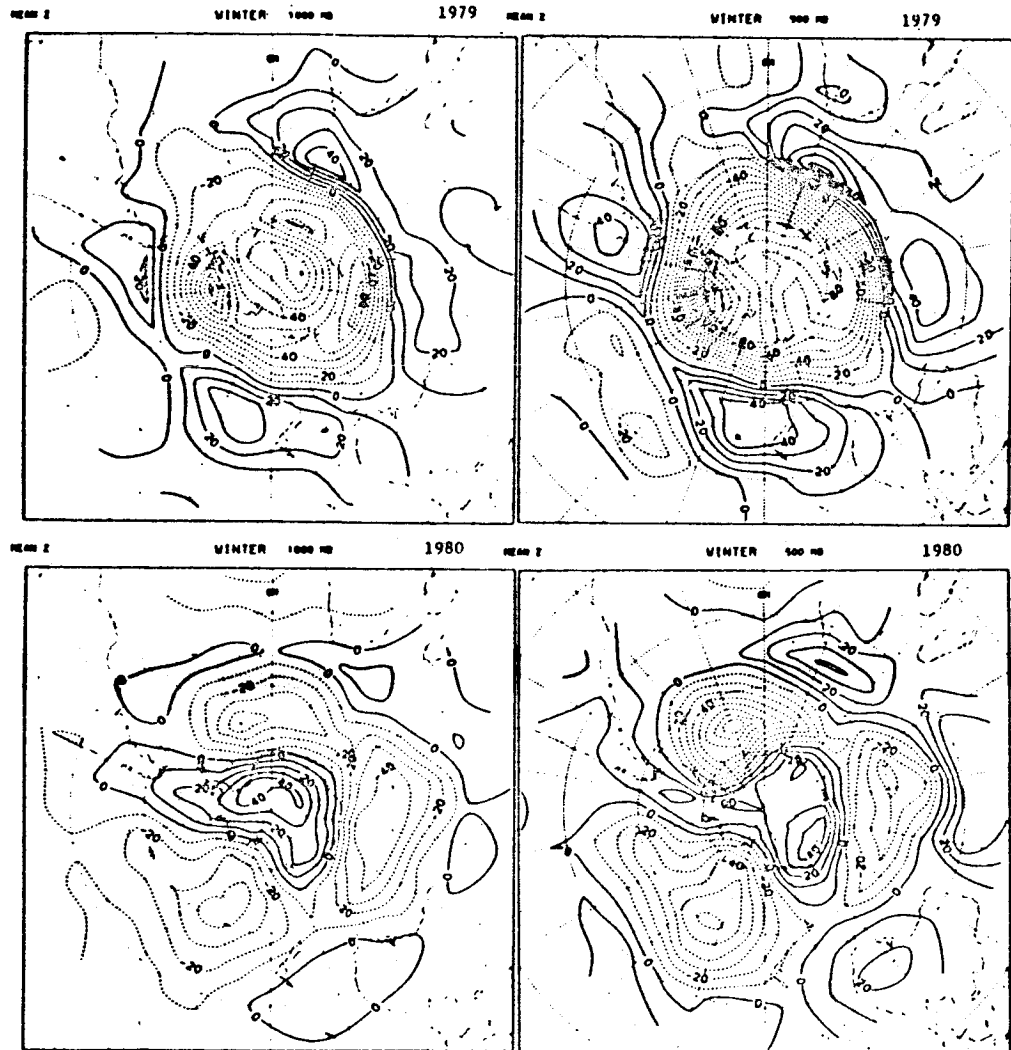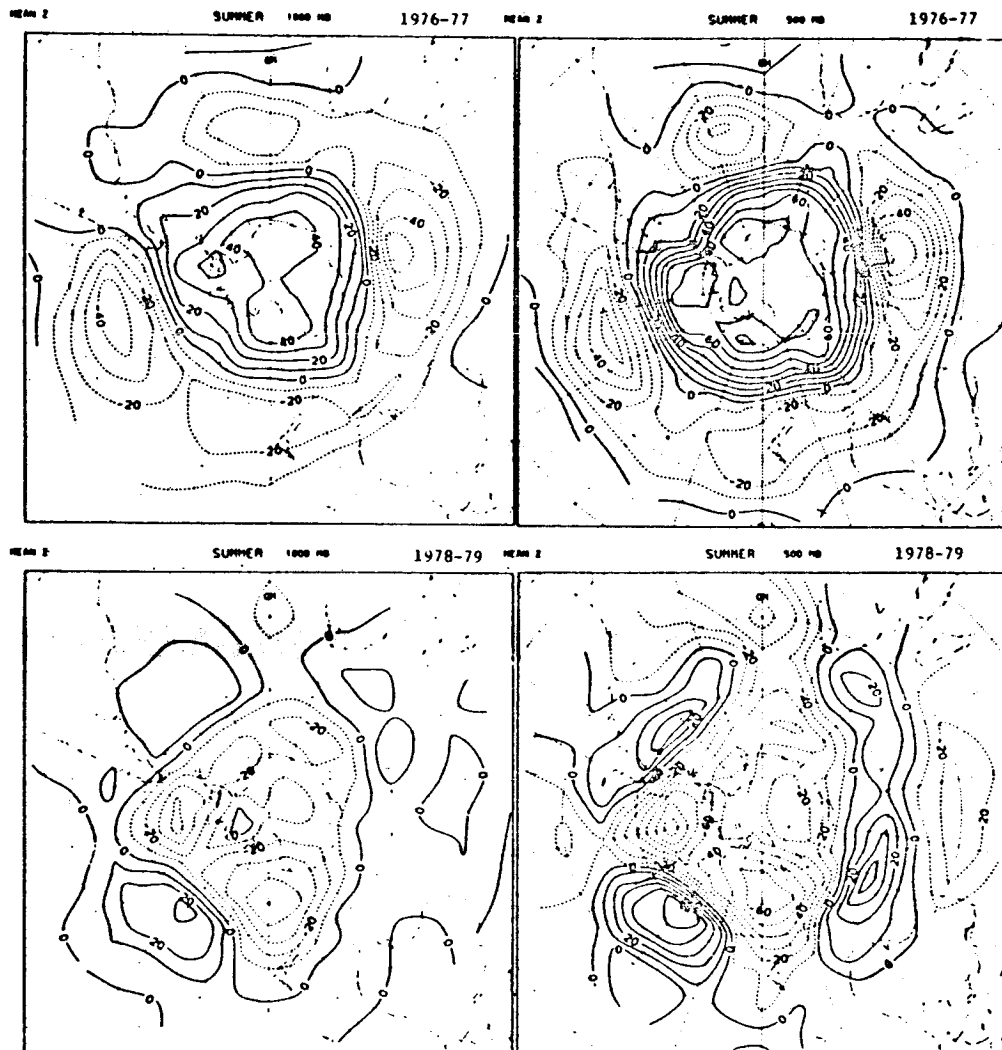
FIGURE 13   Anomalies in geopotential height (gpm) at 1000 mb (left) and 500 mb (right) for the summers of 1976-1977 (top) and 1978-1979 (bottom).   The contour interval is 10 gpm and negative contours are dashed.
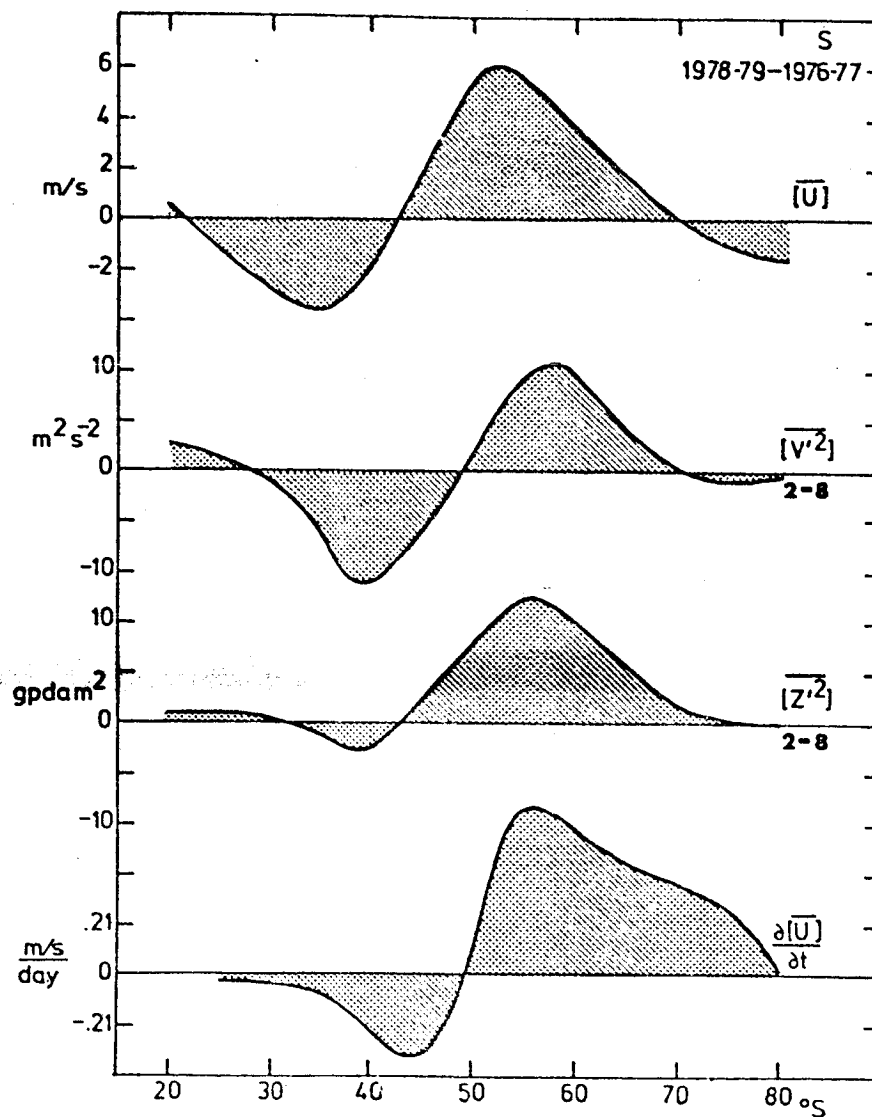
FIGURE 14 Differences between zonal mean quantities for the summers of 1978-1979 minus 1976-1977. Shown from top to bottom are [ū], m/s; [$\overline{v'^2}$] in the 2-8 day band, m² s⁻²; [$\overline{z'^2}$] in the 2-8 day band g p dam²; and the eddy convergence of momentum ∂[ū]/∂t in m/s/day.
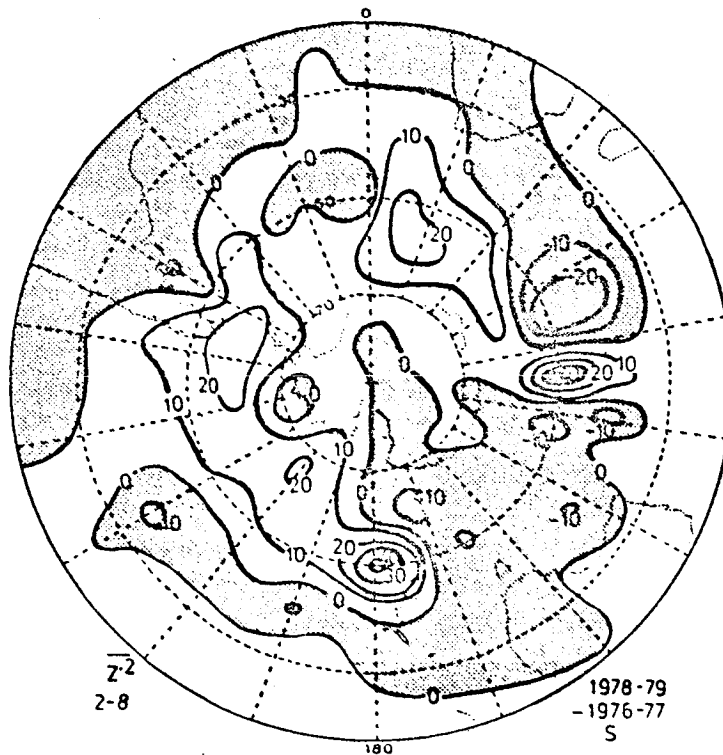
FIGURE 15. Difference in 2-8 day period band variances of geopotential height $\overline{z'^2}$ in summers of (1978-1979) - (1976-1977) g p dam^2.

over the south Pacific and extending across the south Atlantic into the Indian Ocean.

CONCLUSIONS

The foregoing analysis has clearly shown that the circulation over the southern hemisphere during FGGE was not typical. The FGGE year was characterized by an exceptionally deep circumpolar trough, an increase in westerlies from 40° to 70°S and a decrease to the north. In winter therefore, the subtropical jet was weaker than normal, but the polar jet was considerably enhanced, and a double jet structure prevailed. In summer, there was a southward shift in the jet by about 3° latitude. Associated with these changes was a southward shift in storm tracks, as revealed by the high-frequency eddy activity throughout the year. In both seasons, anomalous convergence of momentum by the eddies into the jets helped sustain the abnormal distribution of westerlies against surface friction.

This picture of a systematic southward shift in the jets and storm tracks during FGGE is consistent with expectations based on baroclinic theory and the relationships between the mean flow and location of tracks of high-frequency baroclinic eddies (Trenberth, 1981a; Fredericksen, 1979). Such a systematic shift in the location of features cannot be accounted for by the enhanced observational base during FGGE, although it is suspected that the improved analyses may have contributed to the size of the variances and covariances.

There have been several papers that have remarked on the extremely deep circumpolar trough in the southern hemisphere during FGGE (see Trenberth, 1984 for details), but none apparently that comment on the compensating extraordinarily high sea-level pressure anomalies over the northern hemisphere. The analysis of global redistribution of mass via sea-level pressures suffers from lack of data in the tropics over a long period, and there are some distortions due to the use of sea-level rather than surface pressures (Trenberth, 1981b). Nevertheless, the compensation of mass redistribution as analyzed is quite good and provides convincing evidence of the reality of the gross features of the global anomalies during FGGE. It is important to note that the anomalies in hemispheric sea-level pressures over the northern hemisphere during the northern spring and summer were very large and normally should be expected about 1 year in 100. Regionally, the anomalies are much larger and even more extreme over both hemispheres.

RELATIONSHIPS TO FGGE OBJECTIVES

A brief discussion follows of the implications of this work for attaining the objectives of the Global Weather Experiment (National Research Council, 1978, p. 12).

The observed circulation during FGGE was highly atypical, especially during the northern summer. A major consequence is that testing of models using the FGGE analyses (objective 3) will "tune" them toward an extreme situation. This is undesirable for both weather forecasting and climate simulations unless the reasons for the anomalous circulation are known and included. Thus attention needs to be focused on whether there were anomalous atmospheric forcings through such things as surface effects or diabatic heating and why.

The observational network over the southern hemisphere appears to have been at its best ever, mainly because of the network of FGGE buoys and satellite soundings. It is therefore disturbing to note the huge differences in the zonal mean sea-level pressures analyzed by the Australians and the NMC (Table 3). As noted earlier, some evidence indicates that the Australians may have been overly enthusiastic in analyzing the deep circumpolar trough during FGGE, but there also seems to be a question of whether the buoy data were assimilated properly in the NMC analyses. Further comparisons with the IIIb analyses from other centers are planned to further resolve these issues (objective 2). Future plans for a sparse network of southern hemisphere buoys as part of TOGA implicitly assume that the buoy data will be fully utilized. It is important for the operational centers to ensure that this is the case.

To date, comprehensive diagnostic studies of the southern hemisphere circulation using the FGGE IIIb analyses (objective 4) do not appear to have been done. The first step appears to be establishing confidence limits on the observed flow by comparing the analyses from different centers. Such studies are planned.

Objective 5 is to develop a modeling capability to explore the nature of climatic variations. Little attention has yet been focused on correctly simulating the southern hemisphere flow. In nearly all models, the westerlies are not strong enough, especially in the southern summer. Major improvements are necessary before the problem of interannual and longer term variations, as highlighted in this paper, can even be addressed.

ACKNOWLEDGMENT

REFERENCES

Bengtsson, L., M. Kanamitsu, P. Kallberg, and S. Uppala (1982). FGGE research activities at ECMWF. Bull. Amer. Meteorol. Soc. 63, 277-303.

Frederiksen, J. S. (1979). Baroclinic instability of zonal flows and planetary waves in multi-level models on a sphere. J. Atmos. Sci. 36, 2320-2335.

National Research Council (1978). The Global Weather Experiment-- Perspectives on Its Implementation and Exploitation. FGGE Advisory Panel, U.S. Committee for the Global Atmospheric Research Program, National Research Council, Washington, D.C., 104 pp.

Swanson, G. S., and K. E. Trenberth (1981). Trends in the southern hemisphere tropospheric circulation. Mon. Wea. Rev. 109, 1879-1889.

Trenberth, K. E. (1981a). Observed southern hemisphere eddy statistics at 500 mb: Frequency and spatial dependence. J. Atmos. Sci. 38, 2585-2605.

Trenberth, K. E. (1981b). Seasonal variations in global sea-level pressure and the total mass of the atmosphere. J. Geophys. Res. 86, 5236-5246.

Trenberth, K. E. (1982). Seasonality in southern hemisphere eddy statistics at 500 mb. J. Atmos. Sci. 39, 2507-2520.

Trenberth, K. E. (1984). Interannual variability of the southern hemisphere circulation: Representativeness of the year of the Global Weather Experiment. Mon. Wea. Rev. 112, 108-123.

Trenberth, K. E., and D. A. Paolino, Jr. (1980). Northern hemisphere sea-level pressure data set: Trends, errors and discontinuities. Mon. Wea. Rev. 108, 855-872.

667

Trenberth, K. E., and H. van Loon (1981). Comment of "Impact of FGGE buoy data on southern hemisphere analyses." Bull. Amer. Meteorol. Soc. 62, 1486-1489.

van Loon, H. (1972). Wind in the southern hemisphere. Meteorology of the Southern Hemisphere. Meteorol. Monogr. No. 35, C. W. Newton (ed.), American Meteorological Society, 87-99.

16. PARAMETERIZATION

Organizer   T.N. Krishnamurti

Session Chairman   Akio Arakawa

Speakers   Yoshimitsu Ogura
                          John Molinari
                          Alan Betts

Rapporteur   Bruce Albrecht

278<

RESPONSE OF CUMULUS CLOUDS TO LARGE-SCALE FORCING
AND CUMULUS PARAMETERIZATION

Yoshimitsu Ogura ~~Atmos. Science~~
University of Illinois

ABSTRACT

Using the cumulus ensemble model (Soong and Ogura, 1980), statistical
properties of cumulus clouds that occur in response to the imposed
large-scale forcing were investigated both in the tropical and
midlatitude situtations. A strong drying process was found to occur in
the boundary layer in association with deep convection in a midlatitude
case. The Arakawa-Schubert (1974) cumulus parameterization scheme was
tested semi-prognostically against both the model result and the
observation in a tropical rain event that occurred in GATE. The cloud
heating and drying effects predicted by the Arakawa-Schubert scheme
were found to agree well both with the observation and the model
result. However, it was also found that the Arakawa-Schubert scheme
underestimates both condensation and evaporation rates substantially.
An inclusion of the downdraft effect, as formulated by Johnson (1976),
appears to alleviate this deficiency. This downdraft effect may be
important in predicting the behavior of the boundary layer accurately.

INTRODUCTION

During the past several years, the feedback effects of a group of
cumulus clouds on the large-scale environment in which the group of
clouds is embedded have been studied. To achieve the goal, a model
called a cumulus ensemble model has been developed (Soong and Ogura,
1980). Basically, it is a nonhydrostatic, anelastic moist cloud model
with parameterized cloud physics and turbulence processes. However,
unlike many other cloud models that are aiming at simulating isolated
convective clouds, the cloud ensemble model allows several convective
clouds to develop simultaneously inside the model domain. In addition,
the prescribed large-scale heat and moisture sources are included.
These prescribed terms can be measured either by observations or by the
grid values in a large-scale prediction model. The objective of this
model has been to investigate statistical properties of cumulus clouds
that occur as a result of imposed large-scale forcing. In this
respect, this model may be regarded as an ultrafine mesh, ultralimited
area model nested in a large-scale prediction model.

671
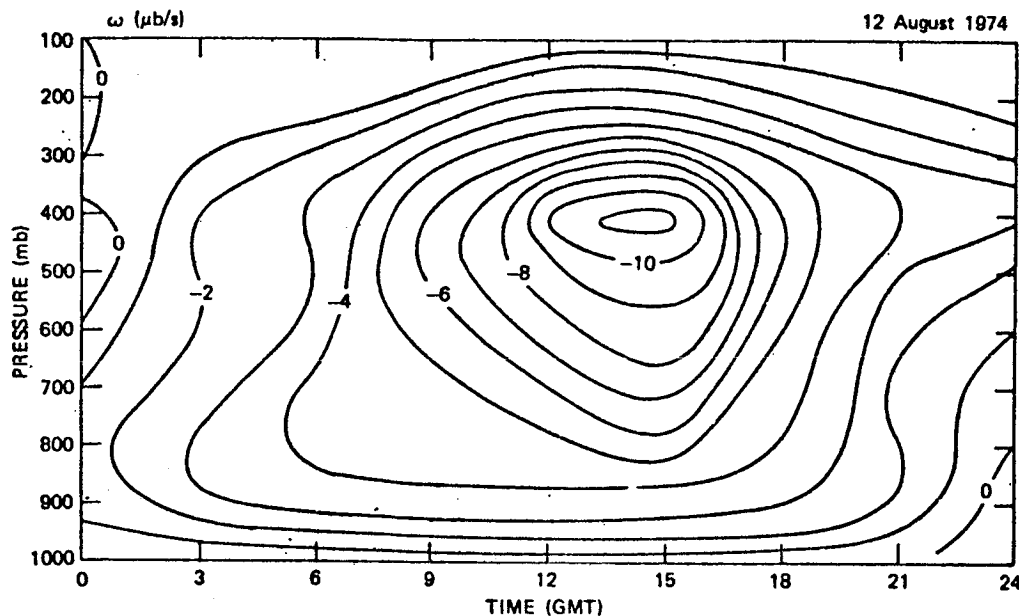
FIGURE 1 Time-pressure section of the vertical p-velocity (ω) at the center of the band that occurred on August 12, 1974 over the eastern Atlantic in units of 10^{-3} mb/s (Ogura et al., 1979).

This paper is divided into two parts. The first part will discuss feedback effects of clouds that occur in response to large-scale forcing, as revealed from the cumulus ensemble model. The second part will discuss how the knowledge gained from this numerical study may be utilized to improve the cumulus parameterization schemes. The full discussion of the cumulus parameterization problem is beyond the scope of this paper. The reader is referred to the latest review article by Frank (1983).

TROPICAL EXPERIMENTS

The cumulus ensemble model was first applied to shallow moist convection by Soong and Ogura (1980) and to tropical deep moist convection by Soong and Tao (1980). Tao (1983) and Soong and Tao (1984) extended their previous work in several aspects, including a discussion of vertical transport of momentum by cumulus clouds. In this paper, the discussion will focus on the cloud heating and drying effects. In the work of Soong and Tao, the tropical rainband event that developed on August 12, 1974 during the GATE Phase II period was considered. Figure 1 shows the evolution of the rainband in terms of vertical velocity (ω) estimated kinematically from the GATE A/B and B scale ship arrays (Ogura et al., 1979). Since the average separation

between the neighboring ships was a few hundred kilometers, ω in Figure 1 should be regarded as the vertical velocity averaged over an area encompassing the rainband.

In general, the heating and drying effects of clouds may be expressed as (Yanai et al., 1973; Ogura and Cho, 1973):

$$Q_1 = -\bar{\pi} \left(\frac{\partial \bar{\theta}}{\partial t} + \bar{v} \cdot \nabla \bar{\theta} + \bar{w} \frac{\partial \bar{\theta}}{\partial z} \right) - Q_R \tag{1a}$$

$$= \bar{\pi} \left(-\frac{\partial \bar{\rho} \, \overline{w'\theta'}}{\rho \partial z} + D_\theta \right) + \frac{L}{c_p} (\bar{c} - \bar{e}) \tag{1b}$$

$$Q_2 = -\frac{L}{c_p} \left(\frac{\partial \bar{q}_v}{\partial t} + \bar{v} \cdot \nabla \bar{q}_v + \bar{w} \frac{\partial \bar{q}_v}{\partial z} \right) \tag{2a}$$

$$= -\frac{L}{c_p} \left(-\frac{\partial \bar{\rho} \, \overline{w'q'_v}}{\rho \partial z} + D_q - \bar{c} + \bar{e} \right) \tag{2b}$$

where π is the non-dimensional pressure given by $(p/P)^{R/c_p}$; Q_r, the radiative cooling rate; D_θ and D_q, the diffusion effects by microscale turbulence on the $\bar{\theta}$ and $\bar{q}_v$, respectively; $\bar{c}$, the rate of condensation of water vapor; e, the rate of evaporation from liquid drops; and other notations are conventional. According to the result of Soong and Tao (1980), the effects of D_θ and D_q are negligibly small compared to other terms and will not be discussed here. The prime symbol in the above equations denotes deviations from area averaged quantities (denoted by the overbar symbol). Q_1 and Q_2 represent the apparent sources of heat and moisture, respectively, and can be measured either by observations or by grid values in a large or regional scale prediction model. Equations (1b) and (2b) represent the cloud heating and drying effects, respectively. They consist of three terms: vertical transport of sensible heat and moisture by cumulus convection, condensation of water vapor that occurs inside cumulus clouds, and evaporation from liquid and ice particles.

Figure 2 shows the result from the cumulus ensemble model applied to the situation in the tropical rainband event for the period 6 to 12 GMT August 12, 1974 (Tao, 1983). It has been well established from observations that the vertical advection terms in equations (1a) and (2a) are 1 order of magnitude larger than the storage and horizontal advection terms in the tropics. Therefore the prescribed heat and moisture sources, estimated as $(\bar{\omega}(\partial \bar{\theta}/\partial p)$ and $\bar{\omega}(\partial \bar{q}/\partial p)$ using the observed $\bar{\omega}$, $\bar{\theta}$, and $\bar{q}$, were introduced into the thermodynamic equations. Clouds were generated in the model by introducing small amplitude perturbations at low levels. The model was run for 6 hours of physical time. At each time step, the horizontal averages of all variables inside the model domain were taken. Finally,

674
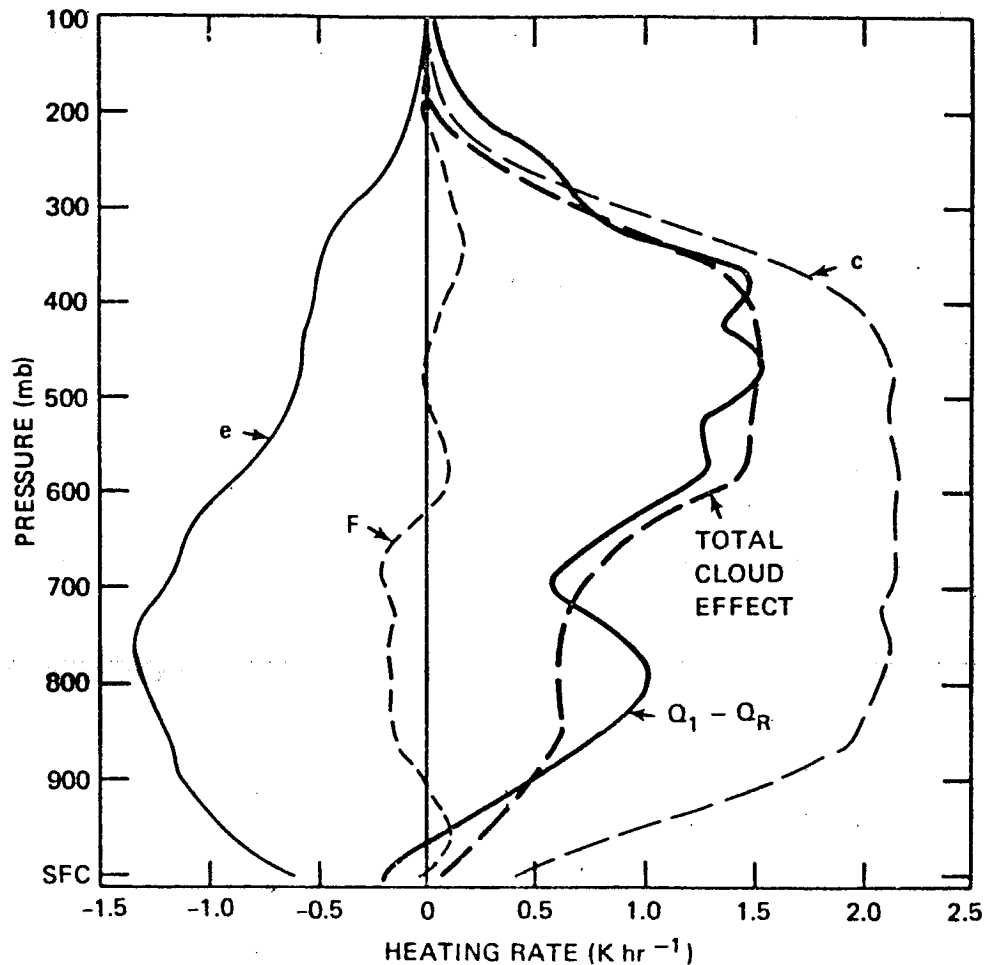
FIGURE 2 Time-averaged heating rate by condensation (c), evaporation (e), and the vertical transport of sensible heat by clouds (F) predicted by the two-dimensional cumulus ensemble model. The sum of the three terms represents the total cloud heating effect. The cloud heating effect estimated from the large-scale heat budget over the period 06 to 12 GMT August 1974 is denoted by Q_1-Q_R (Tao, 1983).

their time averages were taken to represent the response of cumulus clouds to the prescribed large-scale forcing in a statistical sense. Figure 2 shows a close agreement between the time-averaged rate of heating by model clouds and the rate of cooling by large-scale motion estimated from the large-scale heat budget. This implies that, although the atmosphere is continuously cooled by the prescribed heat sink, the heating by clouds almost exactly balances the large-scale heating, so that on the average over 6 hours the temperature does not

change significantly from the initial condition. Figure 2 also shows
that the heating rate by the vertical flux of sensible heat is 1 order
of magnitude smaller than that by condensation at all altitudes, except
of course in the subcloud layer. On the other hand, the maximum
cooling rate by evaporation is comparable with the condensation heating
rate in magnitude.

It is customary in diagnostic and prognostic studies of cumulus
ensembles to divide the area averaged vertical flux $\bar{M}$ into two parts:
the cloud related mass flux (M_c) and the mass flux averaged over the
cloudfree area (i.e., areas between clouds) ($\tilde{M}$). M_c may be further
divided into two parts: mass flux associated with updraft (M_u) and
downdraft (M_d). Thus

$$\bar{M} = M_c + \tilde{M} = M_u + M_d + \tilde{M}.$$

In the cloud ensemble model, M is prescribed. Figure 3 shows the
profiles of M_u, M_d, M_c, and $\tilde{M}$ obtained from the model. The
outstanding feature of this figure is that M_c is nearly equal to $\bar{M}$.

MIDLATITUDE EXPERIMENTS

The cumulus ensemble model is presently being applied to a heavy
precipitation event in midlatitudes. (A good cumulus parameterization
scheme in a GCM should predict the cloud effects accurately in
midlatitudes as well as in the tropics.) In general, synoptic
situations that lead to heavy precipitation in midlatitudes are
substantially different from those in the tropics in several aspects.

First, the midlatitude atmosphere is more unstably stratified than
the tropical counterpart. For example, the typical lifted index
measured at 500 mb for a surface air parcel is $-6^{\circ}K \sim -8^{\circ}K$ in
prestorm situations in the midwestern United States in spring, whereas
the corresponding value observed in GATE was at most $-2^{\circ}K$.
Consequently, the maximum updraft in numerical experiments described
above was roughly 10 m/s, whereas the corresponding value in the
numerical experiment in midlatitude situations, which will be described
shortly, frequently exceeded 20 m/s. Thus the relative importance of
the vertical transports of heat and moisture by clouds is larger in
midlatitude situations than in the tropical counterparts. Second, in
contrast to the tropical situations, the storage and the horizontal
advection terms in equations (1a) and (2a) are not negligibly small
compared to the vertical advection term in midlatitudes. Third, the
vertical wind shear is generally stronger in midlatitudes than in the
tropics. (However this aspect will not be discussed in this paper.)

The situation considered for the midlatitude experiment is the heavy
precipitation event that occurred April 10-11, 1979 (AVE-SESAME-79I)
over the central United States. Kuo and Anthes (1984) calculated the
heat and moisture budgets in this case, which formed the basis of the
input and verification data in the experiment. The result is
encouraging in that the predicted rainfall rate agrees fairly well with
the observation.
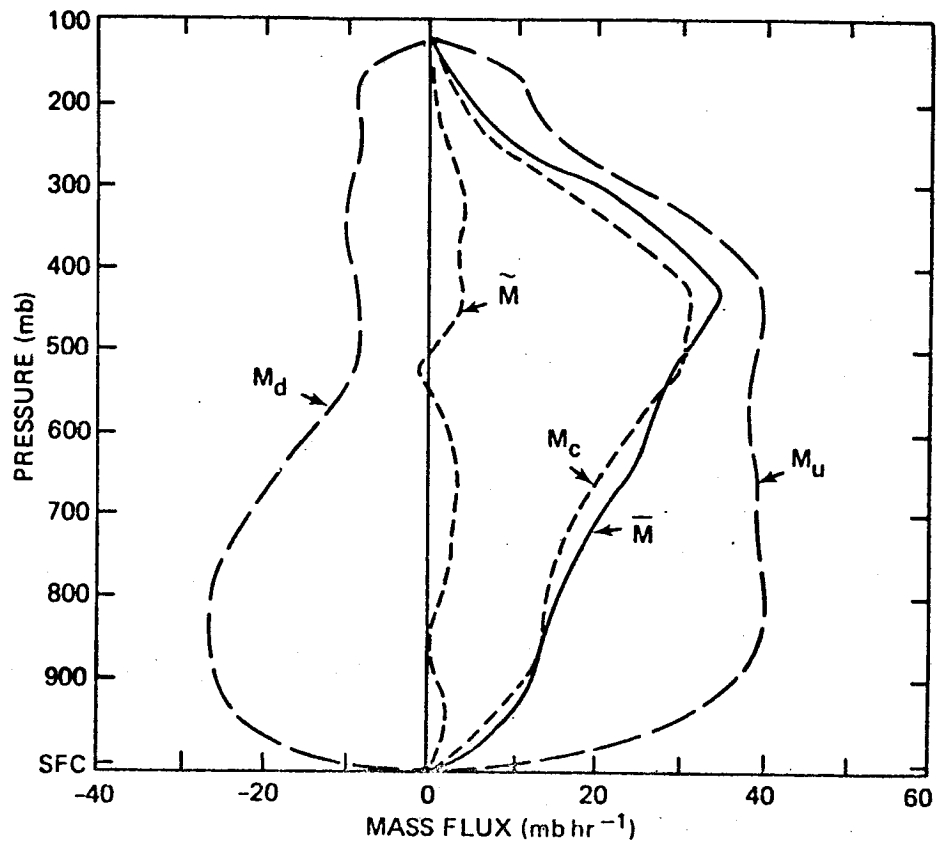
FIGURE 3 Time-averaged mass flux $\overline{M}$, upward mass flux inside clouds M_u, downward mass flux inside clouds M_d, total cloud mass flux M_c (= M_u + M_d), and mass flux in the clear are $\widetilde{M}$ in units of mb Hr^{-1} predicted by the model in the meteorological conditions corresponding to Figure 2 (Tao, 1983).

INTERACTION BETWEEN THE CLOUD LAYER AND BOUNDARY LAYER

A number of experiments have been made to investigate the sensitivity of the cloud effects to the initial soundings and the large-scale forcing. In the series of experiments, the original cumulus ensemble model was slightly modified in that the large-scale forcing was imposed in the form of horizontally uniform but vertically varying internal heat sink and moisture sources.

During the course of these experiments, it was found in many cases that the horizontally averaged variables underwent temporal variations, rather than settling down into steady states, even when the prescribed rates of heating and moistening due to internal sources were kept time
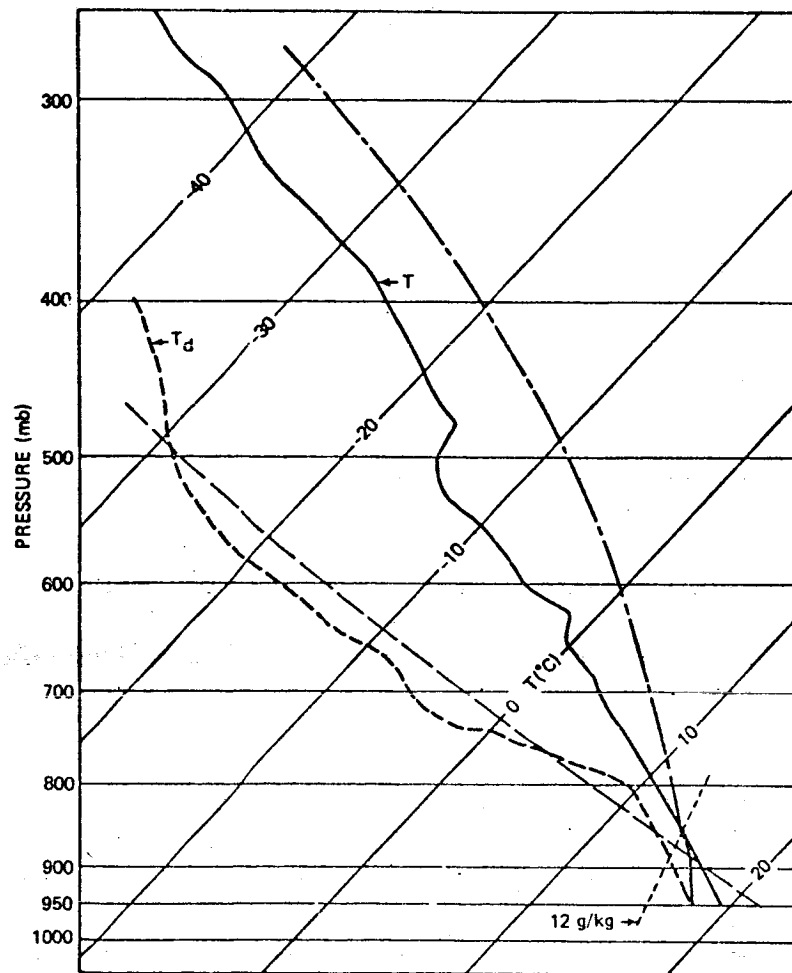
FIGURE 4 Initial temperature and dew-point temperature profiles in a midlatitude case.

independent. The following example illustrates these variations and explains why they occur.

The initial soundings are shown in Figure 4. The air is dry above the 800 mb level to represent typical prestorm conditions over the Midwest in spring. The internal heat sink and moisture sources are shown in Figures 5 and 6. Their profiles were rather arbitrarily determined. However, their magnitudes were chosen so that the total input of moist static energy from the internal sources vanishes. Thus clouds in this experiment are driven by both the continuous supply of moisture at low levels and the continuous cooling at upper levels.

Figures 5 and 6 show the cloud heating and drying effects averaged over the 17-hour simulation, respectively. The cloud heating and
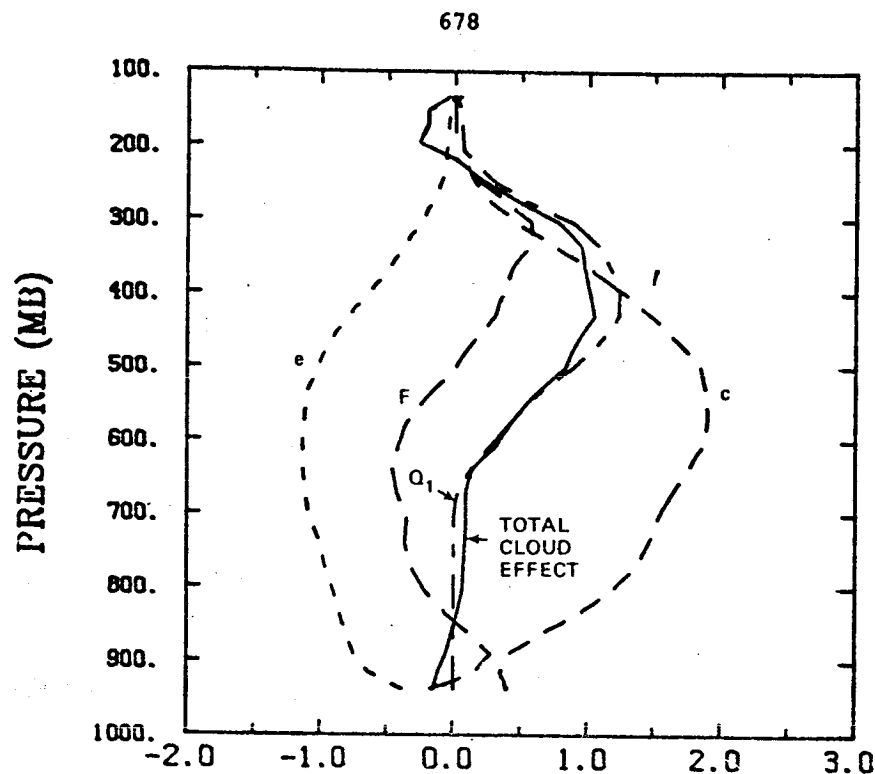
Q1 BUDGET (C/HR)

FIGURE 5   Same as Figure 2, but for the midlatitude case. Q_1-Q_R represents the prescribed rate of cooling due to internal heat sink.

internal cooling did not balance, particularly in the layer between .300 to 550 mb.   This implies that temperatures in this layer tended to decrease on the average.   On the other hand, the layer above 800 mb that was initially dry had been moistened, as one might expect.   An interesting feature of the result lies in the temporal variation of the horizontally averaged precipitation rate shown in Figure 7.   As the moisture increased at low levels, the air became saturated, and rain. started falling at time t = 1.5 hours.   This precipitation lasted about 4 hours and was followed by a period of 4 hours of no significant precipitation.   Even during this period of no precipitation, the model result shows that the major part of the domain was covered by stratiform clouds at upper levels.   The second precipitation event started at 5 = 10.5 hours and it lasted for 2.5 hours.   The precipitation rate was much larger than for the first rain event.   It
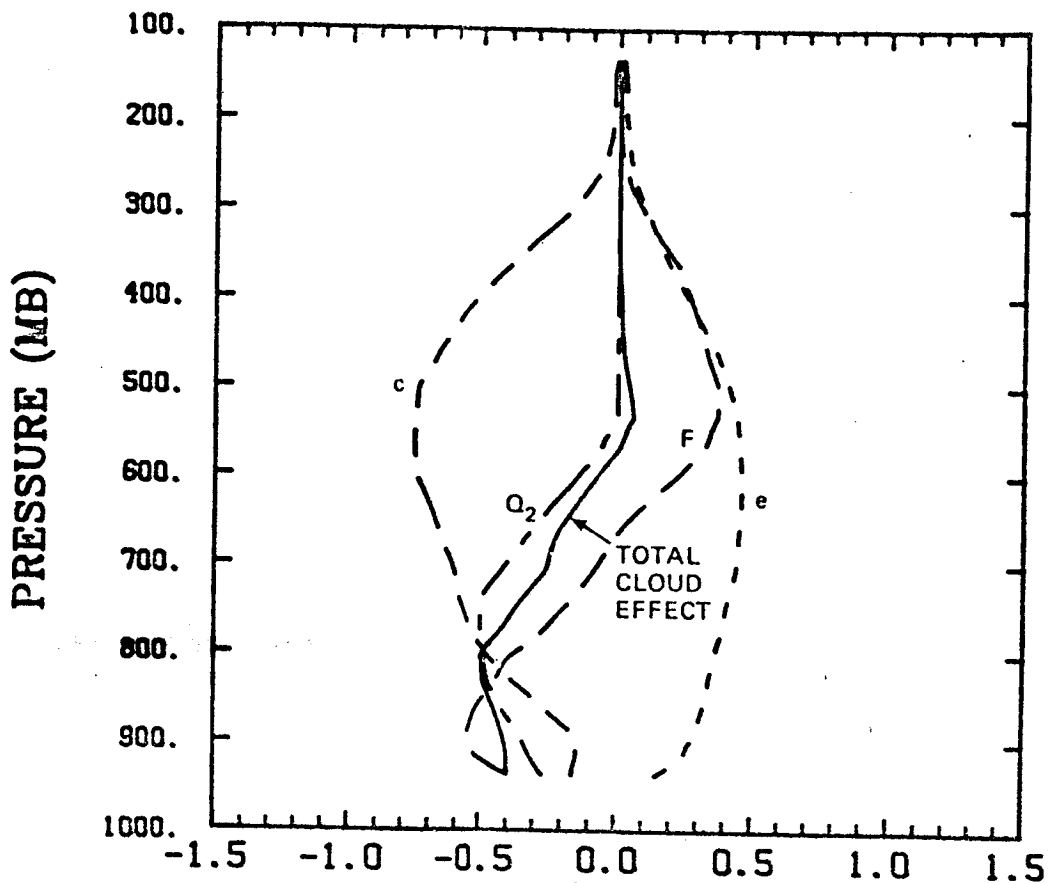
Q2 BUDGET (G/KG/HR)

FIGURE 6 Drying rate by condensation (c), evaporation (e) and the vertical transport of moisture by clouds (F) predicted by the two-dimensional cumulus ensemble model in the midlatitude case. Q_2 represents the prescribed rate of moistening due to internal moisture source.

was again followed by the period of no precipitation with a duration of 3.5 hours.

The physical processes underlying this temporal variation of the precipitation rate are relatively simple. Figure 8 shows the temporal variations of each term in the moisture budget (equation (2b)) at the 980 mb level, being representative of situations at low levels. As the
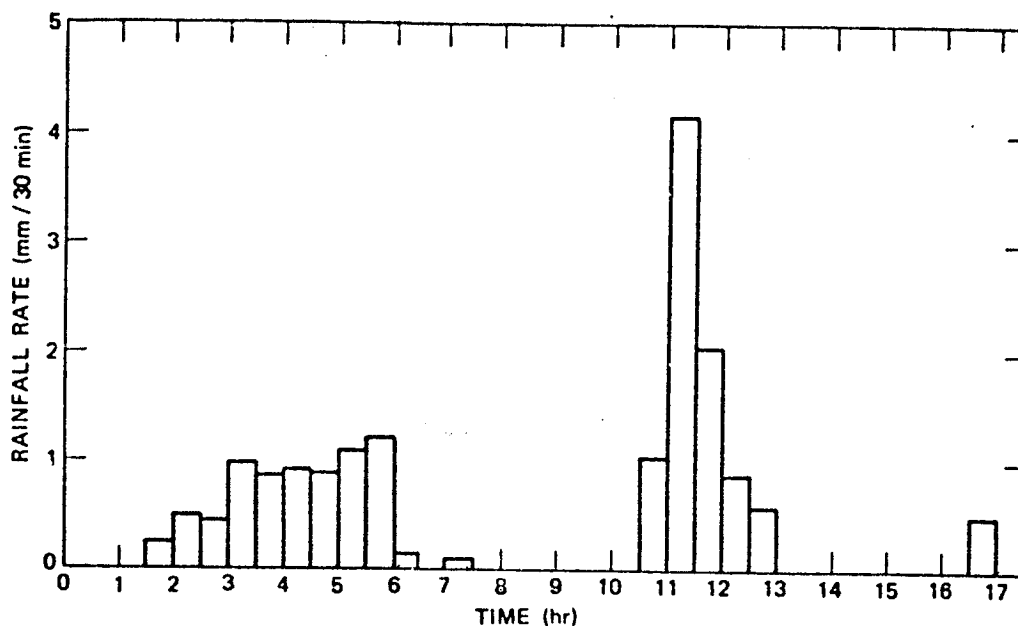
FIGURE 7 Variations of rainfall rate with time predicted by the model.

precipitation develops, the water vapor mixing ratio decreases rapidly, primarily due to the large net vertical flux of moisture. Eventually, air at low levels becomes so dry that deep convection ceases to develop. During the next 4 hours, the moisture at low levels gradually increases due to supply from the internal moisture source. In the meantime, air at upper levels is continuously cooled by the internal heat sink. Consequently, when the air at low levels becomes saturated and the atmosphere is ready to overturn, the atmospheric stratification is more unstable than the inital state; hence more vigorous convection occurs. So vigorous is convection this time that precipitation lasts only 2.5 hours.

This experiment may illustrate the importance of the coupling between the cloud layer and the boundary layer; the updraft depletes moisture from the boundary layer, and the unsatruated downdraft penetrating into the subcloud layer also dries the boundary layer. Simpson and van Helvoirt (1980) discussed the interactions between the clouds and subcloud layer in GATE. Cumulus downdrafts were postulated to be the main interaction mechanism on the scales of interest.

It has been noted above that the model clouds did not completely compensate the prescribed internal heating and moistening, and as a result, the area averaged temperature and moisture profiles tend to continuously depart from the initial conditions at certain heights. This is not unexpected at all since clouds have their own dynamics and physics, and they cannot compensate any large-scale thermodynamic forcing caused by the arbitrary internal heat and moisture sources.
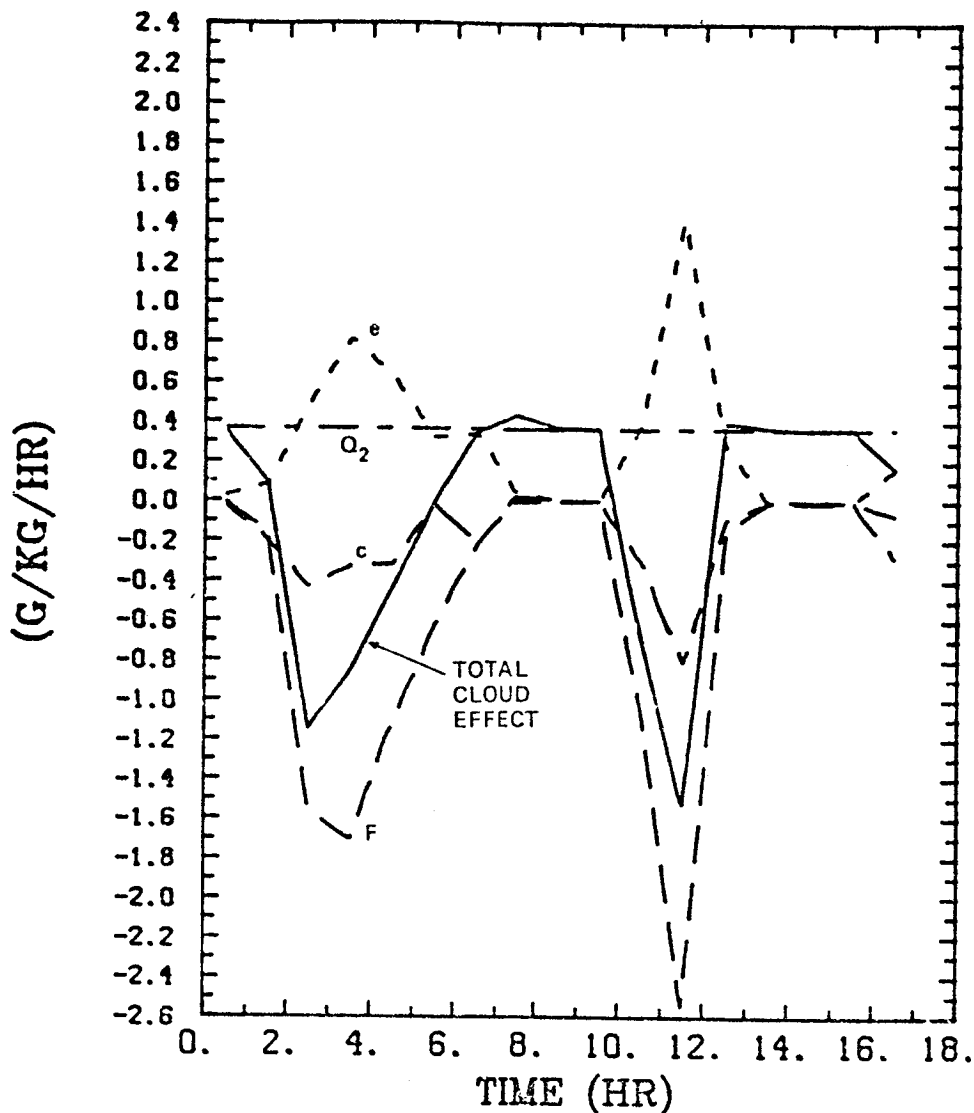
FIGURE 8 Temporal variations of condensation (c), evaporation (e), vertical transport of moisture (F), and the total cloud drying effect (sum of the three terms) at the 890 mb level. Q_2 denotes the prescribed rate of moistening due to internal moisture source.

Why, then, can tropical clouds in Section 2 adjust themselves to the imposed large-scale forcing resulting in a quasi-equilibrium state with the environment? The answer may be in the special nature of the large-scale forcing, special in the sense that the large-scale forcing was estimated as $\bar{\omega}(\partial\bar{\theta}/\partial p)$ and $\bar{\omega}(\partial\bar{q}/\partial p)$, using the observed $\bar{\omega}$, $\bar{\theta}$, and $\bar{q}$.

Ogura (1982) argued that local maxima of $\bar{\omega}$ in the upper troposphere that are often observed in many tropical and midlatitude mesoscale convective systems at their mature stages, including the case shown in Figure 1, are primarily a reflection of a group of growing or already well-developed deep convection (i.e., cloud induced cloudscale and mesoscale vertical velocity) rather than the large-scale ascending motion that might have forced deep convection to develop. This interpretation of the middle or upper level $\bar{\omega}$ is based on the observations that the maximum $\bar{\omega}$ increases both in magnitude and its altitude with development of the radar echo intensity in many cases. The agreement between $\bar{M}$ and the model calculated M_c shown in Figure 3 also supports this interpretation.

If this interpretation is correct for most, if not all, of mesoscale convective systems that develop in the tropics, it may not be surprising to find, as Yanai et al. (1976) actually did for tropical Pacific convective systems, that deep convection is best correlated to upper tropospheric vertical motions. This implies however that this high correlation has no use for predicting occurrence of deep convection simply because the upper tropospheric upward motion is a consequence, not a cause, of deep convection, at least in those cases where preexisting upper level large-scale ascending motion is absent.

Thus a good agreement was achieved between the cloud and large-scale heating and moistening effects in the tropical situation in Section 2 since the large-scale effects were calculated using ω, which we now interpret as basically the cloud induced vertical velocity. Consequently, any reasonably realistic model clouds should not have any difficulty in adjusting themselves to the imposed large-scale forcing that is believed to be not really acting in many cases.

CUMULUS PARAMETERIZATION

This section illustrates how knowledge gained from the cloud modeling study described above may be useful to improve cumulus parameterization schemes. The focus will be on the Arakawa-Schubert scheme (1974), since this scheme has more physics than others, and will be referred to as the A-S scheme.

The A-S scheme has been tested by several authors. The most extensive test was made by Lord (1978, 1982) on the basis of a semi-prognostic method (i.e., one time-step integration) using the GATE Phase III data. The semiprognostic method uses large-scale variables observed at each observation time to compute the large-scale forcing. The A-S scheme has also been tested semiprognostically using data for the tropical rainband event described in Section 2. In doing so, an algorithm different from Lord's has been used in computing the kernel and the large-scale forcing. A subroutine of linear programming named 2X4LP from the IMSL package was found to have a better accuracy in solving the A-S scheme. Three-hourly rawinsonde observations were available for the rainband case. Figure 9 (10) shows the comparison between the heating (drying) rate predicted from the A-S scheme and the observation based on the large-scale heat (moisture) budget. The

683
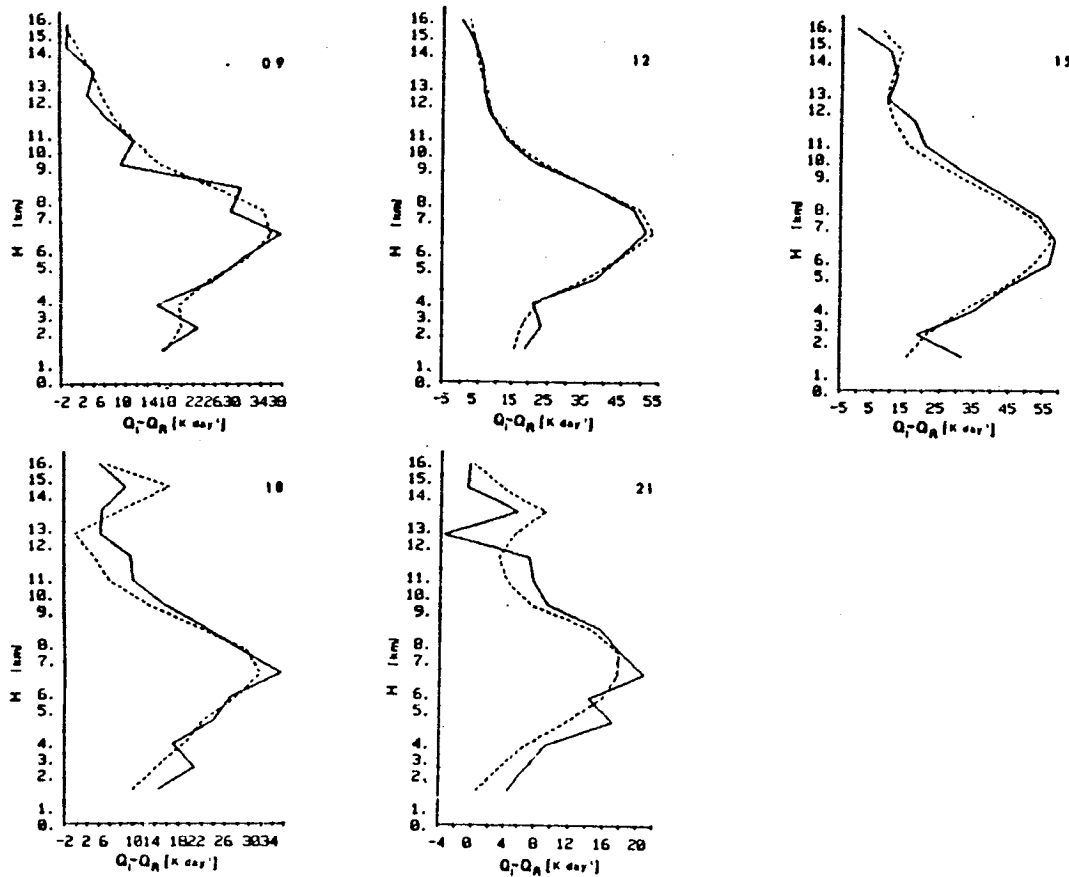
FIGURE 9 Cloud heating effect predicted by the Arakawa-Schubert cumulus parameterization (solid lines) and the apparent heat source estimated from the large-scale heat budget (dashed lines) at each observation time during the period from 09 through 21 GMT August 12, 1974. Note that different scales are used on abscissas.

agreement is rather impressive throughout the developing, mature, and decaying stages of the rainband.

The A-S scheme considers many cumulus clouds with different entrainment constants, and the cloud properties of each class of clouds are specified by a one-dimensional, steady-state, entraining cloud model. Thus the A-S scheme permits the prediction of not only the net cloud heating and drying effects (i.e., the sum of the three terms in equations (1b) and (2b)), but also each term of equations (1b) and (2b) individually. This was computed, and Figure 11 shows the result for the situation at 06 to 09 GMT August 12, 1979. A comparison of Figure 11 with the result from the cumulus ensemble model (Figure 2) shows that the A-S scheme substantially underestimates the rate of cooling by
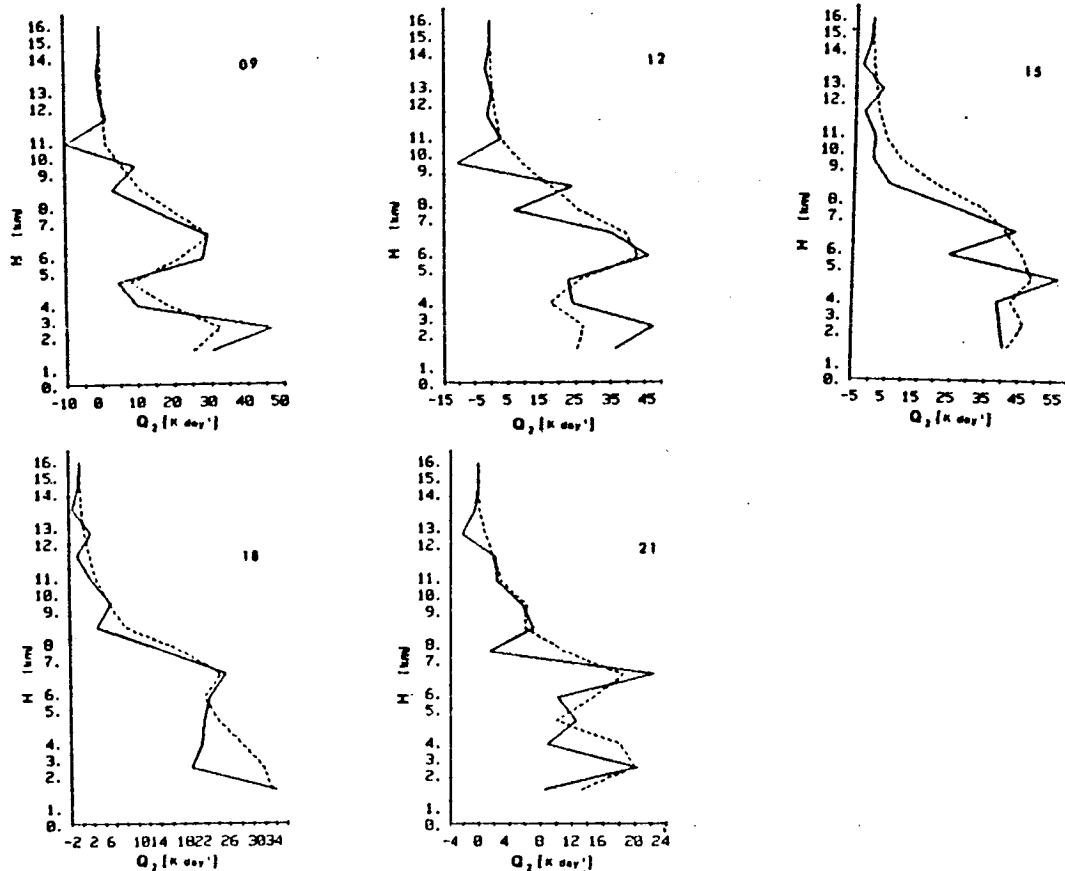
FIGURE 10 Same as Figure 9, but for cloud drying effect and apparent moisture sink.

evaporation. This is not surprising since the A-S scheme does not include the downdraft effect, and all raindrops are assumed to fall out from the system as soon as they form. Evaporation occurs from cloud droplets in the layer of detrainment, which occurs only at the cloudtop level. Interestingly, the A-S scheme underestimates the rate of compensation also, with the result that the net heating rate is just about right.

This result and the discussion on the downdraft effect in Section 4 point a way to improve the A-S scheme. The A-S scheme has been modified by including the downdraft effect, essentially as formulated by Johnson (1976) in his diagnostic study of the cloud effects, but with different values of the parameters. The result is shown in Figures 12 and 13. The agreement between the predicted cloud heating effect and the observation is as good as in Figure 11. However, the predicted condensation and evaporation rates are closer to the model

685
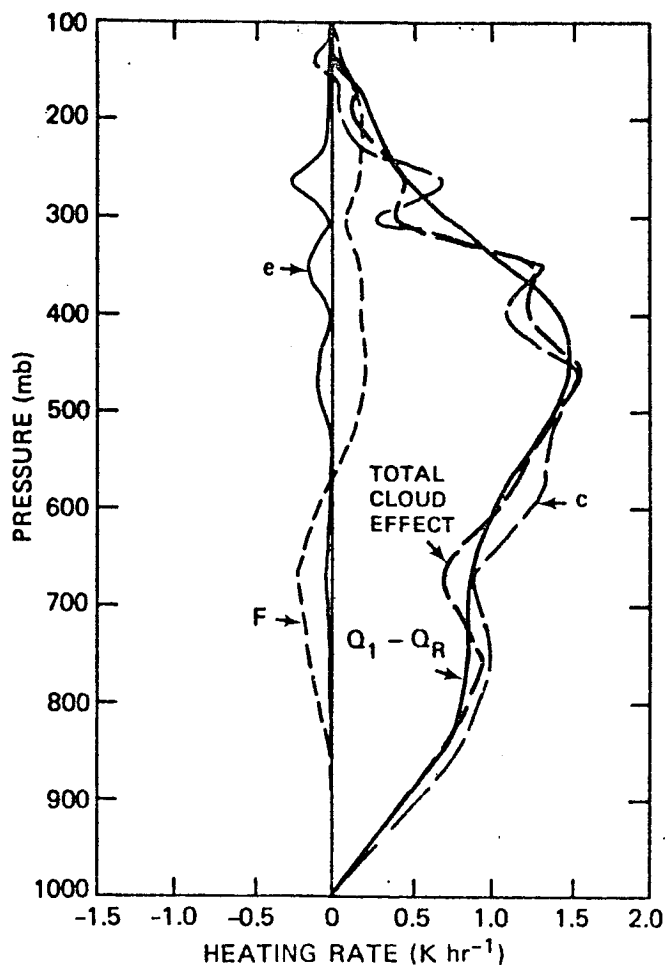
FIGURE 11 Same as Figure 2, but cloud heating effect predicted by the Arakawa-Schubert scheme for the situation at 09 GMT August 12, 1974.

results. More importantly, the modified A-S scheme includes and predicts the downdraft, which agrees fairly well with the model result shown in Figure 3. The proper simulation of boundary layer processes and their interaction with the A-S scheme is critical (Suarez et al., 1983). Hopefully, the inclusion of the downdraft will improve prediction of the boundary layer behavior.

686
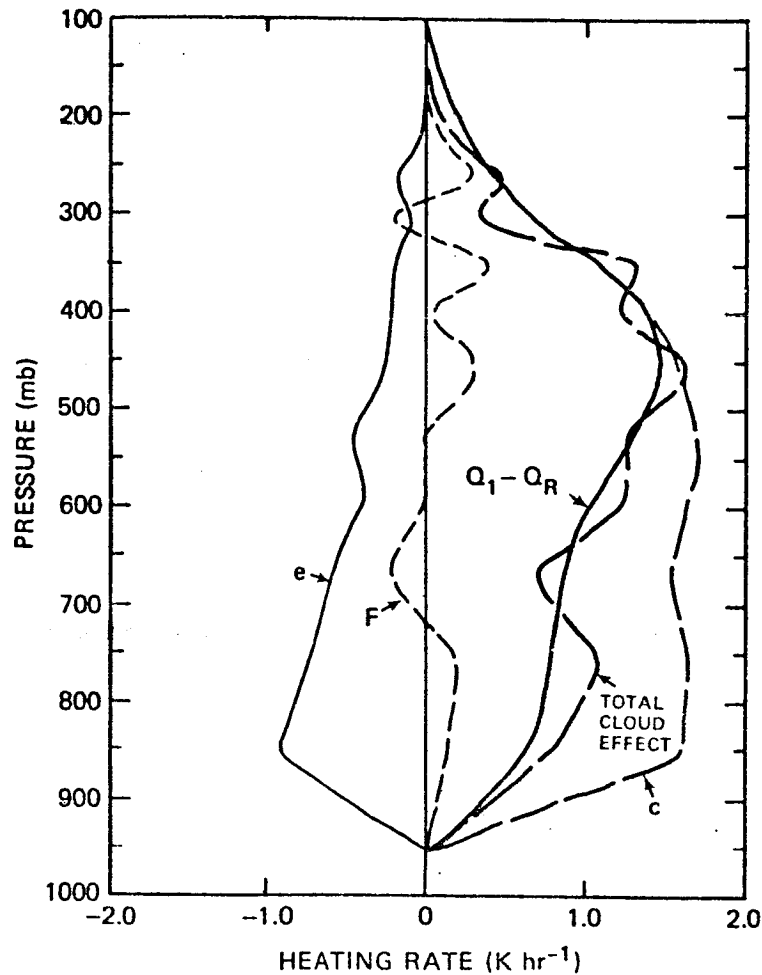
FIGURE 12 Same as Figure 2, but cloud heating effect predicted by the modified Arakawa-Schubert scheme at 09 GMT August 12, 1974.

FIGURE 13   Same as Figure 3, but predicted by the modified
Arakawa-Schubert scheme at 09 GMT August 12, 1974.

REFERENCES

Arakawa, A., and W. H. Schubert (1974).   Interaction of a cumulus cloud
   ensemble with the large-scale environment, Part I.   J. Atmos. Sci.
   31, 674-701.
Frank, W. M. (1983).   The cumulus parameterization problem.   Mon. Wea.
   Rev. 111, 1859-1871.

Johnson, R. H. (1976). The role of convective-scale precipitation downdrafts in cumulus and synoptic-scale interactions. J. Atmos. Sci. 33, 1890-1910.

Lord, S. J. (1978). Development and observational verification of a cumulus cloud parameterization. Ph.D. dissertation, University of California, Los Angeles, 359 pp.

Lord, S. J. (1982). Interaction of a cumulus cloud ensemble with the large-scale environment. Part III: Semi-cumulus parameterization. J. Atmos. Sci. 39, 88-103.

Kuo, Y.-H., and R. A. Anthes (1984). Mesoscale budgets of heat and moisture in a convective system over the central United States. Mon. Wea. Rev. 112 (in press).

Ogura, Y. (1982). A modeling study of mesoscale convective systems. Collection of Lecture Notes on Mesoscale Models, Proc. CIMMS 1982 Symposium, University of Oklahoma, 85-126.

Ogura, Y., and H.-R. Cho (1973). Diagnostic determination of cumulus cloud populations from large-scale variables. J. Atmos. Sci. 30, 1276-1286.

Ogura, Y., Y.-L. Chen, J. Russell, and S.-T. Soong (1979). On the formation of organized convective systems observed over the eastern Atlantic. Mon. Wea. Rev. 107, 426-441.

Simpson, J., and G. van Helvoirt (1980). GATE cloud-subcloud layer interactions examined using a three-dimensional cumulus model. Beitr. Phys. Atmos. 53, 106-134.

Soong, S.-T., and Y. Ogura (1980). Response of tradewind cumuli to large-scale processes. J. Atmos. Sci. 37, 2035-2050.

Soong, S.-T., and W.-K. Tao (1980). Response of deep tropical cumulus clouds to mesoscale processes. J. Atmos. Sci. 37, 2016-2034.

Soong, S.-T., and W.-K. Tao (1984). A numerical study of the vertical transport of momentum in a tropical rainband. J. Atmos. Sci. 41 (in press).

Suarez, M. J., A. Arakawa, and D. A. Randall (1983). The parameterization of the planetary boundary layer in the UCLA general circulation model: Formulation and results. Mon. Wea. Rev. 111, 2224-2243.

Tao, W.-K. (1983). A numerical study of the structure and vertical transport properties of a tropical convective system. Ph.D. dissertation, Department of Atmospheric Sciences, University of Illinois, Urbana-Champaign, 228 pp.

Yanai, M., S. Esbensen, and J. Chu (1973). Determination of average bulk properties of tropical cloud clusters from large-scale heat and moisture budgets. J. Atmos. Sci. 30, 611-627.

Yanai, M., J.-H. Chu, T. E. Stark, and T. Nitta (1976). Response of deep and shallow tropical maritime cumuli to large-scale processes. J. Atmos. Sci. 33, 976-991.

ADVANCES IN PARAMETERIZATION OF CUMULUS CONVECTION IN NUMERICAL MODELS

John Molinari
State University of New York at Albany

ABSTRACT

Observational studies over the last decade have revealed new sources of difficulty in the already complex problem of parameterization of precipitating cumulus convection in large-scale numerical weather prediction models. This paper reviews the structure of mesoscale updrafts and downdrafts and the difficulties they present for cumulus parameterization. An approach is proposed which follows Kuo (1974) but includes cumulus and mesoscale downdrafts in the vertical distributions of heating and moistening. The development of a realistic life cycle behavior in the numerical prediction of a mesoscale convective complex will be shown.

INTRODUCTION

The parameterization of vertical transports of heat, moisture, and momentum by precipitating cumulus clouds remains a major unsolved problem in numerical weather prediction. Although success has been achieved with large-scale models (grid spacing 100 km or more) in the simulation of convectively driven phenomena (e.g., Krishnamurti et al., 1983; Suarez et al., 1983; Miyakoda and Sirutis, 1983), recent studies using FGGE and other data have revealed additional complexity that is not adequately incorporated by current approaches to cumulus parameterization. Among the most significant findings are:

1. The existence of organized, persistent updrafts and downdrafts on a scale larger than that of a convective cloud but still largely unresolvable by the large-scale model grid (Betts, 1973; Zipser, 1977; Houze, 1982).

2. Large vertical transports of momentum and vorticity by cumulus convection (Shapiro and Stevens, 1980; Yanai et al., 1982; Cho et al., 1983), which under some circumstances affect subsequent disturbance evolution more than heat and moisture transports (Schubert et al., 1980).

3. The sensitivity of general circulation model simulations to the parameterization of radiative-convective interactions (Tiedtke, 1984),
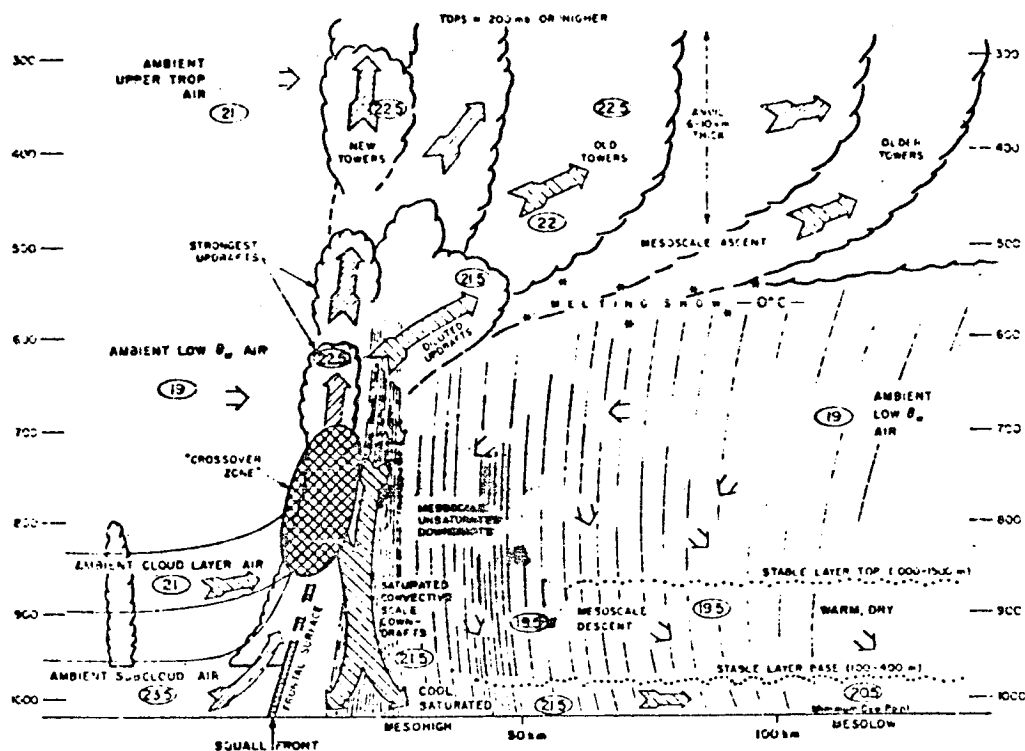
FIGURE 1 Schematic view of a GATE squall line from Zipser (1980).

which influence the model climate as much as fundamental changes in cumulus parameterization.

Only the first of these will be discussed in this paper. Some of the potential difficulties imposed on the large-scale modeler by the existence of mesoscale circulations will be presented. Results of recent numerical simulations by the author which include a bulk parameterization of mesoscale effects will be discussed.

EFFECTS OF MESOSCALE UPDRAFTS AND DOWNDRAFTS ON CUMULUS PARAMETERIZATION

Figure 1 (Zipser, 1980) shows a schematic diagram of a GATE squall line. Behind the propagating line, an extensive region of stratiform precipitation is present. The stratiform rain, which may account for 20 to 50 percent of the total rainfall from the system, is initiated by the spread of hydrometeors from adjacent updrafts, by dying of old

cells, and by condensation in the active mesoscale updraft in the anvil (Churchill and Houze, 1984). The unsaturated mesoscale downdraft is driven by cooling due to melting and evaporation and by precipitation loading.

Radar depiction of the time evolution of a slowly propagating GATE cloud cluster is shown in Figure 2 (Houze and Rappaport, 1984). The mesoscale anvil circulation develops within three to four hours. Significant time variations occur in the anvil, which in this somewhat atypical case, extends from both sides of the major active updraft. Figure 4 (Churchill and Houze, 1984) shows a detailed view from instrumented aircraft of a stationary cloud cluster near Borneo, composited over several hours. Each dot represents the location of an updraft core. One part of the area contains only stratiform precipitation and mesoscale downdrafts, which apparently suppress active updrafts in that region. In this stationary cluster, convective and mesoscale circulations co-exist for several hours.

The presence of the mesoscale circulations greatly complicates cumulus parameterization in large-scale models, for several reasons:

1. The vertical heating and moistening profiles in stratiform regions are significantly different than those for cumulonimubs alone, as shown in Figure 3a, b (Houze, 1982). Hartman et al. (1984) compared simulations of the tropical Walker circulation in a linear steady state model using the mature cluster heating profile and the cumulonimbus profile alone. The cluster profile more accurately reproduced the Walker circulation, and the authors suggested that mesoscale cloud clusters played a major role in tropical heating.

2. The vertical profile of heating undergoes a life cycle as convective-scale circulations evolve into predominantly mesoscale drafts. At a given instant, the heating rate depends greatly on the percentage of total rainfall that is stratiform (Johnson, 1984).

3. The properties of the cloud environment, needed for entrainment calculations in any parameterization based on parcel theory, is quite different within a mature cluster than for initially isolated convection. Use of an undisturbed environment in entrainment calculations would likely underestimate cloud buoyancy.

4. The rapid formation of the anvil, its large extent (sometimes >200 km in length), and its often slow dissipation, even after convection has ended, have great influence on the local radiation budget, especially over land.

The large-scale modeler faces the following difficulty: Initially the unsaturated downdrafts accompany active cumulus-scale updrafts and downdrafts, i.e., occur at the same grid point, and thus must be parameterized. As the convective cluster matures, however, the mesoscale downdrafts cover an increasing percentage of the area. Eventually, the convective updrafts stop, and only the mesoscale circulation remains at the grid point (Houze, 1982), or the convectively active region propagates to an adjacent grid point, leaving a mesoscale downdraft in its wake. In either case, the unsaturated downdraft becomes (at the original point) an explicit
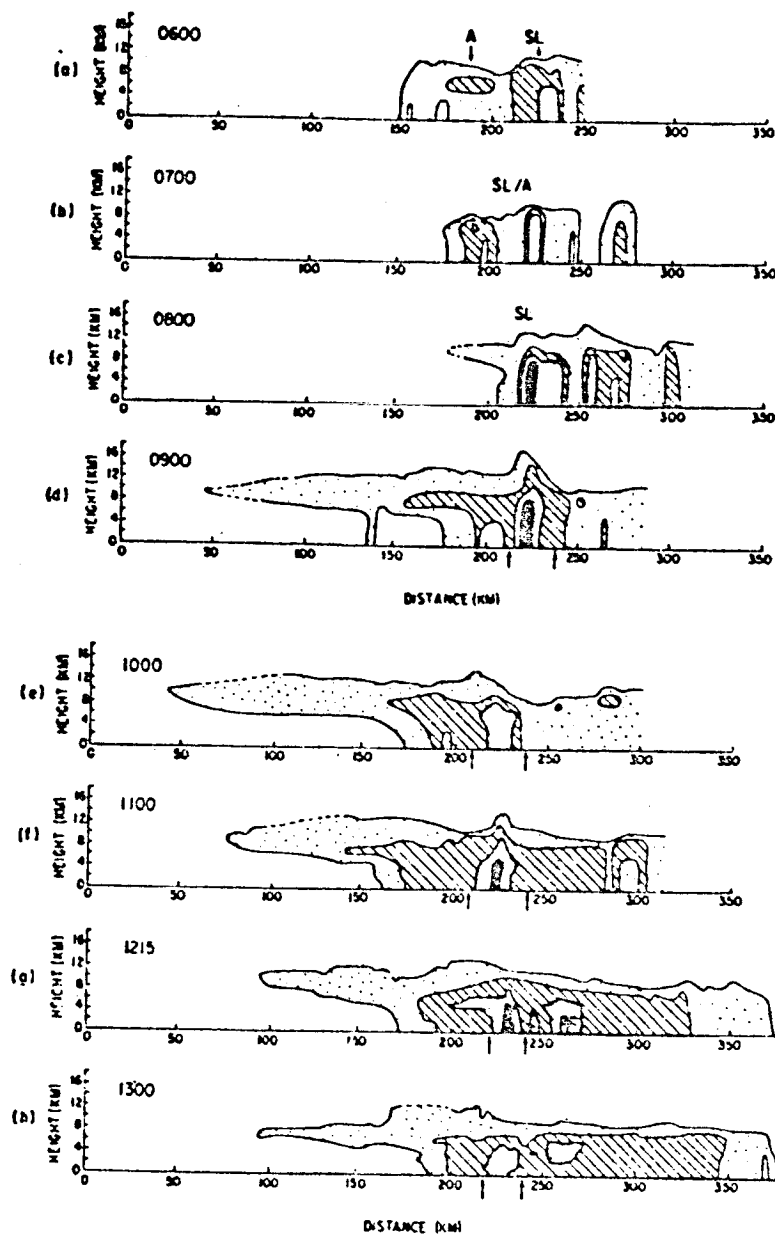
FIGURE 2   Radar depiction of the time history of a slow moving GATE
squall line from Houze and Rappaport (1984).   Cross sections are
parallel to direction of propagation.   Shading represents minimum
detectable signal, 24, 34, and 44 db(Z).

TOTAL HEATING BY NON-RADIATIVE
MESOSCALE PROCESSES
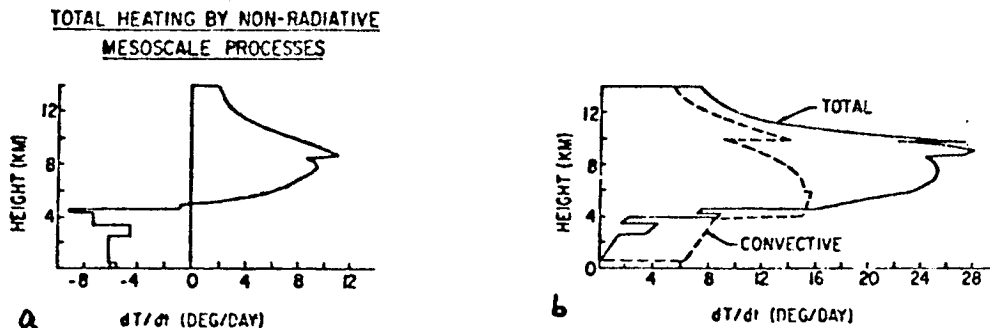
FIGURE 3   (a) Non-radiative heating by mesoscale updrafts and downdrafts only; (b) Total (convective plus mesoscale) heating (solid line) for a mature cloud cluster, and convective heating alone (dashed line). From Houze (1982).

grid-scale phenomenon, unaccompanied by the convective scale, and is no longer parameterized. The large-scale modeler must simulate (1) the vertical distribution of heat and moisture sources due to subgrid-scale convection and radiation, (2) their time variation over the life cycle of the system as mesoscale downdrafts increase in areal coverage, and (3) the grid-scale residue left behind.

   The remainder of this paper will present recent results of the author on a cumulus parameterization based on that of Kuo (1974), but with cumulus and mesoscale downdrafts incorporated into the vertical distribution functions. The approach is tested in a three-dimensional primitive equation prediction of a mesoscale convective complex and is shown to produce a life cycle behavior with many similarities to those observed.

DESCRIPTION AND PROPERTIES OF THE APPROACH

The approach follows the framework of Kanamitsu (1975), Krishnamurti et al. (1976), and Molinari (1982). Because the intensity of convective forcing is proportional to the instantaneous rate at which moisture is supplied to the grid point, definition of the moisture supply is of fundamental importance. Kuo (1983) has shown that, although vertically integrated moisture convergence lags rainfall by increasing amounts with increasing horizontal scale, the quantity

$$I = -\frac{1}{g}\int_{Pt}^{Pb} \omega\frac{\partial q}{\partial p}\,dp \qquad (1)$$

contains no lag on any scale, even 750 x 750 km. Thus Kuo's fundamental assumption of rainfall proportional to rate of moisture supply appears to be valid for deep convection as long as equation (1) is used to define the moisture supply. Equation (1), proposed by Kanamitsu (1975), is adopted in this study.
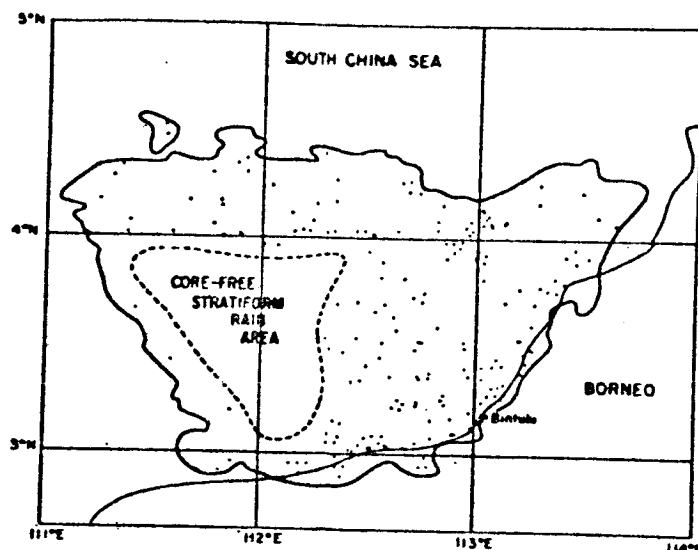
FIGURE 4 Composite radar echo pattern at 3 km over a ten-hour period for a cloud cluster near Borneo. Dots indicate active updraft cores. (From Churchill and Houze, 1984)

The vertical distribution of heating and moistening is defined by the temperature and specific humidity differences between the grid scale and an idealized cloud. Downdrafts are added to the idealized cloud profile by determining a weighted mean of the equivalent potential temperatures (θ_e) and specific humidity for cumulus updrafts, saturated cumulus downdrafts, and unsaturated mesoscale downdrafts, and by extracting the cloud temperature iteratively. The values are weighted by the vertical eddy flux convergence of moist static energy by each component, as determined from the data of Johnson (1980). Details are provided by Molinari (1984).

Stabilization characteristics of the approach are determined by measuring the rate of reduction of updraft temperature excess in one-dimensional integrations from tropical standard atmosphere under steady forcing. Stabilization rate increases with increasing precipitation efficiency. Cumulus downdrafts dominate the stabilization process; mesoscale downdrafts act to stabilize but have much less influence. The stabilization rate is affected by large changes in relative humidity in the mesoscale downdrafts; when they are assumed saturated, stabilization occurs twice as rapidly. When downdrafts are removed, the sounding still moves toward a more stable profile but at less than 20 percent of the rate when downdrafts are included. A slower stabilization rate is simulated in the presence of surface heat and moisture fluxes.

TABLE 1 Total Rain Volume (10^{12} kg)

	Rain Volume	Error (%)
Observed (Bosart and Sanders, 1981)	2.15	--
Full physics	2.41	+12
No downdrafts	2.76	+28
No convection	0.08	-96

RESULTS

The approach is tested in a real data, three-dimensional primitive equation prediction of a mesoscale convective complex (MCC; Bosart and Sanders, 1981) on a 1° latitude/longitude mesh. The effects of downdrafts on the evolution of the convection and the overall role of convection in the MCC are examined with three integrations: a full physics integration that includes both mesoscale and convective scale downdrafts; a second integration identical to the first but with downdrafts removed; and an integration in which no convective heating is allowed, but full physics is present otherwise, including condensation heating produced when saturation is exceeded.

Table 1 compares the total volume of rainfall observed to that predicted. The integration with downdrafts is most accurate; without downdrafts, rainfall is overestimated; and without convection, rainfall is greatly underestimated.

Figure 5a compares the vertical motion at a point of heavy rainfall for hours 3 to 7 of the three integrations. The integration with downdrafts undergoes a life cycle behavior. Upward motion is intially largest in the middle troposphere, then shifts to an upper tropospheric maximum 5 to 6 hours after the start of the rainfall, while downward motion develops in the lower troposphere. During the last hour shown at each grid point, the rainfall is stratiform only, falling at about 1.5 cm/day from saturated upper levels.

Figure 6 shows the change in the apparent heat source Q_1 at the first grid point from hour 2 to hour 5, just prior to the shift to stratiform rainfall. The Q_1 values include heating due to surface fluxes and are normalized by the rainfall rate. The Q_1 profiles show heating at all levels early in the period but low-level cooling and relatively greater upper level heating at the later time.

The life cycle behavior contains many similarities to those described in GATE (Zipser, 1980; Houze, 1982; Johnson and Young, 1983) and in a composite MCC (Maddox, 1983). Most encouraging in these results is the simulation of the grid scale residue of low-level downdrafts and upper level updrafts that remain as the convection propagates eastward.

When downdrafts are removed, the behavior is dramatically altered. Little or no variation occurs in the lower tropospheric ω (Figure

a

PRESSURE (MB)

OMEGA

b

PRESSURE (MB)

OMEGA
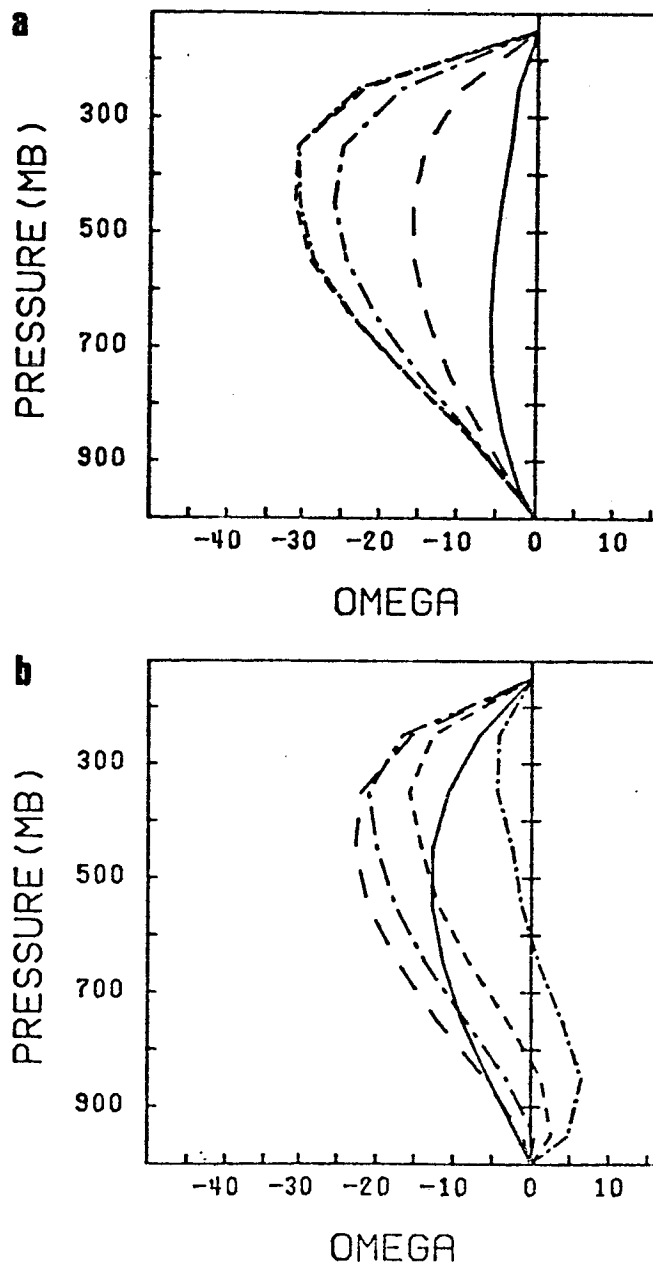
FIGURE 5   (a) Vertical motion in the full physics integration at hour 3
(solid), hour 4 (large dash), hour 5 (large dash-dot), hour 6 (small
dash), and hour 7 (small dash-dot) at the grid point 9,6.   (b) Same as
(a) but in the integration without downdrafts.   (c) Same as (a) but in
the integration without convection.

697

OMEGA
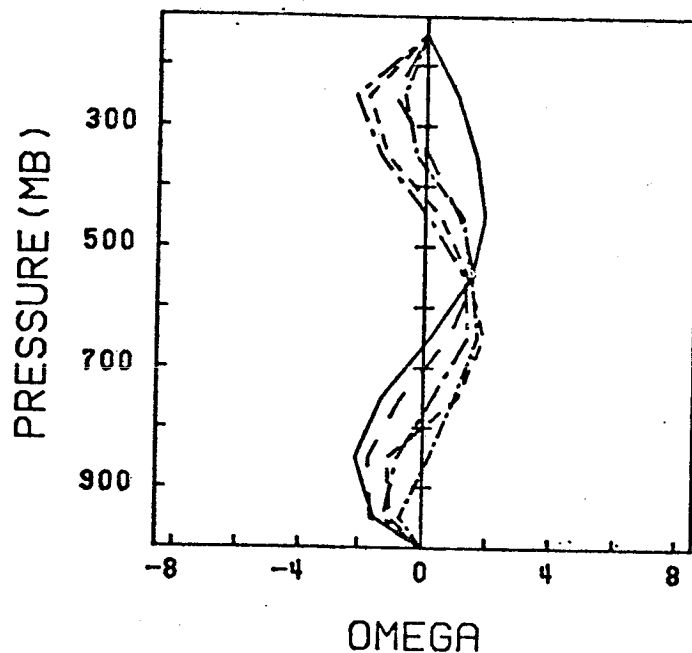
5b), and strong upward motion and intense rainfall occur for several hours. This behavior represents a feedback instability that has frequently been experienced with Kuo's approach without downdrafts (e.g., Kanamitsu, 1975). The column is heated, producing upper level divergence, surface pressure falls, and continued moisture convergence and heating. Figures 7 and 8 show difference fields (no downdraft case minus full physics case) of 1000 mb height and wind at hour 6. Pressure falls and enhanced low-level convergence accompany the excessive rainfall rates in the integration without downdrafts. The overall effect of downdrafts is to improve the rainfall forecast by incorporating the stabilizing influence of low-level cooling by convection, which greatly reduces the chance of the one grid point instabilities that can otherwise occur.

A third integration with convective heating removed gives a measure of its role in maintaining the MCC circulation. The upward motion generated by grid-scale dynamics and physics, independent of convection, is insufficient to produce widespread saturation and rainfall, with a point value maximum of less than 0.5 cm. The original impulse of upward motion (Figure 5c), which is generated largely by low-level warm advection (Corsetti, 1982), remains at low levels; no deep vertical circulation ever develops. The role of convective heating can be shown by difference vectors between the full physics integration and that without convection. Figures 9 and 10 show these vectors at 200 and 800 mb, respectively. Strong outflow above the MCC at hour 3 evolves into an anticyclonic eddy over 12 hours and moves with the heavy rainfall region. The location of this eddy at hour 12 is nearly identical to the observed 200 mb anticyclone given by

698
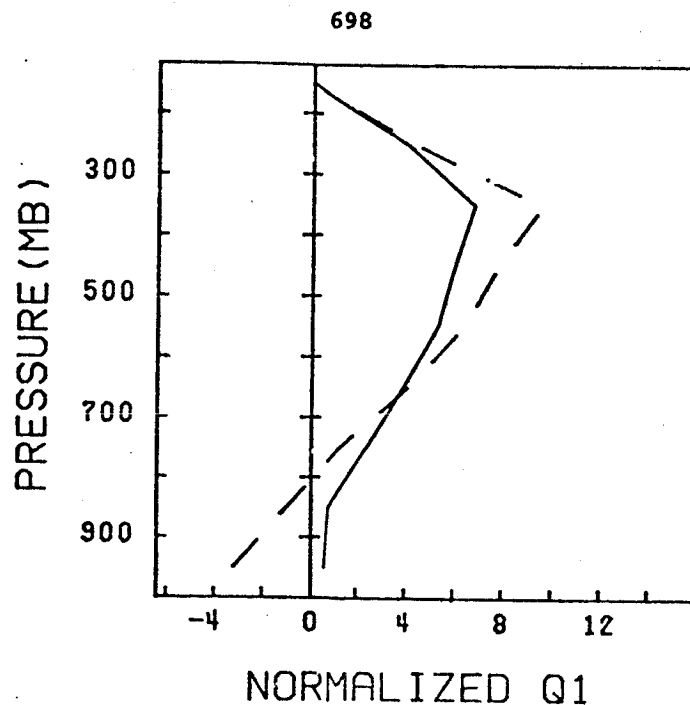
FIGURE 6 Apparent heat source for the 9,6 grid point in the full physics integration at hours 2 (solid) and 5 (dashed).

Corsetti (1982). A low-level cyclonic eddy develops simultaneously (Figure 10). At 500 mb (not shown), the difference vector magnitude is less than 1.5 m/s everywhere, indicating a much less dramatic influence of convection at mid-levels.

CONCLUSIONS

A cumulus parameterization based on the closure of Kuo (1974) is tested in the prediction of a mesoscale convective complex. Predicted total rain volume is most accurate when cumulus and mesoscale downdrafts are incorporated. A strong divergent circulation extends 600 km from the narrow heavy rain region of the MCC in only 6 hours, much like those observed (Fritsch and Maddox, 1981). A realistic life cycle behavior occurs only in the integration with downdrafts. The results indicate that (1) Kuo's closure, linking rainfall to a fraction of the instantaneous moisture supply, may be useful in meso-alpha scale models; and (2) incorporation of downdrafts into Kuo's approach appears to be essential to reproduce the life cycle of convective disturbances in nature.
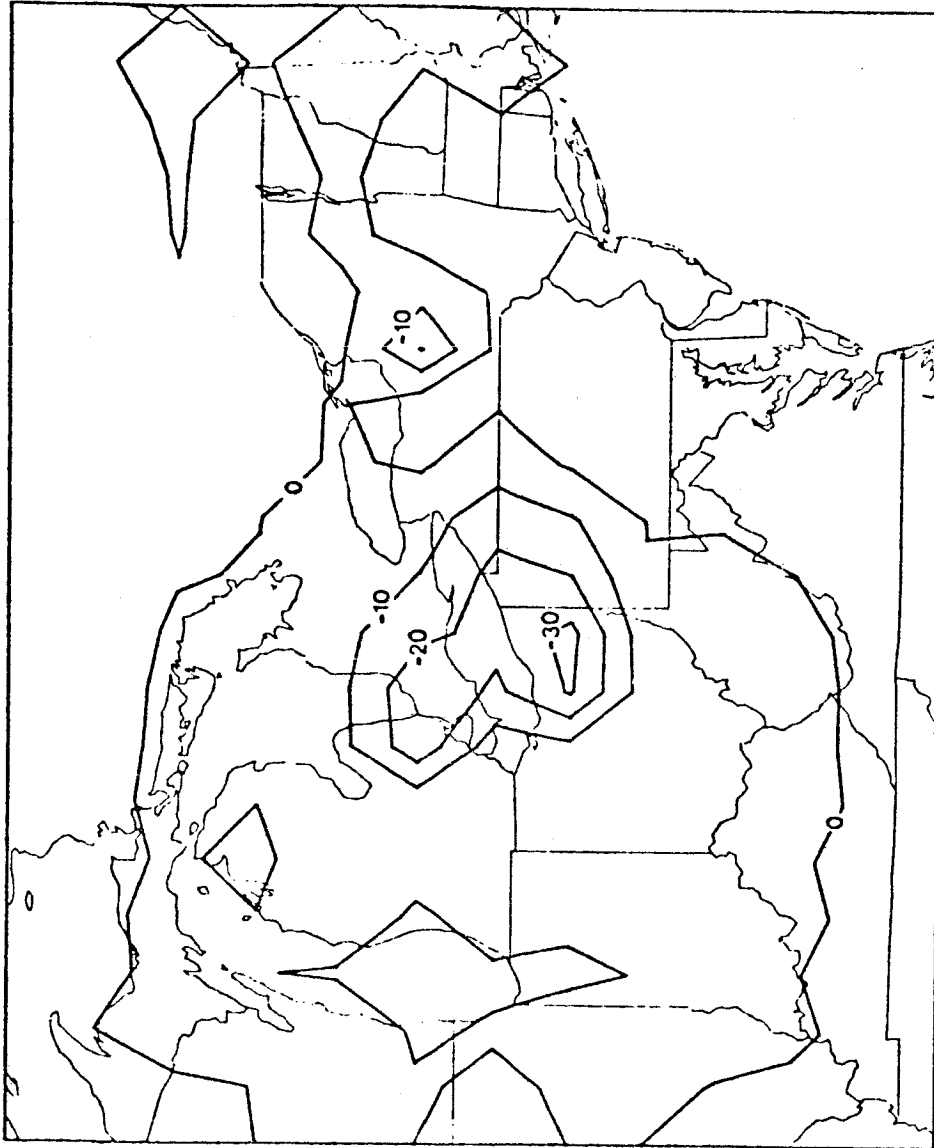
FIGURE 7 Difference vectors at 1000 mb at hour 6 for the no downdraft integration minus the full physics integration.

700

10 M/SEC
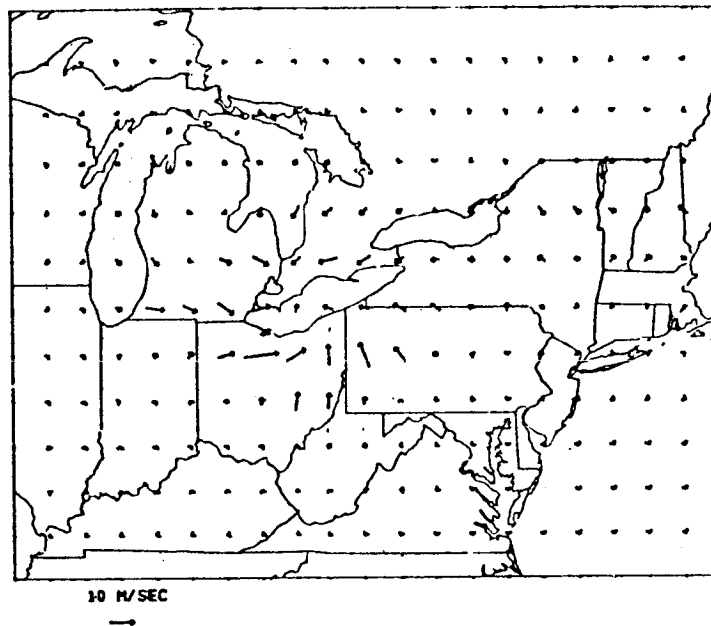
FIGURE 8   Same as Figure 7 but for 1000 mb height.

10 M/SEC
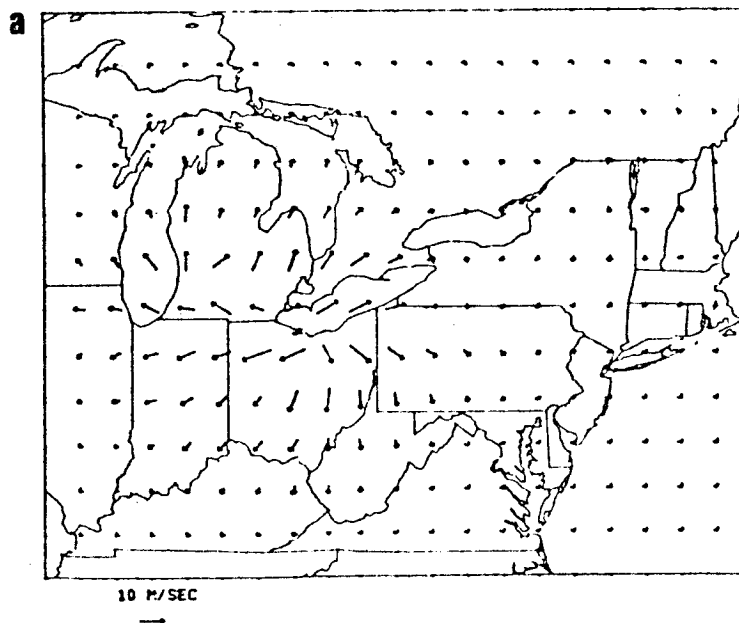
FIGURE 9   (a) Difference vectors at 200 mb between the full physics and
no convection integration for hour 3.   (b) Same as (a) but for hour 6.
(c) Same as (a) but for hour 12.
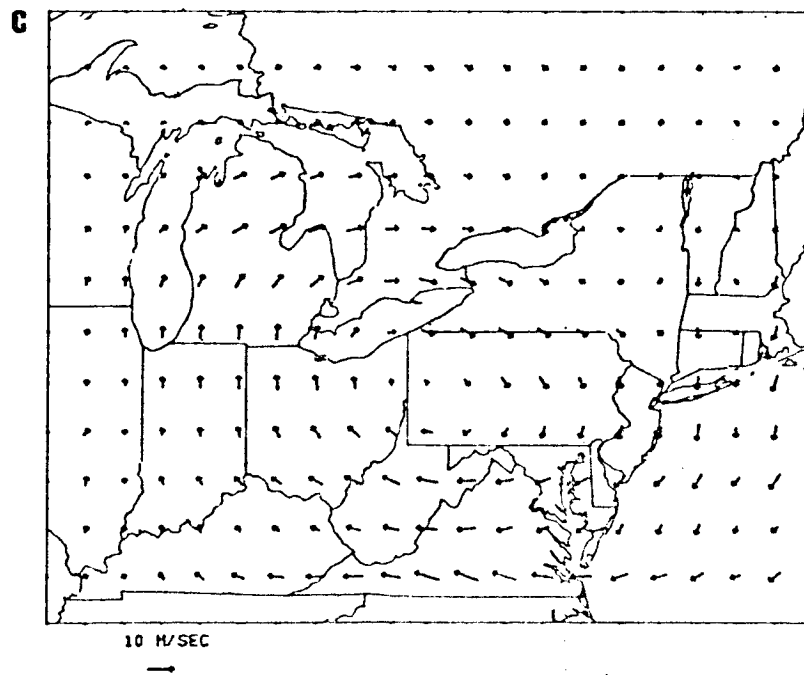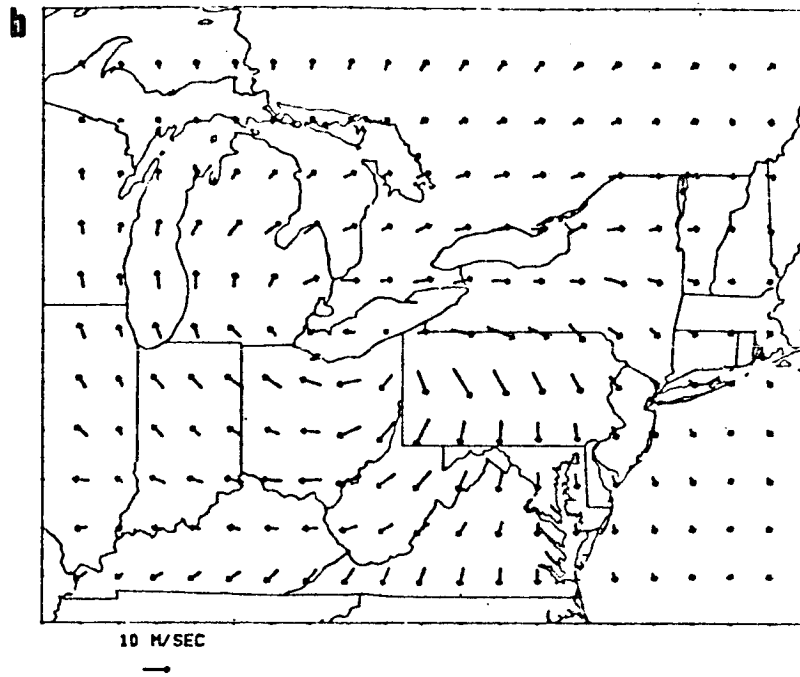
FIGURE 9 b, c
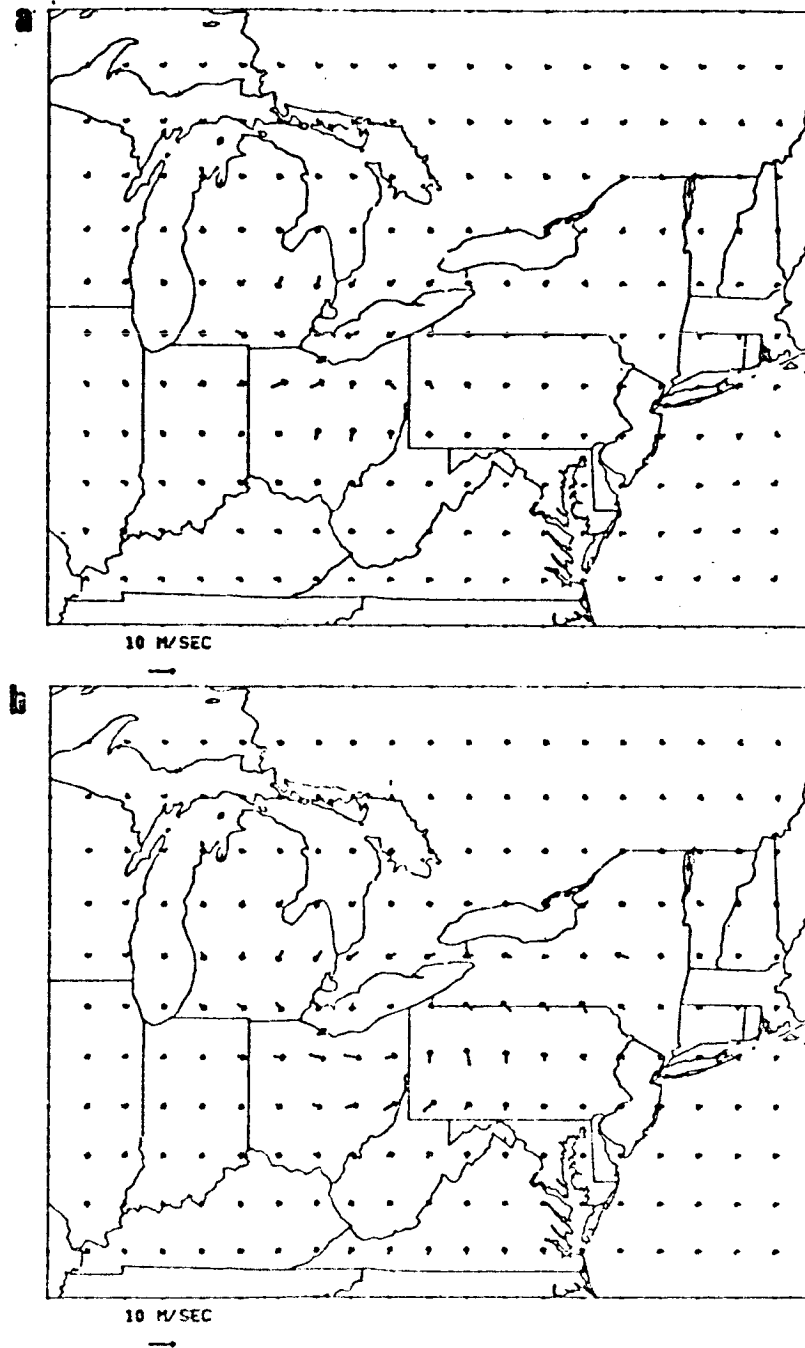
FIGURE 10 (a) Difference vectors at 800 mb between the full physics and no convection integration for hour 3. (b) Same as (a) but for hour 6. (c) Same as (a) but for hour 12.

C

10 M/SEC
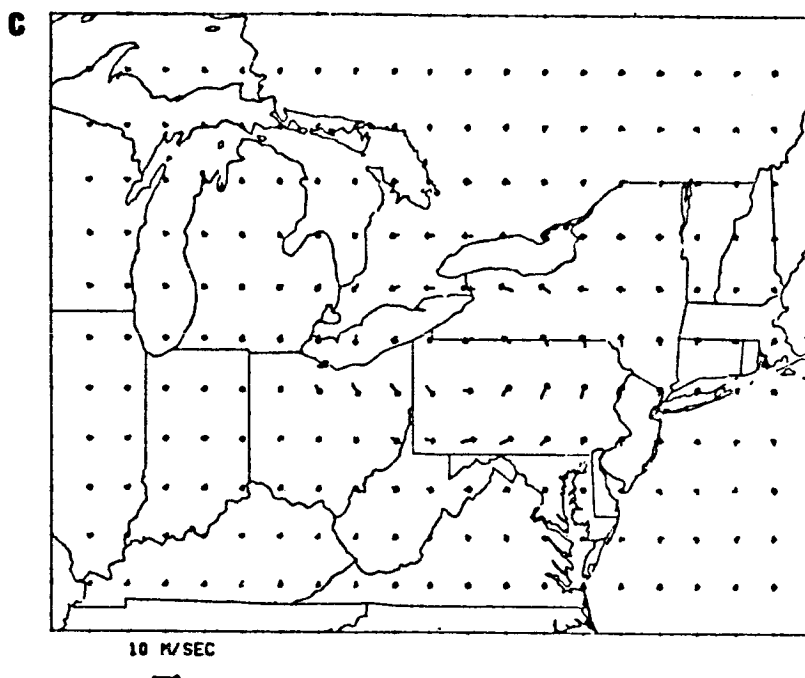
REFERENCES

Betts, A. K. (1973). A composite mesoscale cumulonimbus budget. J. Atmos. Sci. 30, 597-610.

Bosart, L. F., and F. Sanders (1981). The Johnstown flood of July 1977: A long-lived convective system. J. Atmos. Sci. 38, 1616-1642.

Cho, H., M. A. Jenkins, and J. Boyd (1983). A first order vorticity equation for tropical easterly waves. J. Atmos. Sci. 40, 958-968.

Churchill, D. D., and R. A. Houze (1984). Development and structure of winter monsoon cloud clusters on 10 December 1978. J. Atmos. Sci. 41, 933-960.

Corsetti, T. (1982). A numerical simulation of the Johnstown flood of July 1977. M.S. Thesis, Department of Atmospheric Science, State University of New York, Albany, 76 pp.

Fritsch, J. M., and R. A. Maddox (1981). Convectively driven mesoscale weather systems aloft. Part I. Observations. J. Appl. Meteorol. 20, 9-19.

Hartman, D. L., H. H. Hendon, and R. A. Houze (1984). Some implications of the mesoscale circulations in tropical cloud clusters for large-scale dynamics and climate. J. Atmos. Sci. 41, 113-121.

Houze, R. A. (1982). Cloud clusters and large-scale vertical motions in the tropics. J. Meteorol. Soc. Japan 60, 396-410.

Houze, R. A., and E. W. Rappaport (1984). Air motions and precipitation structure of an early summer squall line over the eastern tropical Atlantic. J. Atmos. Sci. 41, 553-574.

Johnson, R. H. (1980). Diagnosis of convective and mesoscale motions during Phase III of GATE. J. Atmos. Sci. 37, 733-753.

Johnson, R. H. (1984). Partitioning tropical heat and moisture budgets into cumulus and mesoscale components: Implications for cumulus parameterization. Mon. Wea. Rev., submitted.

Johnson, R. H., and G. S. Young (1983). Heat and moisture budgets of tropical mesoscale anvil clouds. J. Atmos. Sci. 40, 2138-2147.

Kanamitsu, M. (1975). On numerical prediction over a global tropical belt. Ph.D. Thesis, Department of Meteorology, Florida State University, 281 pp.

Krishnamurti, T. N., M. Kanamitsu, R. Godbole, C. B. Chang, F. Carr, and J. Chow (1976). Study of a monsoon depression (II), dynamical structure. J. Meteorol. Soc. Japan 54, 208-225.

Krishnamurti, T. N., R. N. Pasch, H. Pan, S. Chu, and K. Ingles (1983). Details of low-latitude medium-range numerical weather prediction using a global spectral model I: Formation of a monsoon depression. J. Meteorol. Soc. Japan 61, 188-207.

Kuo, H. L. (1974). Further studies of the parameterization of the influence of cumulus convection on large-scale flow. J. Atmos. Sci. 31, 1232-1240.

Kuo, Y. H. (1983). A diagnostic case study of the effects of deep extratropical convection on the large-scale temperature and moisture structure. Coop. Thesis No. 74, Pennsylvania State University and NCAR, 222 pp.

Maddox, R. A. (1983). Large-scale meteorological conditions associated with midlatitude, mesoscale convective complexes. Mon. Weather Rev. 111, 1475-1493.

Miyakoda, K., and J. Sirutis (1983). Impact of subgrid-scale parameterizations on monthly forecasts. In Convection in Large-Scale Numerical Models, European Centre for Medium Range Weather Forecasts.

Molinari, J. (1982). A method for calculating the effects of deep cumulus convection in numerical models. Mon. Weather Rev. 110, 1527-1534.

Molinari, J. (1984). Incorporation of cloud-scale and mesoscale downdrafts into a cumulus parameterization: Results of one- and three-dimensional integrations. Submitted to Mon. Weather Rev.

Schubert, W. H., J. J. Hack, P. L. Silva-Dias, and S. R. Fulton (1980). Geostrophic adjustment in an axisymmetric vortex. J. Atmos. Sci. 37, 1464-1468.

Shapiro, L. J., and D. E. Stevens (1980). Parameterization of convective effects on the momentum and vorticity budgets to synoptic scale Atlantic tropical waves. Mon. Weather Rev. 108, 1816-1826.

Suarez, M. J., A. Arakawa, and D. A. Randall (1983). The parameterization of the planetary boundary layer in the UCLA general circulation model: Formulation and results. Mon. Weather Rev. 111, 2224-2243.

Tiedtke, M. (1984). The effect of penetrative cumulus convection on the large-scale flow in a general circulation model. Contr. Atmos. Phys.

Yanai, M., C.-H. Sui, and J.-H. Chu (1982). Effects of cumulus convection on the vorticity field in the tropics. J. Meteorol. Soc. Japan 60, 411-424.

Zipser, E. J. (1977). Mesoscale and convective-scale downdrafts as distinct components of squall line structure. Mon. Weather Rev. 105, 1568-1589.

Zipser, E. J. (1980). Kinematic and thermodynamic structure of mesoscale systems in GATE. In Proceedings of the Seminar on the Impact of GATE on Large-Scale Numerical Modeling of the Atmosphere and Ocean, pp. 91-99.

A NEW CONVECTIVE ADJUSTMENT SCHEME

Alan K. Betts
Visiting Scientist
European Centre for Medium Range Weather Forecasts

OBSERVATIONAL AND THEORETICAL BASIS

Cumulus parameterization started with simple attempts to represent the subgrid-scale effects of convective clouds. Manabe et al. (1965) proposed adjustment toward a moist adiabatic structure in the presence of conditional instability, and Kuo (1965, 1974) proposed a simple cloud model to redistribute the heating and moistening effects of precipitating clouds in the presence of grid scale moisture convergence. The work of Ooyama (1971), and Arakawa and Schubert (1974) initiated a great deal of research attempting to parameterize cloud ensembles using a cloud spectrum and a simple cloud model (Frank, 1983). One of the key objectives of the GARP Atlantic Tropical Experiment (GATE) (Betts, 1974) was to study organized deep convection in the tropics to test and develop convective parameterizations for numerical models. GATE diagnostic studies have documented the complexity of tropical mesoscale convection (Houze and Betts, 1981) from the importance of mesoscale updrafts and downdrafts as well as convective-scale processes down to the effects of the cloud microphysical processes of forcing, melting, and water loading. One might conclude from these phenomenological studies that cloud models of much greater complexity might be needed to parameterize cumulus convection (Frank, 1983). Little progress has been made in this direction however, because it is clearly impossible to attempt to integrate at each grid point in a global model, a cloudscale model of much realism.

This paper represents a marked divergence in philosophy. The primary objective of the proposed parameterization scheme (Betts and Miller, 1984) is to ensure that the local vertical temperature and moisture structures, which in nature are strongly constrained by convection, be realistic in the large-scale model. The concept of a quasi-equilibrium between the cloud field and the large-scale forcing [introduced by Betts (1973) for shallow convection, and Arakawa and Schubert (1974) for deep clouds] has been well-established, at least on larger space and time scales (Lord, 1982). This means that convective regions have characteristic temperature and moisture structures that can be documented observationally and used as the basis of a convective adjustment procedure. Betts (1973) and Albrecht et al. (1979) modeled shallow convection using this approach. The main limitation of the

706

moist adiabatic convective adjustment suggested by Manabe et al. (1966) for deep convection is that the tropical atmosphere does not approach a moist adiabatic equilibrium structure in the presence of deep convection. In the scheme proposed here, the temperature and moisture structures will be adjusted simultaneously toward observed quasi-equilibrium structures. This ensures that on the grid scale a global model always maintains a realistic vertical temperature and moisture structure in the presence of convection. This sidesteps all the details of how the subgrid-scale cloud processes maintain the quasi-equilibrium structures one observes. To the extent that one can show observationally that different convective regions have different quasi-equilibrium thermodynamic structures (as a function of wind-field, for example), these could be incorporated using different adjustment parameters. However, in this paper just the simplest scheme to show its usefulness is introduced.

The saturation point formulation of moist thermodynamics (Betts, 1982a) will be used to introduce the observational and theoretical basis of the proposed convective adjustment. The scheme is then applied to a series of data sets from GATE, BOMEX, ATEX and an Arctic air-mass transformation to show the sensitivity of the scheme to different parameters and develop a parameter set suitable for both shallow and deep convection in a global model. The last section (in preparation) will show the effect of the scheme on global forecasts.

Observational Basis

Betts (1982a) has given examples of deep and shallow convective equilibrium structures, and Betts (1983) has discussed equilibrium structure for mixed cumulus layers. Here a few examples are presented that inspired the parameterization scheme. Tephigrams will be presented showing temperature and saturation points ((T, p) at the lifting condensation level: abbreviated SP). Isopleths of virtual potential temperature (θ_{ESV}) for cloudy air will be shown for reference (Betts, 1983), together with ρ, the pressure departure of air at each pressure level from its saturation level.

Deep Convection: Convective Soundings Over the Tropical Ocean

Figure 1 shows the structure of the deep troposphere for the mean typhoon sounding from Frank (1977). The heavy dots and open circles are temperature and saturation points (T, SP) for the eyewall. They show a temperature structure that parallels a θ_{ESV} isopleth below 600 mb and θ_{ES} increasing above, with a nearly saturated atmosphere ($p_{si} -p = \rho = -15$ mb). The crosses and symbols E are (T, SP) inside the eyewall. Here the strong subsidence has produced a very stable thermal structure, but the SP structure is very close to the temperature structure of the eyewall: it has been generated by subsidence of air originally saturated at the eyewall temperature (this does not modify the SP). The midtropospheric subsidence within the eye
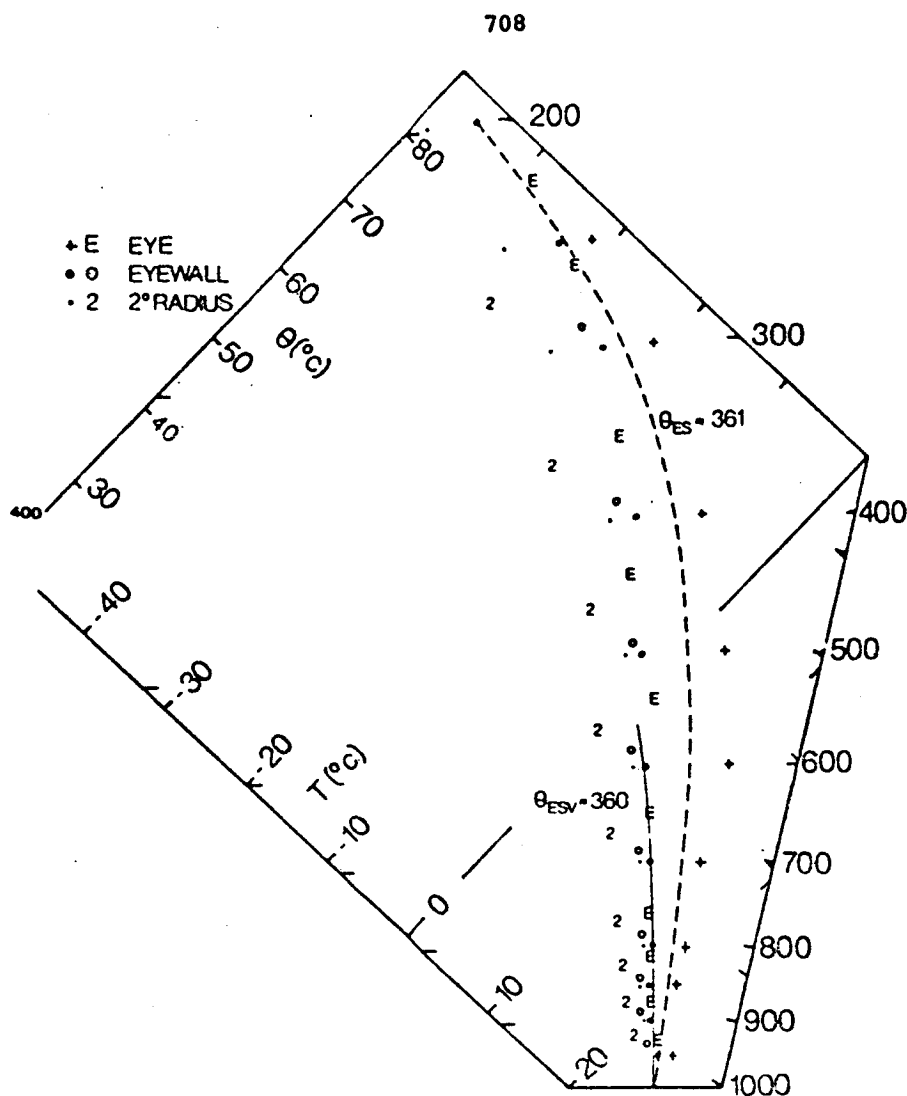
FIGURE 1 Mean typhoon sounding.

(of this composite) is 60 mb. Thus the temperature structure of the eyewall is confirmed by two independent composites.

The light dots and symbols 2 are the (T, SP) at 2° radius from the storm center. Here the atmosphere is further from saturation but has a similar but cooler temperature structure. At 200 mb the eyewall $\theta_{ES} \sim 361^{\circ}$K, while at 2° radius $\theta_{ES} \sim 357^{\circ}$K, with a corresponding change in θ_E at the low levels.

Figure 2 shows the deep tropospheric structure for the wake (Barnes and Sieckman, 1983) of GATE convective band composites. They show a very similar profile to Figure 1, with an initial decrease of θ_{ES} close to a θ_{ESV} isopleth and then an increase above 600 mb, which
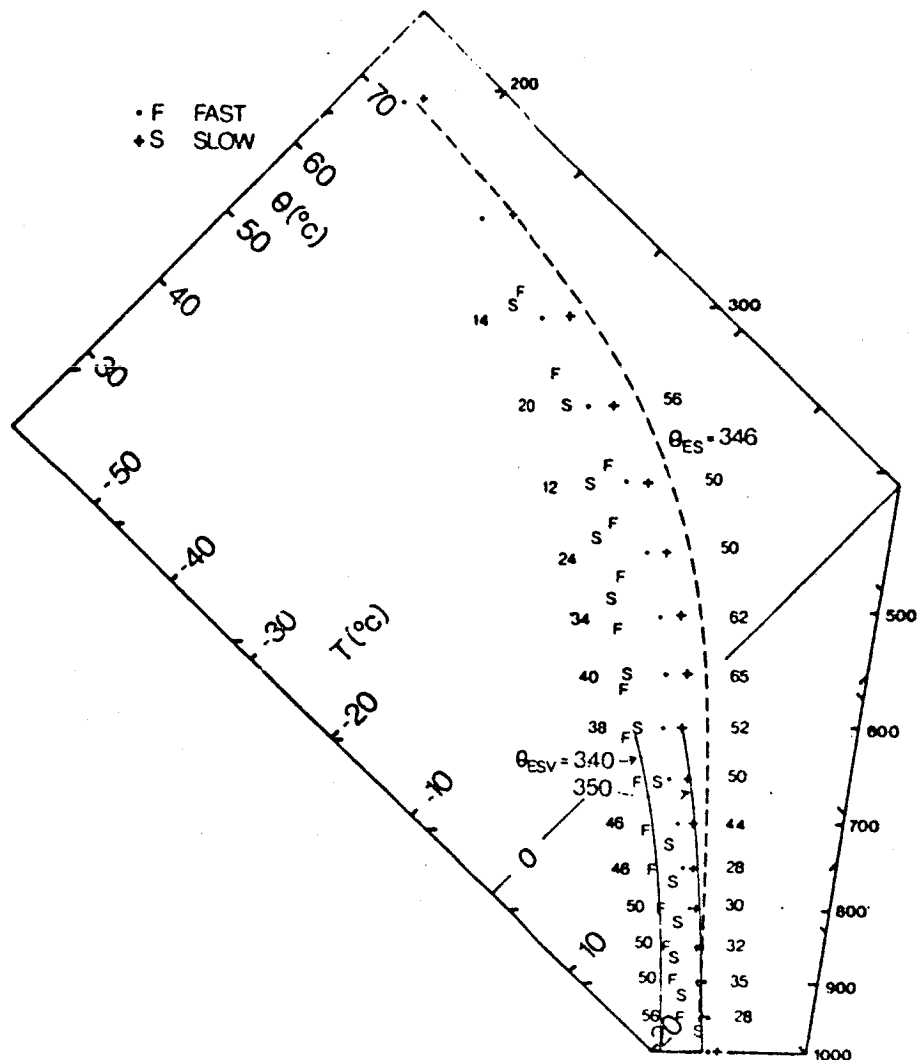
FIGURE 2   Fast and slow moving GATE lines.

is close to the freezing level. The dots and letter F denote the (T, SP) of fast-moving lines (Barnes and Sieckman, 1983), and the cross and letter S denote (T, SP) for slow-moving lines. They show some thermodynamic differences. The ρ values for each p level are shown (fast moving on left, slow on right). For reference, $\rho = -?$ mb corresponds to a relative humidity of 85 percent at 800 mb, 75 percent at 500 mb, and 32 percent at 200 mb at tropical temperatures. The fast-moving line wake has a drier lower troposphere as a result of stronger downdrafts. It's 600 mb temperature is cooler, probably as a response to the falling θ_E in low levels. It is nearly saturated
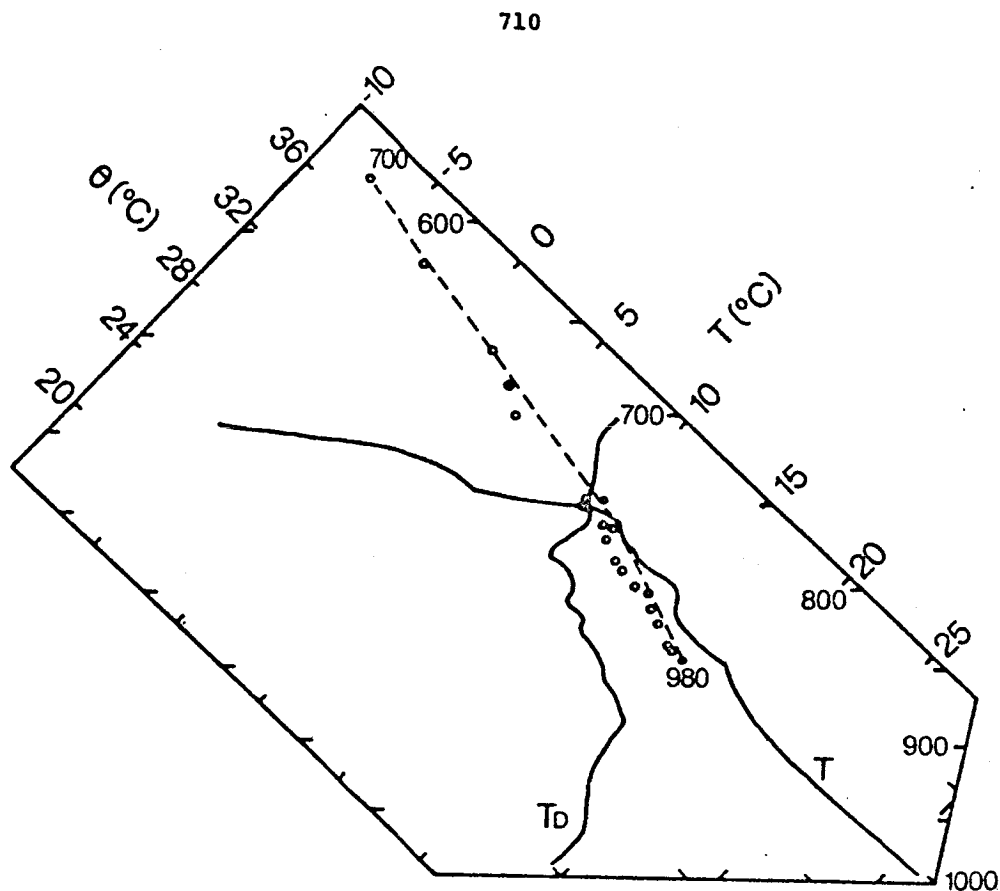
FIGURE 3 Shallow convection mixing line structure.

in the upper troposphere corresponding to extensive anvil clouds. The slow-moving line wake shows the reverse, with a moister lower tropospheric structure and θ_{ES} to 600 mb more closely aligned along a θ_{ESV} isopleth. It however is drier in the upper troposphere. These thermodynamic differences are associated with distinct dynamic features in the wind profile. The fast-moving lines have strong shear between the surface and 650 mb (Barnes and Sieckman, 1984).

Shallow Cumulus Convection: Mixing Line Structure

Cumulus convection is a moist mixing process between the subcloud layer and drier air aloft, and not surprisingly the thermodynamic structure tends toward a mixing line (Betts, 1982a).

Figure 3 shows the (T, T_D) structure (solid lines) and corresponding SPs (open circles) from the surface to 700 mb for a late afternoon convective sounding over land in the tropics. The entire SP structure from 980 mb to 700 mb lies close to the mixing line joining

the end-points. There is a patch of cloud near 750 mb and a dry layer above, but these large fluctuations of T and T_D only appear as SP fluctuations up and down the mixing line. The temperature structure in the cloud layer below the stable layer at 700 mb is nearly parallel to the mixing line.

Convective Adjustment Scheme

The scheme is designed to adjust the atmospheric temperature and moisture structure back toward a reference quasi-equilibrium thermodynamic structure in the presence of large-scale radiative and advective processes. Two different reference thermodynamic structures, which are partly specified and partly internally determined, are used for shallow and deep convection, depending on the height of cloudtop.

Formal Structure

The large-scale thermodynamic tendency equation can be written in terms of SP($\underset{\sim}{S}$), using the vector notation suggested in Betts (1983), as

$$\frac{\partial \overline{\underset{\sim}{S}}}{\partial t} = - v \cdot \nabla \underset{\sim}{S} - \overline{\omega} \frac{\partial \overline{\underset{\sim}{S}}}{\partial p} - g \frac{\partial \overline{\underset{\sim}{R}}}{\partial p} - g \frac{\partial \overline{\underset{\sim}{F}}}{\partial p} \qquad (1)$$

where R, F are the radiative and convective fluxes (including the precipitation flux). The convective flux divergence is parameterized as

$$- g \frac{\partial \overline{\underset{\sim}{F}}}{\partial p} = \frac{E - \overline{\underset{\sim}{S}}}{\tau} \qquad (2)$$

where E is the reference quasi-equilibrium thermodynamic structure and τ is an adjustment time representative of the convective time scale.

Simplifying the large-scale forcing to the vertical advection and combining (1) and (2) gives

$$\frac{\partial \overline{\underset{\sim}{S}}}{\partial t} = \overline{\omega} \frac{\partial \underset{\sim}{E}}{\partial p} + (\underset{\sim}{E} - \underset{\sim}{S})/\tau \qquad (3)$$

Near quasi-equilibrium $\partial \overline{\underset{\sim}{S}}/\partial t \approx 0$ so that

$$(\underset{\sim}{E} - \underset{\sim}{S}) \approx \overline{\omega} \frac{\partial \overline{\underset{\sim}{S}}}{\partial p} \tau \qquad (4)$$

One finds that values of τ from 1 to 2 hours give good results in the presence of realistic forcing. This means that E − S corresponds to about 1 hour's forcing by the large-scale fields, including radiation. For deep convection, the atmosphere will therefore remain slightly cooler and moister than E. Furthermore, for small τ, the atmosphere

will approach $\underset{\sim}{E}$ so that one may substitute $\underset{\sim}{\bar{S}} \approx \underset{\sim}{E}$ in the vertical advection term, giving

$$(\underset{\sim}{E} - \underset{\sim}{\bar{S}}) \approx \omega\tau \ (\partial\underset{\sim}{E}/\partial p) \tag{5}$$

from which the convective fluxes can be approximately expressed using (2), as

$$\underset{\sim}{F} = \int \frac{\underset{\sim}{E} - \underset{\sim}{\bar{S}}}{\tau} \frac{dp}{g} \approx \int (\bar{\omega} \ \frac{\partial\underset{\sim}{E}}{\partial p}) \ \frac{dp}{g} \tag{6}$$

(6) shows that the structure of the convective fluxes is closely linked to the structure of the specified reference profile $\underset{\sim}{E}$. By adjusting toward an observationally realistic thermodynamic structure $\underset{\sim}{E}$, the convective fluxes including precipitation are simultaneously constrained to have a structure similar to those derived diagnostically from (1) (or its simplified form (6)) by the budget method (Yanai et al., 1973; Nitta, 1977).

Adjustment Procedure

The large-scale advective terms, radiation, and surface fluxes are allowed to modify the thermodynamic structure $\underset{\sim}{S}$. Cloudtop is then found using a moist adiabat through the surface θ_E. Cloudtop height distinguishes shallow from deep convection (currently level 11 in the grid point model; about 760 mb). Different reference profiles are constructed for shallow and deep convection that satisfy different energy integral constraints. The convective adjustment, $(\underset{\sim}{E} - \underset{\sim}{S})/\tau$, is then applied. This implicitly redistributes heat and moisture in the atmosphere as it is adjusted toward $\underset{\sim}{E}$.

The deep convection reference profile $\underset{\sim}{E}_D$ is constructed to satisfy the total enthalpy constraint.

$$\int_{P_O}^{P_T} (H_E - H_{\bar{S}}) dp = 0_D \tag{7}$$

where $H = C_p T + Lq$ and p_O, p_T are a surface (or low level) and cloudtop pressure, respectively. The precipitation rate is then given by

$$P = \int_{P_O}^{P_T} (\frac{q_E - \bar{q}}{\tau}) \ \frac{dp}{g} = - \frac{C_p}{L} \int_{P_O}^{P_T} (\frac{T_E - \bar{T}}{\tau}) \ \frac{dp}{g} \tag{8}$$

No liquid water is stored in the present scheme. The adjustment is suppressed if it ever gives $P < 0$.

For shallow convection, the reference profile $\underset{\sim}{E}_S$ is constructed to satisfy the two separate energy constraints

$$\int_{P_o}^{P_T} C_p (T_E - \bar{T}) \, dp = \int_{P_o}^{P_T} L(q_E - \bar{q}) \, dp = 0 \qquad (9)$$

so that the integrated condensation (and precipitation) rates are zero.

Reference Thermodynamic Profiles

The essence of this convective adjustment scheme is these reference profiles. Shallow and deep convection are separated by cloudtop.

SINGLE COLUMN TESTS USING GATE-WAVE, BOMEX, ATEX AND ARCTIC AIRMASS DATA SETS

The convective parameterization scheme was tested and tuned using a series of single column data sets. A GATE-wave data set (derived from Thompson et al., 1979) was used to test and develop the deep convection scheme. BOMEX (from Holland and Rasmusson, 1973) and ATEX (from Augstein et al., 1973; Wagner, 1975) data sets were used to test and develop the shallow convection scheme. A fourth data set for an Arctic air-mass transformation (from Okland, 1976) was used to test both schemes with strong surface fluxes. Only the first part of the GATE tests is shown in this abbreviated paper.

Deep Convection

GATE-Wave Data Set

The grid point model is run as a single column model with prescribed GATE Phase III radiation (from Cox and Griffith, 1979) and prescribed heat and moisture tendencies due to adiabatic processes (from Thompson et al., 1979). The adiabatic forcing terms have a wave structure with an 80-hour period. The model is integrated in time using the convection scheme from an initial sounding. The temperature and moisture structure, the precipitation, and the vertical profile of the convective heating and drying terms as a function of time can be compared with those diagnosed from observations. Most of the sensitivity tests will be done with prescribed surface fluxes (from Thompson et al., 1979), using an 18-level model. A section follows showing results with an interactive boundary layer scheme.

Optimum Parameter Set

First, an optimum parameter set is presented to show how well the scheme can reproduce the structure of the mean GATE-wave (Table 1). The model scheme decreases linearly from -25 at the surface to -50 at the freezing level and returns to -38 at cloudtop.

TABLE 1 Convection Scheme Parameters

τ	O	F	T	α
2 hr	-25	-50	-38	1.5

Figure 4 shows the 80-hour mean vertical structure of the prescribed adiabatic forcing terms and the model physics (convective scheme plus prescribed radiation and surface fluxes). The mean balance is very precise, although the lower troposphere cools and the upper troposphere warms slightly. Figures 5a and 5b show the computed 40- and 80-hour soundings compared with the observations showing the same result. At 40 hours (the wave trough) the agreement between model scheme and the observed mean structure is very good, although the convection scheme does not reproduce the subsequent drying out of the upper troposphere at the ridge (80 hours). Figures 6, 7, and 8 compare the time-height cross-sections for the data (observed structure and diagnosed convective source terms) with these predicted by the model using the convection scheme.

Figure 6 shows the wave in equivalent potential temperature for the data and structure produced using the convection scheme. The agreement is good, although as in Figure 5, the data is warmer and moister at the lowest level. Figure 7 shows the same comparison for relative humidity showing fairly good agreement. The convection scheme does not maintain relative humidity well at 200 mb near cloudtop. Figures 8 and 9 compare diagnosed and computed convective heat source and moisture sink (plus surface fluxes), showing how well the parameterization scheme reproduces the general wave structure of the convective source terms with their maximum at different pressure levels. The agreement is excellent.

Figure 10 compares the observed rainfall and that computed by the model. Good agreement is seen in amplitude but not in phase. The convection scheme, which is closely coupled to the moisture advection, cannot reproduce the observed lag of the precipitation that appears to be due to subgrid-scale storage of moisture, presumably in the cloudfields (Betts, 1978; Frank, 1978).

In general, the parameterization scheme does well in reproducing the structure of the convective source terms and the precipitation. In its present form, it does not reproduce subgrid-scale moisture storage. The deficiencies in the low-level structure seen in Figure 5 can be markedly reduced using an improved resolution and an interactive surface boundary layer. Some deficiencies near cloudtop are always

715
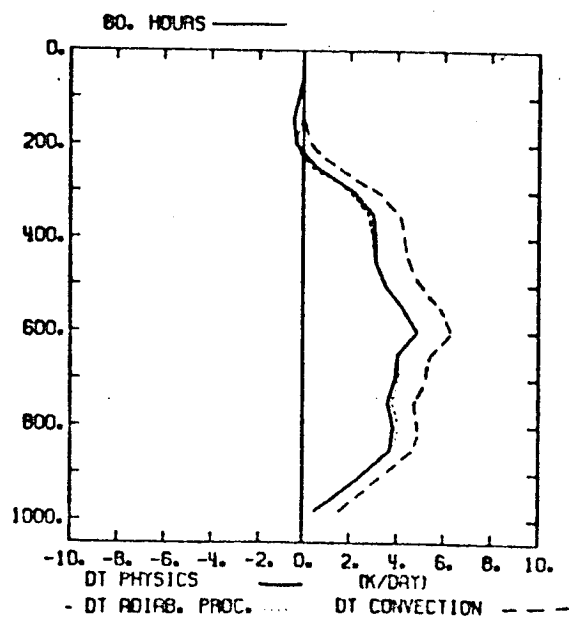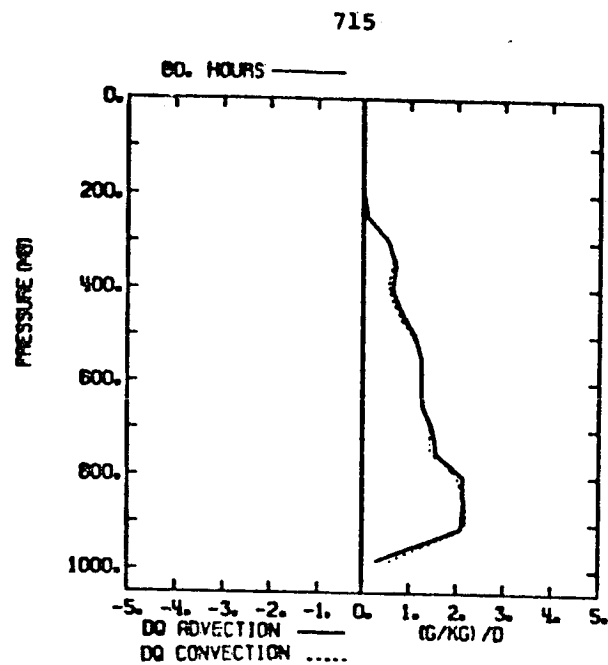
FIGURE 4 Eighty hours mean vertical structure of prescribed adiabatic forcing terms and parameterized convective drying and heating for GATE-wave.
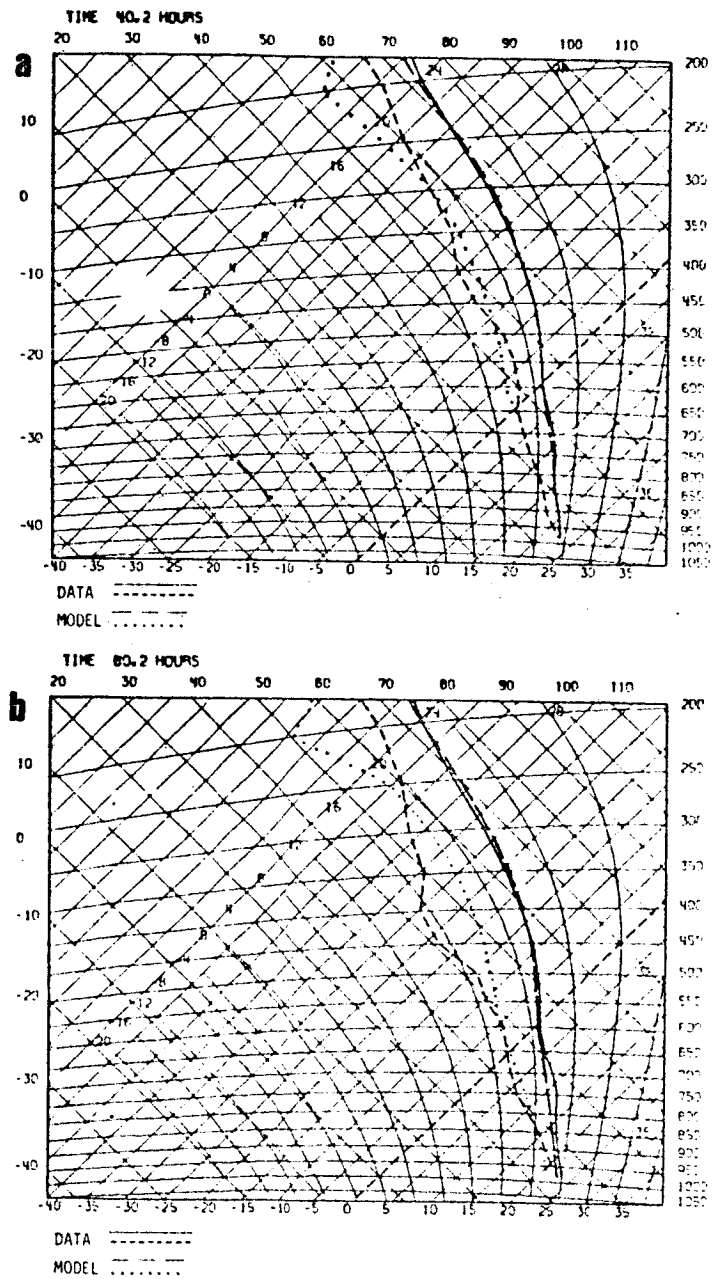
FIGURE 5 (a) Comparison at 40 hours (trough) of observed sounding (T, T_D solid and dashed) and computed sounding (long dash and dots).
(b) Comparison at 80 hours (ridge) of observed sounding (T, T_D solid and dashed) and computed sounding (long dash and dots).

717

EQUIV. POT. TEMP.   (K)   (OBSERVED)

EQUIV. POT. TEMP.   (K)   (MODEL)
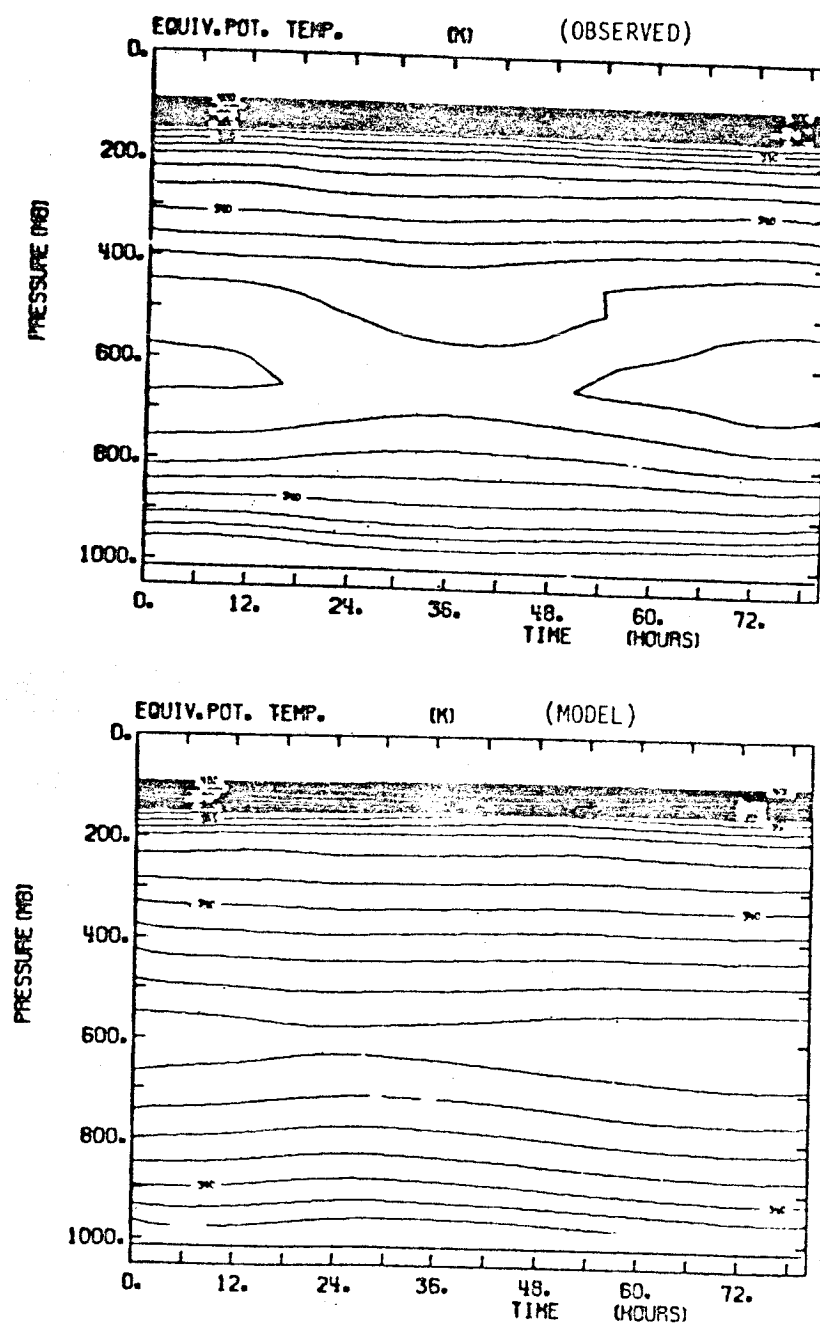
FIGURE 6   Comparison of observed (above) and computed (below) θ_E structure of GATE-wave data.

RELATIVE HUMIDITY (0/0) (DATA)

RELATIVE HUMIDITY (0/0) (MODEL)
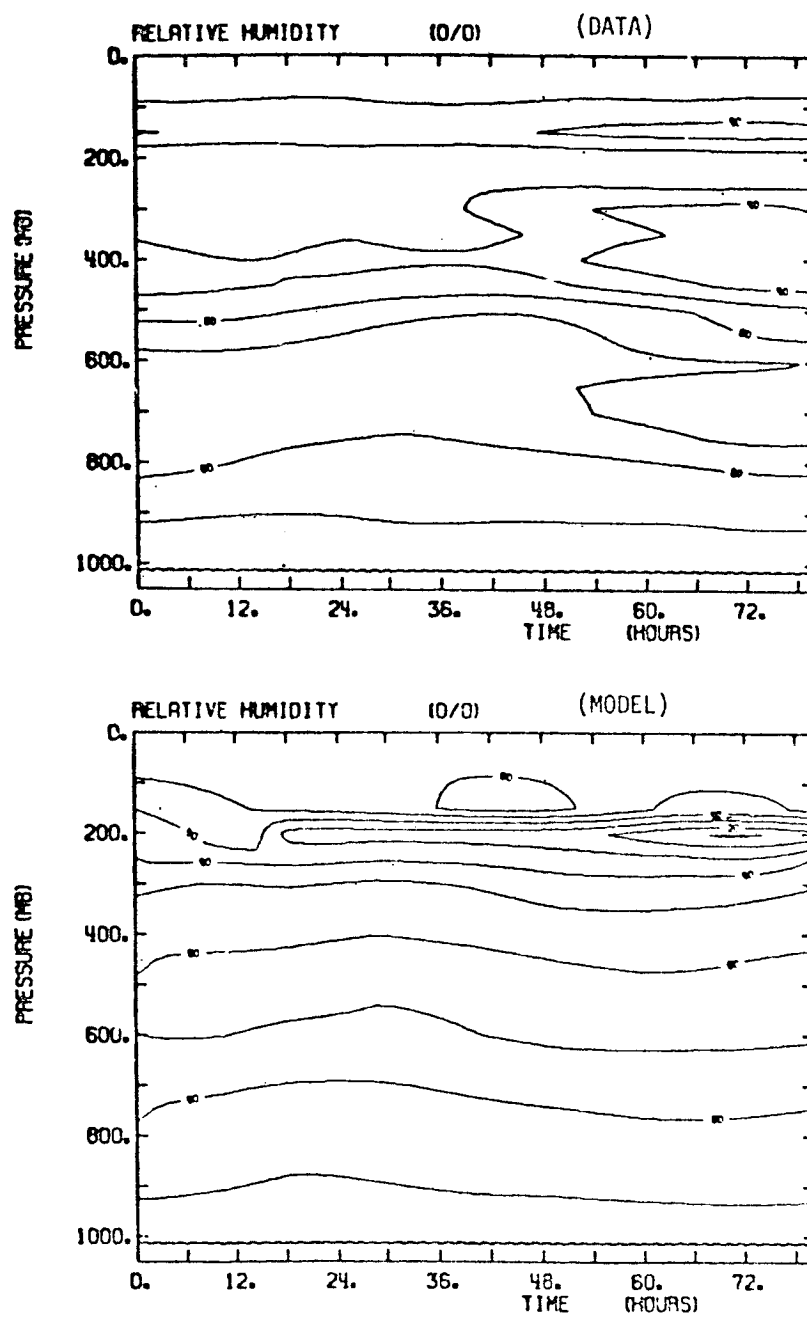
FIGURE 7 Comparison of observed (above) and computed (below) relative humidity for GATE-wave data.

719
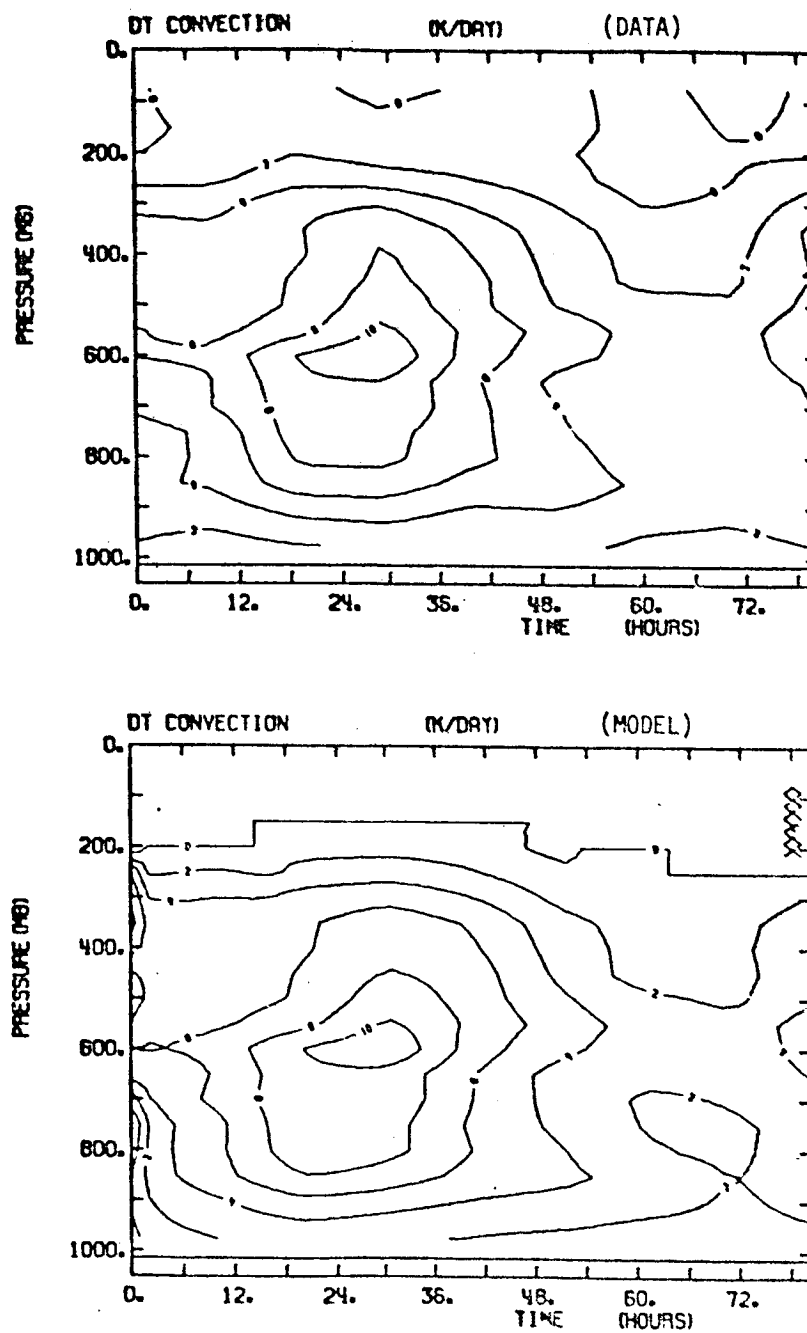
FIGURE 8 Comparison of diagnosed and computed convective heating for
GATE-wave data.

FIGURE 9 Comparison of diagnosed and computed convective drying for GATE-wave data.

721
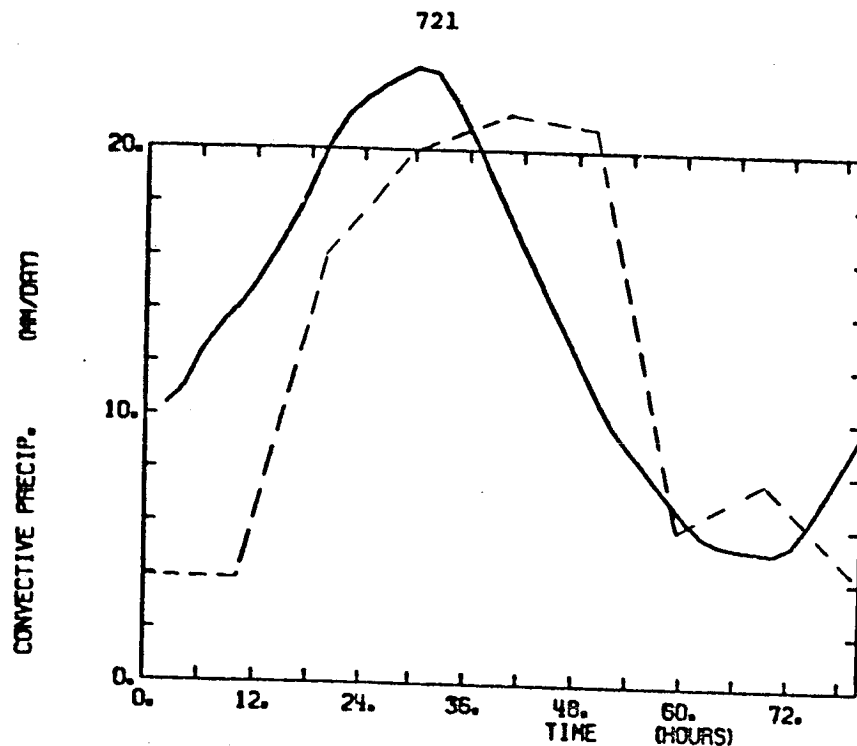
FIGURE 10 Comparison of observed (dashed) and computed rainfall.

likely because the adjustments at this level are always sensitive to the exact specification of cloudtop height in terms of the limited model vertical resolution. Further tuning may be possible. The GATE tests were first run with a cloudtop interpolated between model levels in the specification of the adjustment profile. However this proved to be an unnecessary complication and was dropped from the scheme for the subsequent interactive boundary layer test and global model tests. In this section, the interpolated cloudtop has been retained because a few of the results, although substantially the same, are smoother (cloudtop does not jump between levels) and are therefore easier to intercompare.

ACKNOWLEDGMENTS

REFERENCES

Arakawa, A., and W.H. Schubert (1974). Interaction of a cumulus cloud ensemble with the large-scale environment: Part I. J. Atmos. Sci. 31, 674-701.

Albrecht, B.A., A.K. Betts, W.H. Schubert, and S.K. Cox (1979). A model of the thermodynamic structure of the trade-wind boundary layer: Part II. Theoretical formulation and sensitivity tests. J. Atmos. Sci. 36, 73-89.

Augstein, E., H. Riehl, F. Ostopoff, and V. Wagner (1973). Mass and energy transports in an undisturbed Atlantic trade-wind flow. Mon. Wea. Rev. 101, 101-111.

Barnes, G.M., and K. Sieckman (1984). The environment of fast and slow tropical mesoscale convective cloud lines. Mon. Wea. Rev. 112, 1782-1794.

Betts, A.K. (1973). Non-precipitating cumulus convection and its parameterization. Quart. J. Roy. Meteorol. Soc. 99, 178-196.

Betts, A.K. (1974). The scientific basis and objectives of the U.S. Convection Subprogram for the GATE. Bull. Amer. Meteorol. Soc. 55, 304-313.

Betts, A.K. (1978). Convection in the tropics. Meteorology over the tropical oceans, D.B. Shaw, Roy. Meteorol. Soc., 105-132.

Betts, A.K. (1982a). Saturation point analysis of moist convective overturning. J. Atmos. Sci. 39, 1484-1505.

Betts, A.K. (1982b). Cloud thermodynamic models in saturation point coordinates. J. Atmos. Sci. 39, 2182-2191.

Betts, A.K. (1983). Thermodynamics of mixed stratocumulus layers: Saturation point budgets. J. Atmos. Sci. 40, 2655-2670.

Betts, A.K., and M.J. Miller (1984). A new convective adjustment scheme. Tech. Rpt. No. 43, ECMWF, Reading RG2 9AX, England, 68 pp.

Cox, S.K., and K.T. Griffith (1979). Estimates of radiative flux divergence during Phase III of the GARP Atlantic Tropical Experiment, Part II: Analysis of Phase III results. J. Atmos. Sci. 36, 586-601.

Frank, W.M. (1977). The structure and energetics of the tropical cyclone, Part I: Storm structure. Mon. Wea. Rev. 105, 1119-1135.

Frank, W.M. (1978). The life cycles of GATE convective systems. J. Atmos. Sci. 35, 1256-126?.

Frank, W.M. (1983). The cumulus parameterization problem. Mon. Wea. Rev. 111, 1859-1871.

Holland, J.Z., and E.M. Rasmusson (1973). Measurements of the atmospheric mass, energy and momentum budgets over a 500 km square of tropical ocean. Mon. Wea. Rev. 101, 44-55.

Houze, R.A., and A.K. Betts (1981). Convection in GATE. Rev. Geophys. Space Phys. 19, 541-576.

Kuo, H.L. (1965). On formation and intensification of tropical cyclones through latent heat release by cumulus convection. J. Atmos. Sci. 22, 40-63.

Kuo, H.L. (1974). Further studies of the parameterization of the influence of cumulus convection of large-scale flow. J. Atmos. Sci. 31, 1232-1240.

Lord, S.J. (1982). Interaction of a cumulus cloud ensemble with the large-scale environment. Part III: Semi-prognostic test of the Arakawa-Schubert cumulus parameterization. J. Atmos. Sci. 39, 88-103.

Manabe, S., J. Smagorinsky, and R.F. Strickler (1965). Simulated climatology of a general circulation model with a hydrologic cycle. Mon. Wea. Rev. 93, 769-798.

Nitta, T. (1977). Response of cumulus updraft and downdraft to GATE A/B-scale motion systems. J. Atmos. Sci. 34, 1163-1186.

Ooyama, K. (1971). A theory of parameterization of cumulus convection. J. Meteorol. Soc. Japan 49, 744-756.

Okland, H. (1976). An example of air-mass transformation in the Arctic and convective disturbances of the windfield. Report DM-20, Univ. of Stockholm, 30 pp.

Thompson, Jr., R.M., S.W. Payne, E.E. Reckel, and R.J. Reed (1979). Structure and properties of synoptic-scale wave disturbances in the intertropical convergence zone of the eastern Atlantic. J. Atmos. Sci. 36, 53-72.

Wagner, V. (1975). Relationships between the tropospheric circulation and energetic processes within the Hadley circulation over the Atlantic Ocean. Berichte Inst. Radiometeor. und Maritime Meteor., Univ. Hamburg, No. 26, 83 pp.

Yanai, M., S. Esbensen, and J.H. Chu (1973). Determination of bulk properties of tropical cloud clusters from large-scale heat and moisture budgets. J. Atmos. Sci. 30, 611-627.

17. DESIGN OF OBSERVATIONS

Organizer   Paul R. Julian

Session Chairman   Paul R. Julian

Speakers   Verner E. Suomi
                             Milton Halem

Rapporteur   Richard J. Reed

SOME POSSIBILITIES ON AN OBSERVING SYSTEM
FOR THE WORLD CLIMATE PROGRAM

Verner E. Suomi
University of Wisconsin, Madison

Material presented by V. Suomi is contained in the following publication:

Suomi, V. (1985). Some possibilities on an observing system for the World Climate Program. In Monitoring of Earth, Land, Ocean and Atmosphere: Sensors, Systems and Applications, A. Schnapf (ed.), American Institute of Astronautics and Aeronautics, Technical Progress Series (in press).

333<

SIMULATION STUDIES RELATED TO THE DESIGN OF
POST-FGGE OBSERVING SYSTEMS

M. Halem, R. Atlas, and J. Susskind
NASA/Goddard Space Flight Center

INTRODUCTION

The First GARP Global Experiment (FGGE) led to the planning, design, and implementation of a global observing system that became the prototype for the systems employed operationally in the 1980s. This observing system was mainly an outgrowth of technologies and data analysis requirements developed in the early to mid 1970s. In recent years, new technology such as coherent CO_2 lidar systems and highly sensitive infrared detectors have appeared which offer the potential of more accurate global spaceborne observing systems. At the same time, the advent of supercomputers opened the door to higher resolution general circulation modeling requiring more sophisticated data analysis and diagnostics. This combination of developments suggests the need for advanced spaceborne systems better suited to meet the data initialization problems for higher resolution weather and climate forecasting models. However, a major consideration for the funding agencies is what improvement in forecasting skill can be expected from these new systems and models. In this regard, the Global Weather Experiment provides us with a new baseline for assessing data accuracy, forecasting capabilities, and global analysis, which we can now use to assess the performance of future observing systems.

At this FGGE Workshop, the results of three detailed simulation studies are presented. The first study consists of a comparative assessment of the performance of an advanced moisture/temperature sounder (AMTS) being proposed by NASA as a follow-on replacement to the current HIRS-2 operational sounder aboard the NOAA weather satellites. This study was jointly conducted by participants from GLAS, NESS, the University of Denver, and NMC. The second study was concerned with assessing the relative accuracies of inferred atmospheric states for idealized lidar wind profiling systems, temperature profiling systems, surface pressure systems, and composite systems. The third study, in collaboration with ECMWF, NMC, and GLAS, incorporated the above systems into a highly realistic data analysis/forecast cycle from which a series of forecast impact studies were conducted. These studies, taken together, give us a picture of the potential that emerging technologies can offer in the determination of the basic atmospheric variables required for long-range numerical weather and climate prediction.

OBSERVING SYSTEM DESIGN CONSIDERATIONS

As we study the design of a new generation of global observational
systems, it is also necessary to consider the changing platform
environment and flight operational constraints that will have also
evolved. Table 1 contrasts how future observing systems, in terms of
technology, space platforms, and information systems, will differ from
those which form the current family of operational weather satellites.
The first row of Table 1 indicates that the lead-time for the FGGE
observing system was nearly 15 years from the start of its formal
planning and nearly 20 years from the call by President Kennedy at the
United Nations for such a Global Atmospheric Research Program. If we
assume a similar time span, then 1985-1999 is an appropriate period to
permit the consideration of instrument technologies that, as of yet,
are only emerging.

For example, in recent years, two new technologies have appeared
that offer the potential of making global spaceborne measurements
possible with the accuracy of land-based radiosondes. In particular,
substantial technical progress has been made in the development of
coherent active CO_2 lidar systems (Hardesty et al., 1983; Pace and
LaCombe, 1978) that measure the Doppler shift in the backscatter from
aerosols. From these measurements, it has been shown that one can
infer wind motions with accuracies and vertical resolution of a
rawinsonde (Hall et al., 1983). Studies have been carried out by
Huffaker (1978, 1980), Lockheed (1981), and RCA (1983), indicating the
feasibility of a free-flying space shuttle launched lidar wind
profiling system known as WINDSAT. In addition to overcoming the
significant technological problems involved in the design of
instruments that have to work at the limits of quantum theory,
substantial progress has been made in the signal processing and
computer algorithm developments needed for the extraction of the wind
information (Lawrence, 1983). In addition, recent developments have
shown the feasibility of active incoherent LASERS for pressure
profiling as a function of height with presumably very high vertical
resolution and accuracy.

At the same time, there has been significant progress in obtaining
higher vertical resolution from advanced temperature soundings through
higher spectral resolutions in the wings of specific spectral lines
(Kaplan et al., 1977; Reuter and Susskind, 1984). These passive
systems depend critically on the development of highly sensitive
detector arrays and cryogenic cooling systems. As a result of higher
signal-to-noise sensitivity, passive soundings will thus be able to
provide an order of magnitude increase in spectral resolution and at
least a doubling of spatial evolution. The effect of this increase in
spatial and spectral resolution is to extend our sounding capability to
the full imaging capability in the spectral domain. The impact will be
to create full spectral image displays comparable to visible images.

The satellite platforms that will carry future systems will also
provide a different environment for instrument operation. We can
expect to see a permanent, manned space station supporting interactive
observations, controlled by remote investigators at scattered

TABLE 1 New Planning Considerations in the Design of Global Observational Systems

	FGGE (1965-1979)	FUTURE (1985-1999)
TIME SPAN:		
TECHNOLOGY:	ACTIVE - NONE	ACTIVE - RADAR, CO_2 AND Nd:YAG LIDARS
	PASSIVE - IR, MW, VISIBLE	IMAGING - VISIBLE, SPECTRAL, RADAR BACKSCATTER
PLATFORM:	OPERATIONAL SATELLITES	PERMANENT MANNED SPACE STATION, ATTACHED PAYLOADS
	RESEARCH SATELLITES	RENEWABLE-REVISITABLE SATELLITES
INFORMATION PROCESSING:	HIGHLY CENTRALIZED; MANAGED BY OPERATIONAL AGENCIES	DECENTRALIZED; DISTRIBUTED LOCAL DATA PROCESSING CENTERS
	LIMITED INSTITUTIONAL FACILITIES	EXTENSIVE INSTITUTIONAL PARTICIPATION
	NATIONAL CENTRAL ARCHIVE	CENTRAL RAW DATA ARCHIVES AND ON-LINE REAL DATA MANAGEMENT SYSTEMS; HIGH SPEED DIRECT ACCESS NETWORK SYSTEMS

institutions around the world. As a result, decentralized information processing systems accessing data at distributed data centers will replace central data-handling facilities. Local institutions will perform their data analysis using their own numerical climate and weather forecasting models. Also, from these platforms, space shuttles will be used to revisit, repair, and renew the deployed systems to greatly extend their periods of performance. Thus, highly advanced distributed data management systems, requiring ultrahigh-speed direct network access with massive on-line data storage capabilities, will have to be developed to make practical the scientific utilization from these new observing systems.

Table 2 presents a list of existing or planned atmospheric profiling systems, as well as surface monitoring systems that are being considered for future systems. The largest component in the list of systems' capabilities is in the area of temperature sounding by passive techniques. For wind profiling, the systems are fewer. In addition to cloud-tracking systems, there are spaceborne CO_2 and Nd;YAG lidar systems (Hayes et al., 1984) and improved antenna designs offering the possibility of spaceborne Doppler radar systems. For moisture profiling, tunable differential absorption lidar systems and advanced high-resolution infrared and microwave systems could be used. For measuring the land-ocean-atmospheric boundary interfaces, a variety of active and passive systems sensitive to the surface and boundary layers are used and listed in Table 2. From this broader list, simulation studies were carried out for only a limited number of instruments which are reported herein. For the purposes of this presentation, however, we will only address some of the potential observing systems that might be expected in the near-term future earth-observing system. Additional studies for several other potential systems are being planned.

JOINT NASA/NOAA SOUNDING SIMULATION TEST

In their paper, Kaplan et al. (1977) showed that it was theoretically possible to take advantage of a one or two order of magnitude increase in spectral resolution for infrared temperature sounding by selecting channels in the wings of certain lines or in spectral regions exhibiting a large temperature dependence of the absorption coefficients. Three separate instrument design feasibility studies were carried out in subsequent years by A. D. Little, 1978; Santa Barbara, 1980; and Perkin-Elmer, 1981. A more recent design is given in Chahine et al. (1984). All studies were in agreement that there were no significant technological barriers to the spaceborne qualification of such a temperature and moisture sounder. As a result, NASA and NOAA management initiated the conduct of probably the most extensive and realistic simulation study ever carried out prior to initiating instrument development. The purpose of the test was twofold: first, to assess the expected performance of the proposed AMTS infrared sounder relative to the current HIRS-2 operational sounder and, second, to compare both instrument performances using physical and statistical inversion techniques. The participants included L. McMillin, L. Crone,

TABLE 2 Satellite Atmospheric Profiling Systems

TEMPERATURE	WINDS	MOISTURE
HIGH-RESOLUTION INFRARED SOUNDER (HIRS)	CLOUD-TRACKED IMAGES (VISSR)	AMSU
MICROWAVE SOUNDING UNIT (MSU)	NOAA ERL CO_2 LIDAR	HIRS/MSU
ADVANCED MICROWAVE SOUNDING UNIT (AMSU)	SOLID STATE YAG LIDAR	AMTS
ADVANCED METEOROLOGICAL TEMP S'D'R (AMTS)	DOPPLER RADAR	SMMR
LIDAR TEMPERATURE/PRESSURE SOUNDER		SSMI
HIGH-RESOLUTION INTERFEROMETER SOUNDER (HIS)		LIDAR
VERTICAL ATMOSPHERIC SOUNDER (VAS)		
LIMB SCANNING IR RADIOMETER (LSIR)		

SATELLITE SURFACE SENSING SYSTEMS

TEMPERATURE	PRESSURE	WINDS	SNOW/ICE/SOIL MOISTURE
AVHRR	LIDAR PRESSURE SOUNDER	SCATTEROMETER	VISSR/AVHRR/VAS
HIRS/MSU	FREE FLOATING BUOYS	ALTIMETER	SMMR
SMMR	MICROWAVE SURFACE PRESSURE SOUNDER	SMMR	ESMR
SSMI		LIDAR	HIRS/MSU
			AMTS/AMSU
			LMMR
			LANDSAT-MSS(TM)

HIRS

CHANNEL	ν, cm^{-1}	$\Delta\nu$, cm^{-1}
1	2357.0	23
2	669.0	3
3	679.0	14
4	690.0	13
5	700.0	16
6	2271.5	35
7	716.5	18
8	2243.5	22
9	2210.5	23
10	2190.0	21

U.S. STD. ATMOSPHERE
TEMPERATURE PROFILE

AMTS

CHANNEL	ν, cm^{-1}	$\Delta\nu$, cm^{-1}
1	667.50	0.50
2	668.70	0.50
3	667.00	0.50
4	666.00	0.50
5	652.75	0.50
6	646.65	0.50
7	635.77	0.50
8	2383.74	2.00
9	2386.10	2.00
10	2388.19	2.00
11	2390.19	2.00
12	2392.34	2.00

U.S. STD. ATMOSPHERE
TEMPERATURE PROFILE

PRESSURE, mb

$$\frac{1}{I(\nu)} \quad \frac{dB(\nu,T)}{dT} \quad \frac{d\tau(\nu,P)}{d\ln p}$$

$$\frac{1}{I(\nu)} \quad \frac{dB(\nu,T)}{dT} \quad \frac{d\tau(\nu,P)}{d\ln p}$$

FIGURE 1 Radiance sensitivity function

and D. Wark of NOAA/NESS; N. Phillips of NOAA/NMC; A. Goldman and D. Murray of the University of Denver; J. Susskind and M. Halem of NASA/GLAS; and M. Chahine of NASA/JPL.

Figures 1a and 1b show the sensitivity of the radiant energy to changes in temperature in different levels of a standard atmosphere for the HIRS and AMTS temperature sounding channels. The localized sharpness of the AMTS weighting function and the substantially higher contribution to the radiance at the peaks throughout the atmosphere indicate that under suitable signal-to-noise specifications, the AMTS sounder should provide improved temperature accuracies, especially in the lower stratosphere and near the surface. Figures 2a and 2b show the normalized weighting functions for the water vapor channels of HIRS-2 and AMTS, respectively. Whereas the HIRS-2 essentially resolves, at most, only two broad levels of water vapor between 300 mb and the surface, the AMTS appears capable of providing a water vapor profile of four to five levels.

HIRS 2 WATER VAPOR CHANNELS

AMTS WATER VAPOR CHANNELS
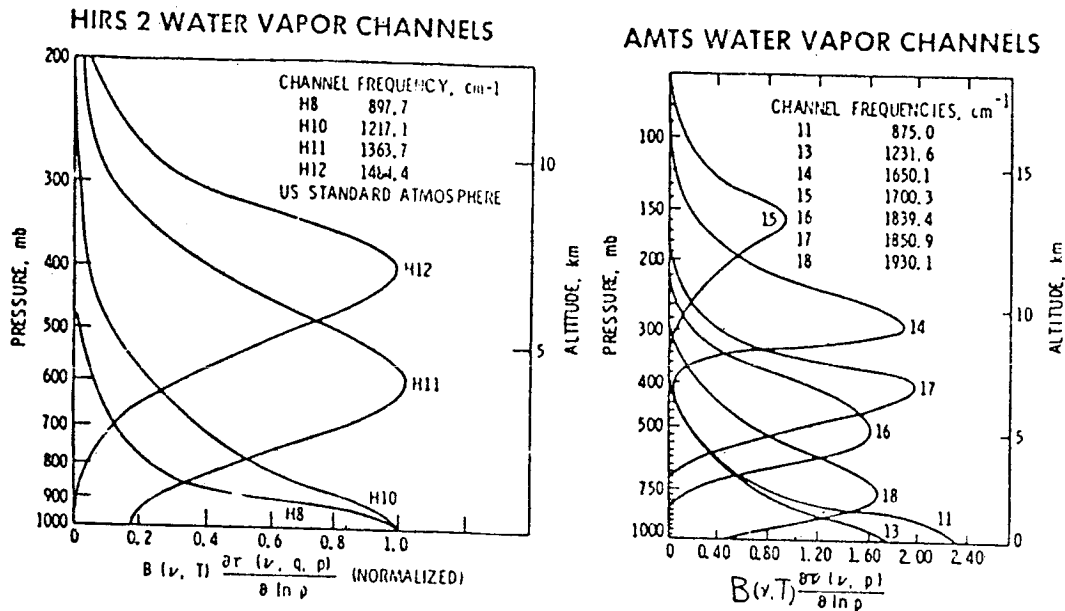
FIGURE 2   Water vapor channels

Elements of Test

Detailed physical simulations of radiances as a function of line-by-line calculations were carried out by Goldman and Murray with rapid algorithms depending on temperature, humidity, and ozone profiles and zenith angles. For this purpose, N. Phillips supplied Goldman and Murray the appropriate profiles. The transmittance code was the same as that described in Susskind et al. (1983). The transmittance coefficients were modified by D. Wark to be representative of physical uncertainties in calculation of transmittance function. In addition, instrumental noise was added to the computed radiances and the effects of reflectivity of solar radiation, land surface temperature and air surface temperature differences were included in the calculation. Two separate sets of radiances to test instrument performance under clear and multilevel dense cloudy conditions were simulated. Microwave sounding radiances for use only in the cloudy test were also provided. Colocated a priori radiosonde and radiance data for a two week period preceding the data in question were made avilable to NOAA and NASA for generation of coefficients in the statistical regression method and for attempting to empirically correct for the differences in the trans- mittance codes used to generate the radiances at the University of Denver and those used to analyze the data of GLAS.

Table 3 summarizes the evaluation of the accuracies for the AMTS processed by the GLAS physical relaxation algorithm and HIRS-2

TABLE 3 Joint Test RMS Errors

JOINT TEST RMS ERRORS

TROPOSPHERE (1000 - 100 MB)		STRATOSPHERE (100 - 16 MB)		SURFACE TEMPERATURE	
AMTS PHYS	HIRS STAT	AMTS PHYS	HIRS STAT	AMTS PHYS	HIRS STAT
1.4	2.1	1.6	2.5	.3	1.0
1.7	2.9	2.0	3.1	.4	1.4

processed by the NESS statistical regression algorithm for both the clear and cloudy cases. The clear results are averaged for 400 test profiles for winter, summer, tropical, and extratropical latitudes. The cloudy results are averaged for the 40 scenes under nighttime cloud conditions of 60 to 90 percent cover. For the clear cases, the AMTS is $0.7^{\circ}C$ more accurate and for cloudy cases the AMTS is $1.2^{\circ}C$ more accurate. The mean rms errors over both the troposphere and stratosphere are $1.5^{\circ}C$ for clear cases and $1.9^{\circ}C$ in cloudy cases. At the surface the ground temperature for land and water are retrieved to better than $0.5^{\circ}C$. Figures 3 and 4 show the average vertical rms errors for clear and cloudy cases at each of 20 layers for both the instruments using both processing methods. The physical relaxation algorithms on average add $0.3^{\circ}C$ to the accuracy and somewhat more cloudy cases while the AMTS instrument itself is better than HIRS-2 by $0.5^{\circ}C$ on average. The largest AMTS improvements in clear cases occur from the surface up to 800 mb and throughout the stratosphere. However, the temperature accuracies and under cloudy situations are improved throughout the troposphere as are the yields (not shown). The significance of these improvements are twofold. First, it indicates the AMTS can make improvements in regions of active weather systems where the accuracy and yields are needed most. Second, the individual AMTS spot accuracies to clear cases at 10 km resolution for ground and sea surface temperatures are $0.3^{\circ}C$. Thus, weekly or monthly averages could be expected to further reduce the standard errors well within the desired limits needed for chronological sea surface temperature studies.

IDEALIZED LIDAR WIND AND TEMPERATURE SIMULATION EXPERIMENTS

The objective we have in performing these simulation experiments is to assess the effect of a particular observing system, in the context of
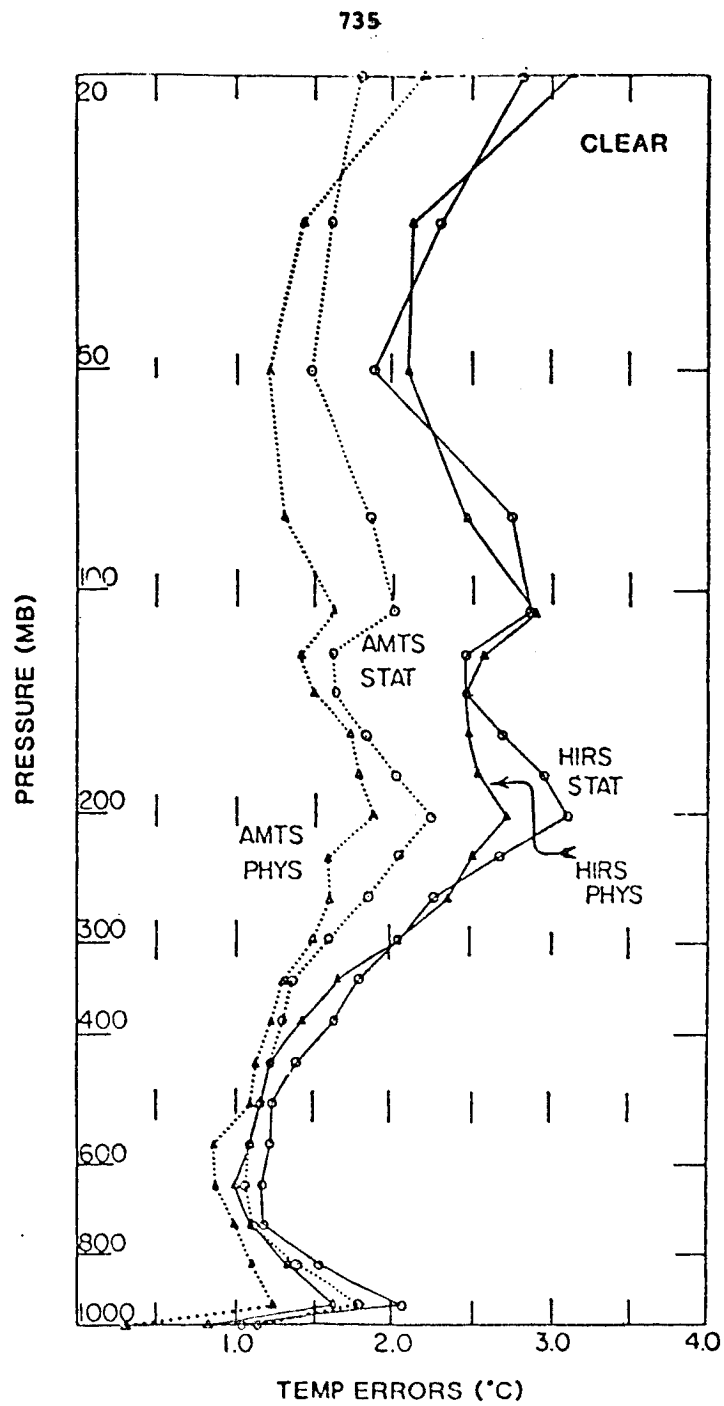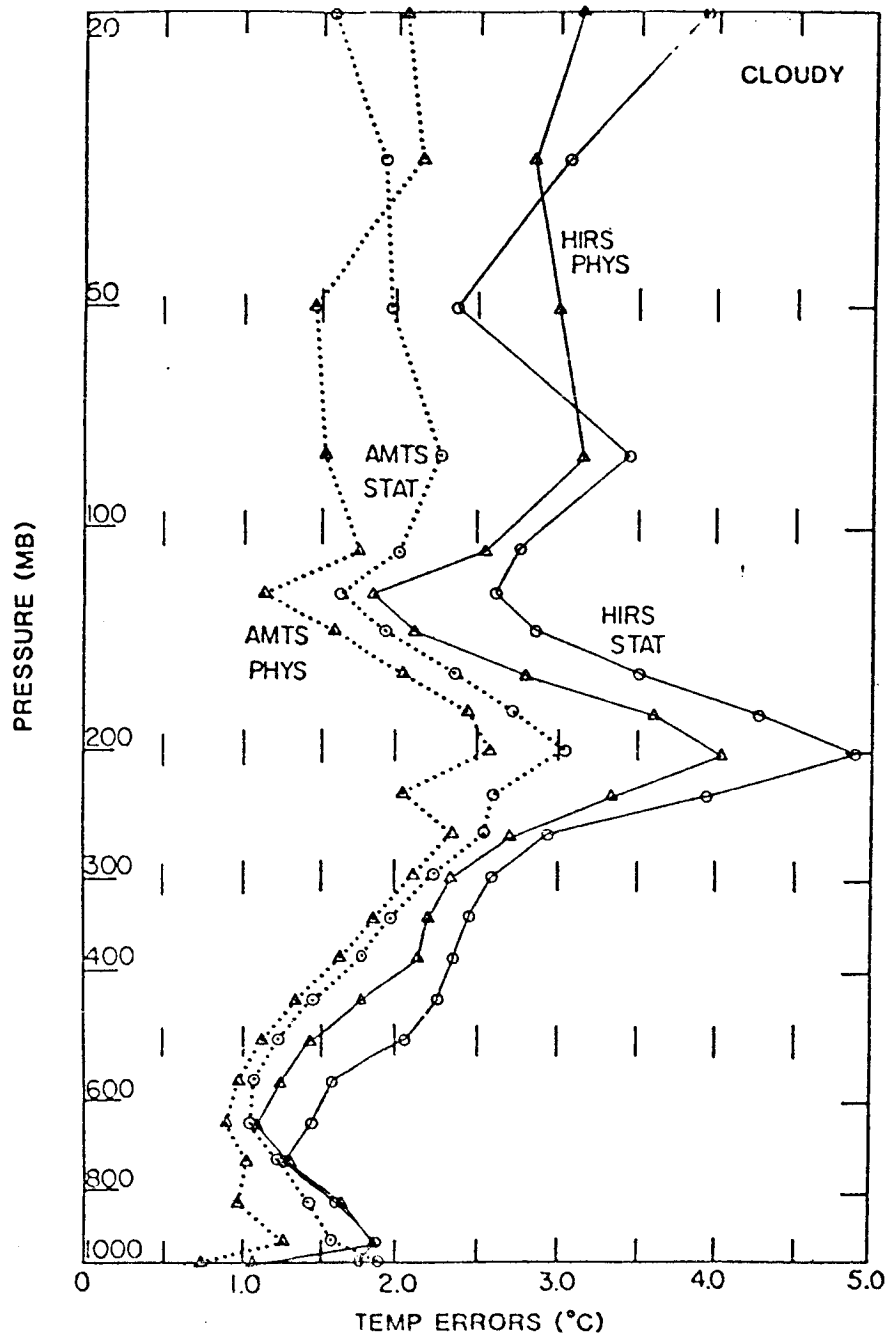
FIGURE 3

FIGURE 4

contributing to an operational analysis. The experiments proceed in three steps. First, one attempts to assimilate a particular observing system configuration and determine its level of performance or accuracy. However, this requires a data set from which one can simulate observations of any degree of accuracy and a data set which can be used to statistically validate the simulated analysis. For this purpose, one can use a long simulated computer integration from a general circulation model containing detailed physical parameterizations of most of the important atmospheric processes. We customarily refer to the continuous sequence of model generated fields as "nature." Since the model outputs are complete in terms of all variables, one could interpolate the model outputs to the proposed locations of an actual observing system with appropriate noise and error statistics added to conform to instrument and flight specifications.

Second, one has to convert the simulated data taken at the points of observation into a gridded field by a process called objective analysis. Thus, in addition to the "nature" assumption, the role of the analysis system itself is also a critical element of the assimilation. Employing an analysis system of which there are several in operational use (Bergman, 1979; Lorenc, 1981; Baker, 1983). In practice, this is very often carried out using the same GCM model for assimilations and for forecasting.

Third, one determines the improvements possible for numerical weather prediction by assessing the forecast sensitivity of the new observing systems. This is done by making forecasts from the respective analysis with and without the observing system in question and then verifying the forecasts against "nature." However, the most critical assumption that pervades all three elements of this study and perhaps the weakest link arguing against the realism of such simulation experiments rests on what we use as "nature," since it provides both the expected data and the validation.

For the purposes of this study, we have attempted to minimize these aspects of the problem by making simplifying assumptions and dealing only with a highly idealized observing system. We assume that we have somehow produced a global instantaneous gridded analysis of any given meteorological field which is perfect. This is done by merely taking the field in question from the "nature" and replacing the evolving analysis by that entire field. For example, if we are studying wind observing systems, we might replace both wind components in the assimilation cycle every 12 hours by the wind components from "nature." However, since we have circuited the analysis cycle by using the "nature" field directly and plan to assess the inferred fields in terms of forecasts, this creates a dual influence of the "nature." In earlier experiments, it has been shown by Williamson (1973) that using the identical model to produce the "nature" and the forecast leads to highly model dependent results.

Recognizing the serious limitations of the "nature" assumption, we have conducted simulation experiments employing three distinct representations of "nature" to avoid the dependence of the results on our "nature" assumption. The three "nature" sets are produced from long integrations made with the GLAS Fourth Order General Circulation

Model (Kalnay et al., 1980) and the ECMWF model (Bengtsson et al., 1982), respectively, and a continuous sequence of real operational analysis produced by the National Meteorological Center. The respective 12-hour forecasts and analyses were kindly provided to the authors for use in this study by Drs. E. Kalnay and L. Bengtsson. The real data analysis consists of National Meteorological Operational analysis and were obtained from the National Climate Center, Asheville, North Carolina.

The simulation experiments are carried out by integrating the GLAS Fourth Order GCM in all three cases for 30 days, continuously updating one or more meteorological fields every 12 hours by the appropriate data set from "nature." This may involve an interpolation to the same grid as the GLAS model. The initial conditions at the start of the GLAS and ECMWF data assimilation cycle are taken from the respective "nature" data set 30 days in advance.* The NMC data assimilation starts from the GLAS initial conditions. The impact of these data is presented in terms of the 12-hour rms forecast fields verified against the respective "nature." Figures 5a, b, and c show the initial conditions of sea level pressure for the three types of "nature" experiments. Figures 6a, b, and c show the corresponding verification fields from "nature." The initial conditions are clearly seen to be relatively uncorrelated with "nature" for the three experiments. Similar differences occur for the other variables.

Inferred Analysis from Primary Variables

Two sets of experiments are analyzed in this section. The first set of experiments are intended to study and quantify the relative forecast impact of analyses inferred from the basic meteorological fields of temperature, pressure, and winds alone. The second set of experiments investigate results of composite systems and their relative forecast impact.

GLAS "Nature"

We first present results of experiments where the data are taken from the GLAS model "nature" described earlier. Figures 7a, b, and c compare the rms 12-hour forecast errors for the synoptic assimilation of complete fields of temperature, wind, and pressure data separately. We verify the forecast rms errors for three derived fields of sea level pressure, 500 mb geopotential heights, and 400 mb zonal winds, respectively. These fields were chosen to assess the ability of a single field to infer not only its own field but the other primary atmospheric states. In the upper panel of each figure, we plotted the rms errors along a typical extratropical latitude, at 50°N, every 12

---

*For ECMWF only 20 days are available.

ARBITRARY INITIAL STATES

GLAS

NMC

ECMWF
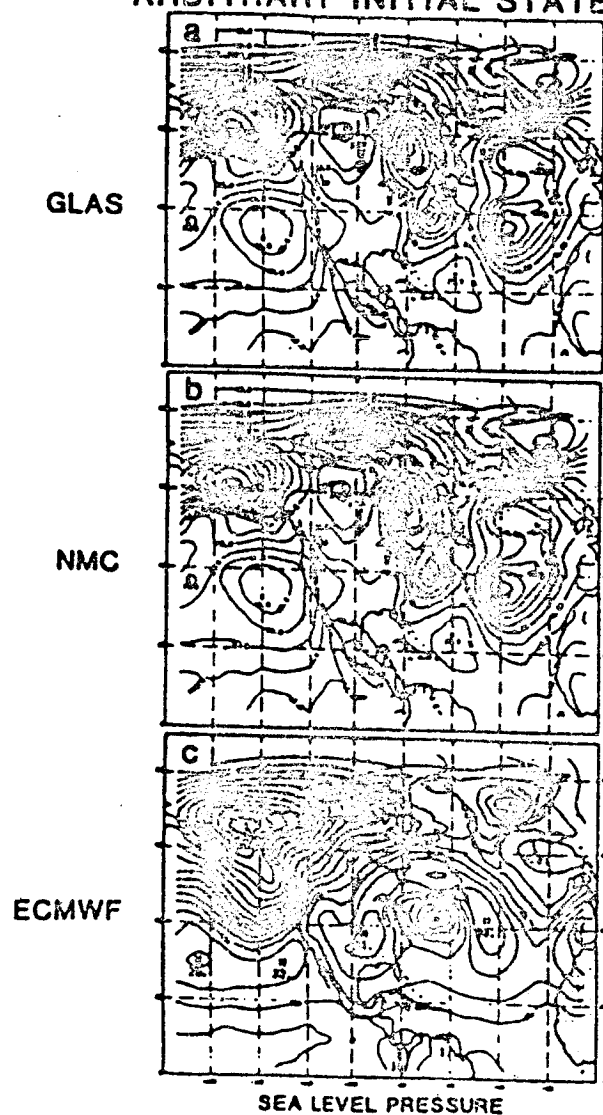
SEA LEVEL PRESSURE

FIGURE 5

hours, and in the lower panel along a tropical latitude, $2°N$. For all three verification fields, the assimilation of sea level pressure data alone has only a slight effect in reducing the initial randomly correlated rms error fields in the extratropics. For example, the mean asymptotic 12-hour forecast error level of sea level pressure is reduced from 16 mb to 10 mb, 500 mb geopotential heights from 200 m to 140 m, and 400 mb zonal winds from 16 m/s to perhaps 14 m/s. The

VERIFICATION

GLAS

NMC

ECMWF

SEA LEVEL PRESSURE
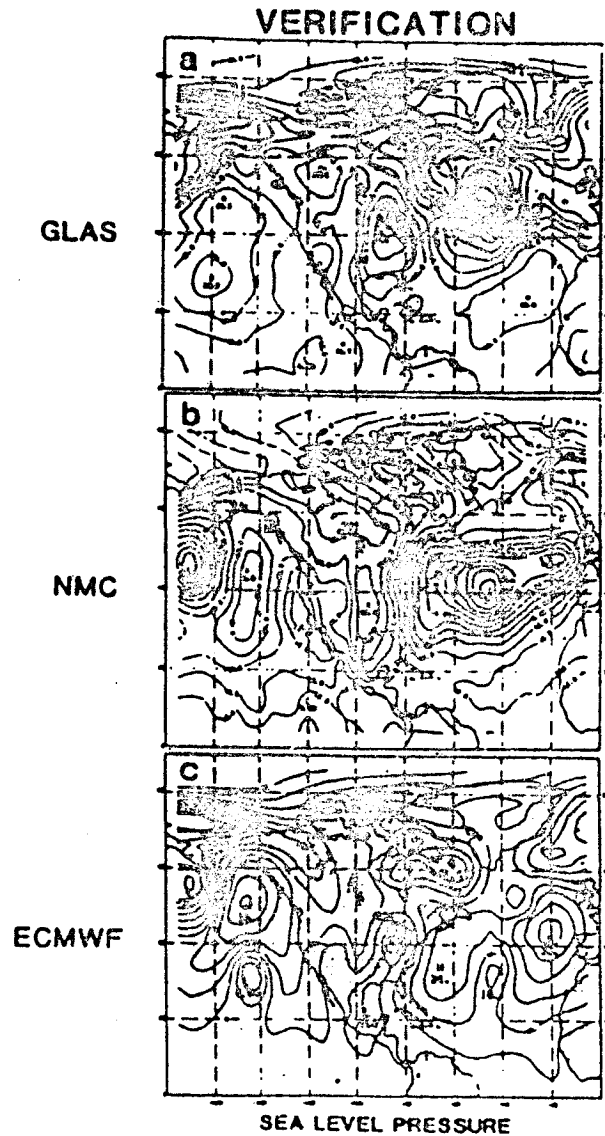
FIGURE 6

temperature data does significantly better, reducing the initial rms errors by more than 50 percent for all of these fields. The wind data, however, virtually eliminate the 12-hour forecast errors in all the verification fields. Moreover, the wind data have a very rapid adjustment period of less than a week to reach its asymptotic error levels, while temperature data require several weeks. The results for these experiments in the tropics again show that pressure makes no
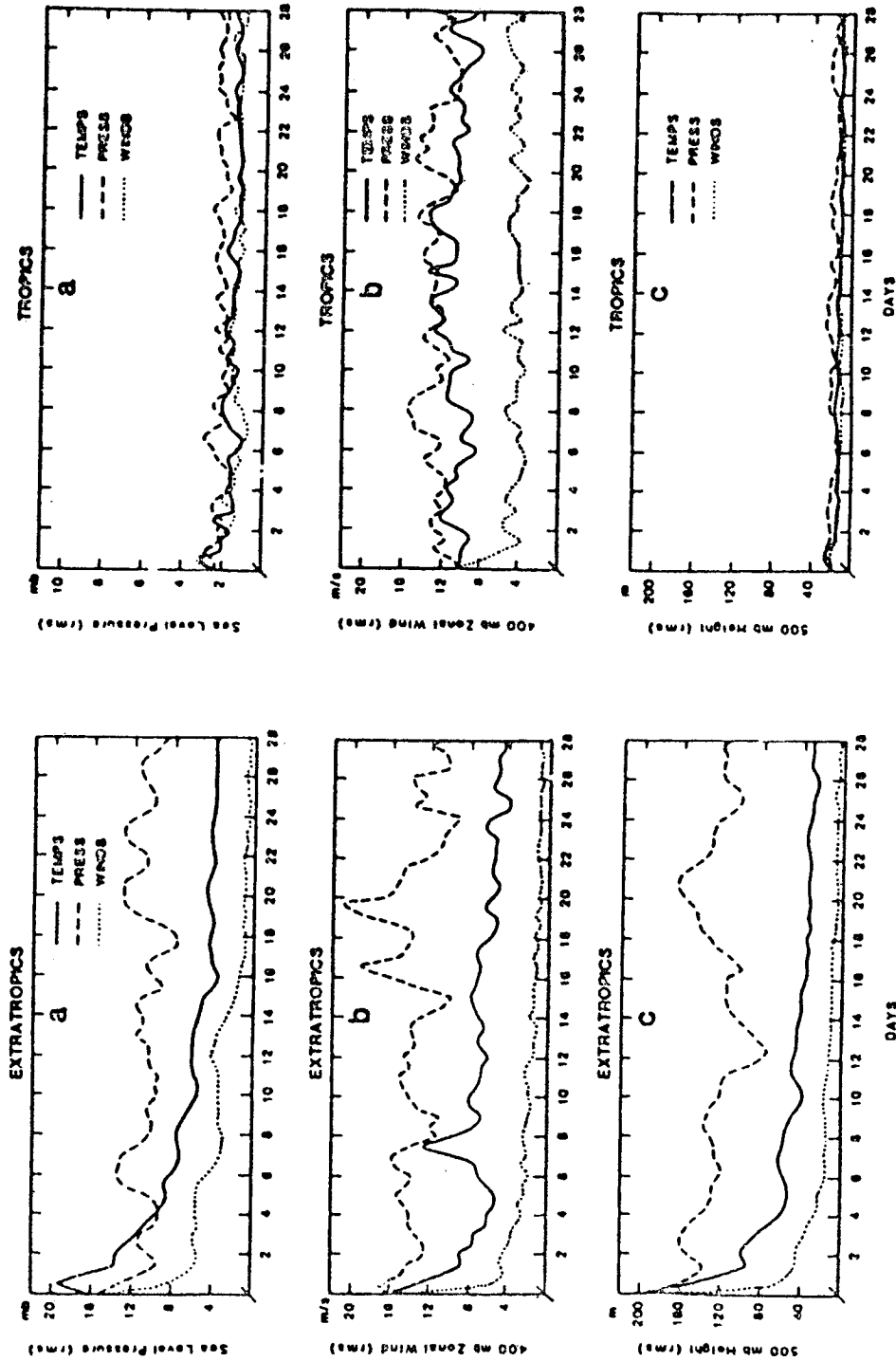
FIGURE 7 12 hr forecast errors (GLAS nature)

reduction in the initial rms errors. Temperature data also shows very little influence on inferring surface pressure fields. The assimilation of wind data in the tropics, however, improves the forecast of wind fields substantially, and has about the same influences as temperature data on the forecast error in 500 mb geopotential and surface pressure fields.

NMC "Nature"

Figures 8a, b, and c again compare the rms 12-hour forecast impact errors of the same fields as before but for temperature and wind fields taken from the real data "nature." Pressure data in these experiments had no effect and are not shown on the charts. Instead, we have added a curve as a reference level which shows the 12-hour forecast of the GLAS Fourth Order Model made from the full FGGE data analysis cycle as reported in Halem et al. (1981). In the extratropics, the insertion of temperature data shows only slight improvements in the 12-hour forecast; 500 mb geopotential heights and zonal winds are almost as good as those obtained using the full FGGE analysis system. There is, however, about a 2 to 4 mb degradation in the 12-hour surface pressure forecasts from the wind data alone. As before, the adjustment process of the inferred fields from wind data seems to occur in about four days.

In the tropics, the results are mixed and require some interpretation. For the sea level pressure 12-hour forecasts, the temperature data alone have an rms 1 to 2 mb more accurate than the FGGE reference level and wind data forecasts, respectively. The situation is reversed for the 12-hour forecast zonal wind fields where wind forecasts are 2 to 4 m/s more accurate than forecasts from FGGE and temperature data. No apparent trends are observable in the 500 mb height forecasts. A possible explanation of these results may be related to the fact that the integrated column density of the NMC height data is obtained from relatively accurate sounding systems whereas the wind data from geostationary cloud winds may have systematic errors inconsistent with the thermal fields. In comparing the accuracies of the 500 mb winds, we may be validating against a data set with the same bias, thereby enhancing the wind simulation since FGGE winds have been influenced by other wind data not included in the NMC fields.

ECMWF "Nature"

In this experiment, we again show in Figures 9a, b, and c the rms 12-hour forecast impact errors of the same fields, but now we use the ECMWF "nature" field. The rms forecast sea level asymptotic pressure error for temperature data in the extratropics is about 12 to 13 mb compared to 4 mb for wind data insertion. This is very similar to the results with real data. The similarity also holds for the 500 mb height fields except that the asymptotic error levels for wind data are substantially better than those with the full FGGE data. The inferred 400 mb zonal winds for the temperature data are now substantially
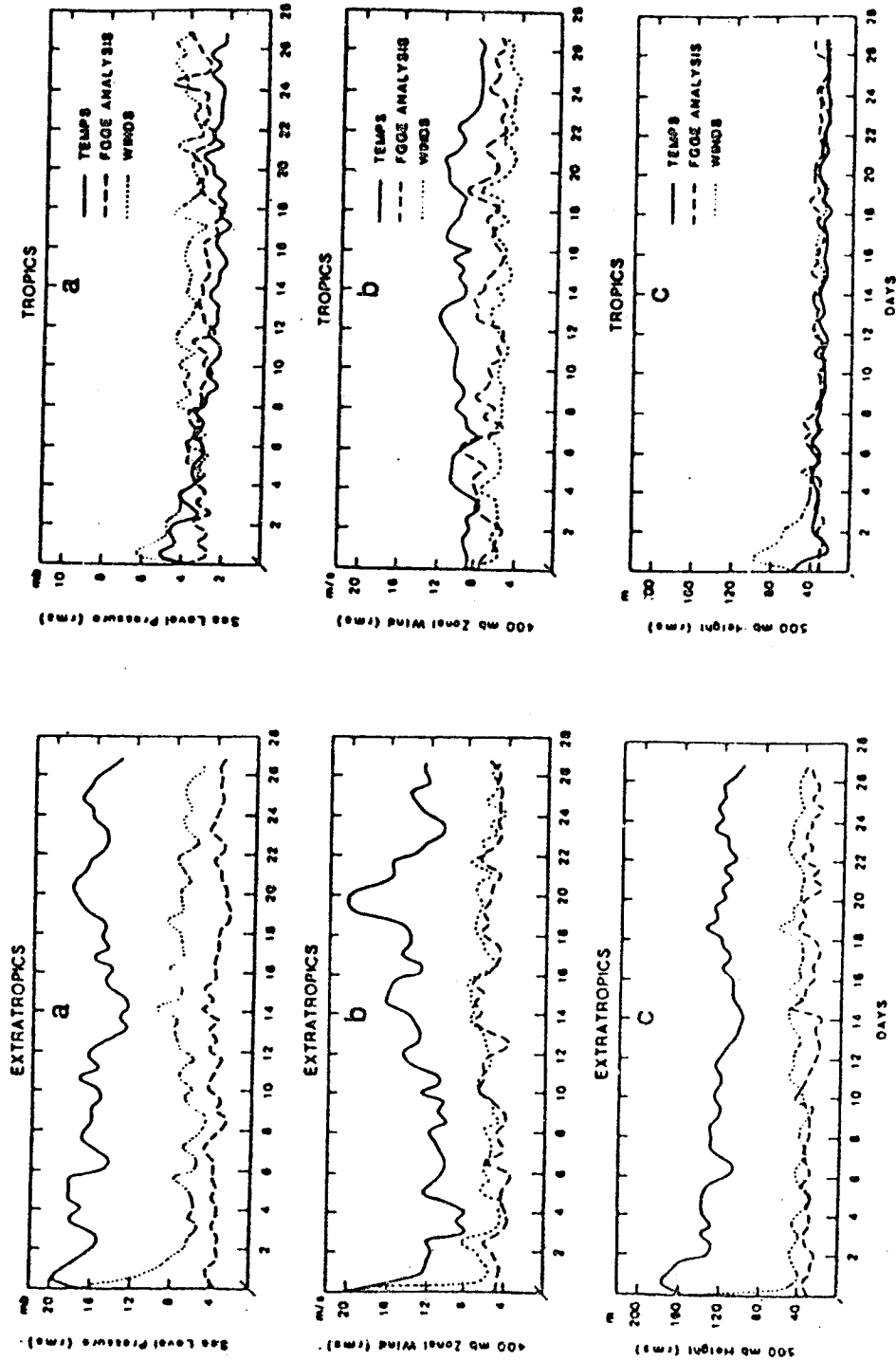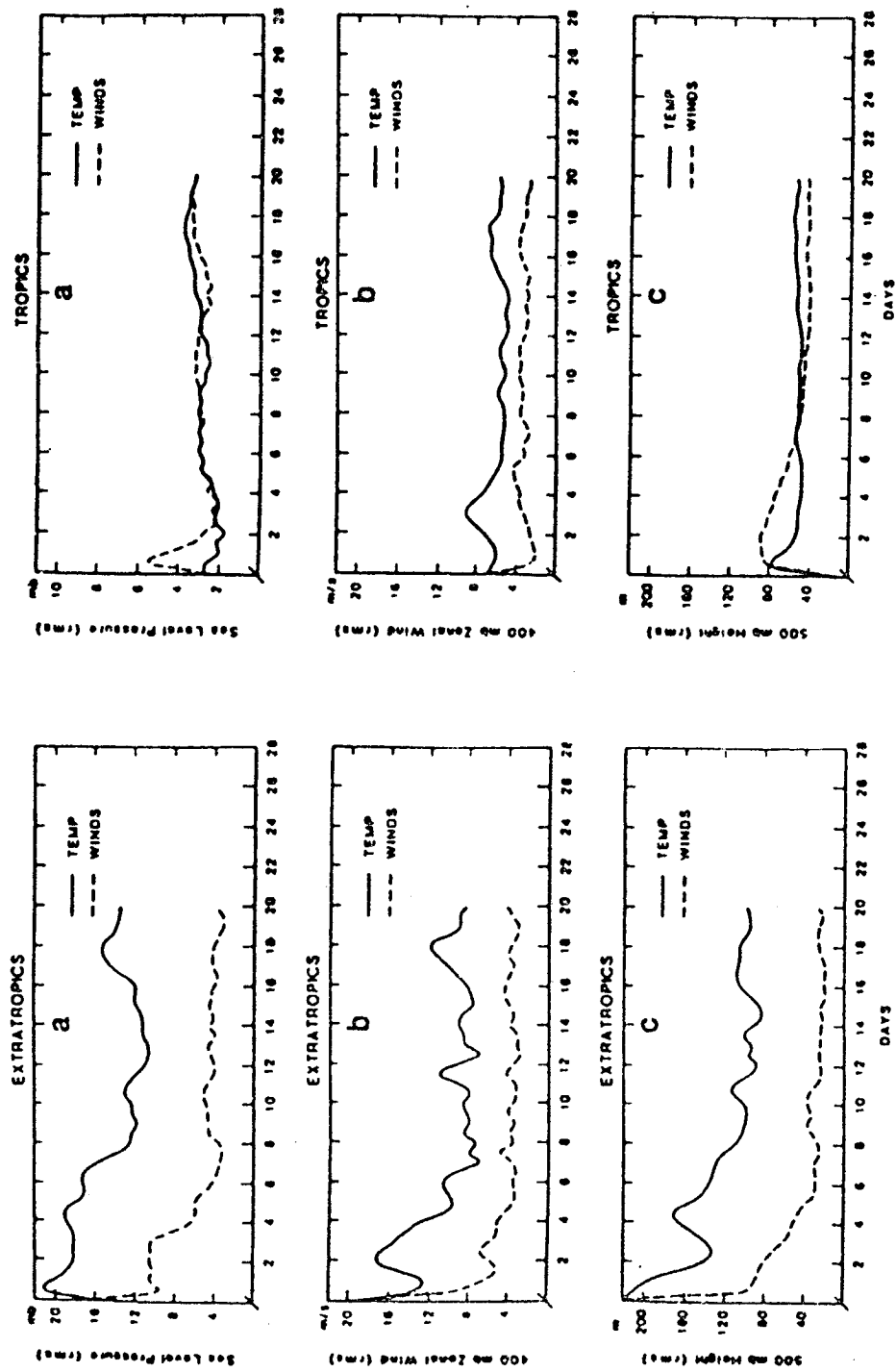
FIGURE 8   12 hr forecast errors (NMC nature)

FIGURE 9 12 hr forecast errors (ECMWF nature)

improved to about 9 m/s while the wind data are about the same as with real data. This indicates that the consistent accurate global temperature fields can reduce the 12-hour forecast wind errors.

The results in the tropics for the ECMWF "nature" experiment are more consistent with the idealized twin simulation experiment than obtained with the real NMC data. The two fields are comparable in the 12-hour forecast errors for sea level pressure wind 500 mb geopotential heights, but wind data forecasts have half the rms zonal wind error than that from temperature data in the tropics.

Simulation Studies for Composite Systems

In the following series of experiments, we couple surface pressure fields with both wind and temperature data since pressure data are readily available over most of the globe from land-based stations and ship reports.

GLAS "Nature"

Figures 10a, b, and c compare the 12-hour forecast errors of temperature and pressure with wind and pressure data for the same basic three validation fields. The "nature" data set for these figures is from the GLAS model. These experiments show that the composite temperature data have reduced the sea level forecast errors to 2 mb, 500 mb heights to 20 m, and zonal winds to about 3 m/s, almost 40 percent less than the errors obtained without the pressure data. The composite wind system had similar asymptotic errors as those without pressure. In the tropics, the use of composite systems had the same asymptotic error levels as the systems without pressure data.

NMC "Nature"

Figures 11a, b, and c show the composite system with the NMC "nature" data set. In these experiments, we observe major reductions in forecast errors for real data composite systems relative to the earlier individual real data systems. For example, the sea level pressure asymptotic levels are 8 mb compared with 16 mb for the previous temperature only experiment, 80 m compared with 120 m for 500 mb geopotential heights ,and 10 m/s compared with 12 m/s. The height and wind forecast errors were about the same for the composite wind system, but the sea level forecast errors were reduced in half to about 4 mb. In the tropics, the results are relatively unaffected by the addition of surface pressure for both composite systems.

ECMWF "Nature"

Figures 12a, b, and c compare the composite system for the third "nature" data set, namely, the "fraternal" ECMWF model. In the
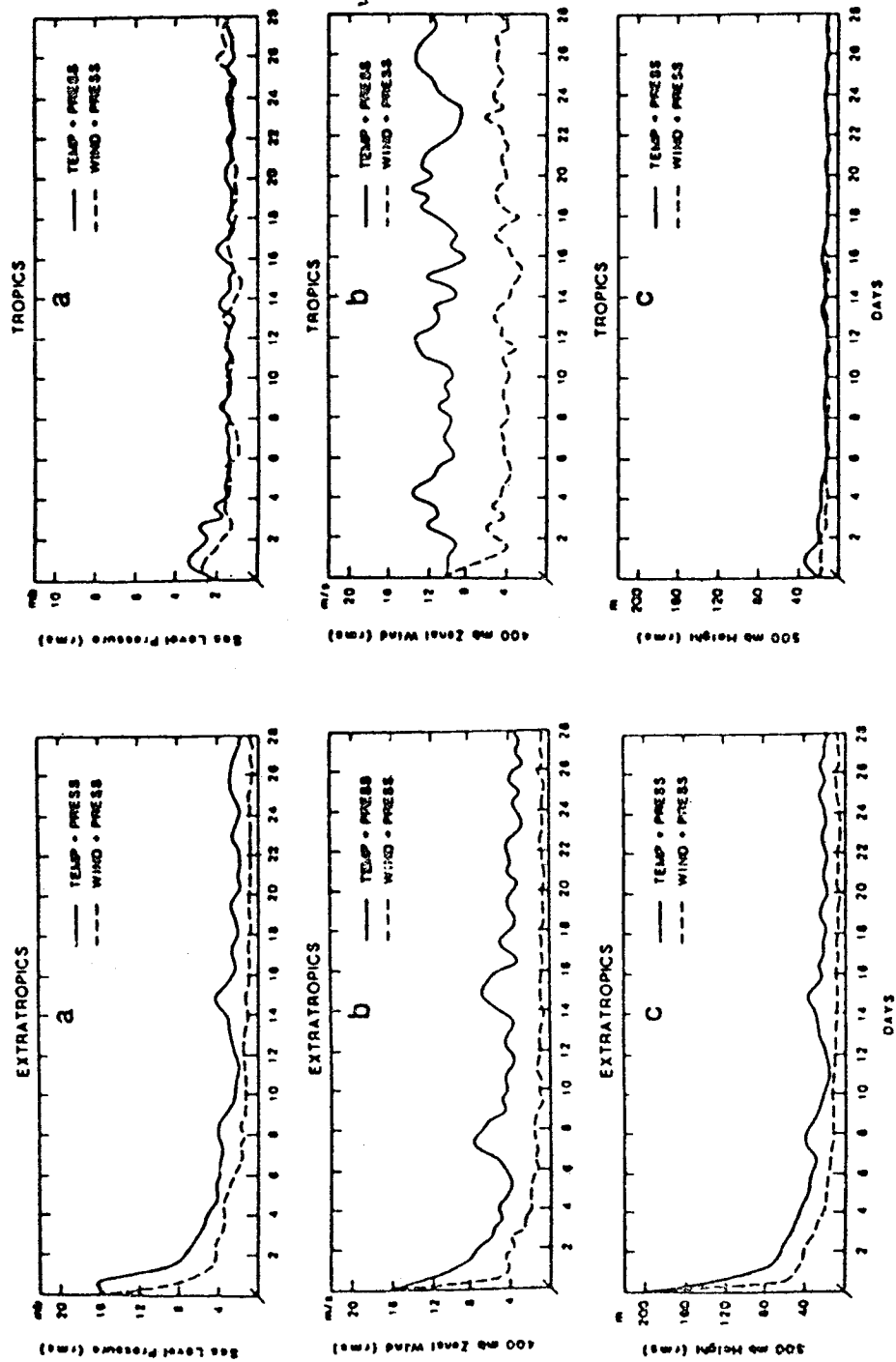
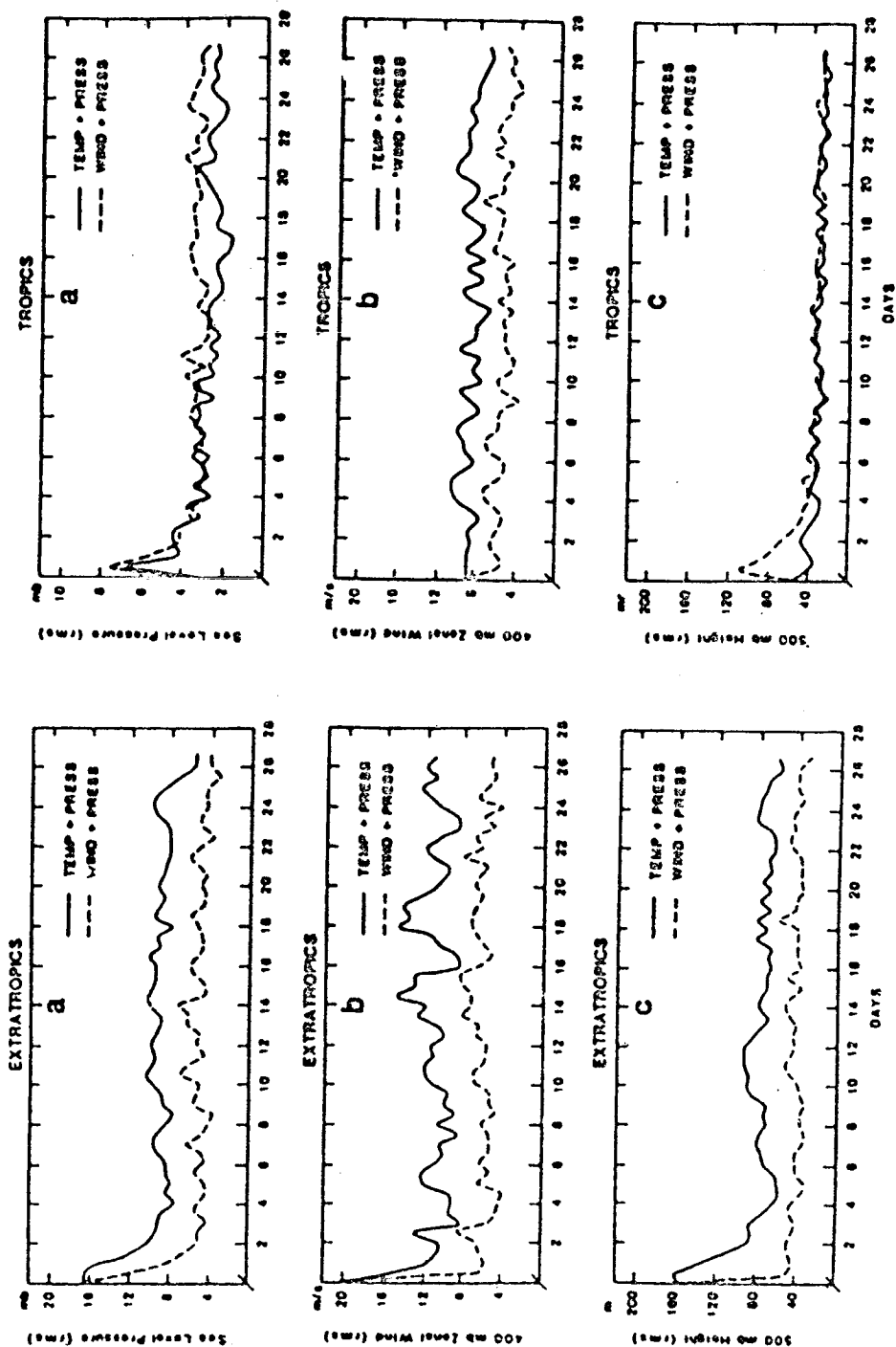FIGURE 10   12 hr forecast errors (GLAS nature)
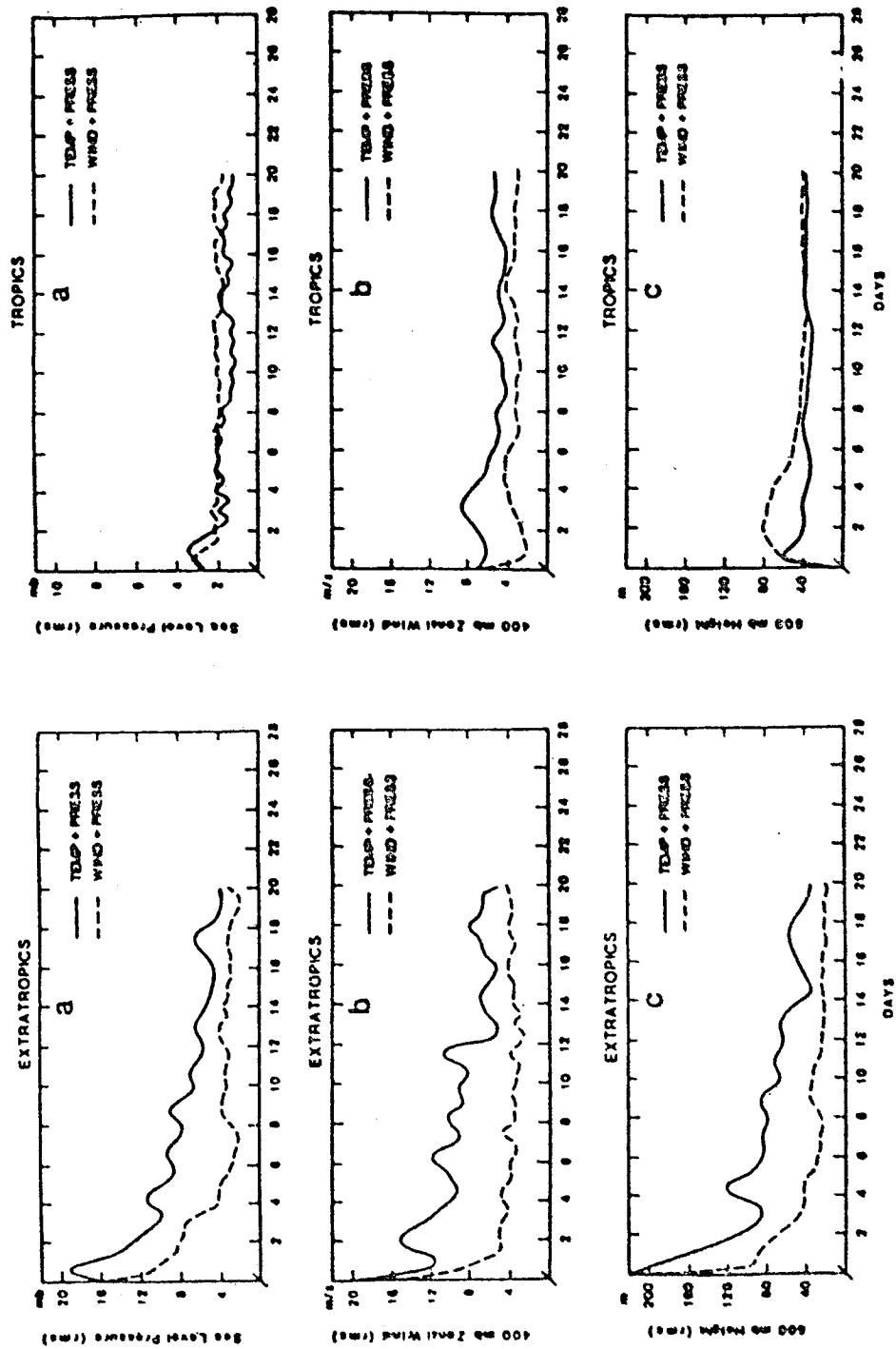
FIGURE 11 12 hr forecast errors (NMC nature)

FIGURE 12   12 hr forecast errors (ECMWF nature)

extratropics, the asymptotic composite temperature system forecast error levels for sea level pressure, 500 mb heights and zonal winds are 4 mb, 40 m, and 6 m/s, respectively. These error levels are half again what the real data error levels were for the composite system and reduced the errors to more than half that of the same fraternal experiment without pressure data. In addition, the error levels are comparable to that of the wind only system for the fraternal experiment. In the tropics, the errors are also significantly reduced with the composite temperature system for sea level pressure and geopotential heights but slightly for zonal winds. Yet, the zonal wind errors at 500 mb are only 4 to 5 m/s compared to 2 to 3 m/s for the wind data system. In both cases, they are significantly better than those obtained for the real data composite systems.

FORECAST/ANALYSIS IMPACT STUDIES OF LIDAR WIND AND PASSIVE TEMPERATURE SOUNDERS

A series of realistic simulation studies was conducted as a cooperative effort between the European Centre for Medium Range Weather Forecasts (ECMWF), the National Meteorological Center (NMC), and the Goddard Laboratory for Atmospheric Sciences (GLAS). The results of real data forecast impact studies indicate that major deficiencies in the global observing system still exist and that the FGGE satellite sounders are far from optimal. Advanced passive infrared and microwave sounders and active scatterometer and lidar sounders in a variety of combinations have recently been proposed to improve the accuracy of satellite observations and extend the useful range of numerical weather prediction. Realistic observing system simulation experiments are required to determine which of the proposed instruments will provide the greatest improvements as well as the optimal design of the future global observing system.

Previous simulation studies have been characterized by the use of the same model to simulate "nature" and observations and to produce forecasts. This "identical twin" problem may distort the conclusions derived from such studies, as discussed in the following section.

In the present study, we attempt to avoid these limitations by designing a more realistic simulation system and calibrating its results by comparison with real data experiments performed with a similar system, and by accurately simulating the expected accuracy and characteristics of observational systems. The simulation system is then used to study the potential impact of advanced passive sounders and lidar temperature, pressure, humidity and wind observing systems.

Design of the Simulation System

The analysis/forecast simulation system consists of four elements.

1. An atmospheric model integration to provide a complete record of the "true" state of the atmosphere (called nature). This record is

then used to fabricate observational reports and to evaluate analyses and forecasts.

2. A conventional data assimilation cycle that is used as the "control experiment." The control experiment is like an operational forecast-analysis cycle based on conventional observations, except that it makes use of fabricated conventional data obtained from the nature run to produce the analyzed fields.

3. A satellite data assimilation that differs from the control in also including fabricated satellite data incorporated in an intermittent or time-continuous manner, in the forecast-analysis cycle.

4. Forecasts produced from both control and satellite initial conditions. Comparison of these forecasts with nature provides an assessment of the impact of satellite data.

Two important considerations are involved in the design of the control assimilation run: the nature of the initial conditions, and the forecast model used. In reality, short-range forecasts have errors stemming from three different sources: (1) inaccuracy of the initial state, (2) model errors that can be ascribed to numerical truncation (horizontal and vertical truncation errors due to insufficient resolution), and (3) model errors that can be ascribed to the "physics" of the model. The latter include parameterization of subgrid processes like radiation, cumulus convection, and friction, as well as sources of external forcing, like orography, sea/land contrast, and even the use of an artificial rigid top boundary condition, common to all numerical models. Numerical and "physical" deficiencies introduce systematic errors in the model integrations that are most evident in the differences between model and observed climatological averages. A striking example of these climatological errors is apparent in the stationary, forced planetary waves. Even though these large-scale waves are numerically well resolved, they are not well simulated by numerical models. In a numerical forecast, a model tends to drift toward its own climatology, so that serious errors in the stationary waves are apparent after even a short time. For realistic simulation studies, all three sources of errors should be simulated. In previous simulation experiments, the same model was used to produce the "true" state and "forecasts." Therefore, the errors in the forecasts were due only to errors in the initial conditions. This method ("identical twin experiment") has the apparent advantage that it isolates the effect of initial data errors and avoids both numerical and "physical" errors. On the other hand, it has a very important shortcoming: since the model and "nature" have the same climatology, the accuracy of the simulated forecasts may be far superior to the accuracy of real forecasts. As a result, the external error growth due to the fact that current models are only approximations of the atmosphere is not present in the "identical twin" experiments. This has the effect of increasing the skill of conventional forecasts at low levels of data coverage, because the perfect forecast model is able to "fill up" data gaps. Consequently, at low levels of data, the impact of an observing system is overestimated, whereas the impact of high levels of data, such as provided by satellites, can be underestimated. In addition, if the

"nature" and "forecast" models are not realistic enough, i.e., do not possess a realistic model climatology, the data impact may be distorted. For example, a forecast model that cannot simulate the "roaring forties" regime in the southern hemisphere will not be helped by better low level winds in the southern hemisphere. The forecast model used should be sufficiently accurate that error growth should be dominated by initial data errors rather than by model dominated errors such as truncation errors. Otherwise, the experiment may overestimate the skill of the forecast and underestimate the influence of the data on the analysis.

Finally, if simulation studies are to provide an accurate indication of how simulated data will influence forecasts in the real world, it is crucial that their error characteristics be realistic. For simulated observational errors to be representative of real observational errors, they should be introduced at actual observing locations and should not be just white noise. Random errors with a standard deviation of the order of GARP errors saturate the spectrum at high frequencies and their effect is mostly averaged out. Horizontal and vertical correlations of error and their dependency on the synoptic situation should be introduced appropriately.

In order to avoid the "identical twin" character of previous studies, the high resolution (1.875° x 1.875° x 15 levels) ECMWF model is used as nature, and the 4° x 5° x 9 levels GLAS model is used as the assimilation and forecast model.

Impact Results

For all of the experiments that have been completed to date, the nature run is a 20-day integration from 0000 GMT November 10, 1979 using the 15 level, 1.875° resolution, ECMWF model. All types of FGGE and conventional data were simulated by NMC by interpolating the nature fields to observation locations and adding assumed or systematic errors to the interpolated values (C. Dey, personal communication). Only satellite temperature soundings were assumed to have systematic errors. Lidar wind profiles were simulated at TIROS observation locations with 1 to 3 m/s accuracy. Wind profiles were not generated at levels below which the integrated cloud amount exceeded 90 percent.

Experiments have been conducted to calibrate the simulation system and determine its realism, and to begin to assess the relative impact of temperature and wind profile observing systems. To this end, two real data assimilation cycles—a control and FGGE (see Halem et al., 1981, for descriptions)—and five simulated data assimilation cycles—control, FGGE, control plus TIROS, control plus perfect temperatures, and control plus wind profiles—were performed for the period 0000 GMT November 10 to 0000 GMT November 25, 1979.

The NMC analysis for 0000 GMT November 10 was used as initial conditions for the real data assimilation cycles. Initial conditions for the simulated data assimilations were provided by a real data control assimilation from 0000 GMT November 4 to 0000 GMT November 10. Eight five-day forecasts were generated from each assimilation at

48-hour intervals beginning on November 11. In addition, a 12-day integration from the ECMWF analysis at 0000 GMT November 10 was generated with the GLAS model. This forecast was then compared to the nature run as a measure of the differences between the two models.

Figure 13 shows that there are substantial differences between the GLAS and ECMWF sea level pressure forecasts from November 10 as verified over North America. For the first four days the differences between the two model forecasts are about as large as the differences between the ECMWF forecast and its analysis. However, from five to eight days the two model forecasts resemble each other more clearly than either forecast represents the analysis. In addition, an examination of global difference fields between the forecasts and between each forecast and the analysis (not shown) reveals that in the northern hemisphere, the model forecast differences are of a larger scale than the forecast versus analysis differences. These results indicate that the simulation system does differ significantly from the identical twin system described previously. But the differences between the models still may not be sufficiently realistic.

Figure 14 summarizes the initial results of our simulation experiments. S_1 skill scores averaged for eight forecast cases are presented for the control, control plus TIROS, and control plus wind profiles for the northern hemisphere; and for the control, control plus TIROS, control plus wind profiles, and FGGE experiments for the southern hemisphere. The FGGE results were nearly identical to the control plus TIROS in the northern hemisphere and are not shown. Similarly, the control plus perfect temperatures were, on the average, similar to the control plus TIROS and are not presented.

From Figure 14, it can be seen that the use of simulated wind profile data shows a significant improvement over the TIROS or FGGE experiments in the southern hemisphere. For the northern hemisphere the impact of both simulated TIROS and wind profiles is only very slightly beneficial on the average. However, in specific cases, significant forecast improvements occur for smaller regions. Figure 15 shows a case of major improvement in the prediction of a storm over the United States which was poorly forecasted with the simulated control system. The use of TIROS data improved the prediction of the low near the Great Lakes. Significant further improvement resulted from either perfect temperatures or wind profiles.

To measure the realism of the simulation results, comparisons were made between the real and simulated data verifications for the same regions. These comparisons showed that the simulated control experiment was unrealistically accurate in the northern hemisphere but realistic in the southern hemisphere. In addition, the impact of TIROS and FGGE data appears to be slightly overestimated requiring a small calibration to the simulation impact results.

SUMMARY

One of the more important accomplishments of FGGE was to provide an international focus to planning, designing and implementing the Global

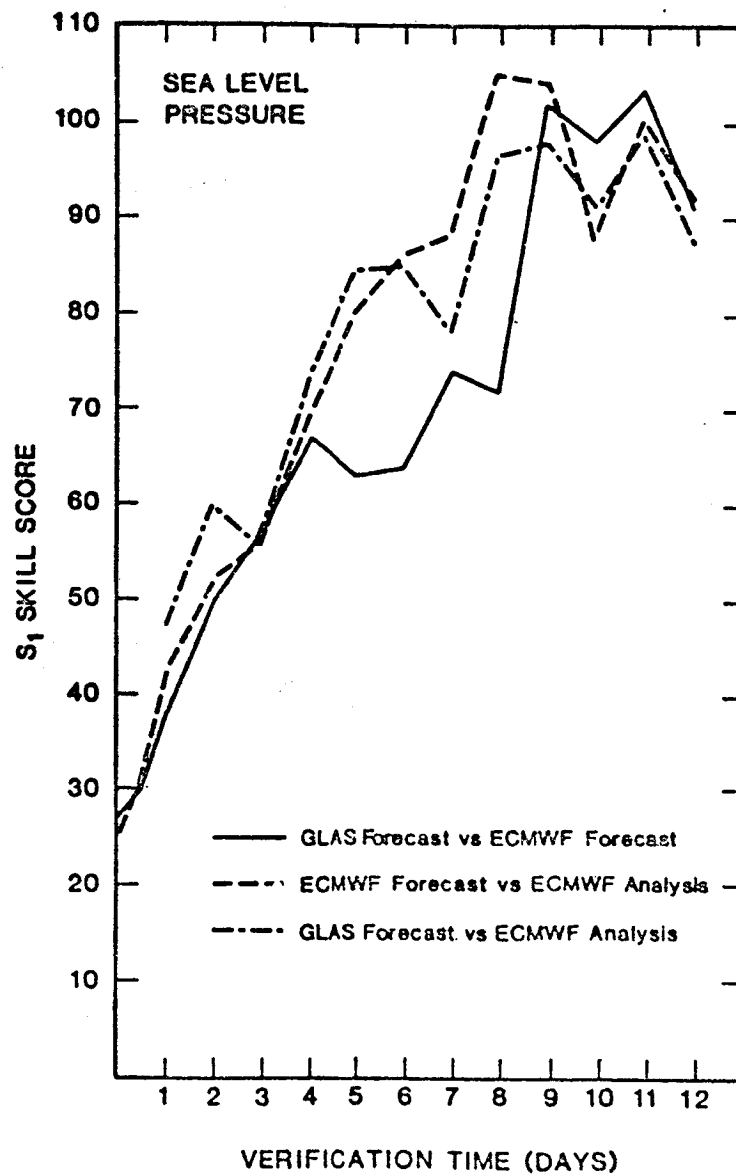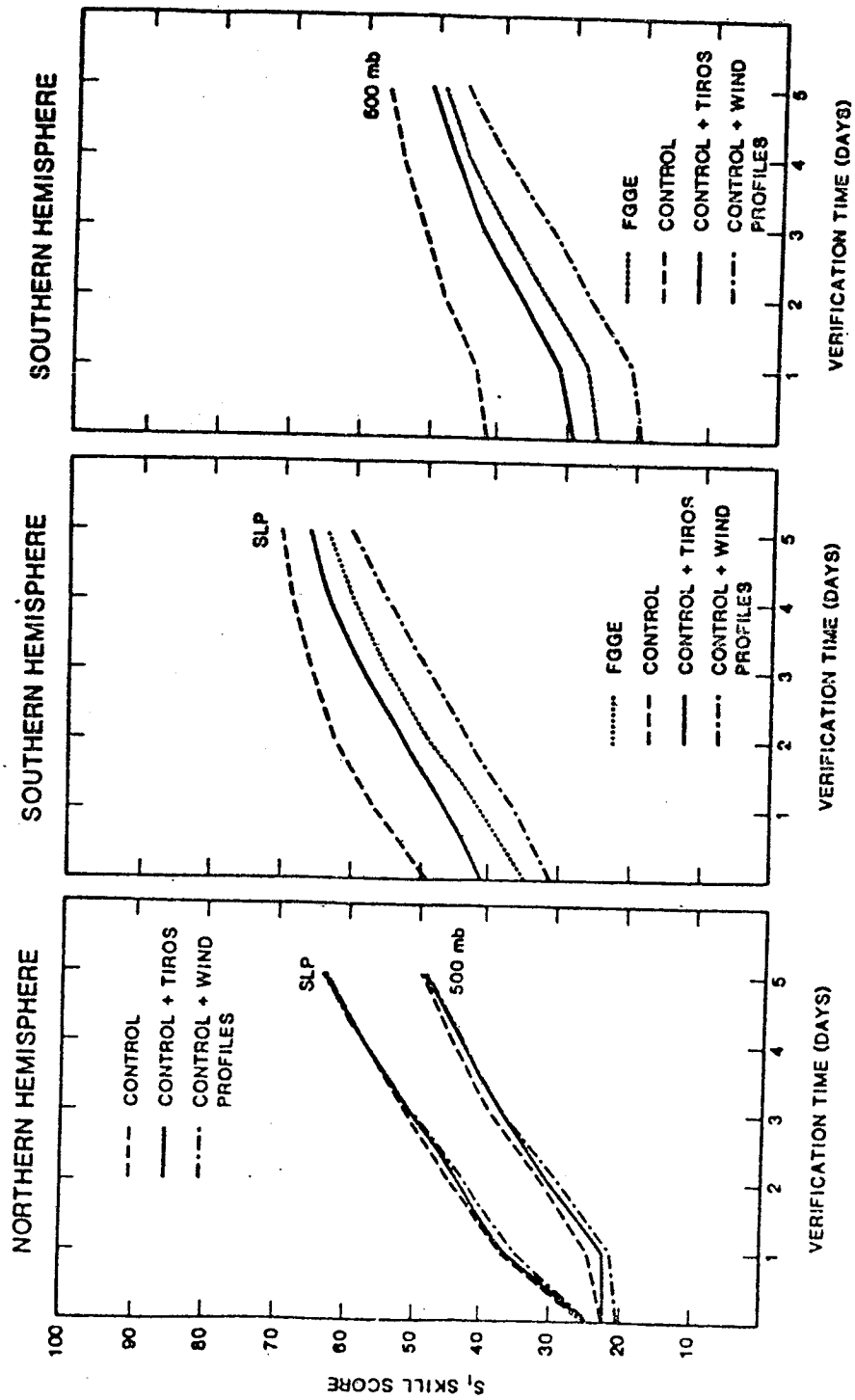FIGURE 13 Sea level pressure S_1 scores for North America for the ECMWF Nature run verified against the ECMWF analysis, and the corresponding GLAS model forecast from the ECMWF analysis at 0000 GMT November 10, 1979 verified against the ECMWF analysis and the ECMWF Nature run.
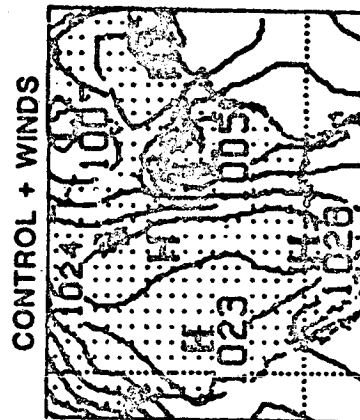
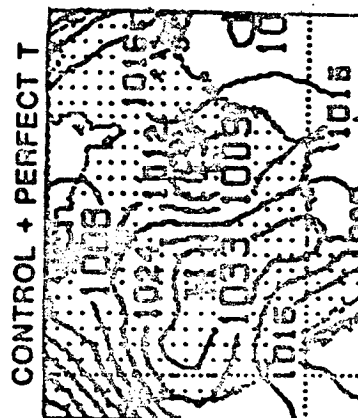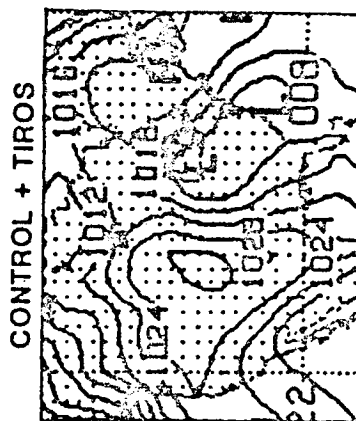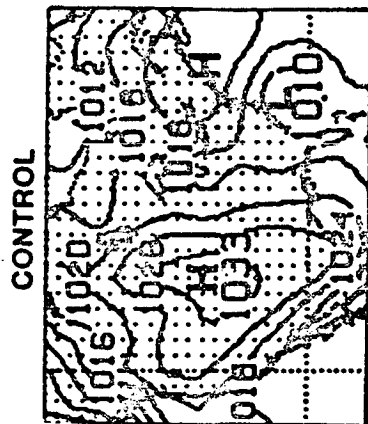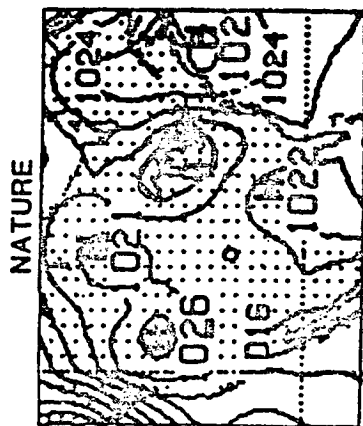FIGURE 14 Simulated data S_1 score verification.

FIGURE 15 Simulated five-day sea level pressure forecasts from November 23, 1979 and verification.

Observing Systems for the next decade. An additional byproduct of the Global Weather Experiment has been a unique data set which can serve as a benchmark for test bedding the design of future observing systems. In this regard, we presented three detailed simulation studies on the potential of next generation active and passive systems to measure and define the global state of the atmosphere. The following summarizes some results drawn from the simulation experiments.

1. AMTS/HIRS Simulation Study. This study examined the performance of the AMTS as calibrated against the operational HIRS-2 and the operational algorithm for the retrieval of temperature profiles. The study was one of the most comprehensive and scientifically credible simulations ever conducted. The major conclusions drawn are that the AMTS outperforms the HIRS even in the presence of clouds and that the NASA/GLAS physical relaxation retrieval process outperforms the operational NESDIS statistical regression process used by NOAA. The overall AMTS improvements in temperature profile accuracies are 0.5°C to 1.0°C better than HIRS. The AMTS thickness heights might be more accurate than those determined from radiosondes. The accuracy of AMTS land and sea surface temperatures are approximately 0.3°C, almost 1.0°C better than HIRS-2.

2. Lidar Wind and Temperature Simulation Studies. These studies establish the ranking of the relative importance of measuring the primary meteorological variables in terms of their ability to improve 12-hour forecasts. The experiments show that global winds are the most important atmospheric variables to measure but that temperatures can be used to infer complete atmospheric states in the extratropics. Surface pressure data alone essentially show no influence. However, surface pressure data combined with temperature data greatly increase the accuracy of inferred states. These experimental results for extra-tropical regions appear model independent since both GLAS and ECMWF simulations were both calibrated with a real NMC data analysis cycle. Model independence in the tropics is still uncertain, but the studies show reasonable support even in these regions.

Specific results obtained show (a) wind and pressure 12-hour forecast asymptotic errors nearly half those of temperatures and pressure in extratropics, (b) asymptotic adjustment to winds almost instantaneous compared with two-week relaxation times for temperature data, (c) incomplete wind profiles significantly degrade accuracies of inferred 12-hour forecast errors, and (d) winds and pressure are the only system that significantly reduces 12-hour forecast zonal wind errors in tropics.

3. Forecast Impact Simulation Studies. The simulated FGGE observing system used in the GLAS analysis and forecast cycles were calibrated against similar real data analyses and forecasts. The calibrated simulation indicates the results to be realistic in the southern hemisphere, but the simulated forecasts in the control experiment appear much more accurate than the real data forecasts in the northern hemisphere. The general conclusions from these studies are that (a) the wind profile data produce more accurate 1 to 5 day forecasts than temperature data, and (b) if the proposed accuracies and

overage for a lidar wind profiler can be achieved, then southern hemisphere analysis and forecasts should become as accurate as those for the northern hemisphere.

REFERENCES

Baker, W.E. (1983). Objective analysis and assimilation of observational data from FGGE. Mon. Wea. Rev. 111, 328-342.

Bengtsson, L., M. Kanamitsu, P. Kallberg, and S. Uppsala (1982). FGGE four-dimensional data assimilation at ECMWF. Bull. Amer. Meteorol. Soc. 69, 29-43.

Bergman, K.H. (1979). Multivariate analysis of temperatures and winds using optimum interpolation. Mon. Wea. Rev. 107, 1423-1443.

Chahine, M.T., N.L. Evans, V. Gilbert, and R.D. Haskins (1984). Requirements for a passive IR advanced moisture and temperature sounder. Applied Optics 23, 979-989.

Halem, M., E. Kalnay-Rivas, W. Baker, and R. Atlas (1981). An assessment of the state of the atmosphere as inferred from the FGGE satellite observing systems during SOP-1. Bull. Amer. Meteorol. Soc. 63, 407-426.

Hall, Jr., F.F., R.M. Huffaker, R.M. Hardesty, M.E. Jackson, T.R. Lawrence, M.J. Post, R.A. Richter, and B.F. Weber (1983). Proceedings of 2nd Topical Meeting on Coherent Laser Radar: Technology and Applications, August 1-4, Aspen, Colorado.

Hardesty, R.M., R.W. Lee, and D.L. Davis (1983). Real-time processes and display of coherent lidar returns. Proceedings of 2nd Topical Meeting on Coherent Laser Radar: Technology and Applications, August 1-4, Aspen, Colorado.

Hays, P.B., and V.J. Abreu (1984). Analysis of a 0.5 micron spaceborne wind sensor. AMS Conf. on Satellite/Remote Sens. and App., June 25-29, Clearwater Beach, Florida.

Huffaker, R.M. (1978). Feasibility study of satellite-borne lidar global wind monitoring system: Part I. NOAA Tech. Memo. ERL WPL-37.

Huffaker, R.M. (1980). Feasibility study of satellite-born lidar global wind monitoring system: Part II. NOAA Tech. Memo. ERL WPL-63.

Kalnay-Rivas, E., and D. Hoitsma (1979). Documentation of the Fourth Order Band Model. NASA Tech. Memo. 80608.

Kaplan, L.D., M.T. Chahine, J. Susskind, and J.E. Searl (1977). Spectral band passes for a high precision satellite sounder. Applied Optics 16, 322-325.

Lockheed Missile and Space Co. (1981). Global Wind Measuring Satellite System--Windsat. Report NOAA Contract H NA 79RS600127.

Lorenc, A.C. (1981). A global three-dimensional multi-variate statistical interpolation scheme. Mon. Wea. Rev. 109, 701-721.

Pace, P.W., and M. LaCombe (1978). A sealed high pulsed rate TEA CO_2 laser. IEEE, J. Quantum Elect. 14, 263.

RCA, Astro-Electronics (1983). Feasibility Study of a Windsat Free Flyer. U.S. Dept. of Commerce, NOAA, Contract NA82RAL001141.

Reuter, D., and J. Susskind (1984). Comparison of AMSU temperature soundings with those produced by HIRS and AMTS. NASA Tech. Memo. 86053, 28-32.

Susskind, J., J. Rosenfield, and D. Reuter (1983). An accurate radiative transfer model for use in the direct physical inversion of HIRS-2 and MSU temperature sounding data. J. Geophys. Res. 88, 8550-8568.

Williamson, D. (1973). The effect of forecast error accumulation on four-dimensional data assimilation. J. Atmos. Sci. 30, 537-543.

18. OCEANOGRAPHY

Organizer	Eli J. Katz
Session Chairman	Eli J. Katz
Speakers	Robert L. Bernstein
	Edward S. Sarachik
	Robert L. Molinari
	Henry M. Stommel
Rapporteur	Edward S. Sarachik

366<

SEA SURFACE TEMPERATURE FROM SATELLITES:
THE IMPACT OF FGGE

Robert L. Bernstein
Scripps Institution of Oceanography

ABSTRACT

Spacecraft instruments first launched at the beginning of the FGGE year
are now producing sea-surface temperature data accurate to about
1°C. At larger scales, the errors are dominated by systematic
effects, some of which are instrumental, but most are geophysical,
i.e., correlated with volcanic aerosols, atmospheric water vapor,
clouds, and surface wind. Progress is being made to identify and
eliminate such errors and thereby provide sea-surface temperature data
on a global basis consistently accurate to 0.5°C, which will be .
needed for studies of climate variability.

During June and October 1978, in preparation for FGGE, the United
States launched three spacecraft: SEASAT, Nimbus-7, and TIROS-N. The
first two were NASA research satellites, while the third was the first
of a new series of NOAA operational weather satellites. The two NASA
satellites both carried identical microwave radiometers intended to
measure sea-surface temperature even through cloud cover. The NOAA
satellite carried two new infrared sensors capable of exploiting
whatever breaks occurred in cloud cover to make the same measurement.
Since then, work by a number of investigators with the resulting data
has shown that these instruments can make important contributions to
ocean science, from scales of a few kilometers and hours to global
dimensions and years. The impact on oceanography is such that almost
all field work now undertaken with ships and buoys includes a satellite
sea-surface temperature component as well. For climate studies that
require many years of data, insufficient time has yet elapsed, but the
accumulating data will clearly soon have great value. For example, the
sea-surface temperature warming of the 1982 El Niño was first detected
by satellite measurements. While some technical problems must still be
overcome, FGGE must claim at least partial credit for a major advance
in this area.

SEASAT and Nimbus-7 both carried the Scanning Multifrequency
Microwave Radiometer (SMMR) developed at the Jet Propulsion Laboratory.
The SMMR measures emitted radiation at five frequencies: 6.6, 10.7,
18, 21, and 37 gHz. The lowest frequency with a spatial resolution of

761

150 km contains most of the sea-surface temperature information, but the higher frequencies are required to make corrections for sea-surface emissivity (a function of sea state and wind) and for atmospheric transmissivity (a function of atmospheric water content).

The TIROS-N satellite and its operational successors (NOAA-6, -7, and -8) each carried the Advanced Very High Resolution Radiometer (AVHRR) and the High Resolution Infrared Sounder/Microwave Sounding Unit (HIRS/MSU). The AVHRR has high spatial resolution (1 km locally, 4 km globally) with measurements in five spectral channels (0.55, 0.90, 3.7, 11.5, and 12.5 micron) in the visible, near infrared, and thermal infrared. The HIRS/MSU has lower spatial resolution (30 km in the infrared) but measures at 24 channels in the infrared and microwave spectrum. Both AVHRR and HIRS/MSU were designed without sea-surface temperature as their primary mission, yet both have demonstrated excellent capabilities to do so.

At the global scale, a recent series of NASA-sponsored workshops conducted at the Jet Propulsion Laboratory (JPL, 1984) have evaluated the satellite sea-surface temperature estimates produced from these instruments by a few groups. Three primary satellite data sets were considered. First were the multi-channel sea-surface temperature (MCSST) operational estimates produced by NOAA from AVHRR data (Strong and McClain, 1984). Next were the data derived from the HIRS/MSU by Chahine of JPL and Susskind from Goddard (Susskind et al., 1982). Third are the Nimbus-7 SMMR estimates produced by Wilheit and Milman at Goddard (Wilheit and Chang, 1980). These three satellite data sets were compared against the routinely reported ship and buoy observations for the months of November 1979, December 1981, March 1982, and July 1982.

In order to compare ship and satellite results, individual observations were binned into monthly, 2° latitude-longitude bins. The statistics on the differences between the ship and satellite bin averages (Table 1) indicate that the AVHRR estimates agree best with the conventional in water data, having standard deviations in the range 0.81 to 1.01°C, about means ranging from -0.54 to +0.26°C. SMMR and HIRS estimates had standard deviations in the range 1.04 to 1.331°C, about means of -0.18 to +0.34°C. Closer inspection of the geographical distribution of the disagreement showed considerable correlation with other geophysical parameters. Most obvious was the problem encountered by the AVHRR following the El Chichon volcanic eruption, when the resulting stratospheric aerosols caused satellite estimates to be too cold by several degrees Celsius in the 0 to 40°N latitude band of maximum aerosol concentration. Techniques for correction of this error source are under development. Other geophysically correlated errors occurred in the AVHRR and HIRS infrared-based data, where sea-surface temperatures were either systematically overestimated or underestimated in regions of high water vapor or cloudiness. Such errors tended to be less than 2°C in the worst case and indicate problems in the algorithms for making corrections for these parameters. The SMMR estimates were found to have problems in high wind areas, probably due to incorrect estimation of the variation of surface emissivity with wind speed. Other SMMR

TABLE 1 Global Binned Difference Temperature (Satellite Minus Ship)
Statistics, Degrees Celcius, from the JPL Workshops. THe July 1982
HIRS data is not yet available.

Satellite Sensor		Nov 1979	Dec 1981	Mar 1982	Jul 1982
AVHRR	mean	0.26	-0.19	-0.06	-0.54
	st dev	0.95	0.83	0.81	0.90
	# obs	2145	4103	4322	3962
SMMR	mean	0.34	0.19	-0.01	-0.18
	st dev	1.28	1.27	1.20	1.08
	# obs	791	1960	1972	1826
HIRS	mean	0.30	0.12	0.31	-
	st dev	1.28	1.23	1.10	-
	# obs	2344	4184	4395	-

problems were unique to the particular instrument design and operation,
rather than microwave radiometry, and are not likely to be repeated in
future instrumentation.

In regional and process-oriented studies, the AVHRR has found
greatest use because of its 1 km resolution. Numerous major
experiments have found satellite data to have a significant impact on
the overall interpretation of data. A list of such experiments
includes the FRONTS 80 experiment, which examined the North Pacific
Subtropical Front north of Hawaii; the Coastal Ocean Dynamics
Experiment (CODE) and the Organized and Persistent Upwelling Structures
(OPUS) programs, both of which looked at coastal upwelling along the
U.S. west coast; the Warm Rings program, studying the dynamics of rings
shed to the north by meanders of the Gulf Stream; and the Equatorial
Pacific Ocean Climate Study (EPOCS) and the Tropic Heat programs in the
eastern and central equatorial Pacific. Phenomena examined by these
investigations range from frontal scales of a few kilometers to
upwelling patterns of tens of kilometers, Gulf Stream meander and eddy
scales of 100 to 200 km, and equatorial current meanders of 1000 km
wavelength.

The primary objective of FGGE was improved atmospheric prediction on
the synoptic scale. The second GARP objective relates to climate, and
programs such as the Tropical Ocean-Global Atmosphere (TOGA)
interaction address this objective with the attendant increased
emphasis on the interaction between ocean and atmosphere at these
longer time scales. Sea-surface temperature measurements globally
distributed and consistently accurate to 0.5°C are required for
climate oriented investigation. The major impact of FGGE in this area
of satellite sea-surface temperature observation thus has been to bring
the state-of-the-art close to satisfying climate research requirements,
although some additional efforts will be needed.

REFERENCES

Jet Propulsion Laboratory (1984). Satellite-Derived Sea-Surface Temperature: Workshop II. JPL Publication 84-5, February 1984.

Strong, A. E., and E. P. McClain (1984). Improved ocean surface temperatures from space—comparisons with drifting buoys. _Bull. Amer. Meteorol. Soc. 65_, 138-142.

Susskind, J., J. Rosenfield, D. Reuter, and M. T. Chahine (1982). The GLAS Physical Inversion Method for Analysis of HIRS/MSU Sounding Data. NASA Tech. Memo. 84936, Goddard Space Flight Center, Greenbelt, Md.

Wilheit, T. T., and A. T. C. Chang (1980). An algorithm for retrieval of ocean surface and atmospheric parameters from the observations of the Scanning Multichannel Microwave Radiometer (SMMR). _Radio Sci._ _15_, 525-544.

MODELING SEA-SURFACE TEMPERATURE AND ITS VARIABILITY

E. S. Sarachik
Pacific Marine Environmental Laboratory
National Oceanic and Atmospheric Administration

ABSTRACT

A brief review is presented of the temporal scales of sea-surface temperature variability, of our progress in modeling sea-surface temperature, and of remaining obstacles to our understanding.

INTRODUCTION

In modeling the mean atmosphere and the annually varying atmosphere, it has been traditional to specify the sea-surface temperature (SST) at the observed values. Indeed, no improvement in the simulation of the mean or annually varying atmosphere could be expected when coupling the atmosphere to an interactive ocean, for under the best of circumstances, the ocean would simply replicate the observed SSTs. It is when one wishes to understand the system perturbed by some internal (e.g., CO_2 doubling) or external (e.g., solar variations) agent for which SST observations are not available that SST must be predicted. Also, when the atmosphere and ocean interact so strongly that the seasonal cycle is perturbed and modes of interannual variability arise (e.g., the El Niño/Southern Oscillation phenomena), the SST must be predicted in order to fully understand the interaction. Under either of these circumstances, the success of atmospheric models will depend strongly on the quality of the SST predictions made for them. It is the purpose of this paper to briefly describe where we stand in modeling SST and SST variability, and how our ideas have evolved from the time of the First GARP Global Experiment (FGGE) to the present (1984).

The varieties of SST variability are shown in the figures. The mean SST is shown in Figure 1a while deviations from the zonal mean are shown in Figure 1b. Since the sun exhibits no zonal asymmetries, it is clear that the ocean must be responsible for much of the zonal asymmetries shown in Figure 1b. A measure of the annual cycle of SST (contours of the difference between the warmest and coldest SSTs at each point) is shown in Figure 2. (A better measure would be contours of the amplitude and phase of the annual cycle of SST, but the author could find no global map exhibiting them.) The interannual variability of SST is well illustrated by the EOF analysis for the Pacific (Weare
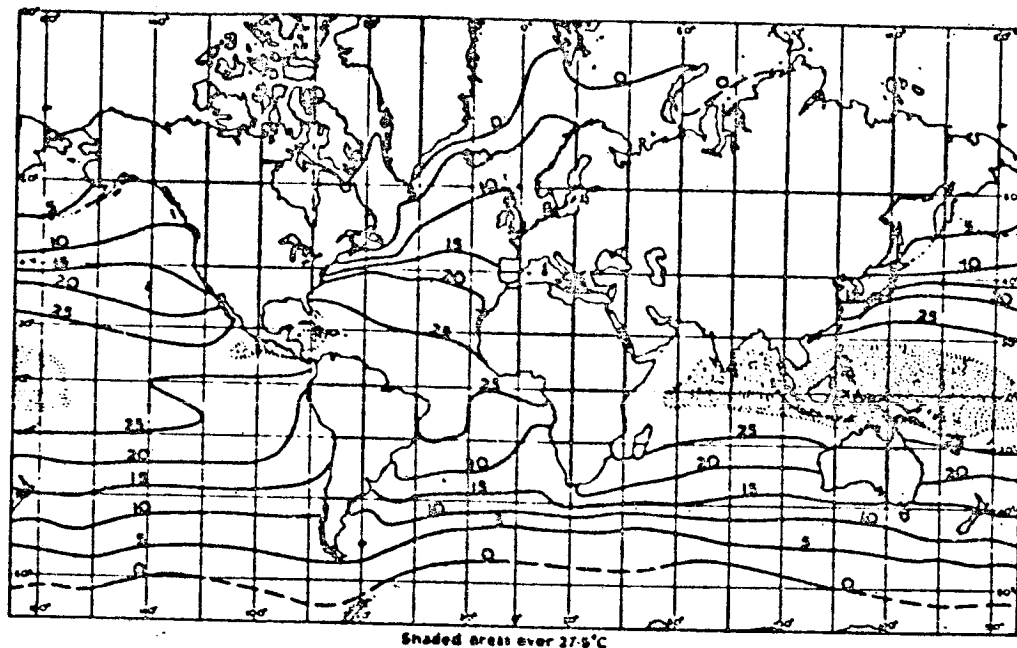
FIGURE 1a Annual mean sea-surface temperatures over the world (°C) (adapted from Dietrich).

et al., 1976) in Figure 3. The maximum amplitude occurs during El Niño periods during which the equatorial Pacific becomes uniformly warm and the northern midlatitude Pacific shows cold anomalies of about a degree. Figure 4 shows the CLIMAP reconstruction of the SST of 18,000 years ago during the last great glacial period.

Ultimately, one would like to understand and be able to simulate all temporal scales of variability of SST. In practice, ocean numerical modeling has advanced no faster than our ability to measure the ocean; many processes that contribute to the slow physics of the ocean, in particular the maintenance of the internal stratification, are simply not understood. Since annual and interannual changes in the ocean are confined to the upper ocean and can therefore, to a first approximation, be decoupled from the slow physics, the best hopes for the immediate future lie in describing these two fast modes of SST variability.

MODELING AT THE TIME OF FGGE

In 1979, most studies (see Garwood, 1979) of SST variability had as their premise that knowing the heat flux into the ocean and being able to predict mixed layer depth and its changes would allow the temperature changes to be computed by a simple one-dimensional model:

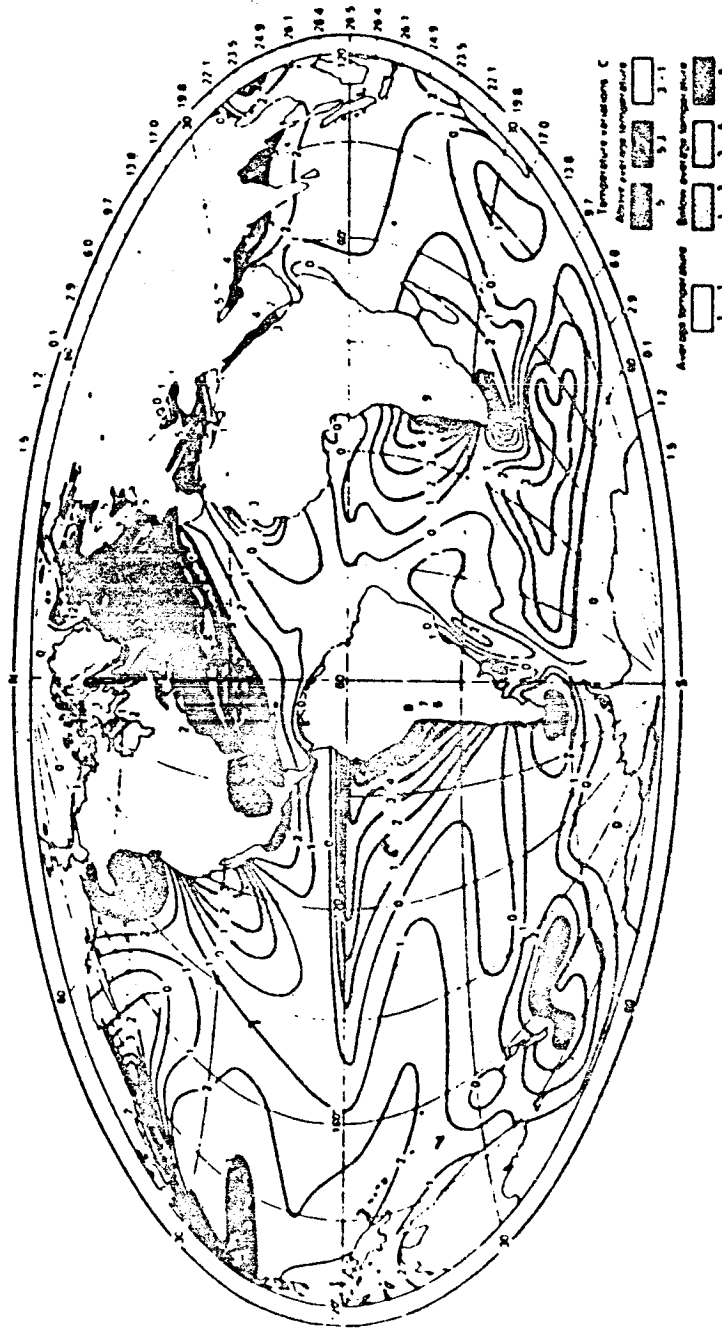FIGURE 1b Sea-surface temperature (°C) represented as a deviation from the average at each latitude (after Dietrich and Kalle, 1957).
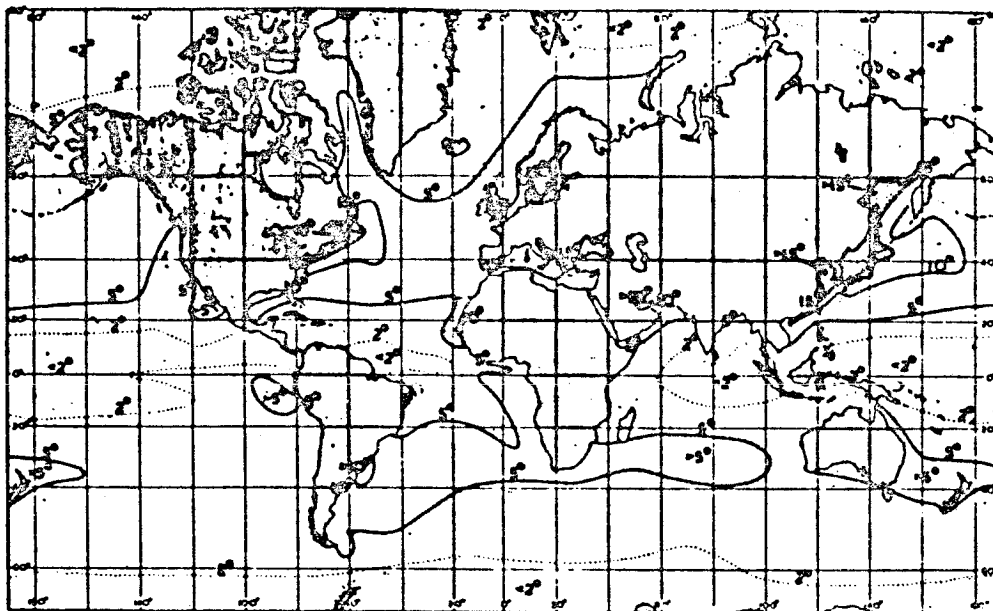
FIGURE 2 Average yearly range of sea-surface temperature (°C).
Warmest–coldest month (adapted from Dietrich 1957).

$$\rho c_p h \frac{d}{dt} (T) = Q(sfc) - Q(e) \tag{1}$$

where the entrainment flux $Q(e) = (dh/dt + w) \Delta T$ was positive only
when the entrainment velocity ($W_e = dh/dt + w$, the volume per unit
area crossing the bottom of the mixed layer) was positive. ΔT is the
discontinuity of temperature at the bottom of the mixed layer and is
simply related to the depth of the layer h and the stratification Γ
beneath. The depth of the layer is usually diagnosed from the
energetic equations: increases of depth are aided by wind stresses and
inhibited by heat flux into the layer either at the top or the bottom
and by friction (see Niiler and Kraus, 1977, for a review of the
methods involved).

There were theoretical reasons for believing that the 1d formulation
should work, at least on the annual time scale. By means of scale
analysis, Gill and Niiler (1973) showed that poleward of 15°, on
relatively large scales (1000s of km), and away from boundary currents,
currents varied too weakly to induce any advective effects on the mixed
layer storage and equation (1) should hold. The combination of
equation (1) and mixed layer models did indeed prove quite successful
at modeling mixed layer depths and SST variability (again, see Garwood,
1979) for those midlatitude stations at which data exist, to the extent
that the surface fluxes could be measured. The method is limited by
our ability to know the fluxes into the ocean Q(sfc) since this flux is

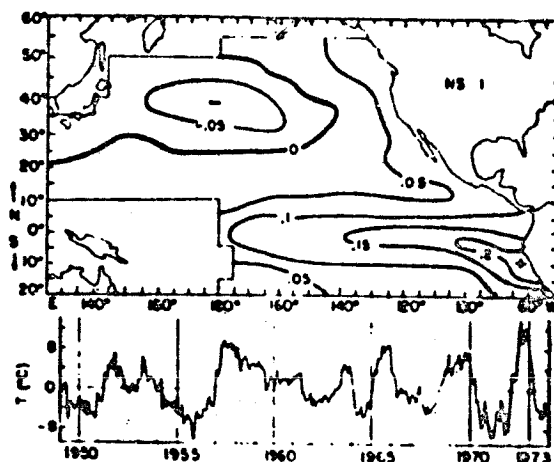FIGURE 3 The amplitude and spatial distribution of the first
(nonseasonal) EOF of Pacific sea-surface temperature variability.

obtained as a (small) sum of the radiative flux, latent heat flux, and
sensible heat flux, all of which are obtained by imperfect bulk
formulae (see Sarachik, 1984).

That the data problem is serious is indicated by a recent direct
attempt to verify that flux variations go entirely into storage (Wyrtki
and Urich, 1982). The discrepancy between heat flux and storage in a
region of the Pacific for which Gill and Niiler's argument should hold
was found to be 50 percent of the storage and was attributed to
advection. The error in storage was about 25 percent of the annual
amplitude, and the error in heat flux was assumed to be an unrealis-
tically low 5 percent of its annual amplitude. Raising the error in
flux to a more realistic 30 percent would put the residual in the range
of zero, in agreement with Gill and Niiler. Without being able to
bound the errors more precisely, the observational verification of Gill
and Niiler remains open.

MODELING SST

Mixed layer models of SST variability break down when advections of
temperature become important. There arose two studies indicating that
heat advections on time scales as short as the seasonal were important.
The first (Oort and Vonder Haar, 1976) indicated that the seasonal
cycle of zonally averaged meridional heat flux was extremely large in
the equatorial regions, with peak-to-peak amplitudes exceeding 10^{16}
W. The second (Merle, 1980), in a study of heat storage and fluxes in
the tropical Atlantic, determined that heat fluxes into zonal strips of
ocean were of the order of magnitude too small (and of the wrong sign)
to account for heat storage variations. Furthermore, heat storage in
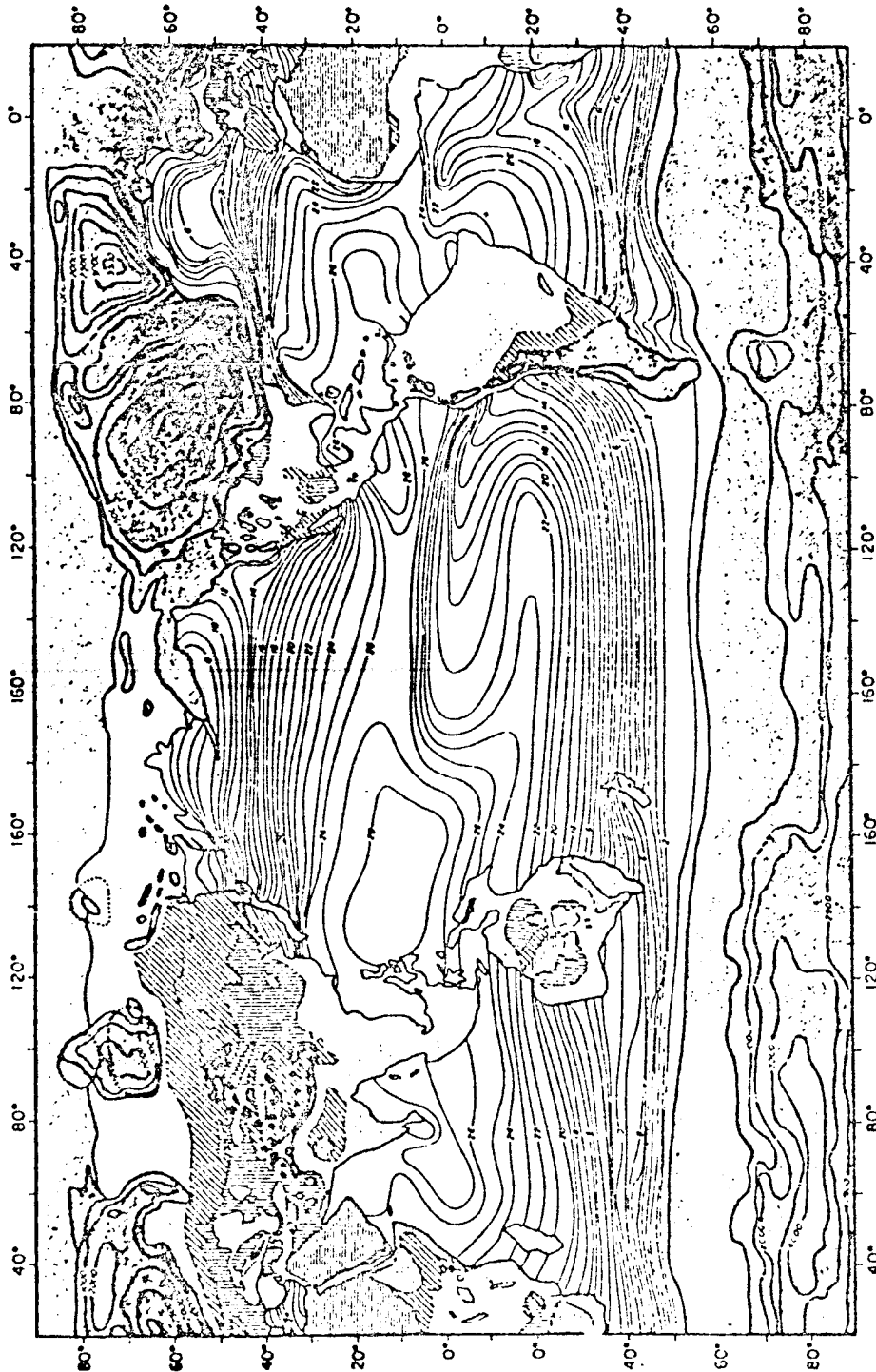the eastern and western parts of the ocean were out of phase with each

FIGURE 4 The CLIMAP reconstruction of sea-surface temperature 18,000 years ago.

other and individually in phase with thermocline depth; and in the Eastern Atlantic, in phase with SST variations. The basic message drawn from Merle's work was that the equatorial ocean was dynamically active in rapidly transferring heat both zonally and meridionally, and that advections cannot be ignored in modeling seasonal changes in SST in equatorial regions; in fact, advections can dominate. Molinari (this volume) also indicates that one-dimensional models failed to predict SST in the equatorial Atlantic during FGGE.

Since thermocline variations are relatively well simulated by simple one-layer reduced gravity equatorial models (e.g., Busalacchi and O'Brien, 1981) and current variations relatively well simulated by a nonlinear reduced gravity model containing two fixed levels above the thermocline (Cane, 1980), the idea naturally arose of making a reduced gravity model with two levels above the thermocline, one of which would be a thermally active mixed layer (Schopf and Cane, 1983). This model is the simplest model capable of simulating the basic features of equatorial currents and thermodynamics and their mutual interactions. One of the initial results of this model was something that in retrospect should have been obvious: the asymmetry in the effects of upwelling and downwelling on SST. Upwelling raises the thermocline and lowers SST directly through entrainment at the base of the mixed layer. Downwelling lowers the thermocline but induces no direct SST effects; SST may increase if horizontal convergence advects in warmer water or may decrease either by horizontal advection or by entrainment at the base of the mixed layer if the wind is strong enough to maintain a positive entrainment velocity. Thus on short time scales, there need be no relation between SST and thermocline depths; whereas on longer time scales, deeper thermoclines are usually associated with warmer SST.

Using the same model, Schopf and Harrison (1983) showed that the SST changes associated with propagating downwelling Kelvin fronts (produced by suddenly applied westerly wind anomalies near the equator) are caused by horizontal advections associated with the anomalous currents associated with the Kelvin front. These advections depend on the pre-existing mean SST gradient. Where the gradient is large, the SST anomalies are large and rapidly propagating; where the pre-existing gradient is small, the SST anomalies are small and slowly propagating. Just such a mechanism was used by Harrison and Schopf (1984) to respectably simulate the initial onset of the El Niño event of 1982-1983 by the action of advections due to the anomalous current associated with a Kelvin front propagating through the mean August 1982 SST field. The lesson learned from this simulation is that the propagation speed and location of the SST anomalies depends on the pre-existing SST gradient.

The obvious extension of this model, a thermally active mixed layer embedded in a higher vertical resolution layered ocean, is currently being constructed by Schopf (personal communication). A model having a mixed layer embedded in a multi-level ocean has been reported by Adamec et al. (1981) and has been used with some success to simulate the short-term effects of a hurricane on the thermal structure of the ocean. Finally, a 27-level numerical model of the equatorial ocean, while having no explicit mixed layer, has been modified to have a
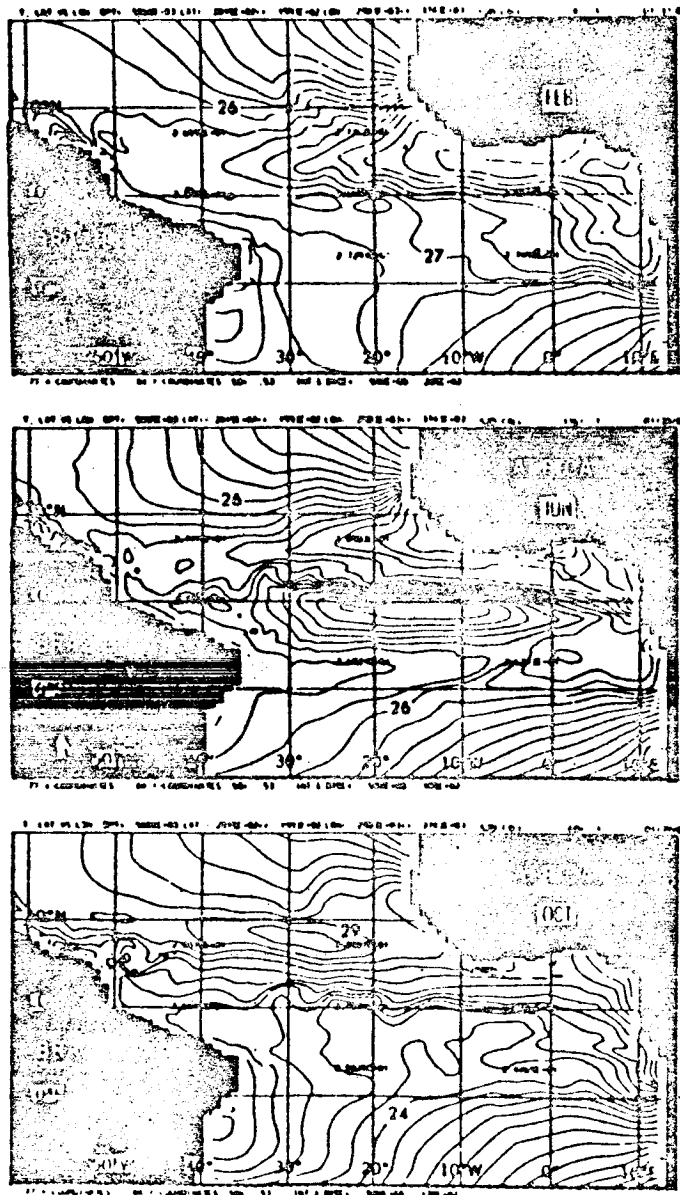
FIGURE 5 Seasonal simulation in the tropical Atlantic (Philander and Pacanowski, unpublished).
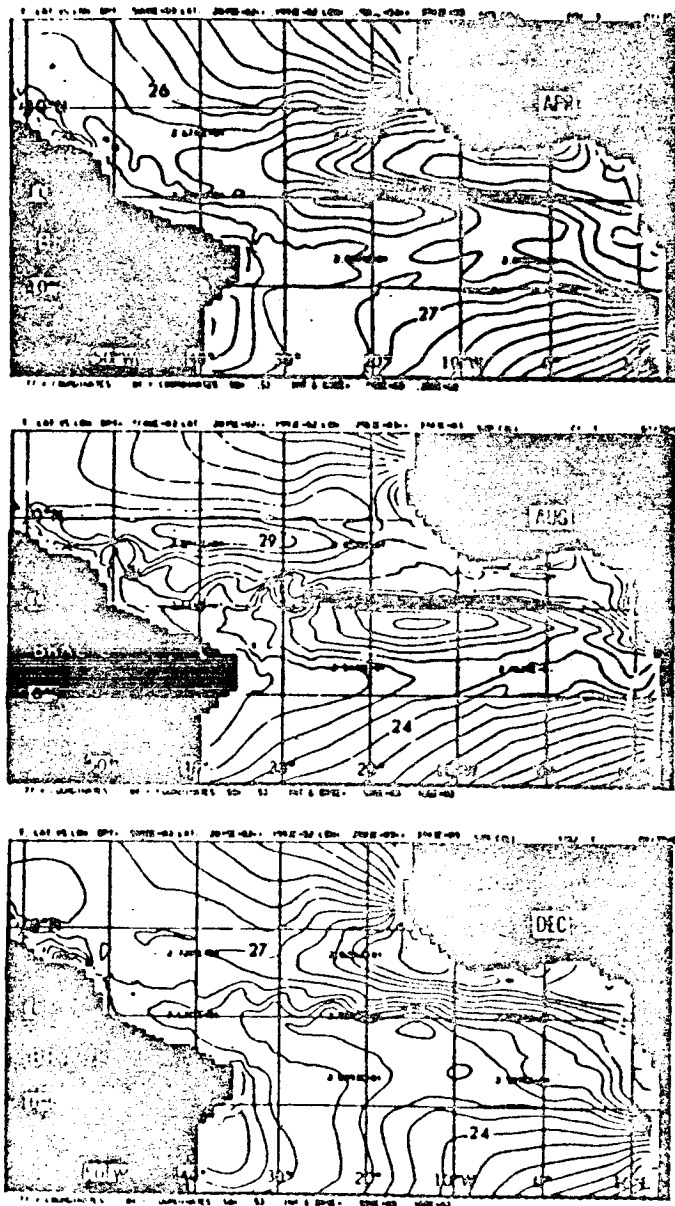
FIGURE 5 (continued)

Richardson number dependent momentum and heat mixing coefficient
(Pacanowski and Philander, 1981). The model, which has had enormous
success in elucidating the dynamics of equatorial currents, has been
recently run in response to climatological winds over the Atlantic (and
parameterized heat fluxes at the surface) and produced a fair
simulation of the annual cycle of tropical Atlantic SSTs (Philander,
personal communication). Two problems seem to be present in the
simulation. First, the (boreal) summer cold tongue in the eastern
Atlantic is instead simulated as an isolated feature on the equator,
disconnected from the coast of Africa. The second is excessively high
temperature in the Gulf of Guinea during all parts of the year. The
probable reason for both problems is the failure of the model to
simulate the cold northward flowing Banguela current, presumably due to
the restricted meridional extent of the domain (20°S to 20°N). On
the other hand, the timing of the cold tongue, the lack of much
temperature variation in the western Atlantic, the region of sharp
gradient along the northern edge of the cold tongue, and indications of
summer upwelling along the northern coast of the Gulf of Guinea are all
well simulated (these preliminary results are shown in Figure 5 and
should be compared to climatology in 6). The same model, without
surface heat fluxes, had already shown itself capable of simulating the
east-west equatorial temperature gradient under the action of the
easterly winds (Pacanowski and Philander, 1981).

OUTLOOK

This section will refer back to the figures showing the temporal scales
of SST variability, and indicate where progress in simulating these
scales of variability is expected and what obstacles might be expected.
Needless to say, none of the scales of variability shown in the figures
have been successfully simulated (preliminary attempts are just
beginning to be made) so that the author will be speaking more as a
prophet than a historian. There are some features of SST variability
that are understood, and some problems that can be anticipated so the
following comments are made with the thought that it will be fun to
reread these comments ten years hence to see just how wrong they prove
to be.

The most difficult problem of all will be to simulate the mean SST
shown in Figure 1 and will have to await the successful implementation
of global coupled atmosphere-ocean models. The problem is that, to a
very large extent, the mean SST is determined by atmospheric processes.
Imagine for a moment that one considers the response to a constant
annually averaged sun and that there were no horizontal heat transports
in either the atmosphere or the ocean: there would then be no heat
flux into the ocean (after the system has reached equilibrium) and at
each point at the surface of the ocean the temperature would be deter-
mined solely by radiative-convective equilibrium in the atmosphere.
There would be a mixed layer (since there would be a zonal surface wind
over the ocean due to the constraints of geostrophy in the atmosphere
in the presence of a warm equator and a cold pole), but the interior of
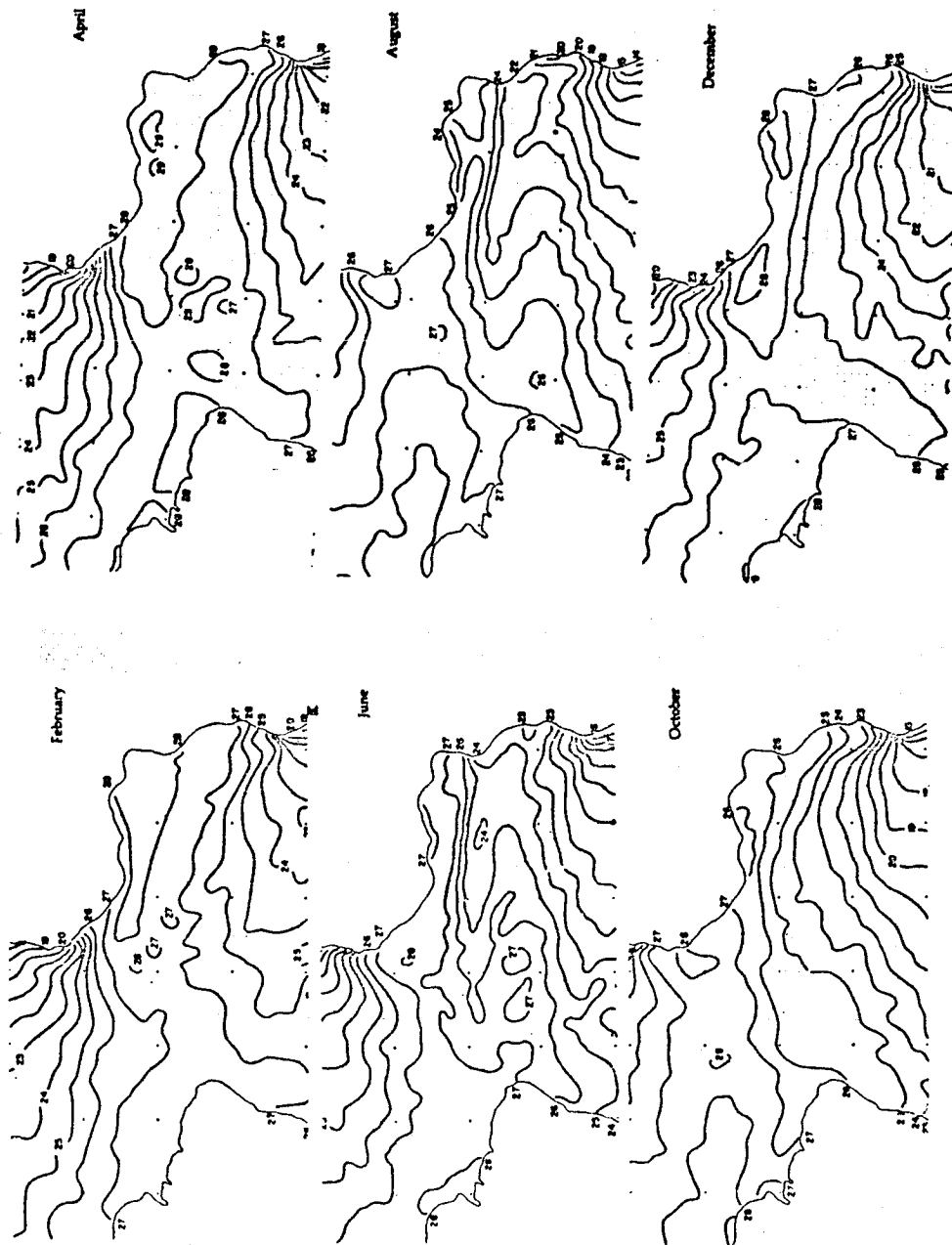
FIGURE 6 Observed climatological SST in the tropical Atlantic (from Hastenrath and Lamb, 1977).

the ocean would have a diffusive form and presumably simply have temperature constant with depth at each position (remember, the system is being artificially constrained to have no horizontal heat transports). We now allow the atmosphere and ocean to develop horizontal heat transports. The system now takes several thousand years to adjust, and when the adjustment is complete, the ocean has a complicated thermocline structure and the SST is altered because there are now steady horizontal heat fluxes that cool the tropics and heat the midlatitude regions. There are now vertical surface heat fluxes into the relatively cooler tropical ocean and out of the relatively warmer midlatitude ocean which close the circuit. One can think of the vertical heat flux into the surface of the ocean as the atmosphere's response to seeing an ocean SST driven away from equilibrium by the action of internal horizontal heat fluxes in both the atmosphere and ocean.

In order to model the mean SST therefore, one will have to get the ocean and atmospheric heat fluxes right, and since presumably the oceanic heat flux depends partly on the slow equatorial cold interior flows, one will have to get much of the slow interior physics of the ocean right. This is a tall order for an ocean model since it depends on processes that are only poorly measured and dimly understood.

Similar comments apply to the CLIMAP reconstruction shown in Figure 4. Unless the heat transport mechanisms are understood well enough to know how the imposition of ice in the Arctic and Norwegian Seas can modify the thermal structure of the north Atlantic, one is unlikely to be able to simulate Figure 4 even if the winds of 18,000 years ago were known. Of course, the winds are not known, and the way to approach the problem is to perform coupled ocean-atmosphere simulations in the presence of the ice and albedo changes indicated in Figure 4. An alternate way to attack the problem is to specify the CLIMAP boundary and SST conditions in an atmospheric model, derive the surface winds and surface heat fluxes that the atmosphere provides, and thereby indirectly evaluate the horizontal ocean heat flux the ocean must have in order to maintain the specified SST. Having the surface winds and fluxes enables one to drive an ocean model to see whether the model is capable of providing the horizontal heat fluxes that were diagnosed from the atmospheric model. This is a mode of decoupled modeling that is very useful, successfully replacing coupled modeling when the SSTs are known from observations. Again, the success of the ocean modeling depends on an understanding of the slow physics of the ocean.

If the question of the slow physics of the ocean is finessed by specifying the mean stratification, then many of the shorter time scale phenomena (presumably confined to the upper part of the ocean) should be calculable. In particular, the seasonal response of SST to the seasonal variation of the winds should be doable (in this regard, the preliminary results of Philander and Pacanowski (unpublished) discussed in the previous section are encouraging).

It seems clear that many of the mechanisms of seasonal SST variability are included in existing models and some of the problems involve difficulty in simulating the mean boundary currents. These

problems could be alleviated when computer advances allow the computational domain to approach global. Other problems involve parameterizations of heat flux into the ocean at the surface (see Schopf, 1983) and the accuracy of the surface winds used to drive the ocean model. Despite these, the author predicts that in ten years the global seasonal variability of SST will have been successfully simulated. To the extent that the anomalous surface winds can be considered known, the author would make the same prediction for the interannual variability characteristic of the ENSO phenomenon, but suspects that more than 20 years will be required to fully model the interactive nature of atmosphere-ocean couplings in this problem.

CONCLUSION

SST modeling has been reinvigorated in the last five years by the explosion of interest in equatorial dynamics; already there is much cause for optimism. Although SST modeling must still be considered in its infancy, it appears that one will be able to understand and model SST variability on annual and interannual time scales using ocean models driven by specified atmospheres. To achieve an understanding of the mean SST and its variations on 10,000 year time scales will require a deeper understanding of the slow physics of the ocean that will probably take a long time to achieve.

ACKNOWLEDGEMENT

REFERENCES

Adamec, D., R. L. Elsberry, R. W. Garwood, and R. L. Haney (1981). An embedded mixed layer ocean-circulation model. Dyn. Atmos. Oceans 6, 69-97.

Busalacchi, A. J., and J. J. O'Brien (1981). Interannual variability of the equatorial Pacific in the 1960s. J. Geophys. Res. 86, 10901-10907.

Cane, M. A. (1980). On the dynamics of equatorial currents with application to the Indian Ocean. Deep Sea Res. 27A, 525-544.

CLIMAP (1976). The surface of the ice-age earth. Science 191, 1131-1137.

Garwood, R. W. (1979). Air-sea interaction and dynamics of the surface layer. Revs. Geophys. Space Phys. 17, 1507-1524.

Gill, A. E., and P. P. Niiler (1973). The theory of seasonal variability in the ocean. Deep Sea Res. 20, 141-177.

Harrison, D. E., and P. S. Schopf (1984). Kelvin wave-induced anomalous advections and the onset of surface warming in El Niño events. Mon. Wea. Rev. (in press).

Hastenrath, S., and P. J. Lamb (1977). Climatological Atlas of the Tropical Atlantic and Eastern Pacific. Univ. of Wisconsin Press, xv pp +97 charts.

Merle, J. (1980). Seasonal heat budget in the equatorial Atlantic Ocean. J. Phys. Ocean 10, 467-469.

Niiler, P. P., and E. B. Kraus (1977). One-dimensional models of the seasonal thermocline. In Modeling and Prediction of the Upper Layers of the Ocean. E. B. Kraus, ed. Pergamon Press.

Oort, A. H., and T. H. Vonder Haar (1976). On the observed annual cycle in the ocean-atmosphere heat balance over the northern hemisphere. J. Phys. Ocean 6, 781-800.

Pacanowski, R., and S. G. H. Philander (1981). Parameterization of vertical mixing in numerical models of tropical oceans. J. Phys. Ocean. 11, 1443-1451.

Sarachik, E. S. (1984). Large scale surface heat fluxes, in Large Scale Oceanographic Experiments and Satellites, C. Gautier (ed.), Reidel Press.

Schopf, P. S. (1983). On equatorial waves and El Niño II: Effects of air-sea thermal coupling. J. Phys. Ocean. 13, 1878-1893.

Schopf, P. S., and M. A. Cane (1983). On equatorial dynamics, mixed layer physics and sea-surface temperature. J. Phys. Ocean. 13, 917-935.

Schopf, P. S., and D. E. Harrison (1983). On equatorial waves and El Niño I: Influence of initial states on wave-induced currents and warming. J. Phys. Ocean. 13, 936-948.

Weare, B. C., A. R. Navato, and R. E. Newell (1976). Empirical orthogonal analysis of Pacific Ocean surface temperatures. J. Phys. Ocean. 6, 671-678.

Wyrtki, K., and L. Urich (1982). On the accuracy of heat storage computations. J. Phys. Ocean. 12, 1411-1416.

HEAT BALANCES OF THE SURFACE MIXED LAYER IN THE EQUATORIAL ATLANTIC AND INDIAN OCEANS DURING FGGE

Robert L. Molinari
Atlantic Oceanographic and Meteorological Laboratory
National Oceanic and Atmospheric Administration

ABSTRACT

Surface meteorological and surface and subsurface oceanographic data collected during FGGE in the equatorial Atlantic and Indian Oceans are used to estimate the terms in a heat balance relation for the mixed layer. The first balance tested is between changes in mixed layer temperature (MLT) and surface energy fluxes. Away from regions of low variance in MLT time series and equatorial and coastal upwelling, surface fluxes can account for 75 percent of the variance in the observed time series. Differences between observed and estimated MLTs indicate that on the average, maximum errors in surface flux are of the order of 20 to 30 W/m^2. In the Atlantic, the addition of zonal advection does not significantly improve the estimates. However in regions of equatorial upwelling, the eastern Atlantic vertical mixing and meridional advection can play an important role in the evolution of MLTs.

The El Nino event of 1982-1983 has dramatized the importance of considering sea-surface temperature (SST) distributions in studies of global climate. The question of whether the ocean plays a passive or active role in such events is still being considered, although evidence strongly supports an active role for SST fields. It is necessary therefore to determine what processes influence the evolution of the SST field in order to quantify the impact of large-scale SST anomalies on global climate.

Merle (1980) observed that in certain regions of the equatorial Atlantic Ocean, energy fluxes through the sea surface play only a secondary role in the heat budget of the near surface layers and that in these regions internal oceanic processes are most important. Spurred partly by the results from GATE, a series of studies on equatorial dynamics have appeared in the literature (O'Brien et al., 1978; Cane 1979; Philander and Pacanowski, 1980). Results from these models show qualitatively how changes in thermocline depth may affect SST. Results from the First GARP Global Experiment (FGGE) permit quantitative computations to define what other processes in addition to thermocline displacement and fluxes through the sea surface can impact SST in the equatorial Atlantic and Indian Oceans.

779

Following McPhaden (1982), the heat balance of the mixed layer on monthly time scales (assuming that MLT is equivalent to SST) can be expressed as:

$$\frac{\partial T}{\partial t} - \frac{1}{\delta t}\left[T(t_1) - T(t_0)\right] + u\left(\frac{\partial T}{\partial x}\right)' + \left(v\,\frac{dT}{dy}\right)' = \frac{1}{\rho c_p}\left[\left(\frac{Q_o}{h}\right)' - \left(\frac{Q_{-h}}{h}\right)'\right] \quad (1)$$

$$\underset{1}{} \qquad \underset{2}{} \qquad \underset{3}{} \qquad \underset{4}{} \qquad \underset{5}{}$$

where primes denote fluctuations about the mean. T is SST, t is time, t_1-t_0 is record length, u is zonal current speed, v is meridional current speed, h is mixed layer depth, Q_o is oceanic heat gain through the sea surface and Q_{-h} is vertical turbulent heat diffusion at the base of the mixed layer. As given in equation (1), changes in MLT, term 1, are expressed in terms of a correction for any trends in the data, term 2; anomalies of horizonatl advection, term 3; surface energy fluxes, term 4; and turbulent diffusion through the base of the mixed layer, term 5. Effects due to horizontal turbulent diffusion and attenuation of penetrative radiation are ignored. As the mean value of terms 3, 4, and 5 can cause trends in MLT, trends not adequately resolved by the one-year time series, term 2 is required to remove the MLT trends.

The balance between changes in MLT and the surface heat flux represents a simplificaton of equation (1) that can be tested with the data collected during FGGE. Neglecting all other terms but these, the integration of equation (1) yields

$$T_E(t) = \frac{1}{\rho c_p}\int_{t_2}^{t}\left(\frac{Q_o}{h}\right)'\,dt + \frac{1}{\delta t}\left[T(t_1) - T(t_0)\right](t - t_2) + T(t_2), \quad (2)$$

where T_E represents an estimated MLT determined only by surface fluxes. The arbitrary constant of integration $T(t_2)$ is chosen such that the mean of the estimated temperature time series is equal to the mean of the observed time series. As McPhaden (1982) stresses, equation (2) "predicts fluctuations and not actual values of mixed layer temperature."

Surface and subsurface oceanographic and meteorological data were collected during FGGE aboard research vessels and merchant ships-of-opportunity. An example of coverage during a typical month is shown in Figure 1. The data collected in the Atlantic have been used in studies of SST fields by Molinari et al. (1984a, b). A similar study has recently begun using data collected during FGGE in the northwestern Indian Ocean. The results from the second study are preliminary and not as complete as those from the Atlantic study.

In both studies, the FGGE SST and surface meteorological data were first averaged onto a monthly 2° by 2° grid. Examples of SST fields are shown in Figures 2 and 3. Large regions of cold water appear in boreal summer in the eastern Atlantic and western Indian Ocean. Both regions apparently play a large role in global climate
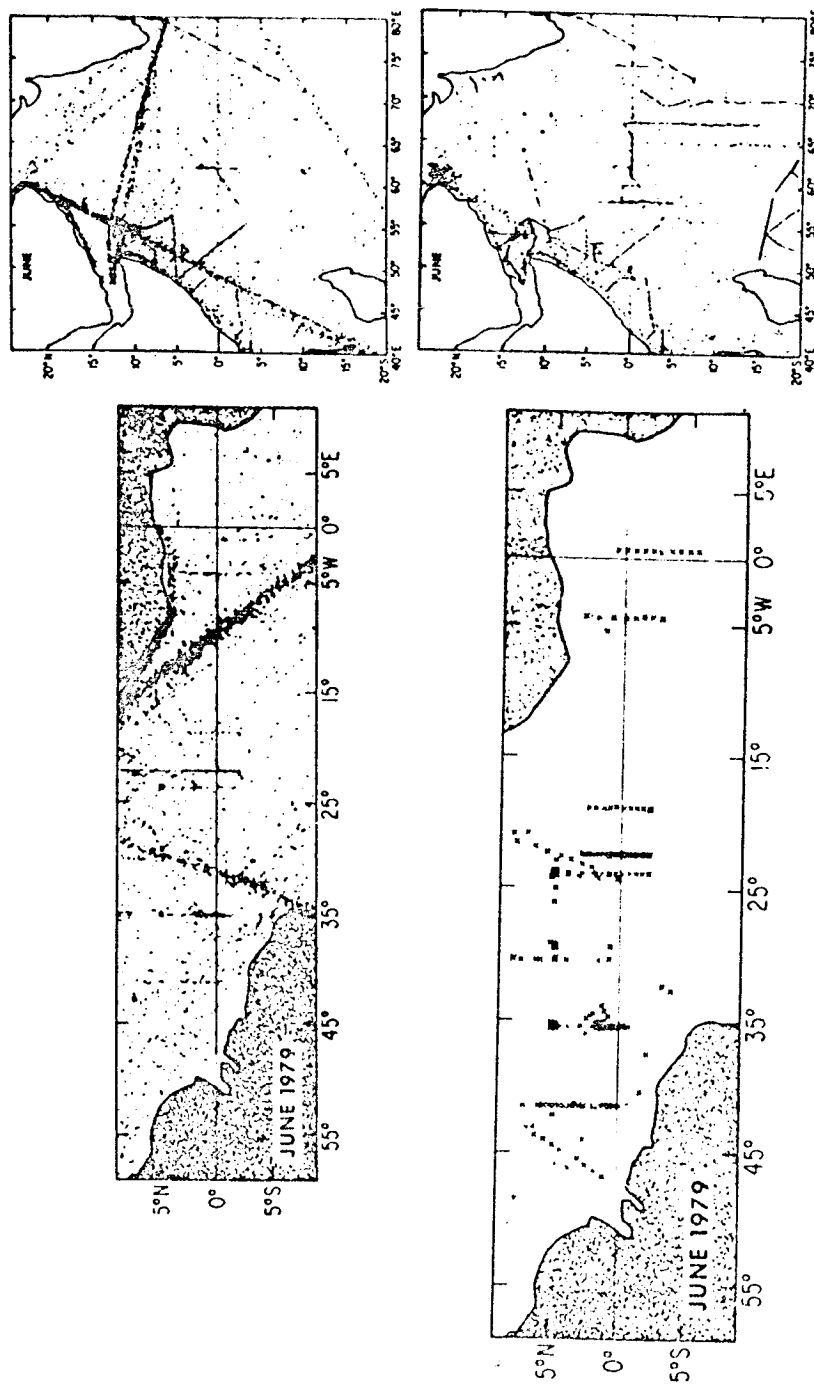
FIGURE 1 Surface data distributions during a typical FGGE month (upper panels) and subsurface data distributions for a FGGE month in the Atlantic Ocean and for all available data in the Indian Ocean (lower panels).
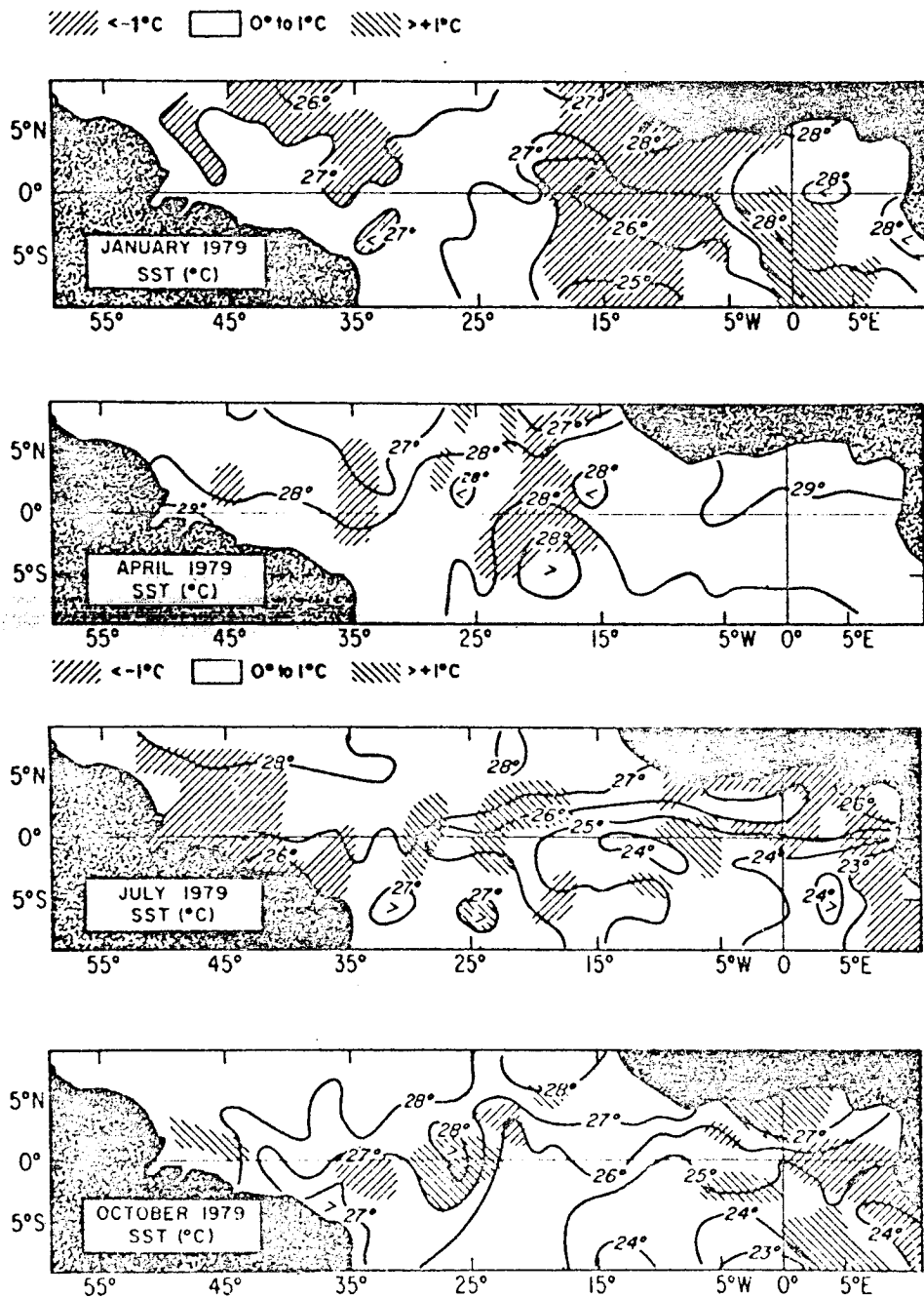
FIGURE 2 Sea-surface temperature (°C) distributions in the Atlantic
Ocean during FGGE, 1979. Cross hatchings represent graphically
determined differences between the 1979 and climatological sea-surface
temperature distributions.
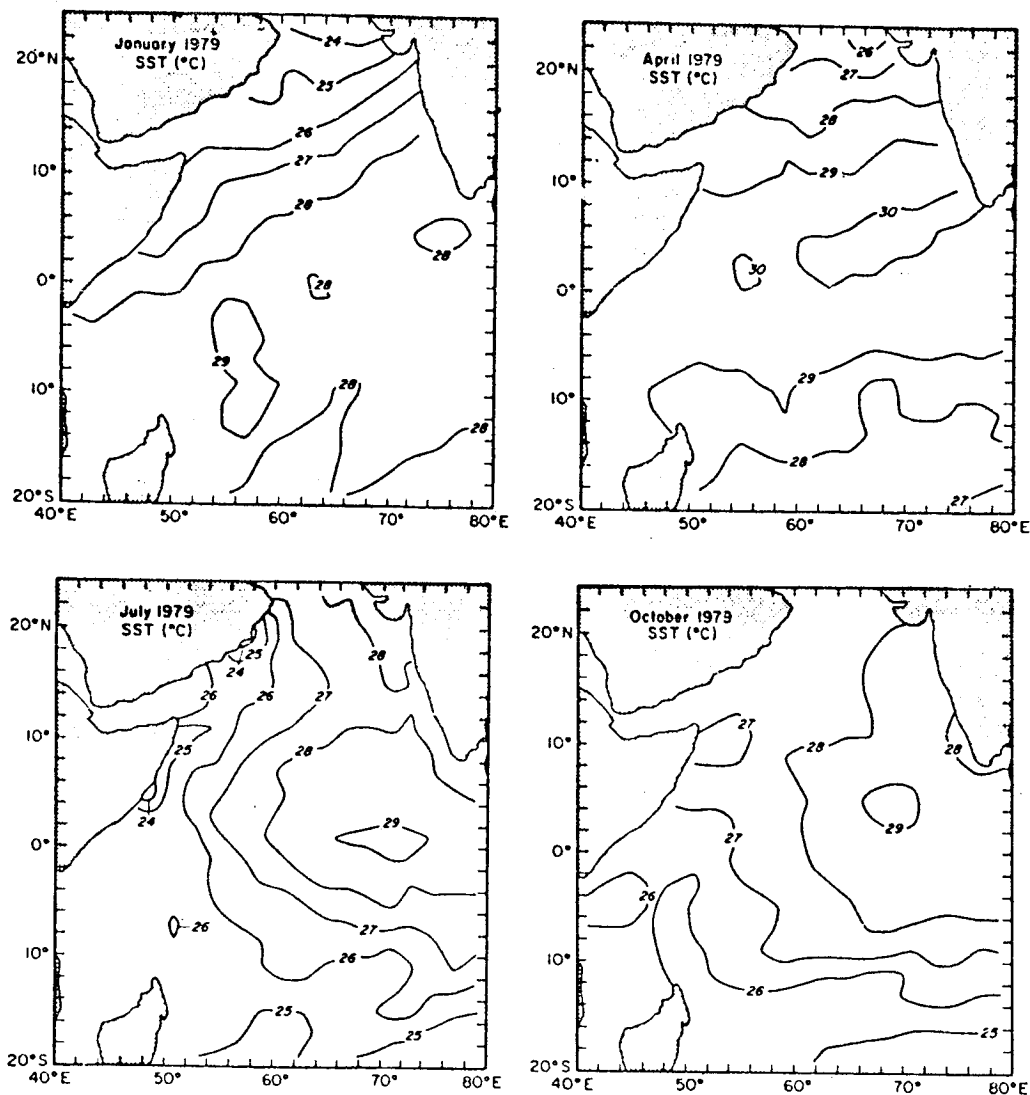
FIGURE 3 Sea-surface temperature (°C) distributions in the Indian Ocean during FGGE, 1979.

(Hastenrath, 1980). Next, distributions of latent and sensible heat flux and net surface longwave and shortwave radiation balances were computed using bulk aerodynamic formulas (Molinari et al., 1984a). The net oceanic heat gain through the sea surface, Q_O equation (2), was then computed as the sum of these fluxes. In the Atlantic, the 1979 distributions of Q_O are quite similar to distributions estimated from climatological data by Hastenrath and Lamb (1978).

Considerable interpolation was required to obtain the distributions of mixed layer depth in the Atlantic (Molinari et al., 1984b). Climatological distributions of mixed layer depth were used for the preliminary Indian Ocean computations because of the absence of basin wide, subsurface data coverage during FGGE. In the Atlantic, the terms on the rhs of equation (2) were averaged onto a monthly $6^\circ \times 10^\circ$ grid. A time series of estimated MLTs were computed using a trapezoidal-rule scheme for evaluation of the integral in equation (2). Similar computations were performed for each 2° by 2° quadrangle of the Indian Ocean grid.

Time series of the observed and estimated MLTs for the Atlantic Ocean are given in Figure 4. Distributions of variance computed from the monthly time series of observed MLT are shown in Figure 5 for the Atlantic and Figure 6 for the Indian Ocean. The coherence squared between the time series of observed MLT and the time series of MLT estimated from equation (2) represents that portion (given as a percentage) of the variance in the observed series that can be accounted for by only fluxes through the sea surface. The distributions of coherence squared are also given in Figures 5 and 6.

Largest variances in MLT accounted for by surface fluxes (>75 percent) occur in the Atlantic Ocean in the latitude band centered at $6^\circ S$. These estimates suggest that surface fluxes are to a large degree responsible for the asymmetry in the cold water tongue observed during boreal summer (Figure 2). Surface fluxes account for little variance along $6^\circ N$ and in the equatorial upwelling region in the eastern Atlantic. The low variance reductions along $6^\circ N$, west of $20^\circ W$, are probably related to the small variances associated with the observed MLT time series. Along 0° in the eastern Atlantic, surface fluxes fail to account for the lower temperatures observed during boreal summer upwelling periods (Figure 4). Upwelling systems are also observed in the quadrangles east of $20^\circ W$ along $6^\circ N$. Similarly, in the Indian Ocean, fluxes through the sea surface play only a minor role in establishing MLT fluctuations both in regions of coastal upwelling (Figure 3) and of low variances in MLT time series (Figure 5). In other areas surface fluxes account for greater than 75 percent of MLT variability.

Two questions remain to be addressed, what is the statistical significance of the heat budget estimates and what are the internal oceanic processes that can account for the unresolved variances in the MLT time series. Tables 1 and 2 (from Molinari et al., 1984a) give estimates of standard errors of the mean for the variables needed to compute net oceanic heat gains. The values are quite similar for both oceans. Within the shipping lanes, maximum likely standard error of means for heat gain are about 40 W/m^2. This uncertainty translates to errors in monthly temperature change ranging from 0.4°C for a mixed layer depth of 75 m to 1.2°C for a mixed layer depth of 25 m. A 10 m uncertainty in mixed layer depth, typical for the Atlantic data (Molinari et al., 1984b), is equivalent to a 0.5°C uncertainty in temperature change for a 25 m mixed layer depth. Thus the largest errors in temperature change would be of the order of 2°C.
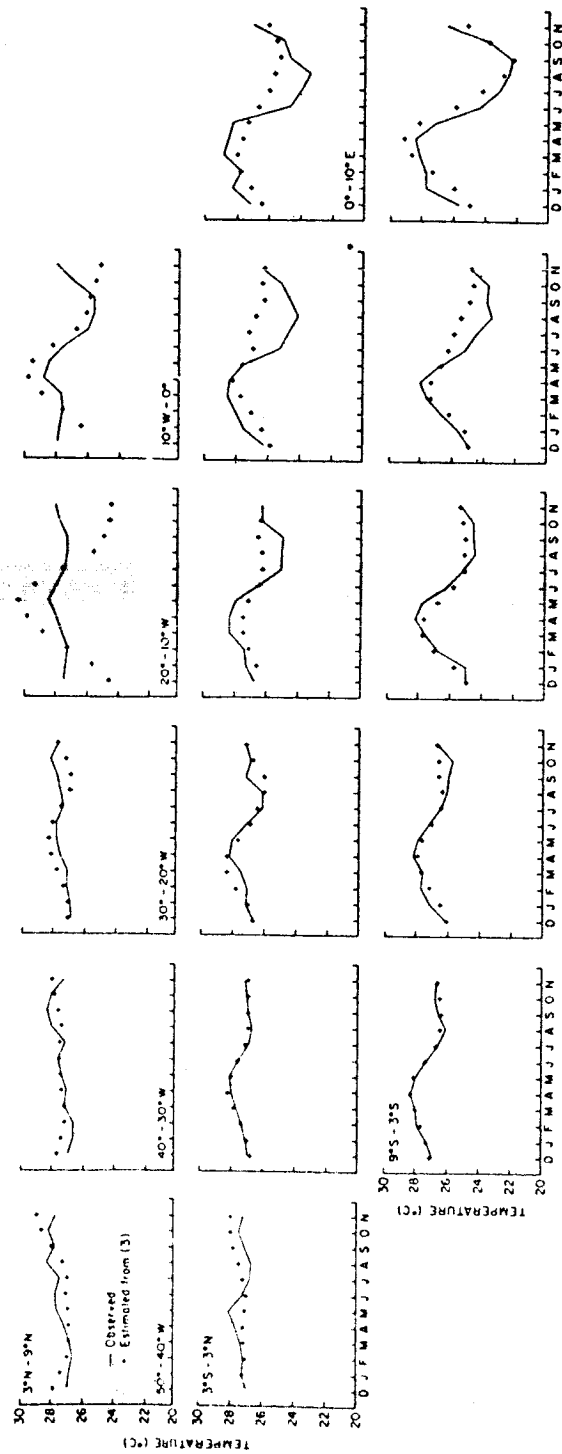
FIGURE 4   Time series of observed mixed layer temperatures and mixed layer temperatures estimated from equation (2) for the $6° \times 10°$ quadrangles of the Atlantic Ocean.
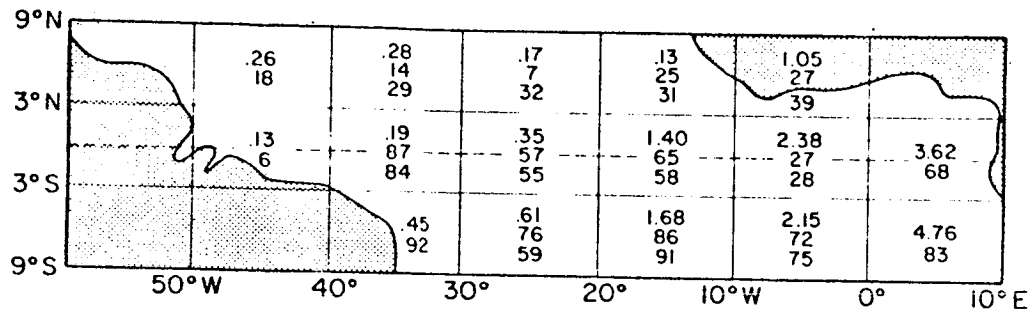
FIGURE 5 Within each quadrangle the top number represents the variance $(^\circ C)^2$ computed from the observed mixed layer temperature time series, the middle number represents the percentage variance in the observed series accounted for by fluxes through the sea surface, and the lower number represents the percentage variance accounted for by fluxes through the sea surface and zonal advection.

However the large variance reductions along $6^\circ S$ indicate that actual errors in surface flux are less. The rms difference between observed and estimated monthly temperature changes along $6^\circ S$ is about $0.5^\circ C$. This uncertainty is equivalent to an uncertainty in surface heat flux of 40 W/m^2 for a 50 m thick mixed layer. Since errors in observed temperatures and mixed layer depth also contribute to the difference between the original and estimated time series, the average uncertainty in Q_0 over the entire basin is probably closer to 20 to 30 W/m^2 than 40 W/m^2. These uncertainties represent errors due to the bulk formulation applied in Molinari et al. (1984a) as well as observational inadequacies. Improvements in the observations are more readily realized than improvements in the bulk formulas. However these later advances are necessary before simple-type models such as applied above can be used in quantitative studies of interannual variability.

The second question to be addressed relates to the oceanic processes that can affect MLT. In Molinari et al. (1984b), the effects of zonal advection on Atlantic MLT fluctuations were estimated using surface current data obtained from merchant ships-of-opportunity. In general, the addition of advection did not significantly improve the variance reductions (Figure 5), although there was some improvement along $6^\circ N$ and along $6^\circ S$ during boreal summer.

Other processes in addition to zonal advection neglected in the derivation of equation (2) include turbulent diffusion at the base of the mixed layer, i.e., the effects of entrainment, meridional advection, and horizontal turbulent diffusion. Adequate data are not available to estimate quantitatively any of these terms. However Molinari et al. (1984b) presented some simple calculations to estimate the possible effects of turbulent diffusion, Q_{-h}, and meridional advection on MLT in the Atlantic Ocean. They expressed Q_{-h} in terms of an entrainment velocity and derived estimates of this velocity from data available in the $6^\circ \times 10^\circ$ quadrangle centered at 0°, $5^\circ W$. The coherence squared between the MLT time series estimated from (2)
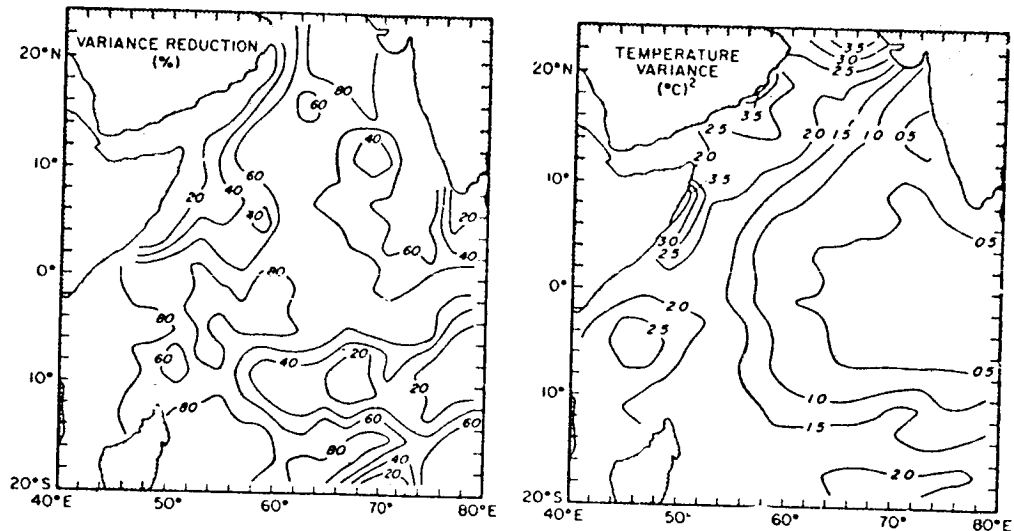
FIGURE 6 Left panel: Distribution of the variance ($^\circ$C)^2 computed from the observed mixed layer temperature time series within each 2° x 2° quadrangle. Right panel: Percentage variance in the observed series accounted for by fluxes through the sea surface.

with Q_{-h} included and the observed time series at 0°, 5°W is 0.6 versus a coherence squared of 0.27 if Q_{-h} is neglected (Figure 5). The improvement in variance reduction is caused by a more realistic representation of cooling during boreal summer. The addition of meridional advection further improves the coherence between observed and estimated time series for a similar reason.

Sufficient oceanographic data to resolve adequately all the terms in (1) will not be available for a considerable time in either the Atlantic or Indian Oceans. The TOGA investigation will provide one opportunity for obtaining such data. Numerical models that include non-adiabatic effects in the surface layers provide a mechanism at the present time for studying surface energy balances. In particular, estimation of terms such as vertical mixing and horizontal advection is possible with the use of multi-level models. Using surface forcing available from FGGE, for example, will permit verification of the model results by actual observations.

ACKNOWLEDGMENTS

TABLE 1   Ensemble Average Standard Error of the Mean Values for Quadrangles Within the Shipping Lanes (> 15 Values) and Outside the Shipping Lanes (< 10 Values)

	Atlantic Ocean		Indian Ocean	
	> 15 values	< 10 values	> 15 values	< 10 values
SST (°C)	0.16	0.31	0.20	0.30
East wind component (ms^{-1})	0.36	0.66	0.59	1.20
North wind component (ms^{-1})	0.38	0.73	0.15	1.08
Air temperature (°C)	0.22	0.42	0.22	0.37
Cloud cover (tenths)	0.4	0.8	0.4	0.8

TABLE 2   Ensemble Average Standard Error of the Mean Values for Quadrangles Within the Shipping Lanes (10 to 15 Values) and Outside the Shipping Lanes (5 to 10 Values)

	Atlantic Ocean		Indian Ocean	
	10-15 values	5-10 values	10-15 values	5-10 values
Saturation specific humidity (g Kg^{-1})	0.38	0.54	0.33	0.40
Specific humidity (g Kg^{-1})	0.38	0.49	0.37	0.46
Sensible heat flux (Wm^{-2})	5.5	8.0	4.2	5.0
Latent heat flux (Wm^{-2})	15.8	23.5	17.9	21.9
Long-wave radiation (Wm^{-2})	3.8	5.5	3.3	4.4
Short-wave radiation (Wm^{-2})	18.3	23.2	13.5	18.6

REFERENCES

Cane, M. A. (1979). The response of an equatorial ocean to simple wind-stress patterns. J. Mar. Res. 37, 233-252.

Hastenrath, S. (1980). Heat budget of tropical ocean and atmosphere. J. Phys. Oceanogr. 10, 159-170.

Hastenrath, S., and P. Lamb (1978). Heat Budget Atlas of the Tropical Atlantic and Eastern Pacific Oceans. University of Wisconsin Press.

McPhaden, M. J. (1982). Variability in the central equatorial Indian Ocean, Part II: Oceanic heat and turbulent energy balances. J. Mar. Res. 40, 403-419.

Merle, J. (1980). Seasonal variation of heat storage in the tropical Atlantic Ocean. Oceanologica Acta 3, 455–463.

Molinari, R. L., J. F. Festa, and E. Marmolejo (1984a). Evolution of sea-surface temperature and surface meteorological fields in the tropical Atlantic Ocean during FGGE, 1979: Part I, Description of surface fields and computation of surface energy fluxes. To appear in Progress in Oceanography.

Molinari, R. L., J. F. Festa, and E. Marmolejo (1984b). Evolution of sea-surface temperature fields in the tropical Atlantic Ocean during FGGE, 1979: Oceanographic fields and heat balance of the mixed layer. Submitted to J. Mar. Res.

O'Brien, J. J., D. Adamec, and D. W. Moore (1978). A simple model of upwelling in the Gulf of Guinea. Geophys. Res. Letters 5, 641–644.

Philander, S. G. H., and R. C. Pacanowski (1980). The generation of equatorial currents. J. Geophys. Res. 85, 1123–1136.

19. FUTURE POSSIBILITIES

Organizer   Norman A. Philips

Session Chairman   Norman A. Philips

Speakers   Edward N. Lorenz
                             Michael Ghil

Rapporteur   Roger W. Daley

396<

FUTURE POSSIBILITIES OF ATMOSPHERIC PREDICTABILITY

Edward N. Lorenz
Massachusetts Institute of Technology

Material presented by E. Lorenz is contained in the following
publications:

Lorenz, E. N. (1982). Some aspects of atmospheric predictability.
  Problems and Prospects in Long and Medium Range Weather Forecasting,
  ECMWF Seminar 1981, pp. 1-20.
Lorenz, E. N. (1982). Atmospheric predictability experiments with a
  large numerical model. Tellus 34, 505-513.
Lorenz, E. N. (1983). Estimates of atmospheric predictability at
  medium range. Predictability of Fluid Motion, 1983 Conference
  Proceedings, American Institute of Physics, La Jolla, Calif., Greg
  Holloway and Bruce West (eds.), pp. 133-139.

FUTURE POSSIBILITIES IN OBJECTIVE ANALYSIS AND DATA ASSIMILATION FOR ATMOSPHERIC DYNAMICS

M. Ghil
Courant Institute of Mathematical Sciences
New York University

ABSTRACT

The central theme of this review article is the role that dynamics plays in estimating the state of the atmosphere from incomplete and noisy data. Objective analysis represents an attempt at relying mostly on the data and minimizing the role of dynamics in the estimation. Data assimilation tries to balance properly the roles of dynamical and observational information. Sequential estimation is presented as the proper framework for understanding this balance, and the Kalman filter as the ideal, optimal procedure for data assimilation.

The optimal filter computes forecast error covariances of a given atmospheric model exactly, and hence data assimilation should be closely connected with predictability studies. This connection is described, and consequences drawn for currently active areas of the atmospheric and related sciences, namely, mesoscale meteorology, long-range forecasting, and upper ocean dynamics. In particular, the paper addresses possibilities offered by judicious data assimilation in understanding barotropic adjustment, a phenomenon that appears to play a crucial role in atmospheric behavior on the scale of weeks to months, and hence in long-range forecasting.

INTRODUCTION

Large-scale atmospheric dynamicists occupy a privileged, and hence difficult, position among their fluid dynamical colleagues. Privileged, since the system studied--the earth's atmosphere on scales of hundreds to tens of thousands of kilometers--is the best observed fluid system of all: $0(10^5)$ scalar observations are routinely made per synoptic period (Bengtsson et al., 1981, preface); this corresponds to $0(10^2)$ observations per significant degree of freedom per significant time interval of dynamic change (Phillips, 1984). Difficult, since this knowledge, coming from fixed stations, aircraft, ships, balloons, drifting buoys, and satellites, is expensive and since the human society in which we live and which pays for it expects an accurate weather forecast in return.

794

Qualitative understanding of the atmosphere is thus necessary but not sufficient for our purposes, and a quantitative estimate of its state in the past and present as well as a quantitative prediction of future states is required. The estimate of the present state is a prerequisite for future prediction, and the accuracy of past prediction is essential for an accurate estimate of the present.

How does the estimation of the present proceed? A good starting point for an answer is Wiener's (1956) article on prediction and dynamics. At the time of his writing, meteorology, like econometrics, could still be considered a semi-exact science, as opposed to the allegedly exact science of celestial mechanics (Horton et al., 1983). Dynamical processes in the atmosphere were still poorly known, while observations were sparse in space and time as well as inaccurate. Consequently, Wiener argued that the best approach to prediction was statistical, relying theoretically on the hope for the system's ergodicity and stationarity, and therewith on certain appropriate theorems of Birkhoff and von Neumann. In practice, this meant ignoring any quantitative dynamical knowledge of system behavior, requiring instead a complete knowledge of the system's past history and using the Wiener-Hopf filter to process this infinite but inaccurate information into yielding an estimate of present and future.

During roughly the same period, synoptic meteorologists were actually producing charts of atmospheric fields at present and future times guided by tacit principles similar to those explicitly formulated by Wiener. The main tool was smooth interpolation and extrapolation of observations in space and time. Still, rudimentary but quantitative dynamical knowledge was incorporated into these estimates of atmospheric states, to wit, the geostrophic relation between winds and heights, and the advection of large-scale features by the prevailing winds.

ANALYSIS, ASSIMILATION AND ESTIMATION

The first step into the present period of estimation was objective analysis, which replaced manual, graphic interpolation of observations by automated, mathematical methods (Panofsky, 1949). Not surprisingly, this step was largely motivated by the use of the recently improved knowledge of atmospheric dynamics to produce numerical weather forecasts (Charney et al., 1950). The main ideas underlying objective analysis were statistical (Eliassen, 1954; Gandin, 1963; Phillips, 1976) like those of Wiener (1956), but in practice various shortcuts of these ideas were implemented in the operational routine of weather bureaus (Cressman, 1959).

Two related developments led to the next step: One was the increasingly accurate nature of numerical weather forecasts; the other was the advent of time-continuous, spaceborne observing systems. Together, they produced the concept of four-dimensional space-time continuous data assimilation in which a model forecast of atmospheric fields is continuously updated with incoming observations (Charney et al., 1969; Smagorinsky et al., 1970). Here the model carries forward

in time the knowledge of a finite number of past observations, subject to the appropriate dynamics, to be blended with the latest observations.

The framework of sequential estimation theory permits a proper understanding of the combination between imperfect dynamics and inaccurate observations, as well as an evaluation of various algorithms for weighting incoming data against a forecast based on past data (Ghil et al., 1981, 1982). The optimal algorithm is given by the Kalman filter, which requires the exact computation of forecast error covariances. This computation can be carried out for a barotropic high-resolution model on the sphere using a Class VI vector-processing computer, and the corresponding Kalman filter is under study and implementation (S.E. Cohn and D. Parrish, personal communication, 1984). It will be possible to implement such a filter for a high-resolution baroclinic model, global or regional, on a Class VII vector machine, to become available within two or three years.

The currently operational version of objective analysis, commonly called optimal interpolation, or OI for short, is a particular sub-optimal filter, which approximates the forecast error covariances matrix by the product of a diagonal matrix of variances, changing in time but not in space, and of a correlation matrix, constant in both time and space (Cohn et al., 1981). The OI algorithm can also be improved by the use of more sophisticated correlation matrices (Balgovind et al., 1983) and of variances changing in space, as well as in time (S.E. Cohn and L. Morone, personal communication, 1984). Finally, computationally efficient filters can also estimate the observational noise of complex observing systems, present and proposed, along with the random noise by which the model equations differ from the true equations governing atmospheric dynamics (Balgovind et al., 1983; Dee et al., 1984). In any case, the gradual and concomitant improvement of model resolution and sophistication, on the one hand, and of data coverage and assimilation methods, on the other, will lead over the next decade to a considerably increased knowledge of large-scale atmospheric dynamics, with model improvement and data improvement mutually enhancing each other (Atlas et al., 1982; Hollingsworth et al., 1984).

NEW APPLICATIONS OF ASSIMILATION

One can only attempt to foreshadow the applications of data assimilation and sequential estimation, as understood from large-scale atmospheric dynamics and the Global Weather Experiment (GWE or FGGE), to mesoscale meteorology and ocean dynamics. The Stormscale Operational and Research Meteorology (STORM) Program, in one case, and the Tropical Ocean-Global Atmosphere (TOGA) and the World Ocean Circulation Experiment (WOCE) Programs, in the other, should provide a major impetus for new applications of sequential estimation and for the extensions to the theory they will suggest.

The still imperfect state of global, high-resolution ocean modeling will probably require improved estimates of systematic model bias, as well as the use and validation of Lagrangian tracer data (Sarmiento,

1984). The special nature of altimetry, scatterometry, and acoustic tomography data will also pose interesting challenges to oceanic data assimilation (Munk and Wunsch, 1982). But the relative scarcity of observations of the ocean, even under intensive field programs like those envisaged, will make the use of predictive models in an assimilation mode even more imperative than for the atmosphere (Ghil et al., 1983; Phillips, 1984). A promising start with such an approach has already been made (Robinson and Leslie, 1984), and more is certainly to come.

The major instrumental breakthrough on which much of the STORM Program appears to hinge is the Wave Propagation Laboratory (WPL) vertical profiler, which provides very accurate wind measurements as frequently as every two minutes (James, 1983). This instrument strongly suggests tradeoffs between temporal and spatial resolution of observations that can be provided by time-continuous assimilation (Ghil et al., 1979). Two methods for implementing such an idea in the meso-α situation can be outlined: (1) a variational method using wind tendencies (Bube and Ghil, 1981; Gal-Chen, 1978; Ghil, 1980; Ghil et al., 1977; Hoffman, 1982), and (2) a generalized Kalman filter capable of using discrete observations taken more frequently than the assimilating model's time steps. An approximation to the latter method consists in advecting each observation according to the estimated wind at the previous time step by an amount proportional to the time elapsed. This replaces a simple in situ average of the measured wind vectors at the instrument location by a spatially weighted average of suitably displaced vectors, using optimally estimated model error covariances (Balgovind et al., 1983; Ghil et al., 1982).

DYNAMICAL RESULTS OF ASSIMILATION

Returning to large-scale atmospheric dynamics, one may wish to address also time scales from weeks to months, i.e., extended-range weather prediction and short-range climate prediction, or long-range forecasting for short. One of the more striking phenomena of low-frequency variability of the atmosphere is its substantially barotropic character (Blackmon et al., 1979). Well-established persistent anomalies of midlatitude atmospheric flow have a pronounced barotropic structure (Dole, 1982), although transitions between a persistent and a rapidly varying atmospheric state are associated with high levels of baroclinic, high-frequency variability. This explains why persistent flow patterns are well captured by barotropic models (Charney et al., 1981; Legras and Ghil, 1983), but transitions or "breaks," as long-range forecasting practitioners call them (Namias, 1982), are somewhat less frequent in such models (Legras and Ghil, 1984).

I propose to call the phenomenon of decrease of baroclinic activity with decreasing frequency barotropic adjustment, by obvious analogy with geostrophic adjustment. In the latter, inertia-gravity energy levels decrease with the period of the motion (Rossby, 1937; Leith, 1980). The mechanism of this adjustment is theoretically well understood: some Rossby waves are baroclinically unstable and have

life cycles of days, while all inertia-gravity waves are neutrally stable and most have life cycles of hours. The "fast" waves are generated by nonlinear interaction of the "slow" waves but are then dispersed and finally dissipated, returning their kinetic energy to the potential energy that generates the unstable Rossby waves. Still, little is known about just how much "fast" energy there is on the spatial synoptic scale, and certainly there is a lot on the mesoscale.

The situation for barotropic adjustment, in contradistinction to the previous one, is just beginning to be understood (Held, 1983). External, barotropic Rossby waves are certainly not slower than internal, baroclinic ones. But it appears that the external ones are not only excited by topographic features or anomalous heat sources but also trapped in quasi-stationary patterns and thus maintained against dissipation. The transient growth and decay of the internal ones occur on the synoptic time scale, i.e., belong to high-frequency variability from the point of view of long-range forecasting.

In the past, the type of question raised here, after theoretical treatment, would have been best referred to a diagnostic study, using long series of objective analyses (Charney et al., 1981; Dole and Gordon, 1983). Alternatively, the time series of atmospheric fields to be interrogated and analyzed for the study of such a theoretical question could have come from a general circulation model (GCM) long-term simulation (Lau, 1983). It is only recently, using FGGE data sets, that a four-dimensional "movie of the atmosphere," created by data assimilation with a GCM, could be used to address such questions successfully (Kalnay and Paegle, 1983; Lindzen et al., 1984).

It would appear perhaps at first sight that using a combination of model with data to address theoretical questions has only the chance of contaminating the purity of the information to be obtained from either alone: about the "true" atmosphere on the one hand, about the properties of the model on the other. As discussed earlier in this paper, on short time scales it can be proven rigorously, more geometrico, that the combination of imperfect model dynamics with imperfect observations gives, by optimal data assimilation, the best quantitative estimate of the true state of the atmosphere. No similar proof is possible when the questions asked are qualitative and apply to the long term rather than being quantitative and short term.

When model dynamics is flawed in an obvious way, as in the use of quasi-nondivergent dynamics for assimilation in the tropics (Kanamitsu, 1981; Phillips, 1981), qualitative results are suspicious. The methodological material reviewed suggests that, relying on an iterative process of improving model dynamics, assimilation methods, and observational systems, much is to be learned about the atmosphere by studying carefully time series of atmospheric fields obtained by judicious four-dimensional data assimilation. This methodological suggestion is strongly reinforced by the already cited qualitative results on the existence of free (Lindzen et al., 1984) and forced (Kalnay and Paegle, 1983) Rossby waves in the atmosphere, results obtained for the first time from the four-dimensional assimilation of FGGE data.

CONCLUSION

These remarks bring us full circle to the beginning, where the need for qualitative understanding of atmospheric behavior was deemed necessary but not sufficient for the purposes of large-scale dynamics, and quantitative estimation and prediction were seen as equally important. The other side of the coin is that the practice of numerical weather prediction in general, and of four-dimensional data assimilation in particular, should serve not only to verify but also to greatly increase our qualitative knowledge. It is hoped that this workshop will leave many participants convinced of the theoretical promise for atmospheric dynamics contained in the FGGE data sets and stimulate them to use these data sets widely in the pursuit of some of the research questions mentioned here.

ACKNOWLEDGEMENTS

REFERENCES

Atlas, R., M. Ghil, and M. Halem (1982). The effect of model resolution and satellite sounding data on GLAS model forecasts. Mon. Wea. Rev. 110, 662-682.

Balgovind, R., A. Dalcher, M. Ghil, and E. Kalnay (1983). A stochastic-dynamic model for the spatial structure of forecast error statistics. Mon. Wea. Rev. 111, 701-722.

Bengtsson, L., M. Ghil, and E. Källén, eds. (1981). Dynamic Meteorology: Data Assimilation Methods. Springer-Verlag, New York, 330 pp.

Blackmon, M., R. A. Madden, J. M. Wallace, and D. S. Gutzler (1979). Geographical variations in the vertical structure of geopotential height fluctuations. J. Atmos. Sci. 36, 2450-2466.

Bube, K. P., and M. Ghil (1981). Assimilation of asynoptic data and the initialization problem. In Bengtsson et al., 1981, pp. 111-138.

Charney, J. G., R. Fjortoft, and J. von Neumann (1950). Numerical integration of the barotropic vorticity equation. Tellus 2, 237-25?.

Charney, J. G., M. Halem, and R. Jastrow (1969). Use of incomplete historical data to infer the present state of the atmosphere. J. Atmos. Sci. 26, 1160-1163.

Charney, J. G., J. Shukla, and K. Mo (1981). Comparison of a barotropic blocking theory with observations. J. Atmos. Sci. 38, 762-779.

Cohn, S. E., M. Ghil, and E. Isaacson (1981). Optimal interpolation and the Kalman filter. Proc. 5th Conf. Numerical Weather Prediction, American Meteorological Society, Boston, Mass., pp. 36-42.

Cressman, G. (1959). An operational objective analysis system. Mon. Wea. Rev. 87, 367-374.

Dee, D. P., S. E. Cohn, and M. Ghil (1984). An efficient algorithm for estimating noise covariances in distributed systems. IEEE Trans. Automatic Control, submitted.

Dole, R. M. (1982). Persistent anomalies of the extratropical northern hemisphere wintertime circulation. Ph.D. Thesis, Massachusetts Institute of Technology, Cambridge, Mass., 225 pp.

Dole, R. M., and N. D. Gordon (1983). Persistent anomalies of the extratropical northern hemisphere wintertime circulation: Geographical distribution and regional persistence characteristics. Mon. Wea. Rev. 111, 1567-1586.

Eliassen, A. (1954). Provisional report on calculation of spatial covariance and autocorrelation of the pressure field. Rept. No. 5, Inst. Wea. Climate Res., Acad. Sci. Oslo, 11 pp.; reprinted in Bengtsson et al., 1981, pp. 319-330.

Gandin, L. S. (1963). Objective Analysis of Meteorological Fields. Gidrometeorol. Izd., Leningrad (in Russian); English transl. Israel Program for Scientific Translations, Jerusalem, 1965, 242 pp. (available from NTIS, as N66-18047).

Gal-Chen, T. (1978). A method for the initialization of the anelastic equations: Implications for matching models with observations. Mon. Wea. Rev. 106, 587-606.

Ghil, M. (1980). The compatible balancing approach to initialization and four-dimensional data assimilation. Tellus 32, 198-206.

Ghil, M., B. Shkoller, and V. Yangarber (1977). A balanced diagnostic system compatible with a barotropic prognostic model. Mon. Wea. Rev. 105, 1223-1238.

Ghil, M., M. Halem, and R. Atlas (1979). Time-continuous assimilation of remote-sounding data and its effect on weather forecasting. Mon. Wea. Rev. 107, 140-171.

Ghil, M., S. Cohn, J. Tavantzis, K. Bube, and E. Isaacson (1981). Applications of estimation theory to numerical weather prediction. In Bengtsson et al., 1981, pp. 139-224.

Ghil, M., S. E. Cohn, and A. Dalcher (1982). Sequential estimation, data assimilation, and initialization, in The Interaction between Objective Analysis and Initialization, D. Williamson (ed.), Publ. Meteorol. 127 (Proc. 14th Stanstead Seminar), McGill University, Montreal, pp. 83-97.

Ghil, M., S. E. Cohn, and A. Dalcher, 1983. Applications of sequential estimation to data assimilation, in _Large-Scale Oceanographic Experiments in the World Climate Research Programme_, WCRP Publ. Series, No. 1, Vol. II, WMO/ICSU, Geneva, pp. 341-356.

Held, I. M. (1983). Stationary and quasi-stationary eddies in the extratropical troposphere: Theory. Chapter 6 in _Large-Scale Dynamic Processes in the Atmosphere_, B. J. Hoskins and R. P. Pearce (eds.), Academic Press, New York, pp. 127-168.

Hoffman, R. N. (1982). SASS wind ambiguity removal by direct minimization. _Mon. Wea. Rev._ 110, 434-445.

Hollingsworth, A., A. Lorenc, S. Tracton, K. Arpe, G. Cats, S. Uppala, and P. Kallberg (1983). The response of numerical weather prediction systems to FGGE IIb data. _Quart. J. Roy. Meteorol. Soc._, submitted.

Horton, C. W., L. E. Reichl, and V. G. Szebehely, eds. (1983). _Long-Time Prediction in Dynamics_. Wiley-Interscience, New York, 496 pp.

James, P. K. (1983). The WPL profiler: A new source of mesoscale observations. _Meteorol. Mag._ 112, 229-236.

Kalnay, E., and J. Paegle (1983). Large amplitude stationary Rossby waves in the southern hemisphere: Observations and theory. _Proc. 1st Conf. Southern Hemisphere Meteorology_, American Meteorological Society, Boston, Mass., pp. 89-92.

Kanamitsu, M. (1981). Some climatological and energy budget calculations using the FGGE IIb analyses during January 1979. In Bengtsson et al., 1981, pp. 263-318.

Lau, N.-C. (1983). Midlatitude wintertime circulation anomalies appearing in a 15-year GCM experiment. Chapter 5 in _Large-Scale Dynamic Processes in the Atmosphere_, B. J. Hoskins and R. P. Pearce (eds.), Academic Press, New York, pp. 111-125.

Legras, B., and M. Ghil (1983). Stationary, periodic, and aperiodic flows in the atmosphere. _J. Méc. Théor. Appl._, special issue 1983, 45-82.

Legras, B., and M. Ghil (1984). Blocking and variations in atmospheric predictability. In _Predictability of Fluid Motions_, G. Holloway and B. J. West (eds.), American Institute of Physics, New York, pp. 87-105.

Leith, C. E. (1980). Nonlinear normal mode initialization and quasi-geostrophic theory. _J. Atmos. Sci._ 37, 958-968.

Lindzen, R. S., D. M. Straus, and B. Katz (1984). An observational study of large-scale atmospheric Rossby waves during FGGE. _J. Atmos. Sci._ (in press).

Munk, W., and C. Wunsch (1982). Observing the ocean in the 1990s. _Phil. Trans. Roy. Soc. Lond._ A307, 439-464.

Namias, J. (1982). Case studies of long period air-sea interactions relating to long-range forecasting. _Proc. Study Conf. Phys. Basis Climate Prediction_, Leningrad, WMO/ICSU, Geneva; reprinted in _Short Period Climate Variations, Collected Works of J. Namias_, Vol. III (1975-1982), University of California, San Diego, pp. 350-393.

Panofsky, H. (1949). Objective weather map analysis. _J. Meteorol. 6_, 386-392.

Phillips, N. A. (1976). The impact of synoptic observing and analysis systems on flow pattern forecasts. Bull. Amer. Meteorol. Soc. 57, 1225–1250.

Phillips, N. A. (1981). Treatment of normal and abnormal modes. Mon. Wea. Rev. 109, 1117–1119.

Phillips, N. A. (1984). Data analysis and modeling, in Global Observations and Understanding of the General Circulation of the Oceans, National Academy Press, Washington, D.C., pp. 222–234.

Robinson, A. R., and W. G. Leslie (1984). Estimation and prediction of oceanic eddy fields. Prog. Oceanogr. (in press).

Rossby, C.-G. (1937). On the mutual adjustment of pressure and velocity distributions in certain simple current systems. J. Mar. Res. 1, 15–28.

Sarmiento, J. L., with M. Kawase (1984). Tracers and modeling, in Global Observations and Understanding of the General Circulation of the Oceans, National Academy Press, Washington, D.C., pp. 235–255.

Smagorinsky, J., K. Miyakoda, and R. Strickler (1970). The relative importance of variables in initial conditions for dynamical weather prediction. Tellus 22, 141–157.

Wiener, N. (1956). Nonlinear prediction and dynamics. Proc, 3rd Berkeley Symposium Math. Stat. Probability, Vol. 3, University of California Press, pp. 247–252.

20. RESEARCH GAPS

Organizer   Donald R. Johnson

Session Chairman   Joseph Smagorinsky

Speakers   Richard J. Reed
                             Eugenia Kalnay

Rapporteurs   Russell L. Elsberry
                             Richard H. Johnson

Speakers made informal summary presentations
resulting from the previous week's sessions. No
formal papers were requested or provided.

APPENDIX

FGGE WORKSHOP
National Academy of Sciences Study Center
Woods Hole, Massachusetts
July 9-20, 1984

Participants

Prof. Bruce Albrecht
Department of Meteorology
512 Walker Building
Pennsylvania State University
University Park, PA 16802

Ms. Vicki Allaback
Space Science and Engineering Center
University of Wisconsin
1225 West Dayton Street
Madison, WI 53706

Dr. Akio Arakawa
Department of Atmospheric Sciences (MK-29)
University of California
405 Hilgard Avenue
Los Angeles, CA 90024

Dr. Ferdinand Baer
Department of Meteorology
University of Maryland
College Park, MD 20742

Dr. Wayman E. Baker
Code 910 (GLAS)
Goddard Space Flight Center
Greenbelt, MD 20771

Dr. David P. Baumhefner
National Center for Atmospheric Research
P.O. Box 3000
Boulder, CO 80307-3000

Dr. Lennart Bengtsson
Director
European Center for Medium-Range
Weather Forecasts
Shinfield Park
Reading, Berkshire RG2 9AX, England

Dr. Robert L. Bernstein
Code A-021
Scripps Institution of Oceanography
La Jolla, CA 92093

Dr. Alan Betts
West Pawlet, VT 05775

Dr. C.-P. Chang
Department of Meteorology (Code 63Cp)
Naval Postgraduate School
Monterey, CA 93943

Dr. Tsing-Chang (Mike) Chen
Department of Earth Sciences
Iowa State University, 326 Curtiss Hall
Ames, IA 50011

Dr. John H.E. Clark
Department of Meteorology (513 Walker)
Pennsylvania State University
University Park, PA 16802

Dr. Roger W. Daley
National Center for Atmospheric Research
P.O. Box 3000
Boulder, CO 80307-3000

Dr. Russell L. Elsberry
Department of Meteorology (63ES)
Naval Postgraduate School
Monterey, CA 93943

Dr. Jay Fein
National Science Foundation (ATM)
1800 G Street, N.W., Room 644
Washington, DC 20550

Dr. Rex J. Fleming
NOAA/OAR (Room 817)
6010 Executive Blvd.
Rockville, MD 20852

Prof. Michael Ghil
Courant Institute of Mathematical Sciences
New York University
251 Mercer Street
New York, NY 10012

Dr. William M. Gray
Department of Atmospheric Science
Colorado State University
Fort Collins, CO 80523

Dr. Richard S. Greenfield
National Science Foundation (ATM)
1800 G Street, N.W., Room 644
Washington, DC 20550

Dr. Milton Halem
Code 930
Goddard Space Flight Center
Greenbelt, MD 20771

Dr. William A. Heckley
European Center for Medium-Range
Weather Forecasts
Shinfield Park
Reading, Berkshire RG2 9AX, England

Dr. Anthony Hollingsworth
European Center for Medium-Range
Weather Forecasts
Shinfield Park
Reading, Berkshire RG2 9AX, England

Dr. Donald R. Johnson
Space Science and Engineering Center
University of Wisconsin
1225 West Dayton Street
Madison, WI 53706

Dr. Richard H. Johnson
Department of Atmospheric Science
Colorado State University
Fort Collins, CO 80523

Dr. Paul R. Julian
Mathematics Department
Dalhousie University
Halifax, Nova Scotia, Canada B3H 4H8

Dr. Eugenia Kalnay
Code 911 (GLAS)
Goddard Space Flight Center
Greenbelt, MD 20771

Dr. Akira Kasahara
National Center for Atmospheric Research
P.O. Box 3000
Boulder, CO 80307-3000

Dr. Eli J. Katz
Lamont-Doherty Geological Observatory
Palisades, NY 10964

Mr. Richard A. Kerr
Science, AAAS
1515 Massachusetts Avenue, N.W.
Washington, DC 20005

Prof. T. N. Krishnamurti
Department of Meteorology
Florida State University
Tallahassee, FL 32306

Prof. Ernest C. Kung
Department of Atmospheric Science
University of Missouri
701 Hitt Street
Columbia, MO 65211

Prof. Conway B. Leovy
Department of Atmospheric Sciences (AK-40)
University of Washington
Seattle, WA 98195

Dr. Andrew Loreno
Meteorological Office
London Road
Bracknell, Berkshire, RG12 2SZ, England

Edward N. Lorenz
Center for Meteorology and Physical
   Oceanography
MIT
Cambridge, MA 02139

Dr. Ronald McPherson
NOAA/National Meteorological Center
World Weather Building, Room 204
5200 Auth Road
Camp Springs, MD 20233

Prof. Carlos R. Mechoso
Department of Atmospheric Sciences
University of California
405 Hilgard Avenue
Los Angeles, CA 90024

Dr. Kikuro Miyakoda
Geophysical Fluid Dynamics Laboratory (NOAA)
Princeton University
P.O. Box 308
Princeton, NJ 08542

Dr. John Molinari
Department of Atmospheric Sciences
State University of New York
1400 Washington Avenue
Albany, NY 12222

Dr. Robert L. Molinari
NOAA/AOML
4301 Rickenbacker Causeway
Miami, FL 33149

Prof. Takio Murakami
Department of Meteorology
University of Hawaii
2525 Correa Road
Honolulu, HI 96822

Mr. James Neilon
NOAA/National Weather Service (W/OTS3)
Gramax Building, Room 604
8060 13th Street
Silver Spring, MD 20910

Prof. Yoshimitsu Ogura
Department of Atmospheric Sciences
University of Illinois (6-113 CSL)
1101 West Springfield Avenue
Urbana, IL 61801

Dr. Jan Paegle
Department of Meteorology
819 Wm. C. Browning Bldg.
University of Utah
Salt Lake City, UT 84112

Dr. Julia N. Paegle
Department of Meteorology
819 Wm. C. Browning Bldg.
University of Utah
Salt Lake City, UT 84112

Dr. Richard L. Pfeffer
Geophysical Fluid Dynamics Institute
Florida State University
Tallahassee, FL 32306

Dr. Norman A. Phillips
NOAA/National Meteorological Center
W32 WWB, Room 204
Washington, DC 20233

Dr. Jeffrey J. Ploshay
Geophysical Fluid Dynamics Laboratory (NOAA)
Princeton University
P.O. Box 308
Princeton, NJ 08542

Dr. Kamal Puri
Australian Numerical Meteorology
   Research Centre
P.O. 5089 AA
Melbourne, Victoria, Australia 3001

Prof. Richard J. Reed
Department of Atmospheric Sciences (AK-40)
University of Washington
Seattle, WA 98195

Dr. Richard D. Rosen
Atmospheric & Environmental Research, Inc.
840 Memorial Drive
Cambridge, MA 02139

Dr. Edward S. Sarachik
NOAA/PMEL, Bldg 3/OCRD
7600 Sand Point Way N.E.
Seattle, WA 98119

Dr. Jagadish Shukla
Center for Ocean-Land-Atmosphere
  Interactions
Department of Meteorology
University of Maryland
College Park, MD 20742

Dr. Pedro Leite Silva-Dias
Departamento de Meteorologia
Universidade de Sao Paulo
Caixa Postal 30627
01051 Sao Paulo, SP, Brazil

Dr. Joseph Smagorinsky
21 Duffield Place
Princeton, NJ 08540

Dr. William L. Smith
NOAA/NESDIS Development Laboratory
1225 West Dayton Street, 2nd Floor
Madison, WI 53706

Prof. Richard C. J. Somerville
Climate Research Group (A-024)
Scripps Institution of Oceanography
La Jolla, CA 92093

Dr. Pamela L. Stephens
National Science Foundation (ATM)
1800 G Street, N.W., Room 644
Washington, DC 20550

Prof. Henry M. Stommel
Woods Hole Oceanographic Institution
Woods Hole, MA 02543

Prof. Verner E. Suomi
Space Science & Engineering Center
University of Wisconsin
1225 West Dayton Street
Madison, WI 53706

Dr. Joel Susskind
Code 911 (GLAS)
Goddard Space Flight Center
Greenbelt, MD 20771

Dr. Steven Tracton
NOAA/National Meteorological Center
W32 WWB, Room 204
Washington, DC 20233

Dr. Kevin E. Trenberth
National Center for Atmospheric Research
P.O. Box 3000
Boulder, CO 80307-3000

Dr. Harry van Loon
National Center for Atmospheric Research
P.O. Box 3000
Boulder, CO 80307-3000

Dr. Hassan Virji
National Science Foundation (ATM)
1800 G Street, N.W., Room 644
Washington, DC 20550

Dr. Thomas H. Vonder Haar
Department of Atmospheric Science
Colorado State University
Fort Collins, CO 80523

Prof. Michio Yanai
Department of Atmospheric Sciences (MK-14)
University of California
405 Hilgard Avenue
Los Angeles, CA 90024

809

Prof. John A. Young
Department of Meteorology (1503)
University of Wisconsin
1225 West Dayton Street
Madison, WI 53706

NRC Staff

John S. Perry
Thomas O'Neill
Doris Bouadjemi